EXPERIMENTAL THERMODYNAMICS • VOLUME VII

MEASUREMENT *of the* THERMODYNAMIC PROPERTIES *of* MULTIPLE PHASES

EDITED BY R.D. WEIR *and* TH. W. DE LOOS

LIST OF CONTRIBUTORS

- B. Davis (Canada)
- V. Dohnal (Czech Republic)
- M.J.B. Evans (Canada)
- K.M. Jaansalu (Canada)
- N.S. Jacobson (USA)
- M.H. Kaye (Canada)
- Th.W. de Loos (The Netherlands)
- J. Matouš (Czech Republic)
- J. Mendez-Santiago (USA)
- A. Navrotsky (USA)
- J.P. Novák (Czech Republic)
- H.A.J. Oonk (The Netherlands)
- R.L. Putnam (USA)
- J. David Raal (South Africa)
- D. Ramjugernath (South Africa)
- K. Řehák (Czech Republic)
- D. Richon (France)
- K.A. Sosin (deceased) (Canada)
- J.Ll. Tamarit (Spain)
- A.S. Teja (USA)
- W.T. Thompson (Canada)
- S.P. Verevkin (Germany)
- R.D. Weir (Canada)
- Emmerich Wilhelm (Austria)
- A. Würflinger (Germany)

FOREWORD

The Division of Physical and Biophysical Chemistry of the International Union of Pure and Applied Chemistry (IUPAC) continues its tradition of meeting the goals of the Union that include the definition and maintenance of standards in the broad field of physical and biophysical chemistry. For thermodynamics in particular, these responsibilities embrace establishing nomenclature, symbols and units, establishing and monitoring pressure and temperature scales, recommending calorimetric procedures, selecting, assessing and evaluating standard reference materials for thermodynamic measurements of all types.

This present volume *Experimental Thermodynamics, Volume VII: Measurement of the Thermodynamic Properties of Multiple Phases* is another in the series to assist the thermodynamics community by providing a summary of the status of the field at a particular moment. It is a book intended to elucidate the current state of knowledge on practical thermodynamic problems to promote international collaboration.

Thanks are due to the 25 authors for their willing cooperation in this undertaking and for their great patience in the face of unavoidable delays as the work proceeded. I would also like to thank my fellow editor Professor Theo de Loos for his invaluable help and sage advice in assembling a logical and smoothly flowing treatise from individual contributions.

Here's the challenge, read it: I warrant there's vinegar and pepper in't.

Sir Andrew in: *Twelfth Night, Act III, Sc IV*
By William Shakespeare

Ron D. Weir
President
Division of Physical and Biophysical Chemistry
International Union of Pure and Applied Chemistry

1 Introduction

TH.W. DE LOOS
Physical Chemistry and Molecular Thermodynamics
Department of Chemical Technology
Delft University of Technology
Delft, The Netherlands

R.D. WEIR
Department of Chemistry and Chemical Engineering
Royal Military College of Canada
Kingston, Canada

Measurement of the Thermodynamic Properties of Multiple Phases
R.D. Weir and Th.W. de Loos (Editors)

1 INTRODUCTION

The Division of Physical and Biophysical Chemistry (DPBPC) of the International Union of Pure and Applied Chemistry (IUPAC) is tasked by the Union with the duty to define and maintain standards in the field of physical and biophysical chemistry that includes the general field of thermodynamics throughout the world. These responsibilities embrace areas such as establishment of nomenclature, symbols and units, the establishment and monitoring of pressure and temperature scales, recommendations for calorimetric procedures, the selection, assessment and evaluation of standard reference materials for thermodynamic measurements of all types. Before 2002, there existed within IUPAC the Commission on Thermodynamics and Thermochemistry, later renamed the Commission on Thermodynamics of the Physical Chemistry Division, whose tasks were to oversee the above responsibilities for thermodynamics. Subsequent to the IUPAC reorganisation in 2002, these responsibilities were subsumed by the DPBPC and executed by means of an Advisory Subcommittee on Thermodynamics and the International Association of Chemical Thermodynamics, which is an Associated Organisation within IUPAC.

Over the past 50 years, the Commission and now the DPBPC have sponsored a series of monographs to help realise their goals. The initial series focussed on *Experimental Thermochemistry* with Volumes I and II edited by F.D. Rossini (1956) and H.A. Skinner (1962) respectively [1,2]. The updated edition of these two works appeared in 1979 as *Combustion Calorimetry* edited by S. Sunner and M. Månsson [3].

In the next series entitled *Experimental Thermodynamics*, the first three volumes focussed on non-reacting systems. The first was *Calorimetry of Non-reacting Systems* edited by J.P. McCullough and D.W. Scott in 1968 [4]. Volume II appeared in 1975, *Experimental Thermodynamics of Non-reacting Fluids*, and was edited by B. Le Neindre and B. Vodar [5] and it was concerned with the measurement of both thermodynamic and transport properties over wide ranges of temperature and pressure. Volume III, *Measurement of Transport Properties of Fluids*, was edited by W.A. Wakeham, A. Nagashima and J.V. Sengers in 1991 [6].

Volume IV, *Solution Chemistry*, edited by K.N. Marsh and P.A.G. O'Hare in 1994 [7], and differs from the previous volumes in that calorimetry of both reacting and non-reacting systems are treated. Volume V, *Equations of State for Fluids and Fluid Mixtures, Parts I and II*, followed in 2000 was edited by J.V. Sengers, R.F. Kayser, C.J. Peters and H.J. White [8].

To cover the steadily expanding fields, Volume VI, *Measurement of Thermodynamic Properties of Single Phases* appeared in 2003 and was edited by A.R.H. Goodwin, K.N. Marsh and W.A. Wakeham [9], and this work set the stage for this new Volume VII, *Measurement of Thermodynamic Properties of Multiple Phases*.

To demonstrate the importance of chemistry in current areas of scientific research and industrial processes of economic significance, the monograph *Chemical Thermodynamics* [10], edited by T.M. Letcher, was published as one of 11 volumes in the IUPAC series 'Chemistry for the 21st Century', followed in 2004 by *Chemical Thermodynamics for Industry* [11].

This current Volume VII is intended to serve as a guide to the scientist, engineer or technician who is concerned with measurements of the thermodynamic properties of multiphase

systems of pure components and of mixtures, involving equilibria between gas, liquid or solid phases. Like the preceding Volume VI, the emphasis is placed on those methods for which reliable, theoretically based equations are available and/or for application to industrial processes. Those individuals who need to evaluate data will find the contents valuable in their assessing the reliability of experimental data obtained by specific techniques.

We as the editors were assigned the task to assemble an international team of distinguished experimentalists to describe the current developments for the measurement of thermodynamic quantities for multiple phases over a range of conditions. We have done this in 16 chapters with 25 authors from nine different countries. Throughout the text, we have adopted the quantities, units, symbols and fundamental constants defined by IUPAC in the text commonly referred to as the *Green Book* [12,13].

Volume VII begins with the treatment of phase changes (liquid + gas), (liquid + solid) and (solid + solid) in pure component systems. Mixtures are treated next with binary and multicomponent systems being considered and these include organic and inorganic compounds, metals, alloys, ceramics and molten salts. Chapters 5–9 deal with vapour–liquid equilibrium at low and high pressures, liquid–liquid, solid–liquid and solid–solid equilibria followed by low-pressure solubility of gases in liquids. In the remaining chapters metallic systems, ceramic systems and molten salts are treated. Activity coefficients using both non-analytical and analytical tools follow. The book concludes with treatment of interfacial tension and critical parameters.

References

1. Rossini, F.D., ed., *Experimental Thermochemistry, Vol I*, Interscience, New York, 1956.
2. Skinner, H.A., ed., *Experimental Thermochemistry, Vol II*, Interscience, New York, 1962.
3. Sunner, S. and Månsson, M., eds., *Combustion Calorimetry*, Pergamon, Oxford, 1979.
4. McCullough, J.P. and Scott, D.W., eds., *Experimental Thermodynamics, Vol I: Calorimetry of Non-reacting Systems*, Butterworth's, London, 1968.
5. Le Neindre, B. and Vodar, B., eds., *Experimental Thermodynamics, Vol II: Experimental Thermodynamics of Non-reacting Fluids*, Butterworth's, London, 1975.
6. Wakeham, W.A., Nagashima, A. and Sengers, J.V., eds., *Experimental Thermodynamics, Vol III: Measurement of Transport Properties of Fluids*, Blackwell Scientific Publications, Oxford, 1991.
7. Marsh, K.N. and O'Hare, P.A.G., eds., *Experimental Thermodynamics, Vol IV: Solution Chemistry*, Blackwell Scientific Publications, Oxford, 1994.
8. Sengers, J.V., Kayser, R.F., Peters, C.J. and White, H.J. Jr., eds., *Experimental Thermodynamics, Vol V: Equations of State for Fluids and Fluid Mixtures, Parts I and II*, Elsevier, Amsterdam, 2000.
9. Goodwin, A.R.H., Marsh, K.N. and Wakeham, W.A., eds., *Experimental Thermodynamics, Vol VI: Measurement of Thermodynamic Properties of Single Phases*, Elsevier, Amsterdam, 2003.
10. Letcher, T.M., ed., *Chemical Thermodynamics*, Blackwell Scientific Publications, Oxford, 2000.
11. Letcher, T.M., ed., *Chemical Thermodynamics for Industry*, Springer, Berlin, 2004.
12. Mills, I., Cvitaš, T., Homann, K.N. and Kuchitsu, K., *Quantities, Units and Symbols in Physical Chemistry*, 2nd ed., Blackwell Scientific Publications, Oxford, 1993.
13. Cohen, E.R., Cvitaš, T., Frey, J.G., Holmström, B., Kuchitsu, K., Marquardt, R., Mills, I., Pavese, F., Quack, M., Stohner, J., Strauss, H.L., Takami, M. and Thor, A.J., *Quantities, Units and Symbols in Physical Chemistry*, 3rd ed., draft, IUPAC, Triangle Park, NC, USA, 2001.

2 Phase Changes in Pure Component Systems: Liquids and Gases

S.P. VEREVKIN
Fachbereich Chemie, Abt. Physikalische Chemie
Universitaet Rostock Hermannstr. 14
Rostock, Germany

Measurement of the Thermodynamic Properties of Multiple Phases
R.D. Weir and Th.W. de Loos (Editors)

2 PHASE CHANGES IN PURE COMPONENT SYSTEMS: LIQUIDS AND GASES

Vapour pressure governs the persistence, volatilization, and transport of chemicals introduced into the environment. Enthalpy of vaporization is also a fundamental quantity characterizing the energetics of the vapour–liquid equilibrium (VLE). The present chapter is an attempt to generalize the state of vapour pressure and vaporization enthalpy investigations that have been made since 1975, when Ambrose reviewed the experimental techniques in the previous book on experimental thermodynamics published under the auspices of IUPAC [1]. An extensive experimental activity has taken place during the intervening period, and the compilations that summarize the achievements in developments of experimental methods include vapour pressure and enthalpy of vaporization data [2–10]. Furthermore there are a number of older but excellent books giving basics of experimental methods [11–13]. In this review, the author attempts to present interesting aspects of experimental techniques, which attracted attention by systematic survey of the scientific papers from 1970 to date, and, possibly, which were not elucidated fully in the aforementioned sources. Astonishingly, it has to be pointed out that basically no new methods could be found in the recent literature. It was rather the application and/or modifications of well-established methods that are of main interest here. In this chapter, only measurements of the vapour pressures of organic substances, which vaporize without chemical change, will be considered, and little will be said about measurements of inorganic compounds, as well as about measurements at high temperatures.

Although numerous techniques exist for measuring vapour pressures, only five general methods have been widely applied to the study of organic compounds. These five generic techniques or methods are referred to as static, ebulliometric (dynamic), effusion (Knudsen and Langmuir methods), transpiration, and calorimetric. The characteristics of each group are discussed and different examples for the practical application from the recent literature are given. It is clear that the classification given here is highly subjective and that other ways of grouping may be possible. Furthermore, any selection of examples is influenced by personal preference. The author apologizes to all those who may have employed interesting variations of vapour pressure methods without their being cited here.

2.1 Static Measurements

In the static methods, vapour pressure is measured in a closed vessel. The temperature of the vessel is held constant for a certain time to permit equilibrium to be established between the condensed phase and the vapour. The sample is carefully degassed and the vessel is evacuated prior to beginning the measurement. Pressure at equilibrium is determined with the aid of any measuring instrument. Many kinds of pressure gauges have been used, including mercury manometers, dead weight piston gauges, Bourdon tubes, and capacitance pressure transducers. High-accuracy instruments are now commercially available (MKS, Ruska, etc.) and

numerous sophisticated home-made devices described in earlier compilations [11–13] are of historical interest. Since samples are often corrosive or are taken to temperatures outside the operating range of the pressure gauge, it is usual practice to isolate the sample from the pressure gauge by using a differential pressure indicator (DPI) such as a U-tube manometer filled with mercury or a metal diaphragm. When the DPI indicates that pressures of an inert reference fluid and the sample are equal, the reference fluid pressure is measured using an appropriate pressure gauge.

Direct vapour pressure measurements tabulated in the literature have ranged over an astonishingly wide temperature range of over 200 K [14–17]. The advantage of the static technique is that it allows for an absolute calibration and accurate temperature determination (± 0.002 K). With a suitably selected pressure sensor, the static method can be applied over a wide range of pressures from 10^{-3} Pa to 10 MPa at any temperature. Disadvantages are its crucial sensitivity to volatile impurities and the time required for a set of measurements, often 2–3 weeks for a sample.

2.2 Ebulliometry

Ebulliometry is the most frequently employed dynamic method. If the boiling is carried out under reflux, and the pressure in the apparatus can be varied, measurement of the boiling temperatures at differing pressures is a convenient way of determining the vapour pressure of the liquid. An ebulliometer is the main part of a vapour pressure measuring apparatus. In principle, it is similar to an ordinary open reflux condenser/boiler that operates at ambient pressure. Ebulliometry is a relatively old technique [18], and as a result, many different boiler designs have evolved. The goal of any design is the promotion of smooth, even boiling and the minimization of superheating. There are two main boiler designs that can be distinguished. The first one is a still with circulation of both the liquid and vapour phases [19–21]. This method is based on the application of a so-called Cottrell pump, which was originally used for the determination of vapour pressures and boiling points of pure components. The second method is similar to the open reflux condenser/boiler and is designed without a Cottrell pump, but has the capability to reduce overheating and bumping of the boiling liquid [22]. Ebulliometers are often designed to measure both boiling and condensation temperatures. The difference between these two temperatures should lie within 0.005 K if the substance is thoroughly purified and decomposition does not occur.

Recent trends in ebulliometry show that this method is preferably used for investigation of VLE for mixtures of organic compounds and the vapour pressure measurements of pure components are merely a starting part for such studies. There are several comprehensive reviews of experimental procedures and equipment for vapour pressure and VLE measurements [19,21,23,24]. Of particular importance is the remarkable retrospection of ebulliometric techniques published by Malanowski [21]. Ambrose [1] has provided detailed insight into the basics of ebulliometric measurements. Analysis of the recent literature reveals that the dynamic method with circulation of both the liquid and vapour phases is applied more frequently than other modifications. A typical ebulliometer, equipped with the Cottrell pump, was designed by Rogalski and Malanowski [20,21]. Two versions of the apparatus were

proposed [21], one for the determination of boiling temperatures or total pressure measurements of pure compounds as well of mixtures, and the second to allow for the withdrawal of samples of the phases in equilibrium for VLE measurements. These types of ebulliometers ensure stable hydrodynamic and thermal conditions under pressures from 300 kPa and from room temperature to 500 K, even in the case when the mixtures investigated consist of substances of widely differing vapour pressure.

The amount of sample required for one experiment with the Rogalski–Malanowski still varies from 20 to 45 cm^3 and this volume seems not to be excessive, especially when the compounds under study are readily available. However, as a rule, most of the interesting compounds for physical–chemical investigations are tediously synthesized by organic chemists, and are usually available in "vanishingly" small quantities. An ingenious apparatus suitable for samples of 4.5–7.0 cm^3 was developed at the Moscow State University by Varouchtchenko *et al.* [25]. The construction is based on a differential ebulliometer of the Swietoslawski type and has been used for the measuring of temperature dependence of the vapour pressure in the temperature range 293–530 K over the pressure range from 2 to 101.6 kPa, and, simultaneously, utilized for determination of the ebulliometric degree of purity of the substances under study.

A highly refined, but simple dynamic still suitable for vapour pressure measurements of pure compounds as well as for VLE has been developed by Raal and Mühlbauer [24,26]. A central feature of this design is the packed equilibrium chamber, which is concentric around a vacuum-insulated Cottrell tube. Since the equilibrium chamber is angularly symmetric, there is no preferred radial direction for the development of concentration gradients.

While for VLE measurements a single ebulliometer is usually applied, a *comparative ebulliometric* method is mostly utilized for the measurement of vapour pressures of pure compounds. In *comparative ebulliometry* [25,27], the condensing temperature of the substance under study and a reference material are measured when the two liquids are boiling at the same pressure. The two boilers are connected to apparatus in which the pressure can be adjusted, cross-contamination of substance and reference material being prevented by making the connections through cold traps. The method avoids the necessity of measuring the pressure directly because the pressure can be calculated from the temperature of the reference material and its known pressure–temperature behaviour. Because of the symmetry of the apparatus, errors tend to be self-cancelling. The fundamentals of the comparative method have been set out by Osborn and Douslin [27]. Substantial additional effort by this working group was instituted to raise the temperature limitations of their apparatus. Changes are reported [28] that resulted in increasing the upper limit of operation of the twin ebulliometers to $T = 650$ K by expeditious choice of the heat-transfer fluid surrounding the platinum resistance thermometers in the ebulliometers as well as by the introduction of decane as a secondary vapour pressure standard in the pressure region of 2–25 kPa.

The development and construction of ebulliometers without the Cottrell pump are due to Ambrose [22]. Previously, it was difficult to operate the ebulliometer below about 20 kPa due to the tendency of the liquid to bump when boiled. This difficulty was completely obviated by the bubble-cap boiler designed by Ambrose [22]. Further changes and simplification of the design of the ebulliometers have been effected by Ewing *et al.* [29,30], who have built and tested all-metal ebulliometers that have ensured smooth boiling especially at high pressures.

The main advantage of the ebulliometric method in comparison with the static method is the possibility of determining sample purity as the pressure is changed only during calibration of the position of the contacts of the mercury-contact pressure gauge against some reference substance. However, one disadvantage of this method is the need for a relatively large amount of material for the measurements. In addition, the substance vapours contact the mercury in the mercury-contact pressure gauge, which is intolerable for some substances and limit their study.

2.3 Knudsen Effusion Methods for Vapour Pressure Measurement

2.3.1 Conventional Mass-Loss Technique

The Knudsen effusion methods, in their original versions, allow the determination of vapour pressure at constant temperature of a single compound by means of the measurement of the weight loss through a small orifice into a vacuum [8,11]. The cell is weighed at the beginning of the experiment and at time intervals using a balance that can be external or internal to the apparatus. Alternatively, the vapour can be condensed on a liquid nitrogen-cooled cold finger or on a surface cooled above the orifice, removed, and then analysed.

Using a classical gas kinetic theory, Knudsen derived an expression for the slow isothermal flow out of a cell with a small hole in it; the vapour pressure of a material in the cell can be calculated from Knudsen's effusion equation [8,11]

$$p = \frac{\Delta m}{ks\tau}\sqrt{\frac{2\pi RT}{M}}, \tag{2.1}$$

where Δm is the loss of mass of a sample during time τ, M the molar mass of the vapour, s the area of an orifice, R the universal gas constant, T the temperature and k the Clausing probability factor, obtained by interpolation from the table given by Dushman [31]. The values of T, s and k are fixed as experimental parameters, and M is known. Thus, m/t remains as the experimentally measured quantity from which the vapour pressure is determined [32–35].

A typical Knudsen effusion apparatus as designed in [32] is presented in Figure 2.1. The vapour pressure p of the samples is calculated from Equation (2.1). A more sophisticated Knudsen effusion apparatus is reported, where the construction enables the simultaneous operation of three Knudsen cells with effusion holes of different sizes [35].

2.3.2 Torsion–Effusion Method

The torsion–effusion (or recoil momentum technique) method is also based on the Knudsen effusion cell. The cell is designed in the form of a closed horizontal cylinder provided with

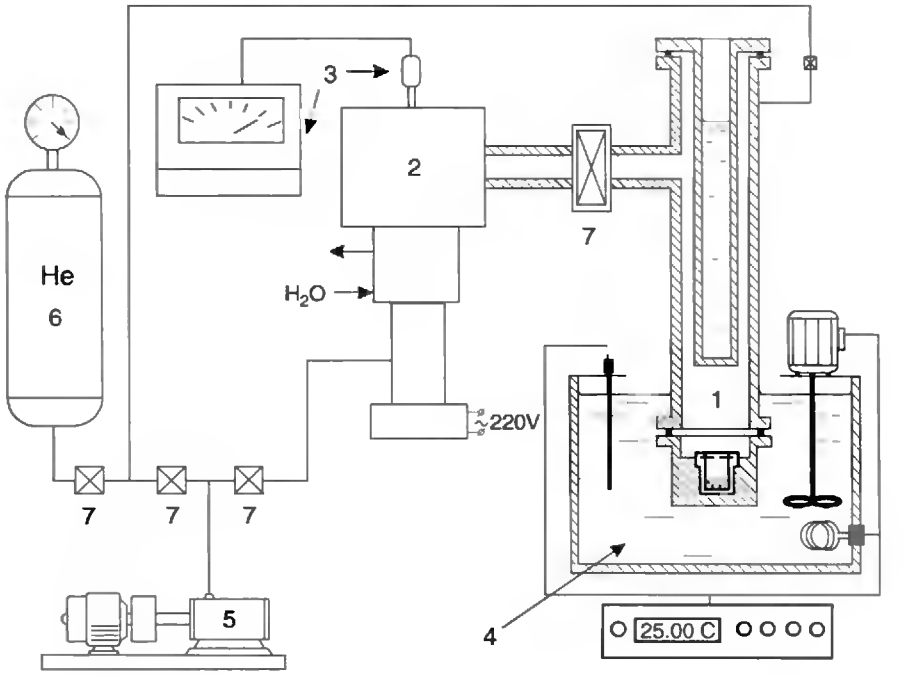

Figure 2.1 The scheme of the apparatus for vapour pressure measurement by the Knudsen method: 1, measuring block (effusion cell with a sample, vacuum connection, cold finger); 2, diffusion oil pump; 3, vacuum measuring gauge; 4, thermostat; 5, roughing-down pump; 6, helium cylinder; 7, bellows gates.

two orifices, one close to each end and on opposite sides of the cylinder. The molecules, effusing through the orifices, exert a force on the cylinder resulting in a torque on the suspension wire. From this torque the pressure can be derived with an associated sensitivity of 10^{-3} Pa.

In the torsion–effusion experiment, the effusion cell is suspended from a thin long wire. The torque produces an angular twist ϕ opposed by the torsional stiffness of the suspension. The torque is directly proportional to the vapour pressure

$$p = 2\phi K/(A_1 l_1 f_1 + A_2 l_2 f_2), \tag{2.2}$$

in which K is the torsion constant, A_1, A_2 and l_1, l_2 are the effective areas of the orifices and their distances from the rotation axis, respectively; and f_1, f_2 are force factors that are related to Clausing orifice transmission probabilities (geometrical factors derived from radius and thickness of the effusion hole [36]) and are tabulated. The torsion constant of the tungsten fibre is determined, for example, by the method of observing the periods of the suspended assembly when cylinders of known but different moments of inertia are added. Calibration is also possible with help of reference compounds. No changes of the torsion constant during the experiments are observed. The torsion angle ϕ of the cell is usually measured by using an optical assembly. The vapour pressure values are obtained

using the simple relation deduced from Equation (2.2). Because torque, which is directly proportional to the vapour pressure, in a torsion–effusion apparatus is counterbalanced electromagnetically, so

$$p = C'I, \tag{2.3}$$

in which I is the electric compensation current and C' the constant in which physical and chemical parameters of the cell and the torsion wire are included. The C' values are experimentally determined by vaporizing standard substances having well-known vapour pressures. The typical assembly [37,38] is drawn in Figure 2.2.

The temperature is measured by a calibrated thermocouple inserted in a second cell equal to the torsion cell and placed beneath it. This method requires a relatively short time of 4–5 days for the complete measuring procedure. However, one serious drawback of the method is that it is not possible to determine exactly the sample temperature and the influence of the background pressure.

2.3.3 Simultaneous Torsion and Mass-Loss Effusion Techniques

For the determination of vapour pressures of low volatile compounds, conventional Knudsen techniques (see Section 2.3.1), as well as conventional torsion–effusion techniques (see Section 2.3.2) are used, all of which have their own merits. The combination of two of these techniques in one set-up offers the opportunity of obtaining supplemental information, which can be employed, for example, in studying the mutual consistency of the methods. Moreover, the extra information can be used for the calculation of additional quantities such as molar mass or composition of the vapour phase [39–40].

The method of weighing effusion is based on Equation (2.1) formulated by Knudsen:

$$p = C\mathrm{d}m/\mathrm{d}t, \tag{2.4}$$

in which $\mathrm{d}m/\mathrm{d}t$ represents the mass loss per unit time from an effusion cell. The constant C among others contains the orifice area, molar mass, and the temperature of the effusing species. In the torsion–effusion experiment with the effusion cell, the vapour pressure is directly proportional to the torque, and is obtained by measurements of the electric compensation current I according to Equation (2.3) and a value of C', which contains apparatus constants only. A set-up in which torsion–effusion is combined with weighing effusion is described in [40].

The advantage of the combined torsion method is that a direct measure of the vapour pressure occurs with the mass loss of the Knudsen method, whereas with the torsion method the molar mass is additionally included. Decomposition, dissociation or association of the sample molecules would be immediately noticed because then the ratio $p_{\text{mass loss}}/p_{\text{torsion}}$ appears significantly different from unity (it is unity for a pure substance). A disadvantage of this method lies in the temperature measurement, which is performed in the measuring cell, but afar from the sample. When the effusion flow rate varies, temperature fluctuations are usually ill defined.

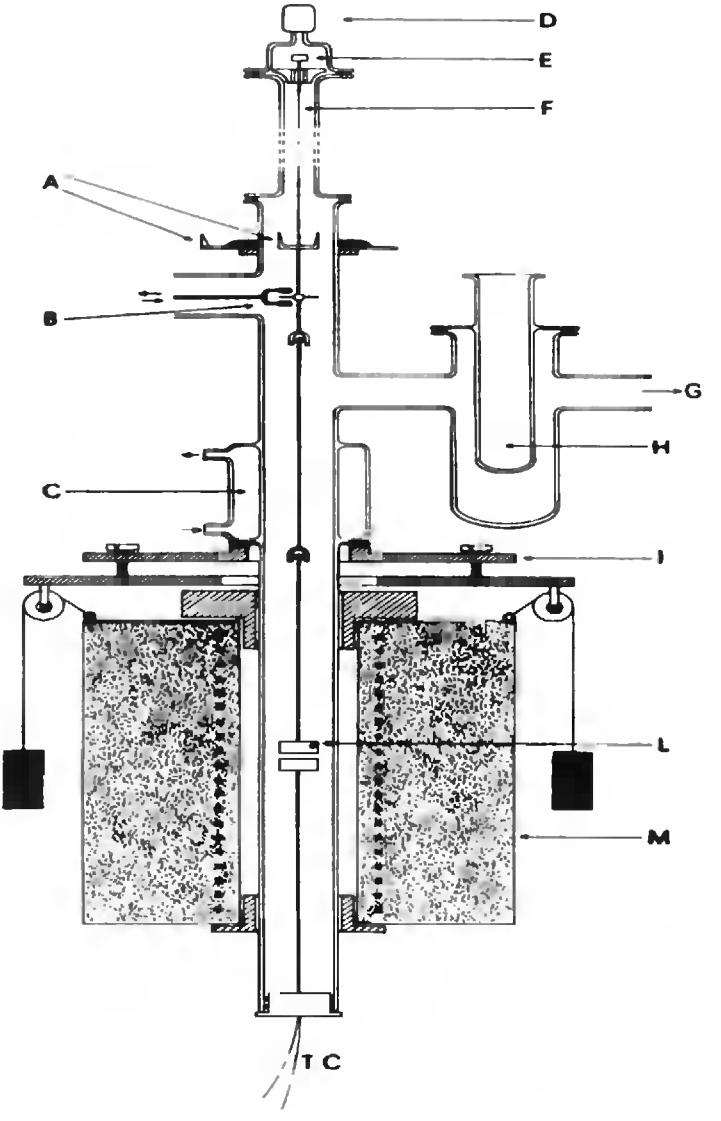

Figure 2.2 Torsion–effusion assembly: A, assembly for torsion-angle measurement; B, magnetic damping apparatus; C, water cooling; D, Penning gauge; E, height regulator of the torsion equipment; F, torsion wire; G, vacuum system; H, liquid-nitrogen trap; I, support and alignment system of the torsion assembly; L, torsion cell; M, furnace; TC, thermocouple.

2.3.4 Isothermal Knudsen Effusion Method in Thermogravimetric-Type Apparatus

Simple weighing of the Knudsen cell before and after effusion is the least precise, and the use of vacuum balances is apparently preferred. Measurements made under isothermal conditions

with mass loss from the cell being recorded as a function of time in a *thermogravimetric* (TG)-type apparatus result in high precision [41–43]. Effusion cell design is decisive for the accurate measurements by using this technique. The cell must be very light, less than 1 g (determined by the capacity of a microbalance) and it must allow the use of samples of a few tens of milligrams. The effusion cell is suspended on the arm of a commercial recording electro-balance. At least 5 mass% of compound under study should be vaporized before measurements are begun. This ensures removal of any volatile impurities possibly present in the sample.

Another measuring principle is based on a homogeneously heated Knudsen cell with the effusion orifice in line with a cooled target, which is connected to a sensitive microbalance [44]. The whole system is mounted within a special high vacuum chamber with a built in cold trap. The Knudsen cell is heated to a pre-selectable test temperature within the temperature range of 223–573 K, controlled by a microprocessor programmer. When an orifice is opened, the impulse of the molecular beam with a defined geometry is detected by the microbalance as a weight loss step. The vapour immediately condenses on the cooled target producing a weight increase with time, proportional to the effusion rate. In the pressure range 10^{-3}–1 Pa, there are two possibilities for the calculation of vapour pressure values: (a) the impulse method gives the vapour pressure without knowing the molar mass of the vapour; (b) the combination with the effusion rate value for the vapour pressure allows the determination of the molar mass. This molar mass determination is precise enough to discriminate between monomeric, dimeric and trimeric vapours. Below 10^{-3} Pa, the impulse values (weight signals) are too small for an exact calculation [44].

2.3.5 Non-Isothermal Knudsen Effusion Method in TG-Type Apparatus

The non-isothermal Knudsen effusion method was developed in response to the need to scan over a wide range of temperatures in a modest time when investigating compounds with extremely low volatility [41]. As the sample cell is in a high vacuum and must receive heat purely by radiation, heat transfer is a key concern. A long time is generally required to reach thermal equilibrium in an isothermal experiment. Achieving a new steady-state temperature typically requires hours. The non-isothermal method is a straightforward modification of the usual Knudsen effusion technique [41], generally requiring few changes in equipment and only a limited change in procedures described above (see Section 2.3.4). The advantage of the non-isothermal technique is that it does not require the cell to reach a steady-state temperature. A temperature ramp is imposed by increasing temperature of the heating block of the TG, but the temperature difference between the block and capsule is no longer of concern. The capsule will rise in temperature at a rate that is in some way related to the rise in block temperature, but it need not track it perfectly. Using the effusion cell of a much lower mass, 0.15 g, its temperature is tracked very well.

2.3.6 Mass-Loss Knudsen Technique with a Quartz Crystal Microbalance

The conventional Knudsen effusion method uses a balance to measure the rate of mass loss through the orifice. A piezoelectric quartz crystal can be used as a weighing device if the

molecules are condensed at its surface, since the thickness increases continuously leading to a change in the resonance frequency (dv/dt). This variation is proportional to the mass-loss rate of the cell (dm/dt) and to the vapour pressure. In the Knudsen effusion and quartz crystal microbalance (QCM) method [45–51], molecules escaping from the orifice are trapped onto an externally cooled QCM. In this case, the mass loss through the orifice is the mass gain of the QCM. The advantages of the QCM are increased sensitivity and insensitivity to vibrational noise. However, for accurate operation of the QCM, the deposited mass must be uniformly distributed on the crystal surface.

The rate of mass loss is related to p, which is the vapour pressure of the condensed phase, by the Hertz–Knudsen–Langmiur equation [45]

$$-(dm/dt)/A = \alpha\gamma(M/2\pi RT)^{0.5}(p_{sat} - p), \tag{2.5}$$

where dm/dt is the mass loss per unit time, A the area of orifice, α the evaporating coefficient, γ the degree of surface roughness, T the local temperature and M the molar mass of the test substance, p_{sat} the local saturated vapour pressure and p the local pressure. Usually $(\alpha \cdot \gamma)$ is supposed to be pressure-independent and is taken to be unity. The enthalpy of sublimation can be obtained from the equation

$$\ln[(dm/dt)T^{0.5}] = \ln B - \Delta_{sub}H/RT, \tag{2.6}$$

where $\ln B$ includes the term $(1/A)(2\pi R/M)^{0.5}$ that remains constant during a measurement. Thus, the enthalpy of sublimation can be obtained even if the mass-loss rate is not exactly known, and instead only a proportional quantity is experimentally available (*e.g.* the thickness, the resonance frequency or the output voltage). Details of the physical principles have been described extensively by Lu and Czandema [51]. The QCM method is used only for substances of low volatility. The high degree of purity of the tested products, which is required for a reliable and precise determination of the evaporation heat, is a limiting condition because the total amount of substance evaporated from or leaving the chamber in this case is vanishing small.

2.3.7 Mass-Loss Knudsen Technique by Heat-Conducting Calorimetry

Calorimetric determination of enthalpies of sublimation in conjunction with a Knudsen effusion cell has been performed by use of two kinds of calorimeters, *i.e.* adiabatic [52–54] and conduction [55–59]. The calorimeters for determining enthalpy of vaporization of low volatile substances should have high sensitivity and stability of the temperature zero line over prolonged time. A Calvet-type heat-conduction calorimeter meets these requirements well and is used for measurements of sublimation and vaporization enthalpies most frequently.

A Calvet microcalorimeter of commercial origin with some modifications is usually used, in which the twin elements are placed symmetrically. The Knudsen cell with a knife-edge effusion hole, containing a known amount of sample can be closed with a silica glass sphere, which can be raised and lowered from the outside by the metallic rod. The working

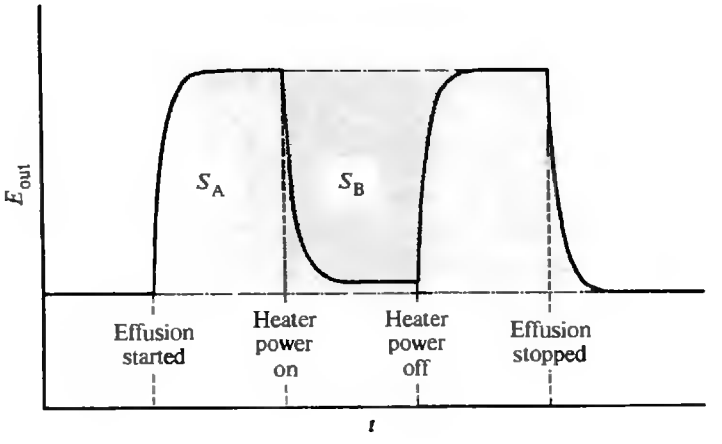

Figure 2.3 Schematic plot of output potential from the microcalorimeter against time for a sublimation calorimetric experiment. A calibration experiment is superposed on a sublimation experiment. S_A is the net area observed for the sublimation experiment and S_B is the area associated with the calibration.

procedure is described in [55,58–61]. The most elaborate sublimation calorimetric system, in which a Calvet microcalorimeter and Knudsen-type sample containers are incorporated, is designed especially for substances that are unstable in air [59]. The output signal of the calorimeter throughout an experiment is schematically depicted in Figure 2.3.

Two areas, S_A and S_B, are determined and the molar enthalpy of sublimation at the temperature of experiment $\Delta_{sub}H(T)$ is calculated on the basis of the equation

$$\Delta_{sub}H(T) = E_{calib}(S_T/S_B)(M/m), \tag{2.7}$$

where E_{calib} is the electrical energy supplied to the calibration heater, $S_T = (S_A + S_B)$ the true area of the sublimation signal, m the mass of the effused sample and M its molar mass. The enthalpy of sublimation by microcalorimetry is determined using relation (2.7). From the direct calorimetric method, the behaviour of $\Delta_{vap}H(T)$ is obtained as a function of temperature. The vapour pressure of the sample is measured simultaneously and obtained by mass loss under isothermal conditions of the Knudsen molecular effusion, using the well-known Equation (2.1). The temperature behaviour of p is expressed by the linear equation, which is the expression of the second-law method, over the range studied, and gives a mean value of $\Delta_{vap}H(T)$. Agreement between the mean values obtained by calorimetry and by the second-law method provides a test of mutual consistency of the experimental results.

2.3.8 Mass-Loss Knudsen Technique with a Mass Spectrometry Method

Mass spectrometry, with its attractive features of high sensitivity and resolution under high vacuum conditions, is an attractive method for effusion studies. In this method, the Knudsen

cell is used as the source of a molecular gas beam that is directed into the ionization chamber of a high-temperature mass spectrometer. The height of a peak in the mass spectrum of a compound is proportional to its partial pressure in the ionization chamber of the spectrometer. Measurements made on the spectra obtained for different temperatures of the equilibrium chamber allow calculation of vapour pressures and enthalpies of vaporization or sublimation. Various kinds of Knudsen cells are employed in combination with various types of instruments: single-focusing magnetic sector field (the standard instrument), double-focusing, quadrupole, time-of-flight and monopole mass spectrometers [62]. Resolution requirements depend upon the mass ranges and separations between adjacent masses of the sample vapour species. The application of mass spectrometry to Knudsen cells has been reviewed by Drowart and Goldfinger [63] and by Chatillon *et al.* [64].

One advantage of this method is that measurements can be made despite the presence of impurities, provided the impurities do not contribute to the peaks chosen for study. Comparison of several peaks in different parts of the spectrum will assist in checking this because, if they are due to a single component only, their ratios should remain constant as the temperature of the equilibrium chamber is changed. Relative insensitivity to impurities has allowed applying high-temperature mass spectrometry to determine the vapour pressure and sublimation enthalpy of buckminsterfullerene at temperatures from 637 to 846 K [65].

The mass spectrometer is not suitable for the precise measurement of the absolute vapour pressure at a single temperature. The measurement depends on the positive ion current for a particular species, which in turn depends on the ion collection efficiency of the instrument and the ionization cross-section of the species concerned. Systematic uncertainties in these will make the absolute vapour pressure imprecise, but should leave the temperature variation unaffected [66].

2.3.9 Knudsen Cell with Differential Scanning Calorimetry

DSC as a Boiling Point Method

Differential scanning calorimetry (DSC) has been an important tool for the study of the thermal behaviour and phase transitions of organic and inorganic substances. By carrying out adequate modifications, a scanning calorimeter can also be developed as an experimental instrument capable of measuring directly the heat transfer involved in the liquid–gas or solid–gas phase transitions of organic substances. Goodrum and Siesel [67] have described such a DSC procedure using sealed standard crucibles with laser-drilled holes. Further improvements to the DSC technique [68–70] have made this method a routine laboratory tool. Minor and easily made modifications to a standard pressure DSC cell are required. In this technique, boiling points can be determined over a broad temperature range with the DSC instrument by non-equilibrium experiments. The heat uptake of the sample is measured as a function of temperature and the enthalpy of evaporation can be measured directly if the whole sample is evaporated. The evaporation curves are better defined when the sample is enclosed and is allowed to evaporate through a pinhole of appropriate size. In DSC experiments, a constant carrier gas flow is maintained in the vicinity of the sample capsule to

prevent recondensation of the sample vapour on the sample holder assembly. The pressure DSC module measures thermal effects from room temperature to 900 K in variable gas atmospheres from ambient pressure up to 7 MPa [68]. Validation of the DSC procedure was performed by studying samples of naphthalene, caffeine and tetradecane [68,69]. The data from the DSC technique are in good agreement with the well-established vapour pressures of these test compounds.

DSC as a Mass-Loss Method

An interesting DSC experimental procedure has been developed for direct measurement of the heat involved in the vaporization of a solid organic compound above its normal melting temperature [71–73]. This technique consists of fusing a solid aromatic hydrocarbon, which is then vaporized by a sudden decrease in the pressure. The direct register of heat flow as function of time by DSC allows quantifying the enthalpy of vaporization of organic compounds. Enthalpies of vaporization are measured in an isothermal mode over a range of temperatures above the melting temperature of a compound, while enthalpies of fusion are determined from separate experiments performed in a scanning mode. The calorimetric measurements are performed using the modified commercial DSC calorimeter [72]. The commercial pans for volatile samples are utilized as vaporization cells, but previously were modified making a hole with a drill of diameter 0.3 mm. The vaporization heat is obtained by knowing the initial mass, the mass lost due to the vaporization at constant pressure, and the area of the measured calorimetric curve. The system was tested successfully with measurements on the naphthalene, iodine, benzoic acid and ferrocene [72].

2.4 Langmuir Effusion Methods for Vapour Pressure Measurement

The Langmuir method in contrast to the Knudsen cell presumes a free evaporation from an open surface. Vapour pressures are determined via the rate of substance vaporization from an open crucible into vacuum or into an inert purge gas. This technique combines the simplistic features of the methods of gas saturation (see Section 2.5) and vapour pressure balance to measure sublimation rates at ambient pressure, namely isothermal thermogravimetry (TG) with an inert gas purge. The TG methods potentially have considerable advantages compared with the conventional methods for determining vapour pressures. These include the relatively small amounts of substance that are sufficient for measurements, the simplicity of the experimental set-up and the short experimental times that are necessary for evaluations.

Price and Hawkins [74,75] formalized a procedure for estimating the vapour pressure of low-volatile substances from TG data obtained in the presence of an inert purge gas at atmospheric pressure using the Langmuir equation. Langmuir considered evaporation from an isolated solid surface into a vacuum and obtained an equation

$$-\frac{\mathrm{d}m}{\mathrm{d}t} = p\alpha\sqrt{\frac{M}{2\pi RT}}, \tag{2.8}$$

where $-dm/dt$ is the rate of mass loss per unit area, p the vapour pressure, M the molar mass of the effusing vapour, R the gas constant, T the absolute temperature and α the vaporization coefficient (usually assumed to be 1). Samples are prepared by placing them in parallel-sided crucibles so that a well-defined surface area is achieved. In the case of solid substances, the material is melted first to obtain a flat surface. Measurements can be made under isothermal and linear-rising temperature conditions using an inert atmosphere instrument purge under ambient pressure.

According to Langmuir, the vaporization constant (α) depends on the experimental set-up and it is independent of the substance being vaporized, provided the vapour is not associated. The value of α is stipulated to be equal to unity in vacuum. The Langmuir equation holds true for a certain rate of mass loss in volatilization from a given container exposing a constant area of interface. In the case of a material volatilizing into a flowing gas stream at one atmosphere rather than *in vacuum*, α can no longer be assumed to be unity. The Langmuir equation can then be rearranged to constitute a material-dependent and a material-independent term. Rearranging Equation (2.8) gives

$$p = kv, \tag{2.9}$$

where $k = \sqrt{2\pi R}/\alpha$ and $v = dm/dt\sqrt{T/M}$. A plot of p against v follows the same trend for a series of compounds with known vapour pressure regardless of chemical structure provided that the sample does not associate in the solid, liquid or gas phase. This allows the calibration constant k to be determined and thus the vapour pressures of unknown materials to be found. The TG method for determination of vapour pressures and sublimation enthalpies by using thermobalances commercially available is described by Price [74,75]. Additionally, it has been demonstrated that "modulated-temperature TG" [76] can be also used for determining the enthalpies of sublimation and vaporization of organic compounds [74].

The use of reference compounds in constructing the vapour pressure plots for the sample compounds is based on the concept of substance independence of the coefficient of evaporation k. The coefficient of evaporation is a measure of the evaporation process that depends on parameters such as the area of the surface from which evaporation is taking place, the vaporization coefficient, and the universal gas constant but does not depend on the material being investigated. Reference compounds are usually selected as those with well-established vapour pressures. Experimental vapour pressures collected in the literature [3,77] are most often approximated by the Antoine equation. Accuracy of the vapour pressures derived by TG depends directly on the quality of vapour pressure data sets of the chosen reference compounds. It is prudent to collect a set of reference substances with vapour pressure data measured over a broad temperature range, which essentially mimic the conditions of the TG experiment. In this context, it is advisable to take some precautions by using the comprehensive compilation [3], which contains vapour pressure results for all classes of organic compounds over a wide range of temperature. This compilation is willingly used by the TG community to extract the Antoine coefficients. However, the origin of the data presented in [3] is unclear. In addition, the methods of measurements are unknown and the associated errors and purities of compounds are not always defined. As a result, caution must be exercised in the use of Antoine coefficients listed in [3].

2.5 The Transpiration Method

The transpiration method, also called the transportation or gas saturation method, is one of the oldest and most versatile ways of studying heterogeneous equilibria involving gases. It was first proposed by Regnault in 1845 [80], but was not used intensively until the advent of automated chromatographic analytical techniques in 1970s. This method has been applied for both organic and inorganic compounds. Unfortunately, this method had long been erroneous because of insufficient saturation of the sample vapour in the carrier gas and the miscalculation of the vapour pressure based on the extrapolation of a flow rate to zero [11]. There are several advantages for this method, for example, it is not influenced by a small amount of volatile impurities and it is possible to measure the equilibrium vapour pressure within a short time, and it is also possible to make measurements in any atmosphere by changing the carrier gas. Vapour pressure can be measured over temperature ranges that are close to ambient. This method is particularly applicable at low vapour pressures around 3 kPa downwards and can be used over a very wide range of temperature. In principle, the method is free of serious errors and has proved to give results that are in excellent agreement with other established techniques for determining vapour pressures of pure substances and enthalpies of vaporization from the temperature dependence of the vapour pressure.

In the transpiration method, a gas, which may be either inert or reactive, is passed over a thermostatically controlled saturator packed with either the pure compound of interest or with an analyte-coated inert support at a rate sufficiently low for equilibrium conditions to be established. The analyte is collected from the saturated vapour using impingers, sorbents or cryogenic traps and the amount of substance transferred is determined by some suitable means. Assuming that Dalton's law of partial pressures applied to the carrier gas stream saturated with the substance i of interest is valid, p_i values are calculated:

$$p_i = m_i RT_a/VM_i, \qquad V = V_{gas} + V_i \, (V_{gas} \gg V_i), \tag{2.10}$$

where R is the gas constant, m_i the mass of transported compound, M_i the molar mass of the compound, and V_i its volume contribution to the gaseous phase. V_{gas} is the volume of transporting gas and T_a the temperature of the device used for measuring the flow rate.

The conventional transpiration apparatus (Figure 2.4) consists essentially of the saturator. About 0.1–0.5 g of the sample under investigation is mixed with glass beads or another support. This material fills the entire length of the saturator. The saturator itself is immersed in a thermo-fluid and kept at constant temperature using a thermostat with an accuracy of ± 0.1 K. The temperature inside the saturator cell is measured by means of a platinum resistance thermometer with an accuracy of ± 0.1 K. The carrier gas, preheated in an additional loop line in the thermostat, enters the saturator, equilibrates with the sample along the tube and the saturated vapour condenses in a cold trap, attached by the connection directly to the exit of the saturator. The saturation vapour pressure p_i at each temperature T_i is calculated from the amount of product collected in the cooling trap within a definite period of time.

The transpiration experiment consists of the following two parts: (1) Determination of the plateau in the plot of the vapour density versus the flow rate of the carrier gas at a suitable temperature, preferably the mean, in the range of measurements. This is important to prove

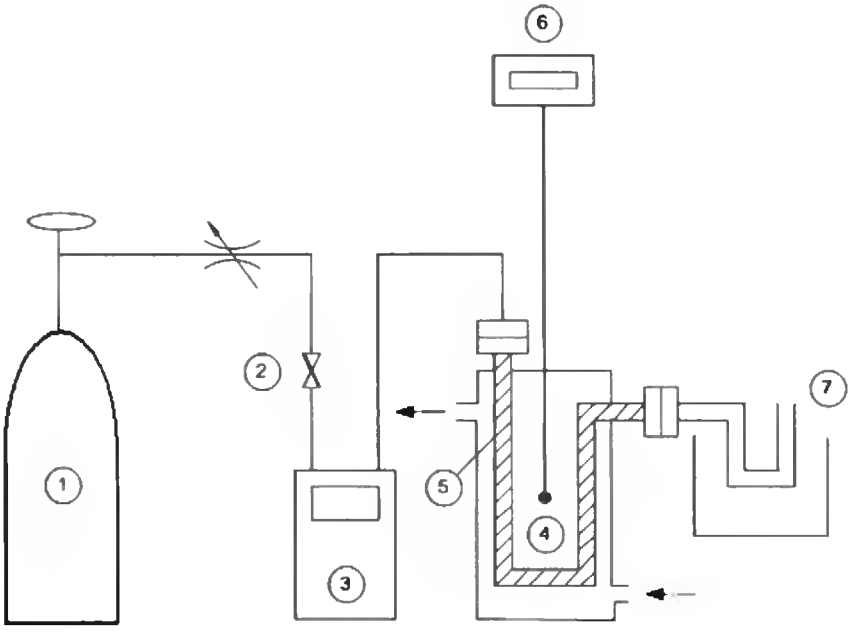

Figure 2.4 Schematic diagram of the transpiration apparatus [81]: 1, carrier gas cylinder; 2, flow valve; 3, digital mass flow meter; 4, equilibrium cell; 5, saturator filled with the sample; 6, thermometer; 7, cooling trap at $T = 243$ K.

saturation conditions. (2) Determination of equilibrium vapour pressures at various temperatures from which the mean enthalpy of vaporization or sublimation is derived. The experimental quantities measured to obtain the above information are as follows: (a) the mass loss m_i of the sample due to the vapour transported away from it by the carrier gas; (b) the rate of flow of the carrier gas over the sample and the total time for which it is passed, from which the total volume of the gas swept over the sample is calculated; (c) the temperature at which the experiment is performed and (d) the ambient temperature T_a at which the volume of the carrier gas is measured. The accuracy of the results obtained depends on the accuracy with which these quantities are measured. Validation of the transpiration procedure with established standards, such as naphthalene, benzoic acid, decane and alcohols, proved its ability to reproduce vapour pressures within 0.5–1.5 per cent, and a typical accuracy of the vaporization enthalpies is within ± 0.2–$0.4\,\mathrm{kJ \cdot mol^{-1}}$ [81].

2.6 Chromatographic Methods

Virtually since its inception, gas chromatography (GC) has been recognized as a powerful method for non-analytic measurements, in particular, for the study of physico-chemical properties, investigation of sorption and catalytic processes, for the measurement of VLE and to obtain data on vapour pressures and vaporization enthalpies. The most common and

thermodynamically well-defined methods include the dynamic approach, in which the retention volume of a solute molecule is measured, and the static or headspace analysis technique, in which the chromatograph is used in a conventional fashion, *i.e.* as a selective and sensitive gas analyser.

2.6.1 Headspace Analysis

A simple indirect headspace analysis for determination of vapour pressures of pure compounds has been developed by Chickos [82]. A typical apparatus consists of a sample compartment attached through a valve to the ballast tank. Equilibrium is achieved by keeping the ballast and sample compartments at the same temperature. An analysis of the contents in the ballast tank of known volume followed by treatment of this quantity by the ideal gas law yields the experimental vapour pressure of the compound under study. Experimental results derived by this method tend to be lower by a few per cent relative to other techniques [83]. This has been attributed to a small contribution of residual adsorption. In spite of the fact that the actual values of the vapour pressures determined by headspace analysis should be considered only as approximate values, it is important to recognize that the temperature dependence of the vapour pressure measured by headspace analysis, and following the $\Delta_{vap}H$, remains reliable [84].

2.6.2 GC-Correlations with Retention Times and Vapour Pressures of Reference Compounds

A number of indirect experimental methods for determining vapour pressure and vaporization enthalpies by using GC are based on measuring retention times. Compared with other methods, the GC technique offers particular advantages in terms of simplicity, speed, solute sample size, as well as purity and stability requirements. Bidleman [85] has outlined the advantage of using the capillary columns to obtain efficient resolutions of mixtures under study. Numerous methods [85–93] were developed intensively for the study of vapour pressures of environmentally relevant chemicals at ambient temperatures, more specifically at the reference temperature 298 K. The average precision of the GC methods, expressed as relative standard deviation, was 9–36 per cent as measured for environmentally relevant organic compounds [9]. Such a disappointing spread of values has not encouraged an extended use of the GC methods in spite of substantial advantages mentioned above. Fortunately, recent systematic attestation of the most frequent GC methods, which have been performed by Koutek *et al.* [86], allowed setting some priorities. In this work, they studied alkane derivatives H-$(CH_2)_n$-Y, where Y denotes Cl, Br, CHO, $COOCH_3$ and $OCOCH_3$, and n varies from 6 to 14. Having an established set of experimental data on retention times from own measurements and sets of reliable vapour pressures available from the literature, a thorough assessment of the most frequently used methods [87–93] has been performed. The GC experimental methods as a rule require the use of one or several reference compounds whose vapour pressures are accurately known over the whole temperature range used by measuring of gas

chromatographic retention times. Nearly all GC methods that have been used at present are, to some extent, either explicitly or implicitly based on an insight that stems from the equation

$$V_{g,i} = RT/Mp_i\gamma_i^{\infty}. \tag{2.11}$$

This equation, assuming the ideal gas behaviour, relates the measured specific retention volume $V_{g,i}$ of a solute i in a stationary phase, whose molar mass is M, to its vapour pressure p_i, activity coefficient at infinite dilution γ_i^{∞} and the gas constant R. Provided that a constant carrier gas flow rate is applied, other retention parameters, for example, adjusted retention times ($t_i' = t_i - t_0$) deduced from the experimental retention times (t_i') and the retention of an "non-retained" substance (the hold-up time, t_0) may be advantageously used in Equation (2.11) instead of $V_{g,i}$.

As has been demonstrated by Koutek *et al.* [86], the average absolute per cent error of methods suggested in [85,87,91,92] scatters at the level of 9–12. Methods suggested in [88–90,93] show the larger average absolute per cent error of 17–25 per cent. Thus, the careful work performed by Koutek *et al.* [86] supports a view that the GC-based methodologies [85,87,91,92] may serve as a very useful complement to existing physicochemical approaches. However, the extension of the methods beyond non-polar and/or moderately polar series of homologues deserves further investigation.

2.6.3 GC-Correlations with Net Retention Times

A simple method to correlate gas chromatographic retention times with experimental vapour pressures of organic compounds was suggested by Chickos *et al.* [94–96]. In short, a plot of $\ln(1/t_a)$ against $1/(T/K)$, where t_a is the retention time of any compound A corrected for the dead volume, results in a straight line. Using this relation, retention time t_a can be calculated at any required temperature, for example, at the reference temperature 298 K. Correlation of the logarithm of reciprocal corrected retention time at a selected temperature ($1/t_a$) with the logarithm of the experimental vapour pressure at a selected temperature results in the linear relationship for over 100 organic compounds from diverse chemical families [94]. Experimental vapour pressures were obtained from the reported Antoine constants [3] evaluated at temperatures consistent with both retention time measurements and range of applicability of the vapour pressure equation, *e.g.* Antoine or Cox. It was suggested by Chickos *et al.* [94–96] that, in cases where compounds are properly selected with regard to the analogy of their molecular structures with reference compounds or standards, this linear relationship obtained by plotting ($1/t_a$) versus logarithm of the experimental vapour pressures of standards with the known and well-established value of vapour pressures can subsequently be used to evaluate the unknown vapour pressures of any structurally related species provided the unknown species are analysed under the same conditions as the standards. Chickos and Hanshaw [96] have described the experimental procedure and validation of the method using alkanes. The linearity between $\ln(p)$ and $\ln(1/t_a)$ was carefully proven for a series of n-alkanes for n-C_{14} to n-C_{20}. In this instance, the $\ln(1/t_a)$ data were extrapolated to $T = 298$ K, and the experimental vapour pressure

data were calculated from the Cox equation, which approximated results recommended in [97]. The linearity ($R^2 = 0.9997$) observed between $\ln(p)$ and $\ln(1/t_a)$ for n-C_{14} to n-C_{20} suggests a mechanism by which vapour pressure data for the larger n-alkanes can be obtained. Using experimental $\ln p$ data at $T = 298$ K calculated from the Cox equation and from extrapolated $\ln(1/t_a)$ values for n-C_{17} to n-C_{23} and using the appropriate equations approximating experimental t_a values, values of $\ln p$ for n-C_{21} to n-C_{23} can be obtained by linear correlation established with the standards n-C_{17} to n-C_{23}.

The range of temperatures for which the Cox equation is applicable for the n-alkanes is from 298 K to the boiling point 575 K [97]. Using, for instance, the vapour pressures of n-C_{17} to n-C_{20} generated from the parameters of the Cox equation as standards [97] and experimental results for $\ln(1/t_a) = f(1/T)$, the stepladder approach just described for obtaining $\ln(p)$ at $T = 298$ K for n-C_{17} to n-C_{23}, vapour pressures of desired n-alkanes at a series of different temperatures can be calculated. Extended comparison of calculated vapour pressures with those available from the literature assures this approach as a highly reliable one. Approximation of these p–T values derived by this GC procedure provides vaporization enthalpies of an alkane under study at any requested temperature, *e.g.* at 298 K.

The same authors described another interesting technique for determining vaporization enthalpies $\Delta_{vap}H(T)$ of organic compounds by using high-resolution GC [94–96]. The technique correlates changes in net retention times of compounds whose enthalpies of vaporization $\Delta_{vap}H(T)$ are known with those of the compound(s) of interest. The best results are obtained when the reference compounds are structurally similar and in the same chemical family. Hydrocarbons and various hydrocarbon derivatives containing one functional group were used for validation of the method. Comparison with literature values of the $\Delta_{vap}H(298\,\text{K})$ of 102 compounds resulted in an average standard deviation of 1.3 kJ · mol^{-1}. In most cases, the difference between the literature value and the value from GC-correlation method lies within the normal errors ± 0.3–0.5 kJ · mol^{-1} associated with vaporization enthalpy determinations.

Similar to the procedure described above for the determination of vapour pressures, a plot of $\ln(1/t_a)$ against $1/(T/K)$ results in a straight line, whose slope when multiplied by the gas constant affords $\Delta_{sol}H$, which is the enthalpy of transfer from solution, *viz.* the stationary phase of the GC column, to vapour. It was found that, in cases where compounds are properly selected with regard to molecular structure, plotting $\Delta_{sol}H$ against the known vaporization enthalpy at temperature T, $\Delta_{vap}H(T)$ also affords a straight line. The equation of this line can subsequently be used to evaluate the unknown vaporization enthalpy of any structurally related material provided that the unknown is analysed at the same time as the standards.

The GC-correlation techniques, developed by Chickos *et al.* [94–96], prove to be an accurate means of determining vapour pressures and vaporization enthalpies of organic molecules. The advantages of this method are its speed and accuracy and small sample sizes required. In addition, whereas most thermo-chemical measurements require purities in excess of 99 per cent, there is no minimum purity requirement for this method. The foremost limitation of this method is that the results are entirely dependent upon the choice of standards and the reliability of their vaporization enthalpies and vapour pressures. However, to our knowledge, methods capable of reflecting the effect of minor structural differences in the position and configuration of substituents on the $\Delta_{vap}H$ better than correlation GC have not existed up to now.

2.7 Calorimetric Measurements of the Enthalpy of Vaporization

Experimental methods for determining the enthalpy of vaporization can be divided into two groups. The first consists of direct methods based on the calorimetric measurement of the enthalpy of vaporization. The second group of indirect methods employs calculation of $\Delta_{vap}H$ from other, experimentally more readily available quantities. This primarily involves the determination of the enthalpies of vaporization from experimental vapour pressures (see Sections 2.1–2.5), from pVT behaviour of both coexisting phases, and from chromatographic data (see Section 2.6). In general, every calorimetric vaporization experiment is based on the determination of the amount of heat required for the vaporization of a unit amount of the substance studied. For measurement of enthalpy of vaporization of volatile compounds, a variety of calorimetric assemblies were developed [2,4,5]. The accuracy of the results depends to a large extent on the complexity of the apparatus and the precision of measuring equipment. For the most part, the calorimeters for determining vaporization enthalpy operate under adiabatic conditions, and all the heat absorbed during vaporization is exactly compensated by an equivalent amount of heat supplied from an external source. Another part of the calorimetric determination of enthalpies of vaporization is performed by use of conduction calorimeters. Because of complexity of the apparatus for adiabatic and conduction calorimetry, commercially available devices are usually adapted for the high-precision measurements. A short description of equipment and measurement procedures is presented here, which is essential to provide understanding of the method currently applied.

2.7.1 Adiabatic Calorimeters

At *low* pressures ($p < 5$ kPa), methods employing vaporization into a vacuum [52,53] and using a carrier gas [98] are convenient. The former permits measurement of the enthalpy of vaporization at very low vapour pressures, even below 1 Pa. The upper limit of applicability of this method is about 25 kPa. The latter method is useful for the pressure range from 0.05 to 25 kPa and the principle of this method has been applied in the commercial LKB-8721 calorimeter. In both methods, the vaporization vessel is open to the calorimeter surroundings during vaporization. By vaporizing into a vacuum, the sample flows out of the vaporization vessel into an evacuated space. The vaporization vessel can then be considered as a Knudsen cell. The experimental arrangements combining a Knudsen cell and a calorimeter are described in detail in Section 2.3.7.

At moderate pressures ($5 < p < 200$ kPa), experimental methods based on a closed system are employed. The vaporization and condensation parts of the apparatus are interconnected and completely separated from the surrounding atmosphere. Usually, only the measured substance is present inside this closed system. Two types can be distinguished. The first type employs a single controlled withdrawal of the vapours from the vaporization compartment into the condensation vessel [99–101], in the second type, the vaporization and condensation parts are connected in a circuit with continuous fluid cycling [102]. The apparatus equipped with control valves designed by Svoboda *et al.* [100] and Majer *et al.* [101] yielded

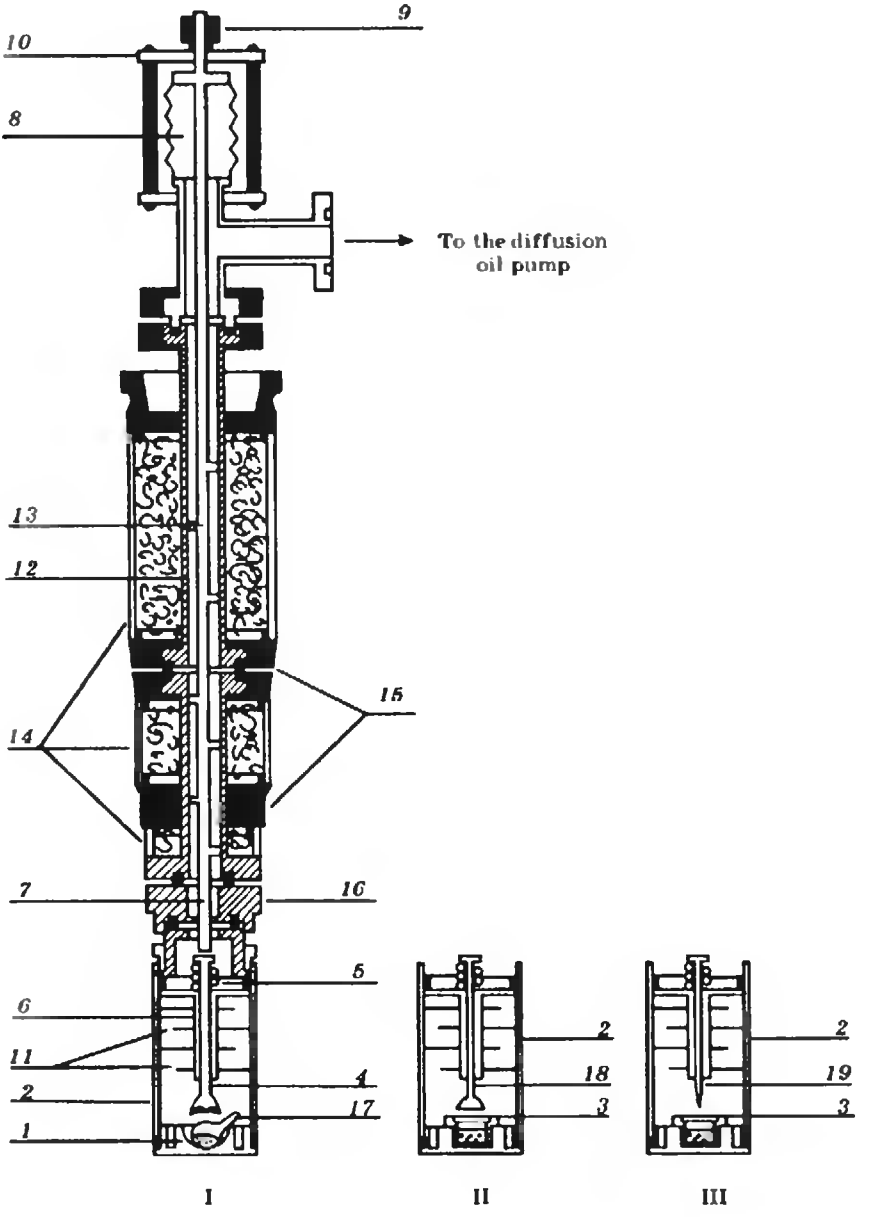

Figure 2.5 Schematic diagram of the calorimetric cell for the differential microcalorimeter [107]. 1, the lower lid; 2, evaporation chamber; 3, effusion cell with a sample; 4, metal rod; 5, spring; 6, directing channel; 7, auxiliary rod; 8, bellows; 9, fixing screw; 10, limiting strap; 11, metal shields; 12, Teflon tube; 13, segmental shields; 14, isolating coats; 15 and 16, metal contacts for the thermostat, 17, glass cell; 18, metal rod with a seal band; 19, metallic rod with a spire. I, evaporation chamber with broken ampoule; II, evaporation chamber with effusion cell closed by metallic rod; III, evaporation chamber with effusion cell obtained by piercing the membrane.

$\Delta_{vap}H$ data for various groups of substances in the interval $T = 298–373$ K with an accuracy of 0.1–0.3 per cent.

2.7.2 Drop Calorimetry Method

The method of drop calorimetry has been proposed for measurement of vaporization enthalpy [103–105]. The sample at room temperature is dropped into a Calvet-type calorimeter with a certain enhanced temperature, which should be sufficiently high to provide a rapid vaporization or sublimation of a sample. The substance is then rapidly heated to the temperature of the calorimeter and vaporizes. The amount of heat transferred is obtained from the peak area in the calorimetric signal. This method is very simple and fast, the measuring error is 1–1.5 per cent for a minimal sample amount of less than 5 mg for calorimeter temperatures of 320–1000 K. Kiyobayashi and Minas da Piedade [105] have described in detail the apparatus, operating procedure and tests.

2.7.3 Differential Calorimetry

The measurement of vaporization enthalpies using a commercial Calvet-type microcalorimeter (Setaram BT 2.15) without modification and using an original design of the vaporization vessel is reported by Viton *et al.* [106]. A modified commercial heat-flow differential microcalorimeter of the Calvet type was developed for the determination of enthalpies of vaporization [107]. A special calorimetric cell (see Figure 2.5) was designed according to the requirements of maximal thermal contact in the measuring zone and prevention of heat loss from the measuring zone. The evaporation can occur either from the broken glass ampoules, or from the special metal ampoules through the orifice in the thin nickel membrane. The glass ampoule is broken with a metal rod. The latter is fixed on a spring, which is moved with an auxiliary Teflon rod. If metal ampoules are used, the orifice is made in advance and is covered with a silicon cap placed on the butt-end of the metal rod. The hole is opened when the measurements begin. It is more convenient if the membrane is pierced with a needle placed on the rod during the experiment as shown in Figure 2.5. The power or the heat flow W is evaluated from the relation $W = \Delta E/K$, where ΔE corresponds to the temperature difference between the core of the calorimeter and the evaporating camera and K is the thermal constant of the cell. The constant for the cells is determined from the results of measurements of enthalpies of vaporization for the reference substances.

2.8 Conclusions

Many experimental techniques for the determination of the vapour pressure are described in the literature, but no single method is applicable for the entire vapour pressure range of industrially significant compounds ($\sim 10^5$–10^{-6} Pa). The choice of a method depends largely on the temperature and pressure range concerned, although there may be considerable overlap

between instruments of each type. Vapour pressure measurements at ambient temperatures, close to the reference temperature 298 K, and low pressures are usually of considerable interest for environmentally relevant compounds, as well as highly desired for scientific calculations to obtain vaporization enthalpies in order to reduce the enthalpy of formation in the condensed state to the gaseous state. The transpiration method is the most suitable for these conditions. Measurements at elevated temperatures and pressures for volatile compounds can be easily performed by calorimetric, static or ebulliometric methods. Measurements at elevated temperatures for low volatile compounds can be better performed by Knudsen cell methods, the transpiration method or by drop calorimetry.

Sometimes an amount of a sample suggested for investigation plays a decisive role by choice of techniques. Conventional ebulliometry requires about 20 g, a static cell about 3–5 g, the conventional Knudsen cell mass-loss effusion set-up about 200–500 mg. For the TG and DSC modification of the Knudsen method or a drop calorimeter, only several milligrams of a sample are required. However, these indications of sample masses are approximate, depending on thermal stability and purity of a sample, and reproducibility of measurements. Also it has been observed that wide variations occur in the data reported by different authors for the same compound. This suggests that several methods covering different experimental conditions should be applied within a research laboratory for proper measurements of vapour pressures and vaporization enthalpies. Under these circumstances, an internal consistency of the results delivered by different techniques should provide requisite reliability.

References

1. Ambrose, D., in *Experimental Thermodynamics, Vol II: Experimental Thermodynamics of Non-Reacting Fluids*, B. Le Neindre and B. Vodar, eds., Butterworths, London, pp. 607–656, 1975.
2. Majer, V. and Svoboda,V., *Enthalpies of Vaporization of Organic Compounds*, International Union of Pure and Applied Chemistry Chemical Data Series, No. 32, Blackwell Scientific Publications, Oxford, UK, 1985.
3. Stephenson, R.M. and Malanowski, S., *Handbook of the Thermodynamics of Organic Compounds*, Elsevier, New York, 1987.
4. Majer, V., Svoboda, V. and Pick, J., *Heats of Vaporization of Fluids (Studies in Modern Thermodynamics*, 9), Elsevier, Amsterdam, 1989.
5. Lebedev, Yu, A. and Miroshnichenko, E.A., in *Thermochemistry and Equilibria of Organic Compounds*, M. Frenkel, ed., VCH Publishers, Inc., New York, pp. 165–375, 1993.
6. Chickos, J.S. and Acree Jr., W.E., *J. Phys. Chem. Ref. Data* **31**, 537–698, 2002.
7. Chickos, J.S. and Acree Jr., W.E., *J. Phys. Chem. Ref. Data* **32**, 515–878, 2003.
8. Wahlbeck, P.G., *High Temp. Sci.* **21**, 189, 1986.
9. Delle Site, A., *J. Phys. Chem. Ref. Data* **26**, 157, 1997.
10. Ipser, H., *Ber. Bunsenges. Phys. Chem.* **102**, 1217, 1998.
11. Nesmeyanov, A.N., *Vapour Pressures of the Elements*, Elsevier, Amsterdam, 1963.
12. Suvorov, A.V., *Thermodynamic Chemistry of Vapour State*, Chemistry, Leningrad, 1970.
13. Margrave, J.L., *The Characterization of High-Temperature Vapours*, Wiley, New York, 1967.
14. Bureau, N., Jose, J., Mokbel, I. and deHemptinne, J.-C., *J. Chem. Thermodyn.* **33**, 1485, 2001.
15. Ruzicka, K., Mokbel, I., Majer, V., Ruzicka, V., Jose, J. and Zabransky, M., *Fluid Phase Equilbr.* **148**, 107–137, 1998.

16. Kasehgari, H., Mokbel, I., Viton, C. and Jose, J., *Fluid Phase Equilbr.* **87**, 133, 1993.
17. Morgan, D.L. and Kobayashi, R., *Fluid Phase Equilbr.* **97**, 211, 1994.
18. Swietoslawski, W., *Ebulliometric Measurements*, Reinhold, New York, 1945.
19. Hala, E., Pick, J., Fried, V. and Vilim, O., *Vapour Liquid Equilibrium*, Pergamon Press, Oxford, 1967.
20. Rogalski, M. and Malanowski, S., *Fluid Phase Equilbr.* **5**, 97, 1980.
21. Malanowski, S., *Fluid Phase Equilbr.* **9**, 197–219, 1982.
22. Ambrose, D., Ewing, M.B., Ghiassee, N.B. and Sanchez Ochoa, J.C., *J. Chem. Thermodyn.* **22**, 589, 1990.
23. Abbott, M.M., *Fluid Phase Equilbr.* **29**, 193, 1986.
24. Raal, J.D. and Mühlbauer, A.L., *Phase Equilibria: Measurements and Computation*, Taylor & Francis Ltd, Washington, DC, 1998.
25. Varouchtchenko, R.M. and Droujinina, A.I., *J. Chem. Thermodyn.* **27**, 355, 1995.
26. Joseph, M.A., Raal, J.D. and Ramjugernath, D., *Fluid Phase Equilbr.* **182**, 157, 2001.
27. Osborn, A.G. and Douslin, D.R., *J. Chem. Eng. Data* **11**, 502, 1966.
28. Chirico, R.D., Nguyen, A., Steele, W.V. and Strube, M.M., *J. Chem. Eng. Data* **34**, 149, 1989.
29. Ewing, M.B. and Sanchez Ochoa, J.C., *J. Chem. Thermodyn.* **30**, 189, 1998.
30. Ewing, M.B. and Sanchez Ochoa, J.C., *J. Chem. Thermodyn.* **32**, 1157, 2000.
31. Dushman, S., in *Scientific Foundations of Vacuum Technique*, J.M. Lafferty, ed., Wiley, New York, 1962.
32. Zaitsau, D.H., Verevkin, S.P., Paulechka, Y.U., Kabo, G.J. and Sevruk, V.M., *J. Chem. Eng. Data* **48**, 1393, 2003.
33. Calado, J.C.G., Dias, A.R., Minas de Piedade, M.E. and Marthino Simoes, J.A., *Rev. Port. Quim.* **22**, 53, 1980.
34. Diogo, H.P., Minas da Piedade, M.E., Fernandes, A.C., Marthino Simoes, J.A., Ribeiro Da Silva, M.A.V. and Monte, M.J.S., *Thermochim. Acta* **228**, 15, 1993.
35. Ribeiro Da Silva, M.A.V. and Monte, M.J.S., *Thermochim. Acta* **171**, 169, 1990.
36. Ferro, D., Piacente, V. and Scardala, P., *Thermochim. Acta* **68**, 329, 1983.
37. Piacente, V., Fontana, D. and Scardala, P., *J. Chem. Eng. Data* **39**, 231, 1994.
38. Piacente, V., Pompili, T., Scardala, P. and Ferro, D., *J. Chem. Thermodyn.* **23**, 379, 1991.
39. De Kruif, C.G. and Van Ginkel, C.H.D., *J. Phys. E* **6**, 764, 1973.
40. De Kruif, C.G. and Van Ginkel, C.H.D., *J. Chem. Thermodyn.* **9**, 725, 1977.
41. Oja, V. and Suuberg, E.M., *Anal. Chem.* **69**, 4619, 1997.
42. Murray, J.J. and Pottie, R.F., *Can. J. Chem.* **52**, 557, 1974.
43. Li, X., Shibata, E., Kasai, E. and Nakamura, T., *Tohoku Daigaku Sozai Kogaku Kenkyusho Iho* **58**, 29, 2002.
44. Kaisersberger, E., Haedrich, W. and Emmerich, W.D., *Thermochim. Acta* **95**, 331, 1985.
45. Offringa, J.C.A., De Kruif, C.G., Van Ekeren, P.J. and Jacobs, M.H.G., *J. Chem. Thermodyn.* **15**, 681, 1983.
46. Burkinshaw, P.M. and Mortimer, C.T., *J. Chem. Soc. Dalton Trans.* 75–77, 1984.
47. Glukhova, O.T., Arkhangelova, N.M., Teplitsky, A.B., Sukhodud, L.F. and Yanson, I.K., *Thermochim. Acta* **95**, 133, 1985.
48. Torres, L.A., Hernandez-Contreras, I., Guardado, J.A. and Gonzalez, M.G., *Meas. Sci. Technol.* **5**, 51, 1994.
49. Goodman, M.A., *J. Chem. Eng. Data* **42**, 1227, 1997.
50. Torres, L.A., Campos, M., Enriquez, E. and Patino, R., *J. Chem. Thermodyn.* **34**, 293, 2002.
51. Lu, C. and Czandema, A.W., *Applications of Piezoelectric Quartz Crystal Microbalances, Vol 7*, Elsevier, Amsterdam, 1984.
52. Morawetz, E. and Sunner, S., *Acta Chem. Scand.* **17**, 473, 1963.

53. Morawetz, E., *Chem. Scripta* **1**, 103, 1971.
54. Sunner, S. and Svensson, Ch., *Trans. Faraday Soc.* **75**, 2359, 1979.
55. Malaspina, L., Gigli, R. and Bardi, G., *J. Chem. Thermodyn.* **3**, 827, 1971.
56. Malaspina, L., Gigli, R. and Bardi, G., *J. Chem. Phys.* **59**, 387, 1973.
57. Sabbah, R., Chastel, R. and Laffitte, M., *Thermochim. Acta* **5**, 117, 1972.
58. Sabbah, R., Chastel, R. and Laffitte, M., *Can. J. Chem.* **52**, 2201, 1974.
59. Murata, S., Sakiyama, M. and Seki, S., *J. Chem. Thermodyn.* **14**, 707, 1982.
60. Meng-Yan, Y. and Pilcher, G., *J. Chem. Thermodyn.* **22**, 893, 1990.
61. Eusébio, E.M., Jesus, A.J.L., Cruz, M.S.C., Leitão, M.L.P. and Redinha, J.S., *J. Chem. Thermodyn.* **35**, 123, 2003.
62. Hilpert, K., *Rapid Comm. Mass Spectr.* **5**, 175, 1991.
63. Drowart, J. and Goldfinger P., *Angew. Chem. Int. Ed.* **6**, 581, 1967.
64. Chatillon, C., Pattoret, A. and Drowart, J., *High Temp. High Press.* **7**, 119, 1975.
65. Korobov, M.V., Skokan, E.V., Borisova, D.Yu. and Khomich, L.M., *Zh. Fiz. Khim.* **70**, 999, 1996.
66. Carson, A.S., in *Thermochemistry and Its Application to Chemical and Biological Systems. NATO ASI Series*, M.A.V. Ribeiro da Silva, ed., Reidel, Dordrecht, pp. 127–141, 1984.
67. Goodrum, J.W. and Siesel, E.M., *J. Therm. Anal.* **46**, 1251, 1996.
68. Boller, A. and Wiedemann, H.G., *J. Therm. Anal. Calorim.* **53**, 431, 1998.
69. Casserino, M., Blevins, D.R. and Sanders, R.N., *Thermochim. Acta* **284**, 145, 1996.
70. Back, D.D., Grzyll, L.R. and Corrigan, M., *Thermochim. Acta* **272**, 53, 1996.
71. Torres-Gomez, L.A., Barreiro-Rodriguez, G. and Galarza-Mondragon, A., *Thermochim. Acta* **124**, 229, 1988.
72. Rojas-Aguilar, A., Orozco-Guareño, E. and Martínez-Herrera, M., *J. Chem. Thermodyn.* **33**, 1405, 2001.
73. Rojas, A. and Orozco, E., *Thermochim. Acta* **405**, 93, 2003.
74. Price, D.M., *Thermochim. Acta* **253**, 367–368, 2001.
75. Price, D.M. and Hawkins, M., *Thermochim. Acta* **315**, 19, 1998.
76. Flynn, J.H. and Dickens, D., *Thermochim. Acta* **15**, 1, 1976.
77. Boublik, T., Fried, V. and Hala, E., *The Vapour Pressure of Pure Substances*, Elsevier, Amsterdam, 1984.
78. Tatavarti, A.S., Dollimore, D. and Alexander, K.S., *Pharm. Sci.* **4**, 45, 2002.
79. Menon, D., Dollimore, D. and Alexander, K.S., *Thermochim. Acta* **237**, 392–393, 2002.
80. Regnault, H.V., *Ann. Chim. (Paris)* **15**, 129, 1845.
81. Verevkin, S.P., Vasiltsova, T.V., Bich, E. and Heintz, A., *Fluid Phase Equibr.* **218**, 165, 2004.
82. Chickos, J.S., in *Molecular Structure and Energetics, Vol 2*, J.F. Liebman and A. Greenberg, eds., VCH Publishers, New York, pp. 67–76, 1987.
83. Chickos, J.S., *Netsu Sokutei* **30**, 116, 2003.
84. Chickos, J.S., Hesse, D., Hosseini, S., Nichols, G. and Webb, P., *Thermochim. Acta* **313**, 101, 1998.
85. Bidleman, T.F., *Anal. Chem.* **56**, 2490, 1984.
86. Koutek, B., Cvacka, J., Streinz, L., Vrkocova, P., Doubsky, J., Simonova, H., Feltl, L. and Svoboda, V., *J. Chromatogr. A* **923**, 137, 2001.
87. Hamilton, D.J., *J. Chromatogr.* **195**, 75, 1980.
88. Spieksma, W., Luijk, R. and Covers, H.A.J., *J. Chromatogr. A* **672**, 141, 1994.
89. van Haelst, A.G., van der Wielen, F.W.M. and Covers, H.A.J., *J. Chromatogr. A* **727**, 265, 1996.
90. Tudor, E., *J. Chromatogr. A* **779**, 287, 1997.
91. Krop, H.B., van Velzen, M.J.M., Parsons, J.R. and Covers, H.A.J., *J. Am. Oil Chem. Soc.* **74**, 309, 1997.
92. Tudor, E., *J. Chromatogr. A* **858**, 65, 1999.
93. Donovan, S.F., *J. Chromatogr. A* **749**, 123, 1996.

94. Chickos, J.S., Hosseini, S. and Hesse, D.G., *Thermochim. Acta* **249**, 41, 1995.
95. Chickos, J.S., Hesse, D.G., Hosseini, S., Liebman, J.F., Mendenhall, G.D., Verevkin, S.P., Rakus, K., Beckhaus, H.D. and Rüchardt, C., *J. Chem. Thermodyn.* **27**, 693, 1995.
96. Chickos, J.S. and Hanshaw, W., *J. Chem. Eng. Data* **49**, 77, 2004.
97. Ruzicka, K. and Majer, V., *J. Phys. Chem. Ref. Data* **23**, 1, 1994.
98. Wadsö, I., *Acta Chem. Scand.* **20**, 536, 1966.
99. Konicek, J., *Acta Chem. Scand.* **27**, 1496, 1973.
100. Svoboda, V., Hynek, V., Vesely, F. and Pick, J., *Collect. Czech. Chem. Commun.* **37**, 165, 1972.
101. Majer, V., Svoboda, V., Hynek, V. and Pick, J., *Collect. Czech. Chem. Commun.* **43**, 1313, 1978.
102. Radosz, M. and Lydersen, A., *Chem. Eng. Tech.* **52**, 756, 1980.
103. Adedeji, F.A., Brown, D.L.S., Connor, J.A., Leug, M., Paz-Andrade, M.I. and Skinner, H.A., *J. Organomet. Chem.* **97**, 221, 1975.
104. Ribeiro Da Silva, M.A.V., Ferrao, M.L.C.C.H. and Jiye, F., *J. Chem. Thermodyn.* **26**, 839, 1994.
105. Kiyobayashi, T. and Minas da Piedade, M.E., *J. Chem. Thermodyn.* **33**, 11, 2001.
106. Viton, C., Chavret, M. and Jose, J., *ELDATA Int. J. Phys. Chem. Data* **2**, 103, 1996.
107. Sevruk, V.M., Simirsky, V.V. and Kabo, G.J., *Zh. Fiz. Khim.* **64**, 3402, 1990.

3 Phase Changes in Pure Component Systems: Liquids and Solids

A. WÜRFLINGER
Physical Chemistry II
Ruhr-Universität Bochum
Bochum, Germany

Measurement of the Thermodynamic Properties of Multiple Phases
R.D. Weir and Th.W. de Loos (Editors)

3 PHASE CHANGES IN PURE COMPONENT SYSTEMS: LIQUIDS AND SOLIDS

The solid–liquid phase transition is thermodynamically first-order, and is therefore characterized by changes in volume and enthalpy (or entropy), which can be used to detect the melting process [1]. Enthalpy changes accompanying phase transitions may be used as standards in calorimetric measurements. An early review of calorimetric methods is given in Ref. [2]. For current developments of heat capacity measurements, the reader is referred to Chapter 7 of Volume VI. Data on heat capacities and entropies, including solid/liquid, for 2500 organic compounds are compiled in [3]. Volume changes on melting can be measured by dilatometric and piezometric methods [4,5]; see also Chapter 5 (density) of Volume VI. Many other physical properties are coupled with a phase transition as well, leading to miscellaneous techniques for the detection of the melting process.

Before expanding on the experimental procedures in more detail, we have to distinguish between various classes of compounds. In general, a crystalline solid melts to an isotropic liquid, thereby losing positional and orientational order. In some cases, a stepwise reduction of these two types of order is observed [6,7]. For example, globular molecules are often able to reorient on their lattice sites far below the melting point without destroying the crystal structure. The onset of such reorientational motion is in general a cooperative process resulting in a solid–solid transition, where the orientational order is lost. This will be treated in the next chapter of this book.

On the other hand, molecules with a strong anisotropic shape may display liquid crystalline phases, where some degree of orientational order is still maintained. Historically, liquid crystals have been classified by Friedel as nematic, smectic or cholesteric [8]. More recently, many other liquid crystalline phases have been discovered to include discotic, cubic or banana-shaped [9–11]. The rich polymorphism observed in liquid crystals means a wealth of phase transitions, which are often investigated simultaneously with the melting process.

The inverse process of the melting is the freezing, which need not necessarily result in the same transition temperature. A liquid may supercool on freezing to yield a glassy state [12] or other metastable solid phases [13]. Reheating of a glass or a metastable solid phase exhibits quite different features. It is therefore indispensable to define clearly the thermal treatment, *viz.* heating or cooling runs and annealing conditions before the measurement. As an example, we show the melting behaviour of carbon tetrachloride [14,15]. On cooling, the liquid freezes to a metastable solid phase I_a. Reheating yields the melting curve $I_a \rightarrow \ell$. Appropriate annealing may transform the solid phase I_a to the stable phase I_b, which melts at a higher temperature as shown in Figure 3.1. It is a general feature that the melting curve of a metastable form is shifted to lower temperatures. Apart from that, the metastability of phase I_a is clearly demonstrated by its spontaneous conversion to I_b during the melting process [15]. Recently, 2,2,2-trichloroethanol was investigated that even revealed three different melting curves [16]. Melting phase diagrams may be much more intricate in multi-component systems. A stable solid phase (*e.g.* fcc) of one component

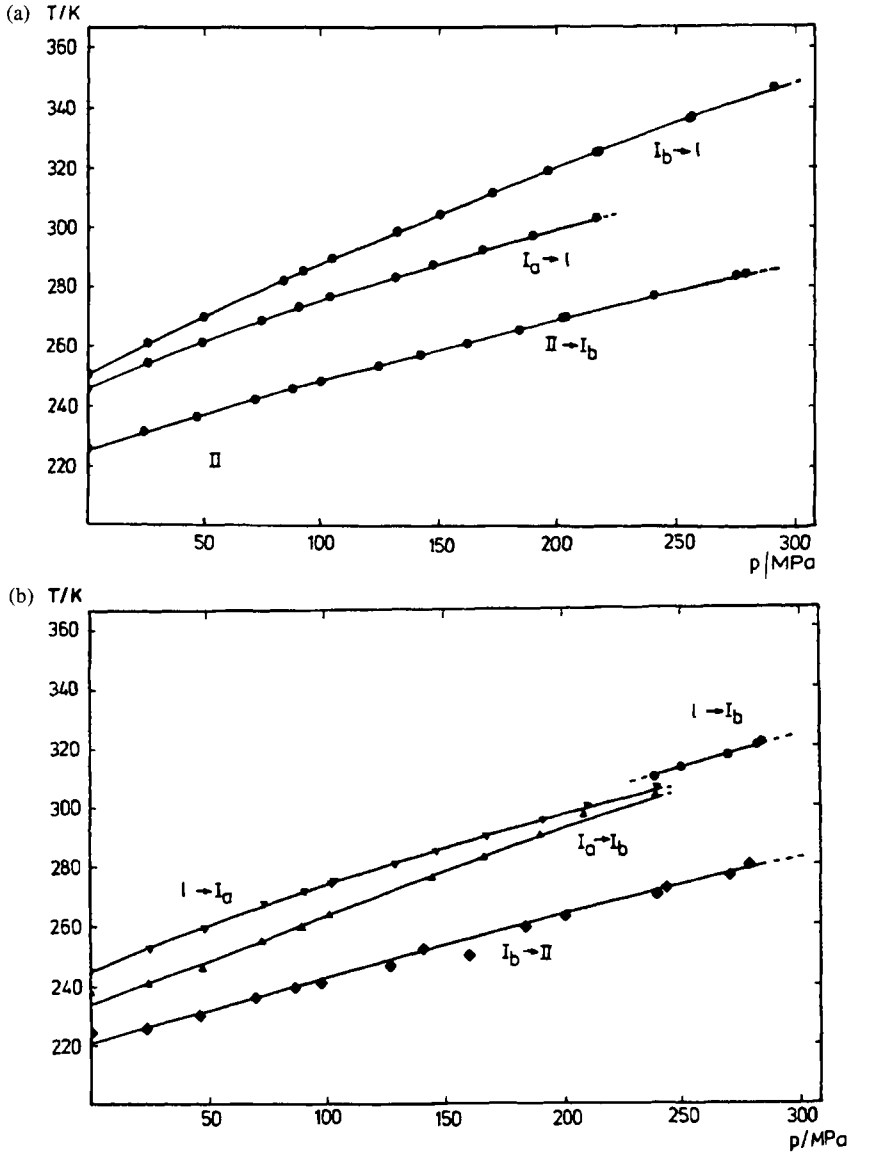

Figure 3.1 Phase diagram of CCl_4: (a) heating, (b) cooling runs.

may be metastable with respect to the other component resulting in crossed isodimorphism in the binary melting diagram [17].

In general, the temperature dependence at constant ambient pressure is considered, which is indeed more easily achieved in comparison with pressure changes. However for any profound understanding of phase transitions, the pressure variable is as important as the influence of temperature. In particular, for "soft" molecular crystals, moderate

pressures may significantly change the phase behaviour and other physical properties [18,19]. Phase diagrams and equations of state for solids have been reported [18,20]. *pVT* data are useful for a full description of thermodynamic properties [21,22]. They enable one to estimate the volume-dependent part of the entropy change at the melting [23] or clearing temperature [24].

Melting curves of compressed gases are of great technological relevance [25]. They are often used as pressure-transmitting media. Moreover, rare gases are good candidates to model melting theories: *e.g.* Solca *et al.* reproduced the melting curves of neon and argon by Monte Carlo simulation [26]; de Konig *et al.* determined the melting curve of argon by a Clausius–Clapeyron method [27]; and Belonoshko *et al.* calculated the melting curve of xenon by molecular dynamics [28]. The melting line of helium is used as a thermometer in low-temperature physics [29]. Modarress *et al.* improved the Lennard–Jones–Devonshire theory for predicting the liquid–solid phase transition [30]. We mention a few results for the melting curves of helium [31–33], neon [33,34], argon [31,35], nitrogen [36,37] and hydrogen [31,38–40].

Polymers usually display a distribution of molar masses, and therefore strictly speaking they are not pure compounds. However, they often exhibit partial crystallinity that places them close to solids. So, we briefly mention just a few of the most recent investigations of their morphology, crystallinity and melting behaviour [41–45] as well as some high-pressure studies including the melting region [46–48]. Equations of state of chain molecular systems have been established [49].

Surface melting [50] can take place when a liquid film is developed on approaching the melting temperature. On the other hand, surface freezing [51] means the formation of a crystalline layer before the bulk freezing point is reached. These interesting phenomena, however, are discounted in this chapter.

3.1 Thermal Methods and Calorimetry

3.1.1 Measurements at Normal Pressure

Adiabatic Calorimetry

Adiabatic calorimetry is one of the classical precision techniques for the determination of enthalpy changes and of heat capacities [2,52–54]. A status report of calorimetric and thermochemical work can be found in a special issue of the *Journal of Chemical Thermodynamics* devoted to experimental methods of thermodynamics [55]. As an example, we mention the calorimetric study of bicyclohexyl, which reveals a series of phase transitions [56]. The equilibrium melting temperatures were measured as a function of fraction of the sample in the liquid state. The resulting triple point temperature was $T_{tp} = (276.83 \pm 0.02)\,K$ with a sample purity of $x = 0.99998$. The enthalpy of fusion $\Delta^{l}_{cr(l)}H_m = 6.859\,kJ \cdot mol^{-1}$ was obtained within a reproducibility of $\pm 10^{-5}$. Energies were measured to a precision of 0.01 per cent, and the temperature resolution was 0.0001 K. Details of the automated and computer-controlled equipment are described in [57].

The calorimetric vessel consists of a platinum inner cylinder with 30 horizontal discs. A surrounding shell provides a uniform temperature profile. Four copper adiabatic shields were controlled to within 1 mK.

Arai *et al.* [58] and Kamae *et al.* [59] designed adiabatic calorimeters for measurements at low temperatures ranging from 20 mK to 25 K. In order to extend the accessible temperature range, an automated calorimeter was constructed, workable in the temperature range from 13 to 530 K [60]. This remarkable temperature range is achieved by using Teflon-insulated wires thereby allowing *in situ* experiments, that is the polymorphism of a substance can be investigated over a wide temperature range without carrying out thermal treatments outside the calorimeter.

Ice Calorimeter

Ditmars [61] gives an account of absolute calorimetric measurements of enthalpies and temperatures of fusion for a number of pure metals starting with zinc for the use of differential scanning calorimetry (DSC) calibration standards. All relative enthalpy measurements were performed with a high-precision ice calorimeter. The melting temperature of zinc (692.745 ± 0.0010) K was obtained with a partial-fusion technique. The accuracy of the enthalpy of fusion (7026 ± 40) $J \cdot mol^{-1}$ is higher than that for previously reported data.

Dynamic Methods

In recent years, dynamic methods such as differential thermal analysis (DTA) and DSC [62–64] have become increasingly popular, as they are especially suitable for small samples. The DTA peak area is roughly proportional to the latent heat evolved in a phase transition; however, quantitative evaluation is limited. The detection of phase transitions can be improved in using derived DTA [5,65]. The DTA can be combined with derivative thermogravimetry to determine melting points of organic acids [66]. Melting is observed as a small peak in the DTG plot of derivative weight against temperature. Both methods yield comparable melting temperatures.

In DSC, the differential energy input between sample and reference yields after integration approximately the enthalpy change of the sample. Callanan *et al.* [67] give a critical comparison of adiabatic calorimetry and DSC. The advantages of DSC are the large accessible temperature range and its acquisition at relatively low cost. However, DSC is not an "absolute" method and it needs suitable reference materials for calibration. Sembira and Dunn [68] describe high-temperature calibration of DTA and DSC using encapsulated samples in quartz. Low heating rates are recommended for the precise determination of heat capacities and enthalpies of transitions [69].

In recent years, new calorimetric methods have been developed, such as temperature-modulated DSC, transitiometry, dynamic and adiabatic scanning calorimetry [53,70–73]. In AC calorimetry, a constant oscillating heating power is imposed on the sample and the resulting temperature oscillations are recorded. This method is particularly useful for the study of pre-transitional effects [74]. In non-adiabatic scanning calorimetry, the power input increases

linearly with time for a certain time interval [75]. It allows the simultaneous measurement of the heat capacity and thermal conductivity. Classical AC calorimetry has a limited frequency window that depends on experimental parameters and sample properties. Honda *et al.* [76] determined the dispersion of the dynamic specific heat of *n*-hexatriacontane. Minakov *et al.* [77] extended the AC technique to higher frequencies (temperature waves transmission spectroscopy) and employed it for simultaneous heat capacity and thermal conductivity measurements of polymers and the liquid crystal 8OCB in the melting region.

Levitation Techniques

Thermophysical measurements on metals, alloys and salts require special methods at high temperatures. Containerless processing techniques have been developed in order to avoid a chemical reaction between the sample and its environment. Baykara *et al.* [78] give a comprehensive review describing various levitation techniques that enable thermophysical measurements up to $T = 4273$ K. Electromagnetic, aerodynamic, electrostatic and acoustic levitation are distinguished. The methods are usually combined with drop calorimetry [79,80] and optical measurement of the temperature [81,82].

Microgravity levitation employed in space labs has turned out to be particularly useful for material processing. Iwasaki *et al.* [83] studied the behaviour of a solid–liquid interface in the supercooled phase during solidification. Crystal growth and temperature distributions were followed by laser interferometry. Wunderlich *et al.* [84] used non-contact modulation calorimetry and electromagnetic heating under ultrahigh vacuum conditions to measure specific heat and enthalpies of fusion for metals and alloys.

Time–Temperature Methods

"Time–temperature" experiments have been widely applied for the determination of the melting behaviour of metals and alloys [5] and organic compounds [85]. Vasilyeva *et al.* [86] report on a new technique for the determination of melting points for A^2B^6 compounds, where A^2 denotes metals of valency 2 (Zn, Cd) and B^6 elements of the group 6 (S, Se, Te). After rapid heating, the melting and evaporation processes were recorded in measurements with an IR photodiode. The variations in the radiation coefficient were connected with the phase transition. Kostanovskii and Kostanovskaya [87] used the thermogram method under laser heating to study the melting of high-temperature materials. The temperature against time curve was measured with a colour pyrometer. The thermograms displayed three characteristic regions below, at and above the melting temperature.

3.1.2 Measurements at High Pressure

Calorimetry

It is difficult to extend classical calorimetry to high pressures because the sample must be enclosed in a container of large mass, and the sample cannot be thermally insulated from the pressure-transmitting medium [88]. Czarnota [89] describes a high-pressure isoperibol

calorimeter for C_p measurements in liquids up to 1200 MPa. The main feature of the construction is to minimize its heat capacity. Later, the system was improved to allow also the evaluation of the enthalpy of liquid–solid transitions [90]. As an example, the author determined the enthalpy of fusion of benzene.

Randzio [91] constructed pressure-controlled scanning calorimeters with power compensation up to 400 MPa. The instrument enables the measurement of the coefficient of thermal expansivity. Furthermore, an example of the isothermal solid-to-liquid transition of benzene is presented. The large volume changes during the phase transition have to be compensated by a special programming system.

DTA and DSC

Both DTA and DSC have been successfully extended to higher pressures, being one of the most convenient methods for the determination of pressure–temperature phase diagrams [5,92,93]. In all cases, it is necessary to prevent the pressure medium from contaminating the sample.

In particular, compressed gases (Ar, He, N_2) are often employed as a pressure medium for studies of molecular crystals at moderate pressures. It was demonstrated that the melting line is significantly altered, if the pressurized gas gets dissolved in the substance [94–96]. Therefore the filled sample capsules, made of indium or lead, are sealed by cold-welding or otherwise closed [94,95]; see Figure 3.2. Maeda *et al.* [97] coated the samples with epoxy adhesives to protect them from the pressure transmitting silicon oil. Rein and Demus [98] designed a DTA apparatus, where the sample is encapsulated in a glass bulb that is submerged in a metallic liquid. Höhne *et al.* [99] developed a power-compensated DSC apparatus that was employed for the investigation of n-alkanes and polymers under pressure. Wagner and Schneider [100] extended the Smit method to elevated pressures of 20 MPa.

Thermobarometry

Buisine and Soulestin [101] have developed a barometric method, which is particularly useful for small quantities. The sample is enclosed in a rigid container of metal. On heating

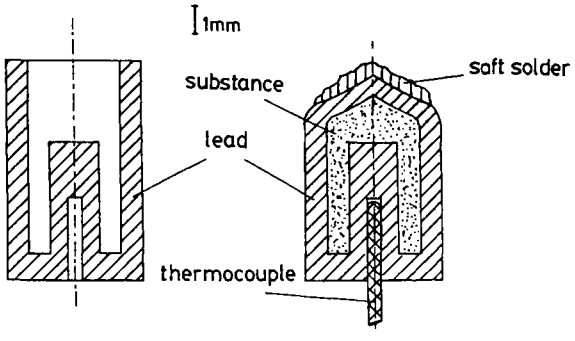

Figure 3.2 DTA high pressure cell.

the cell, its interior pressure increases that can be measured with suitable sensors. The simultaneous recording of temperature against pressure yields the thermobarogram. Outside the transition domain, its slope is $(dp/dT)_V = \alpha/\chi$, α and χ being the thermal expansion coefficient and isothermal compressibility, respectively. If the sample undergoes a first-order transition, the accompanying volume change will cause a significant change of the slope. Thus, the transition can be detected. The authors called this new measuring device a metabolemeter. It was applied to the investigation of many plastic [102] and liquid crystals [103].

Piezothermal Method

Ter Minassian [104] has developed a piezothermal method for the measurements of high-pressure expansivity. The starting point of the method is the thermodynamic relation $(\partial S/\partial p)_T = -\alpha V_m$. By setting $(\partial S/\partial p) \approx (1/T)Q/\Delta p$, the measured quantity is the heat Q liberated during a pressure variation. After corrections for the expansivity of the vessel material, the authors obtained reliable results for the expansivity of the sample with much higher accuracy than obtained in direct volume measurements. Thus, the heat capacity can be derived from the relation: $(\partial C_p/\partial p)_T = -T(\partial^2 V/\partial T^2)_p$. In the case of hexadecane, a remarkable pre-melting was observed. This method was improved for the investigation of weakly first-order transitions in liquid crystals [105].

Thermal Conductivity Measurements

Thermal conductivity, λ, is an important thermophysical property that is related to the thermal diffusivity $a = \lambda/(\rho C_p)$, which is often more convenient to measure. Experimental methods of determining λ under pressure have been reviewed [106]. The hot-wire method was modified for the investigation of solids under high pressure, in which good thermal contact between wire and samples of moderate hardness is achieved [107]. For harder materials, the hot-strip method can be employed [108]. In particular, the behaviour along phase transitions can be studied. On melting, the thermal conductivity decreases considerably and this decrease is less pronounced for orientationally disordered solids. Andersson *et al.* [109] have employed the hot-wire technique for the investigation of various alkanes and plastic crystals.

3.2 Density and Volume Changes

3.2.1 Measurements at Normal Pressure

Density and volume changes can be measured with pycnometers, dilatometers, vibrating tube density meters, with a buoyancy method and piezometers. Volume changes accompanying the melting can be calculated from the densities, which have been independently determined in the solid and liquid phases [5]. However, this chapter is concerned with methods that detect the melting or freezing by a change in density or volume in a single experiment.

Vibrating tube density meters are widely used to determine densities of liquid phases [110]. Freezing of the liquid is usually avoided, and therefore the solid to liquid transition cannot be detected. However, densimeters have been employed successfully for measurements in liquid crystals [111]. Thus, smectic to nematic and nematic to isotropic transitions have been studied [112,113]. Guillon and co-workers [114] investigated several liquid crystals (particularly with smectic phases) using Bekkedahl-type dilatometers. A long calibrated capillary is connected to a cylindrical bulb that contains a known amount of the substance. After degassing the sample, the dilatometer is filled with mercury, the height of which is measured to 0.01 mm after adjustment of the temperature. The dilatometer allows also the determination of the volume changes accompanying first-order phase transitions. Joly and Buisine [115] performed dilatometric measurements with the help of a Michelson's interferometer. Volume changes were derived from modifications of the interference features. The method is particularly suited for very small samples of 0.1 mm^3. Other dilatometric methods employed for liquid crystals have been reviewed by Wedler [111], Bahadur [116] and Grasso *et al.* [117].

Fiske and Stebbins [118] developed a new technique for measuring thermal expansion of liquid inorganic materials at high temperature that should also enable the determination of volume changes due to melting and crystallization. The bottom of the device consists of a chamber containing the sample confined by a molten metal. The top half is a tube graduated by alternating disks of conducting (graphite) and insulating (boron nitride) materials. As the level of the working fluid rises due to volume increase of the sample to be studied, the resistance across the stack of layers drops in a stepwise manner. As an example, the authors measured the thermal expansivity of tin from $T = 708$ to 1718 K with an estimated uncertainty of 5 per cent. High-temperature density measurements can be carried out using the levitation melting technique [78]. Chung *et al.* [119] present a non-contact measurement technique for the density and thermal expansion coefficient of solid and liquid materials. Kimura and Terashima [120] and Rhim *et al.* [121] reviewed thermophysical properties of silicon melt. An anomalous density jump was observed near the melting point. Khairulin *et al.* [122] studied the density of dysprosium fluoride around the melting point with a gamma densimeter.

3.2.2 Measurements at High Pressure

Piezometric methods have been reviewed in detail by Whalley [4], who describes the piezometer as an instrument that determines the compression of a fluid. The volume change caused by pressurizing the system can be measured by the displacement of a piston or the contraction of a bellows cell. The compressed fluid can also be confined by liquid mercury whose meniscus is observed. The volume change of the primary measurement must be carefully corrected from the dilation of the container.

Nelson *et al.* [123] have determined the volume changes for the phase transitions occurring in n-alkanes of mean chain lengths. The sample was enclosed within a capsule of lead that was sealed by a cold-solder technique. The capsule was deposited within a metal bellows, whose remaining volume was filled with a plasticizer. Solid to solid and solid to liquid first-order phase transitions were detected as discontinuities in the dilation of the bellows. Figuière *et al.* [124] used a construction, where the sample was directly filled in the bellows. Sato *et al.* [125] report the results of their measured pVT properties of polymers using a metal

bellows device at temperatures from 313 to 623 K and pressures up to 200 MPa. Calibration of the device was performed with mercury and water. Belonenko *et al.* [126] employed a micro-(pVT) apparatus for measurement of liquid densities up to 500 MPa.

Scaife and Lyons [127] combined a bellows dilatometer with a capacitance cell. Special construction permitted solidification of the sample without serious deformation of the metal. Nevertheless, freezing measurements had to be carried out with great caution. The freezing pressure was approached "from below", thereby exceeding the equilibrium pressure by not more than 5 MPa. The authors used this device to establish the Clausius–Mossotti function for various n-alkanes.

Zoller *et al.* [128] constructed a high-pressure dilatometer using mercury as a confining liquid within the bellows. Additional calibration runs have to be performed, where the sample is replaced by mercury. Using known pVT data of mercury and atmospheric pressure data for the material under investigation (which must be determined in a separate experiment, if necessary) absolute values for the specific volumes as a function of pressure and temperature can be established with an accuracy of (0.001–0.002) $cm^3 \cdot g^{-1}$. In this way, melting properties [129] and the glass transition range [130] of polymers and oligomeric compounds have been determined.

Landau and Wurflinger [131] developed a dilatometer for studying liquid and plastic phases up to 300 MPa (see Figure 3.3). The sample (~2 cm^3) is enclosed in a container of stainless steel, the top of which is closed with a moving piston. Volume changes of the substance cause a displacement of the piston that is recorded inductively. The dilatometer can be calibrated with known pVT data of a reference substance, thus specific volume data with an accuracy of 0.1 per cent can be determined in a way similar as with the Zoller apparatus. However, it is also possible to calibrate with an empty cell using the known compressibility and expansivity of the steel, where the piston is fixed at the upper end of the container [132]. In such a way, isothermal and isobaric calibration runs can be distinguished. In general, isothermal runs are preferred, when the density at atmospheric pressure at the same temperature is known. Otherwise different isotherms must be linked by an isobaric calibration run. At moderate pressures, the measurements can be supplemented with a high-pressure density meter (Anton Paar) [112].

The method was improved in replacing the pressure transmitting gas by compressed oil [133]. The new design allows access to higher temperatures; moreover several runs can be performed with the same filling. pVT data for various orientationally disordered crystals (ODIC) [134] and liquid crystals [135] have been established with the new set-up.

Dollhopf *et al.* [136] constructed a high-pressure dilatometer based on the piston-cylinder principle. Volume data were calculated to form the movement of the Bridgman piston. Contrary to Landau's design, the moving piston has to take up the total pressure. A modified construction was used to determine the pressure dependence of the fusion of indium [137], which serves as a basic standard reference substance. Few other high-pressure dilatometers have been reported for liquid crystals [138–141]. Yamada *et al.* [142] present a calibration method for measuring thermal expansions with a push-rod dilatometer. Measurements of melting points of pure metals for temperature calibration were also carried out. Katayama *et al.* [143] developed a new method by means of X-ray absorption under high pressure using synchrotron radiation. The density was determined from the intensity profile of the transmitted X-rays.

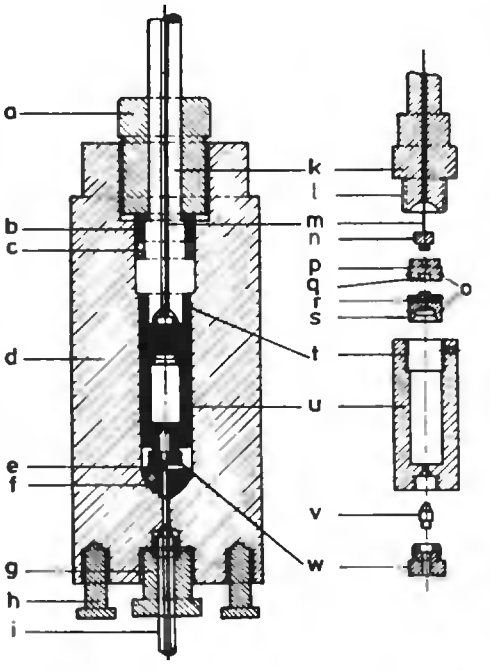

Figure 3.3 High-pressure dilatometer: a – screw cap, b – thrust ring, c – Bridgman sealing, d – pressure vessel, e – thermocouple, f – plastic, g – screw, h – screws for fixing the vessel, i – high pressure capillary tube, k – Bridgman piston, l – thread, m – steel wire, h – screwing, p,s – piston, o – O-rings, q – hollow space, r – indium, t – thread, u – dilatometric cell, v – cone sealing, w – screwing.

3.3 Melting Curves at High Temperatures and Pressures

The determination of melting curves for high-melting inorganic materials requires special techniques. High pressures are achieved with anvil techniques, belt apparatus and shock-wave experiments [25,144,145]. Very often laser-heated diamond cells are used [146–150]. Recent developments are reviewed in [146].

Figure 3.4 shows schematically a diamond cell assembly used for the study of the phase diagram of iron up to $p = 2$ Mbar [147]. Pressures were measured using the ruby fluorescence technique. Temperatures were determined by fitting Planck's radiation function to the spectra. At constant laser power, the largest observed temperature fluctuation at about $T = 3000$ K was 10 K for exposure times of 0.01 s. Melting is observed visually at the onset of convective motion during increasing laser power or with the discontinuous change in the absorption of the laser radiation. The author reports that for all materials studied the melting curves agreed well with those obtained at lower pressures using a piston cylinder apparatus. In a similar way, Godwal *et al.* [148] investigated the melting of lead up to pressures of 1 Mbar and temperatures near 4000 K, and Yoo *et al.* [149] investigated the melting curve of uranium.

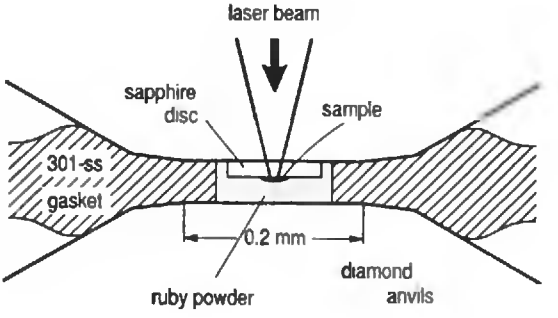

Figure 3.4 The diamond anvil cell.

Jephcoat and Besedin [150] discuss in detail the problems associated with the temperature measurements in diamond anvil techniques. They find an intersection of the melting curves of argon and iron at $p = 47\,\text{GPa}$ and $T = 2750\,\text{K}$, and they propose this as a standard p–T fixed-point. Jeanloz and Kavner [151] critically review the criteria used to detect that melting has taken place in a diamond-cell experiment. In this context, the comparison with experiments by shock wave is particularly important, because they are the only alternative method at very high pressures.

3.4 Miscellaneous Methods

3.4.1 Dielectric Measurements

It is well known that the dielectric constant, ε, of a polar liquid decreases considerably on freezing [152], thus the solid–liquid transition can be easily detected. For polar plastic crystals, the change in ε on freezing is less pronounced, because orientational freedom is retained in the solid "rotator phase" [153]; ε may even increase on freezing. The magnitude of $\Delta\varepsilon$, however, has been often inaccurately determined due to the formation of cracks and holes on solidification. This drawback is avoided in high-pressure experiments in which the holes are squeezed out by the pressure [19,127,154]. For example, a decrease in ε on freezing was reported for *t*-butyl bromide [155]. A re-investigation with a high-pressure cell clearly showed an increase in ε [156]. In order to detect the solid–liquid transition, the capacitor must be rigid enough to withstand crystallization of the substance.

Dielectric relaxation measurements yield the dielectric relaxation time, τ, which displays characteristic changes at a phase transition in particular studies on liquid crystals, have been reviewed [157–159]. In order to measure the complex permittivity, various facilities are required, depending on the frequency range [160,161]. In any case, the influence of lead impedances must be controlled carefully [162].

3.4.2 Ultrasonic Measurements

Ultrasonic measurements have been performed in order to establish melting lines of organic compounds [163]. Crossing the melting line is observed by changes in the attenuation of the

acoustic echoes. The measurements were carried out at constant temperature, starting from the liquid phase and stepwise increasing the pressure, until solidification occurred. Then the pressure is lowered again. The melting pressure was obtained via iterative steps with an accuracy better than 0.05 MPa.

3.4.3 Other Methods

Tiers [164] discussed the visual melting point determination and emphasized the necessity of calibrating the capillary melting point apparatus. He recommended the use of highly pure fixed-point metals (ITS-90) in connection with an oxide-removing flux material. X-ray diffraction was combined with microcalorimetry [165] or polarizing microscopy [166] to study solid–solid and solid–liquid equilibria in pure n-alkanes and alkane mixtures. Pulsed nuclear magnetic resonance (NMR) techniques [167,168] and electrical conductivity measurements [169] have been used for the determination of melting curves.

Acknowledgement

Financial support of the Deutsche Forschungsgemeinschaft is gratefully acknowledged.

References

1. Ubbelohde, A.R., *The Molten State of Matter*, Wiley, Chichester, 1978; Ubbelohde, A.R., *Melting and Crystal Structure*, Clarendon Press, Oxford, 1965; Haase, R. and Schönert, H., *Solid–Liquid Equilibrium*, Pergamon Press, Oxford, 1969.
2. McCullough, J.P. and Scott, D.W., eds., *Experimental Thermodynamics, Vol I: Calorimetry of Non-reacting Systems*, Butterworths, London, 1968.
3. Domalski, E.S. and Hearing, E.D., *J. Phys. Chem. Ref. Data* **25**, 1–525, 1996.
4. Whalley, E., in *Experimental Thermodynamics, Vol II: Experimental Thermodynamics of Non-reacting Fluids*, Ch. 9, B. Le Neindre and B. Vodar, eds., Butterworths, London, pp. 421–500, 1975.
5. Pistorius, C.W.F.T., in *Experimental Thermodynamics, Vol II: Experimental Thermodynamics of Non-reacting Fluids*, Ch. 17, Part 1, B. Le Neindre and B. Vodar, eds., Butterworths, London, pp. 803–834, 1975.
6. Parsonage, N.G. and Staveley, L.A.K., *Disorder in Crystals*, Clarendon Press, Oxford, 1978.
7. Sherwood, J.N., ed., *The Plastically Crystalline State*, Wiley, New York, 1979.
8. Friedel, G., *Ann. Phys.*, **18**, 273, 1922.
9. Demus, D., Goodby, J., Gray, G.W., Spiess, H.W. and Vill, V., *Handbook of Liquid Crystals*, Wiley–VCH, Weinheim, Germany, 1998.
10. Pelzl, G., Diele, S. and Weissflog, W., *Adv. Mater.* **11**, 707, 1999; Wirth, I., Diele, S., Eremin, A., Pelzl, G., Grande, S., Kovalenko, L., Pancenko, N. and Weissflog, W., *J. Mater. Chem.* **11**, 1642, 2001.
11. Stegemeyer, H., in *Topics in Physical Chemistry, Vol. 3*, H. Baumgärtel, E.U. Franck and W. Grünbein, eds., Steinkopff, Darmstadt, Springer, New York, 1994.
12. Angell, C.A., *J. Phys. Chem. Solids* **49**, 863, 1988; Angell, C.A., *J. Non-Cryst. Solids* **13**, 131–133, 1991; Ediger, M.D., Angell, C.A. and Nagel, S.R., *J. Phys. Chem.* **100**, 13200, 1996.

13. Suga, H. and Seki, S., *Faraday Disc.* **69**, 221, 1980.
14. Bean, V.E. and Wood, S.D., *J. Chem. Phys.* **72**, 5838, 1980.
15. Bardelmeier, U. and Würflinger, A., *Thermochim. Acta* **143**, 109, 1989.
16. Jenau, M., Sandmann, M., Würflinger, A. and Tamarit, J.L., *Z. Naturforsch* **52a**, 493, 1997.
17. Pardo, L.C., Barrio, M., Tamarit, J.L., Lopez, D.O., Salud, J., Negrier, P. and Mondieig, D., *Phys. Chem. Chem. Phys.* **3**, 2644, 2001; Pardo, L.C., Barrio, M., Tamarit, J.L., Negrier, P., Lopez, D.O., Salud, J. and Mondieig, D., *J. Phys. Chem. B* **105**, 10326, 2001.
18. Hemley, R.J., *Ann. Rev. Phys. Chem.* **51**, 763, 2000; Hemley, R.J. and Dera, P., in *Rev. Min. Geochem.*, R.M. Hazen and R.T. Downs, eds., **41**, 335, 2000.
19. Würflinger, A., *Int. Rev. Phys. Chem.* **12**, 89, 1993.
20. Holzapfel, W.B., *High Pressure Res.* **22**, 209, 2002; ibid **16**, 81, 1998; Holzapfel, W.B., Hartwig, M. and Reiß, G., *J. Low Temp. Phys.* **122**, 401, 2001; Holzapfel, W.B., Hartwig, M. and Reiß, G., *Z. Kristallogr.* **216**, 473, 2001.
21. Randzio, S.L., *Thermochim. Acta* **300**, 29, 1997.
22. Würflinger, A. and Urban, S., in *Relaxation Phenomena*, W. Haase and S. Wrobel, eds., Springer, Heidelberg, p. 71, 2003.
23 Abe, A., Takeda, T., Hiejima, T. and Furuya, H., *Macromolecules* **34**, 6450, 2001.
24. Würflinger, A. and Sandmann, M., in *Physical Properties of Liquid Crystals: Nematics, Vol 1*, D.A. Dunmur, A. Fukuda and G.R. Luckhurst, eds., Institution of Electrical Engineers, London, p. 151, 2001.
25. Hemley, R.J., ed., *Reviews in Mineralogy: Ultrahigh-Pressure Mineralogy*, Mineralogical Soc. Am., Washington, DC, p. 37, 1998; Russel, J.H., *Rev. Mineralogy: Ultrahigh-Pressure Mineralogy*, Mineralogical Soc. Am., Washington, DC, 1993.
26. Solca, J., Dyson, A.J., Steinebrunner, G., Kirchner, B. and Huber, H.J., *Chem. Phys.* **108**, 4107, 1998; Solca, J., Dyson, A.J., Steinebrunner, G., Kirchner, B. and Huber, H.J., *Chem. Phys.* **224**, 253, 1997.
27. de Konig, M., Antonelli, A. and Yip, S., *J. Chem. Phys.* **115**, 11025, 2001.
28. Belonoshko, A.B., Ahuja, R. and Johansson, B., *Phys. Rev. Lett.* **87**, 1–4, 2001: art. no. 165505 (Oct. 15).
29. Schuster, G. and Wolber, L., *J. Phys. E: Sci. Instrum.* **19**, 701, 1986.
30. Modarress, H., Ahmadnia, E. and Mansoori, G.A., *J. Chem. Phys.* **111**, 10236, 1999.
31. Datchi, F., Loubeyre, P. and Letoullec, R., *Koatsuryoku no Kagaku to Gijutsu* **7**, 778, 1998.
32. Vos, W.L., Van Hinsberg, M.G.E. and Schouten, J.A., *Phys. Rev. B: Condens. Matter* **42**, 6106, 1990.
33. Loubeyre, P., LeToullec, R. and Pinceaux, J.P., *Phys. Rev. Lett.* **70**, 2106, 1993.
34. Vos, W.L., Schouten, J.A., Young, D.A. and Ross, M., *J. Chem. Phys.* **94**, 3835, 1991.
35. Zha, C.S., Boehler, R., Young, D.A. and Ross, M., *J. Chem. Phys.* **85**, 1034, 1986.
36. Vos, W.L. and Schouten, J.A., *J. Chem. Phys.* **91**, 6302, 1989.
37. Mills, R.L., Liebenberg, D.H. and Bronson, J.C., *J. Chem. Phys.* **63**, 4026, 1975.
38. Young, D.A. and Ross, M., *J. Chem. Phys.* **74**, 6950, 1981.
39. Udovidchenko, B.G., Eselson, V.B. and Manzhelii, V.G., *High Temp. -USSR* **31**, 687, 1993.
40. Manzheli, V.G., Udovidchenko, B.G. and Eselson, V.B., *Fiz Nizk Temp. (Kiev)* **1**, 799, 1975.
41. Schick, C., Wurm, A., Merzlyakov, M., Minakov, A. and Marand, H., *J. Therm. Anal. Calorim.* **64**, 549, 2001; Wurm, A., Merzlyakov, M. and Schick, C., *J. Therm. Anal. Calorim.* **60**, 807, 2000.
42. Schmidtke, J., Strobl, G. and Thurn-Albrecht, T., *Macromolecules* **30**, 5804, 1997.
43. Okazaki, I. and Wunderlich, B., *Macromol. Rapid Commun.* **18**, 313, 1997.
44. Androsch, R. and Wunderlich, B., *Macromolecules* **34**, 8384, 5950, 2001; Pak, J. and Wunderlich, B., *Macromolecules* **34**, 4492, 2001; Wunderlich, B., *J. Thermal Anal.* **49**, 513, 1997.

45. Marand, H., Xu, J. and Srinivas, S., *Macromolecules* **31**, 8219, 1998.
46. Höhne, G.W.H., Schawe, J.E.K. and Shulgin, A.I., *Thermochim. Acta* **296**, 1, 1997.
47. Nies, E., *Nato Asi. Ser. Ser. C* **401**, 201, 1993. *Chem. Abstr.* **121**, 36592.
48. Kojima, Y., Takahara, M., Matsuoka, T. and Takahashi, H., *J. Appl. Polymer Sci.* **80**, 1046, 2001.
49. Arora, R.K., Jain, R.K. and Nanda, V.S., *J. Polym. Sci. Pol. Phys.* **39**, 515, 2001; Utracki, L.A. and Simha, R., *Macromol. Theory. Simul.* **10**, 17, 2001.
50. Sondergard, E., Kofman, R., Cheyssac, P., Celestini, F., Ben David, T. and Lereah, Y., *Surf. Sci.* **388**, 1115, 1997.
51. Gang, O., Wu, X.Z., Ocko, B.M., Sirota, E.B. and Deutsch, M., *Phys. Rev. E* **58**, 6086, 1998.
52. McGlashan, M.L., *Chemical Thermodynamics, A Specialist Periodical Report, Vol 1*, The Chemical Society, London, 1973.
53. Randzio, S.L., in *Annual Reports on the Progress of Chemistry*, The Royal Society of Chemistry, p. 433, 1998.
54. Hemminger, W.F. and Höhne, G.W.H., *Calorimetry, Fundamentals and Practice*, Verlag–Chemie, Weinheim, 1984.
55. See special issue about experimental thermodynamics in *J. Chem. Thermodyn.* **30**, 1421–1631, 1998.
56. Chirico, R.D., Cowell, A.B., Good, W.D., Klots, T.D., Knipmeyer, S.E., Nguyen, A., Rau, A.P., Reynolds, J.W., Smith, N.K. and Steele, W.V., *J. Chem. Thermodyn.* **30**, 1423, 1998.
57. Steele, W.V., Archer, D.G., Chirico, R.D., Collier, W.B., Hossenlopp, I.A., Nguyen, A., Smith, N.K. and Gammon, B.E., *J. Chem. Thermodyn.* **20**, 1233–1264, 1988.
58. Arai, N., Sorai, M., Suga, H. and Seki, S., *Bull. Chem. Soc. Jpn.* **50**, 1702, 1977; Murakawa, S., Wakamatsu, T., Nakano, M., Sorai, M. and Suga, H., *J. Chem. Thermodyn.* **19**, 1275, 1987.
59. Kamae, R., Suenaga, K., Matsuo, T. and Suga, H., *J. Chem. Thermodyn.* **33**, 471, 2001.
60. Sorai, M., Kimura, K., Weiss, A. and Strauss, R., *J. Chem. Thermodyn.* **30**, 1441, 1998; Sorai, M., Kaji, K. and Kaneko, Y., *J. Chem. Thermodyn.* **24**, 167, 1992.
61. Ditmars, D.A., *J. Chem. Thermodyn.* **22**, 639, 1990.
62. Hemminger, W.F. and Cammenga, H.K., *Methoden der thermischen Analyse*, Springer, Berlin, 1989.
63. Höhne, G.W.H., Hemminger, W.F. and Flammersheim, H.J., *Differential Scanning Calorimetry*, Springer, Berlin, 1996.
64. Schultze, D., *Differentialthermoanalyse*, Verlag–Chemie, Weinheim, 1969.
65. Kleinhans, H.D., Konrad, R. and Schneider, G.M., *Thermochim. Acta* **61**, 371, 1983; Kleinhans, H.D. and Schneider, G.M., *Thermochim. Acta* **69**, 229, 1983.
66. O'Connel, A. and Dollimore, D., *Instrum. Sci. Technol.* **27**, 13, 1999.
67. Callanan, J.E., McDermott, K.M., Weir, R.D. and Westrum Jr., E.F., *J. Chem. Thermodyn.* **24**, 233, 1992; Callanan, J.E., *J. Therm. Anal.* **45**, 359, 1995.
68. Sembira, A.N. and Dunn, J.G., *Thermochim. Acta* **274**, 113, 1996.
69. Nakasone, K., Takamizawa, K., Shiokawa, K. and Urabe, Y., *Thermochim. Acta* **233**, 175, 1994.
70. Wunderlich, B., *Thermochim. Acta* **355**, 43, 2000; Hu, W. and Wunderlich, B., *J. Thermal Anal. Calorim.* **66**, 677, 2001; Boller, A., Ribeiro, M. and Wunderlich, B., *J. Therm. Anal.* **54**, 545, 1998.
71. Schick, C. and Höhne, G.W.H., *Thermochim. Acta* **377**, 1–2, 2001.
72. Randzio, S.L., *J. Therm. Anal.* **48**, 573, 1997; Randzio, S.L., *Chem. Soc. Rev.* **25**, 383, 1996.
73. Wilken, M., Fischer, K. and Gmehling, J., *Chem. Ing. Techn.* **73**, 1300, 2001.
74. Thoen, J. in *Handbook of Liquid Crystals, Vol 1*, D. Demus, J. Goodby, G.W. Gray, H.W. Spiess and V. Vill, eds., Wiley–VCH, Weinheim, Germany, p. 310, 1998.

75. Yao, H., Chan, T. and Garland, C.W., *Phys. Rev. E* **51**, 4585, 1995.
76. Honda, H., Ogura, H. and Chiba, A., *Meas. Sci. Technol.* **13**, 1, 2002; Honda, H., Tasaki, S., Chiba, A. and Ogura, H., *Phys. Rev. B* **65**, 104112, 2002.
77. Minakov, A., Bugoslavsky, Yu.V. and Schick, C., *Thermochim. Acta* **317**, 117, 1998.
78. Baykara, T., Hauge, R.H., Norem, N., Lee, P. and Margrave, J.L., *High Temp. Sci.* **32**, 113, 1994 (*Volume Date 1991*).
79. Frohberg, M.G., *Thermochim. Acta* **69**, 299, 1983.
80. Kleykamp, H., *Thermochim. Acta* **287**, 191, 1996.
81. McFarlane, J. and LeBlanc, J.C., *High Temp. High Press.* **26**, 605, 1994.
82. Hiernaut, J.P., Sakuma, F. and Ronchi, C., *High Temp. High Press.* **21**, 139, 1989.
83. Iwasaki, A., Hosokawa, S. and Kudo, I., *J. Thermophys. Heat Trans.* **9**, 537, 1995; Iwasaki, A., Kudo, I., Arai, Y., Kawai, T., Watanabe, T. and Takei, H., *Eur. Space Agency, [Spec. Publ.] ESA SP* (1994), ESA SP-1132 (*Vol 4* Final Reports of Sounding Rocket Experiments in Fluid Science and Materials Sciences), p. 123.
84. Wunderlich, R.K., Lee, D.S., Johson, W.L. and Fecht, H.J., *Phys. Rev. B* **55**, 26, 1997.
85. Ott, J.B. and Goates, J.R., *J. Chem. Eng. Data* **41**, 669, 1996.
86. Vasilyeva, I.G., Belyaeva, E.I. and Gibner, Ya.I., *J. Therm. Anal. Calorim.* **52**, 403, 1998.
87. Kostanovskii, A.V. and Kostanovskaya, M.E., *High Temp (Teplofiz Vys Temp.)* **36**, 897, 1998.
88. Loriers-Susse, C., *High Temp.-High Press.* **12**, 119, 1980.
89. Czarnota, I., *J. Chem. Thermodyn.* **23**, 25, 1991; Czarnota, I., *Bull. Acad. Polon. Sci. Ser. Sci. Chim.* **27**, 763, 1979.
90. Czarnota, I., *Meas. Sci. Technol.* **5**, 1345, 1994.
91. Randzio, S.L., *J. Phys. E Sci. Instrum.* **16**, 691, 1983; Randzio, S.L., *J. Phys. E Sci. Instrum.* **17**, 1058, 1984; Randzio, S.L., Grolier, J.P.E. and Quint, J.R., *Rev. Sci. Instrum.* **65**, 960, 1994.
92. Schneider, G.M. *Thermochim. Acta* **88**, 159, 1985; Schmidt, C., Rittmeier-Kettner, M., Becker, H., Ellert, J., Krombach, R. and Schneider, G.M., *Thermochim. Acta* **238**, 321, 1994.
93. Chandrasekhar, S. and Shashidhar, R., *Adv. Liq. Cryst.* **4**, 83, 1979.
94. Bartelt, S. and Schneider, G.M., *Rev. Sci. Instrum.* **60**, 926, 1989.
95. Würflinger, A. and Schneider, G.M., *Ber. Bunsenges. Phys. Chem.* **77**, 121, 1973.
96. Krombach, R. and Schneider, G.M., *Thermochim. Acta* **231**, 169, 1994.
97. Maeda, Y., Cheng, G.P., Kutsumizu, S. and Yano, S., *Liq. Cryst.* **28**, 1785, 2001.
98. Rein, C., Demus, D. *Thermochim. Acta* **237**, 133, 1994.
99. Höhne, G.W.H., Rastogi, S. and Wunderlich, B., *Polymer* **41**, 8869, 2000; Höhne, G.W.H., *Thermochim. Acta* **332**, 115, 1999; Höhne, G.W.H. and Blankenhorn, K., *Thermochim. Acta* **238**, 351, 1994.
100. Wagner, B. and Schneider, G.M., *Thermochim. Acta* **274**, 179, 1996.
101. Buisine, J.M. and Soulestin, B., *Rev. Phys. Appl.* **22**, 1211, 1987; Buisine, J.M., Soulestin, B. and Billard, J., *Mol. Cryst. Liq. Cryst.* **91**, 115, 1983.
102. Tamarit, J.L., Legendre, B. and Buisine, J.M., *Mol. Cryst. Liq. Cryst.* **250**, 347, 1994.
103. Daoudi, A., Longuemart, S., Roussel, F., Kolinsky, C. and Bayle, J.P., *Liq. Cryst.* **28**, 291, 2001; Anakkar, A., Isaert, N., Buisine, J.M. and Nguyen, H.A.T., *Ferroelectrics* **212**, 231, 1998.
104. Ter Minassian, L. and Pruzan, P., *J. Chem. Thermodyn.* **9**, 375, 1977; Pruzan, P., Ter Minassian, L., Figuiere, P. and Szwarc, H., *Rev. Sci. Instrum.* **47**, 66, 1976; Ter Minassian, L. and Millou, F., *J. Phys. E Sci. Instrum.* **16**, 450, 1983.
105. Anakkar, A., Buisine, J.M., Alba-Simionesco, C., Ter Minassian, L., Nguyen, H.A.T. and Destrade, C., *J. Phys. III* **2**, 1029, 1992.
106. Bäckström, G., *High Temp.-High Press.* **17**, 185, 1985; Bäckström, G., *XIII AIRAPT-International Conference on High Pressure and Technolgy*, p. 445, 1991.

107. Hakansson, B., Andersson, P. and Bäckström, G., *Rev. Sci. Instrum.* **59**, 2269, 1988; Andersson, P., *J. Phys. Chem. Solids* **39**, 65, 1978.
108. Andersson, S. and Bäckström, G., *Rev. Sci. Instrum.* **57** 1633, 1986.
109. Andersson, O., Ross, R.G. and Bäckström, G., *Mol. Phys.* **66**, 619, 1989; Forsman, H. and Andersson, P., *J. Chem. Phys.* **80**, 2804, 1984.
110. Majer, V., Crovetto, R. and Wood, R.H., *J. Chem. Thermodyn.* **23**, 333, 1991.
111. Wedler, W., in *Handbook of Liquid Crystals, Vol 1*, D. Demus, J. Goodby, G.W. Gray, H.W. Spiess and V. Vill, eds., Wiley–VCH, Weinheim, Germany, p. 334, 1998.
112. Sandmann, M. and Würflinger, A., *Z. Naturforsch. A* **53**, 787, 1998.
113. Dunmur, D.A. and Miller, W.H., *J. Physique Coll. C3*, **40**, 141, 1979.
114. Guillon, D. and Skoulios, A., *Mol. Cryst. Liq. Cryst.* **39**, 139, 1977; Abied, H., Guillon, D., Skoulios, A., Giroud-Godquin, A.M., Maldivi, P. and Marchon, J.C., *Coll. Polym. Sci.* **266**, 579, 1988; Bruce, D.W., Estdale, S., Guillon, D. and Heinrich, B., *Liq. Cryst.* **19**, 301, 1995.
115. Joly, G. and Buisine, B.M., *J. Therm. Anal.* **37**, 2483, 1991.
116. Bahadur, B., *J. Chim. Phys. Phys.-Chim. Biol.* **73**, 255, 1976.
117. Grasso, D., Fasone, S., Di Pasquale, G. and Castelli, F., *Thermochim. Acta* **140**, 31, 1989.
118. Fiske, P.S. and Stebbins, F., *Rev. Sci. Instrum.* **65**, 3258, 1994.
119. Chung, S.K., Thiessen, D.B. and Rhim. W.K., *Rev. Sci. Instrum.* **67**, 3175, 1996.
120. Kimura, S. and Terashima, K., *J. Cryst. Growth* **180**, 323, 1997.
121. Rhim, W.K., Chung, S.K., Rulison, A.J. and Spjut, R.E., *Int. J. Thermophys.* **18**, 459, 1997.
122. Khairulin, R.A., Stankus, S.V. and Tyagel'skii, P.V., *Inorg. Mater.* **34**, 742, 1998.
123. Nelson, R.R., Webb, W. and Dixon, J.A., *J. Chem. Phys.* **33**, 1756, 1960.
124. Figuière, P., Fuchs, A.H., Ghelfenstein, M. and Szwarc, H., *J. Phys. Chem. Solids* **39**, 19, 1978.
125. Sato, Y., Yamasaki, Y., Takishima, S. and Masuoka, H., *J. Appl. Polym. Sci.* **66**, 141, 1997.
126. Belonenko, V.N., Troitsky, V.M., Belyaev, Y.E., Dymond, J.H. and Glen, N.F., *J. Chem. Thermodyn.* **32**, 1203, 2000.
127. Scaife, W.G.S. and Lyons, C.G.R., *J. Chem. Thermodyn.* **17**, 623, 1985.
128. Zoller, P., Bolli, P., Pahud, V. and Ackermann, H., *Rev. Sci. Instrum.* **47**, 948, 1976; Fakhreddine, Y.A. and Zoller, P., *J. Polym. Sci. B: Polym. Phys.* **32**, 2445, 1994.
129. Lill, H., Rudolf, B. and Cantow, H.J., *Polym. Bull. (Berlin)* **30**, 321, 1993.
130. Eckstein, A. and Schneider, H.A., *J. Therm. Anal.* **46**, 973, 1996.
131. Landau, R. and Würflinger, A., *Rev. Sci. Instrum.* **51**, 533–535, 1980.
132. Riembauer, M., Schulte, L. and Würflinger, A., *Z. Phys. Chem. (Frankfurt) NF* **166**, 53, 1990.
133. Würflinger, A., Sandmann, M. and Weissflog, W., *Z. Naturforsch* **55a**, 823, 2000.
134. Würflinger, A., Mondieig, D., Rajabalee, F. and Cuevas-Diarte, M.A., *Z. Naturforsch.* **56a**, 626, 895, 2001; Würflinger, A. and Pardo, L.C., *Z. Naturforsch.* **57a**, 177, 2002.
135. Würflinger, A. and Urban, S., *Liq. Cryst.* **29**, 799, 2002; Würflinger, A. and Urban, S., *Phys. Chem. Chem. Phys.* **3**, 3727, 2001.
136. Dollhopf, W., Grossmann, H.P. and Leute, U., *Coll. Polym. Sci.* **259**, 267, 1981; Leute, U. and Dollhopf, W., *Coll. Polym. Sci.* **261**, 299, 1983; Leute, U., Dollhopf, W. and Liska, E. *Coll. Polym. Sci.* **254**, 237, 1976; ibid **256**, 914, 1978.
137. Höhne, G.W.H., Dollhopf, W., Blankenhorn, K. and Mayr, P.U., *Thermochim. Acta* **273**, 17, 1996.
138. Kuss, E., *Mol. Cryst. Liq. Cryst.* **76**, 199, 1981.
139. Doerrer, H.L., Kneppe, H. and Schneider, F., *Liq. Cryst.* **11**, 905, 1992.
140. Pollmann, P., in *Handbook of Liquid Crystals, Vol 1*, D. Demus, J. Goodby, G.W. Gray, H.W. Spiess and V. Vill, eds., Wiley–VCH, Weinheim, Germany, p. 355, 1998.
141. van Hecke, G. in *Physical Properties of Liquid Crystals: Nematics, Vol 1*, D.A. Dunmur, A. Fukuda and G.R. Luckhurst, eds., Institution of Electrical Engineers, London, p. 127, 2001.

142. Yamada, N., Abe, R. and Okaji, M., *Meas. Sci. Technol.* **12**, 2121, 2001.
143. Katayama, Y., Tsuji, K., Shimomura, O., Kikegawa, T., Mezoua, M., Martinez-Garcia, D., Besson, J.M., Häuserman, D. and Hanfland, M., *J. Synchrotron Radiat.* **5**, 1023, 1998.
144. Gupta, S.C., *Bull. Mater. Sci.* **22**, 295, 1999.
145. Dlott, D.D., *Ann. Rev. Phys. Chem.* **50**, 251 1999.
146. Proceedings of advances in laser heated diamond cell techniques; *Rev. Sci. Instrum.* **72**(2), 1269–1599, 2001.
147. Boehler, R., *Nature* **363**, 534, 1993; Boehler, R., *Philos. Trans. R. Soc. A* **354**, 1265, 1996.
148. Godwal, B.K., Meade, C., Jeanloz, R., Garcia, A., Liu, A.Y. and Cohen, M.L., *Science* **248**, 462, 1990.
149. Yoo, C.S., Cynn, H. and Soderlind, P., *Phys. Rev. B* **57**, 10359, 1998.
150. Jephcoat, A.P. and Besedin, S.P., *Philos. Trans. R. Soc. A* **354**, 1333, 1996.
151. Jeanloz, R. and Kavner, A., *Philos. Trans. R. Soc. A* **354**, 1279, 1996.
152. Hill, N.E., Vaughan, W.E., Price, A.H., and Davies, M., in *Dielectric Properties and Molecular Behaviour*, T.M. Sugden, ed., van Nostrand, London, 1969.
153. Pethrick, R.A., in *The Plastically Crystalline State*, J.N. Sherwood, ed., Wiley, New York, p. 123, 1979.
154. Whalley, E., Jones, S.J. and Gold, L.W., eds., *Physics and Chemistry of Ice*, 1973.
155. Urban, S., *Adv. Mol. Relax. Int. Proc.* **21**, 221, 1981.
156. Kreul, H.G., Hartmann, M., Edelmann, R., Würflinger, A. and Urban, S., *Ber. Bunsenges. Phys. Chem.* **93**, 612, 1989.
157. Urban, S. and Würflinger, A., *Adv. Chem. Phys.* **98**, 143, 1997.
158. Kresse, H., *Adv. Liq. Cryst.* **6**, 109, 1983; Kresse, H. *Fortschr. Phys.* **30**, 507, 1982.
159. de Jeu, W.H., *Physical Properties of Liquid Crystalline Materials*, Gordon and Breach, London, 1980.
160. Scaife, B.K.P., *Complex Permittivity, Theory and Experiment*, The English Universities Press Ltd., London, 1971.
161. Edelmann, R., Würflinger, A., v. Hornhardt, S. and Stockhausen, M., *Z. Naturforsch. A* **48**, 1231, 1993.
162. Scaife, W.G.S. and Vij, J.K., *J. Phys. E* **9**, 735, 1976.
163. Sun, T.F., Kortbeek, P.J., Biswas, S.N., Trappeniers, N.J. and Schouten, J.A., *Ber. Bunsenges. Phys. Chem.* **91**, 1013, 1987; Sun, T.F., Schouten, J.A., Trappeniers, N.J. and Biswas, S.N., *Ber. Bunsen. Ges. Phys. Chem.* **92**, 652, 1988.
164. Tiers, G.V.D., *Anal. Chim. Acta* **237**, 241, 1990.
165. Mondieig, D., Espeau, P., Roblès, L., Haget, Y., Oonk, H.A.J. and Cuevas-Diarte, M.A., *J. Chem. Soc. Farad. T.* **93**, 3343, 1997; Oonk, H.A.J. and Tamarit, J.Ll., in *Experimental Thermodynamics VII: Measurement of the Thermodynamic Properties of Multiple Phases*, Ch. 9, Th.W. de Loos and R.D. Weir, eds., Elsevier, Amsterdam, pp. 201–274, 2005.
166. Asano, T., *Polym. Bull.* **12**, 543, 1984; ibid **10**, 547, 1983.
167. Ross, S.M. and Strange, JH., *Mol. Cryst. Liq. Cryst.* **36**, 321, 1976.
168. Woznyj, M., Prielmeier, F.X. and Lüdemann, H.D., *Z. Naturforsch. A* **39**, 800, 1984.
169. Greuling, R., *Exp. Techn. Phys.* **36**, 147, 1988.

4 Pure Component Phase Changes: Solid and Solid

K.A. SOSIN[§] and R.D. WEIR
Department of Chemistry and Chemical Engineering
Royal Military College of Canada
Kingston, Canada

The white rabbit put on his spectacles. 'Where shall I begin, please your majesty?' he asked. 'Begin at the beginning', the king said gravely, 'and go till you come to the end: then stop'.

Alice's Adventures in Wonderland, Chapter 12
By Lewis Carroll

[§] Deceased.

Measurement of the Thermodynamic Properties of Multiple Phases
R.D. Weir and Th.W. de Loos (Editors)

4 PURE COMPONENT PHASE CHANGES: SOLID AND SOLID

In the past few decades, research in solid–solid phase transitions, also called *structural phase transformations*, has been active, resulting in well-developed theory and advanced experimental methods. In the limited space of this chapter, our aim is to present only the fundamentals of the discipline and to review selectively the latest literature of the subject.

4.1 Classification of Solid–Solid Phase Transitions

As the name implies, solid–solid phase transitions are associated with changes in the structure of solids. The symmetry aspects of such transitions are fully reflected in the structures of the two or more phases. The high-symmetry phase, usually that at high temperature, is called *prototypic*. Every structural phase transformation is associated with a change in a long-range order parameter η [1]. The order parameter η is non-zero below T_{trs}, the phase-change temperature, and increases on cooling. It becomes zero at T_{trs} and remains zero at $T \geq T_{trs}$. The nature of the order parameter depends on the nature of transition. For instance, in ferroelectric transitions, the polarization P serves as the order parameter.

Solid-phase transformations may occur in two distinctively different ways. One takes place when the bonds holding together atomic or molecular units break completely to form a new structure, totally unrelated to the initial one. Such transitions are called *reconstructive* and their examples are the transformation of graphite into diamond and that of amorphous silica to the crystalline form. Reconstructive transitions are not covered within this chapter. A second type of transformation occurs when a regular lattice changes only slightly, without breaking the links of the network, so that the final structure remains closely related geometrically to the original. Such transitions may take place either through *small displacements*, translational and/or rotational, of the lattice's atomic or molecular units or through changes in *ordering* of such units between equivalent lattice positions. The two types of transitions are primarily driven by order parameters that are mainly atomic. There is, also, another type of non-reconstructive structural phase transitions involving an order parameter linked to electron–lattice interactions, known as *electronic* phase transformations. All three categories are, in fact, idealizations of real transitions, which usually have a 'mixed' character and involve elements of more than one type.

Purely displacive phase transitions can be divided into three subgroups: (a) *Ferrodistortive*, whose displacements are associated with an optic phonon having long wavelength and, therefore, wave vector $\mathbf{k} \approx 0$. They lead to a new phase with the primitive cell having the same number of atoms or formula units. (b) *Anti-ferrodistortive*, with displacements corresponding to an optic phonon of short wavelength (zone boundary), with the number of atoms, or formula units, in the low-temperature phase being a multiple of that number in the prototypic phase. (c) *Thermoelastic*, whose displacements are linked with an acoustic phonon of a long wavelength, represented by a macroscopic strain component.

In many systems, the primary order parameter or distortion has a wave vector that cannot be expressed as a simple rational fraction of a reciprocal lattice vector. The resulting phase

does not have strict translational symmetry and is not exactly crystalline. Transitions of this kind are called *incommensurate.*

Transitions in molecular and molecular-ionic crystals often involve a significant order–disorder component, even if dominated by displacive phenomena. For instance, the KCN crystal is orientationally disordered at temperatures above T_{trs} but, as temperature decreases, ordering leads to rotational–translational coupling and the displacive component becomes prevalent.

The primary order parameter in electronic transitions is a low-energy, degenerate electronic state. If such a state couples with acoustic degrees of freedom, a Jahn–Teller phase transition results, which can occur either at a localized or delocalized level. In the latter case, the transition is called a *band JT transition.*

The behaviour of the order parameter η in the vicinity of T_{trs} provides the basis for distinguishing between first- and second-order phase transitions. In second-order transitions, η decreases smoothly to zero, while in the first-order transitions it collapses rapidly at T_{trs} as shown schematically in Figures 4.1 and 4.2. Based on experiments, one can only classify a transition as 'nearly second order' since a small jump in order parameter may always

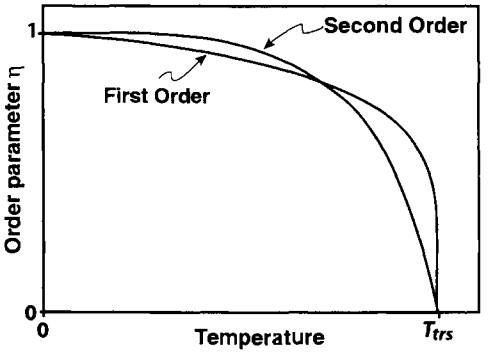

Figure 4.1 Plot of the order parameter against temperature for first- and second-order transitions up to the transition temperature T_{trs}.

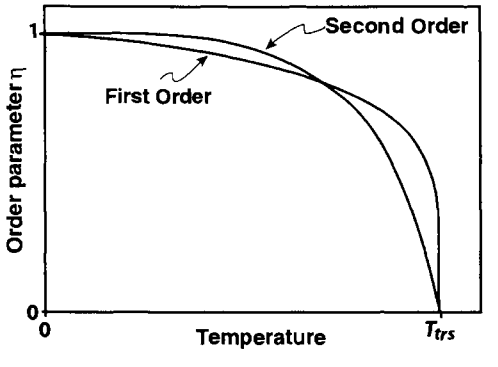

Figure 4.2 Plot of the Gibbs energy G for the Landau model againt the square of the order parameter at temperatures above, below and at the temperature of transition T_{trs}.

go undetected [2]. In addition, there are transitions that cannot be classified as either type. For example, KH_2PO_4 exhibits a phase transition that is neither first nor second order. It shows a tri-critical point at $T = 114\,K$ and pressure close to 200 MPa.

4.2 Thermodynamics of Solid–Solid Phase Transitions

Thermodynamically, the order of the transition is defined as the *lowest discontinuous derivative* of the Gibbs energy function [3]. Thus, if $(\partial G/\partial T)_P$ and $(\partial G/\partial P)_T$ are discontinuous at the transition temperature T_{trs}, the transition is said to be of the first order and if $(\partial^2 G/\partial T^2)_P$ and $(\partial^2 G/\partial P^2)_T$ are discontinuous, the transition is of the second order. Landau proposed the following reasoning ([4], see also [1]). Let us assume that the Gibbs energy $G(\eta; T, H)$ can be expanded as the following power series:

$$G(\eta; T, H) = -H\eta + g_0 + \tfrac{1}{2}g_2\eta^2 + \tfrac{1}{4}g_4\eta^4 + \tfrac{1}{6}g_6\eta^6 + \cdots, \tag{4.1}$$

where coefficients g_n are temperature-dependent, and H refers to the magnetic field strength. The coefficients of odd powers of η are zero, which is true if the crystal has a centre of inversion symmetry at $\eta = 0$. This, however, is a simplification that is not true for all crystals. In equilibrium,

$$\frac{\partial G}{\partial \eta} = -H + g_2\eta + g_4\eta^3 + g_6\eta^5 + \cdots = 0, \tag{4.2}$$

and the coefficient of η^2 in Equation (4.1) must change sign at T_{trs} so that G has a minimum:

$$g_2 = \gamma(T - T_{trs}), \tag{4.3}$$

where γ is a positive constant. When there is no external force, substituting Equation (4.3) into (4.2) and neglecting higher powers of η gives

$$\gamma(T - T_{trs})\eta + g_4\eta^3 = 0, \tag{4.4}$$

which has two roots for the order parameter η: $\eta = 0$ for $T > T_{trs}$ and

$$\eta = \sqrt{\frac{\gamma}{g_4}(T_{trs} - T)}, \tag{4.5}$$

for $T \leq T_{trs}$. With γ assumed to be positive, g_4 must be positive as well. The two solutions illustrate the second-order phase transition plotted in Figure 4.1.

For a transition to be first order, g_4 must be negative, and to avoid G decreasing to $-\infty$, one must retain in Equation (4.1) a positive g_6. With $H = 0$, Equation (4.2) becomes

$$\gamma(T - T_{trs})\eta - |g_4|\eta^3 + g_6\eta^5 = 0, \tag{4.6}$$

so that either $\eta = 0$ or

$$\gamma(T - T_{trs})\eta - |g_4|\eta^2 + g_6\eta^4 = 0, \tag{4.7}$$

or, at $T = T_{trs}$,

$$\eta^2 = \frac{|g_4|}{g_6}. \tag{4.8}$$

Therefore, from η given by Equation (4.8) and at $T = T_{trs}$, the Gibbs energy G has another minimum as shown in Figure 4.2. This figure also makes it clear why, at T_{trs}, the order parameter η shows the sudden 'jump' characteristic for first-order phase transitions.

Landau theory, although rudimentary, provides insight into solid–solid phase transitions. More accurate methods have been since developed and applied in the field [5]. However, they are beyond the scope of this chapter.

4.3 Introduction into Soft Modes and the Central Peak

The discussion in this section will be limited to second-order phase transitions in monatomic lattices. It follows from Equation (4.3) that

$$\frac{\partial^2 G}{\partial \eta^2} = \gamma(T - T_{trs}). \tag{4.9}$$

With $\gamma > 0$ and $T < T_{trs}$, the right-hand side of Equation (4.9) is negative and provides for the possibility of oscillations in η:

$$m\omega^2 = \gamma(T - T_{trs}), \tag{4.10}$$

where m is the mass of the atom. Thus, there is an oscillation (a phonon) with ω decreasing as $(T - T_{trs})^{1/2}$ when T approaches T_{trs} from below. Equation (4.10) leaves uncertainty as to the sign of ω. In structurally stable lattices, the energy of a phonon must be positive and it is suitable to take $\omega > 0$. However, in unstable lattices, ω^2 may become negative because of unusual temperature dependence of the inter-atomic force constants in the crystal and, consequently, ω may be imaginary. Such crystals will spontaneously deform to more stable structures. Modes with ω close to 0 are called *soft* [1]. Such oscillations were first found experimentally in the $\alpha \rightarrow \beta$ transition in quartz [6]. The importance of soft modes arises from the fact that ω^2 is closely related to the inter-atomic forces in the crystal. Measurements of ω close to the transition point provide important information about the lattice in the vicinity of T_{trs} [7]. Interpretation of experimental results is reasonably easy if soft phonons are well described by Equation (4.10). Quite often, however, they are coupled with

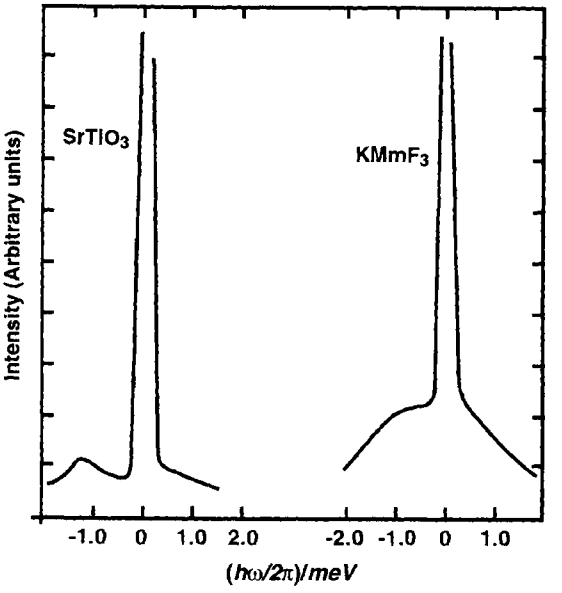

Figure 4.3 Schematic plot of the intensity of the central vibrational modes against angular frequency of the phonons through the region of a phase transition interpreted from the data of Shapiro *et al.* ([82], see also [4]). Left, $SrTiO_3$; right, $KMnF_3$.

other modes such as the optical-acoustic coupling and the task then becomes much more complicated [2].

The rather simplistic explanation of soft modes does not take into account the possibility of damping. The experimental data show, however, that soft modes are usually strongly damped and their line widths are large compared with their frequencies. Damping may account for what has been observed experimentally for a large number of crystal structures, *viz.* the existence of a strong central mode close to T_{trs} with $\omega \approx 0$, whose intensity increases while the line width decreases as $T \rightarrow T_{trs}$ (Figure 4.3). The existence of a *central peak* may be attributed to mode coupling that gives rise to damping. Linear coupling would then lead to a central mode below T_{trs} whereas non-linear coupling would cause a peak to appear above T_{trs}.

Other explanations involve the relation of central modes to critical fluctuations that occur near phase transitions. Such fluctuations would locally produce 'clusters' of the 'new' phase. The cluster dynamics becoming slower with the temperature approaching T_{trs} could also produce a low-frequency central mode in addition to the soft mode [7].

4.4 Phase Transitions in Plastic Crystals and Fullerenes

The existence of a crystalline cubic phase whose molecules may be rotating around one or more of their axes was first introduced theoretically [8] to account for increased heat capacity of hydrogen chloride at the solid–solid transition temperature. Later, Timmermans [9]

observed that certain organic compounds in the solid phase at temperatures just below the melting point were very soft and plastic (some could flow under the influence of gravity), and had entropy of fusion, $\Delta_{fus}S < 2.5R$, which is very low. He linked these properties to the molecular shape of either tetrahedral symmetry or effectively a sphere or ellipsoid, thereby allowing the molecules to rotate freely. Shortly after, Zernike [10] argued that the behaviour of plastic crystals could be explained in terms of an orientational disorder of the structure. The plastic crystals, forming the so-called mesophase, which is the phase 'between' the liquid and the solid phase, have usually cubic symmetry and, at some temperature below the melting point, they undergo a phase transition into 'regular' solid structures of lower symmetry. Plastic crystals are rather difficult to investigate. On cooling, some of these liquids may crystallize into metastable structures that, however, are very slow to transform into stable phases. Undercooling is common and superheating can also occur [11].

Molecules forming plastic crystals are relatively rigid. To help understand these molecules, they may be grouped into three categories, *viz.* (a) neutral molecules that include N_2 and CH_4, that exhibit a high degree of rotational freedom; (b) polyatomic ions such as CN^- and NH_4^+ that form ionic crystals where rotational freedom is more restricted; and (c) side groups, such as methyl CH_3-groups, that may rotate around the bond tying them to the larger organic unit [12].

The orientational disorder combined with the large libration amplitudes of the molecules are the reasons for the large background scattering found in X-ray and neutron diffraction experiments, usually leaving only a small number of distinguishable reflections. Besides, an intense diffuse scattering complicates structural determinations even more. The diffuse scattering, however, is highly structured, thus offering a possibility of yielding additional information both on the structure and on molecular dynamics of the disordered structure. This requires a theoretical model of the structure, in particular, a model of the motion of the molecules or side groups that change their orientation [13]. One such model, constructed by Pauling [14], assumes that the rotating molecules are almost free in their rotations and are only slightly restricted by weak anisotropic potentials. However, the model is of limited applicability, since there are only a few species approximating free rotors such as H_2 and phase II of CH_4. The model of Frenkel [15] can be used for a greater number of structures. In this model, molecules occupy one of n possible orientations. They librate thermally in the potential well, as well as undergo 'jumps' from one equilibrium position to another [13]. The Frenkel model is more general and has been used to interpret diffuse X-ray scattering in a number of crystals; the theory is fairly involved and beyond the space allocated in this chapter. It can be found in [13], along with a number of specific applications.

Solid fullerenes consist of very large molecules, of which C_{60} is probably most common. They are held together by very weak intermolecular interactions. The weakness of these forces is the reason why very small changes in the external environment (p, T) may cause significant changes in the translational, orientational and/or rotational structure of fullerenes [16]. The high-temperature structure of C_{60} at atmospheric pressure is face-centred cubic (fcc). The molecules undergo a quasi-free, almost isotropic, molecular rotation [17]. When cooled, the structure undergoes a phase transition at $T = 260\,K$ and it becomes a simple cubic (sc) phase, while the rotation changes into a rapid ratcheting of molecules between a number of well-defined orientations. In this phase, there are two possible orientational states, which differ with respect to the orientation of the double C=C bond. In the pentagon (P) orientational

state, the double bond in one molecule faces pentagons as its neighbours. However, in the hexagon (H) state, the bond faces hexagons. The P oriented state is preferred at atmospheric pressure, but the energy difference is so small that, around $T = 260\,\mathrm{K}$, the P state constitutes only 60 per cent of the phase. This fraction increases as temperature is lowered and becomes 83 per cent near $T = 90\,\mathrm{K}$ where, due to the thermal energy becoming negligible, the P-to-H reorientation stops. Below $T = 90\,\mathrm{K}$, the P–H orientational disorder stabilizes and gives rise to the existence of an orientational glass. The P-oriented state has a higher density and, therefore, is preferred under pressure [17]. Energies of the two states become identical at $p = 0.2\,\mathrm{GPa}$ [18].

4.5 Experimental Techniques

The presence of solid–solid phase transitions may be detected by means of any one of several different types of experiment. However, to define and understand the mechanism of the transition, a combination of techniques must be used. Much of the current experimental research is concerned with measuring the temperature dependence of the angular frequency $\omega(T)$ of the soft modes.

4.5.1 Thermal Methods

Although there are many thermal methods available, differential thermal analysis (DTA), differential scanning calorimetry (DSC) and adiabatic calorimetry (AC) are probably the most widely used in the detection and characterization of phase transitions. Since the methods are well established and widely used, only a brief description will be given here. For further information on DTA the reader may consult the vast literature, for instance [19]; calorimetric methods are described, among others, in [20].

The DTA is based on recording the temperature difference $\Delta T = T_s - T_r$ between the sample and a reference material, while both are subjected to the same heating programme. The output signal is recorded against T_r. As a matter of convention, endothermic responses, *i.e.* the ones where the sample temperature lags behind that of the reference, show as negative peaks. Good reference materials should possess the following characteristics and (a) should not exhibit any thermal events within the relevant temperature range; (b) should not react with the holder or with the thermometer; and (c) should have values of thermal conductivity and heat capacity similar to those of the sample [11].

Power-compensated DSC instruments allow for the sample and the reference to be kept at the same temperature over a range of temperature, while the sample and the reference are being heated by independently supplied heaters. If the sample undergoes a thermal event, the amounts of energy supplied to the heaters to maintain $\Delta T = 0$ will differ and this difference, which is plotted against the temperature, will become the outcome of the experiment [11].

Both DTA and DSC are excellent methods for detecting the presence of transitions, but they yield enthalpies of transitions with relatively large uncertainties. Adiabatic calorimetry, on the other hand, while being equally useful for detecting the transitions, is capable of measuring $\Delta_{trs}H$, $\Delta_{trs}S$ with very high accuracy as well as the heat capacity at closely spaced intervals of temperature as the transition is traversed. In an adiabatic calorimeter, heat leaks into

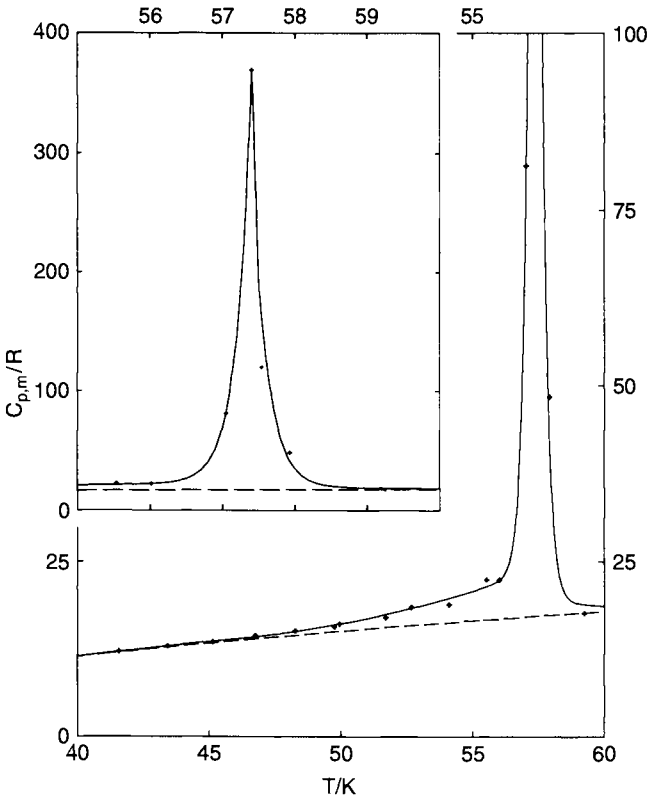

Figure 4.4 Plot of heat capacity against temperature through the region of transition for $(NH_4)_2PtBr_6$ [35].

or out of the system are controlled to be zero and the solid sample is heated by a series of small power boosts of known increments. Before and after each boost, the temperature of the sample is measured. The resulting plot of heat capacity against temperature looks similar to the one illustrated in Figure 4.4, where the λ-shaped peak indicates a phase transition.

4.5.2 Optical Methods

Optical experimental techniques [2,4] include IR reflection, which includes dispersion by Fourier transform spectroscopy, absorption and fluorescence in the visible as well as birefringence and light scattering. The earliest applications of optical methods in the field of solid–solid phase transitions employed birefringence measurements semi-quantitatively to determine order parameters. Subsequently, especially with the advent of the laser, soft modes were studied both by light absorption and scattering that have led to a much better understanding of microscopic phenomena involved. The high-resolution light scattering experiments have provided important input on soft modes that couple with other degrees of freedom and significant contributions have been made to the study of multi-critical points under external pressure and stress. The experiments also showed the limits of mean field theory, which

turned out not to be universally applicable. Some specific applications of optical methods include light scattering and Raman spectra measurements from coupled modes, investigations into the symmetry properties of pure ferro-elastic transitions and cooperative Jahn–Teller systems, non-linear optical studies of phase transitions and multi-critical phenomena.

4.5.3 X-Ray and Neutron Scattering

Elastic Scattering (Diffraction)

Diffraction depends on the interference of beams elastically scattered by electron clouds in the case of X-rays and by nuclei when neutrons are used. Since the typical X-ray and slow thermal neutron wavelength is of the order of 0.1 nm, both are well suited for the study of inter-atomic distances in crystal lattices and solid–solid phase transitions. The generation of X-rays for the diffraction studies is considerably less expensive than neutrons, which require a reactor for their generation. The X-rays, as electromagnetic radiation, interact only with electrons, but they cannot 'see' the electron clouds of the very light atoms, while neutrons 'see' the very light nuclei. Because of their spin, neutrons interact with magnetic fields of electrons and nuclear magnetic moments. The principles and practice of the diffraction are well established [21–23] and it sufficient here to note the Bragg equation

$$2d \sin \theta = n\lambda, \tag{4.11}$$

where $n = 1, 2, 3$, λ is the wavelength of the radiation, d the inter-planar distance and θ is the angle of incidence which is also equal to the angle of reflection. The diffraction law equation (4.11) requires that θ and λ be matched. In doing so, one can either choose a range of wavelengths, so that some of them would match the θ angles for all inter-planar distances d, or choose one wavelength λ_0 and use a whole range of θ angles. The former possibility is realized in the Laue method in which a single crystal is stationary in a beam of X-ray or neutron radiation of continuous wavelength. The latter is employed in the rotating crystal and powder methods. In the rotating crystal method, a single crystal positioned in a beam of mono-energetic X-rays or neutrons is rotated about a fixed axis. During the rotation, the changing θ brings different crystal planes in a position for reflection. In the powder method the sample, in the form of fine crystalline powder whose grains are randomly oriented, is placed in a mono-energetic beam. The large number and random orientations of crystallites act in the same manner as the rotation of a single crystal, *i.e.* diffracted beams emerge from all the crystallites that happen to fulfil the Bragg condition in Equation (4.11).

Inelastic Scattering

Inelastic X-ray scattering (spectroscopy) is used mainly for the identification of atoms and will not be covered within this section. Suffice to note that since thermal neutrons have energies comparable with those of excitations in the solids, the neutrons are very well suited as probes in inelastic scattering experiments. Their wavelength at about 25 MeV is 0.18 nm,

which is comparable with inter-atomic distances in solids, thereby making them an ideal tool to study spatial correlations. The advent of and easier access to cold sources such as liquid hydrogen and deuterium moderators, high fluxes of cold neutrons are now available. These physical properties make it possible to use neutrons to investigate structural changes with small displacements that are involved in some solid–solid phase transitions and to study correlations in space and time.

4.5.4 Ultrasonic Methods

Ultrasonic measurements [24] have been valuable and widely used in studies of condensed matter. They are the tools of choice for the most detailed characterization of the elasticity in solids, as well as any other type of excitations which couple to long-wavelength phonons. Elastic constant measurements are used to locate transition points to determine phase diagrams and, in some cases, to determine the transition order. The type of coupling between strain and order parameter is reflected in the temperature dependence of elastic response functions. The drawbacks are the large size of the samples required and the large number of independent experiments needed for measurements to be accurate, and to characterize fully the properties of a material.

One simple technique to allow for the determination of both sound velocity v_s and sound attenuation α_s, is a pulse method in which a piezoelectric transducer, bonded to a crystal sample having a pair of plane and parallel end faces, generates short pulses of sound waves. These are multiplied and reflected to produce an echo signal in another transducer. From the length of the pulses, the transit time and the decay rate, v_s and α_s may be immediately calculated.

A more modern technique, termed resonant ultrasound spectroscopy [25], has been developed. It dramatically offsets the restrictions of classical ultrasound spectroscopy, *i.e.* the need for large samples and large numbers of independent measurements. Its intrinsic accuracy is high, but it heavily relies on computer programmes for the extraction of physically meaningful information from the raw data.

4.5.5 Magnetic Resonance

All the experimental methods described so far measure *collective* responses of the samples investigated. Magnetic resonance techniques, in contrast, are concerned with *local* system properties. The basis of the techniques is to use magnetic dipole and electric quadrupole moments of the nuclei and the magnetic dipole moment of the electron as local probes implanted within the crystal structure to study local magnetic and electric fields.

Nuclei having a non-zero spin exhibit a non-zero magnetic dipole moment and if the spin is greater than ½, the nuclei also have an electric quadrupole moment. The electron, with its spin ½, also has a magnetic moment. Magnetic moments interact with local magnetic fields, whereas quadrupole moments interact with local electric field gradient tensors, thus giving rise to nuclear magnetic resonance (NMR), nuclear quadrupole resonance (NQR) and electron paramagnetic resonance (EPR). In many crystal systems, the local magnetic field and the local electric field gradient tensor are functions of the order parameter η. As the atomic

fluctuations increase and slow down near the phase transition point T_{trs}, the changes are reflected in the spin–lattice and spin–spin relaxation rates [7].

4.6 Review of Recent Developments

4.6.1 Inorganic Compounds

Ammonium Hexahalometallates $(NH_4)_2MX_6$

Some, but not all, salts of this family undergo transitions into a phase of lower symmetry with decreasing temperature. Some of the transitions are known to involve the small-angle rotations of the MX_6^{2-} (M, transition metal or polyvalent ion; X, halogen) octahedra, others appear to lead to lattice distortion without coupling to the octahedral rotations. Additional librational degrees of freedom are linked to the ammonium ion, either NH_4^+ or ND_4^+ [26]. A number of these compounds, both hydrogenated and deuterated, and with different combinations of metal and halogen atoms, were investigated by adiabatic calorimetry in the temperature range from near absolute zero to above $T = 350$ K. In some instances, X-ray and neutron diffraction techniques were also used. The results are presented in a series of papers: $(NH_4)_2PdCl_6$ in [27] and $(ND_4)_2PdCl_6$ in [28,29]; $(NH_4)_2PtCl_6$ in [30] and $(ND_4)_2PtCl_6$ in [31]; $(NH_4)_2TeCl_6$ in [32] and $(ND_4)_2TeCl_6$ in [33]; $(NH_4)_2TeBr_6$ in [34]; $(NH_4)_2PtBr_6$ in [35]; $(ND_4)_2PtBr_6$ in [36]; $(ND_4)_2SnCl_6$ in [37]; $(ND_4)_2SiF_6$ in [18]; ND_4PF_6 in [38,39]. A comparative study of the thermodynamics, heat capacity, phase transitions and crystal structure of this group is presented in [40]. In a different study, natural and partially deuterated $(NH_4)_2TlCl_6$ was measured [41] using NMR. Above $T = 50$ K, the relaxation curve reveals the classical, hindered reorientation of the NH_4 ion. Below $T = 50$ K, the minima in the temperature dependencies of the spin relaxation times are related to the level crossing.

Inorganic Azides

The acoustic properties were studied for the inorganic azides KN_3, RbN_3, CsN_3, TlN_3, NaN_3 and AgN_3. The internal friction was detected and several phase transitions were identified [42].

BaB_2O_4

The $\alpha \rightarrow \beta$ and $\beta \rightarrow \alpha$ phase transformations during isothermal annealing were investigated using a platinum crucible. Differences between transformation behaviour of bulk crystals and powder were attributed to thermal stress [43].

CCl_4, CF_4 and H_2S at High Pressure

Measurements from X-ray and Raman scattering were used to investigate carbon tetrachloride, carbon tetrafluoride and hydrogen sulphide. For the CCl_4, the phase III to phase IV

transition was found to occur around 2.3 GPa. The space group of the phase IV was Pa3. Above 6 GPa, an intra-molecular vibrational mode of F2 gradually splits into three peaks, which suggests a phase transition to a new high-pressure phase [44]. For the CF_4, the studies were carried out up to 12 GPa. The diffraction pattern of phase III at 7.5 GPa was assigned to a monoclinic lattice with lattice constants $a = 0.6755$ nm, $b = 0.4401$ nm, $c = 0.6766$ nm and $\beta = 103.1°$. For its space group, three different groups of P21, P21/m and P21/c agree with experimental results. The frequency–pressure dependencies of the intra-molecular vibrational modes suggest a phase transition at 8.6 GPa [42]. Diffraction experiments on solid H_2S were performed with a diamond anvil cell and an image plate in order to raise the pressure to 25 GPa. Two unknown structures of phases I′ and IV were found to be cubic T4-P213 and tetragonal D4h20-I41/acd, respectively. In phase I′, the H_2S molecule has six-fold asymmetrical coordination, which causes a displacement from the face-centred arrangement. In phase IV, the molecules form spiral chains along the c-axis with partial loss of molecularity. The chains are linked together by hydrogen bonds [45].

In another study [46], IR-absorption spectra of solid H_2S were measured at high pressures up to 50 GPa at room temperature. The symmetrical stretching overtone vibration $2\nu_1$ showed a red shift in frequency with increasing pressure, and it changed into two components at approximately 11 GPa for the II–IV phase transition. The pressure dependence of the observed $2\nu_1(\nu_2 + \nu_3)$ (which are the bending plus asymmetry and stretching combination bands), and ν_2 vibrations show a phase transition from IV to V at about 30 GPa. The S–H hydrogen bond system continues to exist up to at least 45 GPa; however, its bonding strength is very weak.

GaP and GaAs

Two maxima in the internal friction can be found near $T = 320$ K (peak I) or near $T = 38$ K (peak II) in GaAs (peak I only) and GaP at ultrasonic frequencies near 105 kHz. Peak II can be attributed to some point defect relaxation mechanism, whereas peak I can be explained by a local phase transition that can occur in the stress field of dislocations shifted by ultrasonic deformation. Numerical analysis of the measured Young's modulus yields a reaction order for the transition of 0.69 and activation energy of 113 kJ · mol^{-1} [47].

KNO_2

Phase transitions were studied at temperatures from 77 to 640 K using ultrasonic wave propagation and attenuation methods. First-order transitions were observed at $T = (264, 315, 125–250$ and $343)$ K. The latter transition is associated with an anomaly in the internal friction at $T = 335$ K. The presence of new, unstable phases was observed during cycling [48].

Li_2SO_4 (Powders)

An accurate, high-resolution heat flow calorimeter [49] was used to analyse powder samples of Li_2SO_4 from three different manufacturers. It is shown that some of the results have

more than 10 times smaller uncertainty limits than is usually encountered. Details of the measuring system are given, and reasons for the higher accuracy discussed. The average enthalpy change associated with the transformation between the two high-temperature forms of solid lithium sulphate was $\Delta_{trs}H = (26.1 \pm 1.7)$ kJ · mol^{-1}. The relatively large error, twice as large as expected from the calorimeter's performance, is due to differences between the samples. Also, different transformation temperatures were found for each of the samples. The differences, as well as the shape of the measured heat-flow curves, can be explained in terms of the size distribution of the crystallites. The onset temperatures for the monoclinic to cubic transformation for sample 1 (Aldrich), sample 2 (Merck) and sample 3 (Alfa) are (577.82 ± 0.08), (577.98 ± 0.05) and (578.30 ± 0.03) K. They are believed to represent the transformation temperature of the smallest crystallites present in the sample. For the cubic to monoclinic transformation, the corresponding onset temperatures are (577.90 ± 0.02), (577.84 ± 0.02) and (577.78 ± 0.02) K, respectively. Inter-phase curvature is such that the monoclinic phase is on the concave side of the inter-phase [49].

NH_3 (Solid) at High Pressures

The IR absorption spectra were measured with the diamond anvil cell at room temperature and pressures up to 120 GPa. Two phase transitions were observed: the first, from solid V to VI, at about 40 GPa and the second to solid VII at 70 GPa. Four branch peaks were measured for the NH stretching vibrations. One branch showed a significant frequency decrease from 3200 cm^{-1} at 10 GPa to 3000 cm^{-1} at 120 GPa, while the other two branches markedly showed the peak shifts to higher frequency. No hydrogen-bond symmetry was observed [50].

NOCl

Chlorine NQR studies of solid NOCl at $T = 110$–212 K have confirmed an order–disorder phase transition near $T = 145$ K, found by X-ray diffraction. Unusual hysteretic NQR signal behaviour indirectly proved also a low-temperature phase transition below $T = 100$ K. Fast relaxing mechanisms were also detected [51].

4.6.2 Organic Compounds

n-Alkane ($C_{27}H_{56}$) Crystals of High Purity (Uniaxially Oriented)

The ^{13}C solid-state NMR spectrum and the spin-lattice relaxation time were measured at different temperatures with the orientation axis parallel or perpendicular to the static magnetic field. Rapid local fluctuations and rotations about the molecular chain axis were detected [52]. In a separate study [53], solid transitions of C_{21}, C_{23} and C_{25} *n*-paraffins were investigated from a piezothermal point of view. Pressure scanning allowed the continuous record of the expansivity as a function of pressure up to 500 MPa. The resulting piezo-thermograms and entropies of transformation are presented. Problems related to phase transformations under a shearing stress were considered.

Benzodiazepine Chlordiazepoxide

A novel crystal form, labelled form II, was found and the new polymorphic phase characterized and distinguished from the standard form I by X-ray diffractometry, DSC, IR spectroscopy, microscopy, solution calorimetry and solid-state NMR. The formation of form II was dependent on the solvent, being the predominant form isolated from methanol. Recrystallization from other alcoholic solutions (ethanol, propanol and butanol) and toluene yielded form I. The DSC and powder X-ray diffraction indicated that the two forms were enantiotropically related to a transition of form II to form I occurring between $T = 473$ and 498 K. Hot-stage microscopy in this temperature range revealed a dramatic solid-state transition. Single-crystal X-ray analysis was performed on form II which was found to crystallize in the triclinic space group with $a = 1.0736(2)$ nm, $b = 1.6921(4)$ nm, $c = 1.7041(4)$ nm, $\alpha = 100.76(1)°$, $\beta = 95.27(1)°$, $\gamma = 97.53(1)°$, $Z = 8$ and calculated density of 1.33 $g \cdot cm^{-3}$. When compared with the published crystal structure of form I, the cell symmetry, volume and density were similar. Both structures consisted of four crystallographically independent molecules linked in pairs through intermolecular hydrogen bonding [54].

5-Bromo-9-Hydroxyphenalenone (BHP)

The heat capacities of 5-bromo-9-hydroxyphenalenone (BHP) and its deuteroxy derivative (BDP) were measured from $T = 2$ to 310 K. The heat capacity of BHP is a smooth function of temperature and that of BDP has two peaks at $T = 21.3$ and 33.9 K. By analysing the data on BHP, a tunnel splitting of (64 ± 0.2) cm^{-1} associated with the quantum–mechanical motion of the H atom in the intra-molecular O–H–O H bond was derived, along with the Debye temperature 60.8 K and two Einstein temperatures 131.4 (non-degenerate) and 210.4 K (doubly degenerate). The enthalpy change of 225 $J \cdot mol^{-1}$ and entropy change of 6.8 $J \cdot K^{-1} \cdot mol^{-1}$ were measured for the total thermal effects of the two-phase transitions in BDP. The value of the transition entropy is consistent with the two-fold disorder in the high-temperature phase [55].

t-Butylammonium Tetrafluoroborate

The DTA, DSC and the temperature dependence of the spin–lattice relaxation time T_1 and the second moment M_2 of ^{1}H- and ^{19}F-NMR were studied in $Me_3CNH_3BF_4$ and $Me_3CND_3BF_4$. The data revealed solid–solid phase transitions at $T = 219$ K for $Me_3CNH_3BF_4$ and at $T = 221$ K for $Me_3CND_3BF_4$. The motions of cations and anions in the two solid phases were studied by T_1 and M_2 experiments. The motional modes of the ions and their motional parameters were detected [56].

Methane CH_4

Single crystals of solid methane in phase II can be obtained only from phase I at zero pressure. Large ($\equiv$50 mm^3) single CH_4-I crystals were grown in a cylindrical quartz cell and

successfully cooled below the phase-transition temperature, thus leading to phase II [51]. Brillouin spectra were collected at different crystal orientations corresponding to rotation about the laboratory *z*-axis. The X-ray Laue diffraction techniques were used to orient the crystals. The elastic constants of CH_4 – I were measured from $T = 90$ down to 20.5 K. The constants of CH_4 – II were measured from $T = 19.5$ to 15.5 K. The data were used to calculate the Poisson ratio, bulk and shear moduli, the distribution of the acoustic velocities in high-symmetry planes, and the Debye temperature. Raman spectra of the fundamental modes ν_1 and ν_3 were recorded and their shifts and full-widths at half-height were determined as a function of temperature [57].

Chloranil

The crystal structure of chloranil above and below its phase transition ($T_{trs} = 90$ K) was studied by single-crystal X-ray diffraction. Below T_{trs}, the difference $\Delta\phi$ between the angle of an axis and an O ··· O vector in the chloranil molecule [projected to (010) plane] at any temperature, and the angle at T_{trs}, increases with a power-law relation with a decrease in temperature. The $\Delta\phi$ is an order parameter. The mean-square-displacements of O and Cl atoms increase around T_{trs}. Above T_{trs}, the intermolecular nearest O ··· C distance decreases with a decrease in temperature. Below T_{trs}, the distance–temperature curve has two branches, neither of them decreasing with a decrease in temperature. The transition is thought to be a result of two types of molecular rotations, *viz.* clockwise and counter-clockwise, for neighbouring molecules [58].

$(CH_3)_2NH_2H_2PO_4$

The second moments of the proton magnetic resonance lines and relaxation times in the laboratory frame T_1, were measured in polycrystalline $(CH_3)_2NH_2H_2PO_4$ over the temperature range $T = 88$–360 K [59]. The proton spin-lattice relaxation measurements revealed two minima due to the C-3 reorientations of the methyl groups of $(CH_3)_2NH_2$ cations. Analysis of the relaxation data yields the activation energy barriers of 13.4 and 7.6 kJ · mol^{-1}, respectively. Good agreement was obtained between calculated and measured second moment. The NMR data confirm the phase transition at $T_{trs} = 259$ K known from previous studies [59].

Chlorodifluoromethane

The IR spectra were recorded from $T = 12$ to 105 K. Lattice and internal mode regions were investigated by utilizing two Fourier transform spectrometers, one for the far-IR regions (20–400 cm^{-1}) and the other for the mid-IR region (400–4000 cm^{-1}). Evidence for the solid-state phase transition at $T = (55.0 \pm 0.5)$ K was found. Multiple structure for the nine internal modes was observed over a wide range of temperature, which in most cases resulted from the crystal field rather than from isotopic or other effects. This indicates that both phases are ordered with rather large unit cells, and that the phase transition is of a displacive type. The spectra were compared with those of a recent Raman study and were interpreted on the basis of preliminary structural data from neutron powder diffraction measurement [60].

Cholesterol

The molar heat capacity was measured between $T = 5$ and 425 K. The derived thermodynamic properties were calculated. The solid–solid transition was found at $T_{trs} = 306.7$ K, with an enthalpy of transition of 3886 J · mol^{-1}. The melting temperature was found to be $T_{fus} = 422.3$ K and the enthalpy of fusion is 28.4 kJ · mol^{-1} [61].

Choline Tetrafluoroborate and Iodide

The crystal structure of the highest-temperature and second highest-temperature solid phases of choline tetrafluoroborate and iodide was investigated by X-ray powder diffraction. The structure in the phase at the highest temperature of both salts is NaCl-type cubic [$a = 1.016(2)$ nm, $Z = 4$ for tetrafluoroborate; $a = 1.008(2)$ nm, $Z = 4$ for iodide]. The second highest-temperature phase of tetrafluoroborate and iodide is CsCl-type cubic [$a = 0.6198(6)$ nm and $Z = 1$] and tetragonal [$a = 0.8706(2)$ nm, $c = 0.6144(6)$ nm and $Z = 2$], respectively. The DSC was carried out for the iodide, where the presence of three solid–solid phase transitions was confirmed. Enthalpy and entropy changes of these transitions were evaluated [62].

Cycloheptane

The phases and phase transitions of solid cycloheptane were examined with DTA with two new findings. Phase I samples cooled below $T \sim 200$ K directly transform to phase III, not phase II as reported earlier. Phase III readily supercools through the III–IV transition, yielding a glassy crystal IIIg or transforming into a previously unknown metastable phase, III′, depending on details. These findings can have an impact on the identification of the phases studied in previous reports. Deuterium NMR of phase III shows that the reorientations are not isotropic, indicating that no molecules reside in sites of cubic symmetry. The deuterium spectrum suggests several non-equivalent sites in phase III [63].

Cyclohexane

Both hydrogenated and deuterated forms of cyclohexane were studied by neutron scattering at high pressures [64]. All the solid phases, *viz.* three in C_6H_{12} and four in the deuterated form, were well recognized both in inelastic neutron scattering and in neutron diffraction experiments. The temperature range extended from $T = 160$ K upwards to room temperature, while the pressure ranged from atmospheric to $p = 370$ MPa.

Cyclohexanol

Solid cyclohexanol was studied by adiabatic calorimetry and FIR spectroscopy [65]. The monotropic set of phases II and II was confirmed. Two different ways of obtaining phase II, one passing through an intermediate metastable phase MS, were demonstrated.

DL-α-Amino-*n*-Butyric Acid

DL-α-amino-*n*-butyric acid crystals undergo a reversible solid-phase transformation at $T - 337$ K, from form A to form D. Two different types of characteristic diffuse scattering along c^* were observed during the phase transformation. From the analysis of diffuse scattering, it became clear that the mechanism of the phase transformation involves the following three main movements: (1) displacement of molecular layers by $(a + b)/2$ in the A phase, (2) a reorientation of the methyl group with rotational displacement and (3) a rearrangement of molecular layers forming the D phase [66].

4,4′-Di-*n*-Butyloxyazozybenzene

The phase diagram in the temperature range from room temperature to $T = 388$ K was determined in [67] by neutron diffraction measurements.

Fluoro- and Aminocyclohexane

A thermodynamic study of $C_6H_{11}F$ and $C_6H_{11}NH_2$ is presented in [68]. Phase diagrams have been established up to $p = 300$ MPa using DTA. The enthalpy of phase transition II–I in $C_6H_{11}F$ was found to be much greater than the enthalpy of melting. The opposite is true in $C_6H_{11}NH_2$. Therefore, the latter is not considered as a plastic crystal.

Trans-4-*n*-Hexyl-(4′-Cyanophenyl)-Cyclohexane

The phase diagram up to $p = 300$ MPa and $T = 370$ K was studied by means of DTA [69].

Hexatriacontane (n-$C_{36}H_{74}$)

Hexatriacontane (n-$C_{36}H_{74}$) was studied by DSC and X-ray diffraction. In the original monoclinic single crystal, molecular chains inclined ~27° in the bcc-plane from the normal to the lamellar surface. A solid–solid phase transition starts at $T = 72$ K and finishes at $T = 73.4$ K. Two kinds of mechanisms took place in the formation of the high-temperature monoclinic structure. One arose from the formation of twinned crystals where the transition developed on the frontier of the (110) twin boundary. The other was responsible for changing the molecular staggering by 90° where the crystal axis was unchanged. The two mechanisms appeared simultaneously, resulting in the appearance of polycrystals [70].

n-Undecylammonium Chloride

Molecular motions and structural changes were studied as a function of temperature by NMR and DSC. Reorientation of the NH_3 group was detected. Simultaneous presence of the inter-digitated and the ε-phase was observed [71].

4.6.3 Fullerenes

A comprehensive review of fullerenes with 56 references [72] was published in 1995. It examines some of the important results obtained to-date on their solid state properties that include phase transitions of C_{60} and C_{70} related to orientational ordering, superconductivity in alkali and alkali earth fullerides, and ferromagnetism in the radical ion salt C_{60}. Some aspects of carbon nanotubes and anions are briefly described.

A thermodynamical model describing the co-existence of phases at orientational phase transition in solid fullerenes has been developed [73]. For such a transition in fullerene C_{60} characterized by the comparatively low enthalpy, heterophase fluctuations can lead to the wide temperature region of phase co-existence within about 30 K below the 260 K transition point. By comparison with the theoretical dependence obtained on this basis with the experimental data on X-ray diffraction and heat capacity measurements for C_{60}, the energetic characteristics of the hetero-phase cluster formation were evaluated. The relative contribution of homophase and heterophase fluctuations to breaking the orientational order was discussed.

In [74], the molecular, crystal and electronic structures of fullerenes are discussed, and the mechanism of superconductivity in alkali-doped fullerides M_xC_{60} (M=K, Rb, Cs, Tc, ...) is proposed. It comprises a combination of phonon and high-energy electronic boson exchange, as in the case of cuprates. The electronic boson process would involve bond polarization in interaction with conduction electrons. The theory accounts for the high transition temperature T_{trs} observed in these systems. Predictions based on this mechanism are consistent with the observed isotope effect and the superconducting energy gap in M_3C_{60} fullerides.

Boron-doped carbon fullerenes were examined in [75]. The *in situ* creation of single- and multi-shelled fullerenes and multi-walled nanotubules by electron irradiation of chemical vapour deposit of graphitic B_xC ($x \leq 0.2$) in a high-resolution 300 kV electron microscope is reported. Nanostructure formation occurred through irradiation-induced solid-state phase transformation, in contrast to conventional fullerene/nanotube synthesis from the gas phase. The fullerene and nanotubule chemical composition and bonding character were analysed by EELS, applying a 0.5 nm electron probe. The boron/carbon ratio of the observed curled, closed nanostructures never exceeded ~0.1. Unlike pure carbon anions, most of the B-doped fullerenes exhibited a polyhedral faceted circumference suggestive of B-induced buckling.

Multi-nuclear NMR studies of A_3C_{60} compounds (A, alkali metal) are reported in [76]. Low-temperature ^{13}C-T_1 and high-temperature ^{13}C-Knight shift measurements in various A_3C_{60} compounds revealed spin susceptibility that successfully explains the temperature dependence of ^{13}C-T_1T in K_3C_{60} at $T = 120$ K, while a contribution from C_{60} molecular rotation was observed at higher temperatures. In Na_2AC_{60}, electronic states and molecular dynamics are discussed below and above the fcc-sc structural phase transition temperature.

Reorientational relaxation following a pressure-induced change in the pentagon/hexagon ratio in C_{60} fullerenes was studied and reported in [77]. From the same group came an assessment of the measurements of thermophysical properties as tools to study phase diagrams of fullerenes under pressure [78].

4.6.4 Advances in Experimental Techniques and Interpretation of Results

Adiabatic Calorimetry – Design Improvements

Design improvements in an adiabatic calorimeter make it possible to load or unload the calorimeter in 30 min. A new protocol for adiabatic calorimetric systems is discussed and changes in the data collection and the data calculation programmes are given [72].

Fluoroprobe

A new application was found for the charge-transfer compound Fluoroprobe. With this fluorescent compound, the phase transition in crystalline materials can be observed directly, which is not possible with any other technique [79].

X-Ray Powder Diffraction

A new method for the analysis of non-isothermal kinetic data is now available, which is suitable for treating data of phase transitions or of chemical reactions. The method was made general by using integrated rate equations. For simple kinetic models, kinetic parameters can be achieved from a single measurement, preferably at the slowest heating rate. For complex models, number of measurements with different heating rates are required [80]. In addition, a new "millikelvin (mK)-stabilized cell" having a function of sensing thermal anomalies for the detailed X-ray diffraction study of solid-phase transitions has been developed [81]. The cell is easily mounted on a commercially available goniometer head. The performance was tested using a $CsPbC_{13}$ single crystal, in which a phase transition is known at $T_{trs} = 320\,K$ (47°C) from tetragonal to cubic. An abrupt variation in the distance between some two reciprocal points in the precession pattern was clearly detected in a 0.1 K temperature range centred at $T = 320\,K$ along with two thermal anomalies. The cell will be especially useful to investigate phase transitions occurring over a narrow temperature range.

References

1. Kittel, C., *Introduction to Solid State Physics*, Wiley, New York, 1976.
2. Fleury, P.A. and Lyons, K., in *Structural Phase Transitions I*, K.A. Müller and H. Thomas, eds., Springer, Berlin, p. 10, 1981.
3. Ubbelohde, A.R., *Modern Thermodynamical Principles*, Clarendon Press, Oxford, 85ff. 1952.
4. Fujimoto, M., *The Physics of Structural Phase Transitions*, Springer, New York, p. 3, 1997.
5. Stinchcombe, R.B., in *Magnetic Phase Transitions*, M. Ausloos and R.J. Elliot, eds., Springer, Berlin, 1983.
6. Raman, C.V. and Nedungadi, T.M.K., *Nature* **145,** 147, 1940.
7. Blinc, R. and Žekš, B., *Soft Modes in Ferroelectrics and Antiferroelectrics*, North-Holland, New York, 1974.

8. Simon, F. and von Simson, C.Z., *Physik* **21**, 168, 1924.
9. Timmermans, J., *Bull. Soc. Chim. Belge.* **44**, 17, 1935.
10. Zernike, F., *Ned. Tijdschr. Natuurkunde* **8**, 66, 1941.
11. Dunning, W.J., in *The Plastically Crystalline State*, J.N. Sherwood, ed., Wiley, Chichester, 1979.
12. Huller, A. and Press, W., in *The Plastically Crystalline State*, J.N. Sherwood, ed., Wiley, Chichester, 1979.
13. Fouret, R., in *The Plastically Crystalline State*, J.N. Sherwood, ed., Wiley, Chichester, 1979.
14. Pauling, L., *Phys. Rev.* **36**, 430, 1930.
15. Frenkel, J., *Acta Phys. Chemica U.S.S.R.* **3**, 23, 1935.
16. Sundqvist, B., Soldatov, A., Lundin, A. and Andersson, O., *High Temp. – High Press.* **29**, 119, 1997.
17. Dresselhaus, M.S., Dresselhaus, G. and Eklund P.C., *Science of Fullerenes and Carbon Nanotube,* Academic Press, San Diego, 1996.
18. David, W.I.F. and Ibberson, R.M., *J. Phys. Condens. Mat.* **5**, 7923, 1993.
19. Brown, M.E., *Introduction to Thermal Analysis*, Chapman & Hall, London, 1988.
20. Hemminger, W. and Höhne, G., *Calorimetry Fundamentals and Practise*, Verlag-Chemie, Weinheim, 1984.
21. Bragg, W.L., *Proc. Camb. Phil. Soc.* **17**, 43, 1913.
22. Rudman, R., *Low-Temperature X-Ray Diffraction: Apparatus and Techniques*, Plenum, New York, p. 344, 1976.
23. Askeland, D.R. and Phule, P.P., *The Science and Engineering of Materials*, 4th ed., Thomson, London, p. 1003, 2003.
24. Lüthi, B. and Rehwald, W., *Strucural Phase Transitions I*, Springer, Berlin, pp. 131–184, 1981.
25. Leisure, R.G. and Willis, F.A., *J. Phys. Condens. Mat.* **9**, 6001, 1997.
26. Smith, D., Weir, R.D. and Westrum, E.F. Jr., *J. Chem. Thermodyn.* **22**, 421, 1990.
27. Callanan, J.E., Weir, R.D. and Westrum, E.F. Jr., *J. Chem. Thermodyn.* **24**, 1001, 1992.
28. Swainson, I.P., Powell, B.M. and Weir, R.D. Jr., *J. Solid State Chem.* **131**, 221, 1997.
29. Callanan, J.E., Weir, R.D. and Westrum, E.F. Jr., *Ber. Bunsenges Phys. Chem.* **96**, 1585, 1992.
30. Weir, R.D. and Westrum, E.F. Jr., *J. Chem. Thermodyn.* **22**, 1097, 1990.
31. Weir, R.D. and Westrum, E.F. Jr., *J. Chem. Thermodyn.* **23**, 653, 1991.
32. Callanan, J.E., Weir, R.D. and Westrum, E.F. Jr., *J. Chem. Thermodyn.* **24**, 567, 1992.
33. Callanan, J.E., Weir, R.D. and Westrum, E.F. Jr., *J. Chem. Thermodyn.* **24**, 661, 1992.
34. Callanan, J.E., Weir, R.D. and Westrum, E.F. Jr., *J. Chem. Thermodyn.* **27**, 299, 1995.
35. Callanan, J.E., Weir, R.D. and Westrum, E.F. Jr., *J. Chem. Thermodyn.* **30**, 1483, 1998.
36. Callanan, J.E., Weir, R.D. and Westrum, E.F. Jr., *J. Chem. Thermodyn.* **32**, 1133, 2000.
37. Callanan, J.E., Weir, R.D. and Westrum, E.F. Jr., *J. Chem. Thermodyn.* **22**, 149, 1990.
38. Callanan, J.E., Weir, R.D. and Westrum, E.F. Jr., *J. Chem. Thermodyn.* **22**, 979, 1990.
39. Swainson, I.P., Hammond, R.P., Cockcroft, J.K. and Weir, R.D., *Phys. Rev. B* **66**, 174109, 2002.
40. Weir, R.D. and Westrum, E.F. Jr., *J. Chem. Thermodyn.* **34**, 133, 2002.
41. Grabias, T. and Pislewski, N., *Solid State Nucl. Magn. Reson.* **12**, 37, 1998.
42. Belomestnykh, V. N., *Neorganichenskia Materialy* **29**, 221, 1993 (in Russian).
43. Kimura, H., Numazawa, T. and Sato, M., *J. Mat. Sci.* **31**, 2361, 1996.
44. Kawamura, H., *Koatsuryoku no Kagaku to Gijutsu* **7**, 1998. (*Proc. Int. Conf. AIRAPT 16 & HPCJ 38 on High Press. Sci. & Tech.* **805–807**, 1997 [in English].)
45. Fijihisa, H., *Koatsuryoku no Kagaku to Gijutsu* **7**, 1998. (*Proc Int. Conf. AIRAPT 16 & HPCJ 38 on High Press. Sci. & Tech.* **790–792**, 1997 [in English]); Fujihisa, H., Yamawaki, H., Sakashita, M. and Aoki, K., *Phys. Rev. B: Condens. Mat. Phys.* **57**, 2651, 1998.
46. Shimizu, H., Ushida, T., Sasaki, S., Sakashita, M., Yamawaki, H. and Aoki, K., *Phys. Rev. B: Condens. Mat. Phys.* **55**, 5538, 1997.
47. Klimm, D., *Phys. Stat. Sol. A* **143**, 305, 1994.

48. Belomestnykh, V.N., *Neorganichenskia Materialy* **29**, 100, 1993 (in Russian).
49. Tischler, M., *Thermochim Acta* **231**, 87, 1994.
50. Sakashita, M., *Koatsuryoku no Kagaku to Gijutsu* **7**, 1998. (*Proc. Int. Conf. AIRAPT 16 & HPCJ 38 on High Pressure Sci. & Tech.* **796–798**, 1997 [in English].)
51. Pirnat, J., Trontelj, Z. and Borrmann, H., *Z. Naturforsch A: Phys. Sci.* **53**, 537, 1998.
52. Kitamaru, R., Horii, F., Nakagawa, M., Takamizawa, K., Urabe, Y. and Ogawa, Y., *J. Mol. Struct.* **355**, 95, 1995.
53. Minassian, Ter, L. and Milliou, F.J., *Therm. Anal.* **38**, 181, 1992.
54. Singh, D., Marshall, P.V. and Shields, L., *J. Pharm. Sci.* **87**, 655, 1998.
55. Matsuo, T., *J. Chem. Phys.* **108**, 9809, 1998.
56. Ishida, H., *Z. Naturforsch A: Phys. Sci.* **53**, 796, 1998.
57. Gregoryanz, E., Clouter, M.J., Rich, N.H. and Goulding, R., *Phys. Rev. B: Condens. Mat. Phys.* **58**, 2497, 1998.
58. Kubozono,Y., Yoshida, T., Maeda, H., Kashino, S., Terauchi, H. and Ishii, T., *J. Phys. Chem. Solids* **58**, 1375, 1997.
59. Tritt-Goc, J., Pislewski, N., Pawowski, A. and Goc, R., *Solid State Commun.* **106,** 367, 1998.
60. Anderson, A., *Proc. SPIE-Int. Soc. Opt. Eng.* **2089–2090**, 1993; Anderson, A., Beardsall, A.J. and Fraser, J.M., *Phys. Stat. Sol. B: Basic Research* **182**, 59, 1994.
61. van Miltenburg, J.C., van Genderen, A.C.G. and vandenBerg, G.T.K., *Thermochim. Acta* **31**, 151, 1998.
62. Ishida, H., Ono, H. and Ikeda, R., *Z. Naturforsch A: Phys. Sci.* **52**, 679, 1997.
63. Synderman, D.M., Adams, J.M., McDowell, A.F., Conradi, M.S. and Bunnelle, W.H., *J. Phys. Chem.* **98**, 6234, 1994.
64. Mayer, J., Urban, S., Habrylo, S., Holderna, K., Natkeniec, I., Wurflinger, A. and Zajac, W., *Phys. Stat. Sol.* **166**, 381, 1991.
65. Mayer, J., Rachwalska, M., Ściesińska, E., Ściesiński, J., *J. Phys. France* **51**, 857, 1990.
66. Nakata, K., *Dai-3-bumon* **45**, 39, 1996 (in English).
67. Janik, J.A., Mayer, J., Habrylo, S., Natkaniec, I., Zajac, W., Janik, J.M. and Stanek, T., *Phase Transit.* **37**, 239, 1992.
68. Hamann, F. and Würflinger, A., *Z. Phys. Chem.* **211**, 85, 1999.
69. Sandmann, M., Hamann, F. and Würflinger, A., *Z. Naturforsch.* **54a**, 281, 1999.
70. Asano, T., Mina, M.F. and Hatta, I., *J. Phys. Soc. Jpn.* **65**, 1699, 1996 (in English).
71. Reynhardt, E.C., *Chem. Phys. Lett.* **256**, 548, 1996.
72. Seshadri, R. and Rao, C.N.R., in *Perspectives in Solid State Chemistry*, K.J. Rao, ed., Narosa, New Delhi, 1995.
73. Stephanov, E.V., *Mater. Res. Soc. Symp. Proc.* **359**, 573, 1995.
74. Sinha, K.P., *Nat. Acad. Sci. Lett. (India)* **4**, 127, 1993.
75. Golberg, D., Bando, Y., Kurashima, K. and Sasaki, T., *Appl. Phys. Lett.* **17**, 2108, 1998.
76. Maniwa,Y., *Proc. Electrochem. Soc.* **14**, 1191, 1997.
77. Anderson, O., Soldatov, A. and Sundqvist, B., *Phys. Lett. A* **206**, 260, 1995.
78. Sundqvist, B., Soldatov, A., Lundin, A. and Anderson, O., *High Temp. – High Press.* **29**, 119, 1997.
79. Jenneskens, L., *Chem. Mag. (Rijswijk, Neth.)* **10**, 380, 1994 (in Dutch).
80. Kennedy, J.A. and Clark, S.M., *Mater. Sci. Forum* **228–231** (*Pt. 1, European Powder Diffraction: EPDIC IV, Pt. 1*), 423–427, 1996.
81. Tozaki, K., Ishii, C., Izuhara, O., Tsuda, N., Yoshimura, Y., Iwasaki, H., Noda, Y. and Kojima, A., *Rev. Sci. Instrum.* **69**, 3298, 1998.
82. Shapiro, S.M., Axe, J.D. and Shirane, G., *Phys. Rev. B* **6**, 4332, 1972.

5 Vapour–Liquid Equilibrium at Low Pressure

J. DAVID RAAL and D. RAMJUGERNATH
School of Chemical Engineering
University of KwaZulu-Natal
Durban, South Africa

Measurement of the Thermodynamic Properties of Multiple Phases
R.D. Weir and Th.W. de Loos (Editors)

5 VAPOUR–LIQUID EQUILIBRIUM AT LOW PRESSURE

Accurate measurement of high- and low-pressure multi-component vapour–liquid equilibria (VLE) has presented one of the most compelling experimental challenges to chemical engineers and physical chemists for a considerable time. With the rapidly increasing number of new organic compounds synthesized annually, the number of possible mixtures has become effectively infinite and design engineers cannot hope to have mixture property data banks for more than a small fragment of these. Ultimately, the task of predicting thermodynamic properties from basic molecular parameters is the only realistic goal. Such predictive methods are computationally very intensive (no longer a serious problem), but capable at present of only modest accuracy, insufficient for many purposes. Accurate, rapid and cost-effective measurement of VLE for binary and multi-component mixtures thus remains a considerable priority for the foreseeable future. An examination of published VLE data and limiting activity coefficients for highly non-ideal systems, such as alcohol–hydrocarbon mixtures, reveals quite considerable discrepancies between data sets from different researchers using similar or different equipment types. Moon *et al.* [1], using admittedly demanding criteria, found that only 27 per cent of the low-pressure VLE data sets examined were thermodynamically consistent. As noted by Joseph *et al.* [2], this is a surprising state of affairs after a century of experimental development and improvement and is cause for some introspection. To advance thermodynamic theory, VLE data of the highest possible accuracy, particularly in the difficult dilute regions, must be obtained. In the sections below, we survey measurement techniques, offer some insights into the experimental problem and suggest guidelines for measurement on systems of diverse behaviour.

5.1 Equipment and Procedures

Surveys of experimental equipment and procedures have been given by Hala *et al.* [3], Malanowski [4], Abbott [5] and Raal and Mühlbauer [6]. High-pressure phase equilibrium measurement is generally more difficult than for low pressures and is described in the extensive reviews by Raal and Mühlbauer [7], Mühlbauer and Raal [8] and Ramjugernath [9].

A definition of low-pressure VLE (LPVLE) has been given by Abbott [5] with reference to the equilibrium equation relating vapour and liquid compositions (y_i, x_i):

$$y_i = \frac{x_i \gamma_i p_i^{\text{sat}}}{P\Phi_i}. \tag{5.1}$$

The LPVLE is classified as the domain for which the vapour phase is satisfactorily described by the two-term virial EOS in pressure, and activity coefficients can be presumed pressure independent in Equation (5.1). These restrictions are considered appropriate [5] for pressures up to 0.5 MPa. In practice, LPVLE measurement is often limited to pressures up to or only modestly above 101.3 kPa due to the fragility of glass equipment. Equipment for VLE measurement can be broadly classified into three groups, namely, static methods,

dynamic methods and procedures for measuring infinitely dilute activity coefficients. The latter topic is reviewed separately in Chapters 13 and 14 of this volume.

5.1.1 Static Methods

In the static method, a thoroughly degassed liquid mixture is charged to an evacuated hermetically sealed equilibrium cell immersed in an isothermal environment. When equilibrium is judged to have been reached, *e.g.* as evidenced by constancy of measured pressure, the latter is noted and the equilibrium liquid composition is calculated from the charge composition. This is considered by some to be the truest equilibrium, particularly because there are no gradients in pressure or concentration. A popular procedure, pioneered by Gibbs and Van Ness [10], is to pump the two pure degassed liquids into an evacuated cell with metering piston pumps. For a given mixture, the bath temperature can be changed so that multiple isotherms can be obtained. Degassing was accomplished by Maher and Smith [11] in an assembly of 15 miniature cells connected to a common manifold with Cajon Ultra-Torr fittings and using lengthy freezing–evacuation–thawing cycles. Recent trends are to degas by low-pressure distillation.

An example of a more recent successful static apparatus is that of Fischer and Gmehling [12] (based on an earlier design by Rarey and Gmehling [13]) shown in Figure 5.1.

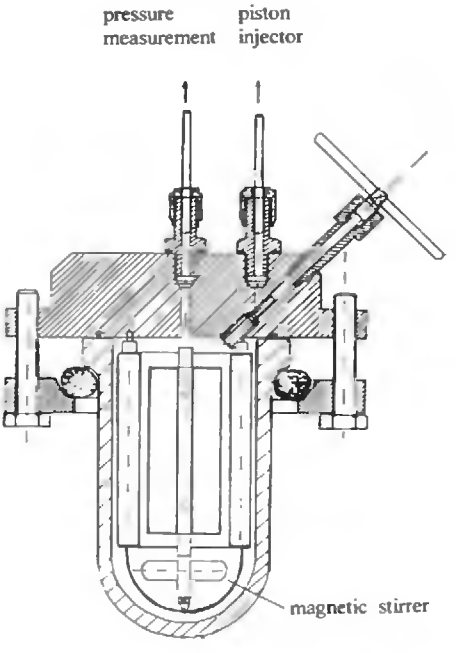

Figure 5.1 Static equilibrium cell of Fischer and Gmehling [12] (With permission from American Chemical Society.)

Good descriptions of the apparatus and the operating procedures, including degassing, are given by Kolbe and Gmehling [14] and Fischer and Gmehling [12]. Their earlier glass equilibrium cell permitted measurements at pressures up to 1.0 MPa. For highest accuracy, it was found necessary to thermostat the proportioning pumps.

Typically, in static methods, equilibrium vapour and liquid compositions are not measured, but are obtained by calculation. This represents a considerable economy of effort, but the P–x isotherm must be of the highest accuracy since subtle changes in curve shape can cause large errors in the calculated y_i, γ and G^E values [11]. A disadvantage of T–P–x data sets is that they cannot be tested for thermodynamic consistency. With excellent new tests of consistency such as those of Van Ness [15] and Moon *et al.* [1] now available, this is a worthwhile consideration.

5.1.2 Computations from Static Cell Data

A considerable variety of calculations arise in connection with low-pressure phase equilibria and have been extensively reviewed by Walas [16], and Raal and Mühlbauer [6]. Here we briefly review only those pertinent to reduction of data from static VLE equipment. In a typical experiment, only the charge composition, x_s, is known in addition to the measured pressure P and the controlled (and measured) temperature T. The first requirement is therefore to obtain the true liquid equilibrium mole fraction, x_1, for a binary mixture. For a static cell, this is a comparatively simple task based on equilibrium–flash relationships and the amount of hold-up in the vapour phase [12,17–19]. A formulation in terms of two new dimensionless groups, R_T and R_G, has been given by Raal and Ramjugernath [20]. Material balances and equilibrium constraints led to the working equation

$$x_1 = \frac{x_{s1}}{1 + (K_1 - 1)E}, \tag{5.2}$$

where K_1 is the equilibrium constant y_1/x_1. E can be considered an equipment characterization parameter (although it also involves system properties), and Equation (5.2) has exactly the same form as that for a dynamic ebulliometer. For the latter however, E is also a function of the vaporization ratio $\phi = V/F$ [21], as discussed for ebulliometers in Chapter 13. When E is resolved in terms of the total equipment interior volume, v^{TOT}, one obtains

$$E = \frac{V'}{S'} = \frac{R_T - 1}{R_G - 1}, \tag{5.3}$$

where the S' and V' are the moles of charge and equilibrium vapour phase hold-up respectively, and R_T and R_G are given by

$$R_T = \left(\frac{v^{TOT}}{S'}\right)\left(\frac{\rho_L}{M_L}\right), \tag{5.4}$$

and

$$R_G = \left(\frac{RTZ}{P}\right)\left(\frac{\rho_L}{M_L}\right). \tag{5.5}$$

M_L and ρ_L are the equilibrium liquid molar mass and density, respectively, and Z the vapour-phase compressibility factor

$$M_L/\rho_L = \sum \frac{x_i M_i}{\rho_i}. \tag{5.6}$$

If the excess volume is neglected, the physical significance of the dimensionless groups is essentially as follows: $R_T \cong$ total equipment volume per unit charge volume and R_G = vapour molar volume per unit liquid molar volume.

Once E has been determined for a given experiment, x_1 can be obtained from Equation (5.2) by fairly simple iterative procedures. The total interior volume, including all fittings, tubing and pressure transducer volume up to the diaphragm, is most conveniently determined by measuring the equilibrium liquid composition x_1 and pressure P for a system of known phase equilibrium behaviour. With x_1, x_{s1} and K_1 known, E is found from Equation (5.2) and hence v^{TOT} from Equations (5.4)–(5.6). A sample calculation is given by Raal and Ramjugernath [20].

For systems of large relative volatility, more specifically large K_1, it is clear from Equation (5.2) that x_1 can differ considerably from the charge composition x_{s1}, even for comparatively small vapour hold-up (small R_T) and moderate pressures [20].

5.1.3 Semi-Micro Cells

In all VLE measurements, the system components must be of the highest purity, particularly if reliable data are to be obtained in the very dilute regions, often of considerable importance in industrial separation processes for high-purity chemicals.

In these regions, any solvent impurity competes with the added solute in influencing system behaviour. Some high-purity chemicals are very expensive and, to cover the full composition range, large amounts of the two components may be required in either a static or dynamic VLE apparatus. Resolution of this problem may lie in the use of *semi-micro* static cells such as those proposed by Wichterle and Hala [22], Wichterle and Boublikova [23] and Maffiolo and Vidal [24]. To overcome some of the drawbacks of these earlier designs, a more robust and versatile design was developed by Raal and Mühlbauer [6]. The apparatus, shown in Figure 5.2, departs from the more conventional static cell types in that there is a small impeller-induced circulation of the vapour phase through the sample loop of a GC valve attached above the cell, *i.e.* the vapour circulation is *internally* induced. The valve system shown permits rapid but not complete degassing and conveyance of the vapour sample directly to a GC. Provision is also made for sampling the liquid phase at equilibrium through a sample septum. Although the pressure measured by the pressure transducer will not be correct due to traces of inert gas, the equilibrium pressure can be *calculated* from the *ratio* of GC peak areas for the vapour, as explained by Raal and Mühlbauer [6]. The $\pm 8\,cm^3$ equilibrium cell is jacketed to maintain isothermal conditions. All fittings in the compartment above the ss flange to which the cell attaches are kept slightly superheated with the block heater shown. Data for the system (cyclohexane + ethanol) obtained with this apparatus were in close agreement with published values.

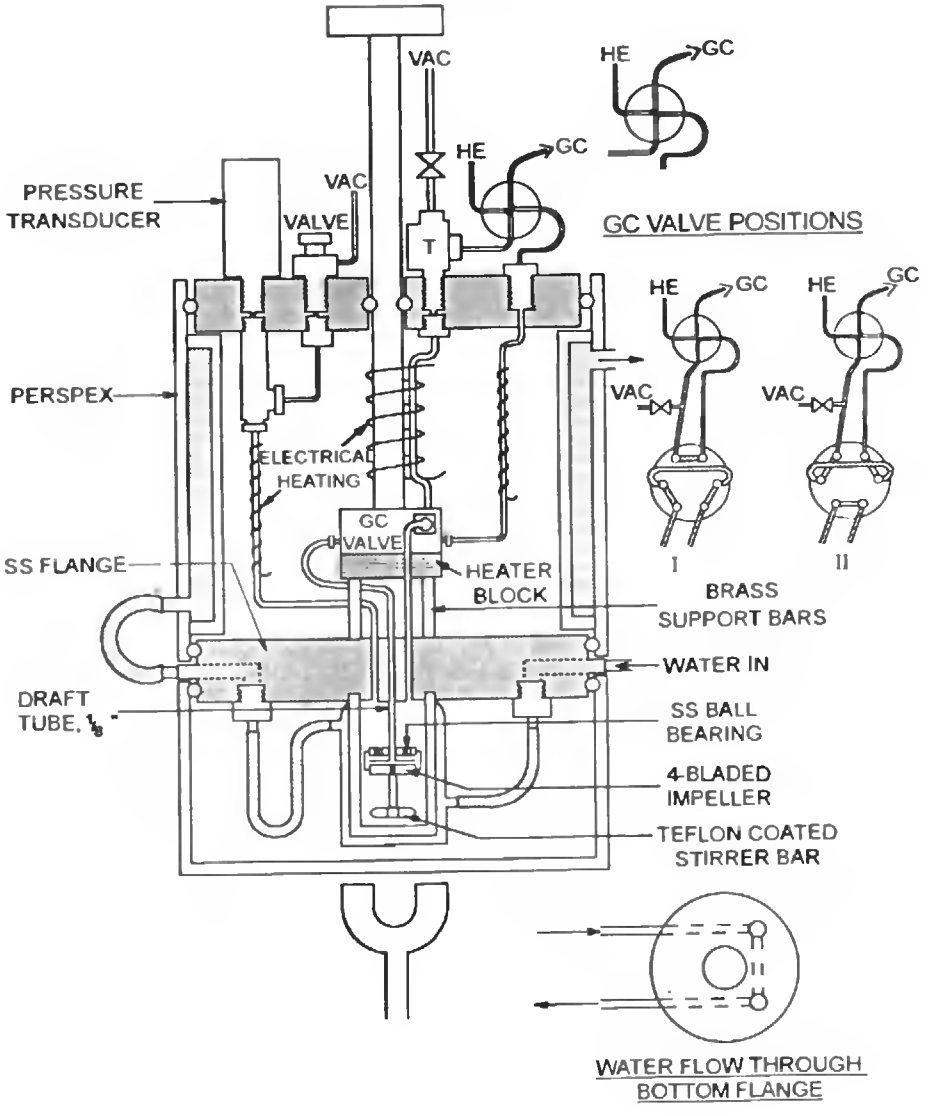

Figure 5.2 Semi-micro cell of Raal and Mühlbauer [6]. (With permission from Taylor & Francis.)

5.1.4 Data Reduction from *P–x* Measurements

The ultimate goal of experimental VLE measurements is to find a correlating equation that can faithfully reproduce equilibrium data over the full composition range. A considerable variety of expressions for the Gibbs excess energy, G^E, differing in complexity and applicability have been developed over the years. The subject is too large and complex to review here. The reader is referred to the texts by Prausnitz *et al.* [25], Walas [16], Abbott and Van Ness [26] and

Raal and Mühlbauer [6]. Evaluation of the constants in an equation for G^E directly from experimental P–x data constitutes a *model-dependent* approach. Such procedures are well known and adequately described in the above texts and will not be repeated here. An interesting procedure for finding the equivalent binary constants in a correlating equation from measured P–x data for a ternary system has been demonstrated by McDermott and Ellis [27].

A considerable number of "model-free" methods have also been developed and can be classified as *direct*, when the vapour composition or relative volatility is solved for, or, *indirect* when G^E or γ_i is first obtained. The methods are of comparable rigour and should yield the same result if there is no appreciable bias or inconsistency in the data. The direct method is based on the *co-existence equation* [26]. In its simplest form, assuming ideal gas behaviour and a liquid molar volume, negligible compared with that of the vapour, the equation for isothermal data becomes

$$\frac{dy_1}{d \ln P} = \frac{y_1(1 - y_1)}{y_1 - x_1}. \tag{5.7}$$

An example of the integration of this equation for the system {water (1) + methyl butenol (2)} for isobaric data has been given by Raal and Brouckaert [28]. In Figure 5.3, we show measured and calculated data, based on the NRTL equation, obtained by Fischer and Gmehling [29] for the system {3-methyl pentane (1) + *N*-methyl-pyrrolidone (2)}, obtained with the static apparatus of Figure 5.1. The data are exemplary and unusually precise in the hydrocarbon dilute region to the extent that an accurate limiting coefficient (γ_1^∞) can be obtained. Finally, how precise must the temperature control be to obtain reliable P–x data and how is this dependent on system properties?

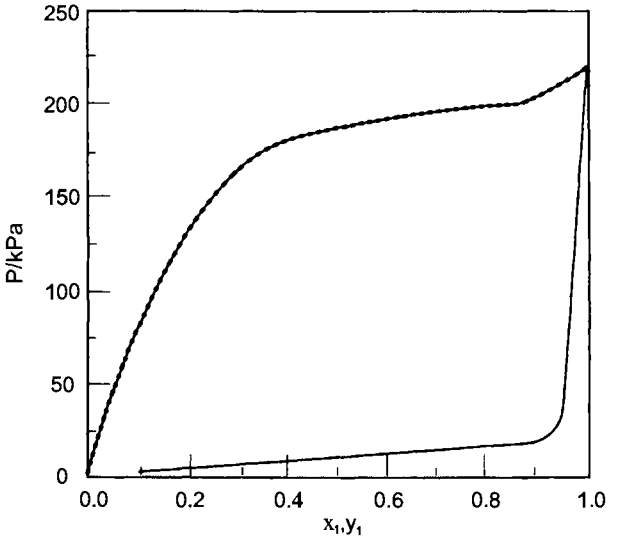

Figure 5.3 Experimental P–x_1 data for the system {3-methyl pentane (1) + *N*-methyl-pyrrolidone (2)} measured with the apparatus of Figure 5.1 [29]. P–y_1 data are calculated. (With permission from Elsevier Publishers.)

5.1.5 Sensitivity of Temperature and Pressure

The greatest difficulty in measurement is nearly always in the very dilute but exceptionally important regions for highly non-ideal systems, such as alcohol–hydrocarbon systems. Special procedures have been developed to find the limiting activity coefficients, γ_1^{∞}. These are reviewed in Chapters 13 and 14. A good indication of how precise temperature or pressure control, the latter for isobaric measurements, must be, can be obtained from the derivative $(\partial T/\partial P)_x$. An expression for the latter can be developed as follows.

Using the triple product relationship,

$$\left(\frac{\partial T}{\partial P}\right)_{x_1} = -\frac{(\partial T/\partial x_1)_p}{(\partial p/\partial x_1)_T}. \tag{5.8}$$

The denominator is most easily developed, *e.g.* from the expression for total pressure:

$$P = \sum y_i P = \sum \frac{x_i \gamma_i p_i^{\text{sat}}}{\Phi_i} \cong \sum x_i \gamma_i p_i^{\text{sat}}. \tag{5.9}$$

Differentiation of Equation (5.9) together with use of the Gibbs–Duhem equation,

$$\sum x_i \mathrm{d} \ln \gamma_i = (V^{\text{E}}/RT)\,\mathrm{d}p. \tag{5.10}$$

gives

$$\left(\frac{\partial p}{\partial x_1}\right)_T = \frac{(p_1^{\text{sat}}\gamma_1 - p_2^{\text{sat}}\gamma_2)\{1 - x_2 \mathrm{d} \ln \gamma_2/\mathrm{d}x_1\}}{1 - p_1^{\text{sat}}\gamma_1 V^{\text{E}}/RT}. \tag{5.11}$$

For the numerator, $(\partial T/\partial x_1)_p$, a more circuitous route has been found as follows:

$$\left(\frac{\partial T}{\partial x_1}\right)_p = \left(\frac{\partial T}{\partial y_1}\right)_p \left(\frac{\partial y_1}{\partial x_1}\right)_p, \tag{5.12}$$

since

$$y_1 \cong x_1 \gamma_1 p_1^{\text{sat}}/P,$$

therefore

$$\left(\frac{\partial y_1}{\partial x_1}\right)_p = \frac{1}{P}\left[x_1\gamma_1\left(\frac{\partial p_1^{\text{sat}}}{\partial T}\right)_p\left(\frac{\partial T}{\partial x_1}\right)_p + p_1^{\text{sat}}\left\{x_1\frac{\partial \gamma_1}{\partial x_1} + \gamma_1\right\}\right]. \tag{5.13}$$

To find a suitable expression for $(\partial T/\partial y_1)_p$, we use the coexistence equation [27] with the vapour phase assumed to be ideal, a satisfactory assumption for our purpose unless there is a strong association:

$$\left(\frac{\partial T}{\partial y_1}\right)_p = -\frac{(y_1 - x_1)}{\Omega\, y_1(1 - y_1)}, \tag{5.14}$$

with

$$\Omega = \frac{x_1\Delta_{vap}H_1 + x_2\Delta_{vap}H_2 - H^E}{RT^2} \cong \frac{x_2\Delta_{vap}H_2}{RT^2} \text{ for dilute solutions} \tag{5.14a}$$

where $\Delta_{vap}H_2$ is the enthalpy of vaporisation of component 2, the solvent.

Substitution of Equations (5.13) and (5.14) into Equation (5.12) gives after some simplification, and with $K_i = y_i/x_i$,

$$\left(\frac{\partial T}{\partial x_1}\right)_p = \frac{-B\{x_1 d\ln\gamma_1/dx_1 + 1\}\gamma_1}{1 + Bx_1\gamma_1(d\ln p_1^{sat}/dT)}, \tag{5.15}$$

where

$$B = \frac{(K_1 - 1)p_1^{sat}}{\Omega P K_1 K_2 x_2}. \tag{5.15a}$$

The expression for $(\partial T/\partial p)_{x_1}$ in the dilute region thus becomes finally

$$\left(\frac{\partial T}{\partial p}\right)_{x_1} \cong \frac{B\gamma_1\{x_1 d\ln\gamma_1/dx_1 + 1\}}{(1 + Bx_1\gamma_1 d\ln p_1^{sat}/dT)(p_1^{sat}\gamma_1 - p_2^{sat}\gamma_2)\left\{1 - x_2\dfrac{d\ln\gamma_2}{dx_1}\right\}} \tag{5.16}$$

Equation (5.16), though cumbersome in appearance, is readily programmed for evaluation. More rigorous forms of Equations (5.11) and (5.16), incorporating vapour-phase non-ideality and the Gibbs–Duhem equation, have been derived and will be presented in a future publication. In addition to the saturation pressures, estimates of the γ_i are required, *e.g.*

$$\ln\gamma_i = A(1 - x_i)^2 \qquad \text{with } A = \ln\gamma_i^{\infty}. \tag{5.17}$$

For the less dilute regions, the one-constant form of the Wilson equation is excellent and recommended [20]. In the calculation, proceeding step-wise from $x_1 = 0$, the temperature at each x_1, is approximated by assuming that $(\partial T/\partial x_1)$ from the previous step $\cong$ constant $= \Delta T/\Delta x_1$. Values of $(\partial T/\partial p)_{x_1}$ evaluated from Equation (5.16) are illustrated for the system {*n*-hexane (1) + ethanol (2)} in Figure 5.4. To interpret these results, *i.e.* a *T–p* sensitivity of about $0.0019\,K \cdot Pa^{-1}$ in the dilute region, the required pressure regulation to reduce the temperature fluctuation to 0.02 K, must be better than 0.0105 kPa, a quite stringent requirement for an isobaric process. For isothermal operation, a variation of 0.05 K in the water bath temperature for example, will produce a pressure response of 26 Pa (not related to composition change), in the concentration region up to about 0.01 mole fraction (from the inverse quantity, $(\partial p/\partial T)_{x_1}$).

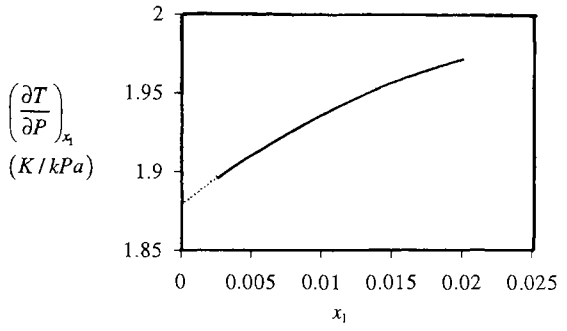

Figure 5.4 Temperature–pressure sensitivity, $(\partial T/\partial p)_{x_1}$, for the system {*n*-hexane (1) + ethanol (2)} at $T = 301$ K, calculated from Equation (5.16).

Limiting activity coefficients for use in Equation (5.16) can be predicted with accuracy more or less sufficient for our purpose by the analytical solution of groups (ASOG) or by the MOSCED or SPACE equation methods, particularly for non-aqueous systems [30].

In the limit as $x_1 \rightarrow 0$, Equation (5.16) reduces simply to

$$\left(\frac{\partial T}{\partial p}\right)^{\infty} = \left(\frac{\mathrm{d}p_2^{\mathrm{sat}}}{\mathrm{d}T}\right)^{-1}. \tag{5.18}$$

Equation (5.16) should prove useful for correcting measured temperature due to controlled pressure fluctuations at any composition (x_1) with the generally short time lag taken into consideration.

5.2 Dynamic Methods

In dynamic methods, the vapour phase, the liquid phase or both phases may be circulated. Recirculating equilibrium stills have accounted for a large proportion of low-pressure VLE data in the literature. A very considerable number of variations of a few basic types have been used and proposed in the literature and the reader is referred to earlier reviews by Hala *et al.* [3], Malanowski [4], Abbott [5] and Raal and Mühlbauer [6].

Despite their popularity, equilibrium stills present a number of problems, some quite serious if accurate data are to be obtained for highly non-ideal systems. Among the more serious are the following:

(i) A failure to attain true equilibrium.
(ii) A partial condensation of equilibrium vapour.
(iii) A failure to attain smooth boiling and a steady state with minimum fluctuations in temperature and pressure.
(iv) Accurate measurement or control of temperature and pressure.
(v) Errors in composition measurement.

5.2.1 Attainment of Equilibrium

In the older Othmer type of apparatus, the vapour formed above a boiling liquid is condensed and recirculated. The equilibrium established in such an apparatus is at best a local equilibrium between a vapour bubble and a small packet of liquid in close proximity with the bubble [31,32]. Continued recycling will not improve the approach to equilibrium. Also, temperature measurement is unsatisfactory. Among attempts at resolution of these problems have been the following:

(a) Vaporize the returning condensate and bubble it through the liquid in the equilibrium chamber.
(b) Circulate both the liquid and vapour using a Cottrell vapour lift pump.
(c) Force a vapour–liquid mixture downwards through a packed equilibrium chamber with subsequent separation of the two streams.

Method (a) can be accomplished in the Jones–Colburn apparatus [33] and its many subsequent variations. For systems with the major resistance to mass transfer in the liquid phase particularly, this mechanism for attainment of equilibrium is first class provided the equilibrium chamber has no stagnant areas. The most serious drawbacks are the difficulty in attaining stable operation and the extreme sensitivity of the results to any small vertical temperature gradients in the upper part of the equilibrium chamber. A successful adaptation of the bubbling chamber has however been found which solves both these problems. In this adaptation [6,28], see Figure 5.5, a novel annular Cottrell pump is used to produce a steady vapour stream and to promote rapid thermal equilibration. The design is unusual in that, although the apparatus appears to be of the vapour and liquid recirculation type, the equilibrium chamber operates as a vapour flow bubbling through a static, adiabatically isolated liquid, a mechanism extensively used in high-pressure VLE apparatus with mechanical circulation of the vapour.

There is a small pressure drop across the liquid in the inner chamber so that the temperature, if measured as shown, will be at a pressure slightly above the controlled and measured value. Temperature calibration should be done *in situ* with a pure liquid. An example of isobaric VLE data measured with the apparatus of Figure 5.5 is shown in Figure 5.6 [28].

Widely used dynamic stills are usually variations and improvements of the original Gillespie still [34], in which the Cottrell pump itself must accomplish phase equilibrium. An example of a recent version is that of Gmehling *et al.* [35], shown in Figure 5.7. As with the earlier Othmer type of apparatus, however, equilibrium must be accomplished *in a single pass* and repeated circulation, no matter how long, cannot produce a closer approach to equilibrium than that of a single pass at steady state.

A much sounder approach for achieving dynamic equilibrium is to force vapour and liquid downward co-currently through a short packed adiabatic chamber as in the apparatus of Yerazunis *et al.* [32]. A successful version of such an apparatus is shown in Figure 5.8 and can be computer controlled to give either isobaric or the generally more useful isothermal data. The apparatus is compact, robust and the equilibrium chamber angularly symmetric. The packing (small wire mesh cylinders) is readily accessible and can be tailored to the system requirements. For a system with high temperature–pressure sensitivity, for

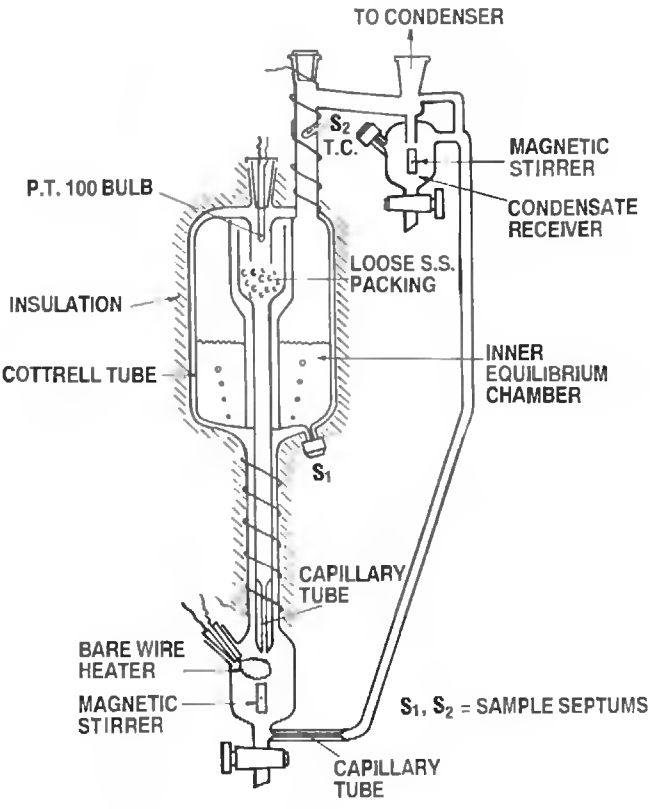

Figure 5.5 Dynamic VLE still with bubbling chamber [28]. (With permission from Elsevier Publishers.)

example, a short section of very open packing with low-pressure drop is advisable to reduce or eliminate vertical temperature gradients. The temperature is measured near the bottom of the packing. The vacuum-jacketed Cottrell tube and the vapour lagging of the equilibrium chamber (in addition to a vacuum outer jacket), to ensure complete adiabaticity, are salient features. Thermodynamically consistent data have been obtained with the equipment, operated by PC in either isobaric or isothermal mode, for several systems by Joseph *et al.* [36].

5.2.2 Partial Condensation of Equilibrium Vapour

In the two designs described above, it is clear that strong precautions are taken to avoid any partial condensation of the equilibrium vapour. Even the smallest amount of condensation in either a static or dynamic apparatus in the equilibrium area will produce considerable error in the vapour composition.

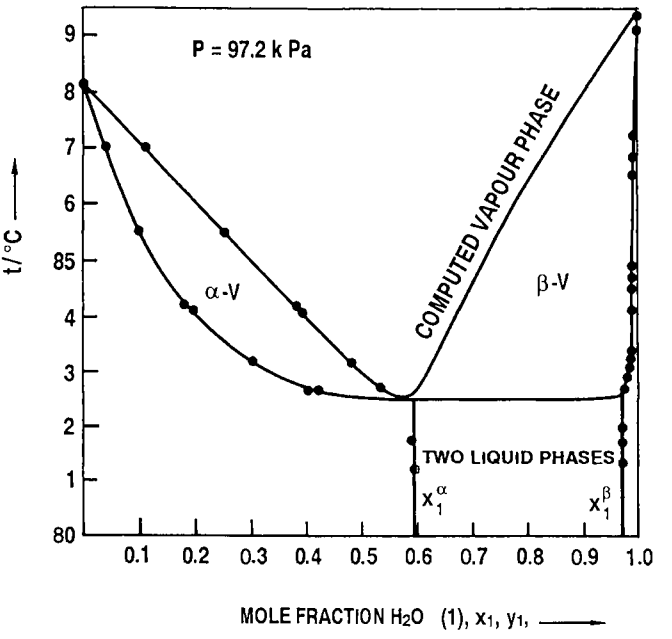

Figure 5.6 Isobaric VLE data for the system {water (1) + methyl butenol (2)} at 97.2 kPa, obtained with the apparatus of Figure 5.4. (With permission from Elsevier Publishers.)

In the first design (Figure 5.5), the vapour take-off tube is superheated as shown and the interior is insulated with a vapour jacket. In the apparatus of Figure 5.8, the annular vapour flow in the concentric tubes surrounding the equilibrium chamber is outstandingly effective in preventing partial condensation. Considerable glass-blowing skill is required to construct either apparatus.

5.2.3 Smooth Boiling

The best results are obtained in a dynamic apparatus when boiling and vapour generation are smooth and free of bumping. The designs described above both have rapid magnetic stirring in the boiling chamber. In the apparatus of Figure 5.8, an internal heater with roughened surfaces assists smooth boiling and gives fine control. For pure solvents, boiling temperature can be boil-up rate dependent, as found by Kneisl *et al.* [37], particularly for systems with large dipole moments and/or molecular association, *i.e.* the plateau region in which one normally operates has a noticeable slope. In the ebulliometers of Thomas *et al.* [38], 30 mesh ground glass particles were fused to the inner wall of the boiler. The production of smooth continuous boiling, particularly for hydrogen-bonded systems, is one of the greatest challenges in dynamic VLE apparatus and a fruitful area for further refinement and research.

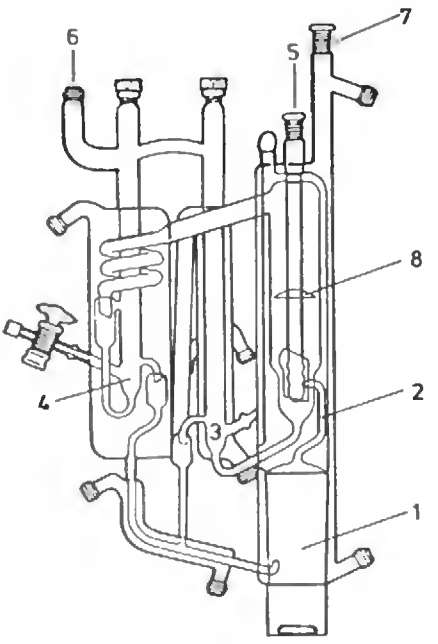

Figure 5.7 Dynamic VLE apparatus of Gmehling *et al.* [35]. (1) Boiling flask; (2) Cottrell pump; (3) liquid-phase collector; (4) condensed-vapour-phase collector; (5) thermometer well; (6) joining flange for manostat; (7) thermometer mounting; (8) shield. (With permission from American Chemical Society.)

5.2.4 Measurement and Control of Temperature and Pressure

With the highly developed electronic circuitry presently available, very precise temperature and pressure measurements are possible by a variety of devices. Digitized signals from Pt-100 sensors or strain gauge pressure transducers are readily transmitted to a PC without signal degradation, preferably through 16-bit or higher precisions, for measurement and control. Capacitance devices for pressure measurement are also popular. Dynamic VLE apparatus can be precisely controlled by a PC with appropriate software to operate in either isobaric or isothermal mode. A relatively simple control strategy such as pulse-width modulation can produce highly accurate, thermodynamically consistent isothermal data [36]. Development and testing of more sophisticated control strategies is continuing in our laboratories. Equation (5.16) can be utilized for this purpose since it contains system-specific properties and at any composition gives the expected temperature response to pressure fluctuations.

5.2.5 Measurement of Composition

Gas–liquid chromatography remains the favoured procedure for sample analysis. The newest flame ionization (FID) and dissociation ionization (DID) detectors have impressive capabilities. Several other specialized detectors for certain classes of compounds have

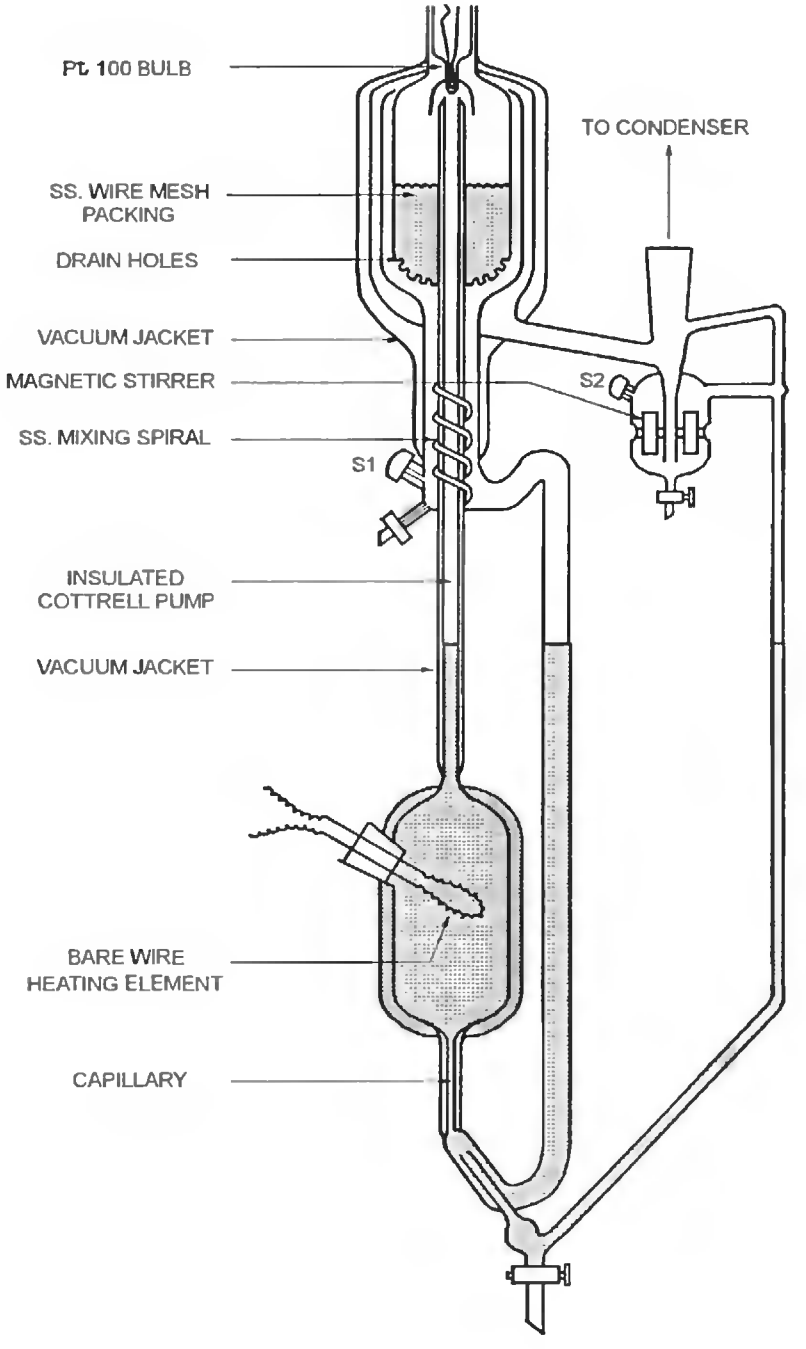

Figure 5.8 Raal modification of the Yerazunis *et al.* [32], dynamic VLE still. Magnetic stirrer in boiler not shown. (With permission from Taylor & Francis.)

been developed. To test and allow for any non-linearity in detector response, the area ratio method of Raal and Mühlbauer [6] is recommended. *In situ* measurements, without sampling, can also be made by Raman spectroscopy, as shown by Kaiser *et al.* [39]. These authors determined both liquid and vapour compositions with an estimated error of ±0.002 mole fraction for the (cyclohexane + toluene) binary mixture. The method appears to be limited to systems without strong inter-molecular forces.

5.3 Conclusions

Equipment of sound design, whether of the static or dynamic type and when carefully operated, can give precise and thermodynamically consistent data even for the most difficult systems. The greatest experimental difficulty is usually in the dilute regions where concentration and temperature or pressure gradients can be very steep. Equipment suitable for one system, or in one region of concentration, may be unsatisfactory for another system or in the other dilute region. The equations for the temperature–pressure sensitivity proposed here, $(\partial T/\partial p)_x$, although subjected so far to only limited testing, should provide guidance as to which type of equipment is best suited to the task. In particular, it quantifies the precision required in the control of either temperature or pressure to produce acceptable tolerances in the measured P or T in selected areas of concentration and should be useful in developing more sophisticated pressure control strategies in which system-specific properties are taken directly into account. It also permits accurate correction of measured temperatures due to pressure fluctuations or vice versa at any composition.

Static equipment such as the highly developed apparatus of the Gmehling school can give very precise isothermal T–P–x data even in the very dilute regions but their thermodynamic consistency cannot be tested. The degassing procedure is time-consuming. The two dynamic stills proposed above have quite different mechanisms for achieving equilibrium, are effective in eliminating superheating of the equilibrium liquid and give excellent results. The T–p–x–y data they yield can be tested for thermodynamic consistency. Multicomponent systems are readily measured. Equilibrium is reached rapidly and, at low pressures, no degassing is required. Future improvements in the operation of such dynamic equipment probably lies in more sophisticated pressure control by improved PC software, *e.g.* to give isothermal P–T–x–y data. The suitability of dynamic equipment relying only on a Cottrell pump to achieve equilibrium in a single pass is considered questionable for systems of high-relative volatility.

References

1. Moon, H.M., Ochi, K. and Kajima, K., *Fluid Phase Equilibr.* **62**, 29–40, 1991.
2. Joseph, M.A., Ramjugernath, D. and Raal, J.D., *Chem. Technol. (SA)* October 23–27, 2001.
3. Hala, E., Pick, J., Fried V. and Vilim, O., *Vapour–Liquid Equilibrium*, Pergamon Press, Oxford, 1967.
4. Malanowski, S., *Fluid Phase Equilibr.* **8**, 197–219, 1982.
5. Abbott, M.M., *Fluid Phase Equilibr.* **29**, 193–207, 1986.
6. Raal, J.D. and Mühlbauer, A.L., *Phase Equilibria: Measurement and Computation*, Taylor & Francis, Washington, DC, 1998.

7. Raal, J.D. and Mühlbauer, A.L., *Dev. In Chem. Eng. Mineral Proc.* **2**, 69–104, 1994.
8. Mühlbauer, A.L. and Raal, J.D., *Chem. Eng. J.* **60**, 1–29, 1994.
9. Ramjugernath, D., *High Pressure Phase Equilibrium Studies*, Ph.D. Thesis, University of Natal, Durban, 2001.
10. Gibbs, R.E. and Van Ness, H.C., *Ind. Eng. Chem. Fund.* **11**, 410–413, 1972.
11. Maher, P.J. and Smith, B.D., *Ind. Eng. Chem. Fund.* **18**, 354–357, 1979.
12. Fischer, K. and Gmehling, J., *J. Chem. Eng. Data* **39**, 309–315, 1994.
13. Rarey, J.R. and Gmehling, J., *Fluid Phase Equilibr.* **83**, 279–287, 1993.
14. Kolbe, B. and Gmehling, J., *Fluid Phase Equilibr.* **23**, 213–226, 1985.
15. Van Ness, H.C., *Pure Appl. Chem.* **67**, 859–872, 1995.
16. Walas, S.M., *Phase Equilibria in Chemical Engineering*, Butterworth, Boston, 1985.
17. Abusleme, J.A. and Vera, J.H., *Can. J. Chem. Eng.* **66**, 964–969, 1988.
18. Pividal, K.A., Birtigh, A. and Sandler, S.I., *J. Chem. Eng. Data* **37**, 484–487, 1992.
19. Hartwick, R.P. and Howat, C.S., *J. Chem. Eng. Data* **40**, 738–745, 1995.
20. Raal, J.D. and Ramjugernath, D., *Fluid Phase Equilibr.* **187**, 473–487, 2001.
21. Raal, J.D., *AIChE J.* **46**, 210–220, 2000.
22. Wichterle, I. and Hala, E., *Ind. Eng. Chem. Fund.* **2**, 155–157, 1963.
23. Wichterle, I. and Boublikova., *Ind. Eng. Chem. Fund.* **8**, 585, 1969.
24. Maffiolo, G. and Vidal, J., *Bull. Soc. Chim. De France* **8**, 2810–2815, 1971.
25. Prausnitz, J.M., Lichtentaler, R.N. and Gomez de Azevedo, E., *Molecular Thermodynamics of Fluid Phase Equilibria*, 3rd ed., PTR, Upper-Saddle River, NJ, 1999.
26. Abbott, M.M. and Van Ness, H.C., *Classical Thermodynamics of Fluid Phase Equilibria*, McGraw-Hill, New York, 1982.
27. McDermott, C. and Ellis, S.R.M., *Chem. Eng. Sci.* **20**, 545–548, 1965.
28. Raal, J.D. and Brouckaert, C.J., *Fluid Phase Equilibr.* **74**, 253–270, 1992.
29. Fischer, K. and Gmehling, J., *Fluid Phase Equilibr.* **119**, 113–130, 1996.
30. Eckert, C.A. and Sherman, S.R., *Fluid Phase Equilibr.* **116**, 332–343, 1996.
31. Joseph, M.A., Ramjugernath, D. and Raal, J.D., *Dev. Chem. Eng. Mineral Process* **10**, 637–651, 2002.
32. Yerazunis, S., Plowright, J.D. and Smola, F.M., *AIChE J.* **10**, 660–665, 1964.
33. Jones, C.A., Schoenborn, E.M. and Colburn, A. P., *Ind. Eng. Chem.* **35**, 660–672, 1943.
34. Gillespie, D.T.C., *Ind. Eng. Chem.* **18**, 575–577, 1964.
35. Gmehling, J., Onken, U. and Schulte, H.W., *J. Chem. Eng. Data* **25**, 29–32, 1980.
36. Joseph, M.A., Raal, J.D. and Ramjugernath, D., *Fluid Phase Equilibr.* **182**, 157–176, 2001.
37. Kneisl, P., Zondlo, J.W. and Whiting, W.B., *Fluid Phase Equilibr.* **46**, 85–94, 1989.
38. Thomas, E.R., Newman, B.A., Nicolaides, G.L. and Eckert, C.A., *J. Chem. Eng. Data* **27**, 233–240, 1982.
39. Kaiser, T., Vossmerbäumer, C. and Schweiger, G., *Bunsenges. Physikaler Chem. Berichte* **96**, 976–980, 1992.

6 Vapour–Liquid Equilibrium at High Pressure

D. RICHON
CEP/TEP
Ecole Nationale Supérieure des Mines de Paris
Fontainebleau, France

TH.W. DE LOOS
Physical Chemistry and Molecular Thermodynamics
Department of Chemical Technology
Delft University of Technology
Delft, The Netherlands

Measurement of the Thermodynamic Properties of Multiple Phases
R.D. Weir and Th.W. de Loos (Editors)

6 VAPOUR–LIQUID EQUILIBRIUM AT HIGH PRESSURE

It is impossible to perform vapour–liquid equilibrium (VLE) measurements at high pressure for all kind of systems using one technique only. The reason for this is that the experiments have to be performed over a wide range of temperatures and pressures and for mixtures of compounds with widely differing physical properties such as volatility, corrosivity, viscosity, thermal stability, density, etc. Also different types of data have to be obtained like Henry's constants or activity coefficients at infinite dilution, p–T–x or p–T–x–y data with or without the simultaneous determination of densities, etc.

The accurate determination of phase equilibria remains sometimes difficult, time-consuming and expensive. So the choice of the right and adequate technique is far from trivial. Over the years, many different apparatuses have been developed and used. It is, however, difficult to compare all of them in a simple way. Some classifications are available in the literature [1–6]. These classifications can be made in several ways. Dohrn and Brunner [6] divided the experimental methods for the determination of high-pressure VLE into two groups based on the way compositions are measured. In this work, we have preferred to make a classification according to how phase equilibria are obtained, namely closed- and open-circuit methods.

6.1 Closed-Circuit Methods

In this group, we have the static–analytic methods, the quasi-static method (circulated phases) and the static–synthetic methods. The major advantage of static methods is their simplicity. The studied system is enclosed in a cell and one waits as long as needed to reach equilibrium. An internal stirring system is usually added to the equilibrium cell in order to reduce the time of equilibration. The equilibrium can be checked by total pressure stability and/or constancy of phase composition as a function of time. Measurements are generally carried out isothermally, with compositions being determined after each pressure change to obtain isothermal p–x–y diphasic envelopes. Equilibrium is reestablished more quickly after a pressure change than after a temperature change, due to the thickness of the walls of the equilibrium cell, especially at very high pressures. We divide the closed-circuit methods into subgroups according to the way of the determination of the phase compositions.

6.1.1 Static–Analytic Methods

These methods require the analysis of the vapour and the liquid phases. This can be done either on withdrawn samples or directly *in situ*. Sampling is a challenging job, because the samples must be representative for the equilibrium phases and the withdrawal of samples must not disturb the equilibria studied, *e.g.* the total pressure must remain constant during sampling. Unfortunately, these conditions are rarely rigorously fulfilled. *In situ* analyses are very attractive but they can be applied in very few cases only.

Sampling

Many different sampling techniques have been developed. Peter and Eicke [7] and Peter *et al.* [8] carried out analyses on part of the samples taken from a container in which they are expanded. It is important to take special care to ensure that the liquid samples do not undergo any vaporisation and to avoid any condensation of the heavy components inside the tubing through which the liquid and the gas samples are withdrawn. Pawlikowski *et al.* [9] use the technique of expanding samples on-line with the same inconveniences. A valve with a sampling loop is used to send a small quantity of the sample into a gas chromatograph (see Figure 6.1). Butcher and Robinson [10] also use the expansion procedure but with analyses by refractometry (see Figure 6.2). Valuev *et al.* [11] developed an instrument somewhat more complex than the preceding, using a ball to close the sampling line (see Figure 6.3) and letting the sample flow in the hollow axis of a needle that rests against the ball. A considerable dead volume is characteristic for this type of sampling. Jacoby and Tracht [12] designed a pressure resistant removable sampling valve (see Figure 6.4), which can be placed in the sampling line and then removed to carry a sample for injection into chromatograph carrier gas as proposed some years before by Yarborough and Vogel [13]. This type of sampling requires at least one shut-off valve and one or more sampling valves. This series of valves creates important and complex-shaped dead volumes which are difficult to sweep. For an experimental run, several times the valves have to be assembled and disassembled, increasing the risk of non-thermal equilibrium in the whole apparatus and the possibility of leaking.

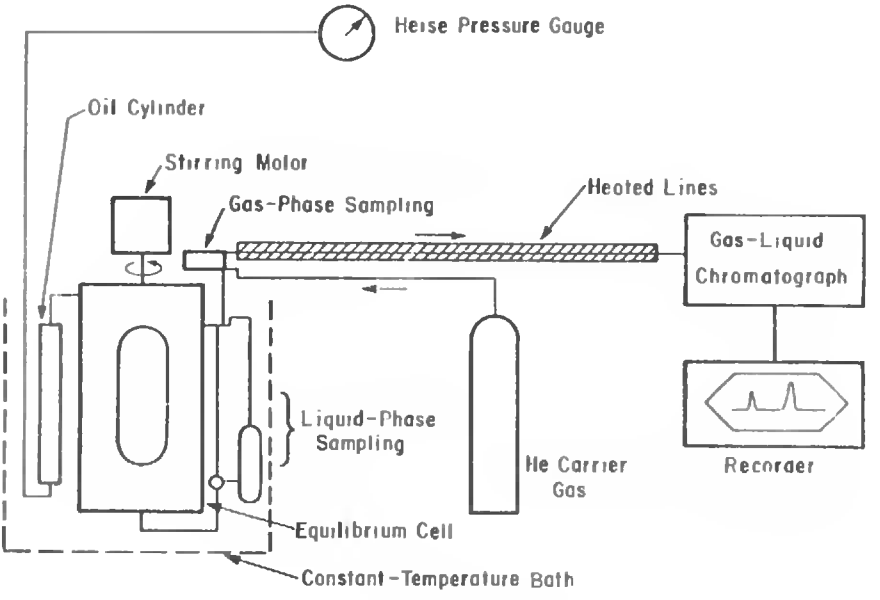

Figure 6.1 Equipment of Pawlikovski *et al.* Reproduced from reference [9] with kind permission of American Chemical Society. Copyright 1982.

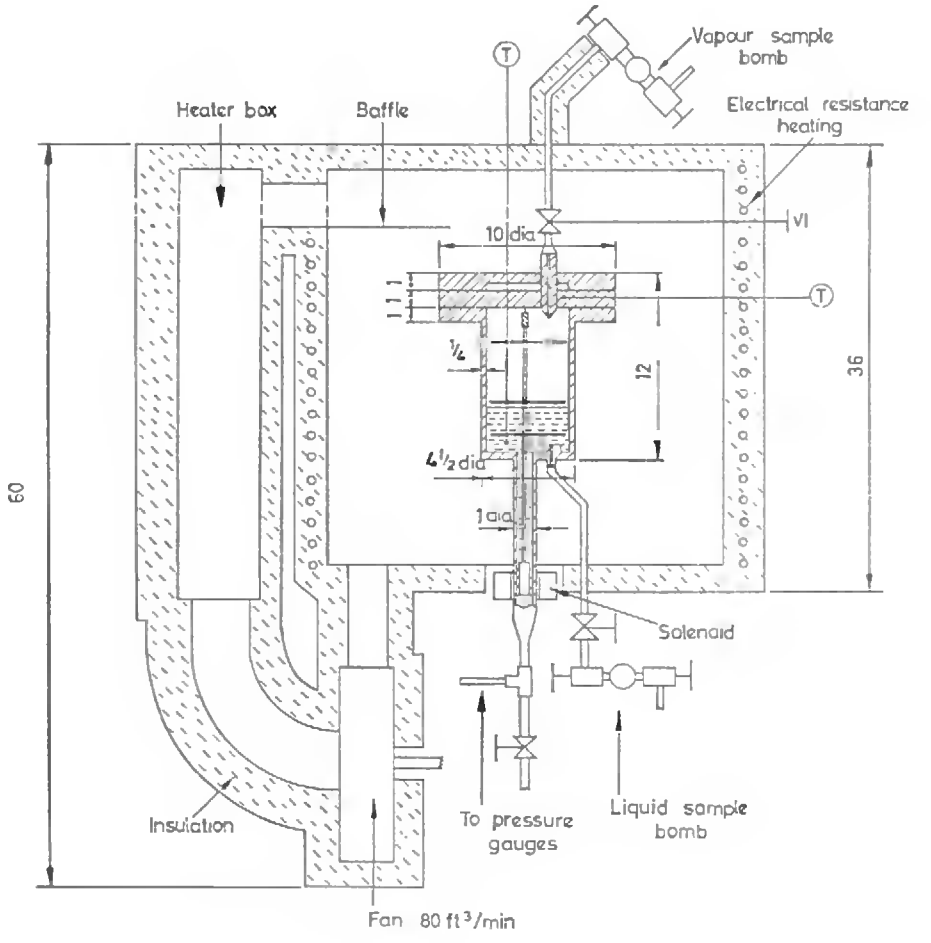

Figure 6.2 Apparatus of Butcher and Robinson [10]. Reproduced from reference [10] with kind permission of Society of Chemical Industry. Copyright 1966.

The samples are more representative for the equilibrium phases if they are withdrawn as close as possible to the equilibrium phase and if they are analysed totally. In addition, the withdrawal of a minimum amount of sample with negligible mass with respect to that of the equilibrium phases is a positive factor to keep the system at equilibrium (constant pressure). A way to take samples at constant pressure, which has been used by several authors, is to use mercury displacement. For example, Ellis *et al.* [14] collect the vapour and liquid samples in containers filled beforehand with mercury (see Figure 6.5). However, the hazards of working with mercury are not negligible and equilibrium temperatures are limited to a relatively small range.

To take samples as close as possible to the wall of the equilibrium cell, Rodgers and Prausnitz [15] have designed a cell with pistons (see Figure 6.6) passing through the walls of the cell. These pistons allow one to take small samples (some nm^3) and to send them

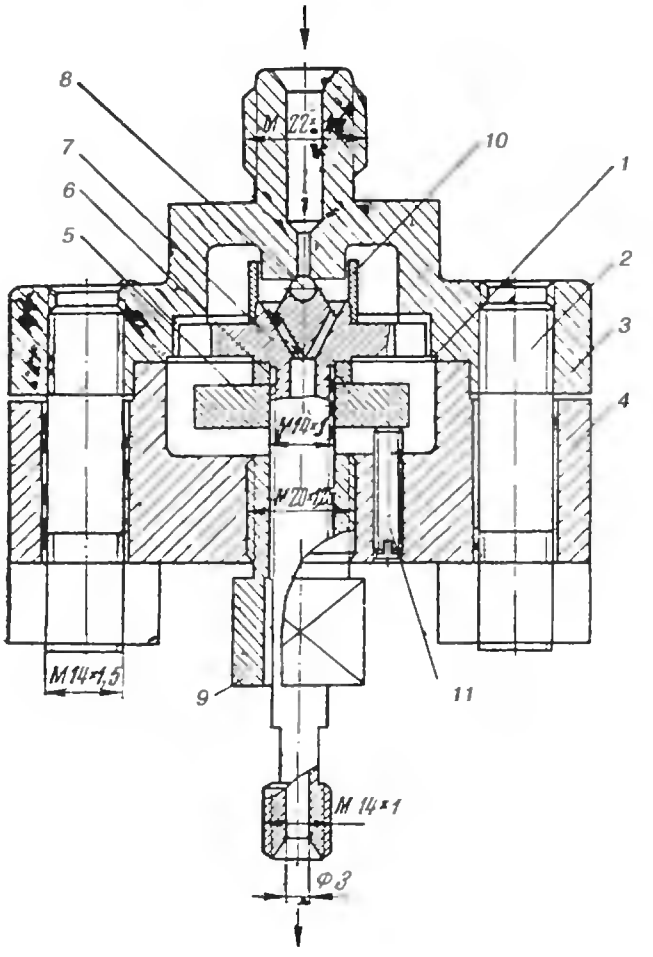

Figure 6.3 Cell of Valuev *et al.*: 1, membrane; 2, screw; 3, valve body; 4, valve cap; 5, nut; 6, disc; 7, axis support; 8, ball; 9, differential screw; 10, security ring. Reproduced from reference [11] with kind permission of Nauka Publishers. Copyright 1972.

directly into a chromatograph carrier gas circuit. Unfortunately, the main problem with this technique is to achieve a reliable sealing between the piston and the wall of the cell. Dorokhov *et al.* [16] developed a new sampling technique by trapping a small sample between two stems inside the equilibrium cell body (see Figure 6.7). The cell body comprises a cavity (4) at the bottom of which a bellows valve obstructs a small channel (3). This channel is closed at its other extremity by a similar valve. To take a sample, the valve (5) is opened, the channel fills up; then the valve (5) is closed while valve (6) is opened, the carrier gas sweeps the sample into the chromatograph. This design has several disadvantages that include the need to have two expansions for each sampling and the fact that region (4) in Figure 6.7 is not well stirred and the small channel (3) acts as a dead volume

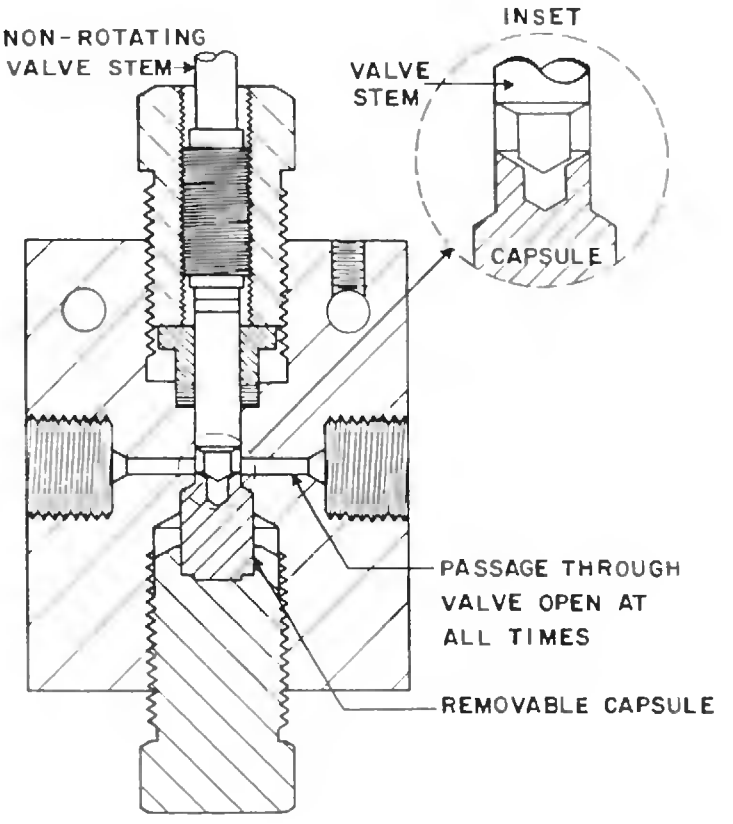

Figure 6.4 Removable sampling valve from Jacoby and Tracht. Reproduced from reference [12] with kind permission of Preston Publications, a Division of Preston Industries, Inc. Copyright 1975.

in the carrier gas circuit and heavy components can remain partially inside the channel and undergo a differential vaporisation. To solve these problems, Figuière *et al.* [17] developed another sampling system with valves (see Figure 6.8). The blocking cones of the valve stems are pushed against the equilibrium cell seating by very strong spring washers to achieve a perfect seal. The stems are moved backward by calibrated shocks allowing to withdraw samples of about 1 nm^3 of both liquid and vapour phase. The carrier gas flowing through the channel machined along the valve stem sweeps the samples totally (no dead volume). Sampling is done very quickly in less than 0.1 s and the sample size can be changed by modifying the aperture shocks. The equilibrium cell of Figuière *et al.* allows experiments up to $T = 673$ K and 40 MPa. The sampling systems of Dorokhov *et al.* and Figuière *et al.* have one important limitation, namely the liquid samples must be vaporised at the equilibrium temperature during a relatively short time and at the chromatograph carrier gas pressure. In the case of the apparatus of Figuière *et al.*, temperature limitation is not so drastic and the equipment can be adapted [18] through simple modifications to equilibrium temperatures lower than boiling temperatures of the heaviest component under study.

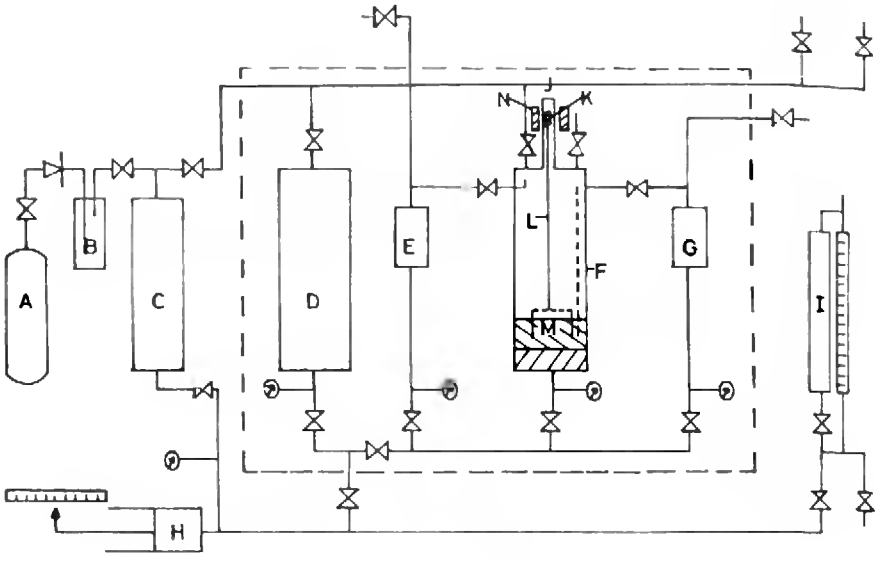

Figure 6.5 Equipment of Ellis *et al.*: A, gas cylinder; B, dryer; C, compressor; D, displacement cell; E and G, sampling cells (65 and 45 cm^3); F, equilibrium cell (500 cm^3); H, volumetric pump; I, mercury reservoir. Reproduced from reference [14] with kind permission of American Institute of Chemical Engineers. Copyright 1968.

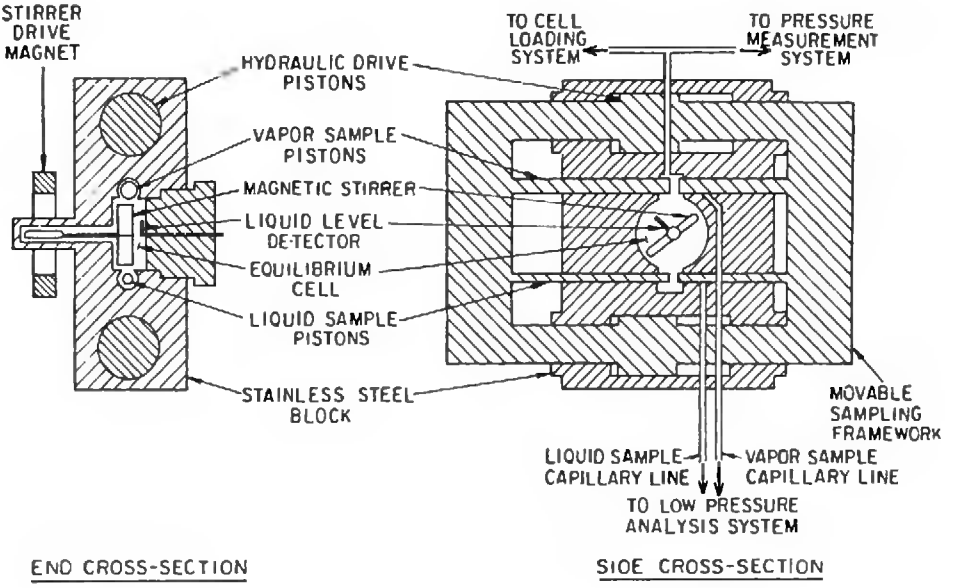

Figure 6.6 Cell of Rodgers and Prausnitz. Reproduced from reference [15] with kind permission of American Chemical Society. Copyright 1970.

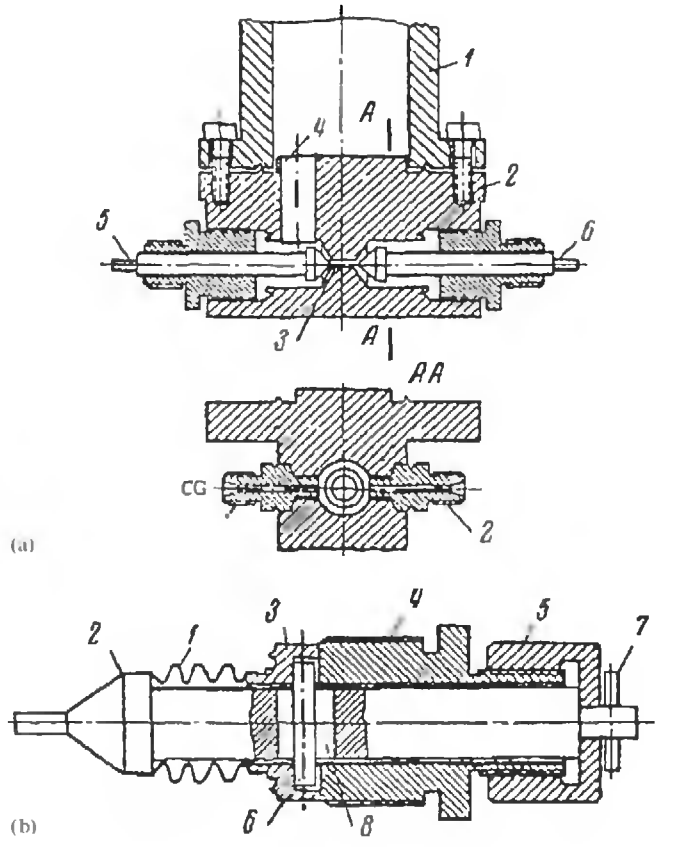

Figure 6.7 Apparatus of Dorokhov *et al.* [16]. (a) Equilibrium cell: 1, cell body; 2, analysis circuit; 3, sampling volume; 4, volume to be sampled; 5 and 6, sampling valves (see b). (b) Sampling valve: 1, bellows; 2, stem; 3, ring; 4, thread; 5, nut; 6, spacer; 7, stop-bolt; 8, screw. Reproduced from reference [16] with kind permission of Nauka Publishers. Copyright 1972.

Miksovski and Wichterle [19] use capillaries, the ends of which enter a transparent cell, to take samples (see Figure 6.9). When equilibrium is reached, the capillaries are opened at the end so that a continuous stream of product rinses the capillary. The flow is sent into the injector of a gas chromatograph for a specified amount of time. More recently, Laugier and Richon [20] designed a new device based on this capillary sampling technique. Figure 6.10 gives a flow diagram of a new version of this type of sampler injector. This pneumatic sampler injector (Armines' patent) presents many interesting features; it allows: samplings up to 60 MPa from cryogenic temperatures to 673 K, continuous adjustment of sample size from about 1 to 100 mg, no dead volumes and independent heating of the sampler. Representative and reliable samples are obtained through *in situ* withdrawing and the whole amount of withdrawn samples is analysed. More recently, an electromagnetic version has been developed (Rolsi™, Armines' patent) and is now available.

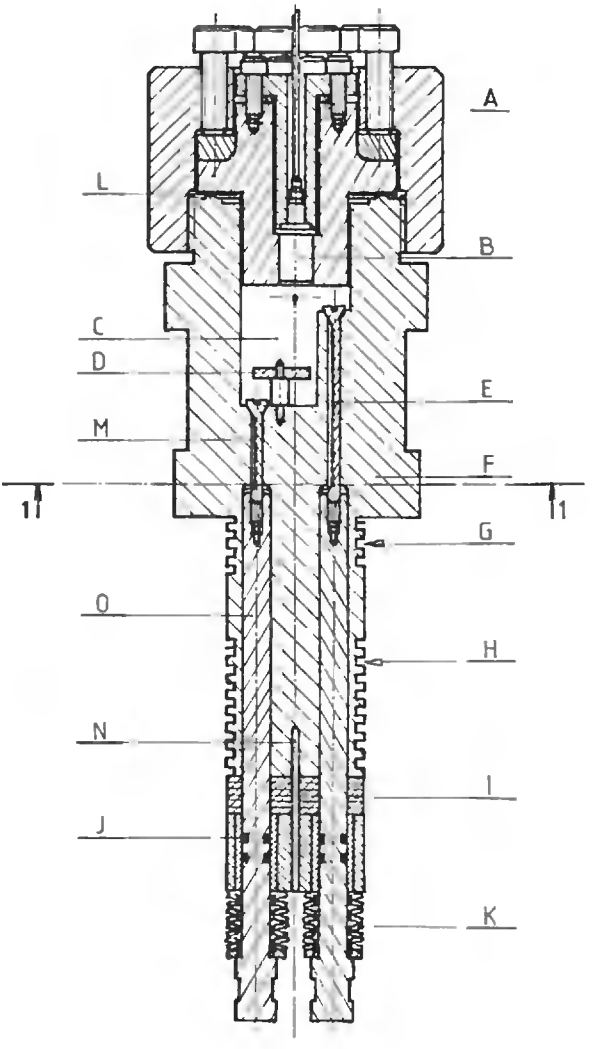

Figure 6.8 Cell of Figuière *et al.*: A, cell cap; B, pressure transducer; C, equilibrium compartment; D, magnetic stirrer; E, valve; F, cell body; G, heating resistance seat; H, cooling coil seat; I, Teflon thermal shield; J, Viton O-ring; K, spring washers; L, copper gasket; M, channel; N, thermocouple well; O, valve pusher. Reproduced from reference [17] with kind permission from American Institute of Chemical Engineers. Copyright 1980.

In Situ Analyses

Instead of taking samples, some authors prefer to perform analyses directly inside the equilibrium cell by using spectroscopic methods. The cell must be equipped with windows that are transparent for the type of radiation involved. Marteau *et al.* [21] use sapphire windows for *in situ* determination of high-pressure phase diagrams of methane–heavy

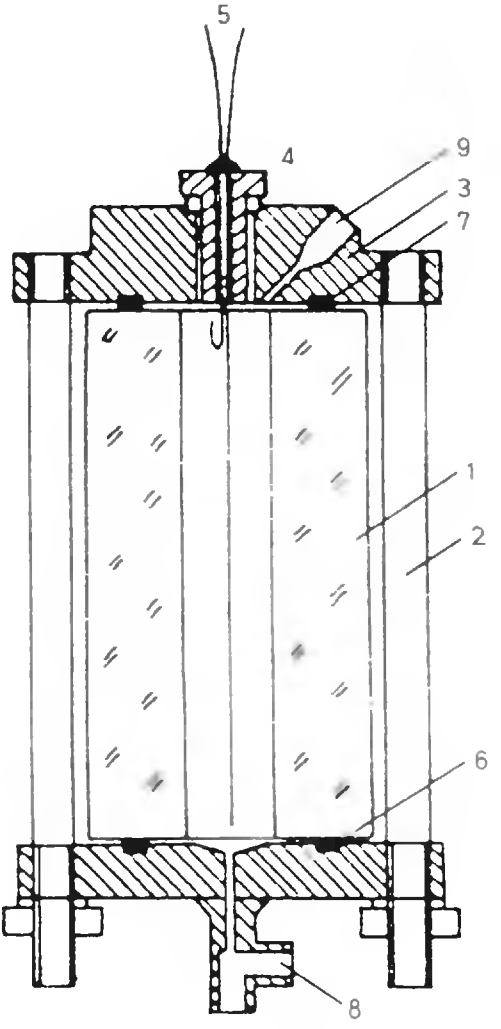

Figure 6.9 Cell of Miksovski and Wichterle: 1, glass tube; 2, bolt; 3, flange; 4, bushing; 5, capillary; 6 and 7, Teflon rings; 8, inlet; 9, outlet. Reproduced from reference [19] with kind permission of the Institute of Organic Chemistry and Biochemistry, Academy of Sciences of the Czech Republic. Copyright 1975.

hydrocarbon mixtures by infrared spectroscopy (see Figure 6.11). Although this method is very attractive, it can, unfortunately, only be applied to very particular cases, since the infrared spectra of compounds are complex and superimposed for mixtures. It becomes difficult with more than two components to obtain precise quantitative determinations. Furthermore, molecular extinction coefficients depend on temperature and pressure, which make calibrations very tedious. In some cases, Raman spectroscopy can be advantageously

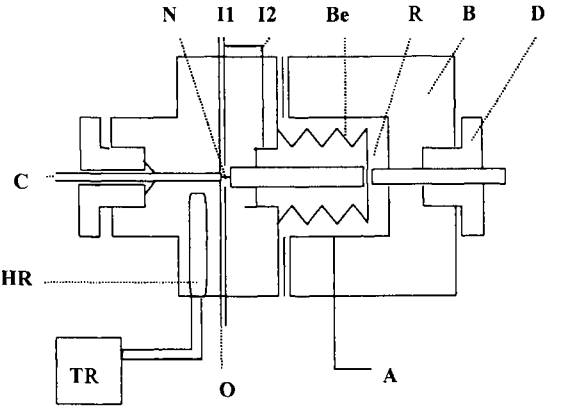

Figure 6.10 Pneumatic sampler from Laugier and Richon: A, compressed air inlet; B, sampler body; Be, bellows; C, capillary; D, differential screw; HR, heating resistance; I1, I2, carrier gas inlet; N, micro stem; O, carrier gas outlet; R, expansion room; TR, temperature regulator.

used, but it has about the same drawbacks. Konrad *et al.* [22] designed a cell with four windows, mounted 2 × 2 at different levels of the cell. This construction allowed the determination of the composition of the liquid and the vapour phase at the same time using near-infrared spectroscopy. Recently, Tuma and Schneider [23] presented a high-pressure cell for the determination of the solubility of solid dyestuffs in near- and supercritical fluids using UV spectroscopy.

6.1.2 Quasi-Static Method (Circulated Phases)

Mechanical Circulation

In several designs, the agitation that is necessary for establishing equilibrium is accomplished by dispersing one phase into the other, instead of using a stirrer bar that is externally activated by a magnetic device. In this case, the vapour phase or the liquid phase or both phases are circulated over a period of time in a closed circuit using a pump. In the equilibrium cell, agitation and mass transfer are enhanced by bubbling the circulating vapour phase through the liquid phase.

Katayama *et al.* [24], Freitag and Robinson [25] (see Figure 6.12), Miksovsky and Wichterle [19] and Nasir *et al.* [26] all chose to bubble the vapour phase through the liquid phase, using a magnetic pump. Katayama *et al.* collect vapour samples in containers relatively far from the equilibrium cell. Freitag and Robinson [25] determine, in addition to the phase equilibrium, the saturated molar volume of the phases, by measuring the refractive index. The cell of Nasir *et al.* [26] is a variable volume cell (Figure 6.13), which permits, in principle, the determination of pVT properties. Weber *et al.* [27] use a cell (Figure 6.14) in which the liquid samples are taken by capillaries closed by a valve and the vapour sample is taken directly from the circulation line. In addition, the cell is equipped with

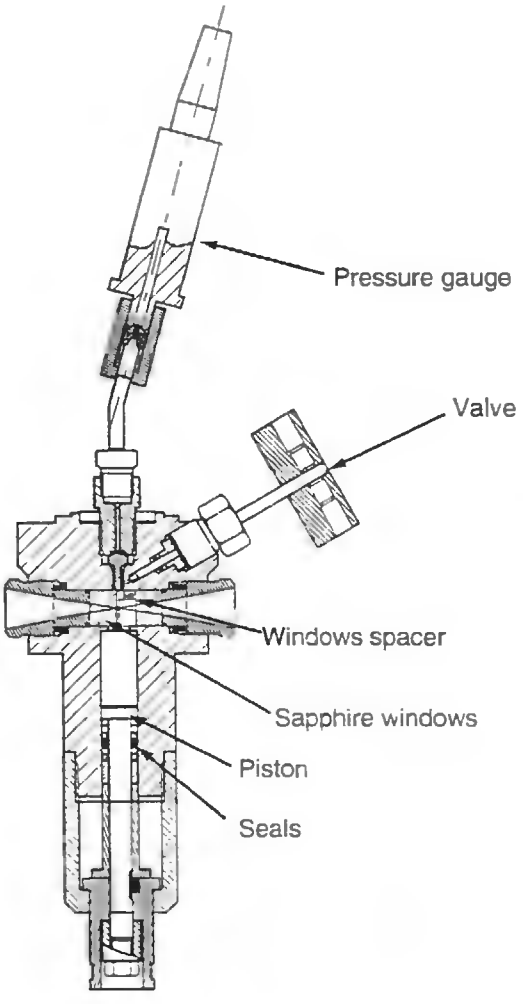

Figure 6.11 Cell of Marteau *et al.* Reproduced from reference [21] with kind permission from Elsevier. Copyright 1996.

an optical system that allows the visual observation of the contents of the cell. Kim *et al.* [28] have chosen to circulate the liquid phase. Samples are taken through sampling valves, one in the circulation line for the liquid sample and another at the bottom of a tube for the vapour sample. The equilibrium of the vapour phase in the sampling tube of internal diameter 3 mm is obtained by diffusion. The time necessary to reach equilibrium under these conditions is very long. In the design of Radosz [29], both the liquid and the vapour are circulated. A variable volume cylinder is used to keep the pressure constant during sampling, which is absolutely necessary when large samples are withdrawn. Fleck and Prausnitz [30] circulate the three phases of triphasic systems with magnetic pumps and the samples are taken directly into the circulation lines (Figure 6.15).

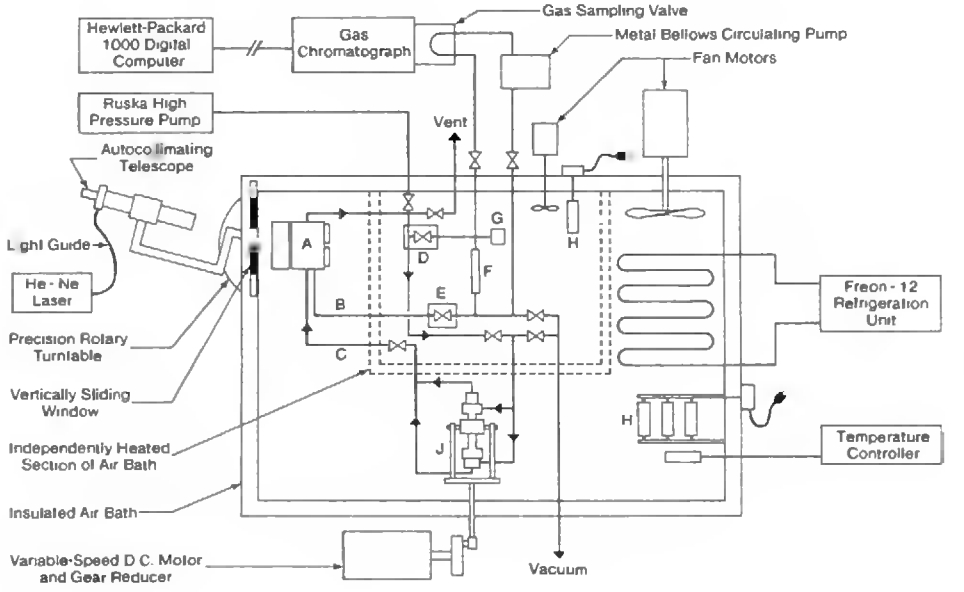

Figure 6.12 Equipment of Freitag and Robinson: A, equilibrium cell; B, liquid sampling capillary; C, vapour recirculation line; D, vapour sampling valve; E, liquid sampling valve; F, sample storage section; G, pressure transducer; H, electric heaters; J, vapour recirculation pump. Reproduced from reference [25] with kind permission from Elsevier. Copyright 1986.

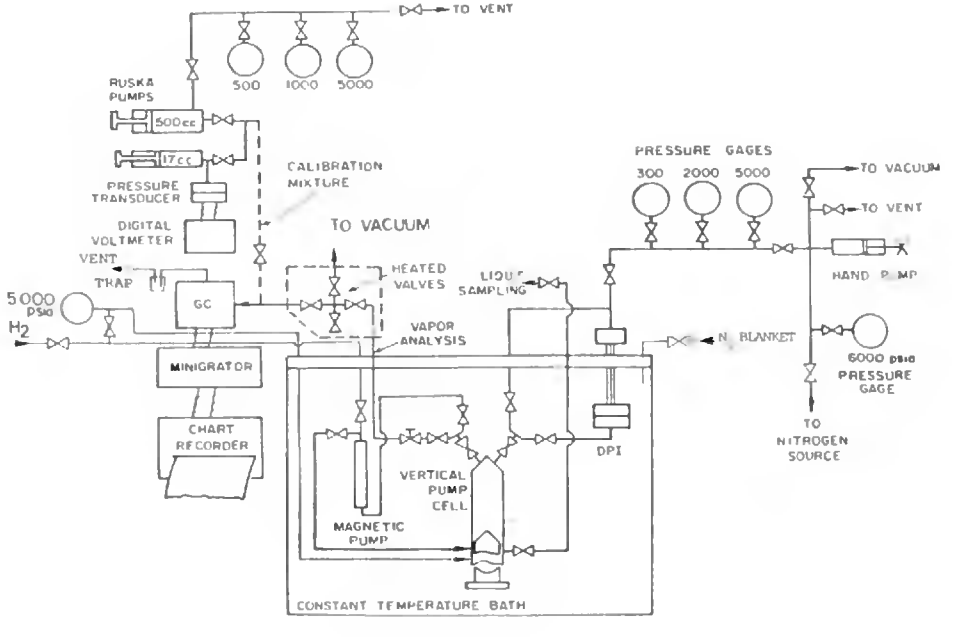

Figure 6.13 Apparatus of Nasir *et al.* Reproduced from reference [26] with kind permission from Elsevier. Copyright 1980.

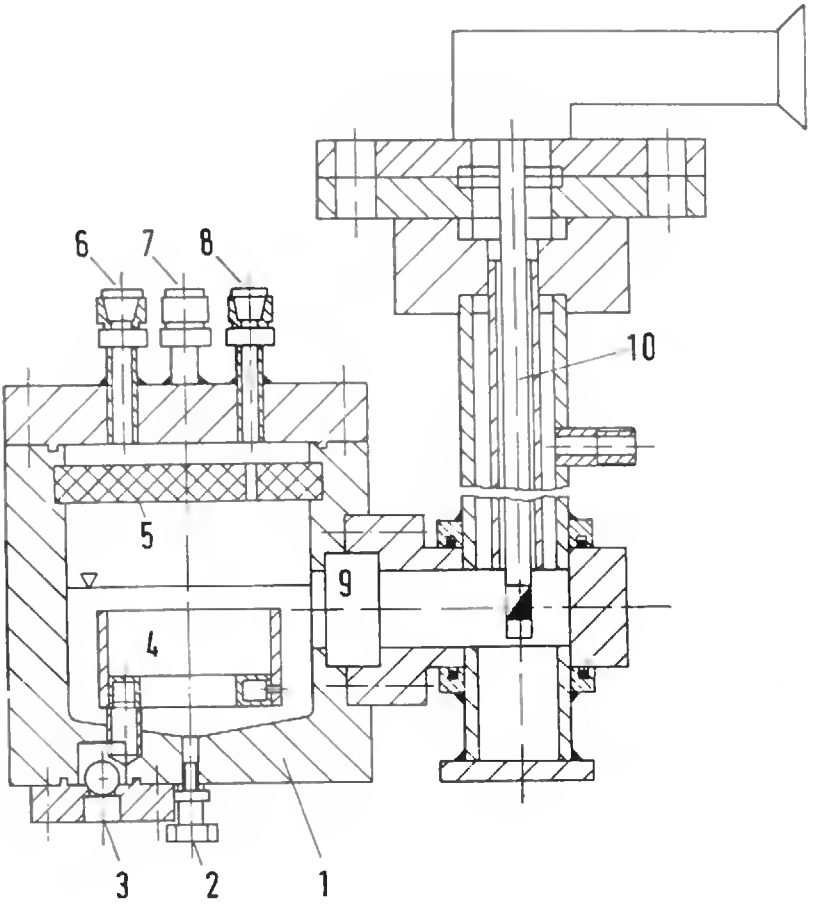

Figure 6.14 Cell of Weber *et al.*: 1, cell body; 2, solvent inlet; 3, gas inlet; 4, distribution nozzle; 5, mist separator; 6, gas outlet; 7, connection for temperature sensor; 8, connection for capillary; 9, high-pressure glass window; 10, inspection and illumination device. Reproduced from reference [27] with kind permission from Elsevier. Copyright 1984.

Thermal Circulation

Sampling

The phenomenon of forced circulation is well known from ebulliometry (see Hala *et al.* [31] and Chapter 5), where the circulation of the phases is achieved by boiling. In the most advanced devices, equilibrium is not reached in the boiling liquid, but during a turbulent and adiabatic flow in a Cottrell pump, which also serves to pump the liquid. Large numbers of ebulliometers have been presented in the literature, but mainly for measurements carried out at relatively low pressure. An example of a device using circulation by ebullition

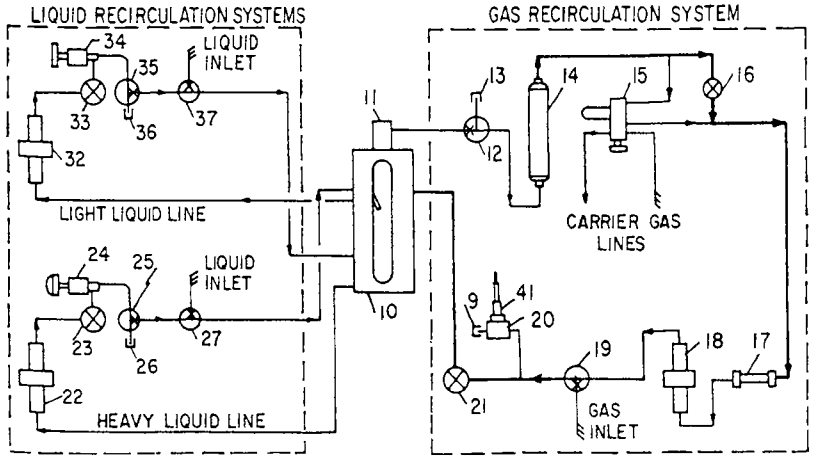

Figure 6.15 Equipment of Fleck and Prausnitz: 10, equilibrium cell; 11, safety cap; 12, 19, 25, 27, 35, 37, three-port valves; 9, 13, 26, 36, caps; 14, 300 cm^3 gas-surge vessel; 15, linear valve; 16, block valve; 17, small gas-surge vessel; 18, 22 and 32, magnetic pumps; 20, transducer receiver; 21, 23 and 33, valves; 24, 34, liquid samplers; 41, flush-diaphragm pressure transducer. Reproduced from reference [30] with kind permission of American Chemical Society. Copyright 1968.

is that of Othmer and Morley [32], which allows measurements up to 1.5 MPa. A diagram of this device is given in Figure 6.16. The evaporated liquid phase is condensed and collected in the condensate reservoir from which it returns to the ebullition reservoir. After a period of 2–3 h, necessary to reach equilibrium, samples are withdrawn from both reservoirs.

In Situ *Analyses*

In principle, it should be easy to fit windows in the wall of the two reservoirs and perform spectroscopic analyses of the contents instead of withdrawing samples for analyses.

6.1.3 Static–Synthetic Methods

The mixture is placed inside an equilibrium cell, by introducing pure components one after the other. The number of moles of each component is determined by weighing or pressure–volume measurements. Weighing is the method that gives the most accurate results, but it is necessary that the equilibrium cell is light enough compared with the weight of the pure components to be weighed, as well as pressure-resistant. Manipulating the cell is a delicate operation and gloves must be used. The manipulations are tedious, as the cell has to be connected to the degassing circuit before each weighing. Loading by pressure–volume measurements (pump) is simple, but requires knowing the pVT properties of the pure compounds, since loadings are carried out at pressures imposed by the nature of the pure

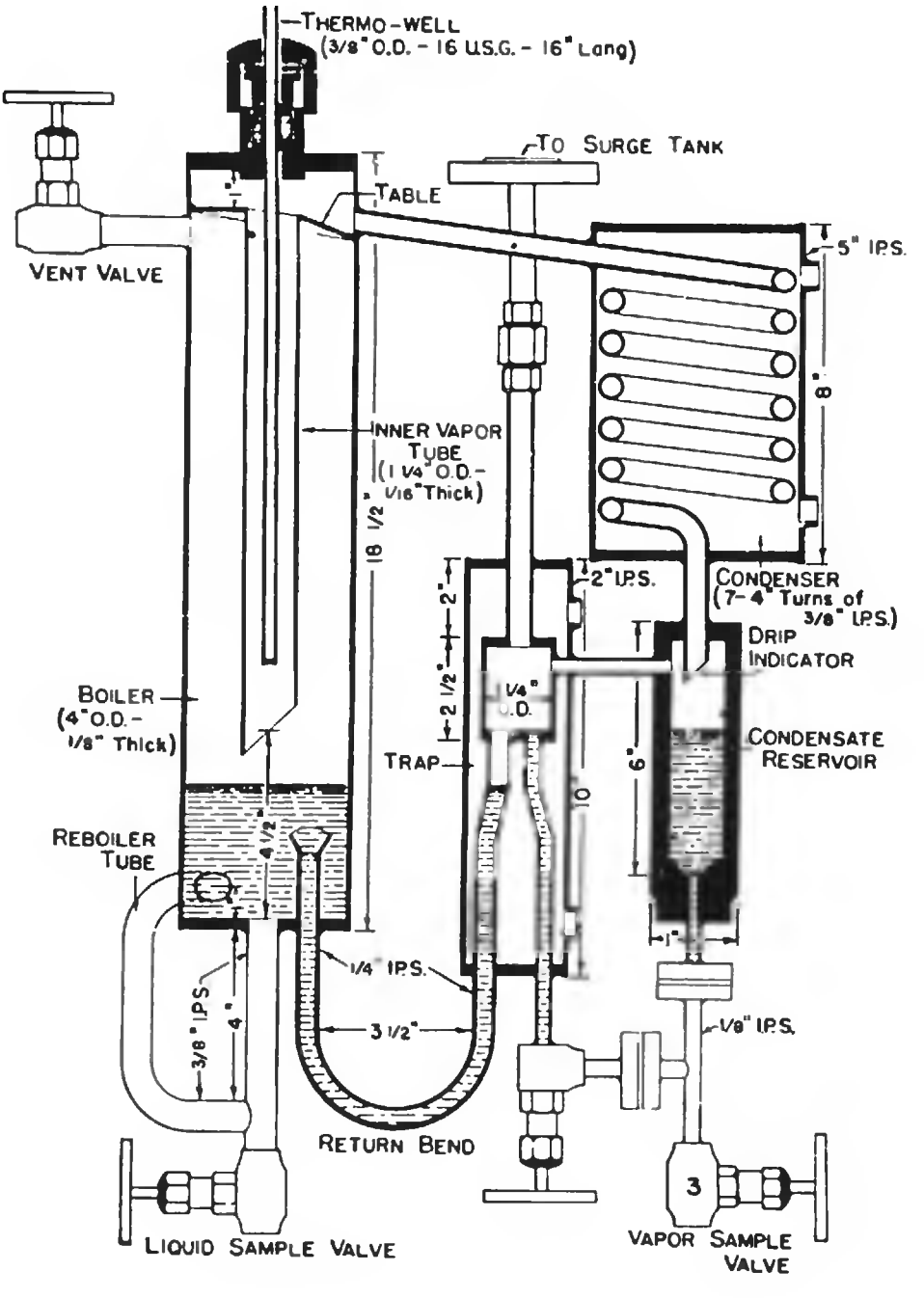

Figure 6.16 Ebulliometer of Othmer and Morley. Reproduced from reference [32] with kind permission of American Chemical Society. Copyright 1946.

compounds under study. Several types of synthetic methods exist: (i) by direct determination of bubble or dew points, (ii) by simultaneous determination of bubble and dew point properties and (iii) by total pressure measurements.

Direct Determination of Bubble or Dew Point Properties

In this case, the equilibrium cell is set either for fixed or variable volume and it is transparent or opaque. When transparent, the change of the system from a one- to a two-phase state is generally observed visually. When the first drop or mist of droplets of liquid appear, the properties of the mixture at the dew point are obtained, and when the first vapour bubble appears, we obtain the properties of the mixture at its bubble point. However, an error is introduced, since the measurements are not made exactly at the dew or bubble point, but only near to them (the second phase has to have a certain volume to be observable). The use of photoelectric cells or spectroscopic beams generally does not improve the accuracy of the measurements as the observed area of the beam is reduced and what happens outside this field is not taken into consideration.

The principles of the method are very simple. For a load of composition z in the vapour state and not in the retrograde region, a pressure increase through volume decrease at constant temperature leads to first exceeding the dew-point pressure and then the bubble-point pressure. The same types of observations are obtained by a temperature decrease at constant volume. For high-pressure measurements, variable volume cells must be preferred as they allow isothermal procedures and equilibration is very fast after a change of the total volume. In contrast, changing the temperature is very time-consuming as cells have thick walls to be pressure-resistant and are generally not made of materials that have a high thermal conductivity.

Semi-Transparent Cells

Most cells are of this type. It is interesting to note that, in addition to vapour–liquid, also liquid–liquid and gas–gas and solid–liquid equilibria can be studied. Roof and Baron [33] have elaborated a cell composed of a metal cylinder around a thick-wall glass tube. The mixture to be studied is placed between the glass tube and the metallic envelope. A movable periscope allows the observation of phase transitions. Kurata and Kohn [34] proposed various Pyrex cells (a typical shape is proposed in Figure 6.17) of different volumes between 1.33 and 12.5 cm^3 to work up to 10 MPa. The complete equipment fitted to these cells gives the possibility of independently measuring pressure and temperature. The volume variations are obtained by mercury displacement. The cells designed by Kurata and Kohn [34] are simpler than that proposed by Katz and Kurata [35]. Kay and Ranbosek [36] presented a similar method with an elaborate loading technique and pressure measurements carried out with a dead weight balance instead of a Bourdon manometer. Other types of equipments are described by Bloomer and Parent [37] and Lu *et al.* [38]. In the Cailletet apparatus described by De Loos *et al.* [39], the sample is confined over mercury in a glass capillary tube, which is sealed at the top. This apparatus allows the observation of the whole mixture and

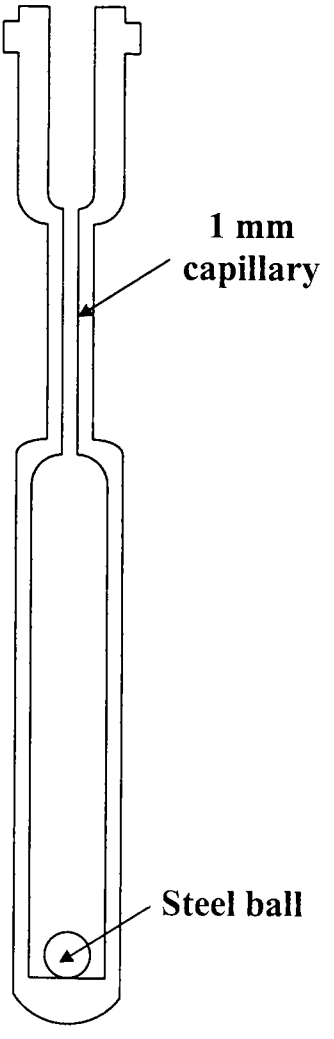

Figure 6.17 Typical Pyrex cell used by Kurata and Kohn.

can be used from $T = 243$ to 500 K at pressures up to 15 MPa. In 1975, Slocum [40] presented a more complex instrument, using strong internal agitation by circulating the light phase into the heavy phase by magnetic stirring.

The light phase is drawn to the top of the axis, E (Figure 6.18) and pulled through the hole, S, in this axis. The cylindrical cell body is made of Pyrex, which does not allow pressures above 7 MPa. The internal volume is adjusted by introduction of mercury. Above 10 MPa, the use of glass presents risk and sapphire is preferred for either the tubes or windows. Schneider [41] describes a relatively simple high-pressure cell for working up to 500 MPa and about $T = 573$ K. The internal pressure (Figure 6.19) is controlled by a Teflon piston, which separates the fluid being studied from the pressurising fluid. Buback and

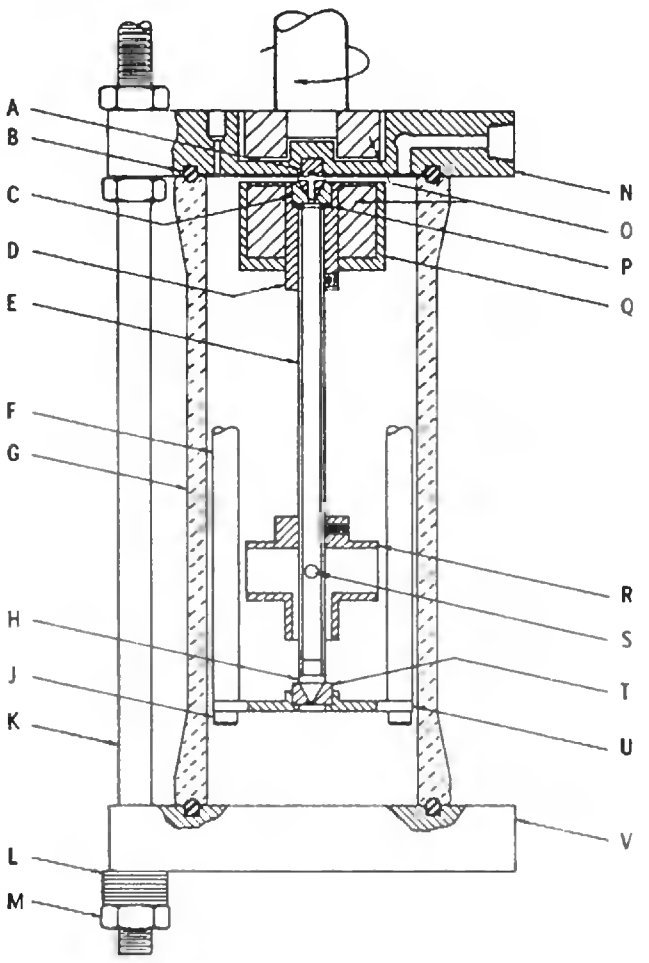

Figure 6.18 Equilibrium cell of Slocum: A, hollow pivot cone; B, O-ring; C, graphitar bearing; D, magnetic cover; E, impeller shaft; F, bearing support rod; G, Pyrex pipe; H, pivot cone; J, socket head cap screws; K, support and tie rod; L, Belleville washer; M, hex-nut; N, upper head; O, magnets; P, wavy washer; Q, magnet can; R, impeller; S, connecting hole in shaft; T, graphitar bearing; U, bearing support; V, lower head. Reproduced from reference [40] with kind permission of American Chemical Society. Copyright 1975.

Franck [42] realised a cell with the pressure controlled by a bellows (Figure 6.20) as in the design of Oeder and Schneider [43] (Figure 6.21). To study complex cases, such as gas–gas equilibria up to 200 MPa, de Swaan Arons and Diepen [44] conceived an equilibrium cell in which mercury is in contact with the mixture (temperature limit is 423 K), an example of such a cell is shown in Figure 6.22. A high-temperature version of this cell for use with temperatures up to 673 K is described by de Loos *et al.* [45]. The last cells referred to above serve also for determining pVT properties since volume measurements are associated with them.

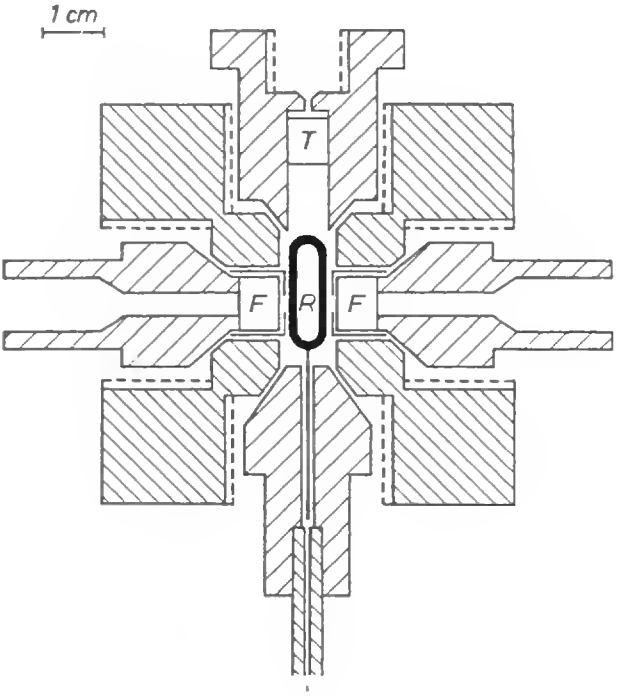

Figure 6.19 Cell of Schneider: F, sapphire window; R, stirrer; T, Teflon piston. Reproduced from reference [41] with kind permission from Oldenbourg Verlag. Copyright 1963.

Blind Cells

Knowing the volume available to a mixture, one can use this information to establish p–V curves at constant temperature or p–T curves at constant volume. At high pressures, due to the necessary thickness of the walls of equilibrium cells (poor thermal conductivity), the isothermal method is preferred in order to reduce the experimentation time. The p–V or p–T diagrams display break points, which become more notable as the equilibrium temperature is lowered and lower than the critical temperature of the mixture. This break point is, in fact, the intercept of two curves: one for the one-phase mixture and one for the two-phase mixture. Contrary to the visual observation method, where phase transitions very near the critical point can be studied easily, the method described here is less accurate in this region as the break point vanishes rapidly on reaching the critical point. The coordinates of the break point give the saturated liquid molar volume times the number of moles and either the bubble or dew pressure or the bubble or dew temperature. As the method does not require the visual observation of the mixture, the equilibrium cells are technologically simpler with fewer problems of air tightness. The method to determine phase boundaries from breaks in p–V curves has been used for many years by Sage and

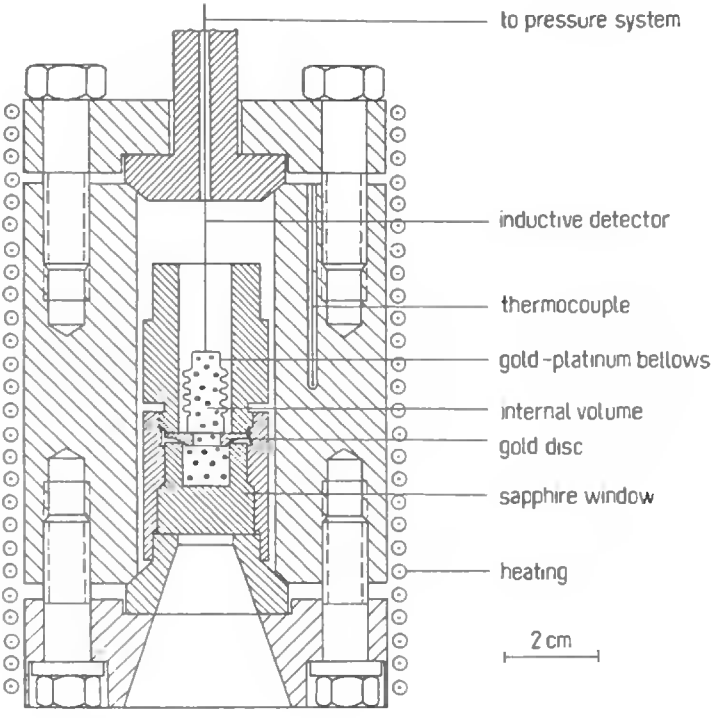

Figure 6.20 Cell of Buback and Franck. Reproduced from reference [42] with kind permission from Wiley-VCH, STM-Copyrights & Licences. Copyright 1972.

Lacey [46], Weise *et al.* [47], Reamer and Sage [48], Reamer *et al.* [49], and others. In all these cases, volume variations are easily obtained by displacement of mercury, which has however many drawbacks related to reactivity, toxicity and volatility of mercury. To avoid the use of mercury, Meskel-Lesavre *et al.* [50] made a cell with a movable piston through a pressurised hydraulic fluid, especially adapted to obtain isothermal p–V curves. Using a hydraulic fluid for volume change presents advantages that include minimising the air tightness problems with pistons and avoiding the constraints between the inside and the outside of bellows. The cell is light enough to be weighed with an analytical balance before and after each loading within 10^{-4} g. The volume of the cell is obtained from the volume of the displaced hydraulic fluid. Thermal expansion and compressibility corrections are necessary to obtain the real volume of the mixture. To avoid these corrections, direct measurements can be achieved using a rod connected to a piston on one side and to a displacement transducer on the other side. In this way, the piston displacement can be determined within 1 μm. Use of mercury limits the temperature range to about 423 K and of pistons from 393 to 523 K depending on the nature of the polymeric rings used to ensure air tightness around the piston. For working at higher temperatures, bellows have to be used [51].

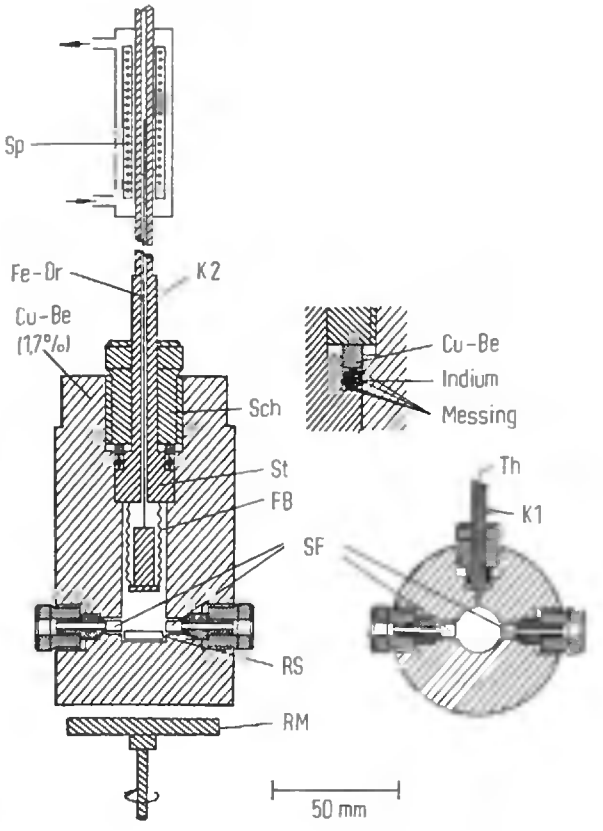

Figure 6.21 Cell of Oeder and Schneider: Sp, thermostated coil for measuring internal volume; Fe-Dr, iron wiring; K2, high-pressure inlet; Sch, screw-bolt; St, Bridgman piston; FB, bellows; SF, sapphire window; RS, magnetic stirrer; RM, driving magnet; Th, thermocouple; K1, capillary inlet tube; Messing, Brass. Reproduced from reference [43] with kind permission from Wiley-VCH, STM-Copyrights & Licences. Copyright 1969.

Simultaneous Determination of Bubble and Dew Point Properties

It can be demonstrated, by application of the phase rule, that at a given temperature and pressure, the density and composition of the liquid and vapour phases in equilibrium are set for a binary mixture, while the mass of each phase depends on the overall composition of the mixture.

Isothermal Method

If the equilibrium state (equal temperature and pressure) can be reproduced for different overall compositions, and if the volume of each phase can be measured, it is possible to

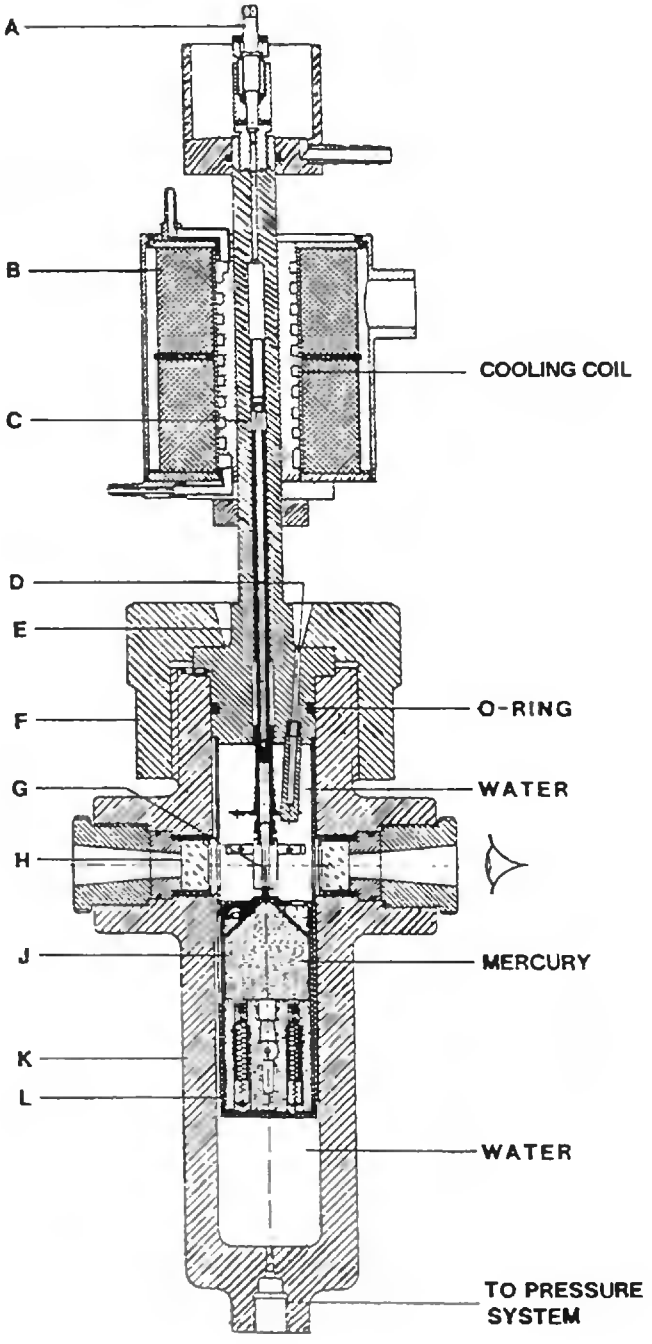

Figure 6.22 Example of cell used in Delft group: A, vent; B, electromagnet for activating the magnetic stirring system; C, soft iron rod; D, shaft for resistance thermometer; E, closing plug; F, closing nut; G, stirrer; H, sapphire window; J, glass sample vessel; K, autoclave body; L, container for sample vessel.

calculate the saturated molar volume and the compositions of each of the two phases, using the mass balance equation

$$n_i^{\alpha} = x_i \frac{V^{L\alpha}}{v_S^L} + y_i \frac{V^{V\alpha}}{v_S^V}, \tag{6.1}$$

($i = 1$ or 2) for a binary mixture, but this type of equation can be extended to multi-component and multi-phase mixtures. The α is the load, n_i the number of moles of component i, V the phase volume and v the saturated molar volume. Superscripts L and V refer to liquid and vapour and subscript S to the saturated state. Specovius *et al.* [52] used a glass cell and a cathetometer was used to determine the position of the interface. Fontalba *et al.* [53] have designed a cell made of titanium alloy for measurements up to 45 MPa. This cell is shown in Figure 6.23. The piston is connected to a stem that extends from the bottom of the cell and is connected to a displacement transducer. The respective volumes of the phases are determined by using a thermistor probe, which receives a constant electrical

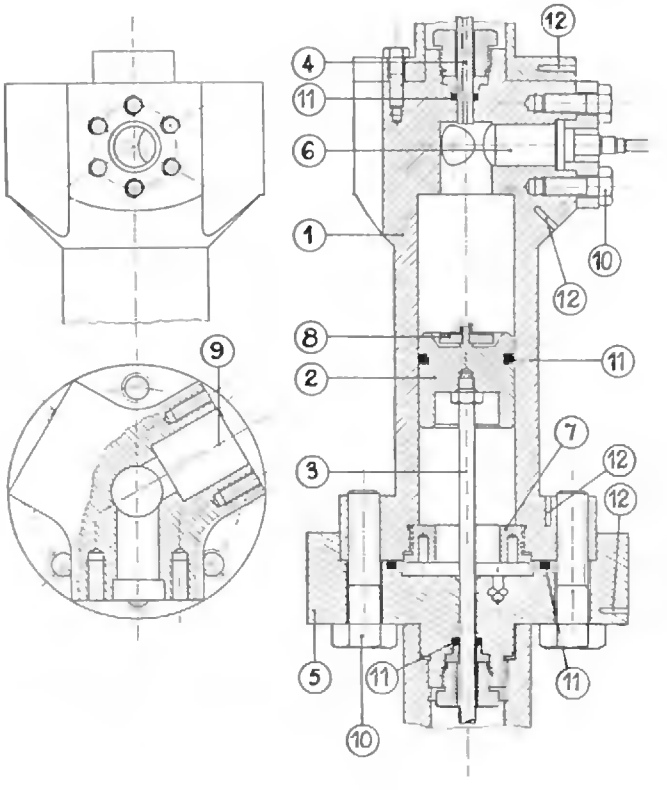

Figure 6.23 Variable volume cell of Fontalba *et al.*: 1, cell body; 2, piston; 3, piston position measuring device; 4, thermistor probe for measuring interface position; 5, pressurizing assembly; 6, membrane pressure transducer; 7, stop-screw; 8, magnetic rod; 9, seat of the loading valve; 10, bolt; 11, O-ring; 12, thermocouple well. Reproduced from reference [53] with kind permission from American Institute of Chemical Engineers. Copyright 1984.

intensity. Any change in thermal conductivity of the medium around the thermistor is noted by a variation of the electrical tension.

The instrumentation needed for the manipulation is simple (Figure 6.24). The experimental procedure that allows maximum use of the possibilities of the equipment is the following: for each loading, the $p(V^V)$ and $p(V^L)$ curves should be measured in the largest pressure range possible up to the bubble points (Figure 6.25). In this way, two loadings will

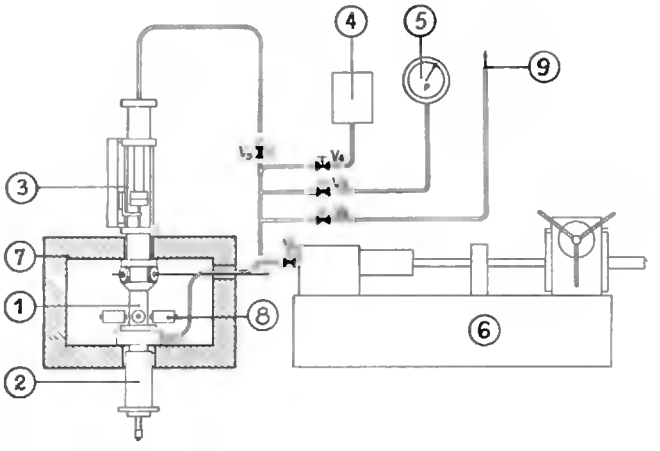

Figure 6.24 Flow diagram of the equipment of Fontalba *et al.*: 1, equilibrium cell; 2, system for measuring the piston position; 3, system for measuring the interface position; 4, pressurization fluid reserve; 5, manometer; 6, high-pressure hydraulic pump; 7, air thermostat; 8, solenoids to create a rotating magnetic field; 9, link-up to vacuum pump; V_{1-5}, shut-off valves. Reproduced from reference [53] with kind permission from American Institute of Chemical Engineers. Copyright 1984.

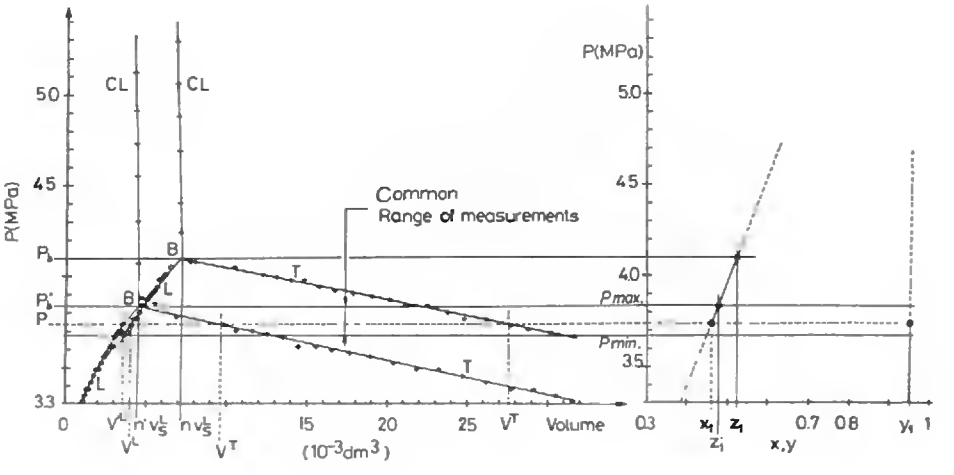

Figure 6.25 Pressure–volume curves from Fontalba *et al.* Reproduced from reference [53] with kind permission from American Institute of Chemical Engineers. Copyright 1984.

suffice to define the dew and bubble curves in a certain range. The closer the total compositions of the two loadings, the larger the studied pressure range will be, and also, the larger the dependency of the mass balance equations, the less precise the accuracy of calculated variables. Similarly the more different the loads, the greater will be the precision, but the smaller the studied pressure range. This gives a choice or a compromise between tracing a precise, but time-consuming, isotherm, or a rapid but less precise curve. This mass balance technique should be avoided when total pressures are low, since the vapour phase has a small number of moles compared to the liquid phase, which yields a very large uncertainty in the vapour phase properties. This difficulty can be overcome by sampling and analysing the vapour phase independently [54]. When the interface position is measured by a thermistor, it is necessary that the phases have sufficiently different thermal conductivity. When an optical method is used, the refractive indices of both phases must be sufficiently different. In both cases, the critical region is difficult to handle due to the fact that all differences in phase properties vanish at the critical point. The method just described can be used theoretically for multi-component and multi-phase systems if the number of phases is equal to or higher than the number of components. However, for a higher number of components, there is a greater number of mass balance equations that have to be solved simultaneously and the smaller is the accuracy of the determined variables. Di Andreth and Paulaitis [55] present an equilibrium apparatus permitting to apply this method to the study of three-phase systems.

Isochoric Method

This method, used by Hall and Eubank [56,57] and Hall *et al.* [58], is comparable with the isothermal method, except that the cell has a fixed volume and pressure is measured as a function of temperature. The densities of the phases are measured with a particular densimeter: a buoy is stabilised in the fluid by the effect of a magnetic field (Figure 6.26). Temperature variations (because of inertia) make the manipulations very time consuming. For each load of given initial composition, pressure is recorded as a function of temperature leading to the determination of a p–T isochor. Other isochors are obtained with the same load by modifying the total volume according to the Burnett method. For two different loads, the isochors meet unless the global compositions of the two loads are too different. Coupled with the Burnett method, several isochors for each loading can be obtained with this technique, and therefore many two-phase points. For a two-phase mixture, two degrees of freedom are available. Therefore at the isochors intersection, the two systems of different overall compositions are characterised by identical phase compositions and phase density. An overall mass balance leads to writing the vaporised volume fraction f^{V} as

$$f^{V} = \frac{\rho^{L} - \rho^{T}}{\rho^{L} - \rho^{V}}, \tag{6.2}$$

where ρ^{L}, ρ^{V} and ρ^{T} are the densities of the liquid phase, the vapour phase and the mean value for the whole system, respectively.

The mass balance for component i leads to

$$\rho_{T} z_i = y_i f^{V} \rho^{V} + x_i (1 - f^{V}) \rho^{L}, \tag{6.3}$$

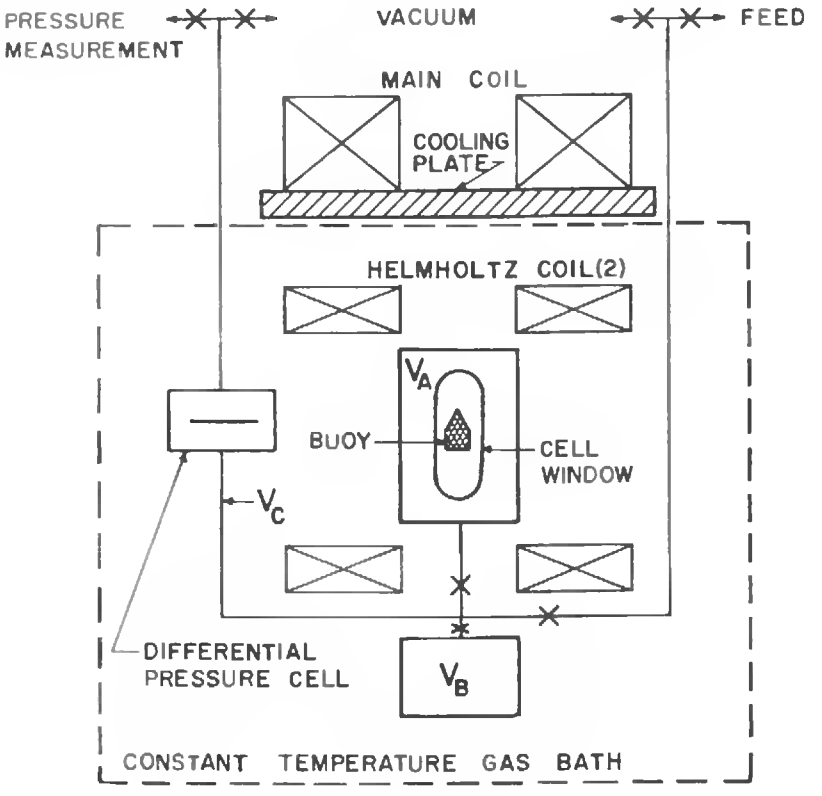

Figure 6.26 Equipment used by Hall and Eubank and Hall *et al.* Reproduced from reference [58] with kind permission from American Institute of Chemical Engineers. Copyright 1975.

ρ^L, ρ^V, ρ^T, f^V and z_i are obtained through direct measurements. The x_i, y_i and z_i are the mass fractions of component i in the liquid and vapour phases and in the loaded mixture. The two unknowns are x_i and y_i; they are calculated by solving two mass balance equations written at the isochors intersection. The proper experimental procedure to apply is the following: (i) measurements are carried out at several pressures for a given load, then on other loads and (ii) $\rho^L(p)$, $\rho^V(p)$ and $\rho^T(p)$ curves are drawn, at constant temperature.

Measurement of Total Pressure

In this method, the composition of a load and the volume available are known, and the total pressure above the two-phase mixture is measured as a function of temperature. This method is simple and rapid. However, the reduced number of experimental measurements, total composition, temperature, pressure and global molar volume, make it necessary to reduce the data by use of a model able to represent phase equilibria and saturated molar

volumes of both phases. There are several possibilities, most of them are based on the Gibbs–Duhem equation. The first approach is used by Prengle and Palm [59], Ramalho and Delmas [60], Prengle and Pike [61], Singh and Benson [62], Hermsen and Prausnitz [63] and Diaz Pena [64], who use an analytical expression for the Gibbs energy G of the liquid phase. The equation of state for the gas phase is assumed to be known as are the volumetric properties of the liquid. The parameters of this Gibbs energy expression are adjusted to the experimental data obtained. The activity coefficients in the liquid phase are calculated, as is the vapour composition. The choice of the analytical expression for G is very important and a bad choice can lead to imprecise results. The second approach [65–67] depends on a first-order differential equation, relating rigorously p, T, x and y in an iterative process.

Gibbs and Van Ness [68] have developed an apparatus to work at relatively low pressures. Loading of components is done using volumetric pumps, which necessitates a good knowledge of the pVT properties of each of the components. The cell of the Ronc and Ratcliff instrument [67], which is derived from that of Gibbs and Van Ness [68], avoids a dead volume between the cell and the pressure measuring device, and offers the possibility of higher working temperatures and pressures. For this type of measurement at higher pressures up to 5+ MPa, a very simple apparatus (Figure 6.27) was designed by Legret *et al.* [69].

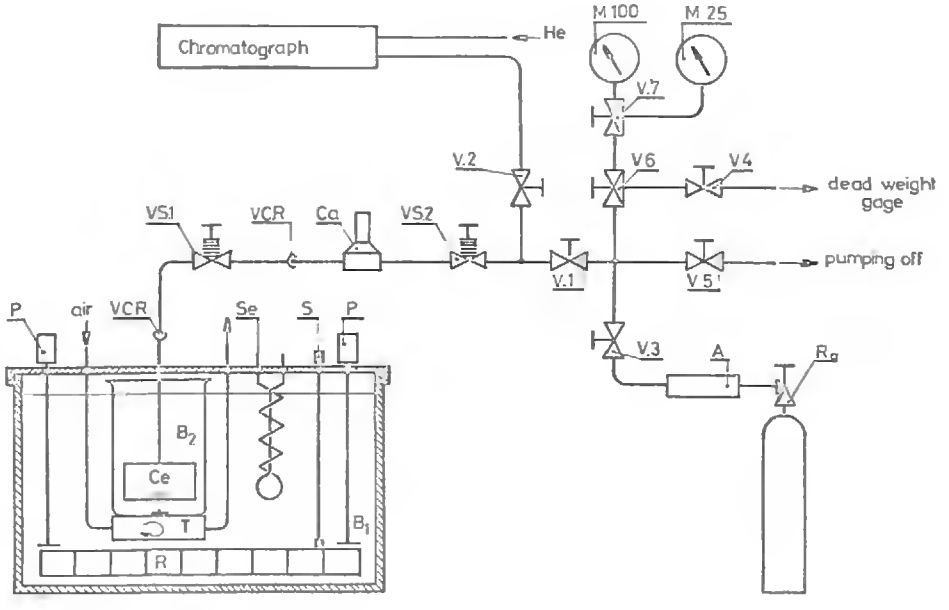

Figure 6.27 Apparatus of Legret *et al.*: A, special cylinder for filling cell with gaseous compounds; B1, B2, thermostated baths; Ca, pressure transducer; Ce, equilibrium cell; M25, M100, Bourdon tube manometer; P, circulating pump; R, heating resistance; Rg, pressure regulator; S, platinum probe; Se, tubing coil; T, gas turbine; V.1–V.5, Whitney valves; V6, V7, three-way valves; VCR, Cajon couplings, VS1, VS2, Nupro bellows valve. Reproduced from reference [69] with kind permission of American Chemical Society. Copyright 1980.

The interpretation of their experimental results for p, T, numbers of moles, n_1^T and n_2^T, and total volume V^T uses mass balance equations of the form

$$V^T = (n_1^V + n_2^V)v_S^V + (n_1^L + n_2^L)v_S^L, \tag{6.4}$$

The total volume is the sum of the liquid volume and of the vapour volume. The v_S^V and v_S^L are the molar volumes of the saturated vapour and liquid phases. From the definition of the mole fractions, we have

$$n_1^L = n_1^T - [V^T - v_S^L(n_1^T + n_2^T)]\frac{y_1}{v_S^V - v_S^L}, \tag{6.5}$$

$$n_2^L = n_2^T - [V^T - v_S^L(n_1^T + n_2^T)]\frac{1 - y_1}{v_S^V - v_S^L}, \tag{6.6}$$

At high pressures, the liquid cannot be considered incompressible. An equation of state, for which the parameters have to be known, is used to link the variation of molar volumes and gas composition to the temperature and liquid composition. An iterative process is begun with $x_2 = z_2$, and initial values of v_S^V, v_S^L and y_1. A new value is obtained for x_2 and is introduced along with new interpolated values of v_S^V, v_S^L and y_1. The process is continued until the x_2 value is constant within the desired precision.

6.2 Open-Circuit Methods

6.2.1 Forced Circulation of the Mixture

Sampling

Equilibrium is attained during the circulation of a mixture. This method involves a separator, which permits collecting all the circulating phases in equilibrium. The mixture is prepared in a container and then circulated either by pumping, pressure gradient or boiling. In the case of a pressure gradient, the mixture is pressurised and circulates in a tube that acts, first, as a heat exchanger and then as the equilibrium device, where equilibrium is attained by turbulent two-phase flow before the phases are separated and analysed. There are several ways of operation not only for circulation, but also for control and analyses. The major advantages of this method, also known as the "dynamic method", over static methods are the short equilibration times and the possibility for use with non-metallic materials. This is particularly advantageous when dealing with thermosensitive or corrosive compounds.

Simnick *et al.* [70] have developed an instrument (Figure 6.28) to work at high temperatures (up to 673 K and 25 MPa) with thermally unstable compounds. It includes a separate pumping system for each component of the system, so that the total composition is monitored. The components are mixed before they are heated in the tube that carries them to the equilibrium cell and the phase separator, from which the liquid and vapour phases

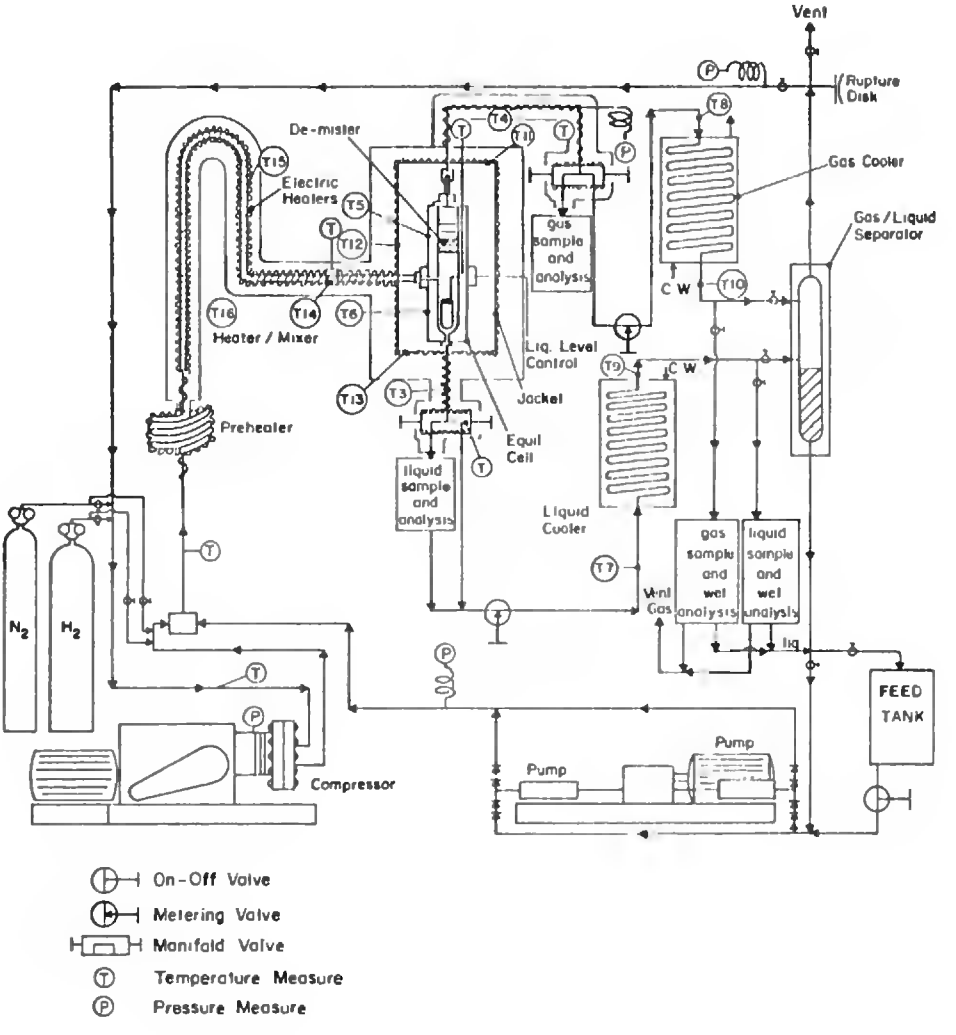

Figure 6.28 Apparatus of Simnick *et al.* Reproduced from reference [70] with kind permission from American Institute of Chemical Engineers. Copyright 1977.

are sampled continuously. All parts of the equipment, which are heated at the equilibrium temperature, are made of stainless steel. The liquid level in the equilibrium cell is known by electrical capacity measurements. This method has its limits and cannot be used with all types of mixtures. Lin *et al.* [71] preferred an optical method, using a cell with sapphire windows (Figure 6.29). Niesen *et al.* [72] use an instrument (Figure 6.30) similar to that of Simnick *et al.*, but with a cell (Figure 6.31) almost identical to that of Lin *et al.* The mixture to be studied is pumped directly from a reservoir and sent into the heating and equilibrium circuit. Gilbert and Paulaitis [73] have developed an equipment (Figure 6.32) based on the principle of the apparatus of the Simnick *et al.* To study the water–acetic acid system,

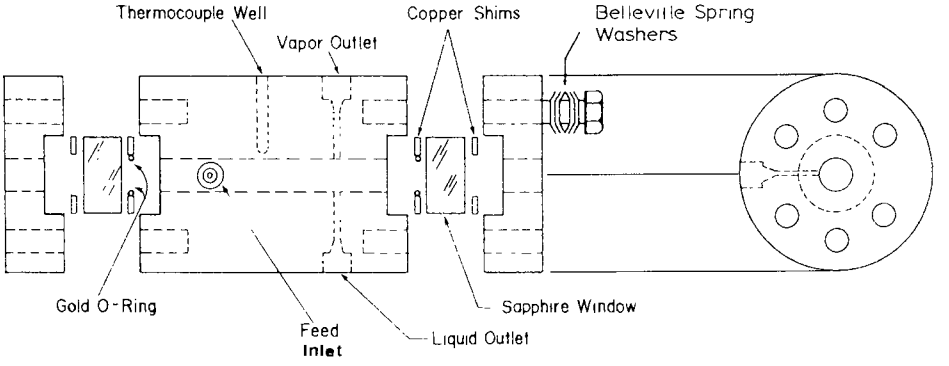

Figure 6.29 Cell of Lin *et al.* Reproduced from reference [71] with kind permission of American Chemical Society. Copyright 1985.

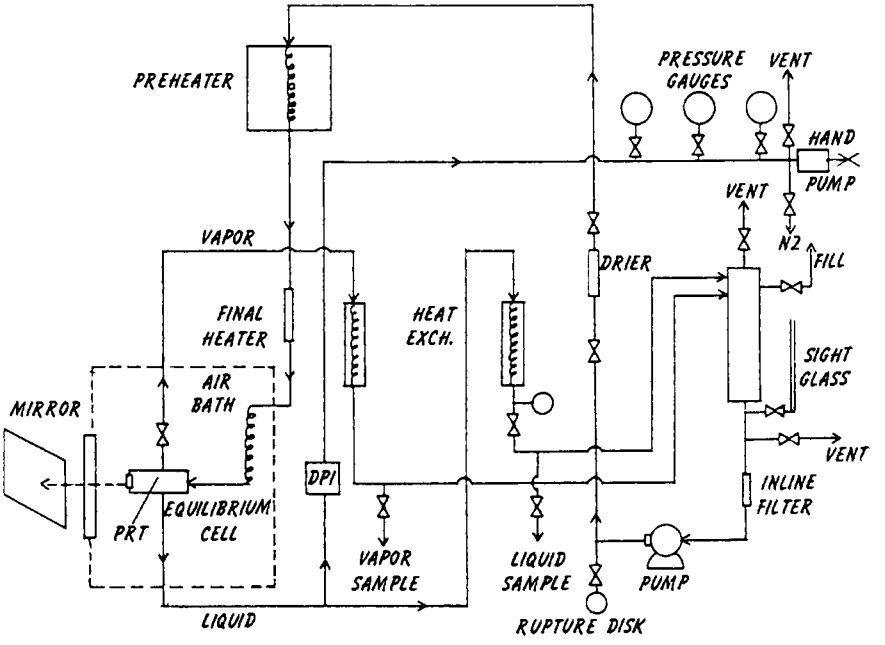

Figure 6.30 Instrument of Niesen *et al.* Reproduced from reference [72] with kind permission from Elsevier. Copyright 1986.

Houzelle *et al.* [74] developed a relatively simple system (Figure 6.33). The mixture is placed in a polymer envelope pressurised from the outside by a gas, which permits a completely smooth flow. The mixture is taken up to high temperatures in a Pyrex coil that empties into an equilibrium cell, also made of Pyrex. The liquid and vapour phases are collected as liquids into cooled containers before being analysed by volumetric titration. For very high

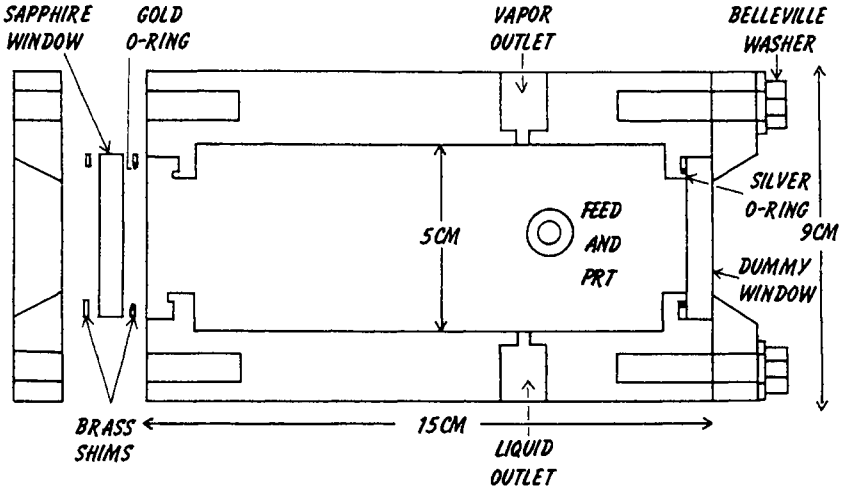

Figure 6.31 Cell of Niesen *et al.* Reproduced from reference [72] with kind permission from Elsevier. Copyright 1986.

temperatures up to 823 K, Laugier *et al.* [75] used a device of similar design, in which all parts submitted to high temperatures are made of quartz. A fluidised alumina bath supplies the calories to the vaporisation coil.

In Situ Analyses: Measurements and Related Methods

It is very easy to perform on line analyses by optical methods, such as spectroscopy or refractometry. Indirect measurement by following the density as a function of pressure at constant temperature is a very powerful method, especially when coupled to a fully automated equipment involving a vibrating tube. This new method proposed by Bouchot and Richon [76a] for pressures up to 40 MPa and $T = 423$ K allows the simultaneous determination of volumetric properties in the compressed and saturated states and the phase equilibria with generation of a considerable amount of data in a very short time. This considerable amount of pVT data allows using neural network models to represent data within experimental uncertainties. Then useful thermodynamic and transport properties are calculated owing to numerical derivations from the Z or ρ represented by the neural models. The enthalpy, entropy, heat capacities C_p and C_v, expansion coefficients α and χ and speed of sound can be calculated with satisfactory accuracy [76b,76c]. A more recent equipment with a hastelloy U-tube allows working up to 70 MPa with mixtures containing components like hydrogen sulphide.

Another method, based on calorimetry, involves the forced circulation of the components with mixing at constant p and T. It is a very attractive way to get phase equilibria in terms of mutual solubilities. The technique described by Richon *et al.* [77] was used extensively by Ott and Sipowska [78] for liquid–liquid equilibria up to 15 MPa. The mutual solubilities are obtained from the plot of the excess enthalpy H^E against composition at constant

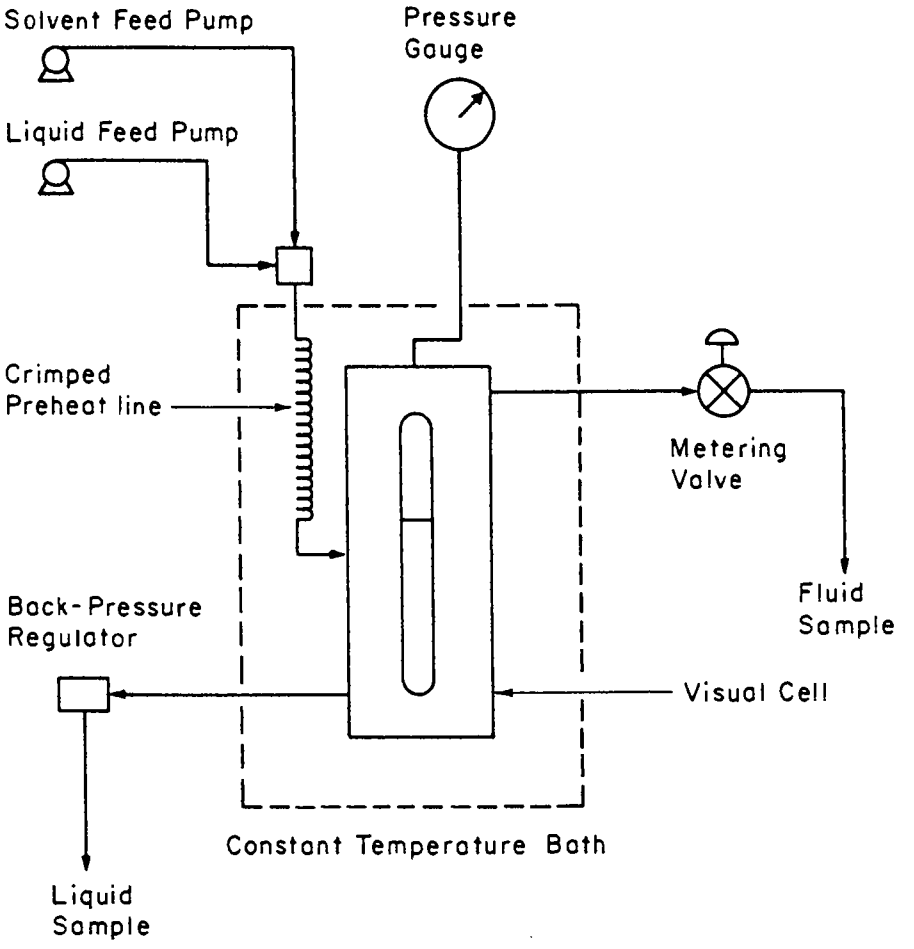

Figure 6.32 Apparatus of Gilbert and Paulaitis. Reproduced from reference [73] with kind permission of American Chemical Society. Copyright 1986.

pressure and temperature, which presents break points at the end of the linear part (two-phase mixture) between the two one-phase branches. Vapour–liquid equilibrium (VLE) are obtained in the same way.

6.2.2 Open Flow of the Gas Phase

These are also dynamic phase methods, as initially the gas phase does not have the equilibrium composition. Equilibrium is reached by saturating phases during the steady flow of the mobile phase in the cell containing the dense phase or phases. It is important that the circulating phase is completely separated from the stationary phase, without entraining any droplets, since the sampling is carried out after mechanical separation of the phases.

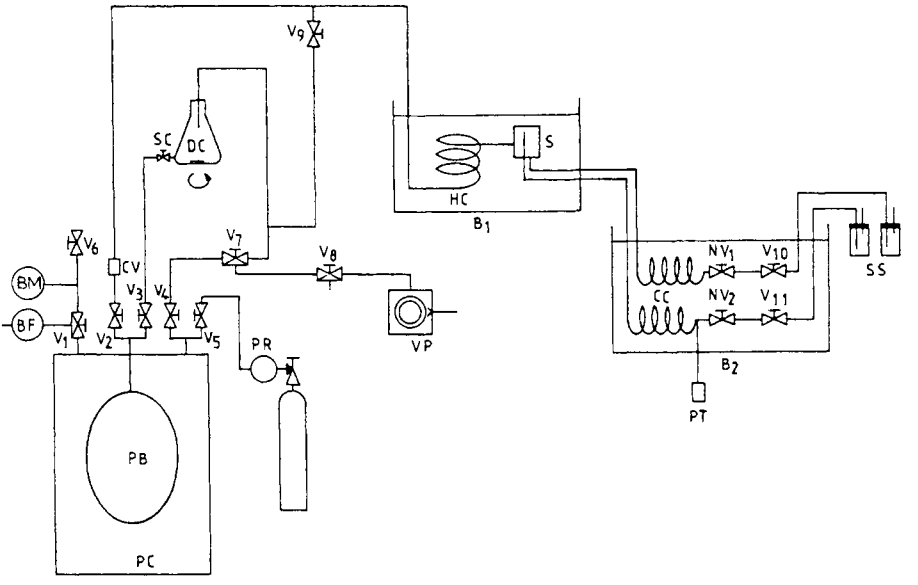

Figure 6.33 Apparatus of Houzelle *et al.*: B_1, oil bath; B_2, water and ice bath; BF, flowmeter; BM, Bourdon manometer; CV, check valve; DC, degassing cell; HC, heating coil; NV, needle valve; PB, polymer bag; PR, pressure regulator; PT, pressure transducer; SC, stopcock; S, separator; SS, sample container; V, valves; VP, vacuum pump. Reproduced from reference [74] with kind permission from Elsevier. Copyright 1983.

These methods, which can seem to be very close to quasi-static methods, are different since the gas phase is not recirculated and thus it is more difficult to obtain complete saturation of the gas phase in one passage. Methods differ by the way of measuring and treating the experimental data.

Circulation of the Gaseous Component in a Cell Containing a Quasi-Saturated Liquid

The liquid component is placed in a cell, while the gaseous component is dispersed into the liquid by bubbling. The phases are sampled at constant temperature and pressure. Kirk and Ziegler [79] developed an instrument (Figure 6.34), similar to that of Dodge and Dunbar [80]. The cell has two compartments. The gas enters at the base of the cell and passes into a spiral through the lower compartment, which is partially filled with pieces of copper and fibre-glass. The liquid phase is sampled using a capillary opening in the lower compartment. The vapour phase is sampled directly in the vapour extraction circuit. This instrument was used up to 12 MPa at cryogenic temperatures.

In a series of papers, Hiza and Herring [81], Herring and Barrick [82], Hiza and Kidnay [83], Hiza *et al.* [84] and Hiza and Duncan [85] have discussed the use of this type of method. Their cell is shown in Figure 6.35. Instead of having the vapour phase run

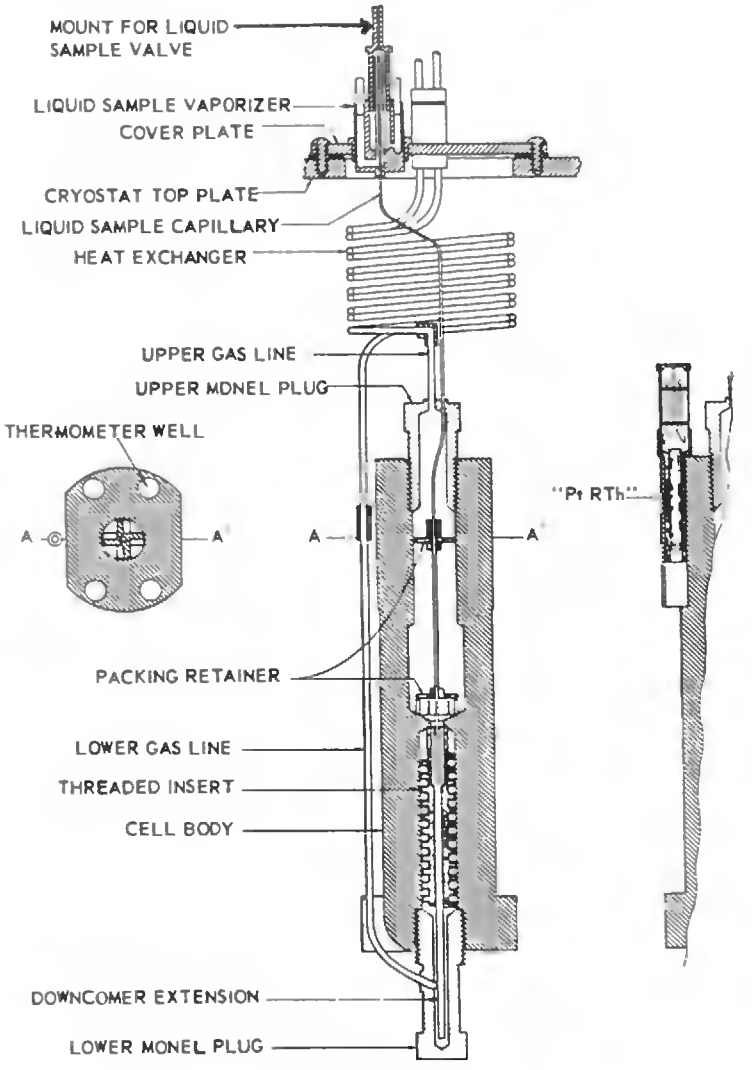

Figure 6.34 Cell of Kirk and Ziegler. Reproduced from reference [79] with kind permission of Springer Science and Business Media. Copyright 1965.

through a complex passage within the liquid, as in the preceding cell, the gas is diffused at the bottom of the cell in the form of small bubbles. Michels *et al.* [86,87] designed an instrument (Figure 6.36) that can be used up to 80 MPa. To begin with, the liquid component is placed into the cell, A, while the gas component (pure or mixture) is in the reservoir, B. The reservoir D contains mercury and oil from the hydraulic press, F. The reservoirs are connected by a tube to permit the circulation of mercury. The pressure in the press is controlled by a manometric balance, G, which also serves to measure the pressure.

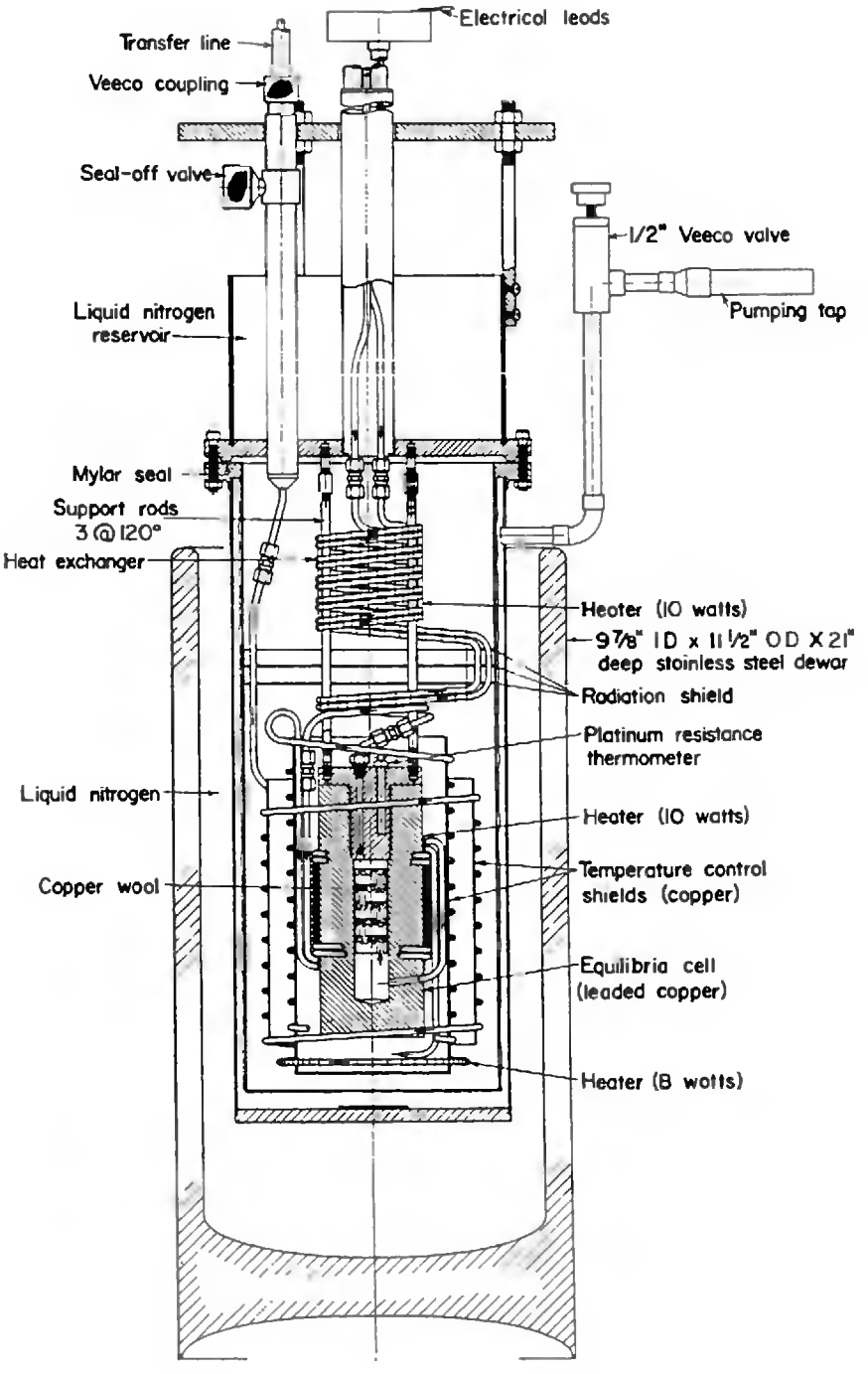

Figure 6.35 Cell of Hiza and Herring. Reproduced from reference [81] with kind permission of Springer Science and Business Media. Copyright 1963.

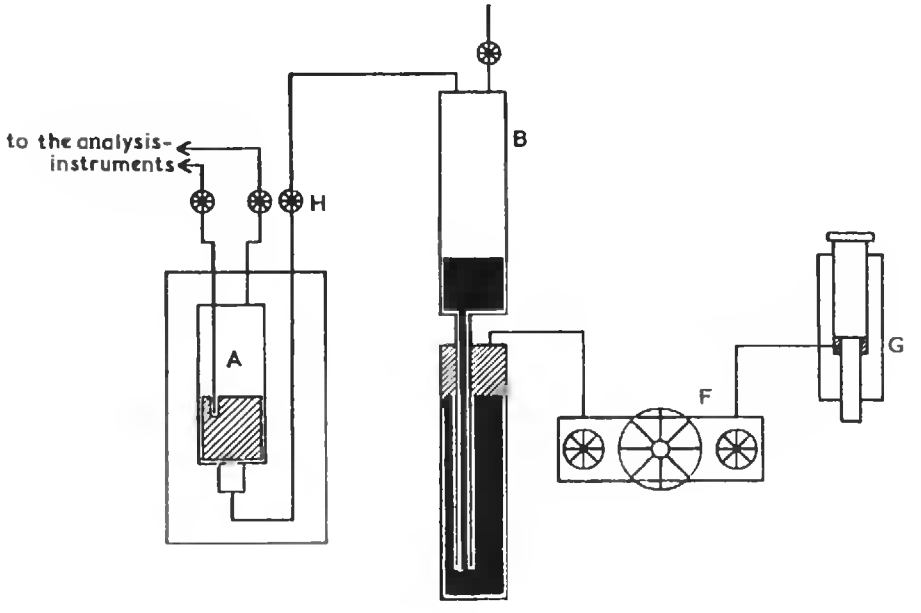

Figure 6.36 Apparatus of Michels *et al.*: A, liquid reservoir; B, gas reservoir; C, tube; D, mercury reservoir; E, top of mercury; F, press; G, pressure gauge. Reproduced from reference [86] with kind permission from Elsevier. Copyright 1950.

When the valve, H, is opened, the gas component is pushed by the mercury, which in turn is pushed by oil through the liquid phase. Control valves allow the continuous extraction of the liquid and vapour phases (about 1000 cm^3 of vapour phase at standard conditions and 2 cm^3 of liquid phase per hour). A detailed diagram of the equilibrium cell of Michels *et al.* is given in Figure 6.37. The components enter a capillary, of 0.15 mm internal diameter, through valve, H and a steel cone, L, which is precisely adjusted in the casing, M. In the surface of the cone, L, are 12 longitudinal grooves, 0.05 mm deep. The gas is distributed in these grooves that lead to the formation of fine bubbles in compartment, N. The porous stopper, V, rests against the steel cone, O, which is adjusted on the cell body, A, with the conical axis, P, to which the nut, R, is screwed. This assembly forms a control system. The liquid phase wets the porous material and the gas bubbles entering in the compartment, N, travel a fairly long distance, which allows them to be saturated. A security spring, S, holds this porous system at the bottom of the cell. Two capillaries, T and U, are emerging into the equilibrium cell, one into the liquid phase and one into the vapour phase. The other ends of the capillaries are connected to the set control valves, X and Y.

Inert Gas Stripping Method

The inert gas stripping technique allows the measurement of activity coefficients or Henry's constants of light solutes in heavy liquid solvents. The inert gas stream carries

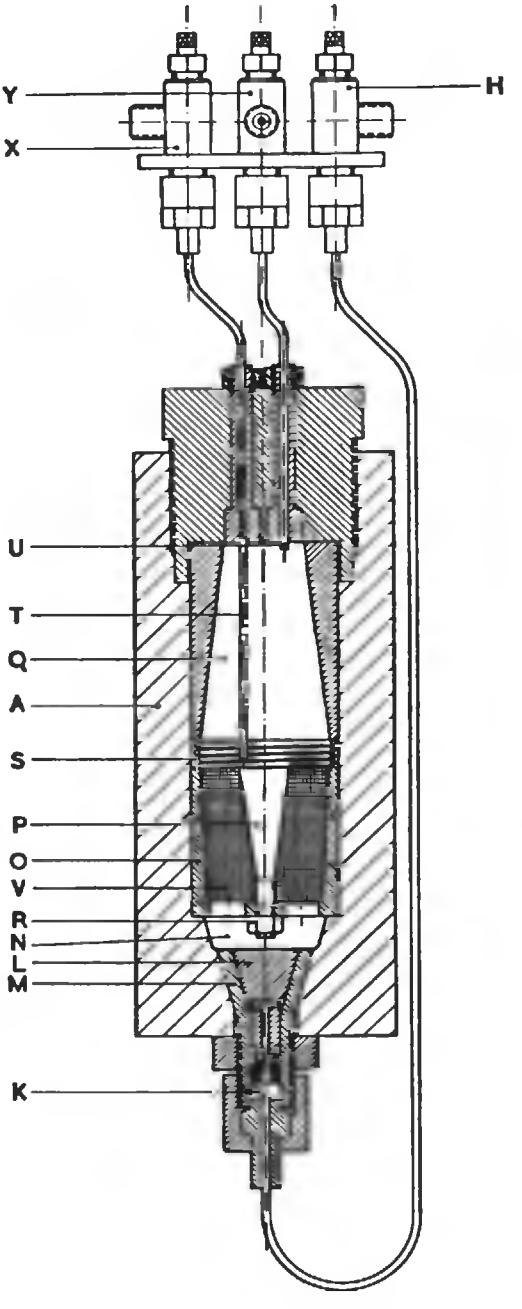

Figure 6.37 Cell of Michels *et al.*: A, reservoir; H, throttling valve; L, steel cone; M, conical sleeve; N, chamber; O, hollow steel cylinder; P, conical steel plug; Q, reservoir; R, nut; S, holding cup; T, U, capillaries; V, fibre glass cloth; X, Y, valves. Reproduced from reference [86] with kind permission from Elsevier. Copyright 1950.

away the volatile components out of the liquid solvent in an exponential decay. The inert stripping gas has a negligible solubility in the solvent and does not participate as a component of the mixture. Equilibrium in the cell is obtained dynamically. It corresponds to a non-steady-state equilibrium as the liquid composition varies continuously until all volatile components are removed. Vapour samples are periodically analysed. This can be advantageously carried out by chromatography. Leroi *et al.* [88] suggested the idea to apply this stripping technique for the determination of thermodynamic properties at infinite dilution. In this case, it is not necessary to calibrate the chromatograph, provided the detector response is linear, as only the variation with time of the solutes concentrations (proportional to detector response) needs to be known. In its original conception, the cell has a tube ended by a fritted glass disc to disperse the gas in the liquid phase. In a more recent version, Antoine *et al.* [89] ensure dispersion by 10 capillaries having a 0.2 mm internal diameter (Figure 6.38). In case the rate of the gas stripping must be high to minimise the time of experiments when not very volatile solutes are used or when the number of moles of solutes is not negligible in the vapour phase, Richon and Renon [90] recommend the use of a cell with minimal vapour phase volume of simple geometry. Richon *et al.* [91]

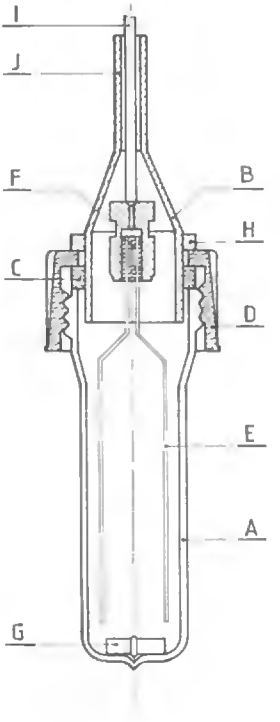

Figure 6.38 Cell of Antoine *et al.*: A, glass cell body; B, vapour collector; C, flat joint; D, screw-nut; E, capillaries; F, leakproof holder of capillaries; G, magnetic stirrer; H, metal ring for adjusting cell volume; I, tube and inlet for gas sample; J, outlet for vapour. Reproduced from reference [89] with kind permission of American Chemical Society. Copyright 1980.

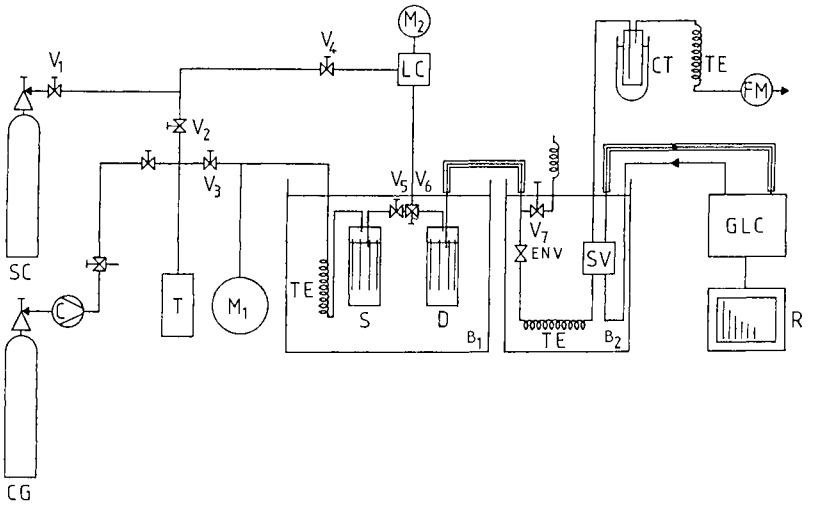

Figure 6.39 Apparatus of Legret *et al.*: B_1, B_2, liquid bath; C, compressor; CG, carrier gas chamber; CT, cold trap; D, dilutor; ENV, expansion needle valve; FM, flowmeter; GLC, gas chromatograph; LC, loading cell; M, manometer; R, recorder; S, saturation device; SC, solute cylinder; SV, sampling valve; T, reserve; TE, thermal exchanger; V, shut-off valve; V_3, double stage pressure regulator. Reproduced from reference [92] with kind permission from American Institute of Chemical Engineers. Copyright 1983.

recommend the use of another type of cell with liquid circulation when dealing with highly viscous fluids, over 50 cP and below 1000 cP.

At pressures much higher than atmospheric pressure, the solubility of the stripping gas is no longer negligible and the stripping gas must be considered as a component of the mixture. Then, the property that is measured at high pressures is the partition coefficient of the solute at infinite dilution between the vapour and the liquid phase. Legret *et al.* [92] describe the corresponding apparatus to work up to 20 MPa and $T = 473$ K (Figure 6.39). The dilutor cell (Figure 6.40) is made of stainless steel and has a dispersion system composed of 50 capillaries of 0.1 mm internal diameter. Each gas bubble is formed slowly, during more than 20 s, at the extremity of capillaries to ensure complete mass transfer.

Saturation of a Gas by Passing it through a Weak Volatile Liquid or a Solid Powder

A solid or a low volatile liquid will dynamically saturate the gas phase at any pressure during its passage through the cell. Krichevsky and Gamburg [93] developed a device (Figure 6.41) to measure the solubility of liquids in compressed gases, based on the bubbling principle. The pure gas enters the extraction tube, 1, through valve, 14. The two thermostats are at different temperatures, with a difference of 10–20 K, so that the gas passes through the

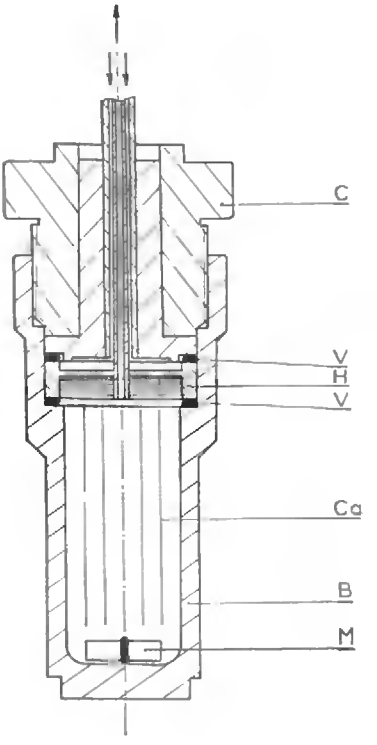

Figure 6.40 Cell of Legret *et al.*: B, cell body; C, cell loading device; Ca, capillaries; H, capillaries holder; M, magnetic stirrer; V, O-ring. Reproduced from reference [92] with kind permission from American Institute of Chemical Engineers. Copyright 1983.

over-heated section. The gas circulation tube, 26, between the two thermostats is heated. Leaving the saturators, the vapour passes through two traps, 2, before entering the condenser, 3, which is kept at very low temperature, and goes on to the humidifiers, 4, and the gas meter, 5. Valves 17 and 18 are also heated. During the time necessary to reach equilibrium, valve 18 is closed while valve 17 is opened so that vapour escapes into the atmosphere. The condenser is shown in Figure 6.42. By weighing the condenser, and knowing the volume of gas that circulates, it is possible to deduce the solubility of the liquid in the gas. Several authors have developed this type of instruments, for carrying out studies of the solubility of solids in supercritical fluids. As an example, the instruments of Schmitt and Reid [94] and Dobbs *et al.* [95] are shown in Figures 6.43 and 6.44, respectively. In Figure 6.43, the supercritical fluid circulates in a weak flow in extraction tubes and exits into a trap where the recuperated solid is weighed at the end of the experiment. Dobbs *et al.* prefer a method that is considered more satisfactory. A sampling valve is used to isolate a small volume of the gas phase leaving the saturator. This sample is expanding it between valves A and B (Figure 6.44). The solid is recovered by circulating a solvent, which is analysed by chromatography.

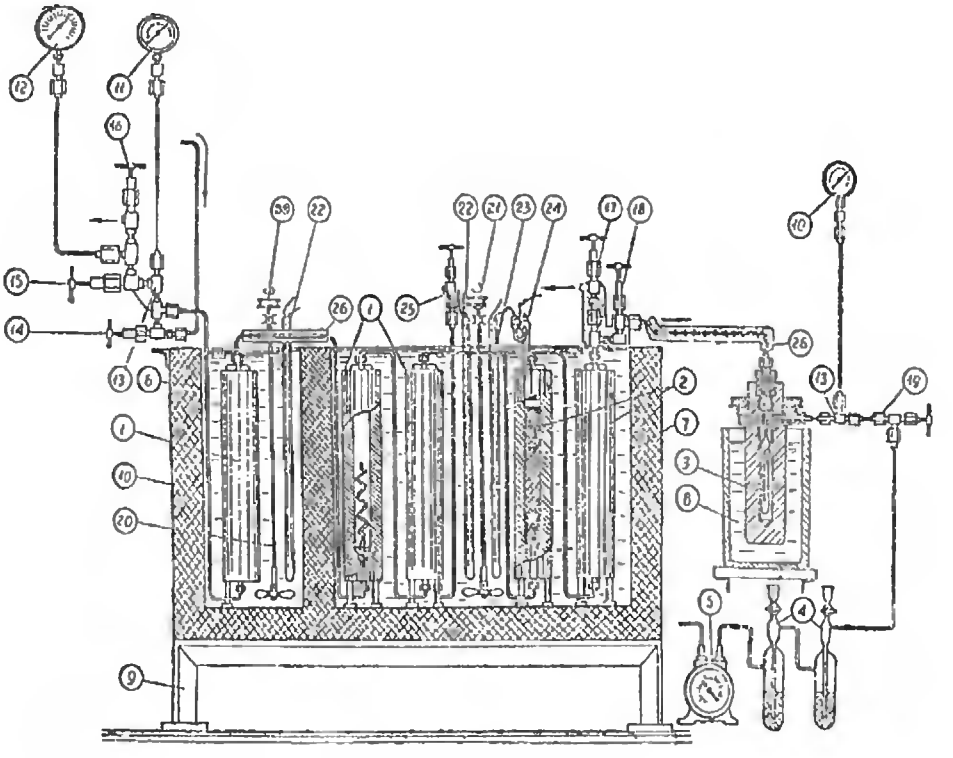

Figure 6.41 Apparatus of Krichevsky and Gamburg: 1, saturators; 2, traps; 3, condenser; 4, humidifiers; 5, gasmeter; 6, thermostating liquid; 7, liquid bath; 8, cooling liquid; 9, holder; 10, Bourdon pressure gauge or liquid bath; 11, Bourdon pressure gauge; 12, precision pressure gauge; 13, connector; 14, inlet valve; 15 to 18, valve; 19, connector; 20, stirrer; 21, motor; 22 to 24, heating resistance; 25, valve; 26, heated tube; 39, motor. Reproduced from reference [93] with kind permission of Nauka Publishers. Copyright 1942.

Retention Time Methods

In retention time methods, chromatography is used as a gas–liquid partition method to obtain thermodynamic properties. Use of this technique was originally suggested by Martin [96] (see Chapter 14). Since this time, its validity has been verified experimentally and theoretically by a number of workers. Ng *et al.* [97] have applied this method to the measurement of the Henry's constants of several light hydrocarbons in heavy hydrocarbons. The solute passes inside the column containing the solvent, undergoes VLE and then spend, inside the column, a period of time related to the value of the desired Henry's constant. Data reduction relies on some quantities, which are not completely defined such as homogeneity of column packing, dead volumes, homogeneity of solvent deposit, etc. As a consequence, uncertainty of determined values is an increasing function of the absolute value of the Henry's constant. Kragas *et al.* [98] describe a new gas–liquid partition chromatography apparatus (Figure 6.45) for the measurement of VLE data at elevated pressures and temperatures.

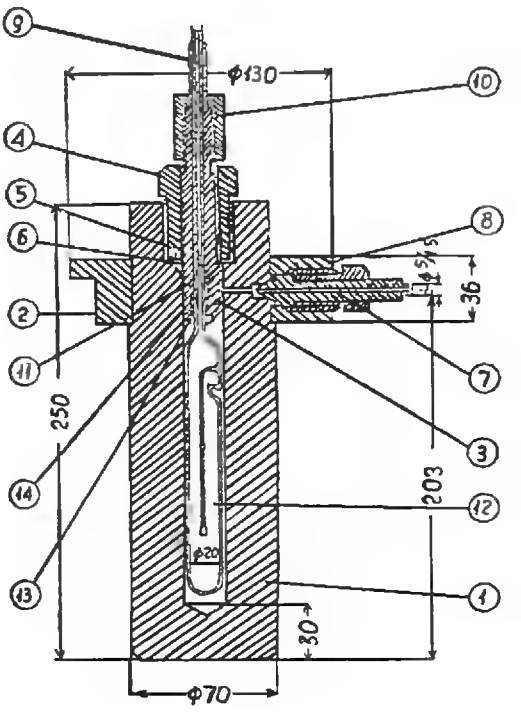

Figure 6.42 Condenser used by Krichevsky and Gamburg: 1, body; 2, supporting ring; 3, filling pump; 4, screw-nut; 5, joint; 6, tube; 7, screw-nut; 8, threaded ring; 9, vapor inlet; 10, screw-nut; 11, leakproof joint for magnet; 12, combustion tube; 13, screw; 14, flat joint. Reproduced from reference [93] with kind permission of Nauka Publishers. Copyright 1942.

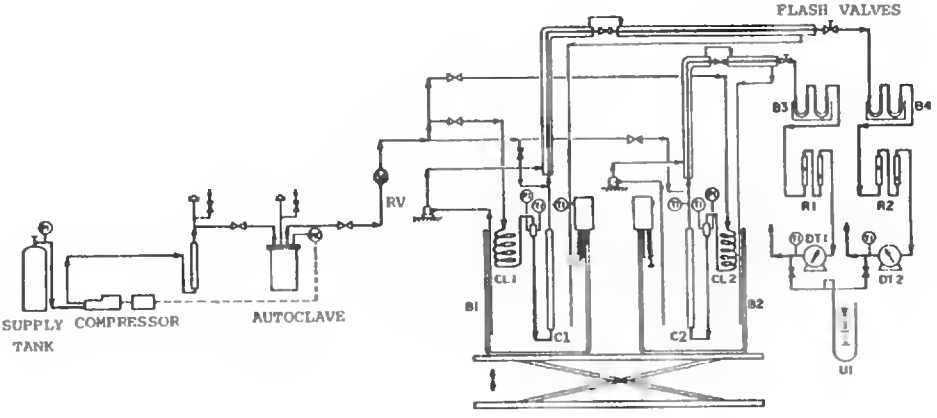

Figure 6.43 Apparatus of Schmitt and Reid: C, equilibrium tubes; CL, heating coils; B1, B2, water bath; B3, B4, U-tubes; R, rotameter; DT, dry test meter; U, manometer; RV, pressure regulator. Reproduced from reference [94] with kind permission of American Chemical Society. Copyright 1986.

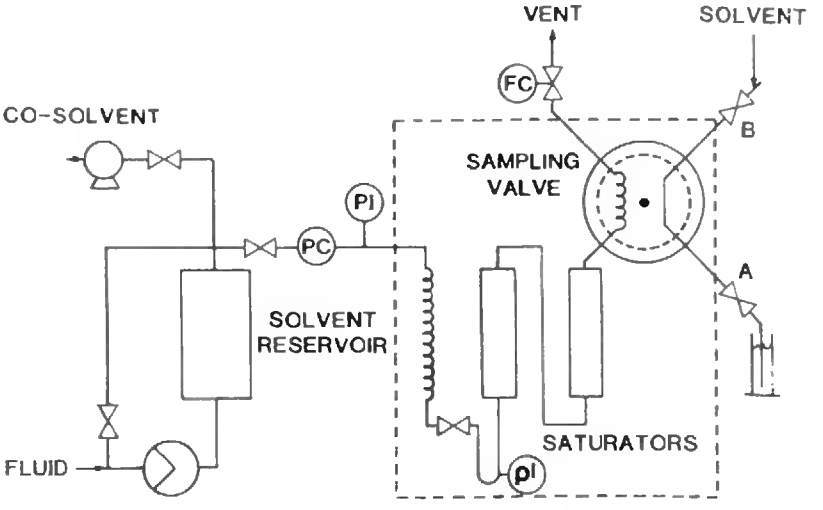

Figure 6.44 Apparatus of Dobbs *et al.* Reproduced from reference [95] with kind permission of American Chemical Society. Copyright 1986.

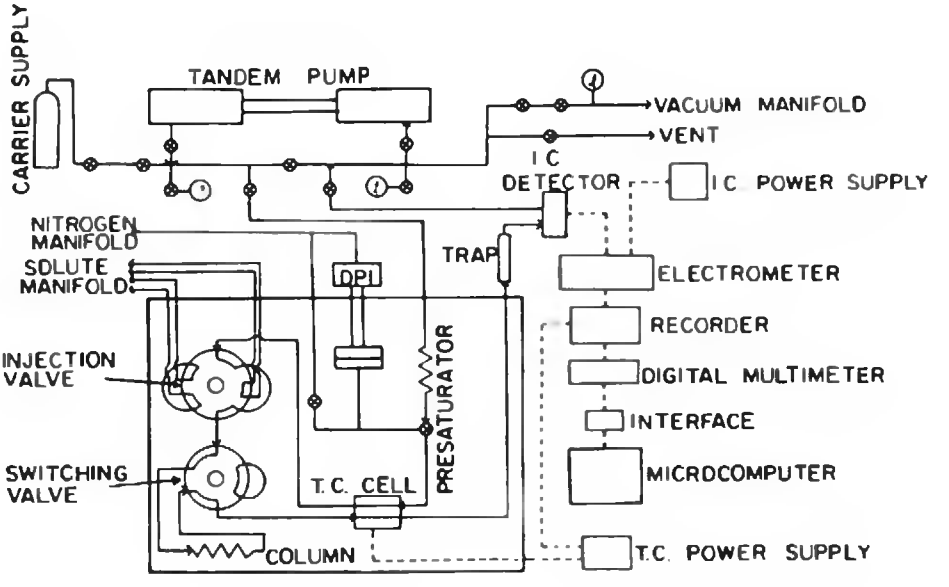

Figure 6.45 Apparatus of Kragas *et al.* Reproduced from reference [98] with kind permission from Elsevier. Copyright 1984.

6.3 Conclusions

Closed-circuit methods can be divided into static–synthetic and static–analytic methods. These methods have the essential advantage that the system investigated can be equilibrated for a sufficient period of time so that equilibrium is assured. Closed-circuit methods can be realised in relatively simple devices, both in conception and in use. Homogeneity inside equilibrium cells can be achieved in various ways: external oscillating movements of the cell, or internal agitation with a magnetic stirrer for static methods and mechanical or thermal agitation through recirculation of one or more phases with quasi-static methods.

Synthetic methods have the advantage that most of them permit the visual observation of the phenomena studied and simple cells can be used since sampling is not necessary. However, the data are generally incomplete. To obtain complete data, relatively complex instrumentation is required. In this case, the synthetic method is competitive or better in comparison with analytical methods only in a certain range of variables and especially because analytical problems are avoided and the risk of leaks is reduced. It is interesting to note that when p, T, x, y data are determined using synthetic methods, it is in general possible to obtain simultaneously pVT properties which can prove to be a major advantage. The synthetic methods use various techniques, like visual or instrumented observation of phenomena (the appearance or disappearance of a phase), measurement of an interface position, the solution of mass balance equations or data processing. The chemical nature and physical properties of the pure components and mixtures are important factors to decide whether or not a method is suitable. For the methods based on the variation of temperature at constant volume or variation of the volume at constant temperature, to determinate break points in p–V or p–T curves, it is necessary to avoid the proximity of the critical point or regions where $(\partial p/\partial x)_V$ and $(\partial p/\partial x)_T$ have very high values and where $(\partial p/\partial T)$ is near zero or tends towards infinity. Visual methods can normally be used in the critical region. In the case of synthetic methods with measurement of phase volumes and solving mass balance equations to calculate the equilibrium concentrations, it is difficult to say which conditions yield the highest precision. This depends on several factors, such as the nature of the components, the range of pressures and the accuracy of each measurement. In addition, the precision of one variable can be improved while that of another is deteriorated. Theoretically, these methods can be applied to multi-component, multi-phase systems but in practice, it is recommended to limit their use to systems with not more than three components to keep sufficient precision. The total pressure measurement method is the method that yields the minimum of experimental information. It depends heavily on the data processing method and for this reason has severe limitations. It is in general applied at low or moderate pressures. At higher pressures, the best results are for systems composed of one volatile and one heavy component.

Analytic methods are basically complementary to synthetic methods, although the same types of measurements can be carried out. The limits of analytic methods are found in the technique of sampling and the technique of analysis. Samples must be small enough in order to avoid disturbance of the equilibrium and should nevertheless be representative for the equilibrium. Most sampling systems presented in the literature do not satisfy these criteria. With a good sampling system, the accuracy of phase compositions is determined by the analytical instrument. In the synthetic method, compositions are determined, *a priori*, from

accurate measurements of volumes or weights. For multi-component mixtures, analytic methods are well adapted, provided, the analytical conditions are known or easy to set up. *In situ* analyses through spectroscopic measurements are very attractive but suffer from other drawbacks, which limit their use to simple systems.

When the residence time for the mixture, at equilibrium temperature, needs to be as short as possible because of thermal instability of the chemicals, methods with open circuits are preferred. Another advantage of these methods is the possibility of collecting a large amount of sample and then using other analytic methods, *e.g.* involving chemical reactions. For measurements near the critical point, static–analytic methods are well adapted if the thermal regulation is stable and homogeneous.

References

1. Tsiklis, D.S., *Handbook of Techniques in High Pressure Research and Engineering*, Plenum, New York, 1968.
2. Schneider, G.M., in *Phase Equilibria of Liquid and Gaseous Mixtures at High Pressures*, B. Le Neindre and B. Vodar, eds., *Vol 2*, Butterworth, London, pp. 787–801, 1975.
3. Eubank, P.T., Hall, K.R. and Holste, J.C., in *A Review of Experimental Techniques for Vapour–Liquid Equilibria at High Pressures*, H. Knapp. and S.I. Sandler., eds., *2nd Int. Conf. Phase Equilibria and Fluid Properties in the Chemical Industry*, Dechema, Frankfurt, 1980.
4. Deiters, U.K. and Schneider, G.M., *Fluid Phase Equilibr.* **29**, 145, 1986.
5. Fornari, R., Alessi, P. and Kikic, I., *Fluid Phase Equilibr.* **57**, 1, 1990.
6. Dohrn, R. and Brunner, G., *Fluid Phase Equilibr.* **106**, 213, 1995.
7. Peter, S. and Eicke, H.E., *Ber. Bunsenges. Phys. Chem.* **74**, 190, 1970.
8. Peter, S., Brunner, G. and Wenzel, H., *Chem. Eng. J.* **7**, 99, 1974.
9. Pawlikowski, E.M., Newmann, J. and Prausnitz, J.M., *Ind. Eng. Chem. Process Des. Dev.* **21**, 764, 1982.
10. Butcher, K.L. and Robinson, W.I., *J. Appl. Chem.* **16**, 289, 1966.
11. Valuev, K.I., Karchenko, A.A. and Lebedev, A.E., *Zh. Fiz. Khim. USSR* **46**, 2135, 1972.
12. Jacoby, R.H. and Tracht, J.H., *J. Chromatogr. Sci.* **13**, 44, 1975.
13. Yarborough, L. and Vogel, J.L., *Chem. Eng. Progr. Symp. Ser.* **63**, 1, 1967.
14. Ellis, S.R.M., Walteris, R.M. and Harris, G.J., *Chem. Eng. Prog. Symp. Ser.* **88**, 16, 1968.
15. Rodgers, B.L. and Prausnitz, J.M., *Ind. Eng. Chem. Fund.* **9**, 174, 1970.
16. Dorokhov, A.I., Zakurenov, V.M. and Nozdrev, V.F., *Russian J. Phys. Chem.* **46**, 1385, 1972.
17. Figuière, P., Hom, J.F., Laugier, S., Renon, H., Richon, D. and Szwarc, H., *AIChE J.* **26**, 872, 1980.
18. Laugier, S., Richon, D. and Renon, H., *FUEL* **62**, 842, 1983.
19. Miksovski, J. and Wichterle, I., *Coll. Czec. Chem. Commun.* **40**, 360, 1975.
20. Laugier, S. and Richon, D., *Rev. Sci. Instrum.* **57**, 469, 1986.
21. Marteau, Ph., Tobaly, P., Ruffier-Meray, V. and Barreau, A., *Fluid Phase Equilibr.* **119**, 213, 1996.
22. Konrad, R., Swaid, I. and Schneider, G.M., *Fluid Phase Equilibr.* **10**, 307, 1983.
23. Tuma, D. and Schneider, G.M., *Fluid Phase Equilibr.* **158–160**, 743, 1999.
24. Katayama, T., Oghaki, K., Maekawa, G., Goto, M. and Nagano, T., *J. Chem. Eng. Jpn.* **8**, 89, 1975.
25. Freitag, N.P. and Robinson, D.B., *Fluid Phase Equilibr.* **31**, 183, 1986.
26. Nasir, P., Martin, R. and Kobayashi, R., *Fluid Phase Equilibr.* **5**, 279, 1980.
27. Weber, W., Zeck, S. and Knapp, H., *Fluid Phase Equilibr.* **18**, 253, 1984.
28. Kim, C.H., Vilmalchand, P. and Donohue, M.D., *Fluid Phase Equilibr.* **31**, 299, 1986.

29. Radosz, M., *J. Chem. Eng. Data* **31**, 43, 1986.
30. Fleck, R.N. and Prausnitz, J.M., *Ind. Eng. Chem. Fund.* **7**, 174, 1968.
31. Hala, E., Pick, J., Fried, V. and Vilim, D., *Vapor Liquid Equilibrium*, 2nd ed., Pergamon Press, Oxford, 1967.
32. Othmer, D.F. and Morley, F.R., *Ind. Eng. Chem.* **38**, 751, 1946.
33. Roof, J.G. and Baron, J.D., *J. Chem. Eng. Data* **18**, 293, 1967.
34. Kurata, F. and Kohn, J.P., *Petroleum Process.* **57**, 103, 1956.
35. Katz, D.L. and Kurata, F., *Ind. Eng. Chem.* **32**, 817, 1940.
36. Kay, W.B. and Ranbosek, G.M., *Ind. Eng. Chem.* **45**, 221, 1953.
37. Bloomer, O.T. and Parent, J.D., *Chem. Eng. Progr. Symp.* **49**, 11, 1953.
38. Lu, M., Newitt, D.M. and Ruheman, M., *Proc. Roy. Soc.* **178**, 506, 1941.
39. de Loos, Th.W., van der Kooi, H.J. and Ott, P.L., *J. Chem. Eng. Data* **31**, 166, 1986.
40. Slocum, E.W., *Ind. Eng. Chem. Fund.* **14**, 26, 1975.
41. Schneider, G.M., *Z. Phys. Chem. (Frankfurt)* **37**, 333, 1963.
42. Buback, M. and Franck, E.U., *Ber. Bunsenges Phys. Chem.* **76**, 350, 1972.
43. Oeder, D. and Schneider, G.M., *Ber. Bunsenges Phys. Chem.* **73**, 229, 1969.
44. de Swaan Arons, J. and Diepen, G.A.M., *J. Chem. Phys.* **44**, 2322, 1966.
45. de Loos, Th.W., Wijen, A.J.M. and Diepen, G.A.M., *J. Chem. Thermodyn.* **12**, 193, 1980.
46. Sage, B.H. and Lacey, W.N., *Trans. Am. Inst. Mining Met. Eng., Petrol. Div.* **136**, 136, 1940.
47. Weise, H.C., Reamer, H.H. and Sage, B.H., *J. Chem. Eng. Data* **15**, 75, 1970.
48. Reamer, H.H. and Sage, B.H., *J. Chem. Eng. Data* **9**, 24, 1964.
49. Reamer, H.H., Sage, B.H. and Lacey, W.N., *J. Chem. Eng. Data* **5**, 44, 1960.
50. Meskel-Lesavre, M., Richon, D. and Renon, H., *Ind. Eng. Chem. Fund.* **20**, 284,1981.
51. Rousseaux, P., Richon, D. and Renon, H., *Fluid Phase Equilibr.* **11**, 153, 169, 1983.
52. Specovius, J., Leiva, M.A., Scott, R.L. and Knobler, C.M., *J. Phys. Chem.* **85**, 2313, 1981.
53. Fontalba, F., Richon, D. and Renon, H., *Rev. Sci. Instrum.* **55**, 944, 1984.
54. Laugier, S., Richon, D. and Renon, H., *Fluid Phase Equilibr.* **54**, 1934, 1990.
55. Di Andreth, J.R. and Paulaitis, M.E., *Fluid Phase Equilibr.* **32**, 261, 1987.
56. Hall, K.R. and Eubank, P.T., *J. Chem. Phys.* **709**, 6691, 1973.
57. Hall, K.R. and Eubank, P.T., *AIChE J.* **20**, 815, 1974.
58. Hall, K.R., Eubank, P.T., Mierson, A.S. and Nixon, W.E., *AIChE J.* **21**, 1111, 1975.
59. Prengle, H.W. Jr. and Palm, G.F., *Ind. Eng. Chem.* **49**, 1769, 1957.
60. Ramalho, R.S. and Delmas, J., *Can. J. Chem. Eng.* **46**, 32, 1966.
61. Prengle, H.W. Jr. and Pike, M.A., *J. Chem. Eng. Data* **6**, 24, 1961.
62. Singh, J. and Benson, G.C., *Can. J. Chem.* **46**, 1249, 1968.
63. Hermsen, R.W. and Prausnitz, J.M., *Chem. Eng. Sci.* **18**, 485, 1963.
64. Diaz Pena, M., *Annal. Phys.* **66**, 377, 1970.
65. Tao, L.C., *Ind. Eng. Chem.* **53**, 307, 1961.
66. Ljunglin, J.J. and Van Ness, H.C., *Chem. Eng. Sci.* **17**, 531, 1962.
67. Ronc, M. and Ratcliff, G.A., *Can. J. Chem. Eng.* **54**, 326, 1976.
68. Gibbs, R.E. and Van Ness, H.C., *Ind. Eng. Chem. Fund.* **11**, 410, 1972.
69. Legret, D., Richon, D. and Renon, H., *Ind. Eng. Chem. Fund.* **11**, 410, 1980.
70. Simnick, J.J., Lawson, C.C., Lin, H.M. and Chao, K.C., *AIChE J.* **23**, 469, 1977.
71. Lin, H.M., Kim, H., Leet, W.A. and Chao, K.C., *Ind. Eng. Chem. Fund.* **24**, 260, 1985.
72. Niesen, V., Palavra, A., Kidnay, A.J. and Yesavage, V.F., *Fluid Phase Equilibr.* **31**, 283, 1986.
73. Gilbert, M.L. and Paulaitis, M.E., *J. Chem. Eng. Data* **31**, 296, 1986.
74. Houzelle, C., Legret, D., Richon, D. and Renon, H., *Fluid Phase Equilibr.* **11**, 179, 1983.
75. Laugier, S., Legret, D., Mulhbauer, R., Renon, H. and Richon, D., *Hydrogen as an energy vector, Commission of the European Communities*, EUR 9782 EN, 386, 1985.

76a. Bouchot, C. and Richon, D., *Ind. Eng. Chem. Res.* **37**, 3295, 1998.
76b. Laugier, S. and Richon, D., *Fluid Phase Equilibr.* **210**, 247, 2003.
76c. Scalabrin, G., Piazza, L. and Richon, D., *Fluid Phase Equilibr.* **199**, 33, 2002.
77. Woycicka, M., Richon, D. and Viallard, A., *C.R. Acad. Sci.* **276**, 983, 1973.
78. Ott, J.B. and Sipowska, J., *J. Chem. Eng. Data* **41**, 987, 1996.
79. Kirk, B.S. and Ziegler, W.T., *Adv. Cryogenic Eng.* **10**, 160, 1965.
80. Dodge, B.F. and Dunbar, A.K., *J. Am. Chem. Soc.* **49**, 591, 1927.
81. Hiza, M.J. and Herring, R.N., *Adv. Cryogenic Eng.* **8**, 158, 1963; Hiza, M.J. and Herring, R.N., *Adv. Cryogenic Eng.* **10**, 182, 1964.
82. Herring, R.N. and Barrick, P.L., *Adv. Cryogenic Eng.* **10**, 151, 1965.
83. Hiza, M.J. and Kidnay, A.J., *Adv. Cryogenic Eng.* **11**, 38, 1966.
84. Hiza, M.J., Heck, C.K. and Kidnay, A.J., *Adv. Cryogenic Eng.* **13**, 343, 1968.
85. Hiza, M.J. and Duncan, A.G., *Adv. Cryogenic Eng.* **14**, 30, 1969.
86. Michels, A., Skelton, G.F. and Dumoulin, E., *Physica* **16**, 831, 1950.
87. Michels, A., Dumoulin, E. and van Dich, J.J.Th., *Physica* **25**, 840, 1959; Michels, A., Dumoulin, E. and van Dich, J.J.Th., *Physica* **27**, 886, 1961.
88. Leroi, J.C., Masson, J.C., Renon, H., Fabries, J. F. and Sannier, H., *Ind. Eng. Chem. Process Des. Dev.* **16**, 139, 1977.
89. Antoine, Ph., Richon, D. and Renon, H., *Ind. Eng. Chem. Process Des. Dev.* **19**, 144, 1980.
90. Richon, D. and Renon, H., *J. Chem. Eng. Data* **25**, 59, 1980.
91. Richon, D., Sorrentino, F. and Voilley, A., *Ind. Eng. Chem. Process Des. Dev.* **24**, 1160, 1985.
92. Legret, D., Desteve, J., Richon, D. and Renon, H., *AIChE J.* **29**, 137, 1983.
93. Krichevsky, T. and Gamburg, D., *Acta Physicochim. USSR* **16**, 362, 1942.
94. Schmitt, W.J. and Reid, R.C., *J. Chem. Eng. Data* **31**, 204, 1986.
95. Dobbs, J.M., Wong, J.M. and Johnston, K.P., *J. Chem. Eng. Data* **31**, 303, 1986.
96. Martin, A.J.P., *Analyst* **81**, 52, 1956.
97. Ng, S., Harris, H.G. and Prausnitz, J.M., *J. Chem. Eng. Data* **14**, 482, 1969.
98. Kragas, T.R., Pollin, J., Martin, R.J. and Kobayashi, R., *Fluid Phase Equilibr.* **16**, 205, 1984.

7 Low-Pressure Solubility of Gases in Liquids

EMMERICH WILHELM
Institut für Physikalische Chemie
Universität Wien
Wien, Austria

It is a very sweet little problem, and I would not have missed it for a good deal.

Sherlock Holmes in: *The Adventure of the Beryl Coronet*
By Sir Arthur Conan Doyle

Measurement of the Thermodynamic Properties of Multiple Phases
R.D. Weir and Th.W. de Loos (Editors)

7 LOW-PRESSURE SOLUBILITY OF GASES IN LIQUIDS

For a century and a half, experimental investigations of thermo-physical properties and phase equilibria of non-electrolyte solutions in general, and of dilute non-electrolyte solutions in particular, have held a prominent position in physical chemistry. The scientific insights gained in these studies have been of immense value in the development of the highly formalized, general discipline of mixture thermodynamics. In combination with specific models of material behaviour, they have been both at the heart of physical and biophysical chemistry as well as chemical engineering. During the last three decades, various aspects of this topic have been included in state-of-the-art surveys, though with greatly differing coverage and from a variety of viewpoints as documented representatively in references [1–21]. Besides purely descriptive presentations of results, of pertinent instruments and corresponding experimental techniques, emphasis was placed, for instance, on formal thermodynamics including critical behaviour, on Kirkwood–Buff type analysis of data, on the use of equation-of-state (EOS) models and group-contribution methods, on molecular simulation, on hydrophobic effects in "simple" model solutions of biological relevance, *etc.* The preponderance of work on aqueous systems reflects the fact that water is our environment's primary and indispensable solvent.

Quantitative research on the solubility of gases in liquids started in the 1850s with the pioneering work of Bunsen "*Über das Gesetz der Gasabsorption*" [22], and many distinguished scientists have contributed to this subject. One can only marvel about the careful experimental work of some of the early researchers, such as Winkler [23], Szeparowicz [24] and Horiuti [25], to name but a few. Their pioneering contributions are still quite acceptable, even by modem standards. The years since about 1970 have seen renewed and intense activities concerning the solubility of gases in liquids. The assortment of modern instrumentation accessible to today's experimentalists has made possible the study of dilute solutions with unparalleled precision, accuracy and speed over wide ranges of temperature and pressure, including the solvent critical region. Why, now, this marked interest in vapour–liquid equilibria (VLE) involving supercritical components, that is to say, where the system temperature exceeds their respective critical temperature? In addition to its profound theoretical interest, this topic includes many important practical applications covering surprisingly diverse areas of the pure and applied sciences [5,8]. For instance, reliable gas solubility data are frequently needed in biomedical technology, the environmental sciences, geochemistry and chemical process design. The latter includes coal gasification, enhanced oil recovery, natural-gas and synthetic-gas purification (gas sweetening), waste water treatment and so forth. Since life cannot exist without water, studies of aqueous solutions of simple non-polar substances, in particular of the rare gases and of simple hydrocarbons, have held a prominent position in biophysics. Studies on such model systems provide information on hydrophobic effects [5,13,26–28] that are thought to be of pivotal importance for the formation and stability of higher order structures of biological substances, such as proteins and nucleic acids, and the stability of cell membranes.

Given this wide scope, it is not surprising that the subject of the solubility of gases in liquids has such a vast literature. Because of this diversity, a certain variation of

experimental as well as theoretical methods used in each of these areas is almost inevitable, and makes it impossible to cover all of them in one short review. Far from being exhaustive, this contribution will therefore focus on just a few selected topics, with the bias reflecting my current interests and idiosyncrasies. For the omission of some important papers and neglecting several related research areas, I would like to offer my apologies in advance.

First of all, I shall be concerned with the concise formulation of the thermodynamic formalism relevant to the solubility of gases in liquids. This will be followed by a critical examination of current methods for the prediction of important auxiliary quantities needed for the practical implementation of the derived relations. That is, estimation techniques for virial coefficients and partial molar volumes at infinite dilution will be discussed. The next sections will be devoted to a brief appraisal of several recent designs of precision apparatus, and to the presentation and correlation of experimental data. Pride of place will be given to experimental methods characterized by an imprecision of *less* than 0.1%. Finally, a few recent high-precision data on selected systems will be presented, including caloric properties, such as enthalpies of solution, obtained *via* van't Hoff analysis of solubilities. Essentially, all of what follows will concern the solubility of a single *pure gas in a single pure liquid solvent*. Gas solubility in mixed solvents, or the solubility of several gases in a pure liquid or a liquid mixture, though undoubtedly of considerable practical interest, will not be considered and no salt effects will be discussed. Further, problems associated with solutions of chemically reacting gases will not be treated to any extent, despite its importance to the chemical industry, since absorption of gases by liquids *with* chemical reaction is an extensive topic by itself. A characteristic feature of these processes is the interplay of equilibrium thermodynamics on the one hand, and time-dependent processes, that is to say mass transfer and chemical reaction, on the other. Enormous effort and ingenuity have gone into the design of absorbers, strippers and reactors, reflecting industry's need to operate under optimal conditions. Those with a specific interest in one or more of these topics are referred to the pertinent sections in references [29–34].

7.1 Thermodynamics

7.1.1 Fundamentals

The purpose of this section is to present a concise overview of classical thermodynamics applicable to *dilute solutions of non-electrolytes*, or more specifically, to *dilute solutions of gases in liquids*. When discussing systems containing more than one component, it is frequently convenient to distinguish between a *mixture* or a *solution*, and a *dilute solution*. In a mixture, all components are on equal footing: thermodynamically, they are all treated in the same manner, that is to say *symmetrically*. In contradistinction, in a dilute solution one (or several) of the components is (are) present in great excess and forms (form) the *solvent* (or *mixed solvent*), while the remaining component(s) at low mole fraction or concentration is (are) classified as the *solute(s)*. Usually, the thermodynamic treatment of dilute solutions focuses on the solute(s), that is to say it will be *asymmetric*. These statements will be elaborated below. We note that there is nothing fundamental in this distinction

between a mixture/solution and a dilute solution since it is merely a heuristic convenience. However, while the designation "*gas solubility*" is to some extent arbitrary, the fact that the solute frequently is supercritical introduces some aspects not encountered in the usual thermodynamic treatment of VLE [5,8,9,12,34–37].

A general criterion for phase equilibrium at temperature T and pressure P is the equality of the fugacity f_i^{π} of each one of the constituent components i in all coexisting phases π [35]. Thus, for the specific case of VLE (π = V or L)

$$f_i^{V}(T, P, \{x_i^{V}\}) = f_i^{L}(T, P, \{x_i^{L}\}), \quad i = 1, 2, \ldots, N, \tag{7.1}$$

where N is the number of components present, $\{x_i^{V}\}$ the set of vapour-phase mole fractions $x_1^{V}, x_2^{V}, \ldots, x_N^{V}$ and $\{x_i^{L}\}$ the set of liquid-phase mole fractions $x_1^{L}, x_2^{L}, \ldots, x_N^{L}$ with $\Sigma x_i^{V} = 1$ and $\Sigma x_i^{L} = 1$. From now on, however, I shall confine attention to binary systems only, where $i = 1$ or 2.

Two *entirely equivalent* formal procedures are commonly used to establish the link with experiment:

(I) In the first, the equilibrium condition, Equation (7.1) is rewritten in terms of the fugacity coefficient of component i in solution defined by

$$\varphi_i^{\pi}(T, P, \{x_i^{\pi}\}) = \frac{f_i^{\pi}(T, P, \{x_i^{\pi}\})}{x_i^{\pi} P}, \quad i = 1, 2, \tag{7.2a}$$

in both phases π = V or L, respectively. This approach is called, for obvious reasons, the (φ, φ) *method*. For pure i in any phase π, the fugacity coefficient is defined by Equation (7.2b) where the asterisk always denotes a property of the pure substance:

$$\varphi_i^{\pi *}(T, P) = f_i^{\pi *}(T, P)/P. \tag{7.2b}$$

(II) In the second, the component fugacities in the vapour phase are again expressed in terms of the respective fugacity coefficients φ_i^{V}, whereas the liquid-phase fugacities of the components are expressed in terms of appropriately normalized liquid-phase activity coefficients. The *symmetric* convention is based on the Lewis–Randall (LR) rule (see below), and leads to

$$\gamma_i^{LR}(T, P, \{x_i^{L}\}) = \frac{f_i^{L}(T, P, \{x_i^{L}\})}{x_i^{L} f_i^{L*}(T, P)}, \quad i = 1, 2. \tag{7.3}$$

The *unsymmetric* convention is based on Henry's law (HL) (see below), and leads to

$$\gamma_i^{HL}(T, P, \{x_i^{L}\}) = \frac{f_i^{L}(T, P, \{x_i^{L}\})}{x_i^{L} h_{i,j}(T, P)}, \quad i, j = 1, 2; i \neq j. \tag{7.4}$$

Here, $f_i^{L*}(T, P)$ is the fugacity of *pure component i* in either a real or a hypothetical liquid state at (T, P) of the solution, and $h_{i,j}(T, P)$ is *Henry's law constant* or, perhaps more descriptive, the *Henry fugacity of i dissolved in j* at (T, P) of the solution. This approach is called the (φ, γ) *method*. The numerical value of the Henry fugacity depends on T and P and also on the identity of the solvent j, the other component, hence the double subscript. Since the

limiting value of the ratio f_i^{π}/x_i^{π} for $x_i^{\pi} \to 0$ at constant T and P is known from experiment to be finite, by de l'Hôpital's rule

$$\lim_{x_i \to 0} \left(\frac{f_i}{x_i} \right) = \left(\frac{\mathrm{d}f_i}{\mathrm{d}x_i} \right)_{x_i=0} = h_{i,j}(T, P), \tag{7.5}$$

where the superscript π has been dropped for convenience. This equation defines the Henry fugacity $h_{i,j}(T, P)$ of i dissolved in j ($i \neq j$) at given T and P for any phase L or V. Thus *Henry's law*

$$f_i(T, P, x_i) = x_i h_{i,j}(T, P), \tag{7.6}$$

applies in the limit as $x_i \to 0$, and must also be approximately valid for small values of x_i.

Henry's law is related to the Lewis–Randall rule through the isothermal–isobaric Gibbs–Duhem equation, whence at the other end of the composition range one obtains at constant T and P

$$\lim_{x_i \to 1} \left(\frac{f_i}{x_i} \right) = \left(\frac{\mathrm{d}f_i}{\mathrm{d}x_i} \right)_{x_i=1} = f_i^*(T, P). \tag{7.7}$$

The $f_i^*(T, P)$ is the fugacity of pure i at (T, P) of the solution and in the *same* physical state. Thus the *Lewis–Randall rule*

$$f_i(T, P, x_i) = x_i f_i^*(T, P), \tag{7.8}$$

applies in the limit as $x_i \to 1$, and must also be approximately valid for values of x_i near unity.

Figure 7.1 shows the composition dependence of the fugacity of component 2 in a binary solution at constant T and P, and illustrates the quantities introduced above. Reality may thus be compared with each one of the two *idealizations* introduced by assuming validity over the *whole* composition range of either (i) the Lewis–Randall rule as expressed by Equation (7.8), which is the dashed line marked LR, or (ii) Henry's law as expressed by Equation (7.6), which is the dashed line marked HL. In other words, by definition ideal-solution behaviour in the sense of the Lewis–Randall rule is characterized by

$$f_i^{\mathrm{LR}}(T, P, x_i) = x_i f_i^*(T, P), \quad 0 \leq x_i \leq 1, \tag{7.9a}$$

and with

$$\gamma_i^{\mathrm{LR}} = f_i^{\mathrm{L}}/f_i^{\mathrm{LR}}, \tag{7.9b}$$

Equation (7.3) is obtained. Ideal-solution behaviour in the sense of Henry's law is characterized by

$$f_i^{\mathrm{HL}}(T, P, x_i) = x_i h_{i,j}(T, P), \quad 0 \leq x_i \leq 1, \tag{7.10a}$$

and with

$$\gamma_i^{\mathrm{HL}} = f_i^{\mathrm{L}}/f_i^{\mathrm{HL}}, \tag{7.10b}$$

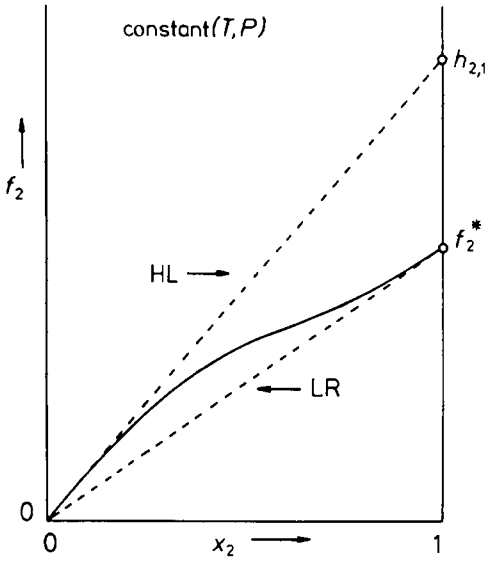

Figure 7.1 Composition dependence (schematic) of component fugacity f_2 in a binary solution at constant (T, P). The f_2^* is the fugacity of pure substance 2, $h_{2,1}$ is the Henry fugacity (or Henry's law constant) of solute 2 dissolved in solvent 1, and x_2 is the mole fraction of solute 2. The dashed lines represent the two most popular *ideal solution models*, that is the one based on the *Lewis–Randall* (LR) rule: $f_2^{LR} = x_2 f_2^*$ and the one based on *Henry's law* (HL): $f_2^{HL} = x_2 h_{2,1}$, respectively.

Equation (7.4) is obtained. Correspondingly, the activity coefficients are said to be normalized symmetrically when Equation (7.3) applies for all components, and

$$\gamma_1^{LR} \to 1 \quad \text{as } x_1^L \to 1$$

$$\gamma_2^{LR} \to 1 \quad \text{as } x_2^L \to 1.$$

They are said to be normalized unsymmetrically, when for the solvent ($i = 1$) Equation (7.3) applies, and for the solute ($i = 2$) Equation (7.4) applies, and

$$\gamma_1^{LR} \to 1 \quad \text{as } x_1^L \to 1$$

$$\gamma_2^{HL} \to 1 \quad \text{as } x_2^L \to 0.$$

It is customary and convenient to set $\{x_i^V\} \equiv \{y_i\}$, and $\{x_i^L\} \equiv \{x_i\}$ and to drop the superscript L where permissible. The VLE condition, Equation (7.1), may therefore be recast in three different, though entirely equivalent, ways ($i = 1, 2$):

$$\varphi_i^V(T, P, y_i) y_i P = \varphi_i^L(T, P, x_i) x_i P, \tag{7.11}$$

$$\varphi_i^V(T, P, y_i) y_i P = \gamma_i^{LR}(T, P, x_i) x_i f_i^{L*}(T, P), \tag{7.12}$$

$$\varphi_i^{\mathrm{V}}(T, P, y_i) y_i P = \gamma_i^{\mathrm{HL}}(T, P, x_i) x_i h_{i,j}(T, P). \tag{7.13}$$

Each equation may serve as a rigorous thermodynamic basis for the treatment of VLE. The decision as to which approach should be adopted for solving actual problems is by and large a matter of taste, yet is subject to important practical constraints. Numerical values for the fugacity coefficients are obtained by using EOS information on the fluid.

VLE involving fairly simple fluids may conveniently be treated in terms of the (φ, φ) approach, Equation (7.11), because the use of a single EOS valid for *both* phases V and L has some computational advantage (and a certain aesthetic appeal). However, the emphasis is on "fairly simple", since no generally satisfactory EOS for dense fluids of practical importance has as yet been established. The situation is further aggravated by the sensitivity of the results on the so-called *mixing rules* and *combining rules*, which have always an empirical flavour.

At low to moderate pressures, thermodynamic analysis, *i.e.* data reduction and VLE calculations, is preferably based upon the classical (φ, γ) formalism expressed by Equations (7.12) and (7.13). Here, an EOS is required only for the low-density vapour phase, while for the liquid phase a suitable activity coefficient model is introduced. The VLE involving two liquid sub-critical components are generally treated in terms of the LR approach, Equation (7.12). Since the emphasis of this contribution is on dilute solutions of gases in liquids, only the (φ, γ) approach incorporating the unsymmetric convention, *i.e.* Equation (7.12) for $i = 1$ and Equation (7.13) for $i = 2$, will be discussed in any detail. In what follows now on dilute binary solutions, component 1 will *always* be the sub-critical solvent present in large excess, and its liquid-phase activity coefficient will be defined accordingly by Equation (7.3). Component 2 will *always* be the dissolved gas (usually, but not necessarily, a supercritical, non-condensable fluid), and its liquid-phase activity coefficient will be defined accordingly by Equation (7.4).

The various quantities corresponding to the two conventions introduced above are, of course, related [8,9,12,34–39]. Comparison of Equations (7.3) and (7.4) shows that ($i, j = 1, 2; i \neq j$)

$$\frac{\gamma_i^{\mathrm{LR}}(T, P, x_i)}{\gamma_i^{\mathrm{HL}}(T, P, x_i)} = \frac{h_{i,j}(T, P)}{f_i^{\mathrm{L}^*}(T, P)}. \tag{7.14}$$

Thus, in the limit $x_i \to 0$ one obtains for the activity coefficient in the symmetric convention (LR) at infinite dilution

$$\gamma_i^{\mathrm{LR}\infty} = \lim_{x_i \to 0} \gamma_i^{\mathrm{LR}} = h_{i,j}/f_i^{\mathrm{L}^*}, \tag{7.15}$$

whence

$$\gamma_i^{\mathrm{HL}} = \gamma_i^{\mathrm{LR}}/\gamma_i^{\mathrm{LR}\infty}, \tag{7.16}$$

and

$$\lim_{x_i \to 0} \gamma_i^{\mathrm{HL}} = 1/\gamma_i^{\mathrm{LR}\infty}. \tag{7.17}$$

Here, for the sake of brevity, the specifications (T, P, x_i), *etc.* have been omitted.

By definition, for component i in solution in any phase π, Equation (7.2a) applies, hence according to Equation (7.5) the important, *generally valid* relation

$$\varphi_i^{\pi\infty}(T, P) = \lim_{x_i^\pi \to 0} \phi_i^\pi(T, P, x_i^\pi) = \frac{1}{P} \lim_{x_i^\pi \to 0} \left\{ \frac{f_i^\pi(T, P, x_i^\pi)}{x_i^\pi} \right\} = h_{i,j}^\pi(T, P)/P, \qquad (7.18)$$

is obtained [37–39], where $\varphi_i^{\pi\infty}(T, P)$ is the fugacity coefficient of component i at infinite dilution in the phase π.

Focusing now on the liquid phase and combining Equations (7.2) and (7.18) with Equations (7.3) and (7.4) yields (all quantities refer to the same temperature and pressure)

$$\gamma_i^{\mathrm{LR}} = \varphi_i^{\mathrm{L}}/\varphi_i^{\mathrm{L}^*}, \qquad (7.19)$$

$$\gamma_i^{\mathrm{HL}} = \varphi_i^{\mathrm{L}}/\varphi_i^{\mathrm{L}\infty}, \qquad (7.20)$$

and

$$\gamma_i^{\mathrm{LR}\infty} = \gamma_i^{\mathrm{LR}}/\gamma_i^{\mathrm{HL}} = h_{i,j}/f_i^{\mathrm{L}^*} = \varphi_i^{\mathrm{L}\infty}/\varphi_i^{\mathrm{L}^*}. \qquad (7.21)$$

These equations show the links between a description based on activity coefficients with a description based on an EOS.

Gas solubilities are usually reported at isothermal conditions. Since the equilibrium pressure at constant temperature varies with composition, for each composition the quantities φ_1^{V}, φ_2^{L}, γ_1^{LR}, γ_2^{HL}, $f_1^{\mathrm{L}^*}$ and $h_{2,1}$ will refer to a *different* pressure. For the reduction and/or correlation of solubility data, it is advantageous (as well as customary) to select at each temperature the vapour pressure $P_{\mathrm{s},i}(T)$ of the solvent as reference pressure (the subscript s always indicates *saturation* conditions). Conversion to any other reference pressure is, in principle, straightforward by taking into account the following relations [8,9,12,35,37]:

$$f_1^{\mathrm{L}^*}(T, P) = f_1^{\mathrm{L}^*}(T, P_{\mathrm{s},1}) I_1(T, P) = P_{\mathrm{s},1} \varphi_1^{\mathrm{V}^*}(T, P_{\mathrm{s},1}) I_1(T, P), \qquad (7.22a)$$

$$I_1(T, P) \equiv \exp\left\{ \int_{P_{\mathrm{s},1}}^{P} \frac{V_1^{\mathrm{L}^*}(T, P)}{RT} \, \mathrm{d}P \right\}, \qquad (7.22b)$$

where use was made of $\varphi_1^{\mathrm{L}^*}(T, P_{\mathrm{s},1}) = \varphi_1^{\mathrm{V}^*}(T, P_{\mathrm{s},1})$. Here, $\varphi_1^{\mathrm{L}^*}(T, P_{\mathrm{s},1})$ is the fugacity coefficient of pure saturated liquid solvent, $\varphi_1^{\mathrm{V}^*}(T, P_{\mathrm{s},1})$ the fugacity coefficient of pure saturated solvent vapour, $I_1(T, P)$ the Poynting correction for the solvent resulting from the pressure dependence of the pure substance fugacity $f_1^{\mathrm{L}^*}$, and $V_1^{\mathrm{L}^*}(T, P)$ the molar volume of the pure solvent.

For the Henry fugacity one obtains in complete analogy

$$h_{2,1}(T, P) = h_{2,1}(T, P_{\mathrm{s},1}) I_2(T, P) = P_{\mathrm{s},1} \varphi_2^{\mathrm{L}\infty}(T, P_{\mathrm{s},1}) I_2(T, P), \qquad (7.23a)$$

$$I_2(T, P) \equiv \exp\left\{\int_{P_{s,1}}^{P} \frac{V_2^{L\infty}(T, P)}{RT}\, dP\right\}, \tag{7.23b}$$

where use was made of Equation (7.18). Here, $\varphi_2^{L\infty}(T, P_{s,1})$ is the fugacity coefficient of the solute at infinite dilution in the liquid phase at $P_{s,1}$. The $I_2(T, P)$ is the Poynting correction for the solute resulting from the pressure dependence of the Henry fugacity $h_{2,1}$, and $V_2^{L\infty}(T, P)$ is the partial molar volume of dissolved gas at infinite dilution.

For the activity coefficients one obtains [8]

$$\gamma_1^{LR}(T, P, x_2) = \gamma_1^{LR}(T, P_{s,1}, x_2) \exp\left\{\int_{P_{s,1}}^{P} \frac{V_1^L(T, P, x_2) - V_1^{L*}(T, P)}{RT}\, dP\right\}, \tag{7.24a}$$

$$\gamma_2^{HL}(T, P, x_2) = \gamma_2^{HL}(T, P_{s,1}, x_2) \exp\left\{\int_{P_{s,1}}^{P} \frac{V_2^L(T, P, x_2) - V_2^{L\infty}(T, P)}{RT}\, dP\right\}, \tag{7.24b}$$

where $V_i^L(T, P, x_2)$ is the partial molar volume of either the solvent $i = 1$ or the solute $i = 2$ at mole fraction x_2.

According to Equation (7.5), the Henry fugacity for solute 2 dissolved in liquid solvent 1 is defined by

$$h_{2,1} = \lim_{x_2 \to 0}\left(\frac{f_2^L}{x_2}\right). \tag{7.25}$$

For VLE, because of the criterion for phase equilibrium expressed by Equation (7.1), f_2^L may conveniently be identified with the fugacity of the solute in the coexisting vapour phase, *i.e.* $f_2^L = f_2^V = \varphi_2^V\, y_2 P$. At the vapour pressure $P_{s,1}$ of the solvent, the Henry fugacity referring to the *liquid phase* is thus rigorously accessible from *isothermal* VLE measurements at decreasing pressure $P \to P_{s,1}$ according to

$$h_{2,1}(T, P_{s,1}) = \lim_{x_2 \to 0}\left(\frac{f_2^L}{x_2}\right) = \lim_{x_2 \to 0,\, y_2 P \to 0}\left(\frac{\varphi_2^V(T, P, y_2) y_2 P}{x_2}\right). \tag{7.26}$$

It is the intercept of a plot of $\varphi_2^V(T, P, y_2)y_2P/x_2$ against x_2 or y_2P. Entirely equivalent expressions relating the Henry fugacity to limiting slopes [see Equation (7.5)] may be derived [8,35]. The vapour-phase fugacity coefficient must be calculated from a suitable EOS.

At the experimental temperature, the liquid-phase constant-pressure activity coefficient in the unsymmetric convention, $\gamma_2^{HL} = f_2^L/(x_2 h_{2,1})$, is subsequently obtained *via*

$$\ln \gamma_2^{HL}(T, P_{s,1}, x_2) = \ln\left(\frac{\varphi_2^V(T, P, y_2) y_2 P}{x_2 h_{2,1}(T, P_{s,1})}\right) - \int_{P_{s,1}}^{P} \frac{V_2^L(T, P, x_2)}{RT}\, dP. \tag{7.27}$$

The argument of the logarithmic term on the right-hand side of Equation (7.27) is a dimensionless group containing the experimental isothermal data as well as the Henry fugacity already extracted therefrom. In order to evaluate the Poynting integral in Equation (7.27), information is needed on the pressure dependence and the composition dependence of V_2^L.

The selected correlating equation for these activity coefficients $\gamma_2^{HL}(T, P_{s,1}, x_2)$ as a function of composition has to be compatible with the number and the precision of the experimental results. Depending on the approximations introduced, such well-known equations as the Krichevsky–Ilinskaya equation are obtained [8] (see Section 7.1.2).

This classical sequential approach outlined above is most frequently adopted in data reduction of gas solubility measurements. It simply reflects the focusing of interest on the solute in a composition range very close to pure solvent, and makes little use of the information thermodynamics supplies on the solvent. For calculations, however, the equilibrium relations are needed for all components. For instance, from Equations (7.12) and (7.13) the total pressure is obtained as

$$P = x_1 P_{s,1} \gamma_1^{LR}(T, P_{s,1}, x_2) \frac{\varphi_{s,1}^{V*}}{\varphi_1^V} \exp\left(\int_{P_{s,1}}^{P} \frac{V_1^L}{RT} \, dP \right)$$

$$+ x_2 h_{2,1}(T, P_{s,1}) \gamma_2^{HL}(T, P_{s,1}, x_2) \frac{1}{\varphi_2^V} \exp\left(\int_{P_{s,1}}^{P} \frac{V_2^L}{RT} \, dP \right), \qquad (7.28)$$

where $\varphi_i^V = \varphi_i^V(T, P, y_2)$ is the vapour-phase fugacity coefficient of either the solvent $i = 1$ or the solute $i = 2$ at mole fraction y_2, and in more compact notation $\varphi_{s,1}^{V*} = \varphi_1^{V*}(T, P_{s,1})$.

Isothermal VLE data that give the variation of P with liquid-phase composition, may be reduced, for example, by Barker's method [40], whereby the functional form of the composition dependence of the activity coefficients is assumed in advance. It may also be applied to Equation (7.28) [8,35].

The reference states based on the Lewis–Randall rule and on Henry's law are states of *pure i* in the physical state of interest. Referring to Figure 7.1, f_2^{L*} is the fugacity of *real* pure liquid $i = 2$ at given (T, P), while $h_{2,1}$ refers to a state of *hypothetical* pure liquid $i = 2$ at (T, P) with a corresponding full set of thermodynamic properties. The $RT \ln \varphi_i$ is a partial molar property in relation to $RT \ln \varphi$, where φ is the fugacity coefficient of the *solution*, whence

$$RT \ln \varphi = RT \sum x_i \quad \ln \varphi_i, \qquad (7.29)$$

which is a quantity equal to the residual molar Gibbs energy G^R of the solution:

$$G^R(T, P, x_2) = G(T, P, x_2) - G^{pg}(T, P, x_2) = RT \ln \varphi(T, P, x_2). \qquad (7.30)$$

Here, G is the molar Gibbs energy of the solution, and G^{pg} refers to the perfect-gas (pg) state. Thus, from Equation (7.18) for the liquid phase

$$\ln \frac{h_{2,1}(T, P)}{P} = \ln \varphi_2^{L\infty}(T, P) = \mu_2^{R\infty}(T, P)/RT, \qquad (7.31)$$

where

$$\mu_2^{R\infty}(T, P) = \lim_{x_2 \to 0} [\mu_2^L(T, P, x_2) - \mu_2^{pg}(T, P, x_2)], \qquad (7.32a)$$

$$\mu_2^{R\infty}(T, P) = RT \ln \varphi_2^{L\infty} = RT \ln \varphi_2^{L*}(T, P) + RT \ln \gamma_2^{LR\infty}(T, P). \quad (7.32b)$$

See also Equations (7.15) and (7.21). Here, μ_2^L denotes the chemical potential of the solute in the real liquid solution, μ_2^{pg} is its chemical potential in the corresponding pg mixture and $\mu_2^{R\infty}$ is the residual chemical potential at infinite dilution. The residual molar Gibbs energy of pure liquid component i is given by

$$G_i^{R*}(T, P)/RT = \ln \varphi_i^{L*}(T, P) = \ln [f_i^{L*}(T, P)/P]. \quad (7.33)$$

Evidently,

$$(\mu_2^{R\infty} - G_2^{R*})/RT = \ln(\varphi_2^{L\infty}/\varphi_2^{L*}) = \ln \gamma_2^{LR\infty} = \ln(h_{2,1}/f_2^{L*}), \quad (7.34)$$

and

$$(\mu_2^{R\infty} - G_1^{R*})/RT = \ln(\varphi_2^{L\infty}/\varphi_1^{L*}) = \ln(h_{2,1}/f_1^{L*}), \quad (7.35)$$

where all quantities are at the same T and P.

Equation (7.35) is of central importance in solvation thermodynamics [18,19,41,42], *i.e.* $(\mu_2^{R\infty} - G_1^{R*})$ is envisaged to be the driving force in an imaginary process that takes place when a solvent molecule is mutated to a solute molecule. In turn, it is related to $(\partial P/\partial x_2)_{T,V}^{\infty}$. At the solvent's critical point, this derivative becomes the *Krichevski parameter* [43,44], a *finite* quantity that governs near-critical dilute mixture behaviour.

For the temperature and pressure dependence of the Henry fugacity, one thus obtains, respectively,

$$\left[\frac{\partial\{\ln (h_{2,1}(T, P)/P)\}}{\partial T}\right]_P = \left[\frac{\partial \ln \varphi_2^{L\infty}(T, P)}{\partial T}\right]_P = -\frac{H_2^{L\infty} - H_2^{pg*}}{RT^2} = -\frac{\Delta H_2^{\infty}(T, P)}{RT^2}, \quad (7.36a)$$

and

$$\left[\frac{\partial\{\ln (h_{2,1}(T, P)/P)\}}{\partial P}\right]_T = \left[\frac{\partial \ln \varphi_2^{L\infty}(T, P)}{\partial P}\right]_T = \frac{V_2^{L\infty} - V_2^{pg*}}{RT} = \frac{\Delta V_2^{\infty}(T, P)}{RT}. \quad (7.36b)$$

Here, $H_2^{L\infty}$ is the partial molar enthalpy of the solute at infinite dilution in the liquid solvent, and H_2^{pg*} and $V_2^{pg*} = RT/P$ are the molar enthalpy and the molar volume of the pure solute, respectively, in the pg state. Equation (7.36a) provides the basis for obtaining partial molar enthalpy changes on solution (enthalpies of solution) ΔH_2^{∞} *via van't Hoff analysis* of high-precision solubility data of gases in liquids [5,8,9,12,17,34–39] (see Section 7.2). The notations ΔH_2^{∞} and ΔV_2^{∞} are generally preferred over $H_2^{R\infty}$ (the partial residual molar enthalpy at infinite dilution) and $V_2^{R\infty}$ (the partial residual molar volume at infinite dilution). Equation (7.36b) was used in deriving Equations (7.23), (7.24b), (7.27) and (7.28), respectively.

Equations (7.36a) and (7.36b) are completely analogous to the expressions giving the temperature and pressure dependence of the pure substance fugacity. From Equation (7.33) it follows, say, for the liquid solvent that

$$\left[\frac{\partial\{\ln (f_1^{L*}(T,P)/P)\}}{\partial T}\right]_P = \left[\frac{\partial \ln \varphi_1^{L*}(T,P)}{\partial T}\right]_P = -\frac{H_1^{L*} - H_1^{pg*}}{RT^2} = -\frac{H_1^{R*}(T,P)}{RT^2}, \tag{7.37a}$$

and

$$\left[\frac{\partial\{\ln (f_1^{L*}(T,P)/P)\}}{\partial P}\right]_T = \left[\frac{\partial \ln \varphi_1^{L*}(T,P)}{\partial P}\right]_T = \frac{V_1^{L*} - V_1^{pg*}}{RT} = \frac{V_1^{R*}(T,P)}{RT}. \tag{7.37b}$$

Here, H_1^{R*} and V_1^{R*}, respectively, are the residual molar enthalpy and the residual molar volume of pure liquid solvent. Equation (7.37b) was used in deriving Equations (7.22), (7.24a) and (7.28), respectively.

A versatile and widely used measure of the solubility of a gas in a liquid is the *Ostwald coefficient* [5,8,36,45]. It is defined by

$$L_{2,1}(T,P) = (\rho_2^L/\rho_2^V)_{equil}, \tag{7.38}$$

where $\rho_2 = n_2/v = x_2/V = x_2\rho$, with the appropriate superscript L or V, is the amount of substance concentration of solute 2 in either the liquid-phase solution or in the *coexisting* vapour-phase solution at T and equilibrium pressure P. The amounts of solvent 1 and solute 2 are denoted by n_1 and n_2, respectively, $v = (n_1 + n_2)V$, $V = \rho^{-1}$ is the molar volume of the solution and ρ is the (total) molar density of the solution. Thus, in contradistinction to the Henry fugacity, the Ostwald coefficient is a *distribution coefficient* pertaining to the solute dissolved in the coexisting phases L and V, and therefore *always* refers to T and P of the actual VLE. Equation (7.38) in conjunction with the equilibrium condition formulated on the basis of Henry's law yields, after some algebraic manipulation [8,9,36], the rigorous relations

$$L_2(T,P) = \frac{RT}{\gamma_2^{HL}(T,P,x_2)h_{2,1}(T,P)V^L(T,P,x_2)} Z^V(T,P,y_2)\varphi_2^V(T,P,y_2), \tag{7.39a}$$

$$L_2(T,P) = \frac{RTZ^V(T,P,y_2)\,\varphi_2^V(T,P,y_2)}{\gamma_2^{HL}(T,P_{s,1},x_2)h_{2,1}(T,P_{s,1})V^L(T,P,x_2)} \exp\left\{-\int_{P_{s,1}}^{P} \frac{V_2^L(T,P,x_2)}{RT}\,dP\right\}. \tag{7.39b}$$

Hence, in the limit as $\rho_2^L \to 0$, with $\rho_2^V \to 0$, $P \to P_{s,1}$ and $V^L \to V_1^{L*}(T,P_{s,1}) = V_{s,1}^{L*}$, the Ostwald coefficient of solute 2 at infinite dilution in solvent 1 is given by

$$L_{2,1}^{\infty}(T,P_{s,1}) = \lim_{\rho_2^L,\,\rho_2^V \to 0,\,P \to P_{s,1}} L_{2,1}(T,P) = \frac{RT}{h_{2,1}(T,P_{s,1})V_{s,1}^{L*}} Z_{s,1}^{V*}\,\varphi_2^{V\infty}(T,P_{s,1}), \tag{7.40}$$

where

$$Z_{s,1}^{V*} = P_{s,1} V_{s,1}^{V*}/RT \tag{7.41}$$

is the compression factor of pure saturated solvent vapour, and $V_{s,1}^{V*}$ is the molar volume of the pure saturated solvent vapour.

The most important application of VLE relations is in the design of separation processes. A frequently used measure of the tendency of a given component to distribute itself in one or the other equilibrium phase is the *vapour–liquid distribution coefficient* or *K value* of solute 2 in solvent 1, defined by

$$K_{2,1}(T, P) = (y_2/x_2)_{\text{equil}}. \tag{7.42}$$

Alternatively it may be expressed as [12,39]

$$K_{2,1}(T, P) = (\varphi_2^L/\varphi_2^V) = \gamma_2^{LR} f_2^{L*}/(\varphi_2^V P) = \gamma_2^{HL} h_{2,1}/(\varphi_2^V P). \tag{7.43}$$

For the K value in the infinite-dilution limit, the following exact equations hold:

$$K_{2,1}^{\infty} = \lim_{x_2, y_2 \to 0,\, P \to P_{s,1}} K_{2,1}(T, P) = \lim_{x_2, y_2 \to 0,\, P \to P_{s,1}} (y_2/x_2)_{\text{equil}},$$

$$K_{2,1}^{\infty} = \varphi_2^{L\infty}(T, P_{s,1})/\varphi_2^{V\infty}(T, P_{s,1}), \tag{7.44}$$

$$K_{2,1}^{\infty} = \gamma_2^{LR\infty}(T, P_{s,1})\varphi_2^{L*}(T, P_{s,1})/\varphi_2^{V\infty}(T, P_{s,1}), \tag{7.45}$$

$$K_{2,1}^{\infty} = \frac{h_{2,1}(T, P_{s,1})}{\varphi_2^{V\infty}(T, P_{s,1}) P_{s,1}}, \tag{7.46}$$

whence the important relation

$$L_{2,1}^{\infty} = \frac{1}{K_{2,1}^{\infty}} \frac{V_{s,1}^{V*}}{V_{s,1}^{L*}} = \frac{1}{K_{2,1}^{\infty}} \frac{\rho_{s,1}^{L*}}{\rho_{s,1}^{V*}}, \tag{7.47}$$

is obtained. Here, $\rho_{s,1}^{L*}$ and $\rho_{s,1}^{V*}$ are the molar densities of pure saturated liquid and vapour, respectively. Note that

$$\lim_{T \to T_{c,1}} L_{2,1}^{\infty} = \lim_{T \to T_{c,1}} K_{2,1}^{\infty} = \lim_{T \to T_{c,1}} (V_{s,1}^{V*}/V_{s,1}^{L*}) = \lim_{T \to T_{c,1}} (\rho_{s,1}^{L*}/\rho_{s,1}^{V*}) = 1, \tag{7.48}$$

where $T_{c,1}$ is the critical temperature of the solvent.

7.1.2 Practical Implementation

In Section 7.1.1, the thermodynamic formalism as applied to (binary) solutions that contain a supercritical component has been summarized concisely. Section 7.1.2 is devoted to a

review of various approximations to the exact relations obtained so far. These approximations are indispensable when practical application is the goal.

Property estimation methods and correlation methods based on generalized corresponding states approaches require reliable data on critical quantities and acentric factors. Since Henry fugacities and related quantities of interest are usually referred to orthobaric conditions, vapour pressure data are indispensable and must be judiciously selected. A valuable source for these quantities is the book by Poling *et al.* [46] on the properties of gases and liquids, now in its fifth edition. More recent compilations of critical temperatures T_c, critical pressures P_c, and critical molar volumes V_c, with recommended values and uncertainties, are available, for instance for n-alkanes [47], branched alkanes and cycloalkanes [48], aromatics [49] and aliphatic alcohols [50]. For water, the Steam Tables [51] recommend $T_c = 647.126\,\mathrm{K}$, $P_c = 22.055\,\mathrm{MPa}$, and $V_c = 55.95\,\mathrm{cm^3 \cdot mol^{-1}}$.

For n-alkanes, Ambrose and Walton [52] report critically selected parameters for a four-constant Wagner-type vapour pressure equation (see also reference [53]), *viz.*

$$\ln(P_{s,1}/P_{c,1}) = (b_1\tau_1 + b_2\tau_1^{1.5} + b_3\tau_1^{2.5} + b_4\tau_1^5)/T_{r,1} \tag{7.49}$$

where $\tau_1 = 1 - T_{r,1}$, and $T_{r,1} = T/T_{c,1}$ is the reduced temperature. For the vapour pressure of water, we always used the Chebyshev polynomial representation of Ambrose and Lawrenson [54]. Comprehensive, continuously updated collections of thermodynamic and thermophysical data of hydrocarbons as well as non-hydrocarbons are provided by the corresponding *TRC Thermodynamic Tables* [55].

The Vapour Phase

When Equation (7.26) is used to determine the Henry fugacity, evaluation from an experimental isothermal data set requires a vapour-phase EOS for calculating φ_2^V. This quantity is again needed in Equation (7.27), that is, when extraction and subsequent correlation of activity coefficients γ_2^{HL} are intended.

The majority of gas-solubility measurements lie in the low to moderate pressure domain, whence the virial EOS, either explicit in pressure or in volume (or molar density $\rho = V^{-1}$), is most convenient for the description of real-gas behaviour. In the former case, truncation after the third virial coefficient yields for the compression factor Z^V of a mixture of N components

$$Z^V(T, \rho^V, \{y_i\}) \equiv P/(\rho^V RT) = 1 + B(T, \{y_i\})\rho^V + C(T, \{y_i\})(\rho^V)^2, \tag{7.50}$$

where the second and third mixture virial coefficients are given by

$$B(T, \{y_i\}) = \sum_i \sum_j y_i y_j B_{ij}(T), \tag{7.51}$$

and

$$C(T, \{y_i\}) = \sum_i \sum_j \sum_k y_j y_j y_k C_{ijk}(T), \tag{7.52}$$

respectively. In conjunction with the exact relation

$$\ln \varphi_i = \int_0^{\rho} \left\{ \left[\frac{\partial(nZ)}{\partial n_i} \right]_{T,\rho/n,n_j} - 1 \right\} \frac{d\rho}{\rho} - \ln Z, \quad \text{constant } T, \{y_i\}, \tag{7.53}$$

one obtains finally

$$\ln \varphi_i^{V} = 2\rho^{V} \sum_j y_i B_{ij}(T) + \frac{3}{2}(\rho^{V})^2 \sum_j \sum_k y_i y_k C_{ijk}(T) - \ln Z^{V}, \tag{7.54}$$

where the summations are over all components. Virial coefficients with identical subscripts refer to pure substances, whereas mixed subscripts designate composition-independent interaction virial coefficients (cross-coefficients). Note that $B_{ij} = B_{ji}$, $C_{ijk} = C_{ikj} = C_{jik} = \cdots$.

The computational convenience associated with a volume-explicit rather than a pressure-explicit EOS leads to the widely used approximation for *low pressures*

$$Z^{V}(T, P, \{y_i\}) = PV^{V}/RT = 1 + BP/RT, \tag{7.55}$$

where B of the mixture is again given by Equation (7.51). The corresponding expression for the fugacity coefficient is now obtained from the exact relation

$$\ln \varphi_i = \int_0^{P} (Z_i - 1) \frac{dP}{P}, \quad \text{constant } T, \{y_i\}, \tag{7.56}$$

where $Z_i = [\partial(nZ)/\partial n_i]_{T,P,n_j} = PV_i/(RT)$, and V_i is the partial molar volume of i in solution. Insertion of Equations (7.55) into Equation (7.56) yields for a binary vapour mixture

$$\ln \varphi_i^{V} = \frac{P}{RT}(B_{ii} + y_j^2 \Delta_{12}), \quad i, j = 1, 2, i \neq j, \tag{7.57}$$

with

$$\Delta_{12} = 2B_{12} - (B_{11} + B_{22}). \tag{7.58}$$

The fugacity coefficient of the gas at infinite dilution in the vapour phase is thus given by

$$\ln \varphi_i^{V\infty} = \frac{P}{RT}(2B_{12} - B_{11}), \tag{7.59}$$

the fugacity coefficient of pure i by

$$\ln \varphi_i^{V*} = \frac{P}{RT} B_{ii}, \tag{7.60}$$

and the compression factor of the mixture may be written as

$$Z^{V}(T, P, y_2) = 1 + (RT)^{-1} P(y_1 B_{11} + y_2 B_{22} + y_1 y_2 \Delta_{12}). \tag{7.61}$$

Frequently, experimental results on second and, in particular, third virial coefficients [56] are not available, whence one has to rely quite heavily on semi-empirical correlation methods [57–61]. For instance, the versatile Tsonopoulos method [58,59] for second virial coefficients is based on the extended corresponding states theorem. The reduced pure substance second virial coefficient at a reduced temperature $T_{r,i} = T/T_{c,i}$ is given by

$$\frac{B_{ii}(T_{r,i})P_{c,i}}{RT_{c,i}} = B^{(0)}(T_{r,i}) + \omega_i B^{(1)}(T_{r,i}) + B^{(2)}(T_{r,i}), \tag{7.62}$$

$$B^{(0)}(T_{r,i}) = 0.1445 - 0.3300T_{r,i}^{-1} - 0.1385T_{r,i}^{-2} - 0.0121T_{r,i}^{-3} - 0.000607T_{r,i}^{-8}, \tag{7.63}$$

$$B^{(1)}(T_{r,i}) = 0.0637 + 0.331T_{r,i}^{-2} - 0.423T_{r,i}^{-3} - 0.008T_{r,i,}^{-8}, \tag{7.64}$$

$$B^{(2)}(T_{r,i}) = \hat{a}_i T_{r,i}^{-6} - \hat{b}_i T_{r,i,}^{-8}. \tag{7.65}$$

Here, the subscript c indicates a critical quantity (*i.e.* critical temperature $T_{c,i}$ and critical pressure $P_{c,i}$ of pure i), and ω_i is the acentric factor. The polar contribution $B^{(2)}(T_{r,i})$ is zero for non-polar or slightly polar substances; for non-hydrogen-bonded polar compounds, $\hat{b}_i = 0$ and $\hat{a}_i$ depends on the compound class. For hydrogen-bonded substances both parameters $\hat{a}_i$ and $\hat{b}_i$ must be used. For instance, for the normal l-alkanols, $\hat{a}_i = 0.0878$, and $\hat{b}_i$ appears to be a function of the reduced dipole moment $\mu_{r,i}$ defined by [39,62]

$$\mu_{r,i} = \left(\frac{N_A \mu_i^2}{4\pi\varepsilon_0 V_{c,i} k_B T_{c,i}} \right)^{1/2}, \tag{7.66}$$

and hence of the chain-length l of n-$C_lH_{2l+1}OH$, though this dependence still needs quantification by data on the higher l-alkanols [63,64]. Here, μ_i is the numerical value of the permanent molecular dipole moment, ε_0 is the permittivity of vacuum, N_A is Avogadro's constant, and k_B is Boltzmann's constant.

If one wishes to use Equations (7.62)–(7.65) to calculate second virial cross-coefficients B_{ij}, appropriate combination rules have to be devised to obtain the characteristic interaction parameters $T_{c,ij}$, $P_{c,ij}$, ω_{ij}, $\hat{a}_{ij}$ and $\hat{b}_{ij}$ to replace the corresponding pure-substance quantities. The following simple recipes have been found useful:

$$T_{c,ij} = (1 - k_{ij})(T_{c,i}T_{c,j})^{1/2}, \tag{7.67}$$

$$P_{c,ij} = Z_{c,ij}RT_{c,ij}/V_{c,ij}, \tag{7.68}$$

$$Z_{c,ij} = \tfrac{1}{2}(Z_{c,i} + Z_{c,j}), \tag{7.69}$$

$$V_{c,ij} = \tfrac{1}{8}(V_{c,i}^{1/3} + V_{c,j}^{1/3})^3, \tag{7.70}$$

$$\omega_{ij} = \tfrac{1}{2}(\omega_i + \omega_j), \tag{7.71}$$

where k_{ij} is yet another binary interaction parameter usually much smaller than 1, and $V_{c,ij}$ is the critical volume of i. The reduced temperature is now defined by $T_{r,ij} = T/T_{c,ij}$.

Equations (7.67)–(7.71) suffice for mixtures of non-polar substances. For non-polar/polar binaries, B_{ij} is assumed to have no polar contribution, while for polar/polar binaries

$$\hat{a}_{ij} = \tfrac{1}{2}(\hat{a}_i + \hat{a}_j), \quad \hat{b}_{ij} = \tfrac{1}{2}(\hat{b}_i + \hat{b}_j), \tag{7.72}$$

Equation (7.67) is definitely the most crucial combination rule of all. For binaries where both components belong to hydrocarbons, or rare gases or simple molecular gases, k_{ij} may be estimated from [65]

$$k_{ij} = 1 - \frac{8(V_{c,i}V_{c,j})^{1/2}}{(V_{c,i}^{1/3} + V_{c,j}^{1/3})^3}. \tag{7.73}$$

Other (semi-)empirical estimation methods may be found in references [34,58,59,63,66,67]. Selected aspects of more fundamental combination rules for unlike energy parameters of two-parameter pair potentials have been discussed in references [68,69].

The Liquid Phase

In the key relation (7.27), the influence of composition upon the liquid-phase fugacity has been separated formally from the influence of pressure. However, rigorous evaluation of the Poynting integral would require detailed knowledge of the pressure dependence as well as the composition dependence of the partial molar volume V_2^L at each temperature of interest. Such comprehensive information will rarely be available, whence for the great majority of solutions approximations at various levels of sophistication must be introduced to make the problem tractable [8]. The situation becomes particularly unsatisfactory at high pressures and/or when the critical region is approached.

With few exceptions, typical gas-solubility measurements do not cover large composition ranges, while at the same time experimental scatter often tends to obscure the composition dependence of the derived constant-pressure activity coefficient γ_2^{HL}. Thus, for purely practical reasons the correlating equations for γ_2^{HL} usually contain only few adjustable parameters, that is to say rarely more than one. The selection of such correlations follows rather closely the well-established recipes for the symmetrically normalized activity coefficients. Take, for instance, the simplest non-trivial expression for the excess molar Gibbs energy, *i.e.* $G^E/(RT) = Ax_1x_2$. From this expression, one obtains the two-suffix Margules equations

$$\ln \gamma_1^{LR} = Ax_2^2, \tag{7.74}$$

$$\ln \gamma_2^{HL} = A(x_1^2 - 1). \tag{7.75}$$

Insertion of Equation (7.75) into Equation (7.27) and approximation of V_2^L by a pressure-independent $V_2^{L\infty}(T, P_{s,1})$ leads to the Krichevsky–Ilinskaya equation

$$\ln\left(\frac{\varphi_2^V(T, P, y_2)y_2P}{x_2h_{2,1}(T, P_{s,1})}\right) - \frac{(P - P_{s,1})V_2^{L\infty}(T, P_{s,1})}{RT} = A(x_1^2 - 1). \tag{7.76}$$

When applied to isothermal, pressure-corrected activity coefficients as discussed above, clearly $A = A(T, P_{s,1})$. If one now assumes $\gamma_2^{HL} = 1$, independent of composition, the Krichevsky–Kasarnovsky equation is obtained:

$$\ln\left(\frac{\varphi_2^V(T, P, y_2)y_2P}{x_2}\right) = \ln h_{2,1}(T, P_{s,1}) + \frac{(P - P_{s,1})V_2^{L\infty}(T, P_{s,1})}{RT}. \tag{7.77}$$

It has frequently been used for the determination of $V_2^{L\infty}$ from gas-solubility measurements at elevated pressures, and accounts, in fact, for a large portion of the existing $V_2^{L\infty}$ data. However, the mole fraction solubility may then be already appreciable and hence the underlying assumptions too severe. Thus, values of $V_2^{L\infty}$ obtained by using the Krichevsky–Kasarnovsky equation should always be regarded with caution and may be unreliable [70,71].

Evidently, the partial molar volume of the solute in the liquid solution is of importance in the reduction and correlation of accurate gas-solubility measurements. Poynting-type corrections are ubiquitous in this area [8,9,12,36,37]. Fortunately, for reasonably small pressure ranges of P to $P_{s,1}$ and at temperatures well below the critical temperature of the solvent, the uncertainties associated with commonly used approximations are frequently quite small. The preferred experimental method for determining $V_2^{L\infty}$ (and V_2^L) is either precision dilatometry or precision densimetry [25,72–79] at very small mole fractions.

The scarcity of experimental results on $V_2^{L\infty}$ (or V_2^L in general) of gases dissolved in liquids is of particular note, whence the revived interest in precision methods for measuring $V_2^{L\infty}$ on the one hand, and in semi-empirical estimation methods on the other [72,73,80–82], becomes understandable. For instance, partial molar volumes of gases at infinite dilution in non-aqueous solvents will usually be predicted to within about ±10% by the empirical Handa–Benson correlation [72,81],

$$V_2^{L\infty}P_{c,2}/(RT_{c,2}) = 0.088 + 2.763TP_{c,2}/(T_{c,2}\Pi_{s,1}^{L*}), \tag{7.78}$$

provided the temperature is well below $T_{c,1}$. Here, $\Pi_{s,1}^{L*} = (T\alpha_{P,s,1}^{L*}/\beta_{T,s,1}^{L*}) - P_{s,1}$ is the internal pressure, $\alpha_{P,s,1}^{L*}$ is the isobaric expansivity, and $\beta_{T,s,1}^{L*}$ is the isothermal compressibility, respectively, of the pure liquid solvent at saturation.

Scaled particle theory (SPT) has been used by Pierotti [83–85] and Wilhelm *et al.* [5], among others, to calculate $V_2^{L\infty}$of non-polar and polar gases in both non-polar and polar solvents according to

$$V_2^{L\infty} = V_{cav} + \beta_{T,s,1}^{L*}(G_{int} + RT). \tag{7.79}$$

Here, $V_{cav} = (\partial G_{cav}/\partial P)_T$, G_{cav} is the partial molar Gibbs energy of cavity formation, and G_{int} is the partial molar Gibbs energy of interaction between a solute molecule and the solvent. The SPT expressions for G_{cav} and V_{cav} are well known and may easily be found in the literature [5,8,37,83–89], together with the relevant approximations for G_{int}. For many solvents, a self-consistent set of molecular parameters, *i.e.* of *effective* Lennard–Jones (6,12) parameters, has been given by Wilhelm and Battino [88]. The correlational and predictive powers of this method can be substantially improved by introducing the concept of *temperature-dependent effective size* parameters as suggested by Wilhelm [90], and more recently by Montfort and Perez [91], Schaffer and Prausnitz [92] and Schulze and Prausnitz [93].

Brelvi and O'Connell [80] correlated the partial molar volume at infinite dilution with the dimensionless spatial integral $\hat{C}_{21}^{L\infty}$ of the infinite-dilution solute–solvent direct correlation function:

$$V_2^{L\infty}/(RT\beta_{T,s,1}^{L*}) = 1 - \hat{C}_{21}^{L\infty}, \tag{7.80}$$

$$\ln\left[-\hat{C}_{21}^{L\infty}(\hat{v}_1/\hat{v}_2)^{0.62}\right] = -2.4467 + 2.12074\tilde{\rho}_1 \quad \text{for } 2.0 \leq \tilde{\rho}_1 \leq 2.785, \tag{7.81a}$$

$$\ln\left[-\hat{C}_{21}^{L\infty}(\hat{v}_1/\hat{v}_2)^{0.62}\right] = 3.02214 - 1.87085\tilde{\rho}_1 + 0.71955\tilde{\rho}_1^2 \quad \text{for } 2.785 \leq \tilde{\rho}_1 \leq 3.2. \tag{7.81b}$$

Here, $\tilde{\rho}_1 = \hat{v}_1\rho_{s,1}^{L*} = \hat{v}_1/V_{s,1}^{L*}$ is the reduced molar density of the solvent (at saturation), and the $\hat{v}_i$ ($i = 1,2$) are characteristic molar reducing volumes. As already pointed out in reference [80], Equations (7.80) and (7.81) should not be used to estimate the partial molar volumes of liquids dissolved in liquids, that is to say it should not be used at temperatures substantially below $T_{c,2}$. For recent work along these lines see O'Connell *et al.* [82].

Finally we note that with [41,42,94]

$$\left(\frac{\partial P}{\partial x_2}\right)_{T,V}^{\infty} = \frac{V_2^{L\infty}}{V_{s,1}^{L*}\beta_{T,s,1}^{L*}} - \frac{1}{\beta_{T,s,1}^{L*}}, \tag{7.82}$$

it follows that

$$\left(\frac{\partial P}{\partial x_2}\right)_{T,V}^{\infty} = \frac{RT}{V_1^{L*}}(\hat{C}_{11}^{L*} - \hat{C}_{21}^{L\infty}), \tag{7.83}$$

where $\hat{C}_{11}^{L*}$ is the dimensionless spatial integral of the solvent–solvent direct correlation function. At the critical point, because here $\hat{C}_{11}^{L*} = 1$, the *Krichevski parameter* is given by [42,95]

$$\left(\frac{\partial P}{\partial x_2}\right)_{T_{c,1},V_{c,1}}^{\infty} = \frac{RT_{c,1}}{V_{c,1}}(1 - \hat{C}_{21}^{L\infty})_{T_{c,1},V_{c,1}}. \tag{7.84}$$

7.2 Instruments, Experimental Techniques, Data Correlation and Selected Results

Recent advances in the design of measuring equipment primarily dedicated to dilute solutions have been quite impressive. They may be classified as follows:

(a) novel designs of apparatus that significantly improve experimental precision and accuracy;
(b) designs that increase the accessible pressure and temperature ranges of already existing instruments;
(c) designs for application to unusual problems;
(d) efforts towards simplifying and accelerating data acquisition.

It is far beyond the scope of this chapter to even attempt to catalogue, let alone to discuss available experimental methods exhaustively. Only a few representative instruments and some closely related problems encountered in data reduction and presentation will be considered. Those potentially interested in building precision equipment are referred to surveys, for instance, by Wilhelm [8,38], Battino and Clever [1,3], and Hallen and Wadsö [96] and to the original literature cited.

Adequate *degassing* of the solvent and reliable *equilibration* procedures to establish true VLE are of paramount importance in all gas-solubility determinations. Failure to reach these goals constitutes the most important source of error in these kinds of measurements.

Various designs of degassing apparatus have been presented in the literature [1,3,5,8]. Perhaps the easiest to fabricate and operate is the one developed by Battino *et al.* [97], which we incorporated in practically all the gas-solubility equipments we constructed and used over the years, be it of the Morrison/Billett type [98], the Scholander type [99], the Ben-Naim/Baer type [66] or the Benson/Krause/Rettich/Battino/Wilhelm (BKRBW) type [100]. Essentially it is a 3 L suction flask equipped with all-Teflon stopcocks, one O-ring joint for introducing the solvent, a magnetic stirring bar (8 cm) and a condenser to minimize solvent loss. The liquid is degassed by vigorous stirring and periodical pumping on the flask through a cold trap. For instance, with this technique the residual air content of water after degassing is easily pushed well below 0.001% of the saturation value at room temperature and atmospheric pressure within 1 h. This degassing apparatus can be readily scaled up or down.

The problem of establishing phase equilibrium between a liquid solvent and a gaseous solute contained in a closed vessel is conceptually simple, yet difficult and demanding in practice. Frequently it takes a long time to reach equilibrium, say 24 h or more. The equilibrator designed by Benson and Krause [101,102], shown in Figure 7.2, appears to be the best design for this purpose. All the high-precision results obtained so far on aqueous systems have shown it to be extremely reliable.

Synthetic as well as *analytic* methods have been reported for VLE measurements. With adequate design and proper handling, both techniques are capable of yielding precise data. The synthetic method is illustrated by the *automated* instruments developed by Tucker and Christian [103], Tucker *et al.* [104] and our group [63,66,67,105] based on the design of Ben-Naim and Baer [106–108]. Typically, the imprecision of experimental solubilities (Ostwald coefficients) obtained with this type of instrument is about 0.5%. In references [63,67] we reported $L_{2,1}(T, P)$ for 102 n-alkanol gas systems and for 99 n-alkane gas systems.

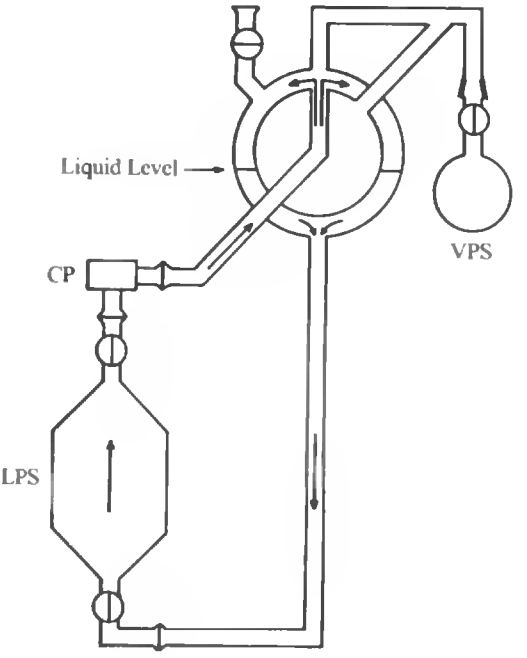

Figure 7.2 Benson/Kraus-type glass apparatus for the equilibration of a gas with a liquid [100,101]: LPS, liquid-phase sample bulb; VPS, vapour-phase sample bulb; CP, centrifugal pump. Arrows indicate the direction of liquid flow. The spherical equilibrator consists of two concentric spheres with inner and outer volumes of about 1 and 2 L, respectively. The re-entrant connection to the inside of the inner sphere conveniently provides a relatively large volume for the vapour phase, so that the dissolution process reduces the pressure to a lesser extent.

In fact, these are the *largest* sets of solubility data on such types of systems ever obtained by one group with one instrument at one time. Figures 7.3 and 7.4 show a few representative results illustrating the dependence of the Ostwald coefficient on chain length l for several series {n-alkane(n-C_lH_{2l+2}) + a gas} and {n-alkan-1-ol(n-$C_lH_{2l+1}OH$) + a gas} at $T = 298.15$ K and $P = 101325$ Pa. Some results on solubilities of Xe were taken from other reliable sources, *i.e.* from the work of Clever [109] and of Pollack and co-workers [110–112]. With the same instrument, Scharlin and Battino [113,114] recently determined the Ostwald coefficients of various freons in H_2O and D_2O as well as in seawater [115]. An analytic method for VLE measurements on dilute solutions of gases in liquids has been developed by Rettich *et al.* [100,116–119]. It is based on the earlier work of Benson *et al.* [101], and of Benson and Krause [102,120]. Vapour- and liquid-phase equilibrium compositions are determined via classical *PVT* measurements, and Henry fugacities are obtained through application of the rigorous prescription embodied in Equation (7.26). The essential parts of the BKRBW high-precision gas-solubility apparatus are shown in the flow diagram in Figure 7.5. The precision and accuracy, which may be achieved with this type of equipment, surpasses that of any previous design, including the one of Cook and Hanson [121]. For the aqueous systems investigated so far, the average combined random error (imprecision) is

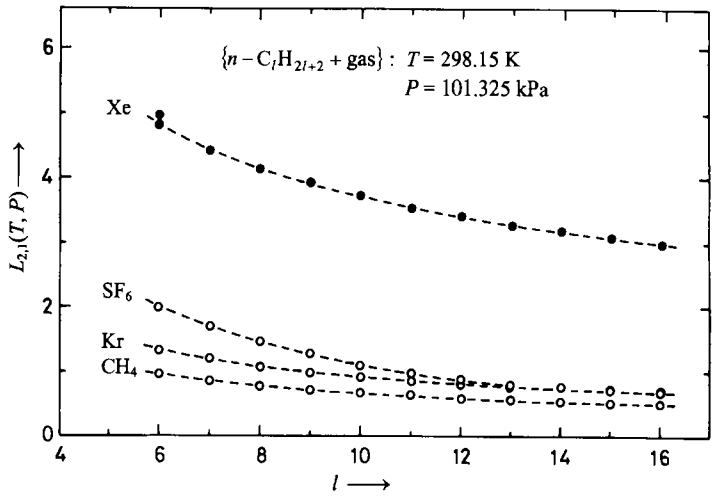

Figure 7.3 Ostwald coefficients $L_{2,1}(T, P)$ for Kr, Xe, CH_4 and SF_6, respectively, dissolved in n-alkanes C_lH_{2l+2} as a function of chain length l for $T = 298.15$ K and $P = 101.325$ kPa, and $6 \leq l \leq 16$. ○, experimental results of Hesse *et al.* [67]; ●, experimental results for the Xe solubilities were taken from Clever [109], Pollack [110] and Pollack and Himm [111]. The dashed curves have been added to aid the eye.

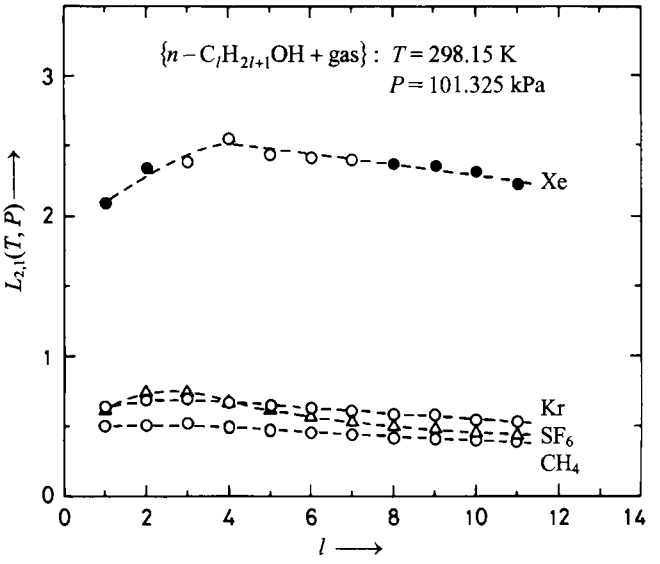

Figure 7.4 Ostwald coefficients $L_{2,1}(T, P)$ for Kr, Xe, CH_4 and SF_6, respectively, dissolved in normal l-alkanols n-$C_lH_{2l+1}OH$ as a function of chain length l for $T = 298.15$ K and $P = 101.325$ kPa, and $1 \leq l \leq 11$. ○, △ experimental results of Bo *et al.* [63]; ● experimental results for some Xe solubilities were taken from Pollack *et al.* [112]. The dashed curves have been added to aid the eye.

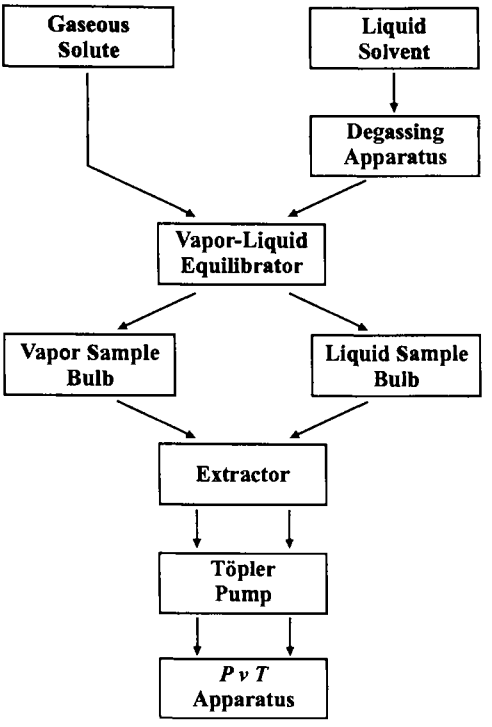

Figure 7.5 Block diagram of the experimental arrangement used in the Benson–Krause–Rettich–Battino–Wilhelm (BKRBW) high-precision gas-solubility apparatus [8,100,101].

estimated to be less than ±0.05%, and the maximum systematic error (inaccuracy) should not exceed ±0.05%. These error estimates have been corroborated by the goodness-of-fit of appropriate correlating equations (see below), and by the highly satisfactory inter-laboratory agreement between our values for the solubility of oxygen in water [100,119] and those of Benson *et al.* [101].

After the retirement of Prof. Rubin Battino in 1997 (now Emeritus Professor at Wright State University, WSU) and I becoming more involved in heading the Institute of Physical Chemistry at the University of Wien, Austria, first as Associate Chairman and then as Chairman, the instruments for measuring gas solubilities located at WSU, Dayton, OH, USA, that is the Ben-Naim/Baer type apparatus and the high-precision BKRBW apparatus, were disassembled, put into crates, and shipped to Prof. Jean-Pierre E. Grolier, then Head of Laboratoire de Thermodynamique des Solutions et des Polymères, Université Blaise Pascal, Clermont-Ferrand, France. With Professor Battino's and my active support, the instruments were reassembled there, and are now again fully operational, as evidenced by two papers on the solubility of CD_4 in water [122], and of C_2F_6 in water [123], respectively.

In order to illustrate international experimental activities in this field during the last several years (*no* exhaustive coverage was attempted!), I have selected a number of papers both from the point of view of showing the diversity of designs as well as of indicating current interest in various types of solutions.

A Ben-Naim/Baer type apparatus has been used by Urieta *et al.* for measuring gas solubilities in isomers of butanol [124–126], and in fluoroalkanols [127]. The Ostwald coefficients of methyl fluoride dissolved in some alcohols have been determined by Silva *et al.* also *via* a synthetic method [128], and recently, this group reported solubilities of some refrigerants in water [129]. This important topic was also taken up by Zheng *et al.* [130]. An experimental method similar to that of Olsen [131], Cukor and Prausnitz [132] and Graaf *et al.* [133] was used in a study by Breman *et al.* [134] on the solubility of H_2, CO, CO_2, C_2H_6 and C_3H_8 in hexadecane, octacosane, 1-hexadecanol, phenanthrene and tetraethylene glycol. Temperatures ranged from about 301 K to 539 K, with pressures as high as 6.5 MPa.

An analytic method is used in the work of Mroczek [135], who determined Henry fugacities of SF_6 dissolved in water from $T = 347$ K to 505 K. It is definitely the most comprehensive investigation of this system; its importance results from the fact that SF_6 is widely used as a ground water and geothermal tracer [136]. Additional VLE data (at $T = 293$ K) and excess enthalpies (at $T = 323$ K) for SF_6 dissolved in H_2O were recently presented by Strotmann *et al.* [137].

N-methylpyrrolidinone is a physical solvent used in the removal of CO_2 from gas streams, and is thus of considerable interest to the gas processing industry. The solubility of ethane in *N*-methylpyrrolidinone was investigated by Henni *et al.* [138] between temperatures of 263.15 K and 393.15 K and at pressures up to 7.1 MPa (see also Melzer *et al.* [139]).

In many (elementary) chemistry textbooks it is stated that "the solubility of gases in liquids decreases with increasing temperature". In fact, such a sweeping claim is *incorrect* when the entire liquid range between the triple point $T_{tr,1}$ and the critical point of the solvent is considered. For many systems, the following behaviour is well documented: at low temperatures (near $T_{tr,1}$), the solubility, say, expressed as mole fraction solubility x_2 of gas dissolved in the solvent for a convenient low partial gas pressure $P_2 = y_2 P$ (traditionally, $P_2 = 1$ atm = 101.325 kPa), first decreases with increasing temperature, then passes through a minimum to increase steeply when the solvent critical temperature is approached. Since the conventional mole fraction solubility is approximately proportional to $1/h_{2,1}$, see Equation (7.13), such a behaviour is, of course, also reflected by the temperature dependence of the Henry fugacity: in such cases $h_{2,1}(T, P_{s,1})$ first *increases* with increasing temperature, then goes through a *maximum* to *decrease* steeply at *high* temperatures when $T_{c,1}$ is approached. As an example, the plot of $\ln h_{2,1}$ against temperature for methane dissolved in water [100,140] is shown in Figure 7.6.

Once experimental Henry fugacities for a given solvent–solute system have been collected over a certain temperature range, the question arises as to their most satisfactory mathematical representation as a function of temperature. In the absence of theoretically well-founded models of general validity, one has to rely on essentially empirical fitting equations, subject, however, to some important thermodynamic constraints. Depending on the choice of variables, that is T or T^{-1}, for expanding the enthalpy of solution, either the Clarke–Glew equation [141,142]

$$\ln[h_{2,1}(T, P_{s,1})/\text{Pa}] = A_0 + A_1(T/\text{K})^{-1} + A_2 \ln(T/\text{K}) + \sum_{i=3}^{n} A_i (T/\text{K})^{i-2}, \qquad (7.85)$$

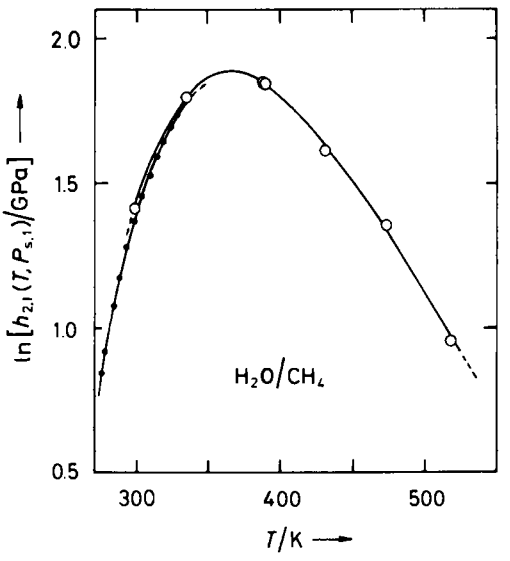

Figure 7.6 Plot of $\ln[h_{2,1}(T, P_{s,1})/\text{GPa}]$ against temperature T for methane dissolved in liquid water. •, Rettich *et al.*, BKRBW apparatus [100]: the average percentage deviation of the Henry fugacity $h_{2,1}$ from the value calculated via the correlating BK function is about ±0.05%; ○, Crovetto *et al.* [140]: the average percentage deviation of the Henry fugacity $h_{2,1}$ from the value calculated via the correlating BK function is about ±2%.

or the Benson–Krause (BK) equation [101,120]

$$\ln[h_{2,1}(T, P_{s,1})/\text{Pa}] = \sum_{i=0}^{m} a_i \, (T/\text{K})^{-i} \tag{7.86}$$

is obtained. Note that the three-term version of Equation (7.85) is the well-known Valentiner equation [143]. On the basis of the ability to fit accurate $h_{2,1}$ data over reasonably large temperature ranges, and of simplicity, the BK power series in T^{-1} appears to be superior. Whatever representation is selected, any correlation for $h_{2,1}(T, P_{s,1})$ over a large temperature range extending up to the critical region must incorporate the thermodynamically correct limiting behaviour for $T \to T_{c,1}$ and $P_{s,1} \to P_{c,1}$ [12,37–39,144] of the Henry fugacity:

$$\lim_{T \to T_{c,1}} h_{2,1}(T, P_{s,1}) = P_{c,1} \varphi_2^{V\infty}(T_{c,1}, P_{c,1}). \tag{7.87}$$

This exact limiting value follows directly from the generally valid Equation (7.18) and the equilibrium condition prevailing at the critical point, that is

$$\varphi_2^{V\infty}(T_{c,1}, P_{c,1}) = \varphi_2^{L\infty}(T_{c,1}, P_{c,1}). \tag{7.88}$$

A somewhat different proof was presented in [8,9,36] exploiting the exact relation between the Henry fugacity and the Ostwald coefficient at infinite dilution, Equation (7.40).

For *volatile* solutes

$$\lim_{T \to T_{c,1}} \mathrm{d} \ln[h_{2,1}(T, P_{s,1})/\mathrm{Pa}]/\mathrm{d}T = -\infty \tag{7.89}$$

as the critical point of the solvent is approached along the coexistence curve [145,146]. Non-classically, the temperature derivative of $\ln h_{2,1}$ diverges as $|T - T_{c,1}|^{\beta-1}$ where the critical exponent $\beta = 0.326$.

In recent years, a number of correlations for $h_{2,1}(T, P_{s,1})$ over large temperature ranges up to the critical temperature of the solvent were developed to incorporate the thermodynamically correct limiting behaviour indicated by Equations (7.87) and (7.89). Inevitably, the focus was on aqueous solutions. Here I note only the contribution of Krause and Benson [147]

$$T_r^2 \ln[h_{2,1}(T, P_{s,1})/\mathrm{Pa}] = b_0 T_r^2 + b_1(1 - T_r)^{1/3} + b_2(1 - T_r)^{2/3}, \tag{7.90}$$

where $T_r = T/T_{c,1}$; of Harvey and Levelt Sengers [148]:

$$T \ln[h_{2,1}(T, P_{s,1})/f^*_{s,1}] = A + B(\rho^{L*}_{s,1} - \rho^*_{c,1}) + CT\rho^{L*}_{s,1} \exp[(273.15 - T/\mathrm{K})\tau^{-1}], \tag{7.91}$$

where τ is a constant varying little with the systems ($\tau \approx 50$); and of Harvey [149], whose equation is a synthesis of the former two:

$$\ln [h_{2,1}(T, P_{s,1})/\mathrm{Pa}] = \ln(P_{s,1}/\mathrm{Pa}) + A/T_r + B(1 - T_r)^{0.355}/T_r + CT_r^{-0.41} \exp(1 - T_r). \tag{7.92}$$

However, if one is concerned with dilute solutions near the critical point of the solvent, Ostwald coefficients (or K values) are potentially more useful. As shown by Wilhelm [8,9,12,36], the Henry fugacity is rigorously related to $L^{\infty}_{2,1}$ by Equation (7.40), which in turn is related to $K^{\infty}_{2,1}$ by Equation (7.47).

A few years ago, Harvey *et al.* [150] suggested that in the neighbourhood of the solvent's critical point the linear relation

$$T \ln K^{\infty}_{2,1} = 2B\Delta\rho^*_1, \tag{7.93a}$$

$$\Delta\rho^*_1 = \rho^{L*}_{s,1} - \rho^*_{c,1}, \tag{7.93b}$$

provides a good estimate of the *true* asymptotic slope ($\rho^*_{c,1} = 1/V_{c,1}$ is the solvent's critical molar density). More evidence comes from data on the initial slope of the critical line (c.l.) [150,151],

$$\left(\frac{\partial P}{\partial x_2}\right)^{\infty}_{T,V,c} = \left.\frac{\mathrm{d}P}{\mathrm{d}x_2}\right|^{\infty}_{c.l.;c} - \left.\frac{\mathrm{d}P_{s,1}}{\mathrm{d}T}\right|_c \left.\frac{\mathrm{d}T}{\mathrm{d}x_2}\right|^{\infty}_{c.l.;c}, \tag{7.94}$$

$$\left(\frac{\partial P}{\partial x_2}\right)^{\infty}_{T,V,c} = R(\rho^*_{c,1})^2 B, \tag{7.95}$$

where the subscript c indicates a derivative taken at the solvent's critical point. However, small differences between $(\partial P/\partial x_2)^{\infty}_{T,V,c}$ calculated from $K^{\infty}_{2,1}$ factors in conjunction with Equation (7.95), and from critical line data *via* Equation (7.94) remain. As an alternative, some time ago, I suggested [12] an *asymptotically linear* relation in the neighbourhood of the critical point of the solvent involving the Ostwald coefficient $L^{\infty}_{2,1}$:

$$T \ln L^{\infty}_{2,1} = b\Delta\rho^{*}_{1}. \tag{7.96}$$

Since

$$T \ln L^{\infty}_{2,1} = -T \ln K^{\infty}_{2,1} + T \ln (\rho^{L^{*}}_{s,1}/\rho^{V^{*}}_{s,1}), \tag{7.97}$$

we note that the density dependences of the two terms on the right-hand side of Equation (7.97) compensate each other in part, whence Equation (7.96) will hold, in general, over a significantly larger range of orthobaric densities than Equation (7.93). This contention has been corroborated by Chialvo *et al.* [152].

Until recently, precision measurements of Henry fugacities over sufficiently large temperature ranges permitting *van't Hoff analysis* of the solubility data, constituted the only reliable source of information on partial molar enthalpy changes on solution ΔH^{∞}_{2}, see Equation (7.36a), and *a fortiori* on partial molar heat capacity changes on solution $\Delta C^{\infty}_{p,2} = \Delta C^{R\infty}_{p,2}$ (partial residual molar heat capacity at constant pressure at infinite dilution) of sparingly soluble gases in liquids. Specifically [8,9,12,17,36–39],

$$\frac{\Delta H^{\infty}_{2}(T, P_{s,1})}{RT} \equiv \frac{H^{L^{\infty}}_{2} - H^{pg^{*}}_{2}}{RT} = -T \frac{\mathrm{d} \ln [h_{2,1}(T, P_{s,1})/\mathrm{Pa}]}{\mathrm{d}T} + \frac{V^{L^{\infty}}_{2}}{R} \frac{\mathrm{d}P_{s,1}}{\mathrm{d}T}, \tag{7.98}$$

and by analogous arguments for $\Delta C^{\infty}_{p,2} = (\partial \Delta H^{\infty}_{2}/\partial T)_{P}$ the following expression is obtained:

$$\begin{aligned} \frac{\Delta C^{\infty}_{p,2}(T, P_{s,1})}{R} &\equiv \frac{C^{L^{\infty}}_{p,2} - C^{pg^{*}}_{p,2}}{R} \\ &= \frac{\mathrm{d}\Delta H^{\infty}_{2}(T, P_{s,1})}{R\mathrm{d}T} - \frac{1}{R}\left[V^{L^{\infty}}_{2} - T\left(\frac{\partial V^{L^{\infty}}_{2}}{\partial T}\right)_{P}\right]\frac{\mathrm{d}P_{s,1}}{\mathrm{d}T} \end{aligned} \tag{7.99}$$

$$\begin{aligned} &= -2T \frac{\mathrm{d} \ln[h_{2,1}(T, P_{s,1})/\mathrm{Pa}]}{\mathrm{d}T} - T^{2} \frac{\mathrm{d}^{2} \ln[h_{2,1}(T, P_{s,1})/\mathrm{Pa}]}{\mathrm{d}T^{2}} \\ &\quad + 2\frac{T}{R}\frac{\mathrm{d}V^{L^{\infty}}_{2}}{\mathrm{d}T}\frac{\mathrm{d}P_{s,1}}{\mathrm{d}T} - \frac{T}{R}\left(\frac{\partial V^{L^{\infty}}_{2}}{\partial P}\right)_{T}\left(\frac{\mathrm{d}P_{s,1}}{\mathrm{d}T}\right)^{2} + \frac{TV^{L^{\infty}}_{2}}{R}\frac{\mathrm{d}^{2}P_{s,1}}{\mathrm{d}T^{2}}. \end{aligned} \tag{7.100}$$

Here, $C^{L^{\infty}}_{p,2}$ is the partial molar heat capacity at constant pressure of the solute at infinite dilution in the liquid solvent at the vapour pressure $P_{s,1}(T)$ of the solvent, and $C^{pg^{*}}_{p,2}$ is the

molar heat capacity at constant pressure of the pure solute in the pg state. The ordinary differential quotients in Equations (7.98)–(7.100) indicate differentiation while maintaining orthobaric conditions: the first term on the right-hand side of Equation (7.98) as well as the first and the second term on the right hand side of Equation (7.100) may all be obtained from any one of the selected fitting equations, say the BK equation (7.86). This leads to

$$\frac{\Delta H_2^{\infty}(T, P_{s,1})}{RT} = \sum_{i=1}^{m} i a_i (T/\mathrm{K})^{-1} + \frac{V_2^{L\infty}}{R}\frac{dP_{s,1}}{dT} \tag{7.101}$$

and

$$\frac{\Delta C_{p,2}^{\infty}(T, P_{s,1})}{R} = -\sum_{i=2}^{m} i(i-1)\, a_i (T/\mathrm{K})^{-1} + 2\frac{T}{R}\frac{dV_2^{L\infty}}{dT}\frac{dP_{s,1}}{dT} - \frac{T}{R}\left(\frac{\partial V_2^{L\infty}}{\partial P}\right)_T\left(\frac{dP_{s,1}}{dT}\right)^2 + \frac{TV_2^{L\infty}}{R}\frac{d^2P_{s,1}}{dT^2}. \tag{7.102}$$

Until recently, the remaining terms on the right-hand side of Equations (7.98) and (7.100) [or Equations (7.101) and (7.102), respectively] containing $V_2^{L\infty}$ and its derivatives with respect to T and P together with $dP_{s,1}/dT$ and $d^2P_{s,1}/dT^2$ – now referred to in the literature [146,147] as *Wilhelm terms* – have been overlooked.

As I have pointed out repeatedly, at temperatures well below the critical temperature of the solvent, the magnitude of these terms will often be smaller than the experimental error of the measurements, and may thus be neglected. However, their contributions increase rapidly with increasing temperature because of the increase of $dP_{s,1}/dT$ and $d^2P_{s,1}/dT^2$, and, of course, of $V_2^{L\infty}$, $dV_2^{L\infty}/dT$ and $|(\partial V_2^{L\infty}/\partial P)_T|$. In fact, the partial molar volume of a gas at infinite dilution in a liquid solvent *diverges* to $+\infty$ at the critical point of the solvent. The effects of this divergence are felt relatively far from the critical point [43]. Using a lattice gas model, in 1972 Wheeler [153] showed that for such a system $V_2^{L\infty}$ will tend to $+\infty$, proportional to the isothermal compressibility of the pure solvent $\beta_{T,s,1}^{L*}$. The partial molar enthalpy at infinite dilution will diverge at the solvent critical point to $+\infty$ in exactly the same manner. Since $C_{p,2}^{L\infty} = (\partial H_2^{L\infty}/\partial T)_P$, the partial molar heat capacity at infinite dilution will diverge as $(\partial \beta_{T,s,1}^{L*}/\partial T)_P$, *i.e.* $C_{p,2}^{L\infty}$ will tend to $+\infty$ as $T_{c,1}$ is *approached from lower temperatures*, and to $-\infty$, as $T_{c,1}$ is *approached from higher temperatures* (at $P = P_{c,1}$). The important experiments of Wood *et al.* confirm these expectations [75,78,154,155].

Little experimental information is available on $(\partial V_2^{L\infty}/\partial P)_T$ appearing in Equations (7.100) and (7.102). This quantity diverges to $-\infty$ as $T \to T_{c,1}$ and $P \to P_{c,1}$, but at temperatures well removed from the critical temperature of the solvent, it is very small. For instance, from the work of Biggerstaff and Wood [75] on argon dissolved in water, we estimated $(\partial V_2^{L\infty}/\partial P)_T = -3 \times 10^{-14}\,\mathrm{m^3 \cdot Pa^{-1} \cdot mol^{-1}}$ at $T = 367\,\mathrm{K}$, and $-6 \times 10^{-14}\,\mathrm{m^3 \cdot Pa^{-1} \cdot mol^{-1}}$ at $T = 428\,\mathrm{K}$ [118].

In Figure 7.7, our results [100] on the partial molar enthalpy change on solution of methane in water obtained *via* Equation (7.101), are compared with values determined calorimetrically [156–159]: excellent agreement is observed over the entire temperature range of

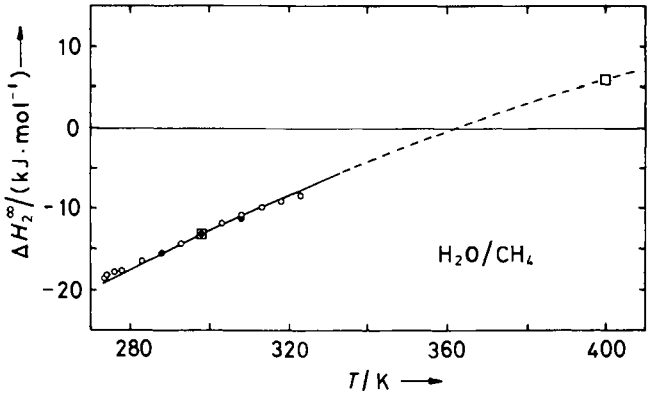

Figure 7.7 Partial molar enthalpy change on solution, $\Delta H_2^{\infty}(T, P_{s,1})$, of methane dissolved in liquid water from $T = 273.15$ K to 400 K:—, Rettich *et al.*, BKRBW apparatus [100], obtained *via* van't Hoff analysis of their solubility data; □, Crovetto *et al.* [140], obtained *via* van't Hoff analysis of their solubility data; ○, Naghibi *et al.* [159], calorimetry; ●, Dec and Gill [157,158], calorimetry. At this scale the calorimetric results of Olofsson *et al.* [156] cannot be distinguished from those of references [157–159].

measurements. Using our data, the extrapolated minimum-solubility temperature, *i.e.* the temperature where the curve of $H_{2,1}(T, P_{s,1})$ plotted against T shows a maximum, is ca. $T = 362$ K, which has indeed been observed by Crovetto *et al.* [140] as shown in Figure 7.6. While their solubility measurements are considerably less precise, with average deviations of about ±2%, they cover a much larger temperature range. As can be seen in Figure 7.7, accord with ΔH_2^{∞} derived from their solubilities *via* van't Hoff analysis is entirely satisfactory.

For several gases dissolved in liquid water, Table 7.1 contains a comparison of $\Delta H_2^{\infty}(T, P_{s,1})$ and $\Delta C_{p,2}^{\infty}(T, P_{s,1})$ obtained from van't Hoff analysis of high-precision solubility measurements [*cf.* Equations (7.98) and (7.100)] with calorimetrically determined values. Besides our own results on solutions of Ar, O_2, CH_4, C_2H_6 and C_2H_4 [100,118,119,160], I have also included those of Krause and Benson on the rare gases He through Xe [147]. Essentially, in this work, Benson and Krause had already adopted our method of data reduction [100]. They included a very small empirical third-order correction term that presumably takes into account the impact of the third virial coefficients and, perhaps, the variation of the Henry's law activity coefficient γ_2^{HL} with composition. The calorimetrically determined partial molar enthalpy changes on solution were all obtained by one of the two types of micro-calorimeters developed either at the Thermochemistry Laboratory in Lund, Sweden, or in the Chemistry Department of the University of Colorado in Boulder, Colorado, USA [162,163]. With the exception of one set of *direct* heat capacity measurements on argon dissolved in water [154], all partial molar heat capacity changes on solution were obtained from the temperature dependence of the enthalpy of solution, *i.e.* from $\Delta C_{p,2}^{\infty} = (\partial \Delta H_2^{\infty}/\partial T)_P$.

Evidently, comparing van't Hoff derived enthalpy changes (*one* differentiation level) and heat capacity changes (*two* differentiation levels) with directly obtained high-quality calorimetric results constitutes a particularly severe test of solubility data. For the sake of

Table 7.1 Partial molar enthalpy changes on solution $\Delta H_2^{\infty}(T, P_{s,1})$ and partial molar heat capacity changes on solution $\Delta C_{p,2}^{\infty}(T, P_{s,1})$ of several gases dissolved in liquid water at $T = 298.15$ K and $P_{s,1} = 3.1691$ kPa: comparison of values obtained *via* van't Hoff analysis of high-precision gas solubility measurements [see Equations (7.98) and (7.100)] with those obtained by calorimetric methods.

Gas	$10^{-3} \cdot \Delta H_2^{\infty}(T, P_{s,1}) / (\mathrm{J \cdot mol^{-1}})$		$\Delta C_{p,2}^{\infty}(T, P_{s,1}) / (\mathrm{J \cdot K^{-1} \cdot mol^{-1}})$	
	Solubility	Calorimetry	Solubility	Calorimetry
He	−0.54[a] [147]	−0.65 [156] −0.52 [161]	122[a] [147]	135 [156]
Ne	−3.64[a] [147]	−3.64 [156] −3.95 [161]	143[a] [147]	145 [156]
Ar	−11.92[a] [147] −11.96 [118]	−12.01 [156] −11.94 [161]	195[a] [147] 192 [118]	200 [156] 189[b] [154]
Kr	−15.34[a] [147]	−15.29 [156] −15.28 [161]	218[a] [147]	220 [156]
Xe	−19.06[a] [147]	−18.87 [156] −19.10 [161]	250[a] [147]	250 [156]
O_2	−11.97 [119] −12.01 [101]	−12.00 [156] −12.06 [162] −12.03 [163]	200 [119] 196 [101]	205 [156]
CH_4	−13.19 [100]	−13.06 [156] −13.18 [157] −13.12 [159]	237 [100]	242 [156] 209 [159] 218 [158]
C_2H_6	−19.50 [100]	−19.30 [156] −19.52 [157] −19.43 [164]	270 [100]	317 [156] 273 [164] 284 [158]
C_2H_4	−16.28 [160]	−16.46 [157]	238 [160]	237 [158]

[a] Krause and Benson [147]: all their enthalpy-of-solution data have the wrong sign.
[b] Biggerstaff *et al.* [154]: this is the only *directly* obtained value. All other $\Delta C_{p,2}^{\infty}$ values have been obtained from the temperature dependence of the enthalpy of solution, *i.e.* $\Delta C_{p,2}^{\infty} = (\partial \Delta H_2^{\infty} / \partial T)_P$.

brevity, in Table 7.1 I have limited the comparison to $T = 298.15$ K, yet essentially the same picture emerges at other temperatures too (see Figure 7.7 and Table 7.2). In general, the agreement is outstanding, *i.e.* usually within the combined experimental error: this is a truly satisfactory reward for both experimental ingenuity and state-of-the-art data reduction.

Table 7.2 provides (smoothed) solubility data and derived caloric quantities ΔH_2^{∞} and $\Delta C_{p,2}^{\infty}$ pertaining to oxygen dissolved in water, as determined by Benson *et al.* [101] and by us [119]. Undoubtedly, because of its central role in physiology, oceanography, limnology, geochemistry, *etc.*, it is the most important solution of all. The solubility of oxygen in liquid water has been studied more extensively than that of any other gas [5] by both physical and chemical methods. In fact, Battino and Clever [1], as well as Wilhelm *et al.* [5] recommended that the solubility of oxygen in water be used as reference for inter-laboratory comparison and equipment calibration. In the temperature range 273.15 K–303.15 K, the two data sets agree to within 0.04%, thereby corroborating the respective claims of precision and accuracy. Any systematic differences are ascribed to the data reduction methods used, that is Benson

Table 7.2 Henry fugacities $h_{2,1}(T, P_{s,1})$, Ostwald coefficients $L^{\infty}_{2,1}$ at infinite dilution, partial molar enthalpy changes on solution ΔH^{∞}_{2}, and partial molar heat capacity changes on solution $\Delta C^{\infty}_{p,2}$ for oxygen dissolved in liquid water at selected temperatures T and the corresponding vapor pressures $P_{s,1}$ of pure water. Our values [119] are compared with those reported by Benson *et al.* [101], and with values obtained from high-precision calorimetry [156,162,163].

T/K	$10^{-9} \cdot h_{2,1}(T, P_{s,1})$/Pa		$10^{2} \cdot L^{\infty}_{2,1}$	$10^{-3} \cdot \Delta H^{\infty}_{2}/(\mathrm{J \cdot mol^{-1}})$			$\Delta C^{\infty}_{p,2}/(\mathrm{J \cdot K^{-1} \cdot mol^{-1}})$		
				Gas solubility		Calorimetry	Gas solubility		Calorimetry
	Rettich *et al.* [119]	Benson *et al.* [101]	Rettich *et al.* [119]	Rettich *et al.* [119]	Benson *et al.* [101]		Rettich *et al.* [119]	Benson *et al.* [101]	
273.15	2.5591	2.5598	4.9256	−17.43	−17.37		239	234	
278.15	2.9242	2.9239	4.3897	−16.26	−16.22		230	226	
283.15	3.2966	3.2955	3.9627	−15.13	−15.12		222	218	
288.15	3.6708	3.6694	3.6194	−14.04	−14.05	−14.03[a]	214	210	
293.15	4.0415	4.0404	3.3415	−12.99	−13.01		207	203	
298.15	4.4038	4.4037	3.1153	−11.97	−12.01	−12.00[a], −12.03[b], −12.06[c]	200	196	205[a]
303.15	4.7533	4.7549	2.9305	−10.98	−11.05		194	190	
308.15	5.0859	5.0901	2.7794	−10.03	−10.11	−9.92[a]	188	184	
313.15	5.3985	5.4060	2.6561	−9.11	−9.21		182	178	
318.15	5.6882	5.7000	2.5557	−8.22	−8.33		176	172	
323.15	5.9531	5.9699	2.4748	−7.35	−7.49		170	167	
328.15	6.1917	6.2143	2.4104	−6.51	−6.66		165	162	

[a] Reference [156].
[b] Reference [163].
[c] Reference [162].

and Krause's then used empirical method against our thermodynamic-based approach, and they should increase with increasing temperature. This trend is indeed observed in Table 7.2. For instance, at the highest experimental temperature (328.15 K), the Henry fugacity reported by Benson *et al.* is 0.36% higher than our value.

For the derived quantities ΔH_2^{∞} and $\Delta C_{p,2}^{\infty}$ for oxygen dissolved in water, the accord with calorimetrically determined values is also excellent [156,162,163]. Taken together, it strongly suggests that our new results [119] are essentially free from systematic errors. We believe that these Henry fugacities $h_{2,1}$ $(T, P_{s,1})$ and the Ostwald coefficients $L_{2,1}^{\infty}$ at infinite dilution of oxygen in water are the most reliable ones to date.

7.3 Concluding Remarks

Albeit the solubility of gases in liquids has been studied for approximately 150 years, obtaining accurate values of Henry fugacities or Ostwald coefficients has often proved to be difficult. On the one hand, this was caused by instruments and related experimental techniques being not entirely adequate for the task, and on the other by data reduction methods and correlation methods not taking full advantage of thermodynamic theory and/or containing too crude approximations. However, during the last two decades, advances in both directions, that is instrument design and more rigorous application of thermodynamics, have been impressive. They are paralleled by advances in the statistical–mechanical treatment of solutions and by increasingly sophisticated computer simulations, which provide new insights and stimulating connections at a microscopic level.

Besides a concise presentation of the thermodynamic formalism relevant to the study of the solubility of gases in liquids, two intimately related topics have been dealt with prominently in this contribution, *viz.* (a) the adequate discussion of solution behaviour over large temperature and pressures ranges including the *critical* region, that is incorporation of the finite value of the Henry fugacity at the critical point of the solvent and the concomitant divergence of its derivatives with respect to temperature and pressure; (b) the reconciliation of results for caloric quantities derived from solubility measurements, that is *via van 't Hoff analysis*, with those measured directly with *calorimeters*.

In the first place, I wrote this review to present the state of the art to the experimentalist from a point of view of a thermodynamicist, though several recent key publications dealing with related non-thermodynamic topics have been included. In fact, cross-fertilization with other disciplines has always been a potent driving force in science. This is particularly true for research concerning the solubility of gases in liquids. Let it suffice to recall that the simplest and most thoroughly investigated hydrophobic effect concerns the poor solubility of non-polar gases in water at low temperatures. Hydrophobic hydration and hydrophobic interaction have been widely studied because of their central role in biology, yet there continues considerable debate about their molecular basis. The increasing number of investigations with a strong biophysical and/or biomedical flavour is thus not surprising. While my own perception of their relative importance may not be shared by all, it appears safe to state that they will greatly stimulate applied research in the coming decade.

Alternatives to the classical thermodynamic approach to gas solubility have been indicated, for instance the use of an EOS valid for both the vapour phase *and* the liquid phase

within the frame of the (φ, φ) approach to VLE. There can be little doubt that this method will become increasingly important [165], yet as long as the interest is focused on dilute solutions of gases in complex liquids consisting of significantly anisotropic molecules, which, perhaps, possess a permanent dipole moment and/or exhibit molecular flexibility and/or association, the Henry's law formalism still appears to be much more convenient and reliable, and thus remains of unquestioned value for modelling the thermodynamic behaviour.

Acknowledgements

It is a pleasure to acknowledge the many years of fruitful scientific collaboration with Prof. Rubin Battino, now Emeritus Professor at Wright State University, Dayton, OH, USA, and several colleagues, post-doctoral fellows and students. It included several extended stays in the USA (E.W.) as well as in Austria (R.B.). Most of our experimental and theoretical work on gas solubility was supported by the Public Health Service of the United States of America *via* grants from the National Institute of General Medical Sciences, a small part was supported by the Petroleum Research Fund, administered by the American Chemical Society.

Notation

In most cases I have adhered to the nomenclature/symbols suggested by IUPAC (see Green Book [166]). Differences are either due to my desire to present a more concise, unequivocal notation, or to compliance with usage generally accepted by the scientific community interested in gas solubilities. Note: a few symbols, which occur only at one or two places in the text, have not been included in the glossary. Some of the symbols listed below may be modified further, with obvious meaning, by adding appropriate superscripts and/or subscripts.

a_i	coefficient in the BK-type fitting equation, Equation (7.86)
$\hat{a}_i$	polar parameter in the Tsonopoulos correlation
A	parameter in the two-suffix Margules equation
A_i	coefficient in the CG-type fitting equation, Equation (7.85)
b	parameter in the Wilhelm equation, Equation (7.96)
$\hat{b}_i$	polar/H-bond parameter in the Tsonopoulos correlation
B	second virial coefficient of a mixture
B_{ii}	second virial coefficient of pure i
B_{ij}	second virial cross-coefficient
$B^{(i)}$	Tsonopoulos parameter (i = 0, 1, and 2)
C	third virial coefficient of a mixture
C_{iii}	third virial coefficient of a pure i
C_{ijk}	third virial cross-coefficient
$C_{p,2}^{pg*}$	molar heat capacity of pure 2 in the pg state

$C_{p,2}^{L\infty}$	partial molar heat capacity of 2 at infinite dilution in the liquid phase
$\Delta C_{p,2}^{\infty} \equiv C_{p,2}^{L\infty} - C_{P,2}^{pg*}$	partial molar heat capacity change on solution of 2 in 1,
$\Delta C_{p,2}^{\infty} = C_{p,2}^{R\infty}$	partial residual molar heat capacity at constant pressure at infinite dilution
$\hat{C}_{21}^{L\infty}$	dimensionless spatial volume integral of the molecular solute–solvent direct correlation function at infinite dilution in the liquid phase
f	fugacity of a solution
f_i	component fugacity of substance i in the solution
f_i^*	fugacity of pure substance i
G^E	excess molar Gibbs energy
G^R	residual molar Gibbs energy of a solution
G_i^{R*}	residual molar Gibbs energy of pure i
G_{cav}	partial molar Gibbs energy of cavity formation
G_{int}	partial molar Gibbs energy of interaction
h_{ij}	Henry fugacity (or Henry's law constant) of solute i dissolved in solvent j
H_2^{pg*}	molar enthalpy of pure 2 in the perfect-gas state
$H_2^{L\infty}$	partial molar enthalpy of 2 at infinite dilution in the liquid phase
H_1^{R*}	residual molar enthalpy of pure liquid solvent 1
$\Delta H_2^{\infty} \equiv H_2^{L\infty} - H_2^{pg*}$	partial molar enthalpy change on solution of 2 in 1,
$\Delta H_2^{\infty} = H_2^{R\infty}$	partial residual molar enthalpy at infinite dilution
I_i	Poynting correction for the pure solvent ($i = 1$) or the solute ($i = 2$) at infinite dilution
k_B	$= 1.380658 \times 10^{-23}\,J \cdot K^{-1}$, Boltzmann's constant
k_{ij}	binary interaction parameter
K_{21}	vapour–liquid distribution coefficient (K value)
L_{21}	Ostwald coefficient of solute 2 dissolved in solvent 1
n	total amount of substance ($=\Sigma n_i$)
n_i	amount of substance i
N_A	$= 6.022137 \times 10^{23}\,mol^{-1}$, Avogadro's constant
P	pressure
$P_i \equiv y_i P$	partial pressure of i
$P_{s,i}$	vapour (orthobaric) pressure of i
R	$= 8.31451\,J \cdot K^{-1} \cdot mol^{-1}$, gas constant
T	thermodynamic temperature
v	$\equiv nV$, volume of a solution
$\hat{v}_i$	characteristic volume of i (Brelvi–O'Connell correlation)
V	molar volume of a solution

V_i	partial molar volume of i
V_i^*	molar volume of pure i
$V_i^{L\infty}$	partial molar volume of i at infinite dilution in the liquid phase
V_1^{R*}	residual molar volume of pure liquid solvent 1
V_{cav}	$= (\partial G_{cav}/\partial P)_T$
x_i	liquid-phase mole fraction
y_i	vapour-phase mole fraction
Z	$\equiv PV/RT$, compression factor

Greek Letters

α_P	$\equiv V^{-1}(\partial V/\partial T)_P$, isobaric expansivity
β_T	$\equiv -V^{-1}(\partial V/\partial P)_T$, isothermal compressibility
γ_i^{LR}, γ_i^{HL}	liquid-phase activity coefficient of i, either for the symmetric LR (Lewis–Randall) convention, or for the unsymmetric HL (Henry's law) convention
Δ_{12}	$\equiv 2B_{12} - (B_{11} + B_{22})$
ε_0	permittivity of vacuum
μ_i	chemical potential of i; numerical value of the permanent molecular dipole moment of i
$\mu_i^{R\infty}$	residual chemical potential of i at infinite dilution
$\Pi_{s,1}^{L*}$	internal pressure of pure liquid solvent 1 at saturation
$\rho \equiv V^{-1}$	(total) molar density; $\rho = \Sigma\rho_i$
$\rho_i \equiv n_i/v = x_i/V = x_i\rho$	concentration or molar density of i
$\bar{\rho}_1 \equiv \hat{v}_1\rho_{s,1}^{L*}$	reduced molar density of solvent 1 at saturation (Brelvi–O'Connell correlation)
$\rho_{s,1}^{L*}$	molar density of pure saturated liquid 1
φ	fugacity coefficient of a solution
φ_i	fugacity coefficient of component i in a solution
$\varphi_i^{V\infty}$, $\varphi_i^{L\infty}$	fugacity coefficient of component i at infinite dilution either in the vapour phase V of the liquid phase L
φ_i^*	fugacity of pure substance i
ω_i	acentric factor of substance i

Superscripts

L	liquid phase
V	vapour phase
pg	perfect-gas state

*	pure substance
∞	infinite dilution
E	excess quantity
R	residual quantity in $\{T, P, x\}$ space
LR	symmetric (*i.e.* Lewis–Randall) convention
HL	unsymmetric (*i.e.* Henry's law) convention
π	phase (V or L)

Subscripts

i, j, k	general indices; usually, $i = 1$ denotes the solvent, and $i = 2$ denotes the solute
ij	"binary" or "interaction" quantity
c	critical (or pseudocritical) quantity
r	reduced quantity
s	saturation (orthobaric) condition

References

1. Battino, R. and Clever, H.L., *Chem. Rev.* **66**, 395, 1966.
2. Wilhelm, E. and Battino, R., *Chem. Rev.* **73**, 1, 1973.
3. Clever, H.L. and Battino, R., in *Solutions and Solubilities, Vol 8, of Techniques of Chemistry*, part 1, M.R.J. Dack, ed.,Wiley, New York, pp. 379–441, 1975.
4. Landolt-Börnstein, 4. Band, 4. Teil, Bestandteil c, *Gleichgewicht der Absorption von Gasen in Flüssigkeiten*, Teil c1: *Absorption in Flüssigkeiten von niedrigem Dampfdruck*, Teil c2: *Absorption in Flüssigkeiten von hohem Dampfdruck*, Springer-Verlag, Berlin, 1976 and 1980.
5. Wilhelm, E., Battino, R. and Wilcock, R.J., *Chem. Rev.* **77**, 219, 1977.
6. *Solubility Data Series (IUPAC)*, Pergamon, Oxford, *Vol 1*, 1979 and later.
7. Mackay, D. and Shiu, W.Y., *J. Phys. Chem. Ref. Data* **10**, 1175, 1981.
8. Wilhelm, E., *CRC Crit. Rev. Analyt. Chem.* **16**, 129, 1985.
9. Wilhelm, E., *Pure Appl. Chem.* **57**, 303, 1985.
10. Matteoli, E. and Mansoori, G.A., eds., *Fluctuation Theory of Mixtures, Advances in Thermodynamics, Vol 2*, Taylor & Francis, New York, 1990.
11. Bruno, T.J. and Ely, J.F., eds., *Supercritical Fluid Technology: Reviews in Modern Theory and Applications*, CRC Press, Boca Raton, Florida, 1991.
12. Wilhelm, E., in *Molecular Liquids: New Perspectives in Physics and Chemistry*, J.J.C Teixeira-Dias, ed., *NATO ASI Series, Series C: Mathematical and Physical Sciences, Vol 379*, Kluwer, Dordrecht, pp. 175–206, 1992.
13. Blokzijl, W. and Engberts, J.B.F.N., *Angew. Chem.* **105**, 1610, 1993; *Angew. Chem. Int. Ed. Engl.* **32**, 1545, 1993.
14. Sandler, S.I., ed., *Modeling for Thermodynamic and Phase Equilibrium Calculations*, Marcel Dekker, New York, 1994.
15. Kiran, E. and Levelt Sengers, J.M.H., eds., *Supercritical Fluids. Fundamentals for Application, NATO ASI Series, Series E: Applied Sciences, Vol 273*, Kluwer, Dordrecht, 1994.

16. White Jr., H.J., Sengers, J.V., Neumann, D.B. and Bellows, J.C., eds., *Physical Chemistry of Aqueous Systems*, Begell House, New York, 1995.
17. Wilhelm, E., *Thermochim. Acta* **300**, 159, 1997.
18. Chialvo, A.A. and Cummings, P.T., *Adv. Chem. Phys.* **109**, 115, 1999.
19. Chialvo, A.A. and Cummings, P.T., in *Supercritical Fluids. Fundamentals and Applications*, E. Kiran, P.G. Debenedetti and C.J. Peters, eds., *NATO Science Series, Series E: Applied Sciences, Vol 366*, Kluwer, Dordrecht, pp. 345–394, 2000.
20. Hummer, G., Garde, S., Garcia, A.E. and Pratt, L.R., *Chem. Phys.* **258**, 349, 2000.
21. Boulougouris, G.C., Voutsas, E.C., Economou, L.G., Theodorou, D.N. and Tassios, D.P., *J. Phys. Chem. B* **105**, 7792, 2001.
22. Bunsen, R., *Ann. Chem. Pharm.* **93**, 1, 1855.
23. Winkler, L.W., *Ber. Dtsch. Chem. Ges.* **24**, 89, 1891; *ibid.*, 3602; *ibid.* **34**, 1408, 1901.
24. Szeparowicz, M., *Sitzungsber. Akad. Wiss. Wien, Math.-Naturwiss. Kl.* **129**, 437, 1920.
25. Horiuti, J., *Sci. Pap. Inst. Phys. Chem. Res. (Tokyo)* **17**, 125, 1931.
26. Ben-Naim, A., *Water and Aqueous Solutions. Introduction to a Molecular Theory*, Plenum Press, New York, 1974.
27. Ben-Naim, A., *Hydrophobic Interactions*, Plenum Press, New York, 1980.
28. Ben-Naim, A., *Solvation Thermodynamics*, Plenum Press, New York, 1987.
29. Astarita, G., *Mass Transfer with Chemical Reaction*, Elsevier, Amsterdam, 1967.
30. Danckwerts, P.V., *Gas–Liquid Reactors*, McGraw-Hill, New York, 1970.
31. Shah, Y.T., *Gas–Liquid–Solid Reactions*, McGraw-Hill, New York, 1979.
32. Prausnitz, J.M., Anderson, T.F., Grens, E.A., Eckert, C.A., Hsieh, R. and O'Connell, J.P., *Computer Calculations for Multicomponent Vapor–Liquid and Liquid–Liquid Equilibria*, Prentice-Hall, Englewood Cliffs, NJ, 1980.
33. Charpentier, J.C., *Adv. Chem. Eng.* **11**, 1, 1981.
34. Prausnitz, J.M., Lichtenthaler, R.N. and Azevedo, E.G., *Molecular Thermodynamics of Fluid-Phase Equilibria*, 3rd ed., PTR, Upper-Saddle River, NJ, 1999.
35. Van Ness, H.C. and Abbott, M.M., *Classical Thermodynamics of Nonelectrolyte Solutions*, McGraw-Hill, New York, 1982.
36. Wilhelm, E., *The Solubility of Gases in Liquids. Thermodynamic Considerations*, in *Solubility Data Series (IUPAC), Vol 10*, R. Battino, ed., Pergamon Press, Oxford, pp. XX–XXVIII, 1982.
37. Wilhelm, E., *Fluid Phase Equilibr.* **27**, 233, 1986.
38. Wilhelm, E., *Thermochim. Acta* **119**, 17, 1987.
39. Wilhelm, E., *Thermochim. Acta* **162**, 43, 1990.
40. Barker, J.A., *Aust. J. Chem.* **6**, 207, 1953.
41. Chialvo, A.A. and Cummings, P.T., *AIChE J.* **40**, 1558, 1994.
42. Chialvo, A.A. and Cummings, P.T., *Mol. Phys.* **84**, 41, 1995.
43. Levelt Sengers, J.M.H., in *Supercritical Fluid Technology: Reviews in Modern Theory and Applications*, T.J. Bruno and J.F. Ely, eds., CRC Press, Boca Raton, FL, pp. 1–56, 1991.
44. Levelt Sengers, J.M.H., in *Supercritical Fluids. Fundamentals for Application*, E. Kiran and J.M.H. Levelt Sengers, eds., *NATO ASI Series, Series E: Applied Sciences, Vol 273*, Kluwer, Dordrecht, pp. 3–38, 1994.
45. Battino, R., *Fluid Phase Equilibr.* **15**, 231, 2001.
46. Poling, B.E., Prausnitz, J.M. and O'Connell, J.P., *The Properties of Gases and Liquids*, 5th ed., McGraw-Hill, New York, 2001.
47. Ambrose, D. and Tsonopoulos, C., *J. Chem. Eng. Data* **40**, 531, 1995.
48. Daubert, T.E., *J. Chem. Eng. Data*, **41**, 365, 1996.
49. Tsonopoulos, C. and Ambrose, D., *J. Chem. Eng. Data* **40**, 547, 1995.

50. Gude, M. and Teja, A.S., *J. Chem. Eng. Data* **40**, 1025, 1995.
51. Haar, L., Gallagher, J.S. and Kell, G.S., *NBS/NRC Steam Tables: Thermodynamic and Transport Properties and Computer Programs for Vapor and Liquid States of Water in SI Units*, Hemisphere Publishing Corporation, New York, 1984.
52. Ambrose, D. and Walton, J., *Pure Appl. Chem.* **61**, 1395,1989.
53. Magoulas, K. and Tassios, D., *Fluid Phase Equilibr.* **56**, 119, 1990.
54. Ambrose, D. and Lawrenson, I.J., *J. Chem. Thermodyn.* **4**, 755, 1972.
55. (a) *TRC Thermodynamic Tables-Hydrocarbons;* (b) *TRC Thermodynamic Tables-Non-Hydrocarbons*, Thermodynamics Research Center Project, Texas A&M University System, College Station, Texas.
56. Dymond, J.H. and Smith, E.B., *The Virial Coefficients of Pure Gases and Mixtures*, Clarendon Press, Oxford, 1980.
57. Hayden, J.G. and O'Connell, J.P., *Ind. Eng. Chem. Process Des. Dev.* **14**, 209, 1975.
58. Tsonopoulos, C., *Adv. Chem. Ser.* **182**, 143, 1979.
59. Tsonopoulos, C., Dymond, J.H. and Szafranski, A.M., *Pure Appl. Chem.* **61**, 1387, 1989.
60. De Santis, R. and Grande, B., *AIChE J.* **25**, 931, 1979.
61. Orbey, H. and Vera, J.H., *AIChE J.* **29**, 107, 1983.
62. Wilhelm, E., *High Temp.–High Press.* **29**, 613, 1997.
63. Bo, S., Battino, R. and Wilhelm, E., *J. Chem. Eng. Data* **38**, 611, 1993; Correction: *J. Chem. Eng. Data* **41**, 644, 1996.
64. Wilhelm, E., *J. Thermal. Anal.* **48**, 545, 1997.
65. Chueh, P.L. and Prausnitz, J.M., *AIChE J.* **13**, 1099, 1967.
66. Tominaga, T., Battino, R., Gorowara, H.K., Dixon, R.D. and Wilhelm, E., *J. Chem. Eng. Data* **31**, 175, 1986.
67. Hesse, P., Battino, R., Scharlin, P. and Wilhelm, E., *J. Chem. Eng. Data* **41**, 195, 1996.
68. Diaz Pena, M., Pando, C. and Renuncio, J.A.R., *J. Chem. Phys.* **76**, 325 and 333, 1982.
69. Kohler, F., Fischer, J. and Wilhelm, E., *J. Mol. Struct.* **84**, 245, 1982.
70. Mathias, P.M. and O'Connell, J.P., *Chem. Eng. Sci.* **36**, 1123, 1981.
71. Carroll, J.J. and Mather, A.E., *J. Solution Chem.* **21**, 607, 1992.
72. Handa, Y.P., D'Arcy, P.J. and Benson, G.C., *Fluid Phase Equilibr.* **8**, 181, 1982.
73. Moore, J.C., Battino, R., Rettich, T.R., Handa, Y.P. and Wilhelm, E., *J. Chem. Eng. Data* **27**, 22, 1982.
74. Bignell, N., *J. Phys. Chem.* **88**, 5409, 1984.
75. Biggerstaff, D.R. and Wood, R.H., *J. Phys. Chem.* **92**, 1988–1994, 1988.
76. Cibulka, I. and Heintz, A., *Fluid Phase Equilibr.* **107**, 235, 1995.
77. Izak, P., Cibulka, I. and Heintz, A., *Fluid Phase Equilibr.* **109**, 227, 1995.
78. Hnedkovsky, L., Wood, R.H. and Majer, V., *J. Chem. Thermodyn.* **28**, 125, 1996.
79. Zhou, T. and Battino, R., *J. Chem. Eng. Data* **46**, 331, 2001.
80. Brelvi, S.W. and O'Connell, J.P., *AIChE J.* **18**, 1239, 1972.
81. Handa, Y.P. and Benson, G.C., *Fluid Phase Equilibr.* **8**, 161, 1982.
82. O'Connell, J.P., Sharygin, A.V. and Wood, R.H., *Ind. Eng. Chem. Res.* **35**, 2808, 1996.
83. Pierotti, R.A., *J. Phys. Chem.* **67**, 1840, 1963.
84. Pierotti, R.A., *J. Phys. Chem.* **69**, 281, 1965.
85. Pierotti, R.A., *Chem. Rev.* **76**, 717, 1976.
86. Reiss, H., *Adv. Chem. Phys.* **9**, 1, 1965.
87. Wilhelm, E. and Battino, R., *J. Chem. Thermodyn.* **3**, 379, 1971.
88. Wilhelm, E. and Battino, R., *J. Chem. Phys.* **55**, 4012, 1971.
89. Wilhelm, E. and Battino, R., *J. Chem. Phys.* **56**, 563, 1972.
90. Wilhelm, E., *J. Chem. Phys.* **58**, 3558, 1973.

91. Montfort, J.-P. and Perez, J.L., *Chem. Eng. J.* **16**, 205, 1978.
92. Schaffer, S.K. and Prausnitz, J.M., *AIChE J.* **27**, 844, 1981.
93. Schulze, G. and Prausnitz, J.M., *Ind. Eng. Chem. Fundam.* **20**, 175, 1981.
94. Chialvo, A.A., *J. Phys. Chem.* **97**, 2740, 1993.
95. Levelt Sengers, J.M.H., *J. Supercrit. Fluids* **4**, 215, 1991.
96. Hallen, D. and Wadsö, I., *Pure Appl. Chem.* **61**, 123, 1989.
97. Battino, R., Banzhof, M., Bogan, M. and Wilhelm, E., *Anal. Chem.* **43**, 806, 1971.
98. Wilhelm, E. and Battino, R., *J. Chem. Thermodyn.* **5**, 117, 1973.
99. Park, T., Rettich, T.R., Battino, R., Peterson, D. and Wilhelm, E., *J. Chem. Eng. Data* **27**, 324, 1982.
100. Rettich, T.R., Handa, Y.P., Battino, R. and Wilhelm, E., *J. Phys. Chem.* **85**, 3230, 1981.
101. Benson, B.B., Krause Jr., D. and Peterson, M.A., *J. Solution Chem.* **8**, 655, 1979.
102. Benson, B.B. and Krause Jr., D., *J. Solution Chem.* **9**, 895, 1980.
103. Tucker, E.E. and Christian, S.D., *J. Chem. Thermodyn.* **11**, 1137, 1979.
104. Tucker, E.E., Lane, E.M. and Christian, S.D., *J. Solution Chem.* **10**, 1, 1981.
105. Hesse, P.J., Battino, R., Scharlin, P. and Wilhelm, E., *J. Chem. Thermodyn.* **31**, 1175, 1999.
106. Ben-Naim, A. and Baer, S., *Trans. Faraday Soc.* **59**, 2735, 1963.
107. Moudgil, B.M., Somasundaran, P. and Lin, I.J., *Rev. Sci. Instrum.* **45**, 406, 1974.
108. Vosmansky, J. and Dohnal, V., *Fluid Phase Equilibr.* **33**, 137, 1987.
109. Clever, H.L., *J. Phys. Chem.* **62**, 375, 1958.
110. Pollack, G.L., *J. Chem. Phys.* **75**, 5875, 1981.
111. Pollack, G.L. and Himm, J.F., *J. Chem. Phys.* **77**, 3221, 1982.
112. Pollack, G.L., Himm, J.F. and Enyeart, J.J., *J. Chem. Phys.* **81**, 3239, 1984.
113. Scharlin, P. and Battino, R., *J. Solution Chem.* **21**, 67, 1992.
114. Scharlin, P. and Battino, R., *Fluid Phase Equilibr.* **94**, 137, 1994.
115. Scharlin, P. and Battino, R., *J. Chem. Eng. Data* **40**, 167, 1995.
116. Rettich, T.R., Battino, R. and Wilhelm, E., *Ber. Bunsenges. Phys. Chem.* **86**, 1128, 1982.
117. Rettich, T.R., Battino, R. and Wilhelm, E., *J. Solution Chem.* **13**, 335, 1984.
118. Rettich, T.R., Battino, R. and Wilhelm, E., *J. Solution Chem.* **21**, 987, 1992.
119. Rettich, T.R., Battino, R. and Wilhelm, E., *J. Chem. Thermodyn.* **32**, 1145, 2000.
120. Benson, B.B. and Krause Jr., D., *J. Chem. Phys.* **64**, 689, 1976.
121. Cook, M.W. and Hanson, D.N., *Rev. Sci. Instrum.* **28**, 370, 1957.
122. Costa Gomes, M.F. and Grolier, J.-P., *Phys. Chem. Chem. Phys.* **3**, 1047, 2001.
123. Bonifacio, R.P., Padua, A.A.H. and Costa Gomes, M.F., *J. Phys. Chem. B.* **105**, 8403, 2001.
124. Pardo, J., Lopez, M.C., Santafe, J., Royo, F.M. and Urieta, J.S., *Fluid Phase Equilibr.* **109**, 29, 1995.
125. Pardo, J., Lopez, M.C., Santafe, J., Royo, F.M. and Urieta, J.S., *Fluid Phase Equilibr.* **119**, 165, 1996.
126. Pardo, J., Lopez, M.C., Mayoral, J.A., Royo, F.M. and Urieta, J.S., *Fluid Phase Equilibr.* **134**, 133, 1997.
127. Sanchez, M.A., Mainar, A.M., Pardo, J.I., Lopez, M.C. and Urieta, J.S., *Can. J. Chem.* **79**, 1460, 2001.
128. Silva, C.S.O., Fonseca, I.M.A. and Lobo, L.Q., *Fluid Phase Equilibr.* **135**, 137, 1997.
129. Miguel, A.A.F., Ferreira, A.G.M. and Fonseca, I.M.A., *Fluid Phase Equilibr.* **173**, 97, 2000.
130. Zheng, D.-Q., Guo, T.-M. and Knapp, H., *Fluid Phase Equilibr.* **129**, 197, 1997.
131. Olsen, J. D., *J. Chem. Eng. Data* **22**, 326, 1977.
132. Cukor, P.M. and Prausnitz, J. M., *J. Phys. Chem.* **76**, 598, 1972.
133. Graaf, G.H., Smit, H.J., Stamhuis, E.J. and Beenackers, A.A.C.M., *J. Chem. Eng. Data* **37**, 146, 1992.
134. Breman, B.B., Beenackers, A.A.C.M., Rietjens, E.W.J. and Stege, R.J.H., *J. Chem. Eng. Data* **39**, 647, 1994.

135. Mroczek, E.K., *J. Chem. Eng. Data* **42**, 116, 1997.
136. Wilson, R.D. and Mackay, D.M., *Ground Water* **31**, 719, 1993.
137. Strotmann, B., Fischer, K. and Gmehling, J., *J. Chem. Eng. Data* **44**, 388, 1999.
138. Henni, A., Lal, D. and Mather, A.E., *Can. J. Chem. Eng.* **74**, 423, 1996.
139. Melzer, W.-M., Schrödter, F. and Knapp, H., *Fluid Phase Equilibr.* **49**, 167, 1989.
140. Crovetto, R., Fernandez-Prini, R. and Japas, M.L., *J. Chem. Phys.* **76**, 1077, 1982.
141. Clarke, E.C.W. and Glew, D.N., *Trans. Faraday Soc.* **62**, 539, 1966.
142. Bolton, P.D., *J. Chem. Educ.* **47**, 638, 1970.
143. Valentiner, S., *Z. Phys.* **42**, 253, 1927.
144. Beutier, D. and Renon, H., *AIChE J.* **24**, 1122, 1978.
145. Schotte, W., *AIChE J.* **31**, 154, 1985.
146. Japas, M.L. and Levelt Sengers, J.M.H., *AIChE J.* **35**, 705, 1989.
147. Krause Jr., D. and Benson, B.B., *J. Solution Chem.* **18**, 823, 1989.
148. Harvey, A.H. and Levelt Sengers, J.M.H., *AIChE J.* **36**, 539, 1990.
149. Harvey, A.H., *AIChE J.* **42**, 1491, 1996.
150. Harvey, A.H., Crovetto, R. and Levelt Sengers, J.M.H., *AIChE J.* **36**, 1901, 1990.
151. Chang, R.F., Morrison, G. and Levelt Sengers, J.M.H., *J. Phys. Chem.* **88**, 3389, 1984.
152. Chialvo, A.A., Kalyuzhnyi, Y.V. and Cummings, P.T., *AIChE J.* **42**, 571, 1996.
153. Wheeler, J.C., *Ber. Bunsenges. Phys. Chem.* **76**, 308, 1972.
154. Biggerstaff, D.R., White, D.E. and Wood, R.H., *J. Phys. Chem.* **89**, 4378, 1985.
155. Biggerstaff, D.R. and Wood, R.H., *J. Phys. Chem.* **92**, 1994, 1988.
156. Olofsson, G., Oshodj, E., Qvarnström, E. and Wadsö, I., *J. Chem. Thermodyn.* **16**, 1041, 1984.
157. Dec, S.F. and Gill, S.J., *J. Solution Chem.* **13**, 27, 1984.
158. Dec, S.F. and Gill, S.J., *J. Solution Chem.* **14**, 827, 1985.
159. Naghibi, H., Dec, S.F. and Gill, S.J., *J. Phys. Chem.* **90**, 4621, 1986.
160. Rettich, T.R., Battino, R. and Wihelm, E., *J. Chem. Thermodyn.* **32**, 1145, 2000.
161. Dec, S.F. and Gill, S.J., *J. Solution Chem.* **14**, 417, 1985.
162. Gill, S.J. and Wadsö, I., *J. Chem. Thermodyn.* **14**, 905, 1982.
163. Dec, S.F. and Gill, S.J., *Rev. Sci. Instrum.* **55**, 765, 1984.
164. Naghibi, H., Dec, S.F. and Gill, S.J., *J. Phys. Chem.* **91**, 245, 1987.
165. Wei, Y.S. and Sadus, R.J., *AIChE J.* **46**, 169, 2000.
166. International Union of Pure and Applied Chemistry, Physical Chemistry Division: *Quantities, Units and Symbols in Physical Chemistry*, 2nd ed., prepared for publication by I. Mills, T. Cvitas, K. Homann, N. Kallay and K. Kuchitsu, Blackwell Scientific Publications, Oxford, 1993.

8 Liquid–Liquid Equilibrium

J. MATOUŠ, K. ŘEHÁK and J.P. NOVÁK
Department of Physical Chemistry
Institute of Chemical Technology
Praha, Czech Republic

Measurement of the Thermodynamic Properties of Multiple Phases
R.D. Weir and Th.W. de Loos (Editors)

8 LIQUID–LIQUID EQUILIBRIUM

This chapter provides information on experimental techniques for determining liquid–liquid phase equilibria. As the mutual solubility of the components of various systems can differ by several orders of magnitude [1], there is no universal method and the experimental techniques are rather diverse. The greatest difficulties are encountered in the analysis of the equilibrium phases, especially in systems with low mutual solubilities. While binary systems can be treated without the use of analytical methods, this tends to be an exception for ternary systems. Thus we will consider methods for determining liquid–liquid equilibria in binary systems separately from ternary and multi-component systems.

8.1 Liquid–Liquid Equilibrium in Binary Systems

Experimental determination of liquid–liquid equilibria in binary systems, *i.e.* determination of the mutual solubility of components, can basically be carried out using three methods, except for special cases: direct analytical, synthetic or turbidimetric and volumetric [2].

8.1.1 Direct Analytical Methods

In these methods, an approach in which the heterogeneous mixture is intensely mixed for a prolonged period of time at constant temperature for 2 h or even much longer is used. The conjugated phases are then left to separate by standing or centrifuging. The time required for complete separation depends on the density difference and the interfacial tension. A period of 24 to 48 h is required for (water + hydrocarbon) mixtures. Usually, however, a shorter time is sufficient, and after several hours both phases are transparent and clearly divided by a sharp boundary. Then samples of the individual phases are taken, *e.g.* using an injection syringe or pipette, and analyzed. Figure 8.1a depicts a classical thermostatted vessel that enables samples to be taken from the individual phases from above using an injection syringe or from below using an outlet stopcock. However, this approach is not really ideal, as the outlet stopcock has dead space and is not usually well thermostatted. In order to prevent mutual contamination of the equilibrium phases during taking of samples from the bottom phase, the classical equilibrium cell was modified so that it is not necessary to pass through the upper phase when taking samples from the lower phase [3]. The consequences of mutual contamination of the phases become increasingly serious with decreasing mutual solubility of the components. The modified cell (Figure 8.1b) consists of a thermostatted jacket, in which the measuring cell with a magnetic stirrer is placed. A side tube is fitted to the bottom of the vessel and is fitted with an injection syringe. The vessel and tube can be closed by using Teflon stoppers. The procedure of determining equilibrium and taking samples of the equilibrium phases is apparent from Figure 8.1c. Lohmann *et al.* [4] used a two-position cell (Figure 8.2), which also prevents mutual contamination in taking samples from the equilibrium phases, which, however, requires larger amounts of substances.

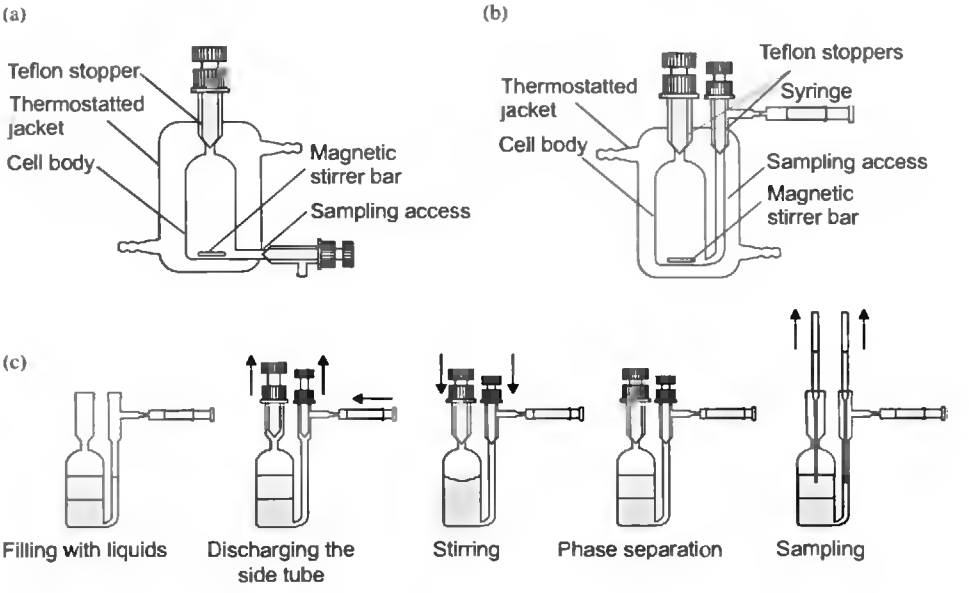

Figure 8.1 Thermostatted cells for determining liquid–liquid equilibria: (a) classical form [2], (b) improved form with a side arm [3], (c) operation.

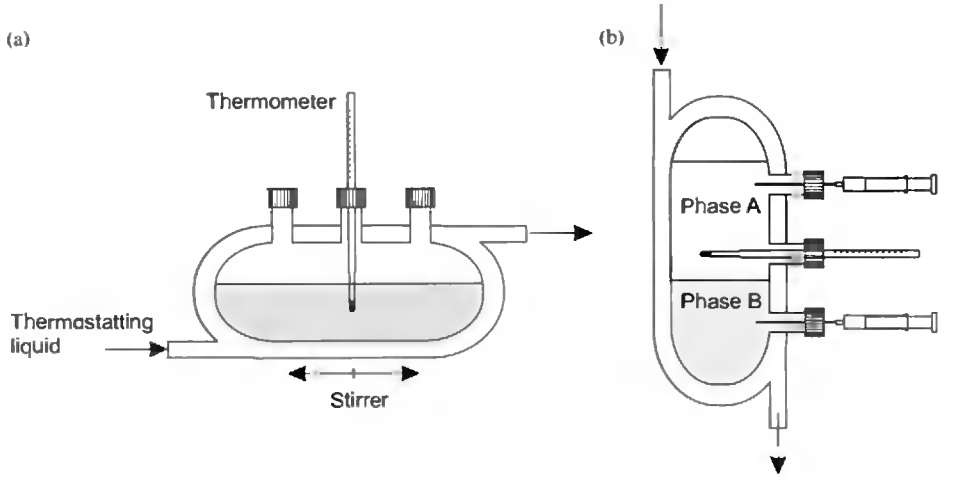

Figure 8.2 A two-position thermostatted cell for measuring of liquid–liquid equilibria: (a) equilibration, (b) separation. (Redrawn with permission from Lohmann *et al.* [4]. Copyright 1998, American Chemical Society.)

Gas and liquid chromatography are primarily used at present for analyses of binary mixtures. However, various physical properties of the substances can be used, *e.g.* the refractive index, density or chemical properties to include reactions of the components during the analytical determination, *e.g.* water, acids and bases. When the physical properties are

employed, it is necessary to carry out the appropriate calibration or to construct calibration curves. Frequently, aqueous systems are encountered in which the Karl–Fischer method [5] is recommended to determine the content of water.

An example of the use of direct analytical methods is the measurement of liquid–liquid equilibria in the system (methyl tert-butyl ether + water) [6]. The ether content in the aqueous phase was determined using gas chromatography by the internal standard method. The water content in the organic phase was determined by Karl–Fischer titration. The direct analytical method is also often advantageous for systems with low mutual solubility of their components where, in contrast, the following two methods are less suitable.

8.1.2 Synthetic or Turbidimetry Method

The principle of this method is to observe the appearance or disappearance of turbidity, resulting from the presence of a second phase, caused either by a change in temperature at constant composition or by the addition of one of the components to the system at constant temperature by titration.

Cloud-Point Method

In determining the temperature of formation of two phases, which is the temperature of dissolution at a given composition, a procedure in which either a known amount of the individual components or a certain amount of a prepared homogeneous sample with known composition is introduced into an ampoule fitted with a stirrer is adopted (Figure 8.3) [7]. The formation or disappearance of the second phase (formation or disappearance of turbidity) caused by a change in temperature is observed at constant stirring. For this purpose, the ampoule is usually placed in a thermostatted jacket and the temperature is increased or decreased at a defined rate, in order to delimit the narrowest possible temperature interval in which the second phase is formed or disappears. The magnitude of this temperature interval, ranging between 0.01 and 1 K, is dependent not only on the experimental conditions, but also on the temperature dependence of the solubility or the temperature coefficient dT/dx. The measurement can also be carried out in the apparatus used for the direct analytical method.

A similar procedure of following the formation or disappearance of turbidity caused by a change in pressure is used in determining the liquid–liquid equilibria at high pressures. Details can be found in Schneider [8].

The simplest method of monitoring the formation or disappearance of turbidity is by visual observation [2]. However, this method is, to a certain degree, subjective and is quite tedious. For these reasons, it is preferable to employ optical methods, based on measuring either the intensity of scattered light or a change in the intensity of transmitted light. For example, Šobr and Hynek [9] constructed an apparatus with horizontal ampoule positioning, based on measuring the intensity of transmitted light. It has the advantage that a relatively small amount of sample is required for the measurement. Semi-automatic determination of the temperature of dissolution through measurement of the intensity of scattered light was used by Hefter *et al.* [10]. The light source was a He–Ne laser coupled with a photo-detector.

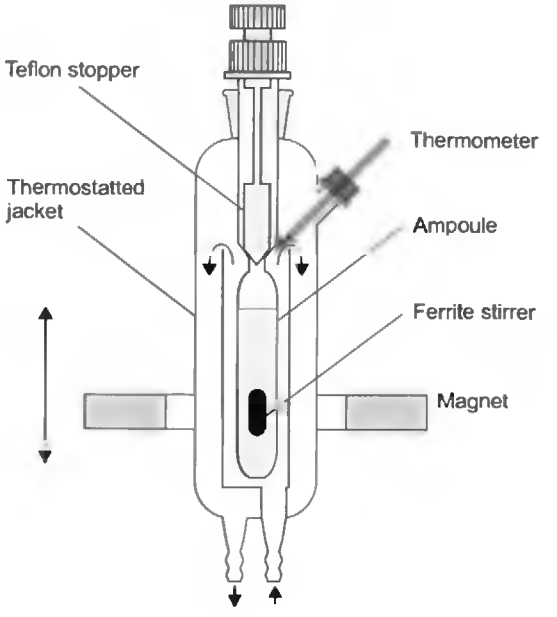

Figure 8.3 Schematic arrangement of the apparatus for measuring liquid–liquid equilibria by the synthetic (cloud-point) method [7].

The sealed ampoule with the studied mixture was placed in a thermostat with programmed temperature and mixed with a magnetic stirrer. A new apparatus based on the same principle that permitted measurement over a broader temperature interval, but with a slight increase in pressure was described by Ochi *et al.* [11]. The experimental arrangement is apparent from Figure 8.4a. This approach has the advantage that critical opalescence can be distinguished from true turbidity. Figure 8.4b depicts the variation of the intensity of scattered light with temperature in the vicinity of the critical point for a system with an upper critical solution temperature (UCST), and Figure 8.4c depicts the same dependence outside the critical region [12]. The cloud-point apparatus designed for determining the liquid–liquid equilibria in small amounts of samples was used by Heintz *et al.* [13]. It was applied to measurements in systems containing ionic liquids.

Titration Method

Titration with one of the components at constant temperature up to the formation of turbidity is carried out in a thermostatted vessel containing a known amount of the other component. The first component is added from the micro-burette while intense stirring is applied. If the sample is over-titrated or as a check possible over-titration, back-titration using the second component can be used. Detection of turbidity is carried out similarly as set forth in the previous section.

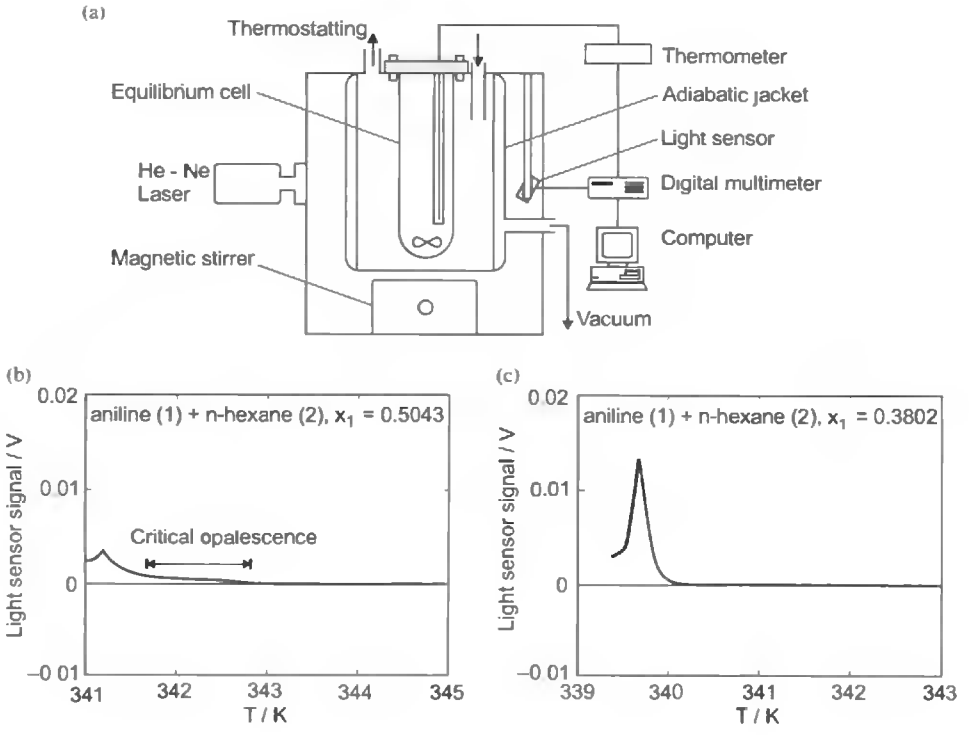

Figure 8.4 (a) Schematic diagram of semi-automated apparatus for determining liquid–liquid equilibria by the synthetic (cloud-point) method, (Redrawn with permission from Ochi *et al.* [11]. Copyright (1996) American Chemical Society.) (b) typical plot of intensity of light scattered vs. temperature (outside the critical region), (c) similar plot in the vicinity of the critical point (UCST). (Redrawn with permission from Ochi *et al.* [12] Courtesy of the Canadian Society of Chemical Engineering.)

Cho *et al.* [14] used a titration method at the boiling point stage. His original version of an ebulliometer was supplemented by Moon *et al.* [15] to include a reservoir for the liquid phase and an optical system permitting determination of the formation or disappearance of turbidity and thus the necessary amount of added component. A He–Ne laser was used as an optical source. When the liquid phase is homogeneous and transparent, the laser beam is straight. However, the laser beam is scattered when turbidity is formed. The experimental arrangement is apparent from Figures 8.5a and b.

In cases with low solubility, where the formation of turbidity during titration cannot be readily indicated, it is preferable to use the procedure of Rifai and Durandet [16] (Figure 8.6). A known weight of the first component, m_1, is transferred to the thermostatted reservoir fitted with a stirrer, to which a calibrated capillary is connected with a mercury seal. The second component is added from a micro-burette with intense mixing until the first portion of the second phase appears. Let its weight be equal to m_2. The mixture is left to stand and, after a sharp boundary is formed, the phase formed is let into the capillary, where its

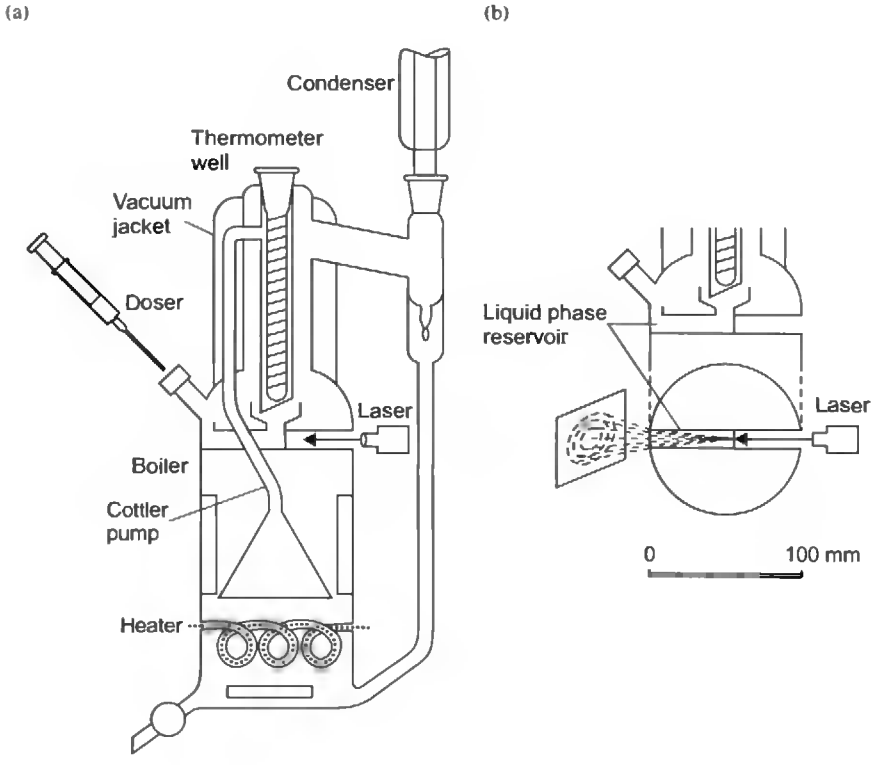

Figure 8.5 (a) Modified ebulliometer to determine mutual solubility at the boiling point, (b) detail of liquid phase reservoir and optical indication. (Redrawn with permission from Moon *et al.* [15]. Copyright 1995, American Chemical Society.)

volume is measured, $V^{(2)}(m_2)$. Then the content of the capillary is forced back into the reservoir and addition of the second component is continued. In principle, two additions following exceeding of the mutual solubility limit are sufficient, but in practice several additions are usually used. It follows from the mass balance that

$$m_1 = \text{const.} = V^{(1)}\beta_1^{(1)} + V^{(2)}\beta_1^{(2)}, \tag{8.1a}$$

$$m_2 = V^{(1)}\beta_2^{(1)} + V^{(2)}\beta_2^{(2)}, \tag{8.1b}$$

where $V^{(1)}$ and $V^{(2)}$ are the volumes of the first and second (forming) phase, respectively, which are a function of the mass m_2, $\beta_i^{(j)}$is the mass concentration ($g \cdot cm^{-3}$) of the ith component in the jth phase. It thus follows that $V^{(2)}$ is given as a function of m_2 by the relationship

$$V^{(2)} = \frac{(m_1\beta_2^{(1)} - m_2\beta_1^{(1)})}{(\beta_2^{(1)}\beta_1^{(2)} - \beta_1^{(1)}\beta_2^{(2)})} = A + Bm_2. \tag{8.2}$$

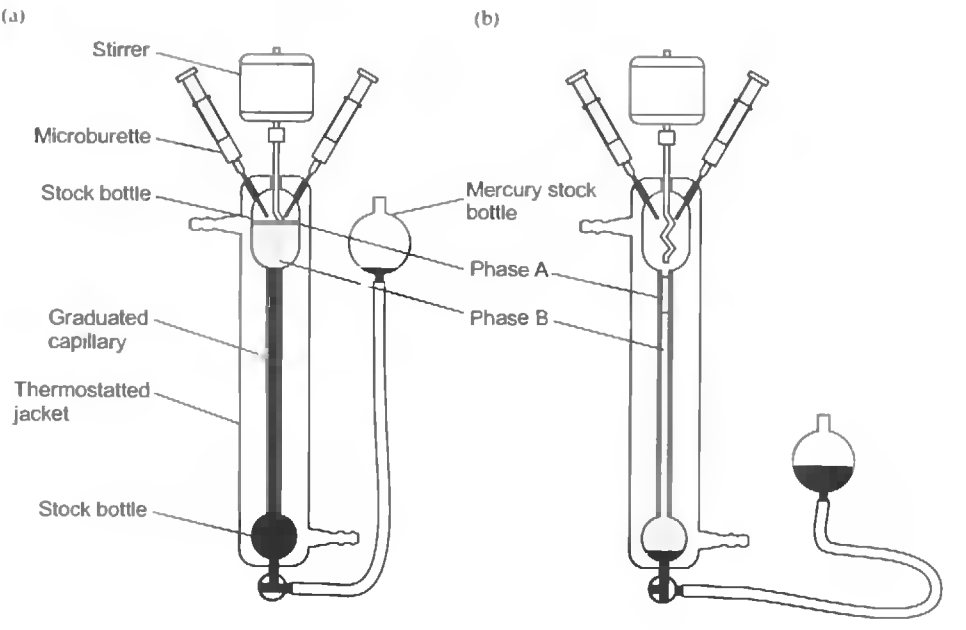

Figure 8.6 Apparatus for determining the phase separation point by Rifai and Durandet [16]: (a) stirring, (b) separation.

The volume of the phase formed is a linear function of the mass of added component 2, which justifies linear extrapolation to zero volume and thus permits determining mass $m_2^0 = -A/B$, required for the formation of the second phase.

8.1.3 Volumetric Method

The volumetric method consists of measuring the volumes of both equilibrium phases at two or more various ratios of components [17]. The measurement must be carried out at constant temperature in calibrated ampoules (Figure 8.7). The contents of the ampoules must be thoroughly mixed, either by vertical movement of a magnetic stirrer or by rotating the ampoule containing, *e.g.* a glass bead. The following balance can be carried out for two sets of measurements on the basis of the mass of the individual components and the determined volumes of the phases.

Each of the components is divided between the two phases and the concentrations in the individual phases at constant temperature do not change. It holds for components 1 and 2 in the first set (I) of measurements that

$$m_{1,\mathrm{I}} = V_{\mathrm{I}}^{(1)}\beta_1^{(1)} + V_{\mathrm{I}}^{(2)}\beta_1^{(2)}, \tag{8.3a}$$

$$m_{2,\mathrm{I}} = V_{\mathrm{I}}^{(1)}\beta_2^{(1)} + V_{\mathrm{I}}^{(2)}\beta_2^{(2)}, \tag{8.3b}$$

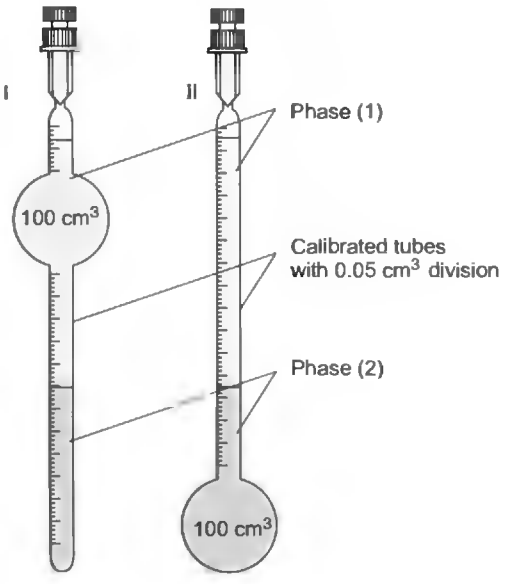

Figure 8.7 Ampoules for determining mutual solubility by the volumetric method [2].

where $V_{\mathrm{I}}^{(k)}$ is the volume of the kth phase in the first set (I) of measurements, $m_{i,\mathrm{I}}$ is the mass of the i-th component of the system in the first set of measurements and $\beta_i^{(k)}$ gives the mass concentration $(m_i/V^{(k)})$ of the ith component in the kth phase. It holds for the second set (II) of measurements that

$$m_{1,\mathrm{II}} = V_{\mathrm{II}}^{(1)}\beta_1^{(1)} + V_{\mathrm{II}}^{(2)}\beta_1^{(2)}\,, \tag{8.4a}$$

$$m_{2,\mathrm{II}} = V_{\mathrm{II}}^{(1)}\beta_2^{(1)} + V_{\mathrm{II}}^{(2)}\beta_2^{(2)}. \tag{8.4b}$$

These equations yield the following relationships for the mass fractions of the first component in the equilibrium phases.

$$w_1^{(1)} = \beta_1^{(1)}/(\beta_1^{(1)} + \beta_2^{(1)}) = \frac{m_{1,\mathrm{I}}V_{\mathrm{II}}^{(2)} - m_{1,\mathrm{II}}V_{\mathrm{I}}^{(2)}}{V_{\mathrm{II}}^{(2)}(m_{1,\mathrm{I}} + m_{2,\mathrm{I}}) - V_{\mathrm{I}}^{(2)}(m_{1,\mathrm{II}} + m_{2,\mathrm{II}})}\,, \tag{8.5a}$$

$$w_1^{(2)} = \beta_1^{(2)}/(\beta_1^{(2)} + \beta_2^{(2)}) = \frac{m_{1,\mathrm{II}}V_{\mathrm{I}}^{(1)} - m_{1,\mathrm{I}}V_{\mathrm{II}}^{(1)}}{V_{\mathrm{I}}^{(1)}(m_{1,\mathrm{II}} + m_{2,\mathrm{II}}) - V_{\mathrm{II}}^{(1)}(m_{1,\mathrm{I}} + m_{2,\mathrm{I}})}\,. \tag{8.5b}$$

The mathematical analysis of the volumetric method was performed by Řehák *et al.* [18]. One of their conclusions is that the method can yield good results on measuring solubilities of liquids with high molar volumes in liquids with low molar volumes. In that event the volumetric method can be used even for measurement of relatively low solubilities.

8.1.4 Indirect Methods

While indirect methods are not intended for the determination of liquid–liquid phase equilibria, the results measured in heterogeneous systems can yield information on these equilibria as a side product. These methods are based on isothermal measurements of certain physical properties of binary solutions in dependence on the concentration. The compositions of the equilibrium liquid phases are given by the intercepts of the linear dependences of the given properties, corresponding to the heterogeneous region, with the dependence of the given property for the homogeneous region. An example is the measurement of the static vapour–liquid equilibrium [19] (Figure 8.8a) and measurement of the concentration dependence of the excess enthalpy $H^E(x_1)$ (Figure 8.8b) in binary systems. In the determination of the vapour–liquid equilibrium by the static method, the dependence of the total pressure on the composition of the liquid phase $P(x_1)$ is measured at constant temperature in both the homogeneous and heterogeneous regions (see also [20]).

Considering the slopes of the measured dependences $P(x_1)$ or $H^E(x_1)$ in the heterogeneous and homogeneous regions, more exact results are usually obtained from mixing calorimetry. In the critical region or at high mutual solubility, static measurement of the vapour–liquid equilibrium and of the concentration dependence H^E cannot be used to determine liquid–liquid equilibria.

8.1.5 Measurement of very Low Mutual Solubility

Very low concentrations are understood to be those that are less than $3 \cdot 10^{-4}$ mole fraction units. These concentrations are typical for aqueous solutions of non-polar organic substances. Obtaining reliable data for these systems is quite difficult, reflected in the contradictory data of various authors. These systems are characterized by high interfacial tension and high resistance to mass transfer between phases, and therefore the time required for equilibrium

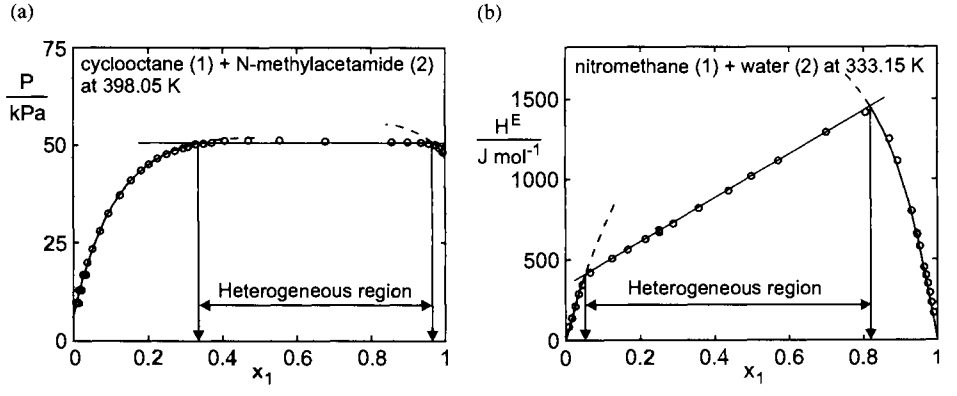

Figure 8.8 Total pressure (a) and heat of mixing, (b) as a function of molar fraction of component 1 at constant temperature. (Redrawn with permission from De Haan *et al.* [19]. Copyright 1995, American Chemical Society.)

saturation by stirring in an equilibrium cell is usually quite long, up to 100 h, and the consequences of any contamination of the second phase in taking samples are very serious.

The aqueous phase also frequently contains suspended organic phase, which must be allowed to settle or be centrifuged. At very low solubility, the content of dissolved substance cannot be determined directly (*e.g.* by chromatography), but rather enrichment must be carried out, *e.g.* usually by extraction or adsorption on solid adsorbents or by stripping [21]. This experimental part is purely analytical in nature and thus the reader is referred to the original literature dealing in detail with this subject [22,23].

If only the solubility of the substance in water is to be determined, a dynamic saturation column method (generator-column technique) can be employed [24–26] (see also Section 8.2.4.3).

Dynamic Flow Method

The above difficulties in measuring low mutual solubilities led to the construction of flow apparatuses. Figure 8.9 depicts the apparatus of Chen and Wagner [27], whose construction follows from the works of Thies and Paulaitis [28]. A micro-pump with flow rate of (46–460) $cm^3 \cdot h^{-1}$ continuously pumps water and the organic component in the selected ratio into the equilibrium cell. To achieve good mixing the mixture passes through a stainless-steel tube (0.635 cm o.d.). The first part of this tube, which acts as a static mixture, is 1.2 m long and contains a cut and twisted thin strip of stainless steel. The second part of this tube, which is 3.6 m long, is filled with glass beads of 1.5 mm diameter and

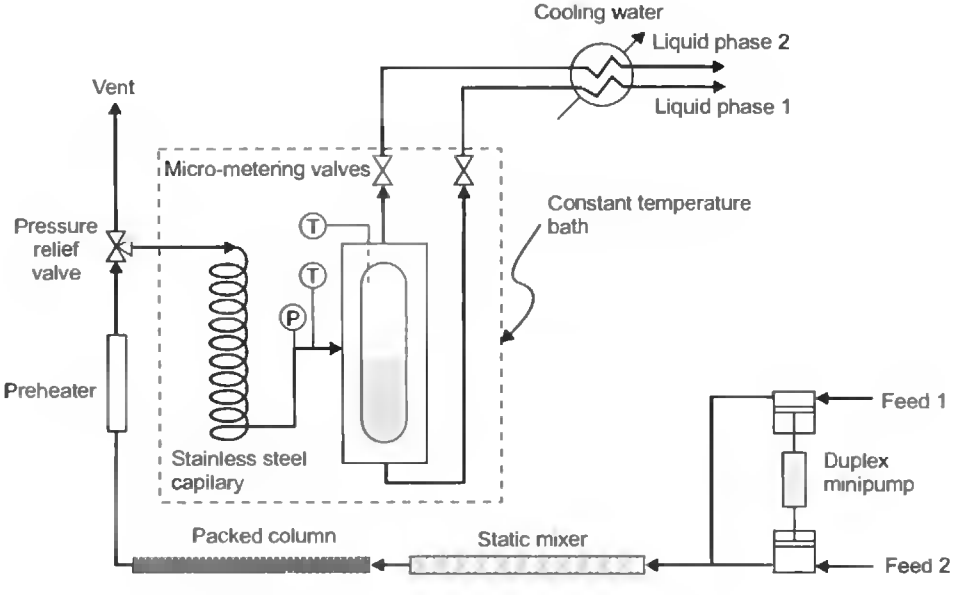

Figure 8.9 Schematic diagram of the apparatus for determining low solubilities by the flow method. (Redrawn with permission from Chen and Wagner [27]. Copyright 1994, American Chemical Society.)

forms the packed column. The end of this tube is fitted with a heating strip to establish the selected preheating of the entering mixture. From this mixing part, the two-phase mixture enters a stainless steel spiral of 10 m length and 0.325 cm o.d. placed in a thermostatted bath (±0.2 K), in which equilibrium is established prior to entering the equilibrium or separation cell (Jerguson JT-40 sight gauge, internal volume 60 cm^3), in which the separation occurs with a retention time of about 1 h. The lighter phase leaves at the top and the heavier at the bottom of the separation cell through micro-metering valves and capillaries into a cooler, and then samples are taken for analysis usually by gas chromatography. Because of the very low concentration of the analyte, further handling of the sample must be very carefully done. Details are described in the work of the same authors [29].

Circulation Apparatus for Solute Vapour Saturation

Sanemasa *et al.* [30] also dealt with the subject of determining liquid–liquid equilibrium in aqueous systems with low mutual solubility of the components. In an attempt to avoid the long period of intense stirring and the subsequent sedimentation of the emulsified organic phase in the aqueous phase, they employed a method of saturation of water by the vapour of the solute suspended by air. It was found that this process of saturation is very fast and reliable. The apparatus is depicted in Figure 8.10a. The air is forced by a diaphragm pump through a saturator filled with the liquid solute and, following tempering, enters the equilibrium cell, in which gradual equilibrium saturation occurs. After the saturation process the aqueous phase is discharged, the solute is extracted by a suitable solvent and analyzed. During discharge of the saturated aqueous phase from the equilibrium cell, the aspirated air also passes through the saturator so that equilibrium pressure of the dissolved component is maintained above the saturated phase. It is apparent from the time dependences, which are depicted in Figure 8.10b, that this is a very fast process. However, this method is not suitable if the dissolved substance has a low volatility.

8.1.6 Measurements in the Vicinity of the Critical Point

In very precise measurements, especially for the purpose of determining the critical point (T_c, x_c) and the critical exponents, basically two approaches can be used. In the first method, the formation of two phases and the position of the meniscus are determined mostly following a temperature step, usually of several mK [31,32]. In the second method, the composition of the conjugated phases is measured *in situ* for prepared mixtures in the vicinity of the critical point. For the dependence on the temperature, a differential refractometer [33] or a magnetic float densimeter [34] is usually used for this purpose. Only a very few of these very demanding measurements, which require extremely precise temperature regulation, have been published. Most experiments have been carried out with systems that exhibit the critical point at ambient temperatures.

If the critical region is sufficiently densely covered by experimental points, the critical temperature can be determined with high precision. However, determination of the critical composition is more difficult, as the dependence of the temperature on the composition is

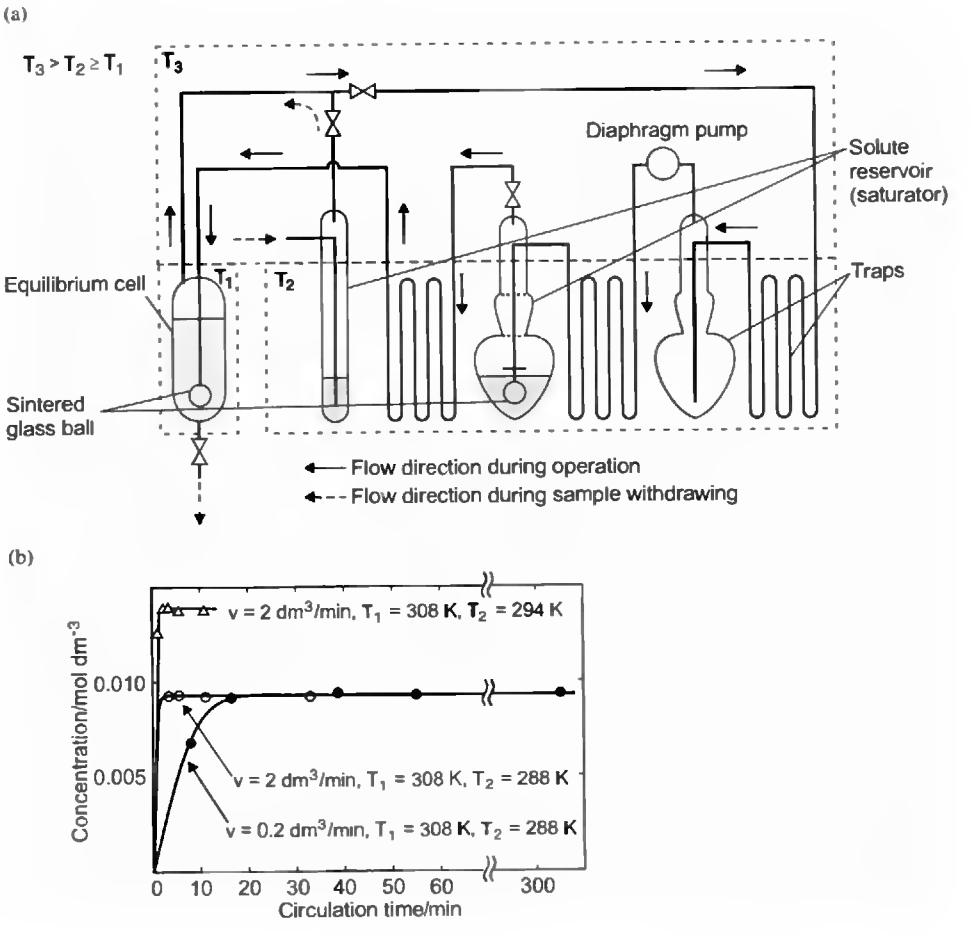

Figure 8.10 (a) Schematic diagram of the apparatus for low solubility determination by saturation with solute vapours, (b) effect of circulation rate (v) on the solubility of benzene. (Redrawn with permission from Sanemasa *et al.* [30], Courtesy of the Chemical Society of Japan.)

usually very small and therefore the binodal is very flat in the critical region. The most suitable procedure for determining x_c is based on studying the position of formation of the meniscus and its vertical motion on a change in temperature for mixtures with various compositions [35]. At the critical composition, the meniscus will be in the centre of the column and its position does not change as the distance from the critical temperature increases slightly. The critical point can be determined relatively precisely by preparing several mixtures in the vicinity of the critical point and measuring the position of the phase boundary formed.

The Cailletet–Mathias rule [2] can also be employed to determine the critical composition x_{ic}:

$$(x_i' + x_i'')/2 = x_{ic}(1 + A\tau), \tag{8.6}$$

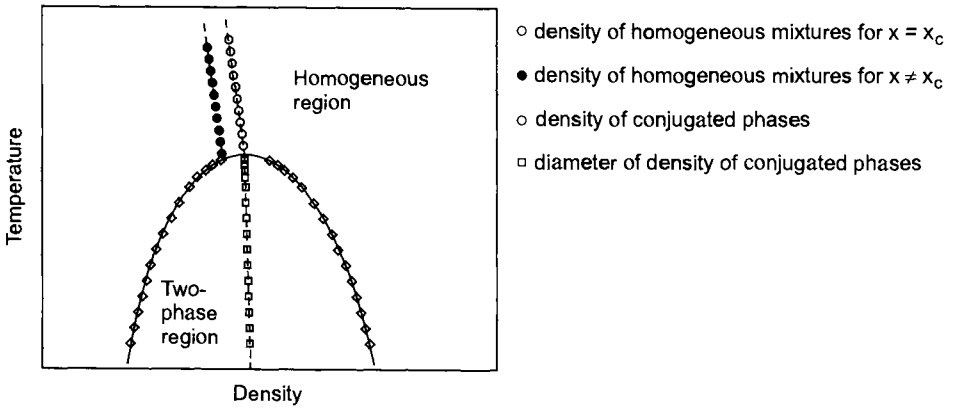

Figure 8.11 Temperature dependence of the densities of conjugate phases and homogeneous mixtures.

where x_i' and x_i'' are mole fractions of the ith component in the conjugated phases, $\tau = (T_c - T)/T_c$ and A is a constant.

Another criterion that can be used to determine the critical composition is the coincidence of the extrapolated average of the densities of the conjugated phases with the density of the mixture in the homogeneous region at the critical point [36] (Figure 8.11). The density of the homogeneous phase can be measured using a vibration density meter.

8.1.7 Test System

Hefter *et al.* [10] recommend the system {water (1) + butane-2-ol (2)} for testing the quality of the apparatus used to determine the liquid–liquid equilibrium. Not only does the two-phase region in this system extend to the higher temperatures (UCST = 386.9 K, $x_{1c} = 0.870$), but it also exhibits a complicated 'Ω' equilibrium curve shape.

8.2 Liquid–Liquid Equilibrium in Ternary and Multi-Component Systems

8.2.1 Determination of the Equilibrium Curves in a Ternary or Pseudo-Ternary System

Although the binodal curve, without knowledge of the tie lines, does not provide complete information on phase equilibrium, as it only delimits the heterogeneous region, its importance is indubitable. When further properties of the studied system are known, the binodal curve can be utilized for determining the compositions of the conjugated phases. Similarly, it is useful to have information on the extent of the heterogeneous region for effective application of the direct analytical method. Determining the binodal curve at laboratory

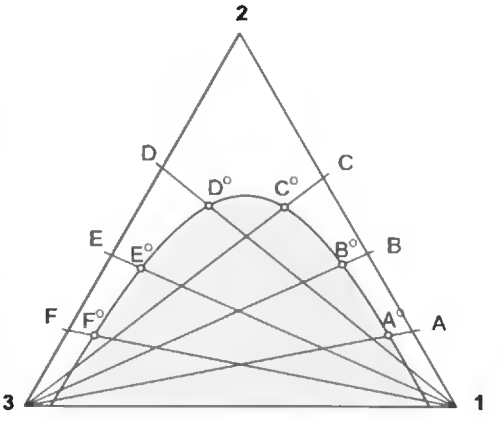

Figure 8.12 Determination of the binodal curve by the titration method.

temperature is fast and, when carried out carefully, sufficiently accurate. This measurement is most frequently carried out by the turbidimetric method or the titration method. A number of mixtures are prepared of components that have unlimited miscibility (1 + 2) or (2 + 3) (Figure 8.12). To a known amount of the mixture, the third or first component is added until turbidity is formed. For example, if we start with mixture B, addition of component 3 leads to a change in the composition along section $\overline{B3}$ and when turbidity is formed a mixture is obtained whose composition corresponds to point B^0. If we start with mixture F and add component 1, point F^0 is determined. As it is necessary to reach a certain excess of the second phase in the formation of turbidity, Rifai and Durandet (see Section 8.1.2, Figure 8.6) proposed a method in which the volume of the separated phase in dependence on the amount of added component is measured. The result is then extrapolated to zero volume of the phase formed. It should be pointed out here that, in contrast to a binary system, the volume of phase formed in the ternary system is not exactly a linear function of the added amount of the third component. The method of Rifai and Durandet has relatively low precision in the vicinity of the critical point, where the volume of the phase being formed depends greatly on the amount of component added and the phases are quite hard to separate.

In order to gain a concept of the binodal surface in the T–x_1–x_2 diagram, the following procedure is useful and is called the cloud-point method. Several mixtures are prepared with a constant ratio of components 1 and 3 and the solution temperature is measured as a function of added amount of component 2. The T–x_2 curves are thus obtained for the pseudo-binary mixture, from which the binodal curves can usually be evaluated by graphical [37] or mathematical interpolation for the selected temperature. A disadvantage lies in the fact that a relatively large amount of experimental data has to be determined.

In order to create a concept of the binodal surface in a quaternary (*i.e.* four-component) system, the pseudo-ternary equilibrium curves are determined [38]. They correspond to sections of the binodal surface with planes in which the molar ratio of two suitably selected components is retained (Figure 8.13). These sections are usually determined by titration. It should be noted that, in contrast to the ternary system, the compositions of the conjugated

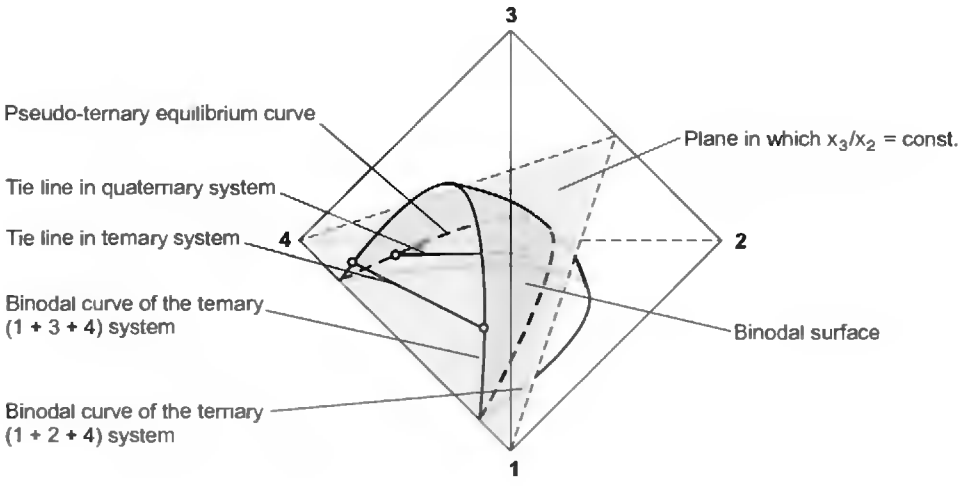

Figure 8.13 Diagram of a quaternary system with one heterogeneous region and the corresponding binodal surface and a pseudo-ternary equilibrium curve.

phases in a quaternary system generally are located on two different pseudo-ternary equilibrium curves. For this reason, these curves are not binodal curves.

8.2.2 Direct Analytical Method

Liquid–liquid equilibria in systems containing three or more components can be determined practically only by the direct analytical method. In this case, the procedure is the same as in the binary system. First, the heterogeneous mixture is mixed intensely for a sufficiently long period of time at constant temperature. After complete separation of the phases, samples are taken for analysis. From an analytical point of view, conditions are more complex than in a binary system, as it is necessary to determine at least two mole fractions in each phase. In general, there are $(n - 1)$ mole fractions in each phase, where n is the number of components. A combination of various physical and chemical methods is used for the analytical determination. Gas and liquid chromatography or a combination of measurement of the density and the refractive index, etc., can be used successfully in these cases. In order for it to be unnecessary to carry out analyses in the immediate vicinity of the equilibrium curves, where there is a danger that the sample will split into two phases, the analytical determination is carried out after dilution with a known amount of one of the components. This also decreases the necessary calibration range. If work is done with substances that are below the normal boiling point under the experimental conditions, the apparatus in Figure 8.1b can be used.

A sophisticated apparatus for studying liquid–liquid-phase equilibria in multicomponent systems was constructed by Huemer *et al.* [39]. The main characteristics of this apparatus (Figure 8.14) are the simultaneous measurement of equilibrium in several cells with the possibility to work at temperatures above the normal boiling point of the mixture and the measurement of the densities of the conjugated phases. The glass equilibrium cells

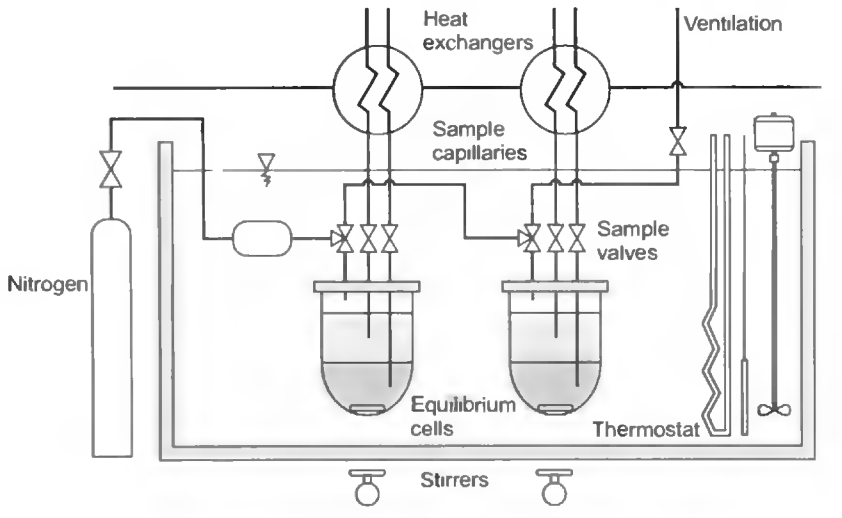

Figure 8.14 Apparatus for measuring liquid–liquid equilibria by the direct analytical method in multi-component systems above their boiling points [39].

are placed in a thermostat and hermetically closed with stainless steel lids fitted with two sampling capillaries ending at different heights in the equilibrium cell to allow sampling of the upper and lower equilibrium phases. The sampling capillaries are closed by a valve. The equilibrium phases are transported by the sampling capillary by over-pressure of an inert gas (nitrogen, 0.1–0.3 MPa), brought into the cell by a capillary, which also prevents boiling of the studied mixture at higher temperatures.

8.2.3 Determination of the Tie Lines in a Ternary System using the Binodal Curve

If the shape of the binodal curve is known along with other properties of this curve, *e.g.* the refractive index, density, etc., it is possible, following measurement of this property in the equilibrium phases, to determine their positions on the binodal curve and thus to determine the tie lines. It is sufficient to determine the composition of only one of the components in both phases for it to be possible to determine their compositions. It is especially easy to use this procedure in cases where one of the components is 'easy' to determine (*e.g.* CH_3COOH by titration with NaOH or using the Karl–Fischer method for water, etc.).

Methods have also been proposed that permit determining the tie lines without analysis. The simplest is the method based on the mass balance and the lever rule following from it. A heterogeneous mixture is prepared with a composition corresponding to point N (Figure 8.15). The two coexisting phases in a thermostatted-separating funnel are separated and then weighed. Assume, for example, the phase that is richer in component 3 is present in twice the amount of that richer in component 1. An auxiliary scale is prepared for the evaluation, in this case in a ratio of 1:2 (Figure 8.15). The zero point of this scale is

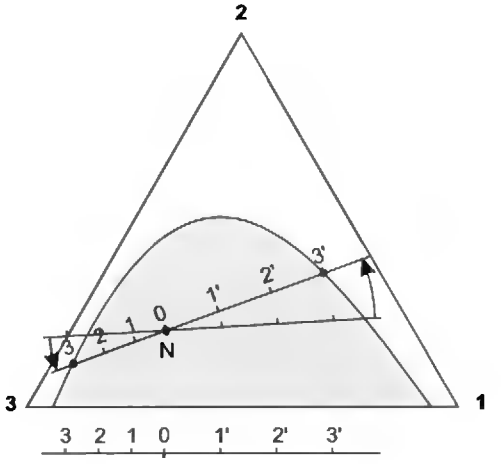

Figure 8.15 Application of the lever rule for determining the composition of the equilibrium phases (tie lines) when the binodal curve is known.

located as point N. The scale is rotated around point N until a position is found where the same numerical value is obtained on both branches of the scale at the points of intersection with the binodal curve. It is necessary to ensure that the binodal curve is plotted in mass fractions, as the weights of the two phases are compared in the experiment.

Another method with graphical plotting based on knowledge of the shape of the binodal curve, recommended by Newsham and Ng [40] and originally proposed by Smith [41], is not extensively used at the present time.

It is experimentally not simple to determine the composition corresponding to the critical point in a ternary system at constant temperature and pressure. Coolidge (see Francis [35]) recommends that two triangles be constructed over each tie line, with sides parallel to the sides of the concentration triangle. A smooth curve connecting the apices of the triangles intersects the binodal curve in the critical point (Figure 8.16). For an asymmetrical system, the curve obtained intersects the binodal curve at a small angle and therefore determining the intercept can be quite imprecise. In this case, it is preferable to construct isosceles triangles above and below the tie line, with sides equal to 60–75 per cent of the length of the tie line according to the size of the triangle.

8.2.4 Determining of the Distribution (Partition) Coefficient

The distribution coefficient of a solute (*i.e.* substance 2), $K_c = c_2^{(1)}/c_2^{(3)}$, is the ratio of the concentrations of this substance in the coexisting equilibrium phases in a system that, in addition to the solute, contains solvents 1 and 3 with limited miscibility. Another definition uses mole fractions and the symbol $K_x = x_2^{(1)}/x_2^{(3)}$. Thus, this is a three-component system and the value of K_c is, in general, dependent on the temperature and composition. The effect of the pressure can be neglected. Measurements carried out at very low concentrations of the solute, namely 10^{-3} mol · dm^{-3}, or extrapolation to zero concentration c_2, can be employed to

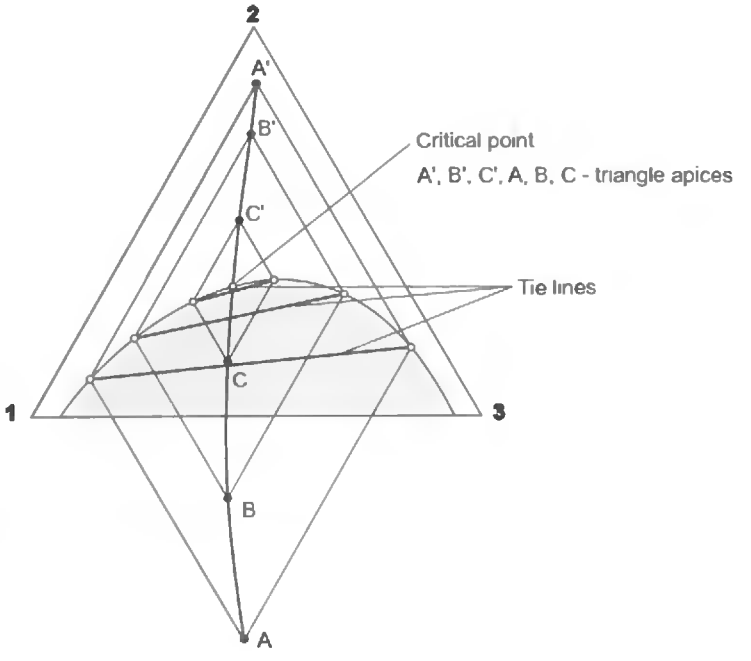

Figure 8.16 Determination of the critical point in a ternary heterogeneous system by the Coolidge method.

determine the limiting value of K_c^{∞}, the Nernst constant. The greatest number of experimental values of distribution coefficients or partition coefficients was determined for various components in {organic solvent (1) + water (3)} systems. Applications in the fields of biology and environmental chemistry very frequently require measurement of the distribution coefficients of substances between {1-octanol (1) and water (3)}, denoted K_{OW}, which depend on the hydrophobicity and biological activity of the solute. The following methods to determine K_{OW}, will be demonstrated for although they have more general applicability [42–44].

Shake-Flask Method

The shake-flask method is historically one of the oldest procedures that, similar to LLE determination, is a direct analytical method. A suitable amount of the solute is added to a heterogeneous mixture of two solvents 1 and 3, and the system is thoroughly mixed (or shaken) at constant temperature until equilibrium is established. Following complete separation of the phases (sometimes using a centrifuge), samples of the phases are taken for analysis. As very low concentrations are involved, the concentration of the solute is frequently determined photometrically or chromatographically (GC or HPLC), or using isotopic labelled components. It should be pointed out here that a large number of distribution coefficients introduced in the older literature were determined in the laboratory at unspecified temperature. In cases where the distribution coefficient is very high, the content of the solute in the aqueous phase cannot

usually be determined directly. In this case, the solute is first extracted from a sample of the aqueous phase by suitable solvent and then the extract is analyzed. The method cannot be used for very high distribution coefficients, *viz.* for $\log K_{OW} < 5.5$ [43]. A disadvantage of the method lies in its tediousness and the formation of colloidal emulsions in the aqueous phase.

Slow-Stirring Method

In this method [45], about 600 cm^3 of water is mixed in a 1000 cm^3 glass-thermostatted cell with 30 cm^3 of 1-octanol, in which the solute was previously dissolved. This mixture is then left for 3–5 days with slow stirring (150 rpm) at constant temperature to establish equilibrium. Slow stirring is intended to prevent the formation of a colloidal emulsion of the organic phase in water. The concentration of the solute is determined using a suitable analytical method usually combined with its extraction from the aqueous phase.

Generator-Column Method

In addition to measurement of the solubility of substances in water, the generator-column method is also used to determine the distribution coefficient K_{OW} [46,47]. The generator column shown in Figure 8.17 consists of a thermostatted tube (length 20–40 cm, 6 mm o.d.) filled with a solid support (*e.g.* Chromosorb W–HP, 100–120 mesh), whose surface is previously saturated with about 1 per cent (by wt) solution of the solute in 1-octanol. Then water is forced through the generator column at a velocity of 20 $cm^3 \cdot h^{-1}$ and collected as the aqueous phase in a collector. An exactly known amount of extraction solvent is present in the collector.

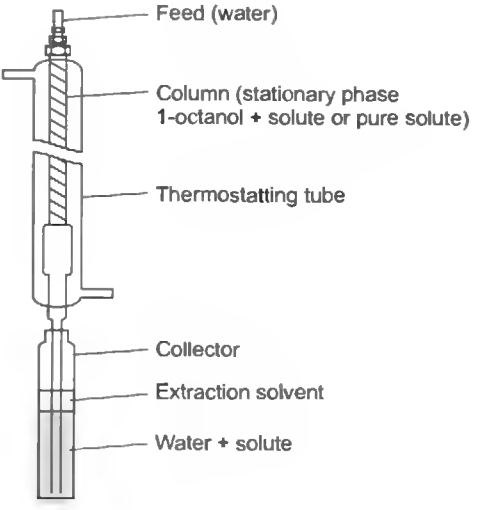

Figure 8.17 Generator column for determining distribution coefficients or aqueous solubility of solutes. (Redrawn with permission from May *et al.* [47]. Copyright 1983, American Chemical Society.)

After collection of a certain amount of aqueous phase in the collector, whose amount is determined by weighing, the content of the collector is thoroughly shaken and the extract is subjected to chromatographic analysis. The evaluation of K_{OW} also requires accurate analysis of the solute in 1-octanol solution. This method is suitable for substances with high K_{OW} values.

Counter-Current Chromatography

Counter-current chromatography (CCC) was developed by Ito *et al.* [48]. The CCC employs two immiscible liquid phases, one of which constitutes the stationary phase and the other the mobile phase. The stationary phase is fixed in the column by centrifugal force. The column consists of a Teflon tube, with a length of approximately 30 m and 1.6 mm i.d., wound around the rotor of a centrifuge operating at 1000 rpm. The mobile phase is continuously added to the column (*e.g.* at 2 $cm^3 \cdot min^{-1}$) by a feed pump. The solute is injected in the same way as in classical liquid chromatography. The column is connected to a spectrophotometric detector, which is employed to evaluate the retention time of the solute. Because of the centrifugal force, the mobile phase passes through the stationary phase in the form of small drops, leading to intensification of the distribution process of substance 2 between solvents 1 and 3. The distribution coefficient is calculated from the relationship

$$K_{OW} = \frac{V_R - V_W}{V_O}, \tag{8.7}$$

where V_O and V_W are the volumes of 1-octanol and water in the column, which correspond to the given experimental conditions of rpm, flow rate and column geometry and that are set when bringing the column into operation. The V_R is the retention volume of the solute, which is calculated from its retention time and the flow rate of the mobile phase.

Figure 8.18 depicts the principle of two types of commercially available CCCs [49,50]:

(a) The hydrostatic equilibrium system (HSES), in which the column rotates around a single axis (Figure 8.18a) and is thus subject to a constant centrifugal force.
(b) The hydrodynamic equilibrium system (HDES), in which the column rotates around two axes (Figure 8.18b) and is thus subject to a variable centrifugal force. This leads to even better mixing of the stationary and mobile phases and thus a more effective distribution process.

The CCC is an absolute method, is relatively fast and can be used for $\log K_{OW} < 4.5$.

Reversed-Phase High-Pressure-Liquid Chromatography (RP-HPLC)

Reversed-phase high-pressure-liquid chromatography (RP-HPLC) is a fast and inexpensive method but a relative method to determine of the distribution coefficient and can be used with high values of $\log K_{OW}$ [51,52]. Reversed phase here means that the mobile phase is water (but in general, a polar solvent) and that the fixed stationary phase is 1-octanol (in general, a non-polar phase). It is based on the existence of a relationship between the distribution coefficient and the capacity factor. In the procedure, parameters a and b in the

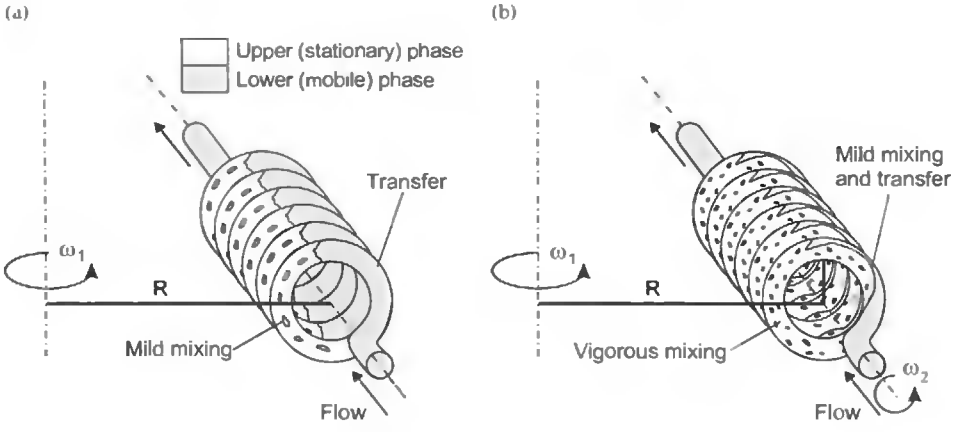

Figure 8.18 Basic CCC systems: (a) the hydrostatic equilibrium system (HSES), (b) the hydrodynamic equilibrium system (HDES). (Redrawn with permission from Foucault [49]. Copyright 1998, American Chemical Society.)

linear relationship between the logarithms of the distribution coefficient K_{OW} and the capacity factor k' are first determined using several reference substances:

$$\log K_{OW} = a + b \log k'. \tag{8.8}$$

The capacity factor k' is given by

$$\log k' = \log \frac{(t_R - t_0)}{t_0}, \tag{8.9}$$

where t_R and t_0 are the retention times of the substance R and an inert substance, respectively. The reference substances used, with known K_{OW} value, should be chemically as similar as possible to the solute.

Distribution Coefficient through the Experimental Limiting Activity Coefficients

The distribution coefficient at infinite dilution can be estimated in an indirect manner using the limiting activity coefficients γ_2^∞ of substance 2 in the individual pure solvents 1 and 3 by the relationship [2]

$$K_x^\infty = \lim_{x_2 \to 0} \frac{x_2^{(1)}}{x_2^{(3)}} \approx \frac{(\gamma_2^\infty)_3}{(\gamma_2^\infty)_1}, \tag{8.10}$$

which assumes that the mutual solubility of components 1 and 3 is very low.

8.3 Basic Monographs

The thermodynamic basis of liquid–liquid equilibrium can be found in the monographs of Haase [53], Prausnitz *et al.* [54,55], Novák *et al.* [2], Renon *et al.* [56] and Storonkin [57]. Experimental determinations of solubilities generally are summarized by Hefter and Tomkins [58]. Data on liquid–liquid equilibrium are given by Sorensen and Arlt [59], Kertes [60] and Kehiaian [61]. Data on aqueous solubility of organic substances were collected by Yalkowsky and Dannenfelser [62], Yalkowsky and He [63] and Freier [1]. Octanol–water partition coefficients were collected by Sangster [64]. Estimation methods for aqueous solubility and octanol–water partition coefficients are given in the monograph by Baum [65].

References

1. Freier, R.K., *Aqueous Solutions, Vols 1* and *2*, Walter de Gruyter, Berlin, 1976.
2. Novák, J.P., Matouš, J. and Pick, J., *Liquid–Liquid Equilibria,* Elsevier, Amsterdam, 1987.
3. Řehák, K., *Chem. Listy.* **93**, 583–585, 1999.
4. Lohmann, J., Roepke, T. and Gmehling, J., *J. Chem. Eng. Data* **43**, 856–860, 1998.
5. Mitchel, J. Jr., *Water*, in *Treatise on Analytical Chemistry Part II, Vol 1*, Section 1, I.M. Kolthoff, P.J. Elving and E.B. Sandel, eds., Interscience, New York, pp. 72–197, 1961.
6. Zikmundová, D., Matouš, J., Novák, J.P., Kubíček, V. and Pick, J., *Fluid Phase Equilibr.* **54**, 93–110, 1990.
7. Matouš, J., Novák, J.P., Šobr, J. and Pick, J., *Collect Czech Chem. Commun.* **37,** 2653–2663, 1972.
8. Schneider, G.M., *Pure Appl. Chem.* **47**, 277–291, 1976.
9. Šobr, J. and Hynek, V., *Sci. Papers Prague Inst. Chem. Technol.* **N2,** 125–132, 1976.
10. Hefter, G.T., Barton, A.F.M. and Chand, A., *J. Chem. Soc. Faraday Trans.* **87,** 591–596, 1991.
11. Ochi, K., Saito, T. and Kojima, K., *J. Chem. Eng. Data* **41**, 361–364, 1996.
12. Ochi, K., Momose, M., Kojima, K. and Lu, B.C.Y., *Can. J. Chem. Eng.* **71**, 982–985, 1993.
13. Heintz, A., Lehmann, J.K. and Wertz, C., *J. Chem. Eng. Data* **48**, 472–474, 2003.
14. Cho, T.H., Ochi, K. and Kojima, K., *Fluid Phase Equilibr.* **11**, 137–152, 1983.
15. Moon, M.H., Ochi, K. and Kojima, K., *J. Chem. Eng. Data* **40**, 468–471, 1995.
16. Rifai, I. and Durandet, J., *Rev. Inst. France Pet. Ann. Combust. Liq.* **17**, 1232, 1962.
17. Hill, A.E., *J. Am. Chem. Soc.* **45,** 1143–1155, 1923.
18. Řehák, K., Voňka, P. and Dreiseitlová, J., *Fluid Phase Equilibr.* **230**, 109–120, 2005.
19. De Haan, A.B., Heine, A., Fischer, K. and Gmehling, J., *J. Chem. Eng. Data* **40**, 1228–1232, 1995.
20. Strotmann, B., Fischer, K. and Gmehling, J., *J. Chem. Eng. Data* **44,** 388–392, 1999.
21. Fichan, I., Larroche, C. and Gros, J.B., *J. Chem. Eng. Data* **44**, 56–62, 1999.
22. Poole, S.K., Dean, T.A., Oudsema, J.W. and Poole, C.F., *Anal. Chim. Acta* **236**, 3–42, 1990.
23. Namieśnik, J., Górecki, T. and Biziuk, M., *Anal. Chim. Acta* **237**, 1–60, 1990.
24. May, W.E., Wasik, S.P. and Freeman, D.H., *Anal. Chem.* **50**, 997–1000, 1978.
25. Dohányosová, P., Dohnal, V. and Fenclová, D., *Fluid Phase Equilibr.* **214**, 151–167, 2003.
26. Dohányosová, P., Sarraute, S., Dohnal, V., Majer, V. and Gomes, M.C., *Ind. Eng. Chem. Res.* **43**, 2805–2815, 2004.
27. Chen, H. and Wagner, J., *J. Chem. Eng. Data* **39**, 470–474, 1994.
28. Thies, M.C. and Paulaitis, M.E., *J. Chem. Eng. Data* **29**, 438–440, 1984.
29. Chen, H. and Wagner, J., *J. Chem. Eng. Data* **39**, 475–479, 1994.
30. Sanemasa, I., Araki, M., Deguchi, T. and Nagai, H., *Bull. Chem. Soc. Jpn.* **55**, 1054–1062, 1982.

31. Nagarajan, N., Kumar, A., Gopal, E.S.R. and Greer, S.C., *J. Phys. Chem.* **84**, 2883–2887, 1980.
32. Beysens, O., *J. Chem. Phys.* **71**, 2557–2565, 1979.
33. Nakata, M., Dobashi, T., Kuwahara, N. and Kaneko, M., *J. Chem. Soc. Faraday Trans. 2*, **78**, 1801–1810, 1982.
34. Greer, S.C., *Ber. Bunsenges. Phys. Chem.* **81**, 1079–1081, 1977.
35. Francis, A.W., *Liquid-Liquid Equilibrium*, Wiley, New York, 1963.
36. Greer, S.C., *Acc. Chem. Res.* **11**, 427–432, 1978.
37. Hradetzky, G. and Lempe, D.A., *Fluid Phase Equilibr.* **69**, 285–301, 1991.
38. Nagata, I., *J. Chem. Eng. Data* **31**, 70–74, 1986.
39. Huemer, H., Woertl, K. and Moser, F., *Fluid Phase Equilibr.* **11**, 311–323, 1983.
40. Newsham, D.M.T and Ng, S.B., *J. Chem. Eng. Data* **17**, 205–207, 1972.
41. Smith, A.S., *Ind. Eng. Chem.* **37**, 185, 1945.
42. Hansch, C., *Acc. Chem. Res.* **2**, 232–239, 1969.
43. Chessells, M., Hawker, D.W. and Connell, D.W., *Chemosphere* **22**, 1175–1190, 1991.
44. Finizio, A., Vighi, M. and Sandroni, D., *Chemosphere* **34**, 131–161, 1997.
45. Paschke, A., Popp, P. and Schueuermann, G., *Fresenius J. Anal. Chem.* **360**, 52–57, 1998.
46. Tewari, Y.B., Miller, M.M., Wasik, S.P. and Martire, D.E., *J. Chem. Eng. Data* **27**, 451–454, 1982.
47. May, W.E., Wasik, S.P., Miller, M.M.,Tewari, Y.B., Brown-Thomas, J.M. and Goldberg, R.N., *J. Chem. Eng. Data* **28**, 197–200, 1983.
48. Ito, Y., Weinstein, M., Aoki, I., Harada, R., Kimura, E. and Nunogaki, K., *Nature* **212**, 985–987, 1966.
49. Foucault, A.P., *Anal. Chem.* **63**, 569–579 A, 1991.
50. Berthod, A. and Bully, M., *Anal. Chem.* **63**, 2512–2519, 1991.
51. Braumann, T., Weber, G. and Grimme, L.H., *J. Chromatogr.* **261**, 329–343, 1983.
52. Kaune, A., Brueggemann, R. and Kettrup A., *J. Chromatogr. A* **805**, 119–126, 1998.
53. Haase, R., *Thermodynamik der Mischphasen*, Springer, Berlin, 1956.
54. Prausnitz, J.M., Lichtenthaler, R.N. and Azevedo, E.G., *Molecular Thermodynamics and Fluid-Phase Equilibria,* PTR, Upper-Saddle River, NJ, 1999.
55. Prausnitz, J.M., Anderson, T.F., Grens, E.A., Eckert, C.A., Hsieh, R. and O'Connell, J.P., *Computer Calculations for Multicomponent Vapor-Liquid and Liquid-Liquid Equilibria,* Prentice-Hall, Englewood Cliffs, NJ, 1986.
56. Renon, H., Asselineau, L., Cohen, C. and Raimbault, C., *Calcul sur Ordinateur des Equilibres Liquide-Vapeur at Liquide-Liquide*, Edition Technip, Paris, 1971.
57. Storonkin, A.V., *Termodinamika geterogennykh sistem*, Izd. Leningr. University, Leningrad, 1967.
58. Hefter, T.G. and Tomkins, R.P.T., eds., *The Experimental Determination of Solubilities, Vol 6*, Wiley Series in Solution Chemistry, Wiley, West Sussex, England, 2003.
59. Sorensen, J.M. and Arlt, W., *Liquid-Liquid Equilibrium Data Collection*, Dechema, Frankfurt, 1979, 1980.
60. Kertes A.S., ed., *Solubility Data Series*, Pergamon Press, Oxford, 1979–1996.
61. Kehiaian, H., ed., *Int DATA Ser, Sel Data Mixtures, Ser A*, TRC, Chem. Dept., A&M University, College Station, 1973.
62. Yalkowsky, S.H. and Dannenfelser, R.M., *Arizona Database*, College of Pharmacy, University of Arizona, Tucson, 1990.
63. Yalkowsky, S.H. and He, Y., *Handbook of Aqueous Solubility Data*, CRC Press, Washington, DC, 2003.
64. Sangster, J., *LOGKOW DATABANK*, Sangster Res. Lab., Montreal, 1993.
65. Baum, E.J., *Chemical Property Estimation. Theory and Application*, Lewis Publishers, Boca Raton, FL, 1998.

9 Condensed Phases of Organic Materials: Solid–Liquid and Solid–Solid Equilibrium

H.A.J. OONK
Faculties of Chemistry and Geosciences
Utrecht University
Utrecht, The Netherlands

J.Ll. TAMARIT
Department of Physics and Nuclear Engineering
Technical University of Catalonia
Barcelona, Spain

Measurement of the Thermodynamic Properties of Multiple Phases
R.D. Weir and Th.W. de Loos (Editors)

9 CONDENSED PHASES OF ORGANIC MATERIALS: SOLID–LIQUID AND SOLID–SOLID EQUILIBRIUM

This chapter is devoted to solid–liquid and solid–solid phase equilibria in systems where two organic components give rise to mixed crystals of the substitutional type. The systems are generally defined as $\{(1 - x)$ mole of substance A $+ x$ mole of substance B$\}$, and some typical phase diagrams, the pressure exerted on the system being constant, are shown in Figure 9.1.

In the case of Figure 9.1a, the two components, A and B, of the system are isomorphous [1–4] and give rise to a continuous series of mixed crystals. In the case of Figure 9.1b, the molecules of A and of B are homeomorphous [5,6] and can replace one another in a crystal lattice; the crystal lattices of A and B, however, being different. In the phase diagram, the *single*-phase field for mixed crystals of the α- and β-types are, necessarily, separated by a $(\alpha + \beta)$ two-phase region. An example is found in the combination of naphthalene and 2-fluoronaphthalene [1,7]. Incidentally, the type of diagram (Figure 9.1b) is also shown by a pair of substances like 1,4-dichlorobenzene and 1-bromo-4-iodobenzene [8]: the two crystalline solids are isomorphous in the sense of having the same crystal structure characteristics, but the degree of molecular homeomorphism is not high enough for a continuous series of mixed crystals. In the phase diagram, the symbols α and β must be replaced by α_{I} and α_{II}. In the case of Figure 9.1c, the two substances have a high degree of molecular homeomorphism and give rise to a continuous series of mixed crystals at temperatures corresponding to the bottom of the phase diagram. The two-phase region is the result of the fact that substance A undergoes a transition from type of solid β to type of solid α. An example is A = 1,4-dichlorobenzene and B = 1,4-dibromobenzene [9].

From the point of view of experimentation, even when polymorphism is absent (see hereafter), equilibria involving mixed crystals are less accessible than equilibria involving only liquid and vapour phases. To make this clear, we consider the phase diagram (Figure 9.1a) as an example. The two important characteristics displayed by the diagram are (i) the change from the low-temperature state of matter, or form of material, to the high-temperature state, and (ii) the fact that the phases in equilibrium have different compositions. In the case of

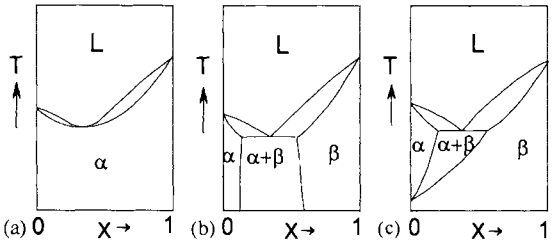

Figure 9.1 Plot of temperature against composition for solid–liquid phase diagrams in systems showing the formation of mixed crystals.

equilibria between liquid and vapour, and as a result of the high degree of mobility of the molecules in these states, the adjustment of the compositions of the phases is a matter of little time. In the case of the equilibrium between mixed crystals and liquid mixtures, the situation is quite different. It comes down to a difference in time needed (i) to realise the change from solid to liquid, and (ii) to adjust the compositions of solid and liquid to their equilibrium values, which amounts to a matter of seconds for the first process (i), against days or weeks for the second process (ii). It corresponds to a difference in time-scale that has its effect on every element of the investigation from sample preparation, via the actual experiment, to the interpretation of experimental data, and the (thermodynamic) processing of the information.

Ideally, mixed crystalline samples, used for investigations, are homogeneous in composition, such as is a liquid mixture, say of water and ethanol. But unlike the liquid mixture, mixed crystalline organic material cannot be prepared just by putting together the components: invariably a fluid phase is required as a medium. That fluid phase can be the liquid or gaseous mixture of the component substances, as well as the solution in a solvent. The use of a fluid medium corresponds to an unfavourable side effect, which amounts to some uncertainty about the degree of homogeneity of the material, because from the equilibrium point of view the transition, from one mixed state to the other, is accompanied by a change in composition. The history of a sample determines its behaviour during the actual experiment. The lower the degree of homogeneity, as a rule, the lower the accuracy of the signals will be.

The immobility of the molecules in the mixed solid state implies that, during an experiment, the occurrence of true thermodynamic equilibrium between coexisting phases is rather the exception than the rule. In spite of this inconvenience, the material 'seems to know' when it should change from one state to the other (item (i) above). In any case, not knowing precisely the equilibrium compositions of the phase means that a dedicated method is needed to extract the pertinent thermodynamic information from the experimental observations.

The crystallographic characterisation of the solid phase(s) is an integral part of research on mixed crystals, in particular, of course, when polymorphism makes its appearance. Ideally, thermodynamic and crystallographic methods are put into action simultaneously. On several occasions, thermodynamic input is needed to give a conclusive interpretation of crystallographic observations, and vice versa. Quite often the substitutional disorder of mixed crystals enhances the occurrence of other kinds of disorder, such as conformational disorder and orientational disorder. The enhanced freedom of molecular movement needs, apart from crystallography, spectroscopic methods to be studied. Viewed the other way round, spectroscopic methods are important tools in arriving at an unambiguous characterisation of the solid state(s).

A complicating and at the same time fascinating element of materials research is the phenomenon of metastability, the occurrence of metastable forms. In the case of mixed crystals, it is often found that a form that is metastable for one of the components becomes stable for the other. Returning to Figure 9.1b, the properties of the β-type of mixed crystals, including pure B, can be used to predict the properties of the β-form of substance A, even if the latter has not yet made its experimental appearance [10–19]. The various aspects of research of mixed crystals, addressed in the preceding paragraphs, will be elaborated in the following sections. From an applied science point of view, mixed crystals offer the opportunity of using composition as a parameter to optimise the properties of a material [20–30].

9.1 Thermodynamic Treatment

9.1.1 The Gibbs Energy Function

At constant pressure, the molar Gibbs energy of a homogeneous mixture in the system {(1 − x) mole of substance A + x mole of substance B} can be represented by the following function of thermodynamic temperature (T) and mole fraction (x),

$$G(T, x) = (1 - x)G^*_A(T) + xG^*_B(T) + RT\,\mathrm{LN}(x) + G^E(T, x). \tag{9.1}$$

The G^*_A and G^*_B represent the molar Gibbs energies of pure A and pure B, respectively; $R = 8.31451\ \mathrm{J \cdot K^{-1} \cdot mol^{-1}}$ is the gas constant; LN(x) is a short notation for

$$\mathrm{LN}(x) = (1 - x)\ln(1 - x) + x \ln x. \tag{9.2}$$

The $G^E(T, x)$ is the excess Gibbs energy or, in other words, the deviation from ideal mixing behaviour. For the thermodynamic treatment of a system whose phase diagram is represented by Figure 9.1a, two functions of the type of Equation (9.1) are needed: one for the liquid mixtures, superscript 'liq', and another for the solid mixtures of the α-type, superscript 'solα'. A third function is needed for a system corresponding to Figure 9.1b; for the solid mixtures of the β-type (superscript 'solβ').

Realising that LN(x) is a standard expression, it is obvious that the thermodynamic properties of a mixture are known when G^*_A and G^*_B are known as a function of temperature, and G^E as a function of temperature and mole fraction. The excess Gibbs energy is conveniently represented by the formula

$$G^E(T, x) = A\left(1 - \frac{T}{\theta}\right)x(1 - x)[1 + B(1 - 2x)], \tag{9.3}$$

to which we will refer as the $AB\theta$ formula, or model. The function has three system-dependent parameters, A, B and θ. The parameter A, with the dimension of energy, is a measure of the magnitude of the excess function. The dimensionless parameter B is a measure of the asymmetry of the function with respect to $x = 0.5$. The parameter θ, with the dimension of temperature, is a measure of the temperature dependence of the excess Gibbs energy. In terms of the $AB\theta$ model, the expressions for the excess enthalpy (H^E, the enthalpy of mixing) and the excess entropy (S^E) are

$$H^E(T, x) = H^E(x) = Ax(1 - x)[1 + B(1 - 2x)] \tag{9.4}$$

and

$$S^E(T, x) = S^E(x) = \frac{A}{\theta}x(1 - x)[1 + B(1 - 2x)]. \tag{9.5}$$

Moreover, in the model, the excess enthalpy and the excess entropy are independent of temperature, and it implies that the excess heat capacity is zero.

In terms of Equations (9.1) and (9.3), the expressions for the partial molar Gibbs energies, *i.e.* the chemical potentials of the components A and B are

$$\mu_A\left[\equiv G - x\frac{\partial G}{\partial x}\right] = G_A^* + RT\ln(1-x) + x^2\,[G_1 + G_2(3-4x)] \qquad (9.6a)$$

and

$$\mu_B\left[\equiv G + (1-x)\frac{\partial G}{\partial x}\right] = G_B^* + RT\ln x + (1-x)^2\,[G_1 + G_2(1-4x)]. \qquad (9.6b)$$

Without disturbing the description of the systems, read, without appreciably affecting the interpretation and processing of experimental data, one can also neglect the heat capacities of the pure components A and B. It implies that

$$G_{A,B}^*(T) = H_{A,B}^*(T) - TS_{A,B}^*(T), \qquad (9.7)$$

where H_i^* represents the molar enthalpy and S_i^* the molar entropy, can be written as

$$G_{A,B}^*(T) = H_{A,B}^* - TS_{A,B}^*, \qquad (9.8)$$

which is a linear function of temperature. The change from Equation (9.7) to Equation (9.8) comes down to observing that, over the relatively small temperature interval of the change of state, the enthalpies and entropies of the components are considered as constants.

9.1.2 The Lowest Possible Gibbs Energy

In Figure 9.2, the molar Gibbs energy, Equation (9.8) as a function of temperature, is plotted for two forms, solid α and liquid, of substance B. The two functions intersect at T_B^0, the melting point of solid α. For $T < T_B^0$, the liquid will change spontaneously into solid α, which corresponds to lowering the Gibbs energy, and for $T > T_B^0$, solid α will change spontaneously into liquid.

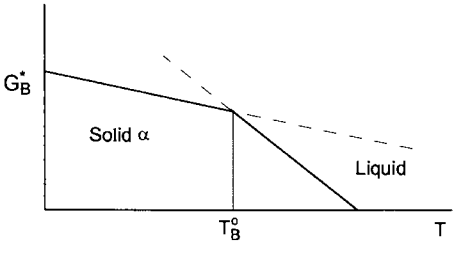

Figure 9.2 Plot of the molar Gibbs energy against temperature for solid α and liquid of pure substance B.

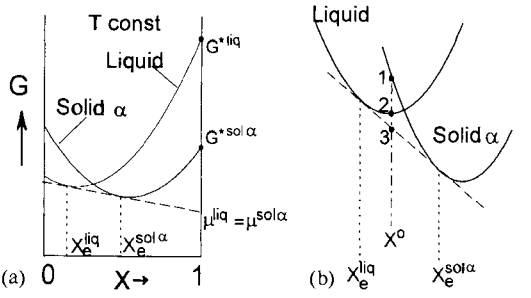

Figure 9.3 (a) Plot of molar Gibbs energy versus mole fraction at a given constant temperature for liquid mixtures and mixed crystals of type α. (b) Enlarged part of Figure 9.3a. The dots represent molar Gibbs energies of a sample of overall composition x^o: 1, if it were completely solid; 2, if it were completely liquid; 3, for a coexisting combination of a liquid and a solid phase.

The melting temperature, T_B^0, is the solution of the equation

$$G_B^{*sol\alpha}(T) = G_B^{*liq}(T), \tag{9.9}$$

or in the difference notation

$$\Delta_\alpha^{liq} G_B^*(T)[\equiv G_B^{*liq}(T) - G_B^{*sol}(T)] = 0. \tag{9.10}$$

In Figure 9.3a, the situation is shown, where for a given constant temperature, the molar Gibbs energies as a function of x are plotted for liquid mixtures, and for the α-form of mixed crystals of the two substances A and B.

The temperature is selected such that the two functions intersect one another. The points of contact of the common tangent line, drawn to the two curves, have mole fractions that are indicated as x_e^{liq} and $x_e^{sol\alpha}$. For an experimental sample containing both A and B and kept at the selected constant temperature, and having an overall mole fraction (x^o) smaller than x_e^{liq}, the lowest Gibbs energy is obtained when the sample is entirely liquid. Likewise for $x^o > x_e^{sol\alpha}$, the lowest possible Gibbs energy corresponds to homogeneous mixed crystalline material of composition x^o.

For $x_e^{liq} < x^o < x_e^{sol\alpha}$, the lowest possible Gibbs energy is obtained for coexisting solid and liquid phases having compositions of $x_e^{sol\alpha}$ and x_e^{liq}, respectively; see Figure 9.3b.

The amounts of material in the two coexisting phases are related by the Lever rule, *viz.*

$$\frac{n(sol\alpha)}{n(liq)} = \frac{x_e^{liq} - x^o}{x^o - x_e^{sol\alpha}}. \tag{9.11}$$

In terms of the chemical potentials of A and B, μ_A and μ_B, the compositions of the coexisting phases, x_e^{liq} and $x_e^{sol\alpha}$ are the solution, for the selected temperature, of the two equations

$$\mu_A^{liq}(T, x^{liq}) = \mu_A^{sol\alpha}(T, x^{sol\alpha}), \tag{9.12a}$$

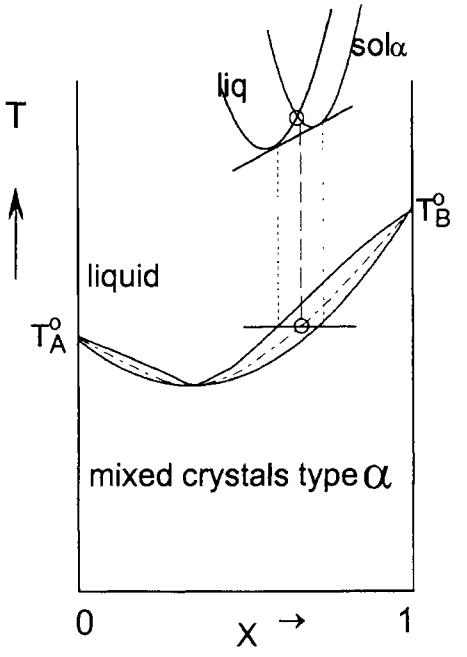

Figure 9.4 Solid–liquid phase diagram with temperature plotted against mole fraction. The relation is shown between the isothermal Gibbs energy section and characteristic points of the phase diagram. These points are on the *solidus*, *liquidus* and EGC (dash-dotted curve).

$$\mu_B^{liq}(T, x^{liq}) = \mu_B^{sol\alpha}(T, x^{sol\alpha}). \tag{9.12b}$$

The loci in the $T-x$ plane of the points of contact, *i.e.* the complete solution of the two Equations (9.12a) and (9.12b), are two curves which are named *solidus* and *liquidus*; see Figure 9.4. The third curve, which is drawn in Figure 9.4 as the dash-dotted line, is the locus of the points of intersection of the two Gibbs energy functions. The curve is named Equal-G Curve (EGC) [31] and it is the solution of the equation

$$G^{liq}(T, x) = G^{sol\alpha}(T, x). \tag{9.13}$$

In the $T-x$ plane, the position of the EGC is an intermediate one, between *liquidus* and *solidus*.

9.1.3 Limiting Cases of Experimentation

From the point of view of experimentation, there is an essential difference between the case implied in Figure 9.2 and the case implied in Figure 9.3, which is a difference that

has far-reaching consequences. For a pure substance, the case of Figure 9.2, the transition from solid to liquid is a quasi-instantaneous event, and it means that it is relatively easy to realise the equilibrium between the solid and the liquid phase. In the case of Figure 9.3, on the other hand, and assuming that an amount of mixed crystalline material is brought to and kept at the selected temperature, there is an amount of time needed to reach the situation of minimal Gibbs energy. The time needed depends on the nature of the system, the phases and also the experiment. The time required may be many times larger than the time the investigator wishes to spend on the experiment. In the context of these observations, one might distinguish between two extreme experimental situations of heating a mixed crystalline sample until it has completely melted. In the first situation, the experiment is carried out at infinitesimal speed, and, for the material selected, the molecules have a finite mobility. Assuming that the sample is perfectly homogeneous, it will start to produce liquid at the *solidus* temperature. The last amount of solid will disappear at the *liquidus* temperature and during the process of melting when there is enough time to adjust the composition of the solid phase by re-crystallisation via the liquid phase. In the converse situation, there is no mobility in the solid state, and the heating rate is sufficiently high that the solid is forced to produce liquid of the same composition during the complete process of melting. In this situation, the material is forced to behave like the pure components: the Gibbs energy change as a function of temperature is just like Figure 9.2, and the material will change into liquid, the moment the point of intersection is reached. In this situation, therefore, the whole sample will melt at the EGC temperature!

As a result, in work on organic mixed crystals special attention should be given to the interpretation and analysis of temperatures observed in heating experiments. The observed temperatures of beginning and end of melting may deviate, to a certain extent, from the *solidus* and *liquidus* temperatures corresponding to minimal Gibbs energy. In spite of this, the average of the observed temperatures is expected to be in the vicinity of the EGC.

9.1.4 Analysis of the Phase Diagram

One of the main objectives of the research, dealt with in this chapter, is the determination of the thermodynamic mixing properties, *viz.* the determination of the A, B and θ values of the various mixed crystalline forms, such as solid α and solid β, of the systems studied. The sources of experimental information are phase diagram data and heat effects determined by calorimetry. To realise the goal set, we start from the assumption that the thermodynamic properties of the pure components, and, also, the thermodynamic mixing properties of the liquid state, are known. In addition to this, the assumption is made that the excess Gibbs energy of the liquid mixtures is too small to have a noticeable influence on the determination of the mixing properties of the mixed solid state. At this point, we will limit ourselves to the analysis of phase diagram data. The details of the calorimetry are given in Section 9.2.

In Figure 9.5, two cross-sections are shown of the excess Gibbs energy function defined by Equation (9.3), the $AB\theta$ model. At this point, a few observations about the

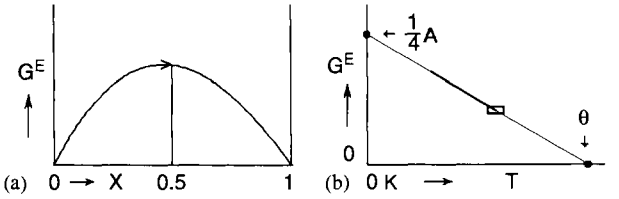

Figure 9.5 Cross-sections of the excess Gibbs energy function defined by Equation (9.3): (a) at constant temperature as a function of mole fraction; (b) for the equimolar mixture as a function of temperature.

function and its use are appropriate. The choice of the first and second component, *i.e.* the substances A and B, respectively, will be considered first. In most of the systems studied, A and B are members of a chemically coherent group of substances, such as the n-alkanes. If so, substance B invariably is the one with the larger molecules. As an example, consider A = hexadecane and B = octadecane. In those cases, the parameter B has a positive value, typically in the vicinity of $B = 0.15$, and it implies that the maximum in Figure 9.5a lies at the left-hand side of $x = 0.5$. Next, the model is such that the excess enthalpy, Equation (9.4), the enthalpy of mixing, is identical with the excess Gibbs energy at $T = 0\,\mathrm{K}$. The equimolar enthalpy of mixing is equal to 0.25 times the value of the A parameter, see Figure 9.5b. In other terms, if a plot is made of G^{E} values as a function of T, the excess enthalpy, H^{E}, can be plotted on the ordinate axis, *i.e.* the axis $T = 0\,\mathrm{K}$.

Let us now suppose that the small rectangle in Figure 9.5b corresponds to the transition range of the form implied, to another form, or to liquid. The range is relatively small and it means that the excess Gibbs energy does not change very much. The consequence, taking into account the experimental uncertainties, is that the temperature characteristics of the transition can be used to determine G^{E} for the mean temperature, T_{m}, of the range, but should not be used to determine the dependence of G^{E} on temperature. To underline this, we write

$$G^{\mathrm{E}}(T = T_{\mathrm{m}}, x) = x(1 - x)\{G_1(T = T_{\mathrm{m}}) + G_2(T = T_{\mathrm{m}})(1 - 2x)\}, \qquad (9.14)$$

the G_1 and G_2 being the parameters that can be derived from the data.

The relation between G_1 and G_2 and the parameters A, B, θ is

$$G_1 = A(1 - T_{\mathrm{m}}/\theta), \qquad (9.15a)$$

$$G_2 = AB(1 - T_{\mathrm{m}}/\theta). \qquad (9.15b)$$

Depending on the nature and the quality of the data, the actual derivation of the parameters G_1 and G_2 from phase diagram data can be realised by either of the two approaches detailed hereafter.

Before doing so, we introduce two operators Δ and Δ_e. The operator Δ is used in the manner of

$$\Delta Z = Z^{\beta} - Z^{\alpha}, \quad \text{for } x^{\beta} = x^{\alpha} = x;\ \alpha = \text{solid } \alpha;\ \beta = \text{solid } \beta, \text{ or liquid.} \tag{9.16}$$

The condition $x^{\beta} = x^{\alpha}$ does apply only if the property Z is a function of x: the operator is also used for form-dependent properties that are independent of composition; *e.g.* $\Delta G_1 = G_1^{\beta} - G_1^{\alpha}$. The operator Δ_e is used in the manner

$$\Delta_e Z = Z^{\beta}(x = x_e^{\beta}) - Z^{\alpha}(x = x_e^{\alpha}), \tag{9.17}$$

where x_e^{α} and x_e^{β} are the equilibrium mole fractions of B in the phases α and β, respectively.

In the first of the two approaches, the EGC is the intermediate between the phase diagram characteristics and the excess Gibbs energies of the forms α and β. The EGC is the solution of Equation (9.13), which is, in the Δ notation

$$\Delta G(T, x) = 0. \tag{9.18}$$

After the substitution of Equation (9.1), for α and for β, Equation (9.18) changes into

$$(1 - x)\Delta G_A^*(T) + x\Delta G_B^*(T) + \Delta G^E(T, x) = 0. \tag{9.19}$$

Next, after substitution of Equations (9.7) and (9.8) for the pure-component properties, and, in view of the remark made before, replacing $\Delta G^E(T, x)$ by $\Delta G^E(T = T_m, x)$, the EGC equation becomes

$$(1 - x)(\Delta H_A^* - T\Delta S_A^*) + x(\Delta H_A^* - T\Delta S_A^*) + \Delta G^E(T = T_m, x) = 0. \tag{9.20}$$

From Equation (9.20), it follows that the temperature of the EGC, T_{EGC}, as a function of x, can be represented by the following equation:

$$T_{EGC}(x) = T_{zero}(x) + \frac{\Delta G^E(T = T_m, x)}{(1 - x)\Delta S_A^* + x\Delta S_B^*}, \tag{9.21}$$

where T_{zero} the zero line, is given by

$$T_{zero}(x) = \frac{(1 - x)\Delta H_A^* + x\Delta H_B^*}{(1 - x)\Delta S_A^* + x\Delta S_B^*}. \tag{9.22}$$

The zero line is determined by pure-component properties only: ΔH^* the enthalpy and ΔS^* the entropy change at the transition; $\Delta S_A^* = \Delta H_A^*/T_A^0$ and $\Delta S_B^* = \Delta H_B^*/T_B^0$, T_A^0 and T_B^0 being the transition temperatures of the pure substances A and B.

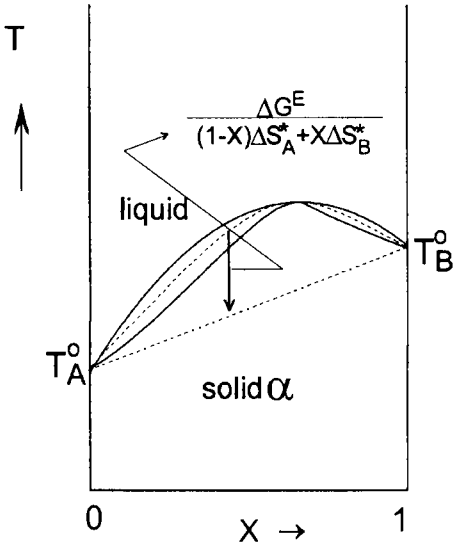

Figure 9.6 Plot of the temperature against mole fraction. In the T–x plane, the distance from EGC (dashed) to the zero line (dotted) is equal to the excess Gibbs energy difference divided by the weighed mean of the entropy of transition of the pure components.

In the T–x plane, the zero line as a rule is close to the straight line connecting T_A^0 and T_B^0. From Figure 9.6, it follows that the function $\Delta G^E(T = T_m, x)$ can be read easily from the phase diagram: its value is the distance in K from EGC to the zero line, multiplied by the mean entropy of transition of the pure substances.

The T–x phase diagram, as a result, allows the calculation of a set of ΔG^E values as a function of x. The mathematical processing of these data, in terms of the ΔG^E analogue of Equation (9.14), leads to the values of the parameters ΔG_1 and ΔG_2.

Computer programs based on the EGC methodology of phase diagram analysis are LIQFIT [32] and its Windows version WINIFIT [33]. The program LIQFIT was developed, originally, to use a set of *liquidus* data, in order to calculate the complete solid–liquid phase diagram (see also Section 9.2.2).

In the second approach, which is based on the equilibrium conditions in terms of chemical potentials, Equations (9.12a) and (9.12b), the phase diagram information to be furnished consists of triplets T, x_e^α, x_e^β with the equilibrium compositions of the two coexisting phases as a function of temperature. In the Δ_e notation the equilibrium conditions, Equations (9.12a) and (9.12b), become

$$\Delta_e \mu_A = 0, \tag{9.23a}$$

$$\Delta_e \mu_B = 0. \tag{9.23b}$$

Limiting ourselves to the equilibrium between a solid phase α and an ideal liquid phase, the Equations (9.23a) and (9.23b), after substitution of Equations (9.7) and (9.8), and (9.6a) and (9.6b), change into

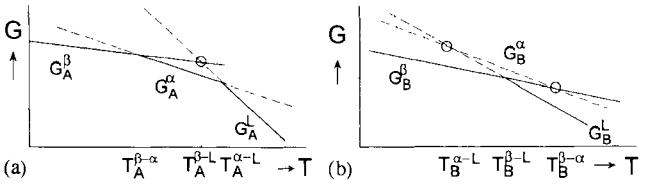

Figure 9.7 Plot of Gibbs energy versus temperature (a) for pure substance A, and (b) for pure substance B corresponding to Figure 9.1c. The dashed lines reflect metastability, and the open circles denote metastable melting points.

$$RT \ln \frac{(1 - x^\alpha)}{(1 - x^{\text{liq}})} + (x^\alpha)^2[G_1^\alpha + G_2^\alpha(3 - 4x^\alpha)] = \Delta H_A^* - T\Delta S_A^*. \qquad (9.24a)$$

$$RT \ln \frac{x^\alpha}{x^{\text{liq}}} + (1 - x^\alpha)^2[G_1^\alpha + G_2^\alpha(1 - 4x^\alpha)] = \Delta H_B^* - T\Delta S_B^*. \qquad (9.24b)$$

For given G_1^α and G_2^α, the two equations can be solved, to yield, as a function of T, the equilibrium mole fractions of the coexisting phases, x_e^α and x_e^{liq}. Conversely, read in the case of phase diagram analysis, the equilibrium compositions are used to calculate the values of G_1^α and G_2^α.

9.1.5 Polymorphism

In Figure 9.7, the pure component Gibbs energies are shown for the case represented by Figure 9.1c, where substance A displays a transition from the form β to the form α, and B does not.

At the transition temperature, the β-form of substance A can be converted into the α-form, and vice versa. It is the kind of polymorphism referred to as enantiotropism. The important thing to note here, is that, if the α-form would not exist, the β-form would melt at a lower temperature than the α. The open circle in Figure 9.7a marks, what is called, the metastable melting point of β. Let us now assume that Figure 9.7b represents the Gibbs energy relationships for substance B. The α-form of substance, invariably, is metastable with respect to β, and the kind of polymorphism is referred to as monotropism. The fact that α is metastable does not mean that it fails to exist as there are many examples of monotropism where the metastable form makes its physical appearance. In other cases, the α-form has a virtual status with properties that can be computed or obtained by extrapolation. Whatever the case may be, metastable melting points, or in general metastable transition points of pure components are properties that play an integral part in the thermodynamic analysis of phase diagrams.

For the thermodynamic treatment of phase diagrams like Figures 9.1b and 9.1c, three Gibbs energy functions of the type of Equation (9.1) are needed. The constituents of these

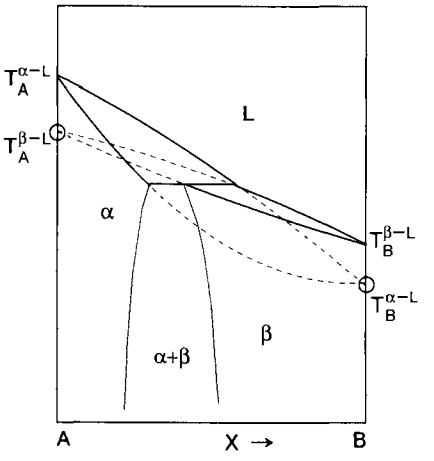

Figure 9.8 Plot of temperature against mole fraction to illustrate a case of crossed isodimorphism. The stable phase diagram can be regarded as the result of two solid–liquid phase diagrams each crossing the other. Dashed curves: metastable extensions of *solidi* and *liquidi*; open circles: metastable melting points.

functions are the pure-component properties of A and B, along with the excess Gibbs energies for each of the three forms, *viz.* α, β, and liquid, be it that in this work the excess Gibbs energy of the latter is neglected. The phase diagram Figure 9.1b, as an example, can be regarded as the stable result of two solid–liquid phase diagrams, each crossing the other. In the case of such a phase diagram, the term 'crossed isodimorphism' is applied, see Figure 9.8 [10–12,15–17,19].

9.2 Experimental

9.2.1 Sample Preparation

Mixed crystalline material, as a rule, is prepared in a roundabout way, by using a fluid phase as a medium. In its simplest form, the fluid phase is the liquid mixture of the components, and the mixed crystalline material is prepared by instantaneous solidification. One speaks of 'quenching of the melt' and the quench can be carried out in liquid nitrogen.

In this section, the issue of sample preparation and homogeneity is elaborated by the example of the system (1,4-dichlorobenzene + 1,4-dibromobenzene). More precisely, the example taken is pertaining to the monoclinic form α of 1,4-dichlorobenzene [34,35]; the form in which the substance is isomorphous with crystalline 1,4-dibromobenzene. At temperatures above $T = 306\,\mathrm{K}$, the stable form of the chloro substance is triclinic (β) [36], whose melting point is 0.19 K higher than the metastable melting point of α; in the present context, the existence of the β-form, and its small single-phase field in the phase diagram of the binary system, can be ignored.

The starting point of our discussion is the paper by Campbell and Prodan, which appeared in 1948 [37]. The authors constructed an apparatus for the determination of cooling curves. Samples, having a volume of about 20 cm^3 and being liquid at the start, are cooled at an initial rate of 0.3 $K \cdot min^{-1}$ and, during the experiment, stirred by employing a fluctuating air pressure. A typical cooling curve is shown in Figure 9.9; the filled circle clearly marks the onset of crystallisation, *i.e.* the *liquidus* temperature in the case of a mixed sample; the open circle would correspond to the *solidus* temperature. The set of *liquidus* and *solidus* temperatures, determined by Campbell and Prodan for the sample system, are shown in Figure 9.10.

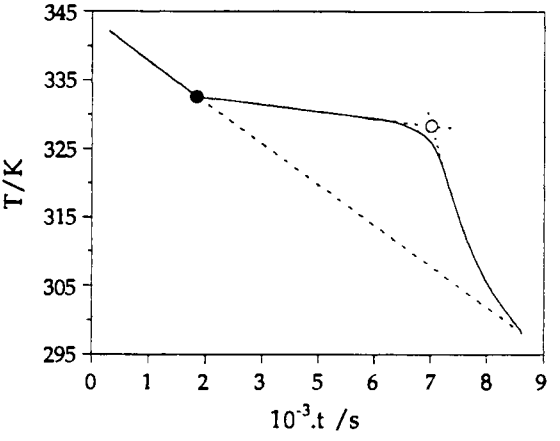

Figure 9.9 Typical cooling curve with temperature plotted against time for the apparatus of Campbell and Prodan [37]. Filled and open circles correspond, according to the authors, to the *liquidus* and *solidus* temperatures of the phase diagram.

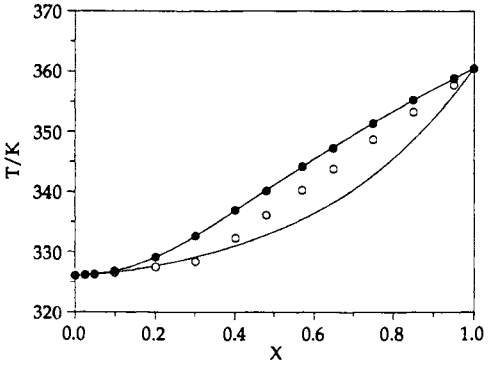

Figure 9.10 Plot of the temperature against mole fraction for the system (1,4-dichlorobenzene + 1,4-dibromobenzene). The filled and open circles represent temperatures read from cooling curves, see Figure 9.9. Solid curves represent the calculated phase diagram [38].

The curves, shown in Figure 9.10, are the *liquidus* and *solidus* that are obtained by LIQFIT, neglecting the small deviation from ideal mixing behaviour in the liquid state. More precisely, they represent the phase diagram that is calculated when the procedure is directed to the *liquidus* data. In terms of the constants in Equation (9.14), the calculated phase diagram corresponds to the following rounded values $G_1^{\alpha} = 1500\,\mathrm{J \cdot mol^{-1}}$ and $G_2^{\alpha} = 400\,\mathrm{J \cdot mol^{-1}}$.

From Figure 9.10, it unambiguously follows that the temperatures taken for *solidus* temperatures are thermodynamically inconsistent with the *liquidus* temperatures. This is a general disadvantage of the cooling curve method, be it that in most of the cases the reported *solidus* temperatures are too low (and not too high, as is the case in Figure 9.10). The following reasoning makes this clear.

From Figure 9.10 it follows that an equimolar mixture when cooled from the liquid state, assuming that undercooling will not take place, is starting to crystallise at about $T = 341\,\mathrm{K}$. The first crystals that are formed, as follows from the phase diagram, have a composition of about $x = 0.72$. When crystallisation goes on, the time is too short to reach thermodynamic equilibrium between the crystallising liquid and the whole of the deposited solid. At best, there will be equilibrium between the entire liquid and the last deposited layer of solid. And owing to the fact that the first deposited layers have $x > 0.5$, the last crystallising layers must have $x < 0.5$. This means that the last amount of liquid will crystallise at a temperature that is lower than the *solidus* temperature for $x = 0.5$.

A revealing experiment has been the following, carried out in an adiabatic calorimeter [38]. In the calorimeter, an original liquid sample, with $x = 0.51$, was kept for 5 days at 1 K below the *liquidus* temperature, and subsequently cooled at an average rate of $3\,\mathrm{K \cdot day^{-1}}$, until room temperature. Thereafter, it was subjected to the normal experimental procedures: at $T = T_a$, the sample is kept under adiabatic conditions for (typically) 600 s, then an electrical energy input $\Delta E = 25\,\mathrm{J}$ is provided, whereafter the sample is kept again under adiabatic conditions for 600 s, the temperature becomes a constant, $T = T_b$. The heat capacity of (calorimeter + sample), at the mean temperature, is given by $\Delta E/\Delta T$, where $\Delta T = T_b - T_a$. After correction for the heat capacity of the calorimeter, the number of joules per mole or gram is calculated, which is necessary to raise the temperature of the material by 1 K. A plot of this property against temperature is referred to as a heat capacity diagram [39]. The outcome of the experiment on the sample solidified in the calorimeter, as described, is shown in Figure 9.11, along with the ideal melting curve.

The ideal curve is calculated for overall and continuous thermodynamic equilibrium. It shows a sharp rise at the *solidus* temperature, and a sharp fall at the *liquidus* temperature. From Figure 9.11, it follows that the real sample already starts to melt at a temperature close to the melting point of 1,4-dichlorobenzene ($T = 326.24\,\mathrm{K}$). It can also be observed that melting is complete at the *liquidus* temperature. By gradual cooling of an initially liquid mixture, as a result, mixed crystalline material is obtained that lacks overall homogeneity. Instead, the deposited solid material has a gradient in composition, corresponding to some kind of a layered structure. The first deposited layer has a composition, which is the equilibrium composition for the *liquidus* temperature of the overall sample composition. The last layer has a composition that is close to the composition at the lowest temperature of the equilibrium diagram, lowest melting component or at the minimum, if the diagram has a minimum.

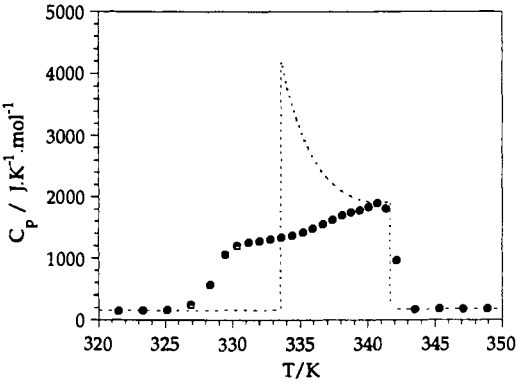

Figure 9.11 Heat capacity plotted against temperature for the system (1,4-dichlorobenzene + 1,4-dibromobenzene) [38]. The points represent the values obtained for the solid to liquid change for a sample (x = 0.51) prepared from a liquid mixture by slow cooling in the calorimeter. The dashed figure is the ideal melting curve.

In the opposite direction, on heating, the last deposited layer will be the first to melt, and the first deposited the last to melt. The heating curve, so to say, will be the mirror image of the cooling curve.

From the observations made so far, it is plausible to conclude that the experimental determination of reliable *solidus* temperatures will be possible only if the experimentalist has at his or her disposal mixed crystalline samples that are homogeneous throughout. A special technique for the preparation of grams of homogeneous material is zone levelling. The technique belongs to the class of 'zone melting' techniques that are characterised by a small molten zone that redistributes the material while travelling slowly through a tube with solid material. In the case of zone levelling, the liquid zone passes, a number of times, through the tube from left to right, and back, from right to left. A special apparatus for the growth of organic mixed crystals has been constructed and described by Kolkert [40,41]. With Kolkert's apparatus, 2 or 3 weeks are needed to prepare some 4 g of homogeneous material; the travel speed of the liquid zone is of the order of 4 cm · day^{-1}. The technique was applied by Bouwstra *et al.* [42–44] to investigate the system (*trans*-azobenzene + *trans*-stilbene). Their heat capacity diagrams, by adiabatic calorimetry, indeed, showed the ideal appearance of the calculated curve in Figure 9.11. Moreover, their calorimetric observations were in full agreement with the calculated phase diagram. The importance of the work on zone levelling is that it has been demonstrated that by the coupling of this technique and adiabatic calorimetry, reliable *liquidus* and *solidus* data can be obtained. The work has been a landmark and a starting point for the exploration of less sophisticated and time-consuming methods. As a particular example, we will discuss the work by van der Linde [38] and van der Linde *et al.* [45], on samples prepared by rapid co-precipitation from a highly volatile solvent. The pure substances 1,4-dichlorobenzene and 1,4-dibromobenzene, in the desired proportions, were dissolved in diethyl ether, after which mixed crystalline material was forced to precipitate through fast evaporation of the solvent. The quasi-instantaneous method allows the preparation of samples, typically with a mass of 5 g, in less than half an hour.

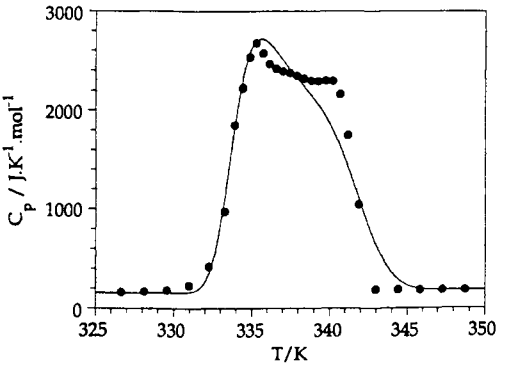

Figure 9.12 Plot of heat capacity against temperature for the system (1,4-dichlorobenzene + 1,4-dibromobenzene) for the solid to liquid change in a sample (x = 0.52) prepared by rapid co-precipitation from a solvent. The solid curve is the melting curve in terms of the ULTRACAL model [38,45].

As a representative example, and for comparison with Figure 9.11, Figure 9.12 gives the measured heat capacities of the sample, having x = 0.52. From a comparison of Figures 9.11 and 9.12, it follows that the experimental points in the latter are close to the ideal melting curve. Most importantly, as has been shown [45], the temperatures at the highest slopes at the rising and falling edges, which are the points of inflexion at the edges of the experimental diagram, virtually coincide with the *solidus* and *liquidus* temperatures, respectively of the phase diagram.

With respect to the accuracy of the experimental data, 0.1 K is a representative figure for the uncertainties in (i) the *liquidus* temperatures by Campbell and Prodan [37], and (ii) the *solidus* and *liquidus* temperatures, derived from the heat capacity diagrams for samples prepared by rapid co-precipitation. From the point of view of phase diagram temperatures, the method preparing samples in this way yields results close to the standard set by zone levelling. For the research on mixed crystals this is an advantage. Does it mean that the work on zone levelling has been superfluous? Certainly not, as follows from the experimental observations detailed hereafter.

In the thermodynamics section above, a distinction was made between two experimental situations: (i) heating at low speed when the molecules have some mobility, and (ii) heating at high speed in combination with negligible mobility. It was argued that in situation (i) melting would start at the *solidus* temperature and be complete at the *liquidus* temperature. In this section, we have shown that samples prepared by zone levelling and measured by adiabatic calorimetry fully meet these expectations; and that the same is true for the samples prepared by rapid precipitation. For the limiting case of situation (ii), it was argued that the mixed crystalline material should melt isothermally at the EGC.

From the very first measurements [40,41] by differential scanning calorimetry (DSC), it became apparent that samples prepared by zone levelling exhibit a unique melting behaviour. Experiments extending over the full scale of a binary system were carried out for (1,4-dichlorobenzene + 1,4-dibromobenzene) [46]. The DSC heating curves, shown in Figure 9.13, are representative of the whole set of observations, and they include the melting curves of the pure components.

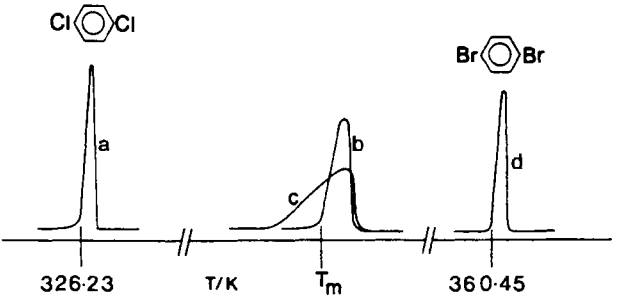

Figure 9.13 Heating curves obtained by DSC for the system (1,4-dichlorobenzene + 1,4-dibromobenzene). The heating rate of 0.62 K · min^{-1} on 1 mg samples was used. Curves (a) and (d) refer to the pure components; curve (b) to the sample taken from mixed crystalline material prepared by zone levelling; curve (c) recorded after melting and solidifying of the sample giving rise to curve (b).

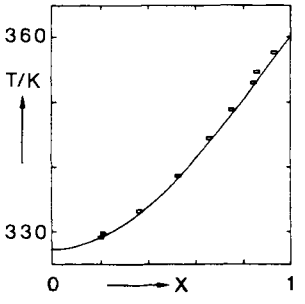

Figure 9.14 Plot of 'melting points' for crystalline samples of (1,4-dichlorobenzene + 1,4-dibromobenzene). The samples were prepared by zone levelling, and the temperatures correspond to the temperature T_m in Figure 9.13 curve (b). The curve is the EGC, corresponding to the phase diagram shown in Figure 9.10.

Curve (b) is typical of samples taken from mixed crystalline material prepared by zone levelling. The curve resembles the melting curves of the pure components. This means that the mixed material is melting quasi-isothermally at the temperature T_m. The melting temperature, T_m, can be read from the curve in a clear and unambiguous manner. The complete set of observed 'melting points', T_m, is plotted as a function of composition in Figure 9.14.

The most striking aspect of the 'melting points' is that they are in the direct vicinity of the EGC of the system. In other words, the melting behaviour of the samples comes close to the behaviour expected for limiting case (ii).

From the experimental results, detailed in this section, it follows that the three characteristic curves of the phase diagram, *liquidus*, *solidus* and EGC, all represent an experimental reality. They can be located by experimental methods. It is also clear that the choice of the measuring technique and the preparation of the samples have a decisive influence on

what is actually measured. Out of the three characteristic curves, the *liquidus* is the most accessible one to experimental determination. The EGC is the least accessible of the three. The material prepared by zone levelling allows, apart from the *liquidus*, the determination of the *solidus* and the EGC, be it in different experiments. The material prepared by co-precipitation from a solvent, and when measured in an adiabatic calorimeter, is giving rise to heat capacity diagrams that virtually coincide with the diagrams produced by the material prepared by zone levelling. In DSC experiments, on the other hand, only the zone-levelled samples manage to melt isothermally, on the EGC. The difference in DSC behaviour can be related to the fact that zone levelling results in compact material, and co-precipitation in a fine powder. The latter has free space to enhance, via vapour, the mobility of the molecules. The material prepared by co-precipitation results in DSC thermograms that resemble the heat capacity diagrams, Figure 9.12, obtained by adiabatic calorimetry. Owing to the fact that the outcome of the experiments is a function of experimental methods and sample history, it is recommended that experiments are synchronised with thermodynamic computations, namely phase diagram analysis.

9.2.2 Microcalorimetry

In the section 'sample preparation', the technique of adiabatic calorimetry has been discussed at some length. This section is restricted to microcalorimetry. When compared with adiabatic calorimetry, microcalorimetry has the enormous advantage of requiring less time and less material. Through microcalorimetry, samples as small as a few milligrams are scanned at a rate, which is as a rule between 1 and $10\,K \cdot min^{-1}$. In adiabatic calorimetry, samples have masses that range from 0.5 g to some 10 g, and a complete experiment easily takes two weeks. Adiabatic calorimetry, on the other hand, is a byword for accuracy and precision. And not insignificantly, adiabatic calorimetry is a better guarantee for thermodynamic equilibrium.

For the purpose of research on mixed crystals, the principal techniques are differential thermal analysis (DTA) and DSC. The adjective 'differential' expresses the fact that the measured quantity is a difference between the sample and a reference, both being kept under the same experimental conditions [47]. In the case of DTA, the measured difference is a difference in temperature. However, for DSC, it is a difference in heat flow.

In the case of organic materials, it is desirable to encapsulate the sample under an inert atmosphere. This is to prevent evaporation, and to avoid sample oxidation. It must be realised that the material under investigation has a certain vapour pressure, and that the dead volume of the sample container, as a result, will be saturated with vapour. During a heating experiment, the vapour pressure increases, and it means that there is some uncertainty as to the pressure exerted on the material at a solid–solid or a solid–liquid transition. Strictly speaking for the case of containers with no other material than the system to be studied as well as for pure substances, triple points are measured rather than normal melting points [48–51].

In the majority of cases, the influence of vapour pressure on solid–solid and solid–liquid transition temperatures can be neglected as their contribution is less than the experimental uncertainties.

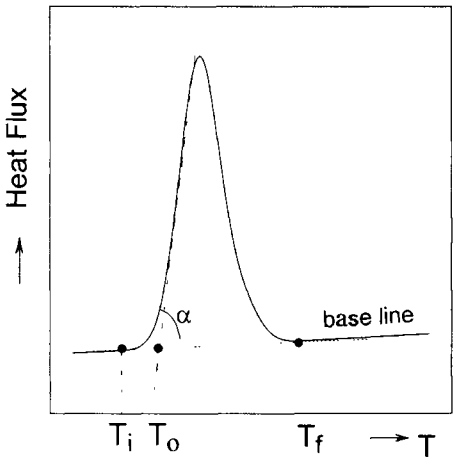

Figure 9.15 Plot of heat flux against temperature to produce a microcalorimetric thermogram that corresponds to the melting of a pure substance.

The Thermogram

The microcalorimetric thermogram shown in Figure 9.15 is meant to correspond to the melting of a pure substance. The horizontal axis is for temperature, the temperature of the block (on which sample capsule and reference are mounted) to be precise.

The melting of a pure substance is an isothermal event, which implies that over the whole rising edge of the thermogram the temperature of the sample does not change. At the end of the event, the recording returns to the baseline in a more or less exponential manner. At T_f, which is called the final peak temperature, the recording is back at the baseline. At the ascending edge of the thermogram, T_i, which is called initial peak temperature, is the temperature at which the recording starts to deviate from the baseline; and T_o is the so-called onset temperature. Obviously, the onset temperature is representative of the melting temperature of the process. More precisely, instruments are calibrated with pure substances such that the observed onset temperatures are identified with their melting temperatures. One can observe that the part of the peak between T_i and T_o is a matter of instrumental inertia. The angle α, between ascending edge and baseline, is a property of the instrument and, in addition, a function of the applied heating rate. At the falling edge and neglecting the inertia at the top of the peak, the temperature of the sample increases from T_o to T_f. For a point on the falling edge, the temperature of the sample is found with an auxiliary straight line, parallel to the ascending edge, *i.e.* at an angle α with the baseline: the temperature is given by the intersection of the auxiliary line and the baseline. Obviously, the difference between T_o and T_f is a function of the mass of the sample.

For a mixed crystalline sample having a certain composition x, the change from solid to liquid, as a rule, is a non-isothermal event. The thermogram of the event will be the result of a complex interplay between the characteristics of the instrument, the applied heating rate, the thermodynamic characteristics of the solid to liquid change and the preparation of the sample. A typical thermogram is shown in Figure 9.16, and the key question

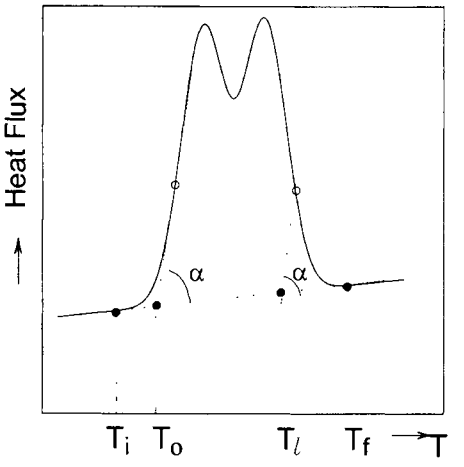

Figure 9.16 Thermogram representing the melting of a mixed crystalline sample with the heat flux plotted against temperature.

is, how to read from the thermogram the *solidus* and *liquidus* temperatures that correspond to composition x. For the interpretation that follows here, it is assumed that the sample has been prepared by rapid evaporation from a solvent, and, moreover, that it manages to behave like the sample measured by adiabatic calorimetry, see Figure 9.12.

If so, the *solidus* temperature should correspond to the onset temperature, T_o. Note that reading values of T_o from the thermogram may be less precise than in the case of Figure 9.15. Furthermore, the point of inflexion at the falling edge should correspond to the end of melting. Subsequently, the *liquidus* temperature, T_l, is found as is shown in Figure 9.16, that is to say, respecting the angle α [52].

A practical, alternative method, for the reading of *solidus* and *liquidus* temperatures from thermograms like Figure 9.16, is the so-called shape-factor method [53]. The method is rather similar to the one detailed in the foregoing paragraph. It also compares the thermogram of the mixed sample with the thermogram(s) of the pure substance(s), taken under the same experimental circumstances.

A typical result of microcalorimetry work is the phase diagram shown in Figure 9.17. The diagram pertains to the system (2-methylnaphthalene + 2-chloronaphthalene), one of the very few systems showing a solid–liquid phase diagram with a maximum [54]. The data shown are *liquidus* points from two different investigations, and for one of the investigations from three different instruments. The solid curves in Figure 9.17 are the optimised (LIQFIT) *solidus* and *liquidus* curves. The observations to be made here are (i) that an individual experimental *liquidus* point may deviate from the mean trend by a maximum of about 1 K; and (ii) that from investigation to investigation, differences may easily run up to 3 or 4 K. Clearly, the accuracy of microcalorimetric *solidus* and *liquidus* temperatures is less than the accuracy of the ones determined by adiabatic calorimetry.

The remaining uncertainties in the latter are 0.1 K (see above). A lower limit for the remaining uncertainties in microcalorimetric *solidus* and *liquidus* data is 0.5 K.

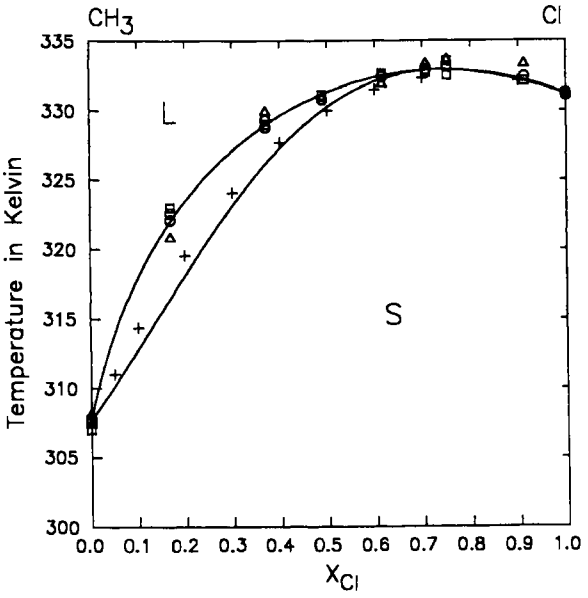

Figure 9.17 Optimised phase diagram of the system (2-methylnaphthalene + 2-chloronaphthalene) with temperature plotted against mole fraction. The symbols are microcalorimetric *liquidus* points obtained with different instruments [54] (○ Seiko DSC 120; △Perkin-Elmer DSC 2; □ Setaram DSC 111); + data by Meresse [55].

Heat Effect

The area under the peak of a thermogram, making allowance for the course of the baseline, is a measure of the heat effect of the process (see Figure 9.18).

As a function of composition, the measured heat effect gives direct information on the excess enthalpy function, because

$$\Delta_\alpha^\beta H(x) = (1 - x)\Delta_\alpha^\beta H_A^* + x\Delta_\alpha^\beta H_B^* + \Delta_\alpha^\beta H^E(x). \tag{9.25}$$

An example of experimental results is shown in Figure 9.19 for the system (2-methylnaphthalene + 2-chloronaphthalene), which corresponds to the solid–liquid change displayed in Figure 9.17. In order to visualise the 'excess effect', the property on the y-axis of Figure 9.19 is not simply the molar enthalpy of melting, but the 'enthalpy of melting divided by kJ · mol^{-1} minus two times the value of the mole fraction'. The curve shown in Figure 9.19 is based on

$$\Delta H(x)/(\text{kJ} \cdot \text{mol}^{-1}) = \{(1 - x)11.96 + x14.05 + 2.60x(1 - x)[1 + 0.20(1 - 2x)]\}, \tag{9.26}$$

where Δ stands for Δ_{sol}^{liq}. It implies $\Delta H_A^* = 11.96\,\text{kJ} \cdot \text{mol}^{-1}$; $\Delta H_B^* = 14.05\,\text{kJ} \cdot \text{mol}^{-1}$; and in terms of the $AB\theta$ model, assuming ideal liquid mixing behaviour, it gives rise to $A = -2.60\,\text{kJ} \cdot \text{mol}^{-1}$; $B = 0.2$ for the mixed crystalline state.

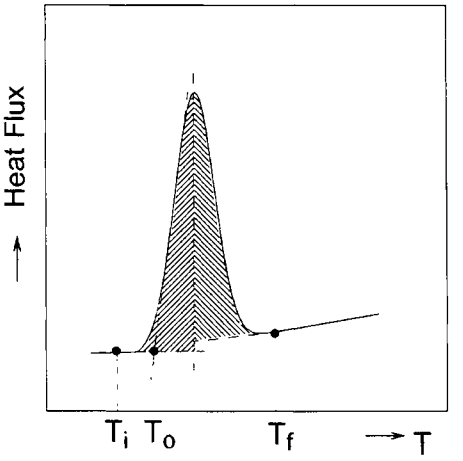

Figure 9.18 Plot of heat flux against temperature. The heat effect of a process follows from the area under the peak.

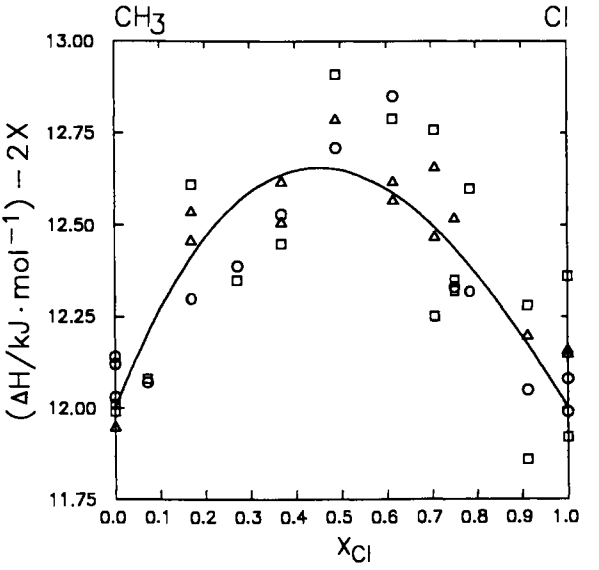

Figure 9.19 Plot of the enthalpy of melting (see text) against mole fraction 2-chloronaphthalene in the system (2-methylnaphthalene + 2-chloronaphthalene). The symbols refer to instruments. See Figure 9.17 [54].

With regard to experimental accuracy, it follows from Figure 9.19 that an individual data point may deviate from the mean trend to a maximum of about 0.25 kJ · mol^{-1}, which is 2 per cent of the total effect. At this point, it should be emphasised that the power of microcalorimetry is that it gives, at the same time, the phase diagram and the enthalpy effect of the transition. The phase diagram is an expression of the excess Gibbs energy difference for

the mean temperature of the transition ($\Delta_\alpha^\beta G^E(T = T^x_{mean})$). The heat effect directly gives the excess enthalpy difference $\Delta_\alpha^\beta H^E(x)$. Subsequently, and when combined, the two functions yield the excess entropy difference, because

$$\Delta_\alpha^\beta G^E(T = T_{mean}, x) = \Delta_\alpha^\beta H^E(x) - T_{mean}\Delta_\alpha^\beta S^E(x). \tag{9.27}$$

In other terms, and in the case of the (2-methylnaphthalene + 2-chloronaphthalene) system for which the liquid state is taken as an ideal mixture, microcalorimetry yields the complete information on the excess Gibbs energy of the system, *i.e.* the values of the parameters A, B and θ. From Equation (9.25), for the excess enthalpy of the mixed crystalline state, here denoted by α,

$$H^{E,\alpha}(x) = -2600x(1 - x)[1 + 0.2(1 - 2x)]\ J \cdot mol^{-1}. \tag{9.28}$$

From the phase diagram, by means of LIQFIT,

$$G^{E,\alpha}(T = 326.5\,K, x) = -1795x(1 - x)[1 + 0.2(1 - 2x)]\ J \cdot mol^{-1}. \tag{9.29}$$

From the two expressions: $A = -2.60\,kJ \cdot mol^{-1}$, $B = 0.2$ and $\theta = 1050\,K$. Owing to the fact that the relative uncertainty in the excess enthalpy (see Figure 9.19) and hence in the parameter A is rather high, the uncertainty in θ may easily run up to 200 K.

With respect to excess properties and their experimental uncertainties, quite a different situation is met with the rotator state of the system (nonadecane + heneicosane). This time the excess enthalpy difference, liquid minus rotator, is negative, and in an absolute sense, four times the difference between liquid and solid displayed by the (methyl + chloronaphthalene) system, see Figure 9.20. Again, the deviation of an individual point from the general trend is about $0.25\,kJ \cdot mol^{-1}$ at most. The large ΔH^E is contrasting with the excess Gibbs energy difference ΔG^E, which is really very small.

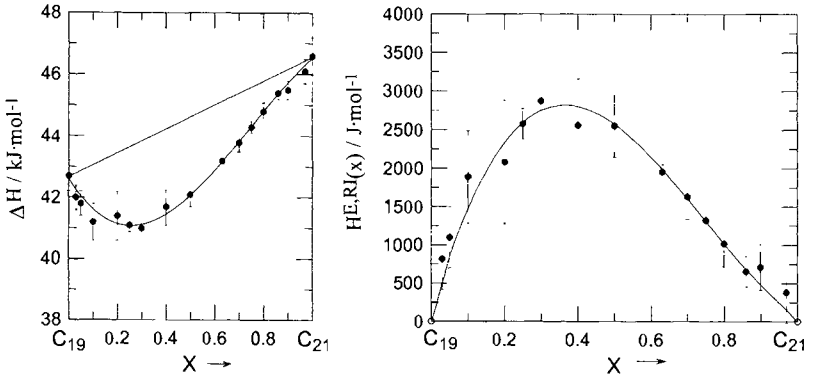

Figure 9.20 Plot of the enthalpy and excess enthalpy of melting against mole fraction heneicosane for the system (nonadecane C_{19} + heneicosane C_{21}) [56].

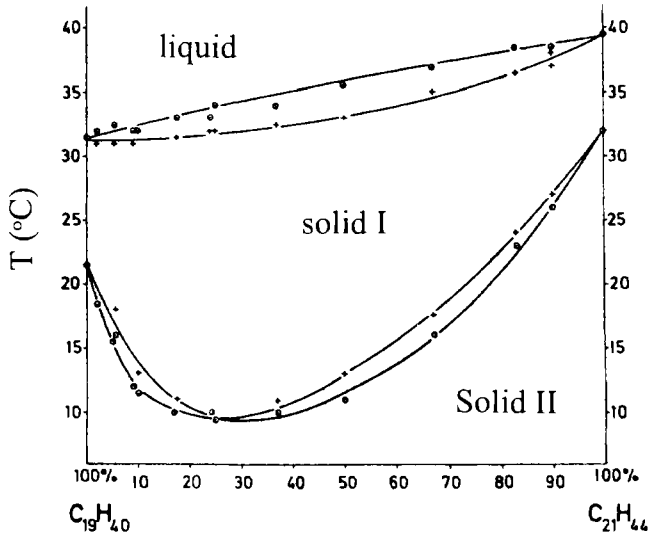

Figure 9.21 The phase diagram of the system (C_{19} + C_{21}) by [57a] and based on high-pressure DTA [57b].

As can be seen in Figures 9.21 and 9.22, the (RI + L) two-phase regions bend only slightly downwards. It means, from Equation (9.21), that there is a small negative ΔG^E and subsequently, from Equation (9.27), it follows that the quotient of ΔH^E and ΔS^E will be close to the T_{mean} in the vicinity of $T = 310$ K. More precisely, that quotient is calculated as $T = 319$ K. Owing to the fact that liquid mixtures of C_{19} and C_{21} are virtually ideal, the calculated $T = 319$ K comes down to the value of $\theta = 319$ K for the rotator state of the system.

Presence of Three Phases in Equilibrium

The system to which the phase diagram Figure 9.28 (see page 231) applies has a three-phase equilibrium, a situation that under isobaric conditions is invariant: as long as there are three phases, the temperature does not change. A sample consisting of two solid phases will start to produce liquid at the three-phase equilibrium temperature, which is named the eutectic temperature in the case of Figure 9.28, and peritectic temperature in cases where the composition of the liquid does not lie between the composition of the solid phases. The sample will remain at the eutectic temperature until one of the solid phases is exhausted. At the eutectic arrest, the instrument will register an isothermal melting peak that resembles the melting peak of a pure substance. After the arrest, the non-isothermal melting of the remaining solid continues, and it is complete when the *liquidus* temperature is reached. The complete thermogram typically has the appearance of the thermogram displayed in Figure 9.23. After the eutectic arrest and up to the *liquidus* temperature, the heat flux as it depends on temperature is determined by the Lever rule, Equation (9.11).

Directly after the eutectic arrest, the heat flux falls down, almost to the baseline. As a result, the enthalpic effect at the arrest can easily be determined. The eutectic enthalpic effect is

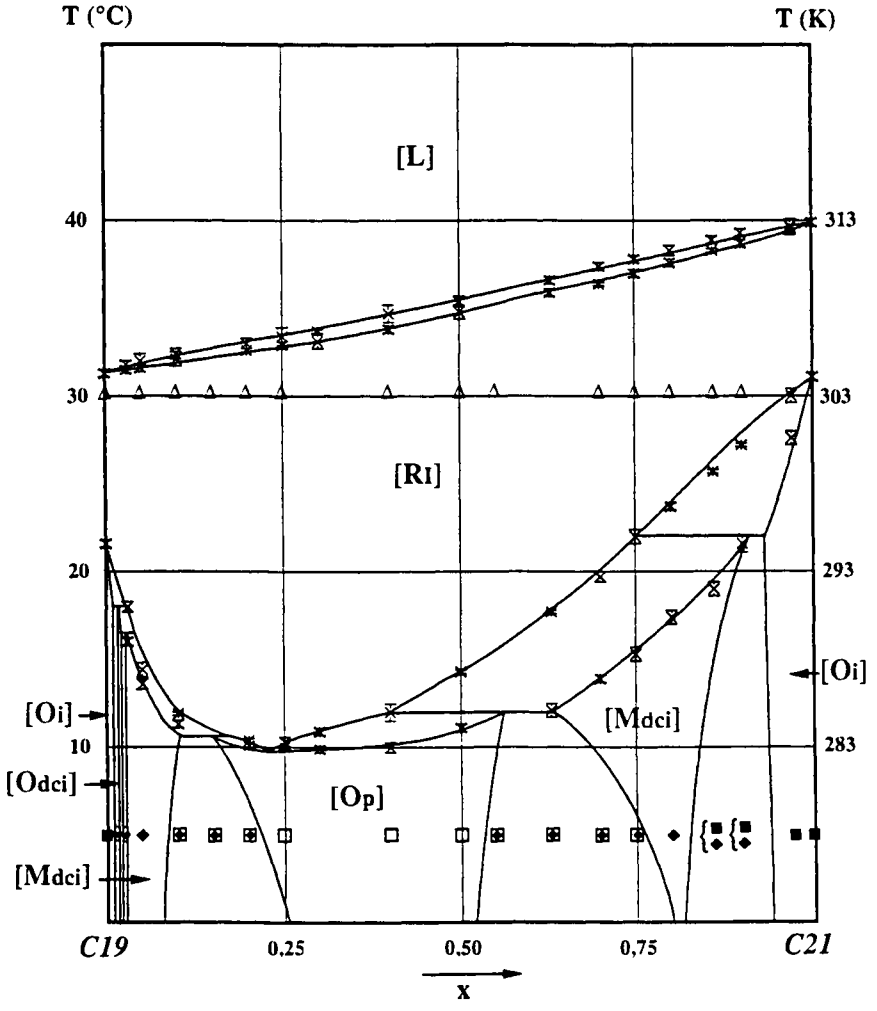

Figure 9.22 The phase diagram of the system (C_{19} + C_{21}) by [56,58] based on isoplethic thermal analysis (x) and isothermal X-ray diffraction at T = 278 and 303 K. The isothermal X-ray measurements at T = 278 K gave rise to the spectra shown in Figure 9.31 [56,58].

maximal when the overall composition of the sample is equal to the equilibrium liquid composition at the eutectic temperature. The effect, again determined by the Lever rule, becomes zero when the overall composition is equal to the composition of either one of the solid phases at the three-phase equilibrium. These observations imply that the compositions of the phases at the three-phase equilibrium can be read from a plot of eutectic enthalpic effect as a function of overall composition, the so-called Tamman plot. An example is given in Figure 9.24, which corresponds to Figure 9.28, for overall compositions at the right-hand side of the eutectic composition.

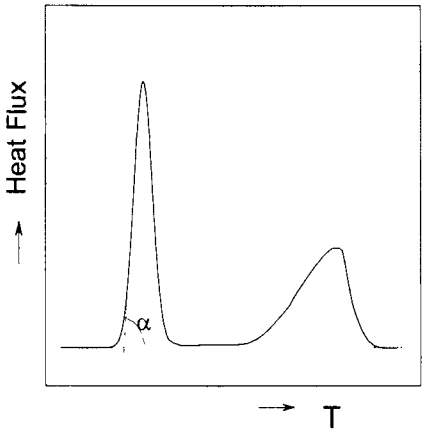

Figure 9.23 Thermogram typical of melting that starts at a eutectic arrest in a plot of heat flux against temperature.

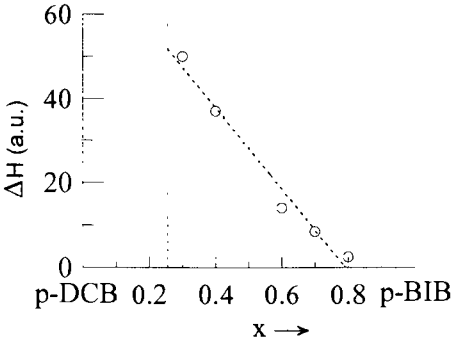

Figure 9.24 Plot of the enthalpy change at the eutectic against mole fraction 1-bromo-4-iodobenzene for the system (1,4-dichlorobenzene + 1-bromo-4-iodobenzene) [8]. See also Figure 9.28.

9.2.3 X-Ray Diffraction

The structural characterisation of the solid phases is an essential part of thermodynamic research on solid–liquid and solid–solid equilibria. This is especially true in the case of organic substances and their mixed crystals. The essential characteristic of organic, molecular materials, when compared with inorganic ionic materials and metals, is the circumstance that the building unit is a polyatomic entity. From substance to substance, the building units or molecules do show a variety in size and shape. For a given substance, the flexibility of the molecules may find expression in the existence of a variety of conformations. With respect to the crystalline state, a given set of molecules may give rise to different arrangements, whether or not in combination with conformational and orientational disorder. The experimental technique par excellence to reveal the richness in structure and to realise the structural characterisation of a crystalline solid is X-ray diffraction.

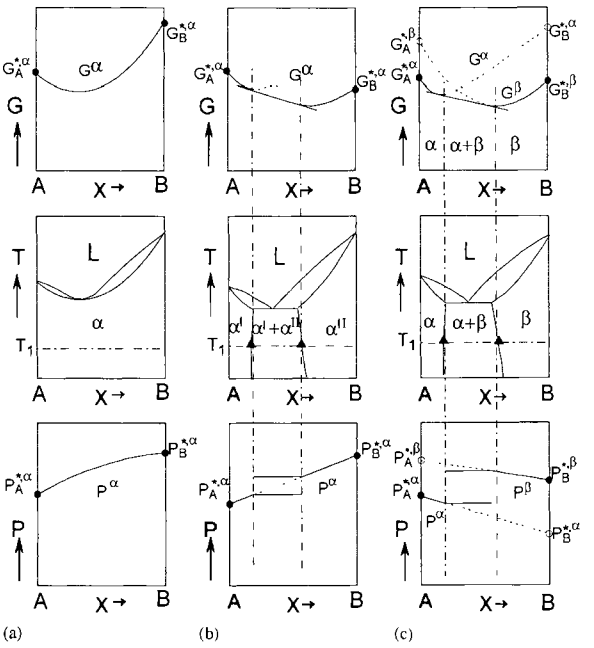

Figure 9.25 The three basic situations are shown for the formation of mixed crystals between two substances A and B at given constant temperature and pressure. Upper part: molar Gibbs energy as a function of the mole fraction of B, x. Middle part: phase diagrams. Lower part: some property of the mixed crystal as a function of x at a temperature T_1. Case (a): A and B have the same crystal structure characteristics and give rise to the formation of mixed crystals in all proportions. Case (b): same crystal structure characteristics; there is, in spite of that, a miscibility gap in the solid phase. Case (c): A and B have different structures; it necessarily involves a range in mole fraction where the formation of mixed crystals is interrupted.

For a pair of substances, A and B, and when considered at a given, fixed temperature and pressure, one can distinguish between three different cases, represented by Figures 9.25a–c. The upper part of the figures shows the Gibbs energy plotted against composition, the lower part represents a property, P, related to structure, suppose the Bragg angle of a given X-ray reflection, all of them corresponding to the solid phase(s) at temperature T_1 for the phase diagrams plotted at the central part.

In the case of Figure 9.25a, there is one Gibbs energy function, and it implies that A and B are isomorphous: they have the same unit-cell characteristics, space group and number of molecules per unit cell, and, within the unit cell, the same arrangement of molecules. In this case, any physical property P^{α} changes from $x = 0$ (pure A) to $x = 1$ (pure B) in a continuous manner.

In the case of Figure 9.25b, and unlike the case of Figure 9.25a, A and B do not mix in all proportions, in spite of the fact that they have the same structure characteristics. Denoting by $x_e^{\alpha I}$ and $x_e^{\alpha II}$ the compositions of the phases that can be in equilibrium, the following observations can be made. For overall compositions between $x_e^{\alpha I}$ and $x_e^{\alpha II}$, the sample is heterogeneous, and P being the Bragg angle of a reflection (for instance), the diffraction

pattern will show a double peak corresponding to $P^{\alpha}(x^{\alpha} = x_e^{\alpha I})$ and $P^{\alpha}(x^{\alpha} = x_e^{\alpha II})$. For overall compositions outside the miscibility gap, samples are homogeneous and P^{α} values 'at the left-hand side' are in line with the values measured 'at the right-hand side' of the gap.

In the case of Figure 9.25c, the stable forms of the pure components have different structure characteristics: two Gibbs energy functions are needed, one for the α-type of structure and one for the β-type of structure. Similarly, there are two different P functions, P^{α} and P^{β}. In a case like this, the phase diagram inevitably will show a two-phase region, and P values measured on homogeneous samples 'at the left-hand side' of that region will not be in line with the values measured 'at the right-hand side'.

For a number of typical examples of real systems, considered hereafter, a distinction is made between isothermal measurements and isoplethic (constant composition) measurements. In the case of the former, the composition is varied, and in the case of the latter the temperature is changed.

Isothermal Measurements

CH_3CCl_3 + CCl_4 [59]

The 1,1,1-trichloroethane and carbon tetrachloride are substances that have plastic-crystalline mesophases, orientationally disordered crystals (ODICs) in which the spherically shaped molecules have orientational freedom. The special aspect about the two is that, when plastic crystalline, they show a dimorphic behaviour of the monotropic type [60–62]. This is to say that they give rise to two different forms, such that one of these forms is metastable under all circumstances of temperature. Moreover, the two substances have the same metastable form; it is face-centred cubic (fcc). The stable form of the substances is rhombohedral (R). The fcc form is produced from the liquid state on cooling, and on further cooling it changes into the R-form. When the fcc crystals after having been formed are heated instead of cooled, they directly change into liquid, *i.e.* without changing first into R.

Mixtures of the two substances exhibit exactly the same polymorphic behaviour as the two components, whatever the composition. The complete situation is shown in Figure 9.26, where the metastable melting loop is superimposed on the stable phase diagram. The thermoanalytical result, Figure 9.26, has been proven in an independent manner by isothermal X-ray diffraction [59]. The outcome of the X-ray investigation, on the pure components and four mixed samples, is shown in Figure 9.27.

In conclusion, in relation to Figure 9.25, the system corresponds to the superposition of two diagrams of type *a*; one for the stable and one for the metastable plastic-crystalline mixtures.

1,4-Dichlorobenzene + 1-Bromo-4-Iodobenzene [8]

Like 1,4-dibromobenzene (Br Br), the substance 1-bromo-4-iodobenzene (Br I), at room temperature, has the same type of structure as 1,4-dichlorobenzene (Cl Cl). But unlike Br Br, Br I does not mix in all proportions with Cl Cl: the Br I molecules are less compatible in size with

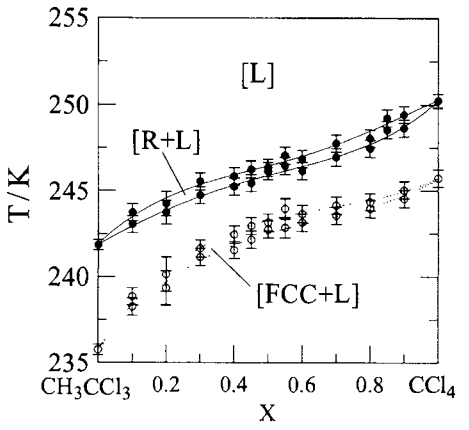

Figure 9.26 The phase diagram for the system (CH_3CCl_3 + CCl_4) with temperature plotted against mole fraction carbon tetrachloride. The metastable melting loop, dashed curves, of the fcc-type of plastic crystals is superimposed on the stable phase diagram shared by the rhombohedral plastic-crystalline and liquid states. Filled and open circles represent experimental data by DSC [59].

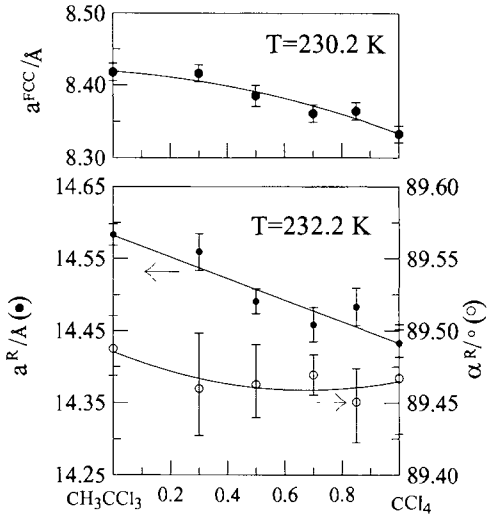

Figure 9.27 Plot of lattice parameters against mole fraction carbon tetrachloride for the system (CH_3CCl_3 + CCl_4) at T = 230.2 and 232.2 K. The unit-cell parameters were obtained by X-ray powder diffraction. The upper part represents the parameter a of the metastable fcc crystals. The lower part represents the parameters a(○) and α (▲) of the rhombohedral crystals [59].

the Cl Cl molecules than are the Br Br ones. The combination of Cl Cl and Br I, therefore, is a clear example of the case represented by Figure 9.25b. The solid–liquid phase diagram of the system is shown in Figure 9.28. The broad solid-state region of de-mixing is giving rise to a three-phase equilibrium of the eutectic type. At the bottom of the diagram, an impression is given of the doubling of X-ray reflections for overall sample compositions 'inside the

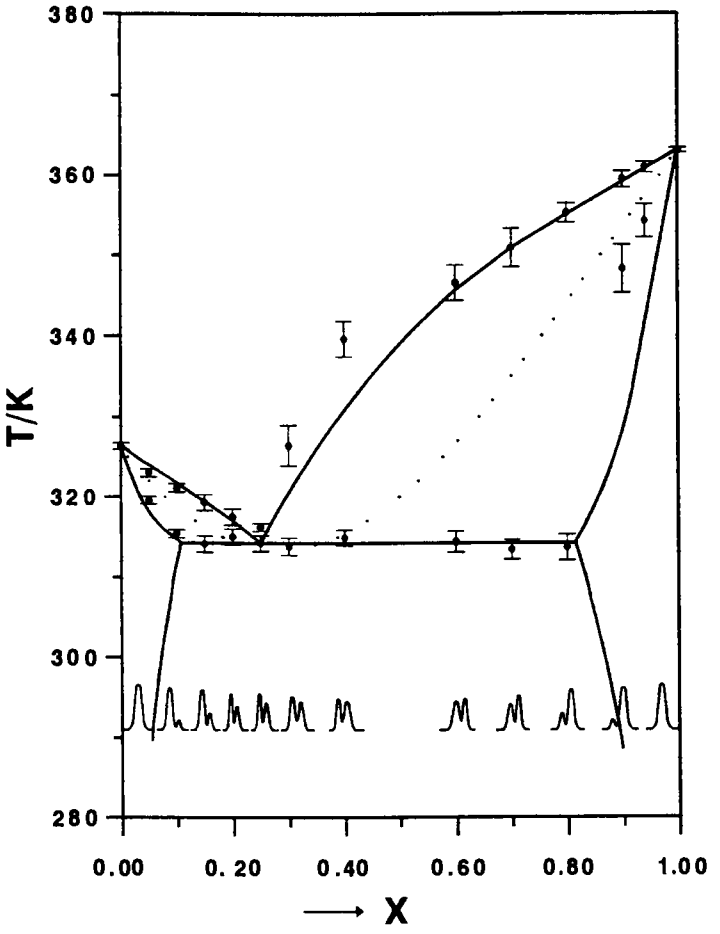

Figure 9.28 The optimised solid–liquid phase diagram for the system (1,4-dichlorobenzene + 1-bromo-4-iodobenzene) with temperature plotted against mole fraction 1-bromo-4-iodobenzene. The filled circles are DSC observations. At the bottom, an impression is given of the change with overall sample composition of the (210) X-ray reflection [63].

region of de-mixing'. As an aside, in a clear manner Figure 9.28 reflects the usefulness of the combined approach of X-ray analysis, microcalorimetry and thermodynamic analysis.

2-Amino-2-Methyl-1,3-Propanediol + 1,1,1-Tris(hydroxymethyl)propane [14]

Systems where the two components are non-isomorphous, and correspond to Figure 9.25c, are quite numerous. An example, again involving ODIC, is the system (AMP + PG). The AMP is the acronym for 2-amino-2-methyl-1,3-propanediol, $NH_2(CH_3)C(CH_2OH)_2$, and the PG for 1,1,1-tris(hydroxymethyl)propane, $(CH_3)C(CH_2OH)_3$. The stable ODIC form of AMP is body-centred cubic (bcc), and the stable ODIC form of PG is fcc [64–66] (Figures 9.29 and 9.30).

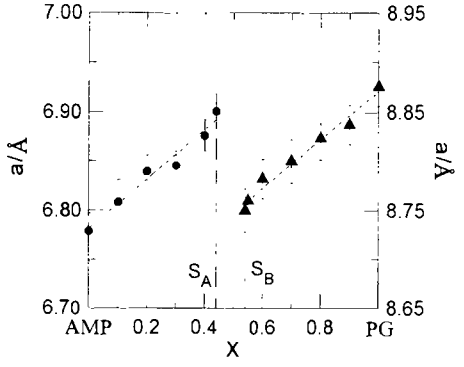

Figure 9.29 Plot of the lattice parameter a against mole fraction PG for the system (AMP + PG). The cubic cell parameter was determined by isothermal X-ray diffraction at $T = 363$ K. Filled circles are for body-centred, and filled triangles for face-centred cubic lattices [67].

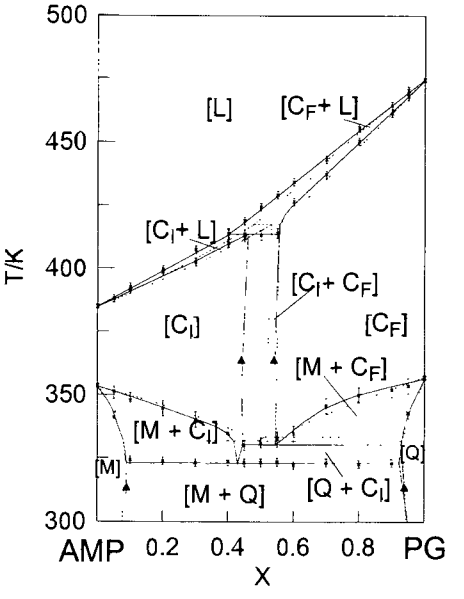

Figure 9.30 The phase diagram for the system (AMP + PG) with temperature plotted against mole fraction PG. Solid curves: experimental phase diagram, based on DSC measurements (X), and isothermal X-ray powder diffraction (▲). Dotted curves: calculated phase diagram [14].

Nonadecane + Heneicosane [58]

The normal alkanes (C_nH_{2n+2}), C_n for short, have a rich polymorphic nature which is different for odd and even members of the family, and, moreover, a function of chain length. Interestingly, part of the polymorphic nature is related to the appearance of a mesostate, which is the rotator state. In the rotator state, the elongated molecules have rotational freedom around their long axis.

In Figure 9.21, the phase diagram of the system (C_{19} + C_{21}) is shown as determined by Würflinger [57b]. The phase diagram has three single-phase fields. These are, from top to bottom, for the liquid, the rotator and the 'ordinary'-solid state. In the rotator state, the system has the form RI, which is one of the possible rotator forms. Phase diagrams, in agreement with Figure 9.21, have also been published by Mazee [68] and by Maroncelli *et al.* [69]. The diagrams agree as to the nature of the 'ordinary'-solid state, *viz.* a continuous series of mixed crystals in the form, the type of structure taken by the pure components. The important point to mention at this point is the fact that the careful measurements, on which the diagram of Figure 9.21 is based, did not reveal the fine structure at the bottom of the diagram.

The fine structure is shown in Figure 9.22, which corresponds to the appearance of intermediate forms like Mdci (monoclinic, space group Aa) and Op (orthorhombic, Pca 2_1), in addition to the form O_i (orthorhombic, P_{cam}) taken by the pure components. The unit-cell parameters of the various forms are close to one another. It means that the energetic differences between the forms are small, and it explains why microcalorimetric methods fail to reveal the subtle distinctions. Figure 9.31 shows, as a function of composition, the X-ray spectra on which the distinction between the forms is based.

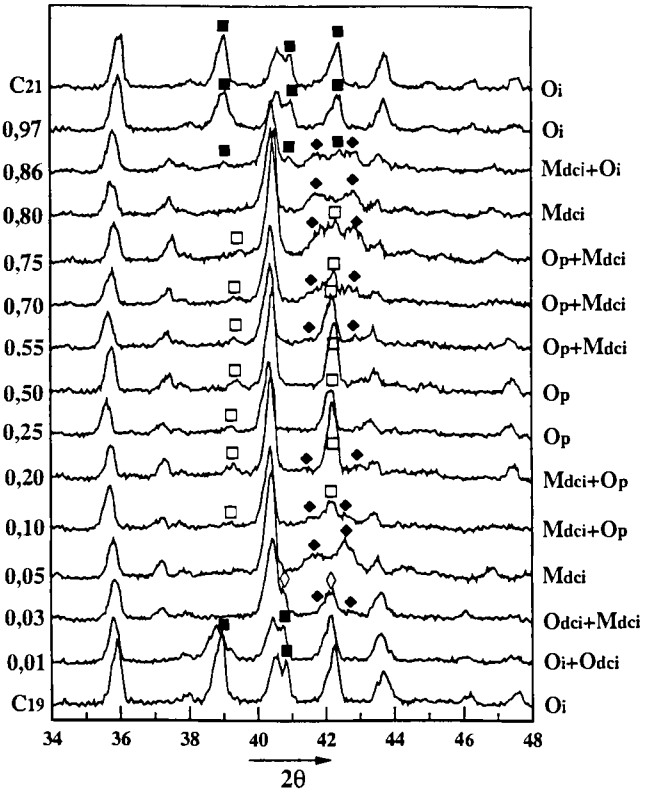

Figure 9.31 X-ray diffraction patterns for the system (C_{19} + C_{21}) plotted against the 2θ angle of reflection with composition as the parameter at $T = 278$ K [58].

Isoplethic Experiments as a Function of Temperature

In the technique introduced by Guinier, X-ray powder diffraction is combined with the possibility of heating the sample under observation. During an experiment, the X-ray film is moved with a linear speed. The technique offers the opportunity not only to subject the sample to a certain heating rate, but also to keep the sample at isothermal conditions and so far for a variety of desired temperatures. The position of the X-ray pattern on the film corresponds to the temperature of the sample (heating experiment at a certain rate), or to the progress of time (isothermal experiment). The power of the technique is that it unites the advantages of thermal analysis-with-characterisation-of-phases with the possibility of applying a wide range of time-scales.

2,2-Dimethyl-1,3-Propanediol + Tris(hydroxymethyl) Aminomethane [70]

Like AMP and PG, see above, the substances neopentylglycol (NPG), 2,2-dimethyl-1,3-propanediol, $(CH_3)_2C(CH_2OH)_2$ and tris(hydroxymethyl) aminomethane (TRIS, 2-amino-2-hydroxymethyl-1,3-propanediol, $NH_2C(CH_2OH)_3$) have a plastic-crystalline mesostate [71]. In the case of NPG, the stability relationships are [64,72]:

Ordinary solid (T_{trs} = 314.4 K)	ODIC	(T_{trs} = 402.8 K) liquid
Monoclinic (M)	fcc (C_F)	
$P2_1/c$; $Z = 4$	$Z = 4$	

and for TRIS

Ordinary solid (T_{trs} = 406.8 K)	ODIC	(T_{trs} = 442.7 K) liquid
Orthorhombic (O)	bcc (C_I)	
$Pn2_1a$; $Z = 4$	Im_3m; $Z = 2$	

The experimental phase diagram of the (NPG + TRIS) system is shown in Figure 9.32 and the phases that make their appearance are L, C_I, C_F, O and M.

Hereafter, a series of experiments is described to give an indication of how the phase diagram was established, and, in particular, to illustrate the influence of time-scale. The experiments on mixed samples were made on originally solid samples that had been obtained from liquid mixtures, which were allowed to cool down to room temperature typically during 30 min.

Initially, the system was studied by thermal analysis by DSC experiments on 5 mg samples at a scanning rate of $2\,K \cdot min^{-1}$. The experiments revealed the existence of three different three-phase equilibria: [M + C_F + 0] at T = 310.2 K; [C_F + C_I + 0] at T = 392.5 K and [L + C_F + C_I] at T = 410.7 K.

In spite of the coherence between the DSC observations, there was an alarming peculiarity. It is the fact that the DSC peak, which would correspond to the arrest at the [C_F + C_I + O]

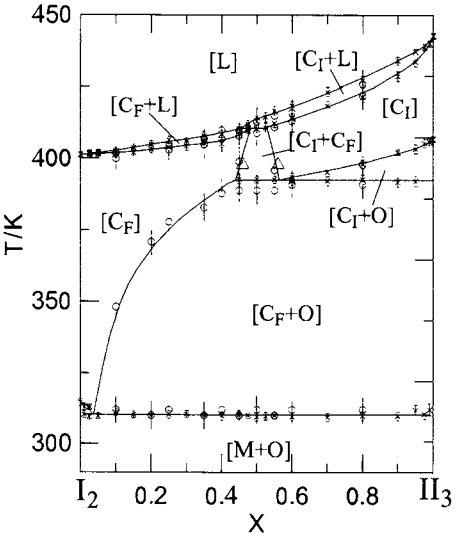

Figure 9.32 Phase diagram for the system (I_2 = NPG + II_3 = TRIS) with temperature plotted against mole fraction TRIS. ×: as determined by DSC; o: by the Guinier technique; Δ: isothermal X-ray diffraction [70].

three-phase equilibrium, was observed for samples containing up to 95 mole% of NPG (the peak in question is the first one of curve 'a' in Figure 9.35). This circumstance would represent an inconsistency in the phase diagram data as was found by a set of trial calculations of the [O + C_F] equilibrium.

In this situation, it was decided to study the behaviour of the samples by means of the Guinier technique at a rate of 0.1 K · min^{-1}, which is 20 times slower than that used in the DSC experiments. The results are shown, in part, in Figure 9.33 and this time they are free from severe inconsistencies. From the diffraction patterns, it can be seen that the transition from the [O + C_F] two-phase region to the [C_F] single-phase region takes place at $T \sim 378$ K for the sample with $x = 0.25$; at $T \sim 383$ K for $x = 0.35$ and at $T \sim 388$ K for $x = 0.40$. Additional Guinier experiments, the results of which are not shown here, showed that, for $0.45 < x < 0.57$, the [O + C_F] domain is left at $T \sim 390$ K as the system enters into the [C_F + C_I] two-phase region. Guinier experiments on samples with $x = 0.60$ and 0.80 showed that the [C_F + O] domain is left at $T \sim 391$ K. The sample with $x = 0.80$ clearly showed the transition from [C_F + O] to [C_I + O]. The sample with $x = 0.60$, on the other hand, only revealed a change from [C_F + O] to C_I. This means that the composition of the C_I phase, at the three-phase equilibrium, is in the vicinity of $x = 0.60$. From isothermal X-ray experiments at $T = 398$ K, it was determined that the composition of C_I at $T = 392.5$ K is $x = 0.57$. The experimental phase diagram, based on the evidence discussed so far, is the one shown in Figure 9.32.

As a conclusive check of the correctness of the phase diagram, as far as experimentation is concerned, some additional experiments have been carried out. The results of these experiments are shown in Figures 9.34 and 9.35. Figure 9.34 pertains to X-ray experiments,

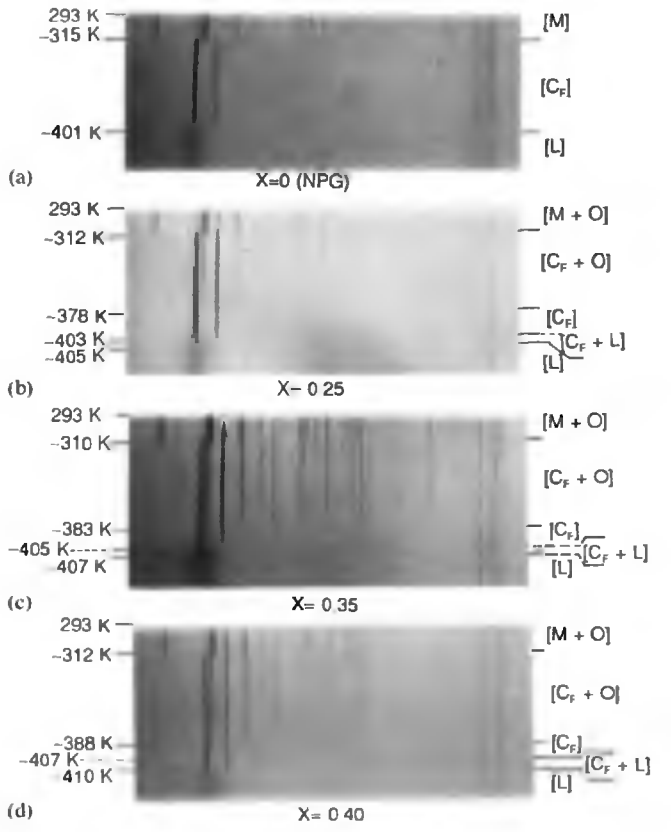

Figure 9.33 Guinier–Simon spectra for the system (NPG + TRIS). (a): pure NPG; (b), (c), (d): samples with mole fraction TRIS $x = 0.25$; $x = 0.35$; $x = 0.40$, respectively [70].

during which the sample with $x = 0.15$ is kept at $T = 388\,\mathrm{K}$. The figure shows the evolution of the X-ray pattern with time. It can be observed that it takes about 60 min for the (111) reflection of the orthorhombic 'phase' to disappear completely.

In the other set of experiments, samples with $x = 0.30$ first were kept at $T = 388\,\mathrm{K}$ within the DSC instrument for a specified time, and then scanned, until they had melted completely. From Figure 9.35, where curve (a) corresponds to the 'direct' procedure, it follows that the eutectic-like peak disappears as time passes. It is further evidenced that the sample becomes homogeneous: in the T–x plane the point ($x = 0.30$; $T = 388\,\mathrm{K}$) is in the [C_F] single-phase field.

9.2.4 High-Order Phase Transitions

From a thermodynamic point of view, phase transitions are classified as first-order or high-order phase transition. Whatever the phase transition of a pure substance, the Gibbs energy of the system remains continuous, read $\Delta_\alpha^\beta G = 0$. First-order phase transitions are

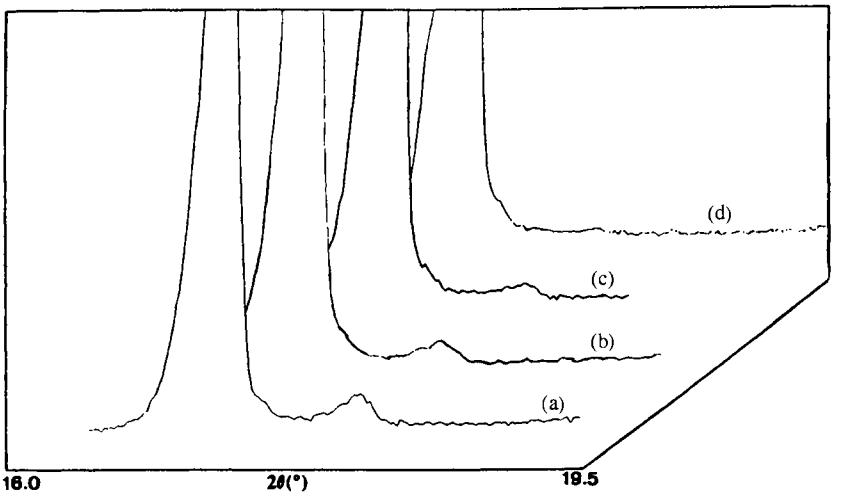

Figure 9.34 X-Ray patterns for the system (NPG + TRIS) with mole fraction TRIS $x = 0.15$ permanently at $T = 388$ K. Curves a, b, c, d: the sample has been at $T = 388$ K for 5, 15, 38 and 60 min, respectively [70].

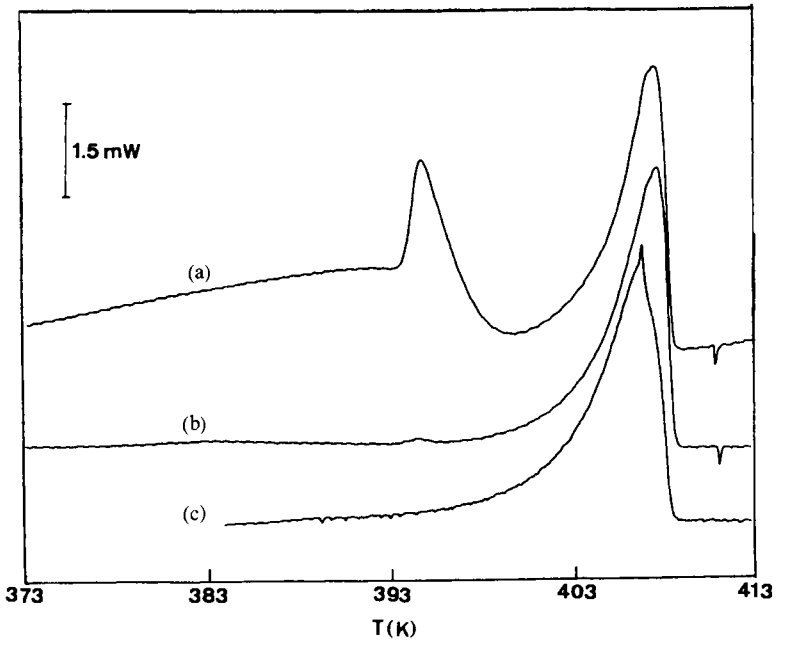

Figure 9.35 DSC thermograms for the system (NPG + TRIS) with mole fraction TRIS $x = 0.30$. Curve (a) direct heating from $T = 293$ K; Curves (b), and (c) are obtained after the sample has been kept at $T = 388$ K for 300 min, and 960 min, respectively [70].

characterised by a discontinuity in the first derivatives of the Gibbs energy with respect to temperature (entropy) and pressure (volume). Such transitions are associated with latent heats, or the enthalpy change, and discontinuities in volume, which generally give rise to drastic structural changes at the transition point. Thus, changes in crystal symmetry along with heat effects could be taken as the necessary experimental evidence for first-order phase transitions. As far as second- or higher-order phase transitions are concerned, both entropy and volume of the system remain continuous, while the second derivatives of the Gibbs energy, namely heat capacity, thermal expansion and isothermal compressibility, display a discontinuous change. For these cases, the crystal symmetry of both phases is related. According to the Landau theory for second- or high-order phase transitions, it is always possible to identify an order parameter that decreases continuously with decreasing temperature from the high-temperature disordered phase (the more symmetrical structure) to the low-temperature ordered phase (the less symmetrical structure). In such a description, phase transition is associated with an ordering process characterised by the order parameter that becomes zero at the transition point. Consequently, coexistence between the high- and the low-temperature phase is never reached. From an experimental point of view, one can only determine a phase transition to be nearly second order, since it is possible that a small discontinuity in the order parameter or other physical properties may be undetected.

2-Chloronaphthalene (R = Cl) is known to display a second-order phase transition. Below the liquid phase, this substance crystallises at $T = 330.2$ K in a disordered phase I that transforms to another disordered structure (phase II) at $T = 313.0$ K. Table 9.1 gathers the crystallographic properties of both phases. The structures may be described as a stacking of molecular sheets that are parallel to the *ab* plane. The positions and orientations of the naphthalene rings are also nearly the same in both monoclinic unit cells. In phase II, the molecular entity is statistical owing to re-orientational disorder, as can be inferred from the four β-positions of the naphthalene ring that are occupied by a statistical atom $[f(\mathrm{Cl}) + (1 - f)(\mathrm{H})]$ with experimental occupancy factors f at $T = 293$ K of 0.64, 0.11, 0.09 and 0.16 for Cl(12), Cl(13), Cl(16) and Cl(17), respectively [73]. On heating form II, the occupancy factors tend to become equal. As a consequence, the molecular entity in the high-temperature phase I, appears to be centro-symmetrical with a more or less statistical equi-distribution of the chlorine atom on the four sites of the naphthalene ring. Thus, phase I corresponds to a unidirectional superstructure of phase II with *c* parameters related by $c_{\mathrm{II}} = 2c_{\mathrm{I}}$ (see Table 9.1). A straightforward order parameter comes, as suggested by the authors, from the relation of the occupancy factors [74]. To account for more detail about this phase transition, the superstructure and structure Bragg reflections were followed around the transition temperature. Figure 9.36 shows the evolution of the

Table 9.1 Lattice parameters of 2-chloronaphthalene for the high-temperature phase I and the low-temperature phase II [74].

Form	Space group	T (K)	Z	a (nm)	b (nm)	c (nm)	β (deg)
II	$P2_1/n$	293	4	0.7662	0.5944	2.1300	120.32
I	$P2_1/a$	315	2	0.7733	0.5963	1.0667	120.00

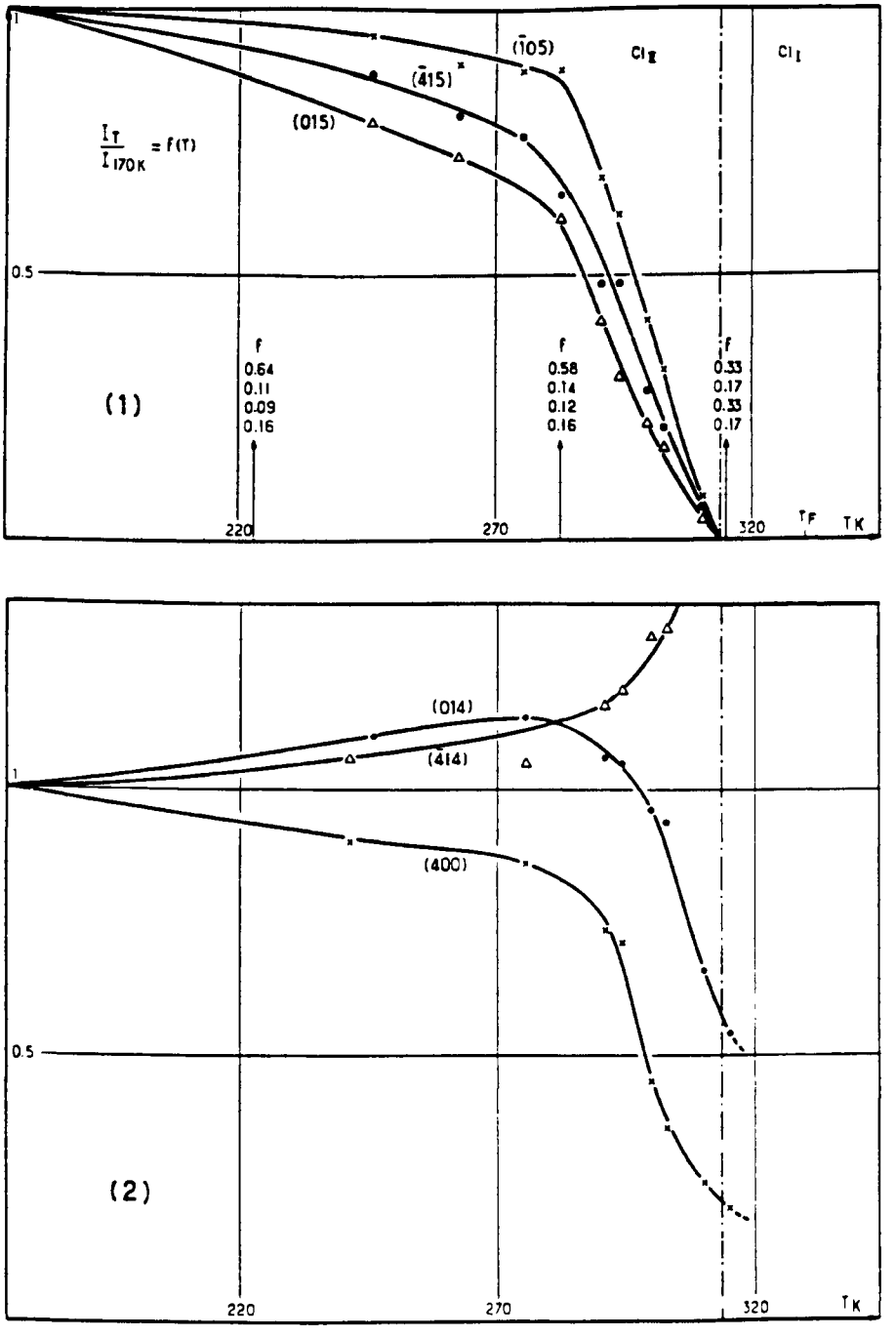

Figure 9.36 Variation of the superstructure (1) and structure Bragg reflections (2) around the II to I second-order phase transition of 2-chloronaphthalene [74].

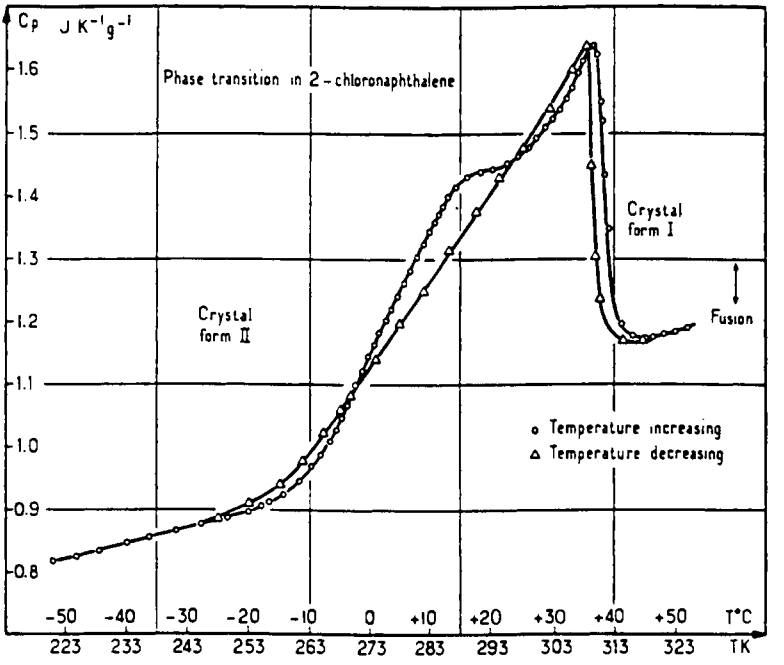

Figure 9.37 Plot of specific heat against temperature for 2-chloronaphthalene to illustrate the change through the II to I second-order phase transition [75a,75b].

superstructure and structure reflections. As can be seen from this figure, superstructure reflections change slowly with temperature until about $T = 260$–$270\,K$, the temperature domain where the thermodynamic effects on the specific heat become evident (see Figure 9.37). Subsequently, these superstructure reflections strongly change; to disappear at the transition point at $T = 313.0\,K$. On the contrary, the variation with temperature of the structure reflections crosses the transition point without discontinuity. Consequently, the volume occupied by a molecule does not change when going from phase II to phase I (see Figure 9.38).

The existence of a second-order phase transition for a pure substance invariably gives rise to a similar transition when molecular mixed crystals are formed. In Figure 9.39, the {2-chloronaphthalene (R = Cl) + 2-methylnaphthalene ($R = CH_3$)} system is shown. The high-temperature phase of R = Cl (here denoted as β) and the corresponding phase of $R = CH_3$ are able to form molecular mixed crystals over the whole composition range. At room temperature, only a small region of mixed crystals corresponding to the low-temperature phase (here phase α) of R = Cl is observed. The continuity of the a, b and β, as well as for c (phase I) and $c/2$ (for phase II) as a function of composition is demonstrated in Figure 9.40. As for second-order transitions in pure substances when temperature is the driving force, there is no phase coexistence when mixed crystals undergo such a transition as a function of temperature or mole fraction.

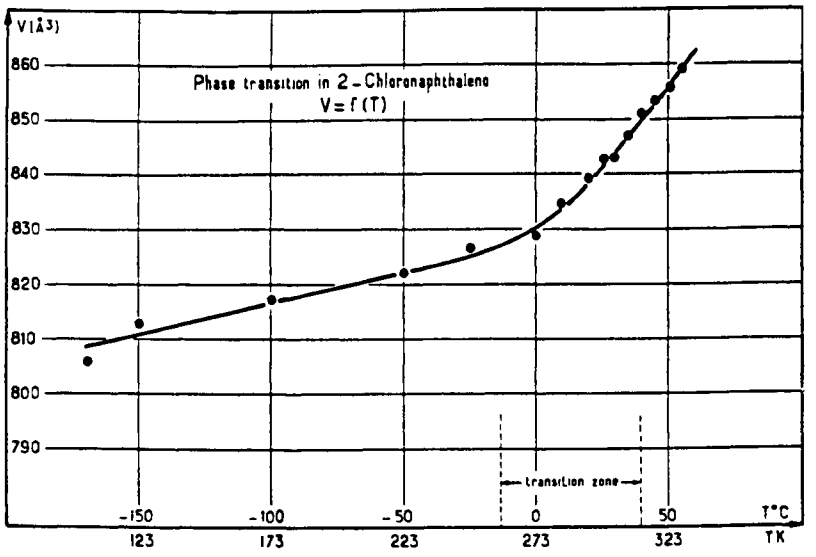

Figure 9.38 Plot of volume occupied by four molecules against temperature for 2-chloronaphthalene to illustrate the change through the II to I second-order phase transition [75a,75b].

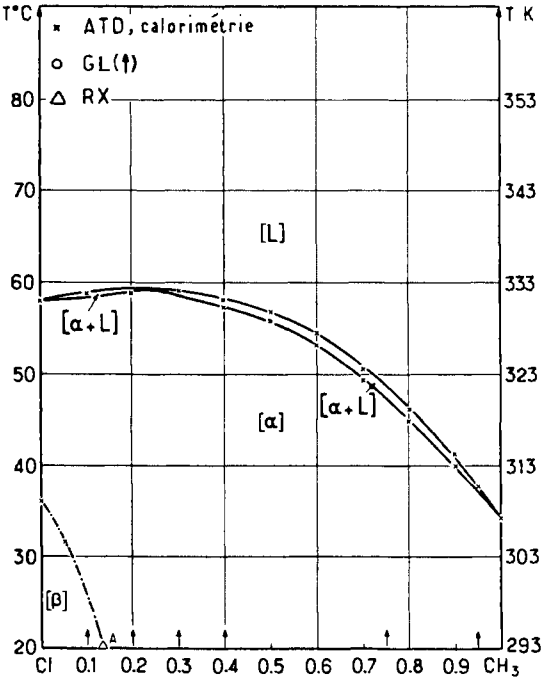

Figure 9.39 Phase diagram for the system {2-chloronaphthalene (R = Cl) + 2-methylnaphthalene (R = CH_3)} with temperature plotted against mole fraction (R = CH_3).

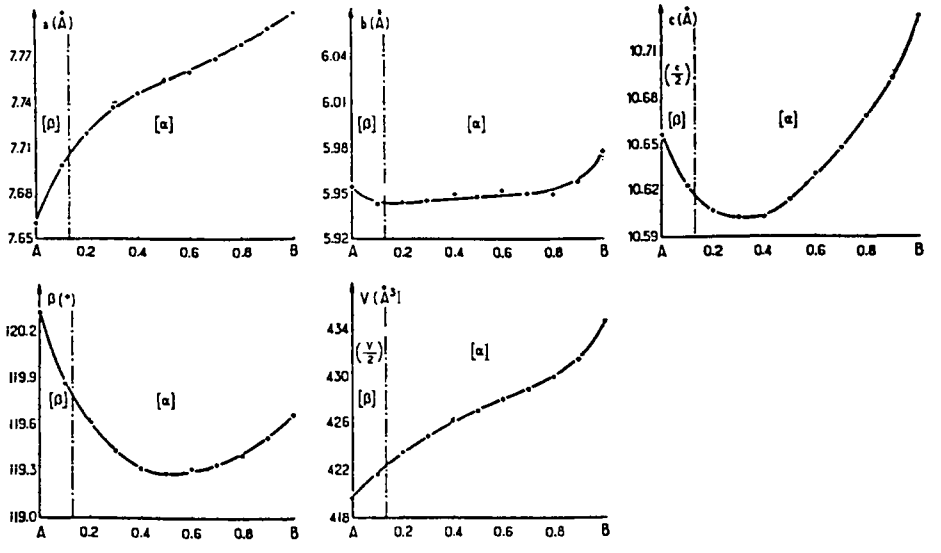

Figure 9.40 Plot of lattice parameters against mole fraction (R = CH_3) for the system {2-chloronaphthalene (R = Cl) + 2-methylnaphthalene (R = CH_3)}, at 293 K.

9.3 Key Systems

9.3.1 Naphthalene + 2-Naphthol

The bicyclic aromatic substance naphthalene is non-polymorphic; it is stable, and it can easily be purified. Naphthalene, accordingly, is an excellent material for the calibration of instruments used in thermodynamic studies. Naphthalene-based binary systems are used for testing the performance of set-ups for crystallisation processes. In mixed crystals research, an important role has been played by the set of substances formed by naphthalene and its 2-R-derivatives. R, in this case, is a substituent on the 2-position of the naphthalene molecule:

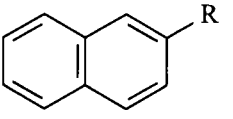

R = F, Cl, Br, OH, SH, CH_3

At the level of individual, isolated molecules every pair out of the set is giving rise to a high value of the coefficient of molecular homeomorphism, ε_k. The coefficient ε_k, introduced by Kitaigorodskii [5,76], expresses the geometrical similarity between two different isolated molecules, and it is defined as

$$\varepsilon_k = 1 - \Delta/\Gamma. \tag{9.30}$$

Table 9.2 Coefficients of molecular homeomorphism ε_k for pairs, R_1 and R_2, of 2-R-substituted naphthalenes.

R_1	R_2				
	F	Cl	CH_3	SH	Br
H	0.982	0.893	0.892	0.863	0.847
F		0.912	0.889	0.883	0.864
Cl			0.965	0.976	0.958
CH_3				0.958	0.957
SH					0.969

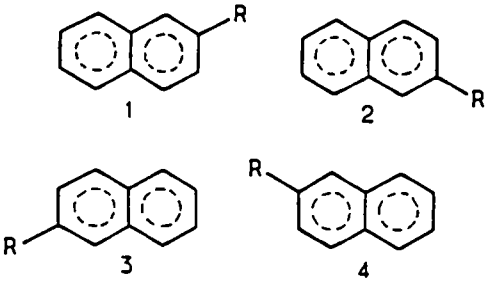

Figure 9.41 The four orientations of the molecules [3].

The two molecules are superimposed such that the intermolecular overlap is maximal. Then, there is an overlapping part, of which the volume is Γ, and there are no overlapping parts of which the total volume is Δ.

In Table 9.2, ε_k values are given for pairs of molecules out of the series of 2-R-substituted naphthalenes, including naphthalene (R = H) itself [3].

At the level of the crystalline unit cell, cell members of the set display the same characteristics. At their melting temperature, and before melting, the substances are monoclinic; space group $P2_1/a$, with two molecules per unit cell ($Z = 2$). These characteristics imply a centro-symmetrical structural unit. In the case of the derivatives, this is realised by fourfold, orientational disorder, see Figure 9.41. Denoting the occupancies of the different orientations by p_i, then necessarily $p_1 = p_3$, and $p_2 = p_4$.

In spite, however, of the high degree of molecular homeomorphism and the same unit-cell characteristics, not every pair out of the set gives rise to a continuous series of mixed crystals. This means that the members of the set do not share the same structural form. Following Kitaigorodskii, the situation can be looked upon as sketched in Figure 9.42. Within the structural setting of $P2_1/a$ and $Z = 2$, there are two competitive packings for occupying the lowest possible Gibbs energy. Following Michaud *et al.* [16], we will denote the two different forms by $\alpha 1$ and $\alpha 2$. The form $\alpha 2$ is the form in which naphthalene is stable. The 2-R-derivatives with R = F, Cl, Br, CH_3 take $\alpha 1$ as their stable form.

An example of phase diagram is shown in Figure 9.43 for the combination of naphthalene (R = H) and 2-fluoronaphthalene (R = F). At the naphthalene side, there is a

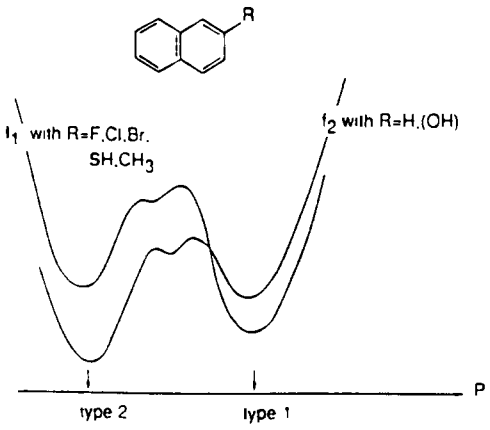

Figure 9.42 Imaginary Gibbs energy function plotted against packing parameter P for the $P2_1/a$ unit cell with two molecules, showing that the stable form of naphthalene is different from the stable form of most of its derivatives [2].

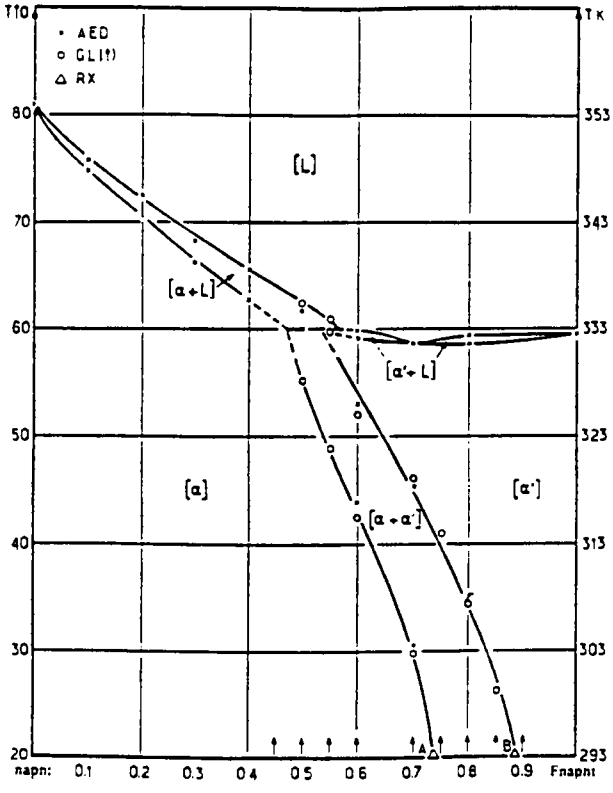

Figure 9.43 Experimental phase diagram of the system (naphthalene + 2-fluoronaphthalene). Experimental data are from microcalorimetry (×), isothermal powder diffraction (Δ) and isoplethic powder diffraction (o) [1,3].

Table 9.3 Cell parameters a, b, c and β of naphthalene (R = H), 2-naphthol (R = OH) and of stable and metastable 2-fluoronaphthalene (R = F). The temperature is T at which the diffraction experiments were carried out [1].

R	Form	T(K)	a (nm)	b (nm)	c (nm)	β (deg)
H	$\alpha 2$	293	0.8262	0.5984	0.8678	122.80
OH		383	0.8356	0.5903	0.9061	119.88
F	$\alpha 1$	293	0.7776	0.5954	0.8685	105.99
F	$\alpha 2$	293	0.8336	0.5915	0.8999	122.23

single-phase field of the $\alpha 2$-type of mixed crystals; at the fluoro side, a single-phase field for the $\alpha 1$-type of mixed crystals. The system, therefore, is an example of crossed isodimorphism, *cf.* Figure 9.8. By means of a thermodynamic analysis [10], the metastable melting points were calculated as $T = 333$ K for R = H, and $T = 312.5$ K for R = F.

In addition, the unit-cell dimensions of metastable 2-fluoronaphthalene could be obtained by extrapolation of the data measured on mixed crystals in the $\alpha 2$-field [3]. The numerical values of the cell dimensions are included in Table 9.3.

Among naphthalene's derivatives, a particular position is taken up by 2-naphthol (R = OH). This occurs because of the fact that the type of crystalline structure of 2-naphthol with $P2_1/a$ and $Z = 2$ has a stability range of just 0.6 K; from $T = 392.6$ K to the melting point $T = 393.2$ K. The unit-cell parameters, included in Table 9.3, could be determined thanks to the fact that a polycrystalline sample, obtained after melting in a sealed Lindemann glass capillary, could be kept supercooled at $T = 383$ K for 1 h, sufficiently long for data acquisition. Below $T = 392.6$ K the substance takes the, so-called, γ-form, with space group Ia and $Z = 8$.

From the numerical data in Table 9.3, it follows that the differences between the forms $\alpha 1$ and $\alpha 2$ are small. The distinction between $\alpha 1$ (R = F) and $\alpha 2$ (R = H; R = F) seems to be most pronounced for the parameters a and β. On these lines and at first sight, the data for 2-naphthol (R = OH) are in favour of $\alpha 2$. This means that naphthol is isomorphous with naphthalene, and that the two substances should give rise to a continuous series of mixed crystals (the ε_k value of the combination is 0.95) if there were not the complicating influence of polymorphism of 2-naphthol.

The experimental determination of the solid–liquid equilibrium goes back to Rudolfi [77]. Rudolfi's diagram has the 'cigar-type' of two-phase region, typical of the equilibrium between liquid mixtures and mixed crystals, over the whole range of compositions. The same type of phase diagram was published by Vetter *et al.* [78]. Vetter's work is unique in the sense that true equilibrium compositions of coexisting phases were determined. Their experimental method is based on zone melting. By means of a thermodynamic analysis [79], full agreement was found between experimental data and the calculated phase diagram. The phase diagram was calculated with the enthalpy of melting values of 19.1 kJ · mol^{-1} for naphthalene and 22.6 kJ · mol^{-1} for 2-naphthol, and assuming ideal liquid mixing behaviour. The deviation from ideal behaviour, Equation (9.14), in the mixed crystalline state was calculated as

$$G^{E,sol}(T \sim 375\,K, x)/(J \cdot mol^{-1}) = x(1 - x)[750 + 125(1 - 2x)]. \qquad (9.31)$$

Vetter's experimental data, read from the published phase diagram, are assembled in Table 9.4.

Table 9.4 Compositions of coexisting liquid (x_e^{liq}) and solid (x_e^{sol}) phases for the system {(1 − x) naphthalene + x naphthol} [78].

T(K)	x_e^{liq}	x_e^{sol}
353.3	0.000	0.000
359.0	0.090	0.182
363.0	0.182	0.329
367.2	0.276	0.464
371.5	0.372	0.571
375.7	0.471	0.667
379.8	0.571	0.757
383.9	0.675	0.820
387.7	0.781	0.892
391.8	0.889	–
395.5	1.000	1.000

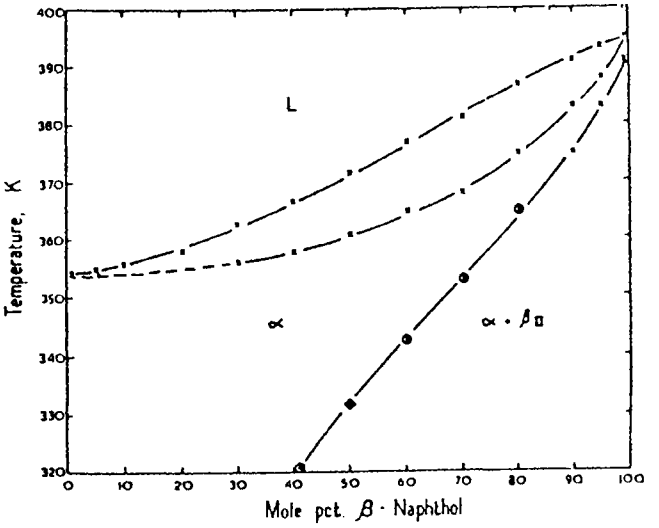

Figure 9.44 Plot of temperature against mole% β-napthol to show the phase diagram for the system {(1 − x) naphthalene + x2-naphthol} according to Baumgarth *et al.* [80]. Crosses: Microcalorimetry; circles: X-ray diffraction.

The diagram, which is shown in Figure 9.44, was determined by Chanh and co-workers, and published in 1969 [80]. The type of solid–liquid phase behaviour displayed by the diagram is in agreement with the results of Rudolfi and those of Vetter *et al.* [78]. The boundary, at the α side, of the (α + γ(β in the figure)) two-phase region had been determined by means of isoplethic X-ray powder diffraction.

Following the 1969 publication, a series of conflicting phase diagrams was published. A phase diagram showing a single three-phase equilibrium was published by Robinson *et al.* [81] and phase diagrams showing two different three-phase equilibria were published by

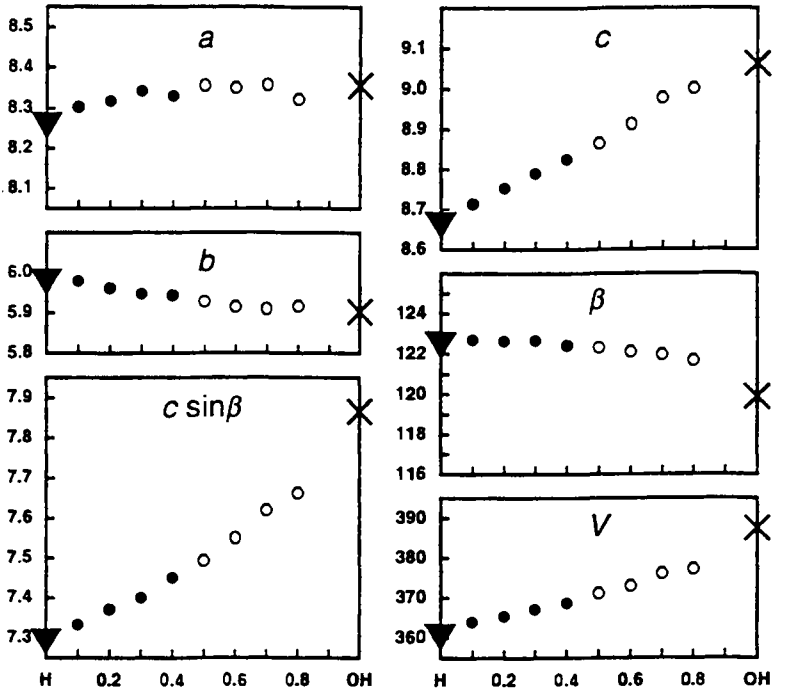

Figure 9.45 Lattice parameters plotted against mole fraction 2-naphthol for the system (naphthalene + 2-naphthol) for stable (•) and non-stable quenched (o) mixed crystals at room temperature. (X) Lattice parameters of the α-form of 2-naphthol at $T = 383$ K [16].

Robinson and Scott [82] and by Meresse [55]. The effect of these publications was that the status of 2-naphthol, in terms of the $\alpha 1$ versus $\alpha 2$ distinction, was called into question again.

A series of decisive experiments, in order to settle the true status of 2-naphthol, was carried out by Michaud *et al.* [16] and Michaud [83]. The title of Michaud's 1998 publication is significant: 'Is 2-naphthol isomorphous with 2-fluoronaphthalene or with naphthalene?' Michaud's results, some of which are detailed below, demonstrate that 2-naphthol is isomorphous with naphthalene, and, consequently, not with 2-fluoronaphthalene.

In Figure 9.45, the cell parameters of mixed crystalline samples are shown as a function of composition; the figure includes the values taken by the pure components as they are given in Table 9.3. The mixed samples, the parameter values of which are shown, were obtained by quenching from the liquid state. After quenching, the samples were analysed by X-ray diffraction. It is clearly seen that the results for 2-naphthol (crosses) are in line with the results for the mixed samples (circles). Besides, from studies on the thermal expansion of naphthalene [74,84], it is known that the change with temperature is too small (and plausibly so for 2-naphthol) to question the conclusion worded in the foregoing sentence.

In another series of experiments, the compositions of the coexisting solid phases, $\alpha 2$ and γ, were determined as a function of temperature. Mixed samples, to start with, were prepared by rapid crystallisation from a solvent. In this way, a finely powdered material is obtained, see above, leaving space for mobility of the molecules in order to reach equilibrium.

Thereafter, the samples were kept under isothermal conditions, during 24 h, and at a number of selected temperatures. Subsequently, the samples were quenched and directly analysed at room temperature by X-ray diffraction.

9.3.2 Tricosane ($C_{23}H_{48}$) + Pentacosane ($C_{25}H_{52}$)

The n-alkanes (C_nH_{2n+2}; hereafter denoted as C_n) have a rich polymorphic nature, which, apart from temperature and pressure, depends on the value and the parity of n, the number of carbon atoms in the molecules. At the level of individual, stretched molecules, there is an inversion centre when the number, n is even, and a mirror plane when n is odd (Figure 9.46).

In the crystalline state, the odd-numbered alkanes, in the range C_9–C_{45}, manifest themselves in four different ordered forms with orthorhombic or monoclinic symmetry and five rotator forms, where the molecules have orientational disorder along their long axis [85–90].

In the case of the even-numbered alkanes, the polymorphic behaviour is even more complex. Even alkanes from C_8 to C_{22} have triclinic ordered forms. From C_{26} onwards, several monoclinic forms are found, and, subsequently, a number of orthorhombic forms [91,92].

Unlike the odd-numbered alkanes, which invariably have a stable rotator phase before melting, the even-numbered alkanes have rotator phases only from C_{22} onwards [85,90,93,94].

The rotator phases, as do the low-temperature, ordered phases, display layered structures with long-range positional order. The structural characteristics of the five known forms of rotator phases, RI, RII, RIII, RIV and RV are very similar. The molecules, ordered in a layered structure, which can be a monolayer (RIII and RIV), a bilayer (RI and RV) or even a trilayer (RII), are always parallel, and are either tilted (RIII, RIV and RV) or perpendicular to the layers (RI and RII); see Figure 9.47.

Pairs of n-alkanes with a small difference in the number of carbon atoms ($\Delta n = 1$ or $\Delta n = 2$) readily mix in the solid state, *i.e.* give rise to the formation of mixed crystals. It is generally observed that forms, which make their appearance for pure alkanes from a certain value of n onwards, are stabilised in binary systems at considerably lower values of n.

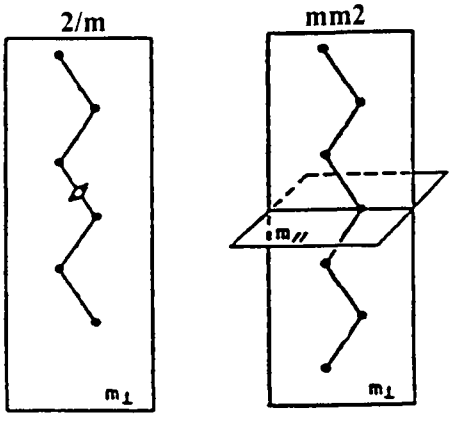

Figure 9.46 The symmetries of the n-alkane molecules, for even (left) and odd (right) alkanes [58].

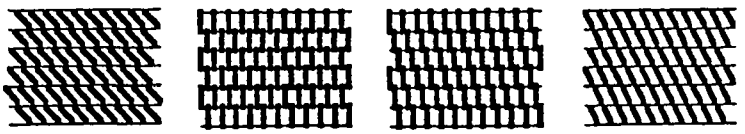

(a) **RV** (b) **RI** (c) **RII** (d) **RIV**

Figure 9.47 Sketch of the layered structure of the rotator forms. Reproduced from reference [88] with kind permission from American Institute of Physics. Copyright 1993.

Table 9.5 Crystallographic data for the various forms observed for tricosane (C_{23}) and pentacosane (C_{25}); from Robles *et al.* [85]. The temperatures given are the ones at which the unit-cell dimensions were determined.

C_n	Form	Space group	Z	T(K)	a (nm)	b (nm)	c (nm)	β (deg)
	Oi	Pcam	4	291	0.7467	0.4983	6.219	
	Odci	Pnam	4	312	0.7546	0.4989	6.226	
C_{23}	RV	Aa	4					
	RI	Fmmm	4	315	0.804	0.494	6.303	
	RII	R$\bar{3}$m	3	318	0.480		9.47	
	Oi	Pcam	4	291	0.7449	0.4968	6.726	
	Odci	Pnam	4	312	0.7529	0.4980	6.733	
	Mdci	Aa	4	320	0.7573	0.5011	6.7631	91.64
C_{25}	RV	Aa	4					
	RI	Fmmm	4	320	0.802	0.493	6.737	
	RII	R$\bar{3}$m	3	324	0.479		10.27	

As an example, the first pure even-numbered alkane with a stable rotator phase is C_{22}, compared with (C_{14} + C_{16}), which is the first (even + even) binary system with a rotator single-phase field. In addition, many of the binary systems in the low-temperature region have single-phase fields corresponding to forms that do not appear for their pure components.

A typical system for detailing the complexity of binary alkane systems is the combination of tricosane (C_{23}) and pentacosane (C_{25}). The pure components, to start with, have the following phase sequences, starting from room temperature.

$$\begin{array}{lll} C_{23} & \text{Oi} \rightarrow \text{Odci} \rightarrow & \text{RV} \rightarrow \text{RI} \rightarrow \text{RII} \rightarrow \text{liquid} \\ C_{25} & \text{Oi} \rightarrow \text{Odci} \rightarrow \text{Mdci} \rightarrow & \text{RV} \rightarrow \text{RI} \rightarrow \text{RII} \rightarrow \text{liquid} \end{array}$$

The notations of the 'ordered' low-temperature forms are from Rajabalee [95]. The O and M stand for orthorhombic and monoclinic, respectively. The index i (from the French impair = odd) is used to indicate that the form is observed for odd-numbered alkanes only. The index dc stands for conformational disorder: in the crystal lattice the molecules have so-called end-gauche defects [96]. The crystallographic data of the various forms of C_{23} and C_{25} are assembled in Table 9.5. Figure 9.48 represents the microcalorimetric thermogram observed for C_{23}.

The phase diagram of the binary combination, (C_{23} + C_{25}), is shown in Figure 9.49. It is the result of a careful investigation by means of DSC and X-ray diffraction (XRD), carried

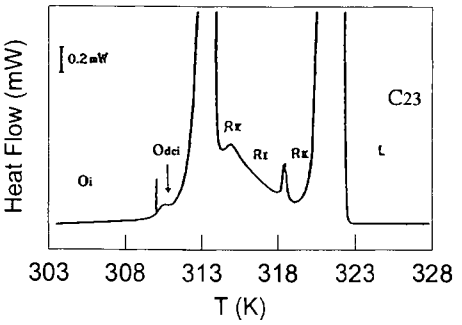

Figure 9.48 Microcalorimetric thermogram for tricosane (C_{23}) with heat flow plotted against temperature [97].

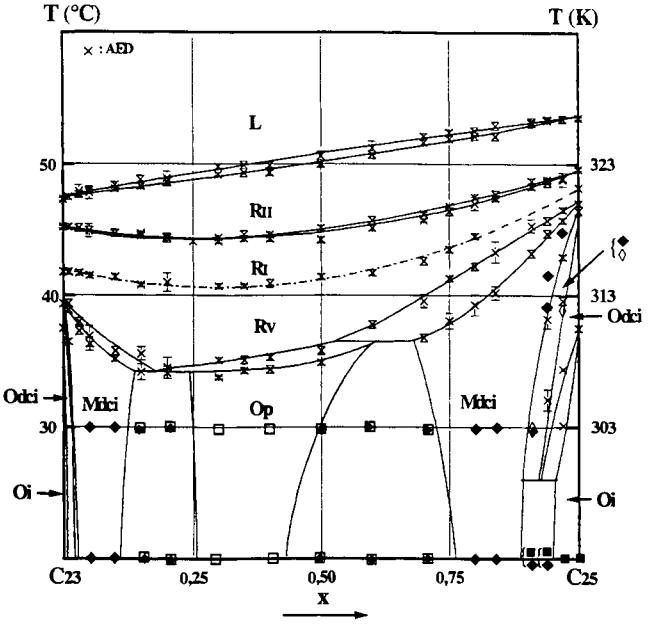

Figure 9.49 Experimental phase diagram, determined by DSC and XRD, with temperature plotted against mole fraction C_{25} for the system $\{(1 - x)$ tricosane $(C_{23}) + x$ pentacosane $(C_{25})\}$. The open and filled squares and diamonds refer to the phases observed by XRD [97].

out by Rajabalee *et al.* [95] and Rajabalee [97]. The fact that the diagram, Figure 9.49, displays some disagreement with the diagram by Dirand and co-workers [98–100] is an expression of the complexity of the subject. To be precise, these authors did neither detect the form Mdci for C_{25}, nor the second-order change (see below) from RV to RI.

In addition to the forms appearing in Table 9.5, the phase diagram shows a single-phase field for a new form, indicated as Op. The form is orthorhombic; the index p is from the French pair (=even), meaning that the form is observed for even pure alkanes (with $n \geq 28$). The appearance of Op is another example (*cf.* R in $(C_{14} + C_{16})$; see above) of the

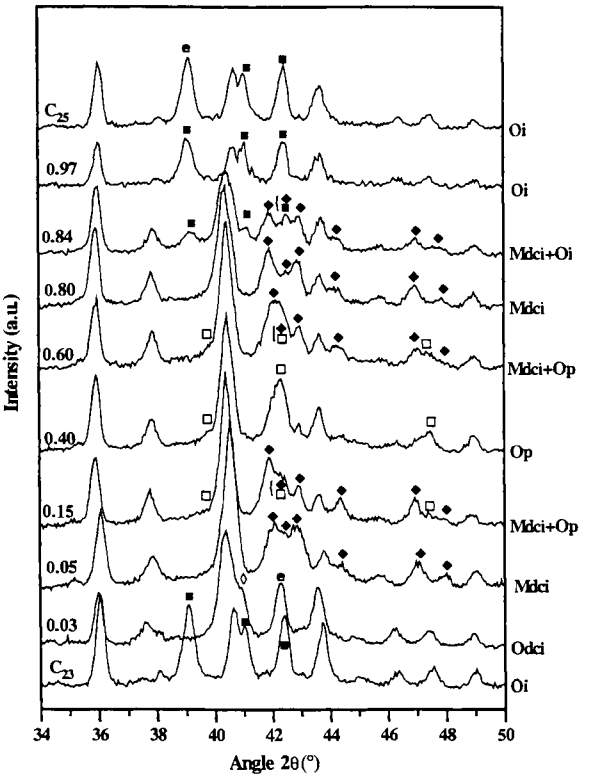

Figure 9.50 Part of X-ray diffraction patterns at $T = 293$ K plotted as a function of mole fraction in the system $\{(1 - x)\, C_{23} + x\, C_{25}\}$ [97]. Symbols are the same as in Figure 9.49.

fact that in binary systems forms are stabilised, which, for the pure components, appear for higher values of n. Likewise there is a Mdci single-phase field at the C_{23} side of the diagram, whereas Mdci is not observed for pure C_{23}. In Figure 9.50 [97], it is shown how the distinction between the low-temperature forms is made.

From bottom to top in Figure 9.49, the $T-x$ phase diagram has three different zones. The zone at the low-temperature side is for the 'ordinary'-solid state (S). The zone at the high-temperature side for the liquid (L), and the intermediate zone form the rotator mesostate (R). From zone to zone, there are great changes in the structural and energetic properties of the material. Within a given zone, inside the ordinary solid and rotator zones, the differences between the different forms are small. These facts are expressed, in a clear manner, by Figures 9.51–9.53. In Figure 9.51 curve (b), the 'normal' recording, with its two peaks, clearly reveals the transition from S to R, and from R to L. The fine structure of the changes is revealed by curve (a) in Figure 9.51, but only in part, because XRD is needed to disclose the change from Oi to Odci (Figure 9.52). In Figure 9.53, enthalpy effects as a function of composition are shown for three different changes. The greatest effect is for the change from R to L. The effect of the change inside the R zone, from RI to RII, is small, even in relation to the uncertainties in the data for R to L. In the case of the effect for the change from S to RV,

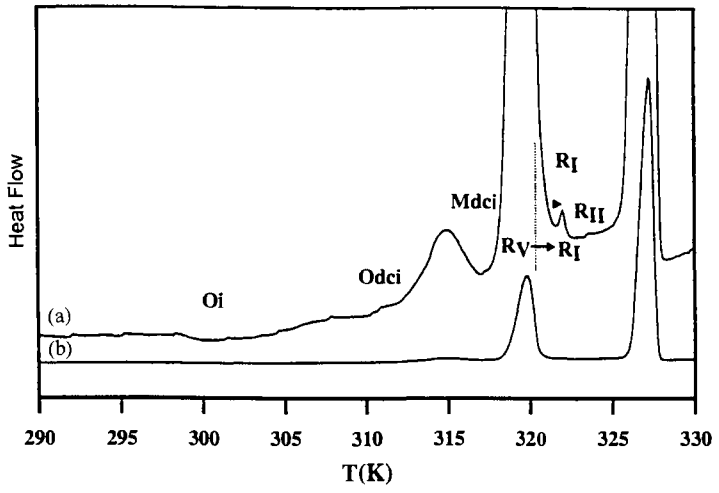

Figure 9.51 The system $\{(1 - x)\,C_{23} + x\,C_{25}\}$ for $x = 0.97$. DSC thermogram: (a) enlargement [97]; (b) 'normal' recording.

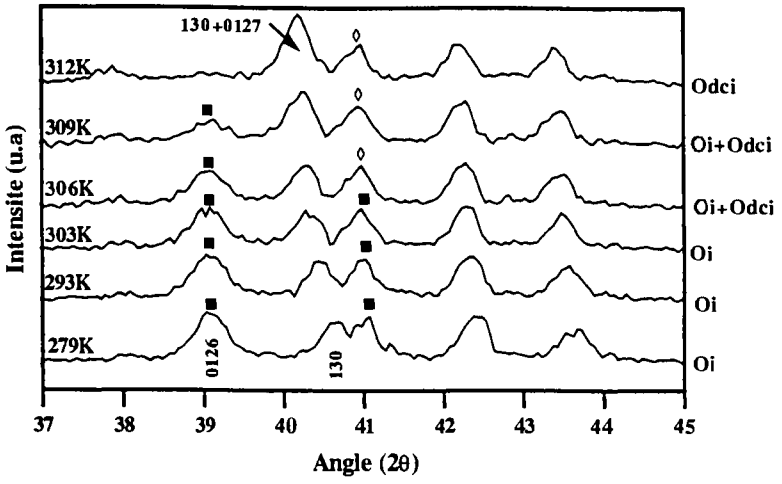

Figure 9.52 The system $\{(1 - x)\,C_{23} + x\,C_{25}\}$ for $x = 0.97$. Part of XRD pattern related to the change from Oi to Odci [97].

the fact that over the whole range of composition the data points are more or less in line demonstrates, again, that the differences between the various forms of S must be small.

The enthalpy effect of the transition from R to L, the enthalpy of melting as a function of x has a downward curvature. It means, that the excess enthalpy difference, $\Delta^{L}_{R}H^{E}$, is negative; see Equation (9.25). Realising that the excess enthalpy in the liquid state virtually is zero (see [98]), the negative $\Delta^{L}_{R}H^{E}$ implies a positive value for $H^{E,R}$, the excess enthalpy of the rotator state (this time in the form RII). A mathematical fit of the experimental heat of melting data, as shown in Figure 9.53, gives rise to the following expression (*cf.* Equation (9.5)),

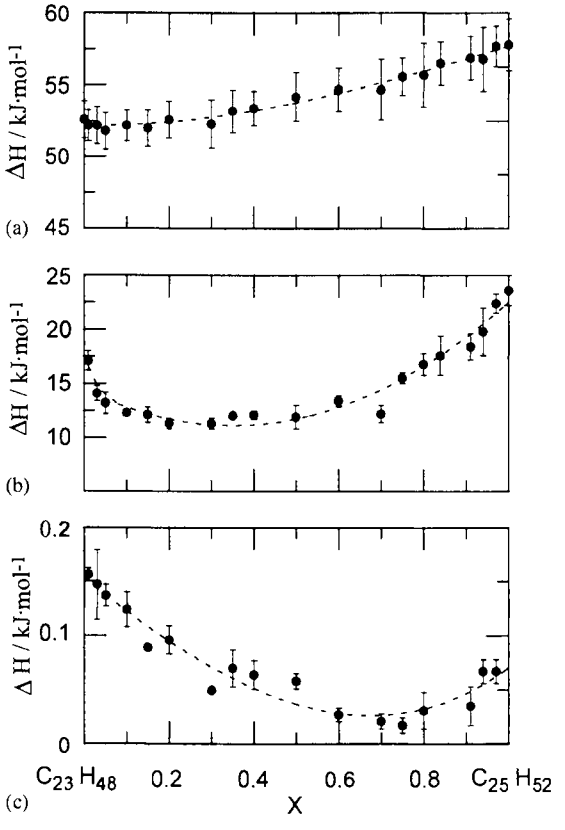

Figure 9.53 A plot of enthalpy effects against composition for $\{(1 - x)\ C_{23} + x\ C_{25}\}$. Top, from rotator to liquid; intermediate, from ordinary solid to rotator; bottom, from RI to RII (data from Rajabalee [97]).

$$\Delta^{L}_{RII}H(x)/(\text{kJ} \cdot \text{mol}^{-1}) = \{(1 - x)52.18 + x57.69 - 4.58x(1 - x)[1 + 0.28(1 - 2x)]\}. \qquad (9.32)$$

In terms of the $AB\theta$ model, Equations (9.3), (9.4), and the liquid mixtures being ideal, the result corresponds to the values of $A = 4580\,\text{J} \cdot \text{mol}^{-1}$ and $B = 0.28$ for the mixed state of the system in the form RII.

From the phase diagram, Figure 9.49, it can be read that the melting loop, *i.e.* the (RII + L) two-phase region, does not deviate much from the straight line connecting the melting points of the pure components. It means according to Equations (9.21) and (9.22), and Figure 9.6 that the excess Gibbs energy difference between R and L, $\Delta^{L}_{R}G^{E}$, is very small. Taking the liquid state as an ideal mixture, $G^{E,L} = 0$, this is to say that, for the mean temperature of the two-phase region, the excess Gibbs energy of the mixed rotator state practically is zero. And this, subsequently, means, Equation (9.3), that the value of θ must be close to the mean temperature, *i.e.* $\theta \cong 320\,\text{K}$.

From Figure 9.53c, it follows that the excess heat of transition, $\Delta_{RI}^{RII}H^E$, of the equimolar mixture is about $-75\,J \cdot mol^{-1}$. It implies that value of the parameter A for the RI form is about $300\,J \cdot mol^{-1}$ greater than $4580\,J \cdot mol^{-1}$ for the RII form. There is no reason to assume that the values of B and θ for the RI form will differ from those of RII form beyond the uncertainties of the latter.

The third heat effect displayed in Figure 9.53 is the enthalpy effect of the transition from the ordinary solid state to the rotator state.

Unlike the change R → L, the change from S to R does not correspond to the change from a mixed state of one given form to another mixed state in one form. The forms taken by S are Odci, Mdci and Op and of the four forms, Mdci and Op have the largest single-phase fields. This circumstance has important consequences, in particular for the thermodynamic analysis of the data. Generally in situations like this, thermodynamic analysis requires for each of the forms involved the enthalpies of transition and the transition temperatures of the two pure components.

In the case of the n-alkanes, the fortunate situation is met that the thermodynamic properties of the member substances change with chain length in a monotonous fashion, whether or not independent of parity. This means that correlations can be made in terms of the number of carbon atoms n. In addition, such correlations are powerful tools for checking the consistency of the data, and to fix the numerical values of open places. As an example, and for our purpose, in Figure 9.54, it is shown how the enthalpy of transition, from S to R, varies with chain length for the odd-numbered alkanes. Similarly, in Figure 9.55, the temperatures of transition are shown as a function of chain length.

In Figure 9.54, alkanes of the form Op are missing. The reason is that for the pure substances the form Op does not make a stable appearance. Note that the Op transition temperatures in Figure 9.55 are extrapolations of binary data.

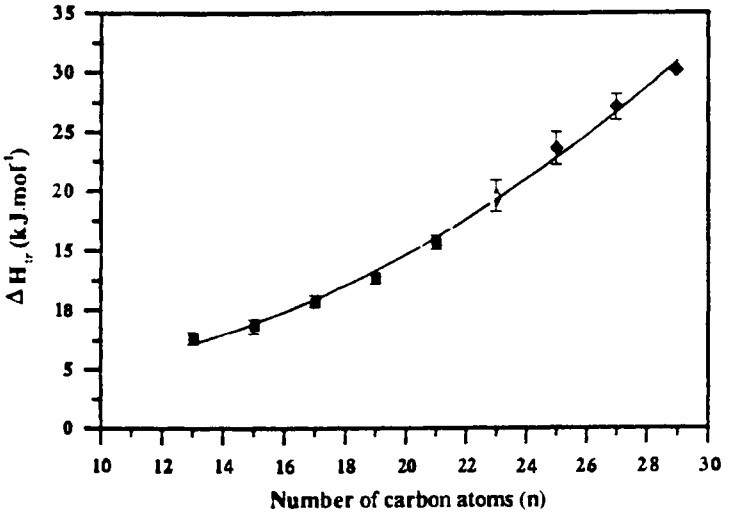

Figure 9.54 Plot of enthalpy of transition from S to R plotted against chain length for the odd-numbered n-alkanes. The forms taken by S are Oi (■), Odci (◇) and Mdci (◆) [95].

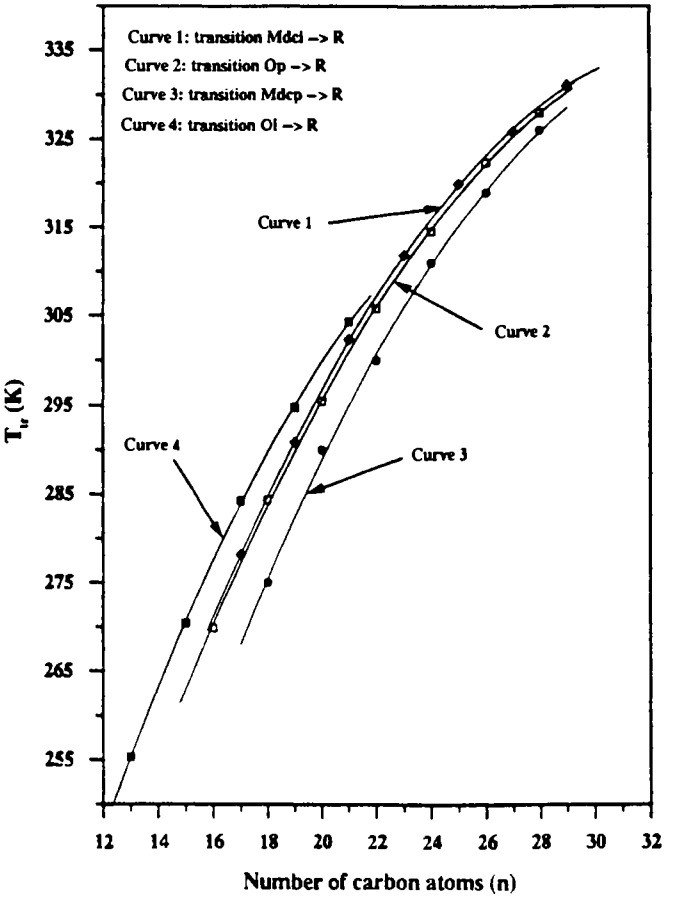

Figure 9.55 Plot of the temperature of transition against chain length from S to R for the various forms taken by S [95].

In the thermodynamic analysis of the (C_{23} + C_{25}) system by Rajabalee *et al.* [95], it has been assumed that the Op to R transition enthalpies are in line with the data for the other forms, *i.e.* with the data in Figure 9.54. A correlation of the thermodynamic properties of the 'ordinary'-solid state S has been made for 14 systems in the range from (C_{17} + C_{18}) to (C_{26} + C_{28}) [101]. The values of the parameter A in S are typically about seven times higher than the A values in R. The A values increase with increasing $\Delta n/\overline{n}$, which is the difference in the number of carbon atoms divided by the mean number. For the system (C_{23} + C_{25}), the value of $\Delta n/\overline{n}$ is 2/24. The following relationships have been constructed for the A values in R (A^R), and in S (A^S) [101,102].

$$A^R/(\text{kJ} \cdot \text{mol}^{-1}) = \left[51.09\left(\frac{\Delta n}{\overline{n}}\right) + 376.5\left(\frac{\Delta n}{\overline{n}}\right)^2\right], \tag{9.33a}$$

$$A^{S}/(\mathrm{kJ}\cdot\mathrm{mol}^{-1}) = \left[660\left(\frac{\Delta n}{\bar{n}}\right) - 1903\left(\frac{\Delta n}{\bar{n}}\right)^{2}\right]. \qquad (9.33b)$$

With respect to the θ parameter, which reflects the dependence of the excess Gibbs energy on temperature, the situation is as follows. The forms in R, like those in S, have a common value for θ. The R-forms are characterised by $\theta = 320\,\mathrm{K}$ [102,117], and the S-forms by $\theta = 335\,\mathrm{K}$ [101].

9.3.3 2,2-Dimethylpropane + Carbon Tetrachloride

The 2,2-dimethylpropane {$C(CH_3)_4$, neopentane} and carbon tetrachloride (CCl_4) belong to the class of substances that give rise to a mesostate. The molecules of the substances in the class have a quasi-spherical shape, and the mesostate is meant by the use of the terms plastic crystals and ODICs. In the plastic-crystalline mesostate, the molecules have dynamic orientational disorder.

The system (neopentane + carbon tetrachloride), and especially its plastic-crystalline state, has been the subject of many studies. In part, the interest in the system is related to the fact that the two different molecules have almost the same size, and both have a non-polar character [103].

Carbon tetrachloride, as far as the ODIC state is concerned, displays monotropic behaviour. There are two different forms, one of them invariably being metastable. The stable form (R) is rhombohedral; the metastable form (C_F) is fcc. When liquid carbon tetrachloride is cooled, it first crystallises to C_F, which, on further cooling changes into R. If, after crystallisation to C_F, the material is heated, it does not change into R, but melts at a temperature about 5 K below the melting point of R. In the ordinary solid state, carbon tetrachloride takes the form M, which is monoclinic.

In the case of neopentane, the only experimentally observed ODIC form is C_F, the fcc form. In the ordinary solid state, the substance takes the form Q, which is either tetragonal [104–106] or hexagonal [60].

A survey of enthalpy changes and transition temperatures is given in Table 9.6. The combination of the two substances, the binary system $\{(1 - x)\ C(CH_3)_4 + x\ CCl_4\}$, has been studied by means of adiabatic calorimetry, by Chang and Westrum [107,116]. Chang and Westrum investigated five mixed samples; the experimental phase diagram, Figure 9.56, is part of their results.

After the establishment of the true polymorphic nature of the two substances, it has become clear that part of the proposed phase diagram must be incorrect. Due to the fact that the two substances have different stable ODIC forms, C_F and R, there must be a (C_F + R) two-phase region, which in Figure 9.56 is missing. The (ODIC + liquid) part of the system, therefore, is a case of crossed isodimorphism (see above). In such cases, the stable phase behaviour can be regarded as the result of two, each other crossing (solid + liquid) loops, where part of the thermodynamic interpretation is related to the establishment of the metastable melting points. As a matter of fact, the metastable melting point of CCl_4 is experimentally known: it is the melting point of the form C_F, see Table 9.6.

Table 9.6 Summary of enthalpy changes and transition temperatures for neopentane $\{C(CH_3)_4\}$ and carbon tetrachloride (CCl_4) [18].

$C(CH_3)_4$	$T_{Q->F}$ (K)	$\Delta H_{Q->F}$ ($J \cdot mol^{-1}$)	$T_{F->L}$ (K)	$\Delta H_{F->L}$ ($J \cdot mol^{-1}$)			Ref.
	140.5		256.8	3093.0			[107]
	140.0	2570.7 ± 1.3	254.2	3190.0 ± 1.3			[60]
	130.2		253.5				[104]
	140.5	2630	256.8	3090			[108]
	140.0	2570	256.5	3250			[109]
	139.0	2560	253.8	3240			[110]
CCl_4	$T_{M->R}$ (K)	$\Delta H_{M->R}$ ($J \cdot mol^{-1}$)	$T_{F->L}$ (K)	$\Delta H_{F->L}$ (m) ($J \cdot mol^{-1}$)	$T_{R->L}$ (K)	$\Delta H_{R->L}$ ($J \cdot mol^{-1}$)	Ref.
	225.5				250.3		[111]
	225.35 ±0.5	4581 ± 13			250.3	2515 ± 8	[112]
	226.6 ± 1.0	4477 ± 180	244.8 ± 1.0	1753 ± 180	247.8 ± 2.0	2494 ± 200	[62]
			245.7 ± 0.1	1848 ± 2	250.28 ± 0.10	2558 ± 4	[113]
				1787 ± 5		2530 ± 12	[114]
	225.7 ± 0.1	4631 ± 20	246.00 ± 0.01	1830 ± 70	250.53 ± 0.01	2562 ± 6	[115]

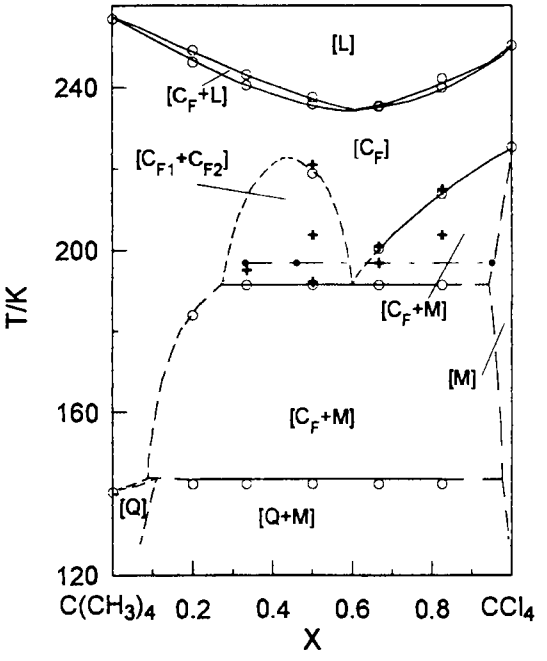

Figure 9.56 The system $\{C(CH_3)_4 + CCl_4\}$. The phase diagram showing temperature plotted against mole fraction CCl_4. Data by Chang and Westrum [107,116].

The matter of the system's phase diagram has been taken up again by Salud *et al.* [18]. A complete thermodynamic analysis of the system was made, including a re-interpretation of Chang and Westrum's heat capacity diagram. Out of the five mixed samples studied by Chang and Westrum, the one having $x = 0.501$ is the most interesting. Its heat capacity diagram, Figure 9.57, differs from the others, by the presence of the stumpy peak in the figure between the second and third of the sharp peaks. The stumpy peak was tentatively ascribed by Chang and Westrum by the presence of a region of demixing, with an upper critical solution temperature. In Salud's view, the peak corresponds to the passage of the (R + C_F) two-phase region, analogous to the heat capacity diagram, Figure 9.12, for the passage of a (solid + liquid) two-phase region. The integrated enthalpy effect of the peak is in agreement with the overall result of the thermodynamic analysis. See below.

The thermodynamic analysis of the plastic-crystalline to liquid part of the system is representative of the treatment of crossed isodimorphism. In terms of input information, methodology and optimised result, the thermodynamic analysis can be detailed as follows.

The input used consists of the

(i) calorimetric data on pure components, Table 9.6, and on the mixed samples, as studied by Chang and Westrum;
(ii) characteristic phase diagram temperatures: the transition temperatures of the pure components, Table 9.6; the temperatures read from the heat capacity diagrams; the metastable melting point of CCl_4, which is $T = 245.7$ K [113];

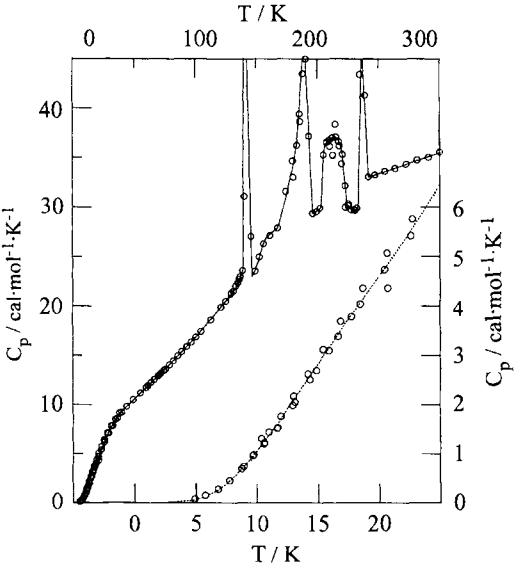

Figure 9.57 Plot of heat capacity against temperature for the system $\{(1 - x)\ C(CH_3)_4 + x\ (CCl_4)\}$ at the composition $x = 0.501$, determined by Chang and Westrum (from the data of Chang and Westrum [107]).

(iii) excess Gibbs energy in the liquid state:

$$G^{E,liq}(x)/(kJ \cdot mol^{-1}) = x(1 - x)[1.25 - 0.04(1 - 2x)], \quad (9.34)$$

(iv) the value of $2350\,J \cdot mol^{-1}$ for the enthalpy of melting of metastable $C(CH_3)_4$, see hereafter.

As usual, the thermochemical data on the pure components and the phase diagram are used to calculate the excess Gibbs energy difference between the solid and liquid states. This function, $\Delta G^E(x)$, when combined with $G^{E,liq}(x)$, yields the excess Gibbs energy of the solid state $G^{E,sol}(x)$. Subsequently, $G^{E,sol}(x)$, which is in fact $G^{E,sol}(T = T_m, x)$, is combined with the heat of mixing, the excess enthalpy of the solid state, $H^{E,sol}(x)$, to yield the function, $S^{E,sol}(x)$, the excess entropy of the solid state. Therewith the three system-dependent parameters A, B and θ are fixed.

In a straightforward manner, the (C_F + L) branch of the phase diagram produces the function

$$G^{E,C_F}(x, T_m = 237\,K)/(kJ \cdot mol^{-1}) = x(1 - x)[1.85 - 0.05]. \quad (9.35)$$

In the case of the (R + L) branch, the procedure is less straightforward, owing to the fact that the metastable melting point of $C(CH_3)_4$ is not known. In this situation, a series of trial and error calculations is made: the metastable melting point is varied until the most satisfactory result is obtained. The outcome is $T = 220\,K$ for the metastable melting point of neopentane, and for the excess Gibbs energy

$$G^{E,R}(x, T_m = 230\,K)/(kJ \cdot mol^{-1}) = x(1 - x)[1.30 - 0.49x(1 - x)]. \quad (9.36)$$

The enthalpy relationships are visualised in Figures 9.58 and 9.59. Figure 9.58 is a representation of the experimental enthalpy effects of the transitions from the plastic-crystalline state to liquid. Again there are two branches, and the figure shows how, by extrapolation, the enthalpy of melting of metastable neopentane is obtained.

The distances, in Figure 9.58, from the enthalpy of melting curves to the dashed lines, correspond to the excess enthalpy differences, $\Delta_s^l H^E(x)$. Together with the known excess enthalpy of the liquid state, these differences give the excess enthalpies of the two mixed states. With respect to the liquid state, experiments have revealed that its excess entropy is very small and for that reason the excess enthalpy can be identified with the excess Gibbs energy, Equation (9.8). The excess enthalpies of the mixed ODIC states are shown in Figure 9.59. For comparison, Figure 9.60 shows the excess enthalpy according to the interpretation by Chang and Westrum [107].

The calculated parameters of the $AB\theta$ model, Equation (9.3), following from the excess Gibbs energies, Equations (9.35) and (9.36), together with the excess enthalpies, Figure 9.58, are assembled in Table 9.7.

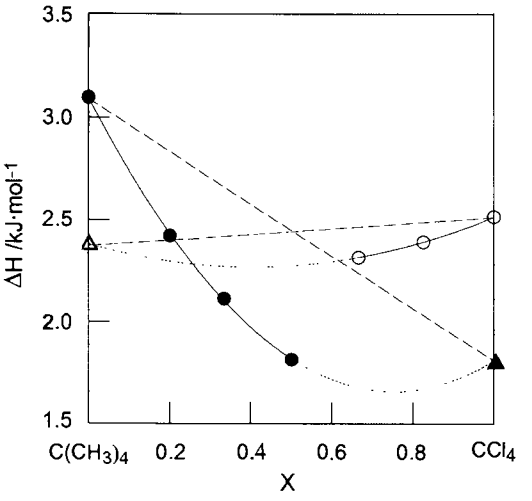

Figure 9.58 Plot of enthalpy of melting against composition for the system $\{(1 - x)\ C(CH_3)_4 + x\ CCl_4\}$ for the two ODIC mixed states C_F (●) and R(○), as reported by Chang and Westrum [107]. Triangles represent enthalpies of melting of metastable phases [18].

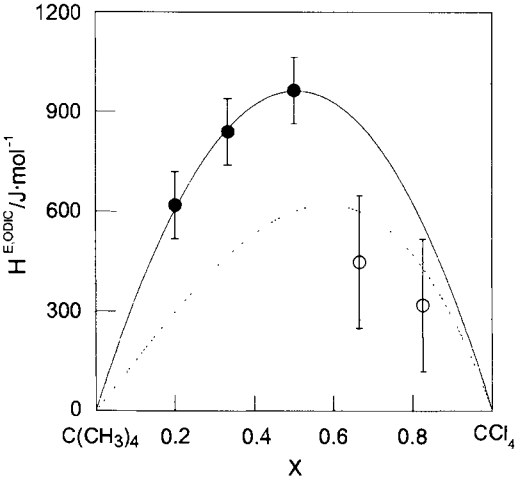

Figure 9.59 Plot of calculated excess enthalpies of the two mixed ODIC states C_F (●), and R (○) against mole fraction CCl_4 for the system $\{C(CH_3)_4 + CCl_4\}$ [18].

Finally, the complete phase diagram resulting from the analysis described above, along with the analysis of the low-temperature region, is shown in Figure 9.61. The phase diagram still needs a certain improvement with respect to the solubility of $C(CH_3)_4$ in the M-form of CCl_4.

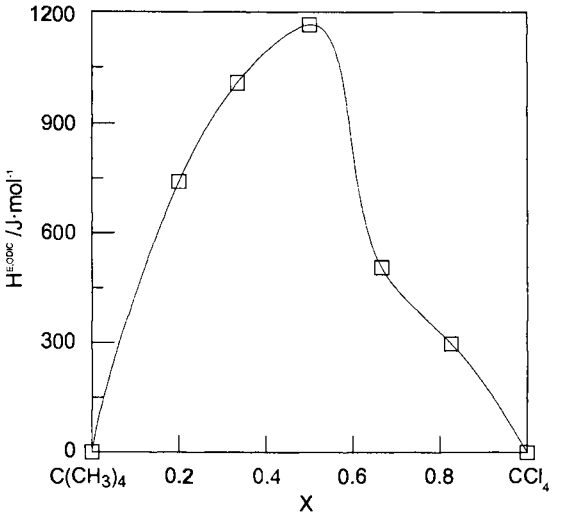

Figure 9.60 Plot of the excess enthalpy of the mixed ODIC state against mole fraction CCl_4 for the system $\{C(CH_3)_4 + CCl_4\}$, according to the interpretation by Chang and Westrum [18,107].

Table 9.7 The parameters of the $AB\theta$ model for the system $\{(1 - x)\ C(CH_3)_4 + x\ CCl_4\}$ for the two mixed ODIC states, C_F and R.

	A/(kJ · mol^{-1})	B	θ/K
C_F	3.95 ± 0.42	−0.11 ± 0.02	456 ± 80
R	2.68 ± 0.48	−0.26 ± 0.21	503 ± 90

9.4 Empirical Relationships

Up to 2001, the thermodynamic and structural properties of mixed crystals have been determined for a variety of isolated systems, and for series of systems out of groups of chemically coherent substances. The investigation on families of systems, such as the (alkane + alkane) systems has been especially rewarding. Several empirical relationships have been discovered between the excess properties themselves and between excess properties and exo-thermodynamic parameters. A brief overview, of the relationships found, is presented in this section.

9.4.1 Enthalpy–Entropy Compensation

In this work, a restriction has been made to isobaric systems, and it means that the principal properties considered are the excess enthalpy H^E and the excess entropy S^E. The excess enthalpy and excess entropy can be looked upon as the changes ΔH and ΔS, involved in the

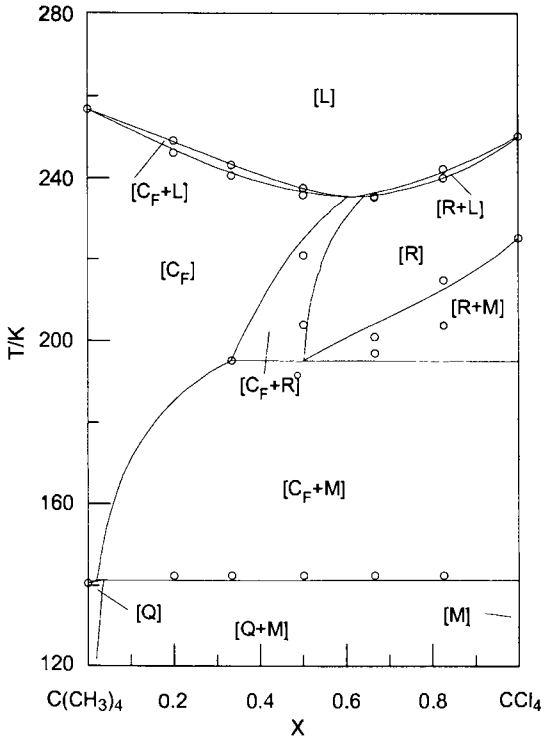

Figure 9.61 Calculated phase diagram with temperature plotted against mole fraction CCl_4 for the system $\{C(CH_3)_4 + CCl_4\}$ [18].

formation of the real mixture from the (hypothetical) ideal mixture of the same components under the same conditions of temperature and composition. In this sense the formation of mixed crystals is just an event, among many others involving an enthalpy and entropy change Experimental research has shown that for many events (i) ΔH and ΔS are virtually independent of temperature over a considerable range of temperature; and (ii) that their quotient $\Delta H/\Delta S$ is virtually constant within a class of similar systems. The quotient having the dimension of temperature is often referred to as the compensation temperature to indicate that for that temperature, the change in Gibbs energy $\Delta G\,(=\Delta H - T\Delta S)$ becomes zero (or rather passes zero) [117].

For mixed crystals and in terms of the $AB\theta$ model, the quotient between ΔH and ΔS, between H^E and S^E is given by the parameter θ, see Equations (9.4) and (9.5). To start with, we may recall Section 9.3.2, where it was agreed that the alkane system (C_{23} + C_{25}) would have, for its rotator mixed state, a value for θ of about 320 K. In Figure 9.62, (C_{23} + C_{25}) is one of the binary alkane systems for which the equimolar excess enthalpy is plotted against the equimolar excess entropy. The points shown in the figure are practically on a straight line, which is evidence of the property that the complete family of systems is characterised by a common value of the parameter θ, which is $\theta = 320$ K.

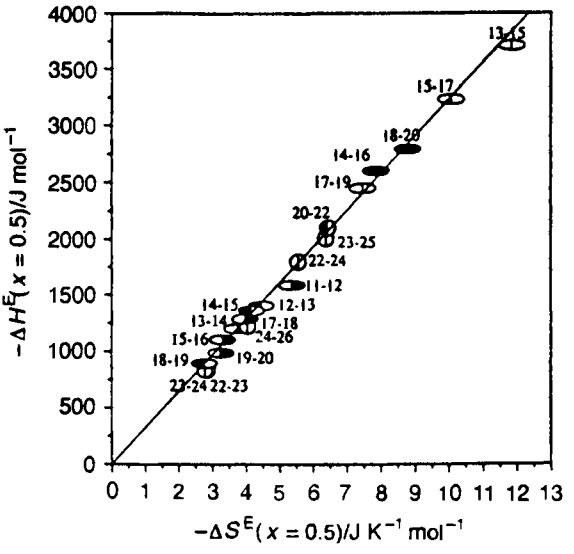

Figure 9.62 Equimolar excess enthalpy plotted against equimolar excess entropy for the mixed crystalline rotator form RI of binary n-alkane systems [118].

Table 9.8 Groups of mixed crystalline systems characterised by a uniform temperature θ of excess enthalpy/excess entropy compensation.

Group	n	States	EGC range T_{irs}/K	θ/K	References
n-Alkanes	18	R→L	250–324	320	[118]
n-Alkanes	14	S→R	270–321	335	[101]
Dihalobenzenes	10	S→L	312–356	500	[119]
Polyols	10	P→L	316–516	630	[120]
Alkali halides	13	S→L	825–1021	2565	[121]

Notes: The n denotes the number of member systems studied. The transitions studied involve two states out of ordinary solid (S), rotator R, plastic crystalline (P) and liquid (L). For EGC range, see text.

The mixed crystalline rotator state (R) of the binary n-alkane systems corresponds to a class of similar systems in the context of enthalpy–entropy compensation. Likewise, the common value of $\theta = 335$ K is displayed by the 'ordinary'-solid state (S) of the n-alkane systems [101].

In Table 9.8, a survey is given of the families of mixed crystals, studied so far by the REALM (Réseau Européen sur les Alliages Moléculaires), that are characterised by a uniform value of the parameter θ. In Table 9.8, the alkali halide group is the group of common-ion binary alkali halide systems. The term dihalobenzenes stands for the group of systems of which the components are 1,4-dihalobenzenes with halo = Cl, Br, I; the term polyols is used for a group of neopentane derivatives containing substituents out of the series

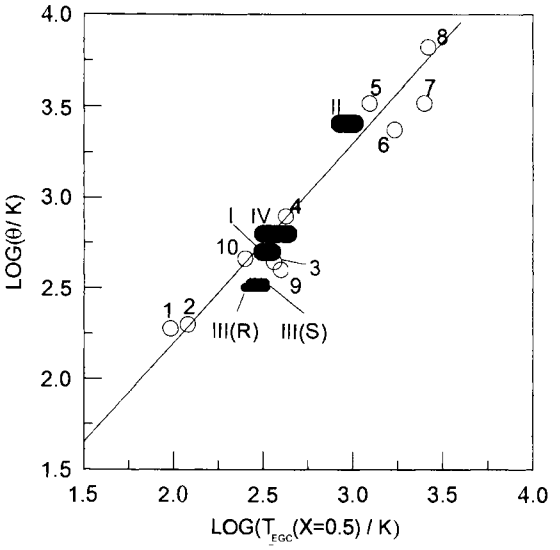

Figure 9.63 Plot of the compensation temperature θ as log θ against equimolar EGC temperature of melting T_m as log T_{EGC}. Apart from the groups of systems shown in Table 9.8 (I, *p*-dihalobenzenes; II, alkali halides; III, alkanes (R for R–L and S for S–R) and IV, polyols), the figure includes the data available for a number of isolated systems: (1) (Ar + Kr) and (2) (Kr + Xe) [122]; (3) (L-carvoxime + D-carvoxime) [123]; (4) (1,2,4,5-tetrachlorobenzene + 1,2,4,5-tetrabromobenzene) [46]; (5) (Ni + Au) [124]; (6) (Pd + Au) [125]; (7) (SrO + BaO) and (8) (MgO + CaO) [126]; (9) (CBr_4 + C_2Cl_6) [15]; (10) (CCl_4 + $C(CH_3)_4$) [18].

$-CH_2OH$, $-NH_2$ and $-NO_2$. The heading EGC range applies to the range on the temperature scale of the equimolar EGC temperatures of the member systems of the group.

The numerical values in Table 9.8 are such that the uniform compensation temperature θ increases with the position of the transition range on the temperature scale. Moreover, the θ values increase faster than the EGC temperatures. To visualise these trends, the values of log θ are plotted in Figure 9.63 against the logarithm of the equimolar EGC temperatures for the transitions of R to L and of S to L. Also included in the log–log representation are the positions of a number of isolated, individual systems.

In a robust way, the evidence contained in Figure 9.63, and corresponding to a relationship between compensation temperature and melting temperature, can be given by

$$\frac{\log(\theta/\mathrm{K})}{\log(T_m/\mathrm{K})} = 1.10 \pm 0.05. \tag{9.37}$$

An alternative formula, having the advantage of using melting temperatures of the pure components, which is more accessible than T_m, is

$$\theta = (4.00 + 0.16)\frac{T_A^0 \cdot T_B^0}{T_A^0 + T_B^0}, \tag{9.38}$$

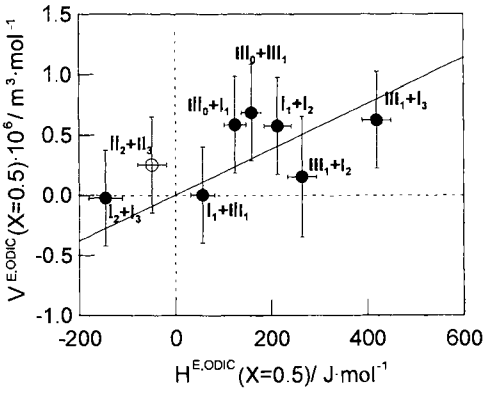

Figure 9.64 Equimolar excess volume plotted against equimolar excess enthalpy for the neopentane derivatives showing a fcc symmetry (filled circles) and a bcc (open circles) in the plastic-crystalline state [120].

where T_A^0 and T_B^0 are the melting temperatures of the pure components [127]. The type of relationship in Equation (9.38) was introduced by Tanaka *et al.* [128] for the compensation temperature of liquid metallic solutions. Clearly, Equations (9.37) and (9.38) have the character of rules of thumb; neither Equation (9.37) nor Equation (9.38) expresses the experimental fact that the groups of systems shown in Table 9.8 have uniform (system-independent) compensation temperatures.

Another interesting compensation relationship has been proposed between the excess enthalpy and the excess volume. In such a case, H^E and V^E compensate for one another in such a way that the excess internal energy ($U^E = H^E - pV^E$) becomes zero at a 'compensation pressure' for a group of systems. This has experimentally been evidenced for the neopentane derivatives and it is shown in Figure 9.64, for which compensation pressure has been estimated to be 0.5 GPa [120].

9.4.2 Mismatch Parameters

Unlike θ, the parameter A of a given system, out of a group like the n-alkanes, is not system-independent. The A parameter reflects the energetic interaction between the molecules A and B of the two components A and B. The parameter A will be zero if this interaction is neutral, *i.e.* the mean of the interaction between A and A and between B and B molecules. The parameter A will be negative if there is a net attraction between A and B molecules, and positive in the case of a net repulsion. Therefore, the statement that parameter A is not system-independent is rather obvious. The replacement of a C_{19} molecule in a lattice of C_{19} molecules by a C_{21} molecule corresponds to a net repulsion. Intuitively, it is 'less easy' to replace the C_{19} molecules by a C_{23} than by the C_{21} molecule: the positive value of A for (C_{19} + C_{23}) will be greater than the value of A for (C_{19} + C_{21}). In other words, the greater the difference in size, the greater is the mismatch between the molecules A and B, the

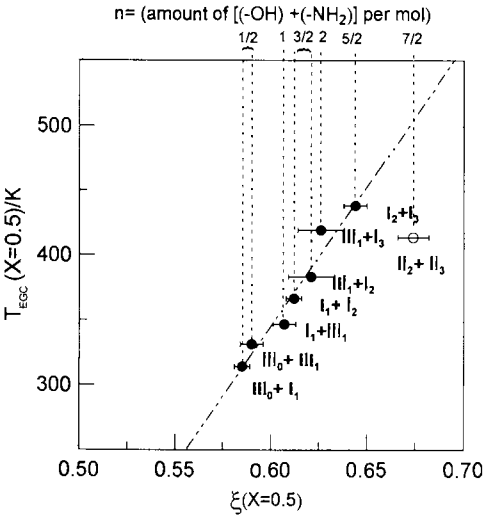

Figure 9.65 Plot of the EGC temperature against the packing coefficient, both for the equimolar mixed crystals, as well as the mean number of the hydrogen bonds (upper axis) of the ODIC phases (fcc, filled circles; bcc, open circles) of the systems of neopentane derivatives [120].

greater the value of parameter A. Mismatch in size, however, is not the only factor that accounts for the A parameter as there are systems with negative A, after all. For the neopentane derivatives containing substituents of the series $-CH_2OH$, $-NH_2$ and $-NO_2$, the intermolecular interactions are accounted for by dynamical hydrogen bonds. In such a case, the packing coefficient is a system-dependent property closely related to the mean number of $-OH$ groups (n) in the two-component system as indicated in Figure 9.65, which shows the increasing of the equimolar melting temperature with the packing parameter as well as with n.

A convenient vehicle for demonstrating these matters is found in the collection of systems based on naphthalene and its 2-R derivatives (R = F, Cl, Br, SH, CH_3), introduced in Section 9.3.1. Recalling Kitaigorodskii's coefficient of molecular homeomorphism, ε_k in Equation (9.30), one can observe that the parameter m_k

$$m_k = 1 - \varepsilon_k, \tag{9.39}$$

expresses the geometrical mismatch between the molecules of the system. As a direct link with the experimental phase diagrams, in Figure 9.66 the values of ΔT are plotted against m_k. The ΔT equals the distance, for $x = 0.5$, from the zero line to equal the G curve

$$\Delta T = T_{zero}(x = 0.5) - T_{EGC}(x = 0.5), \tag{9.40}$$

in the experimental solid–liquid phase diagram. Realising that, within the collection of systems, the entropies of melting of the components do not differ very much, and that it is likely that the same holds true for the values of θ of the mixed solid state of the binary systems, it follows that ΔT, Equation (9.40), is a direct reflection of parameter A of a system.

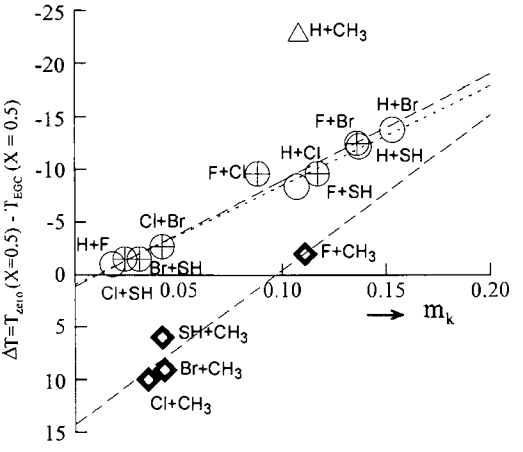

Figure 9.66 Plot of ΔT in Equation (9.40) against parameter m_k for the binary systems out of naphthalene and its 2-R derivatives. For the form in which naphthalene is metastable and 2-fluoronaphthalene is stable, the distance in the phase diagram, for $x = 0.5$ from the EGC to the zero line, Equation (9.40), is plotted against the geometrical mismatch between the molecules of the two components, Equations (9.39) and (9.30) (data from Oonk *et al.* [2]).

The collection of systems, dealt with in Figure 9.66, can be split into four groups, *viz.*:

(i) (halo + halo) group, constituted by six systems, the two components of which have R = halo (=F, Cl, Br and also SH);
(ii) (H + halo) group; four systems; one of the components is naphthalene, the other has R = halo;
(iii) (CH_3 + halo) group; four systems; one of the components is 2-methylnaphthalene, the other has R = halo;
(iv) system (naphthalene + 2-methylnaphthalene).

The (halo + halo) group is representative of families of systems that are composed of two members out of a chemically coherent group of substances having the same crystalline form. Examples are the n-alkanes in the form RI; the 1,4-dihalobenzenes with space group $P2_1/a$ and $Z = 2$; the alkali halides having the NaCl type of structure, and of which common-ion combinations are considered; the neopentane derivatives showing a fcc symmetry in the plastic-crystalline state. Generally, two members out of such a coherent group give rise to mixed crystals; provided, however, that the geometrical mismatch between the two is not too large. The 1-bromo-4-iodobenzene is able to mix in all proportions with 1,4-dibromobenzene, but not with 1,1-dichlorobenzene. Chemical coherence implies that the intermolecular interactions, between A and A, B and B, and between A and B molecules, have the same physical nature. The importance of this observation is that for these systems (i) the excess behaviour of the solid state can be related to geometrical mismatch, and (ii) the excess behaviour of the liquid mixtures can be neglected, in most of the cases. Geometrical mismatch, invariably, comes down to a net repulsion, *i.e.* a positive excess enthalpy, a positive value for the parameter A. And logically, the greater the mismatch, the greater the excess enthalpy; and also, absence of mismatch will be absence of excess enthalpy and will

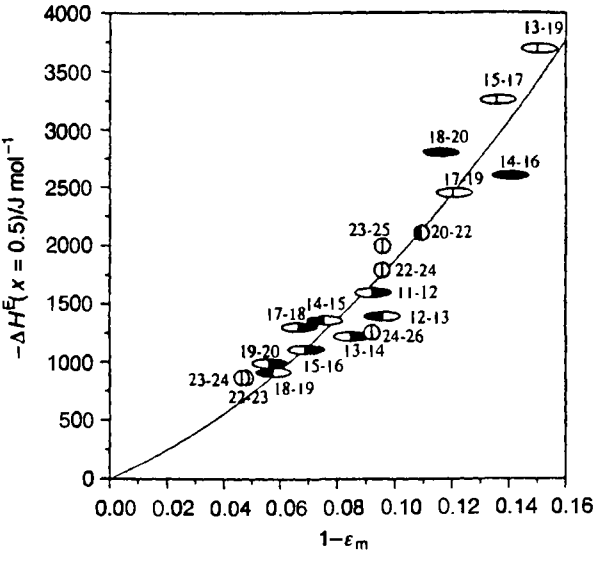

Figure 9.67 Plot of equimolar excess enthalpy against geometrical mismatch ($1 - \varepsilon_m$) based on degree of crystalline isomorphism for the mixed crystalline rotator state of binary n-alkane system. The symbols have the same meaning as in Figure 9.62 [27,118].

correspond to ideal behaviour. In Figure 9.66 as a result, the data symbols for the (halo + halo) group are on a curve having a positive slope and emanating from the origin. These characteristics also make their appearance in Figure 9.67, which pertains like Figure 9.62, to the n-alkane systems and their rotator state. Besides, the mismatch parameter used in Figure 9.67 is an equivalent of m_k, Equation (9.39), such that the coefficient ε_k of molecular homeomorphism is replaced by ε_m, the coefficient of crystalline isomorphism. Values of $(1 - \varepsilon_m)$ are close to the values of $\Delta n/n_s$, which is the difference in chain length divided by the chain length of the smaller molecule.

Like the (halo + halo) group, the systems of the (H + halo) group and the system (H + CH_3) have positive excess enthalpies. Invariably, a positive excess enthalpy goes together with a positive excess entropy and also with a positive excess Gibbs energy, as long as the experimental temperature is below the compensation temperature θ, which is almost always the case.

Positive solid excess Gibbs energies in the $T-x$ phase diagram cause the solid–liquid loop to bend downwards. Positive excess Gibbs energies also may give rise to limited miscibility and the presence of a miscibility gap. If such is the case for a given temperature, then the Gibbs energy as a function of composition will have two points of inflexion. In the $T-x$ plane, the locus of the points of inflexion is a curve that is named spinodal, and a maximum or minimum on this curve is a critical point. The critical point is also the *extremum* of the binodal, which is the locus of the compositions of the coexisting phases; see Figure 9.68. In terms of the $AB\theta$ model, Equation (9.3), the spinodal is given by the equation

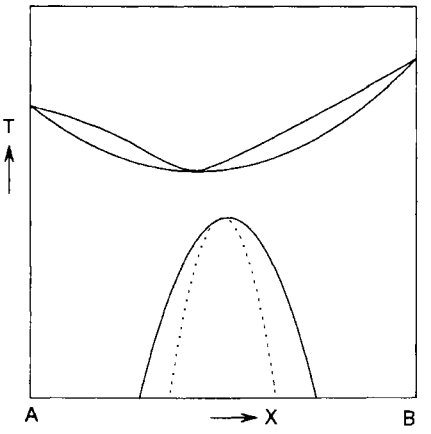

Figure 9.68 Plot of temperature against mole fraction to show the phase diagram with the downwardly bent solid–liquid loop in combination with solid-state miscibility gap, typical of positive solid-state excess Gibbs energy. Dashed curve: spinodal.

$$T_{\text{spin}}(x) = \frac{[2A + 6AB(1 - 2x)x(1 - x)]}{R + (1/\theta)[2A + 6AB(1 - 2x)]x(1 - x)]}. \tag{9.41}$$

The mole fraction value at the critical point x_c is determined by the value of B: x_c is the physically real solution of the equation

$$(18B)x^2 - (2 + 18B)x + (1 + 3B) = 0. \tag{9.42}$$

The temperature at the critical point, the critical temperature T_c, is obtained on the substitution of the value of x_c in the spinodal Equation (9.41). For the simple case that $B = 0$, the critical point has $x_c = 0.5$ and T_c is given by

$$T_c = \frac{A}{2R + (A/\theta)}. \tag{9.43}$$

The value of the 'asymmetry parameter' B, as a rule, is rather small, a representative figure being $|B| = 0.15$. Its influence on T_c is rather limited as is shown by the following example. From Figure 9.62, the A value for the rotator state in (C_{17} + C_{19}) is about 9.6 kJ · mol^{-1}. This value, along with $B = 0.15$ and $\theta = 320$ K, gives rise to $T_c = 209$ K, when substituted into Equation (9.41), and to $T_c = 206$ K, when substituted into Equation (9.43). Besides, it would mean that if, for (C_{17} + C_{19}), the rotator state would still exist below, say $T = 200$ K, it would split up into two phases, having the same rotator form but different compositions. As a result, the value of T_c is determined in the first place, by the value of A, and Equation (9.43) is a good indication of T_c.

The majority of experimental systems, involving mixed crystals, display positive values for the parameter A. In the case of the naphthalene derivatives, positive A values are found,

not only for the (halo + halo) group, but also for the (H + halo) group and the system (naphthalene + 2-methylnaphthalene).

Systems with negative A are very rare. The effect of geometrical mismatch has to be overcompensated by some kind of attractive effect caused by the difference in chemical nature of the constituents, or by the possibilities offered by space group symmetry. Difference in chemical nature is displayed by the combination of substituted methyl and substituted halogen [55]. In the case of (2-methylnaphthalene + 2-fluoronaphthalene), see Figure 9.66, the attractive effect of (methyl + halo) is balanced, so to say, by the repulsive effect caused by mismatch. The possibilities of space group symmetry find expression in the category of systems where the two components are a pair of enantiomers, a pair of optical antipodes. The best-known example in this category is (L-carvoxime + D-carvoxime) [122,129].

9.5 Concluding Remarks

The $AB\theta$ model for the excess Gibbs energy of binary mixtures, in spite of its simplicity, is an adequate and realistic instrument for mixed crystals.

The parameter A of the model is a measure of the net energetic interaction between the components of a given system in a given form. Within a family of systems, where the two components belong to a chemically coherent group of substances, the values of A are positive, and system-dependent, such that they can be correlated to the geometric mismatch between the components. The relationship, for such a family, between the values of A and a well-chosen mismatch parameter, can be used to fill in open places, and also, as an opening to the properties of systems in a related family and having a comparable form.

The asymmetry parameter B is dimensionless; $|B| = 0.15$ is a typical indication of its value. In a system composed of two members from a chemically coherent group of substances, and defined such that the second component is the larger one, B has a positive value. In addition, the value of B fully determines x_c, the mole fraction of the critical point of the region of demixing.

The parameter θ, having the dimension of temperature, is an indicator of the change of the excess Gibbs energy with temperature. In contrast to parameter A, θ has system overstepping characteristics: several families of systems are characterised by a common, system-independent value of θ; and within the realm of mixed crystals there is a unifying principle, albeit coarse. The θ, therefore, has a certain degree of predictability.

References

1. Haget, Y., Oonk, H.A.J. and Cuevas-Diarte, M.A., in *Les Equilibres entre Phases, JEEP XVI*, J. Kaloustian and J. Pastor, eds., Faculté de pharmacie, Marseille, pp. 35–36, 1990.
2. Oonk, H.A.J., van der Linde, P.R., Haget, Y., Bonpunt, L., Chanh, N.B. and Cuevas-Diarte, M.A., *J. Chim. Phys.* **88**, 329, 1991.
3. Haget, Y., Bonpunt, L., Michaud, F., Negrier, P., Cuevas-Diarte, M.A. and Oonk, H.A.J., *J. Appl. Cryst.* **23**, 492, 1990.

4. Haget, Y., *J. Chim. Phys.* **90**, 313, 1993.
5. Kitaigorodskii, A.I., *Organic Compounds Crystallography*, Consultant Bureau, New York, p. 225, 1961.
6. Kitaigorodskii, A.I., *Molecular Crystals and Molecules*, Academic Press, London, 1973.
7. Chanh, N.B. and Haget-Bouillaud, Y., *Acta Crystallogr.* **B28**, 3400, 1972.
8. Oonk, H.A.J., Calvet, T., Cuevas-Diarte, M.A., Tauler, E., Labrador, M. and Haget, Y., *Thermochim. Acta* **250**, 13, 1995.
9. Haget, Y., Housty, J.R., Maiga, A., Bonpunt, L., Chanh, N.B., Cuevas-Diarte, M.A. and Estop, E., *J. Chim. Phys.* **81**(3), 197, 1984.
10. van Duijneveldt, J.S., Chanh, N.B. and Oonk, H.A.J., *CALPHAD: Coupling Phase Diagrams Thermochem.* **13**, 83, 1989.
11. Cuevas-Diarte, M.A., Espeau, P., Haget, P., Mondieig, D., Robles, L. and Oonk, H.A.J., in *Les Equilibres entre Phases, JEEP XXI*, R. Bouaziz and G. Coquerel, eds., Faculté des sciences et des techniques, Rouen, pp. 63–66, 1995.
12. López, D.O., van Braak, J., Tamarit, J.Ll. and Oonk, H.A.J., *CALPHAD: Coupling Phase Diagrams Thermochem.* **19**, 37, 1995.
13. Barrio, M., López, D.O., Tamarit, J.Ll., Negrier, P. and Haget, Y., *J. Solid State Chem.* **124**, 29, 1996.
14. Salud, J., López, D.O., Barrio, M., Tamarit, J.Ll., Oonk, H.A.J., Haget, Y. and Negrier, P., *J. Solid State Chem.* **133**, 536, 1997.
15. van Braak, J., López, D.O., Salud, J., Tamarit, J.Ll., Jacobs, M.H.G. and Oonk, H.A.J., *J. Crystal Growth* **180**, 315, 1997.
16. Michaud, F., Negrier, P., Haget, Y., Alcobé, X., Cuevas-Diarte, M.A. and Oonk, H.A.J., *J. Chim. Phys.* **95**, 2199, 1995.
17. Haget, Y., Chanh, N.B., Meresse, A., Bonpunt, L., Michaud, F., Negrier, P., Cuevas-Diarte, M.A. and Oonk, H.A.J., *J. Appl. Crystallogr.* **32**, 481, 1999.
18. Salud, J., López, D.O., Jacobs, M.H.G., Barrio, M., Tamarit, J.Ll. and Oonk, H.A.J., *J. Solid State Chem.* **154**, 390, 2000.
19a. Pardo, L.C., Barrio, M., Tamarit, J.Ll., Negrier, P., López, D.O., Salud, J. and Mondieig, D., *J. Phys. Chem. B* **105**, 10326, 2001.
19b. Pardo, L.C., Barrio, M., Tamarit, J.Ll., López, D.O., Salud, J., Negrier, P. and Mondieig, D., *Chem. Phys. Lett.* **355**, 339, 2002.
20. Barrio, M., Font, J., Muntasell, J., Navarro, J. and Tamarit, J.Ll., *Sol. Energy Mater.* **18**, 109, 1988.
21. Haget, Y., Mondieig, D. and Cuevas-Diarte, M.A., CNRS Patent FR91/08695 and foreign corresponding patent applications, 1991.
22. Labrador, M., Tauler, E., Cuevas-Diarte, M.A., Mondieig, D., Housty, J.R. and Haget, Y., *Mater. Res. Bull.* **26**, 1227, 1991.
23. Mondieig, D., Haget, Y., Cuevas-Diarte, M.A., van der Linde, P.R. and Oonk, H.A.J., *Mater. Res. Bull.* **26**, 1091, 1991.
24. Barrio, M., Font, J., López, D.O., Muntasell, J. and Tamarit, J.Ll., *Sol. Energy Mater.* **27**, 127, 1992.
25. Cuevas-Diarte, M.A., Labrador, M., Mondieig, D. and Haget, Y., CNRS and Universitat de Barcelona, co-deposited Patent FR/9208553 and foreign co-pending patent applications, 1992.
26. Espeau, P., Robles, L., Cuevas-Diarte, M.A., Mondieig, D. and Haget, Y., *Mater. Res. Bull.* **31**, 1219, 1996.
27. Mondieig, D., Marbeuf, A., Robles, L., Espeau, P., Poirier, B., Haget, Y., Calvet, T. and Cuevas-Diarte, M.A., *High-Temperature High-Pressure* **29**, 385, 1997.
28. Espeau, P., Mondieig, D., Haget, Y. and Cuevas-Diarte, M.A., *Packag. Technol. Sci.* **10**, 253, 1997.

29. Haget, Y., Mondieig, D. and Cuevas-Diarte, M.A., *Molecular Alloys for Storing and Restoring Thermal Energy by Phase Change*, European Patent EP 0 548 334 B1. 09.29.1999, Munich, 1999.
30. Haget, Y., Mondieig, D. and Cuevas-Diarte, M.A., *Molecular Alloys and Restoring Thermal Energy by Phase Change*, United States Patent, 6,136,217. Oct. 10.24.2000, Alexandria, VA, 2000.
31. Oonk, H.A.J., *Phase Theory: The Thermodynamics of Hetereogeneous Equilibria*, Elsevier Science Publishers, Amsterdam, 1981.
32. Jacobs, M.H.G. and Oonk, H.A.J., *LIQFIT: A Computer Program for the Thermodynamic Assessment of T–X Liquidus or Solidus Data*, Utrecht University, Utrecht, 1990.
33. Daranas, D., López, R. and López, D.O., *WINIFIT 2.0: A Windows Computer Program for the Thermodynamic Assessment of T-X Phase Diagrams using the C.I.C. (Crossed Isopolymorphism Concept)*, Technical University of Catalonia, Barcelona, 2000.
34. Fourme, R., Clec'h, G., Figuière, P., Ghelfenstein, M. and Szwarc, H., *Mol. Cryst. Liq. Cryst.* **27**, 315, 1974.
35. Croatto, U., Bezzi, S. and Bua, E., *Acta Crystallogr.* **5**, 825, 1972.
36. Housty, J. and Clastre, J., *Acta Crystallogr.* **10**, 695, 1957.
37. Campbell, A.N. and Prodan, L.A., *J. Am. Chem. Soc.* **70**, 533, 1948.
38. van der Linde, P.R., *Ph.D. Thesis*, Utrecht University, Utrecht, 1992.
39. Westrum, E.F., Furukawa, G.T. and McCullough, J.P., in *Experimental Thermodynamics, Vol. 1*, J.P. McCullough and D.W. Scott, eds., Butterworths, London, p. 133, 1968.
40. Kolkert, W.J., *Ph.D. Thesis*, Utrecht University, Utrecht, 1974.
41. Kolkert, W.J., *J. Crystal Growth* **30**, 213, 1975.
42. Bouwstra, J.A., de Leeuw, V.V. and van Miltenburg, J.C., *J. Chem. Thermodyn.* **17**, 685, 1985.
43. Bouwstra, J.A. and Oonk, H.A.J., *CALPHAD: Coupling Phase Diagrams Thermochem.* **6**, 11, 1982.
44. Bouwstra, J.A., van Genderen, A.C.G., Brouwer, N. and Oonk, H.A.J., *Thermochim. Acta* **88**, 97, 1980.
45. van der Linde, P.R., Bolech, M., den Besten, R., Verdonk, M.L., van Miltenburg, J.C. and Oonk, H.A.J., *J. Chem. Thermodyn.* **34**, 613–629, 2002.
46. van Genderen, M.J., Mondieig, D., Haget, Y., Cuevas-Diarte, M.A. and Oonk, H.A.J., *CAL PHAD: Coupling Phase Diagrams Thermochem.* **19**, 49, 1995.
47. Hemminger, W. and Sarge, S.M., in *Handbook of Thermal Analysis and Calorimetry, Vol. 1: Principles and Practice*, M.E. Brown, ed., Elsevier Science, Amsterdam, 1998.
48. Rouland, J.C., Souleau, C. and Céolin, R., *J. Thermal Anal.3* **30**, 1081, 1985.
49. Céolin, R., Toscani, S., Agafonov, V. and Dugue, J., *J. Solid State Chem.* **98**, 366, 1992.
50. Céolin, R., Toscani, S. and Dugue, J., *J. Solid State Chem.* **102**, 465, 1993.
51. Céolin, R., Agafonov, V., Louër, D., Dzyabchenko, A., Toscani, S. and Cense, J.M., *J. Solid State Chem.* **122**, 186, 1996.
52. Höhne, G.W.H., Cammenga, H.K., Eysel, W., Gmelin, E. and Hemminger, W., *Thermochim. Acta* **160**, 1, 1990.
53. Courchinoux, R., Chanh, N.B., Haget, Y., Calvet, T., Estop, E. and Cuevas-Diarte, M.A., *J. Chim. Phys.* **86**, 561, 1996.
54. Calvet, M.T., Cuevas-Diarte, M.A., Haget, Y., Mondieig, D., Kok, I.C., Verdonk, M.L., van Miltenburg, J.C. and Oonk, H.A.J., *J. Chem. Phys.* **110**, 4841, 1999.
55. Meresse, A., *Ph.D. Thesis*, University of Bordeaux I, Bordeaux, 1981.
56. Métivaud, V., Rajabalee, F., Mondieig, D., Haget, Y. and Cuevas-Diarte, M.A., *Chem. Mater.* **11**, 117, 1999.

57a. Würflinger, A. and Schneider, G.M., *Ber. Bunsenges Physik. Chem.* **77**, 121, 1973.

57b. Würflinger, A., *Ph.D. Thesis*, Ruhr-Universität, Bochum, 1972.
58. Métivaud, V., *Ph.D. Thesis*, University Bordeaux I, Bordeaux, 1999.
59. Pardo, L.C., Barrio, M., Tamarit, J.Ll., López, D.O., Salud, J., Negrier, P. and Mondieig, D., *Chem. Phys. Lett.* **308**, 204, 1999.
60. Rudman, R. and Post, B., *Mol. Cryst.* **5**, 95, 1968.
61. Rudman, R., *Mol. Cryst. Liq. Cryst.* **6**, 427, 1970.
62. Pardo, L.C., Barrio, M., Tamarit, J.Ll., López, D.O., Salud, J., Negrier, P. and Mondieig, D., *Phys. Chem. Chem. Phys.* **3**, 2644, 2001.
63. Oonk, H.A.J., Mikailitchenko, D. and Marbeuf, A., *Chem. Mater.* **11**, 2866–2871, 1999.
64. Barrio, M., *Ph.D. Thesis*, Technical University of Catalonia, Barcelona, 1993.
65. Barrio, M., Font, J., López, D.O., Muntasell, J. and Tamarit, J.Ll., *J. Phys. Chem. Solids* **55**, 1295, 1994.
66. Barrio, M., Font, J., López, D.O., Muntasell, J., Tamarit, J.Ll. and Haget, Y., *J. Chim. Phys.* **91**, 189, 1994.
67. Salud, J., *Ph.D. Thesis*, Technical University of Catalonia, Barcelona, 1999.
68. Mazee, W.M., *Anal. Chim. Acta* **17**, 97–106, 1957.
69. Maroncelli, M., Strauss, H.L. and Snyder, R.G., *J. Chem. Phys.* **89**, 5260–5267, 1985.
70. Barrio, M., López, D.O., Tamarit, J.Ll., Negrier, P. and Haget, Y., *J. Mater. Chem.* **5**, 431, 1995.
71. Tamarit, J.Ll., Pérez-Jubindo, M.A. and de la Fuente, M.R., *J. Phys. Condens. Matter.* **7**, 5469, 1997.
72. Tamarit, J.Ll., Barrio, M., López, D.O. and Haget, Y., *J. Appl. Crystallogr.* **30**, 118, 1997.
73. McCullough, J.P., Fenke, W.L., Messerly, J.F., Todd, S.S., Kincheloe, T.C. and Waddington, G., *J. Phys. Chem.* **61**, 1105, 1957.
74. Meresse, A., Chanh, N.B., Housty, J.R. and Haget, Y., *J. Phys. Chem. Solids* **47**, 1019, 1986.
75a. Chanh, N.B., Haget, Y., Meresse, A. and Housty, J., *Mol. Cryst. Liq. Cryst.* **45**, 307, 1978.
75b. Chanh, N.B., Clastre, J., Gaultier, J., Haget, Y., Meresse, A., Lajzerowicz, J., Filhol, A. and Thomas, M., *J. Appl. Crystallogr.* **21**, 10, 1988.
76. Kitaigorodskii, A.I., *Mixed Crystals*, *Vol. 33*, Springer, Berlin, p. 243, 388 pp., 1984.
77. Rudolfi, E., *Z. Phys. Chem.* **66**, 705, 1909.
78. Vetter, H., Rössler, S. and Schildknecht, H., in *Symposium über Zonnenschmelzen und Kolonnen kristalliseren*, H. Schildknecht, ed., Kernforschunsanstalt, Karlsruhe, Germany, p. 57, 1963.
79. Oonk, H.A.J. and Pleysier, H.L., *Sep. Sci.* **6**, 685, 1971.
80. Baumgarth, F., Chanh, N.B., Gay, R., Lascombe, J. and Le Calvé, N., *J. Chim. Phys.* **66**, 862, 1969.
81. Robinson, P.M., Rosell, H.J., Scott, H.G. and Legge, C., *Mol. Cryst. Liq. Cryst.* **11**, 105, 1970.
82. Robinson, P.M. and Scott, H.G., *Mol. Cryst. Liq. Cryst.* **18**, 143, 1972.
83. Michaud, F., *Ph.D. Thesis*, University of Bordeaux I, Bordeaux, 1994.
84. Pratt Brock, C. and Dunitz, J.D., *Acta Crystallogr. B* **38**, 2218, 1982.
85. Robles, L., Mondieig, D., Haget, Y. and Cuevas-Diarte, M.A., *J. Chim. Phys.* **95**, 92, 1998.
86. Snyder, R.G., Maroncelli, M., Qi, S.P. and Strauss, H.L., *Science* **214**, 188, 1981.
87. Urabe, Y. and Takamizawa, K., *Technology Reports of Kyusyu University* **67**, 85, 1994.
88. Sirota, E.B., King Jr., H.E., Singer, D.M. and Shao, H.H., *J. Chem. Phys.* **98**, 5809, 1993.
89. Sirota, E.B., King Jr., H.E., Shao, H.H. and Singer, D.M., *J. Phys. Chem.* **99**, 798, 1995.
90. Espeau, P., Robles, L., Mondieig, D., Haget, Y., Cuevas-Diarte, M.A. and Oonk, H.A.J., *J. Chim. Phys.* **93**, 1217, 1996.
91. Kobayasi, T., Kobayasi, Y., Ito, Y., Chatani, H. and Tadokoro, H., *J. Chem. Phys.* **72**, 2024, 1980.

92. Poirier, B., *Ph.D. Thesis*, University of Bordeaux I, Bordeaux, 1995.
93. Robles, L., *European Ph.D. Thesis*, University of Bordeaux I, Bordeaux, 1995.
94. Espeau, P., *European Ph.D. Thesis of the University of Bordeaux I*, Bordeaux, 1995.
95. Rajabalee, F., Métivaud, V., Mondieig, D. and Haget, Y., *J. Mater. Res.* **14**, 2644, 1999.
96. Hastie, G.P. and Roberts, K., *J. Mat. Sci.* **29**, 1915, 1994.
97. Rajabalee, F., *Ph.D. Thesis*, University Bordeaux I, Bordeaux, 1998.
98. Dirand, M., Achour, Z., Jouti, B., Sabour, A. and Gachon, J.C., *Mol. Cryst. Liq. Cryst.* **275**, 293, 1996.
99. Jouti, B., Bourdet, J.B., Bouroukba, M. and Dirand, M., *Mol. Cryst. Liq. Cryst.* **270**, 159, 1995.
100. Jouti, B., Provost, E., Petitjean, D., Bouroukba, M. and Dirand, M., *Mol. Cryst. Liq. Cryst.* **287**, 275, 1996.
101. Rajabalee, F., Metivaud, V., Oonk, H.A.J., Mondieig, D. and Waldner, P., *Phys. Chem. Chem. Phys.* **2**, 1345, 2000.
102. Oonk, H.A.J., Mondieig, D., Haget, Y. and Cuevas-Diarte, M.A., *J. Chem. Phys.* **108**, 715, 1988.
103. Rey, R., Pardo, L.C., Llanta, E., Ando, K., López, D.O., Tamarit, J.Ll. and Barrio, M., *J. Chem. Phys.* **112**(17), 7505, 2000.
104. Mones, A.H. and Post, B., *J. Chem. Phys.* **20**, 755, 1952.
105. Rush, J.J., *J. Chem. Phys.* **46**, 2285, 1967.
106. Graaf, L.A. and Sciesinski, J., *Physica* **48**, 79, 1970.
107. Chang, E.T. and Westrum Jr., E.F., *J. Phys. Chem.* **74**, 2528, 1970.
108. Enokida, H., Shinoda, T. and Mashiko, Y., *Bull. Chem. Soc. Jpn.* **42**, 84, 1969.
109. Aston, J.G. and Messerly, G.H., *J. Am. Chem. Soc.* **58**, 2534, 1936.
110. Benson, D.K., Burrows, R.W. and Webb, J.D., *Sol. Energy Mat.* **13**, 133, 1986.
111. Koga, Y. and Morrison, A., *J. Chem. Phys.* **62**, 3359, 1975.
112. Hicks, J. and Hooley, J., *J. Am. Chem. Soc.* **66**, 1064, 1944.
113. Arentsen, J.G. and van Miltenburg, J.C., *J. Chem. Thermodyn.* **4**, 789, 1972.
114. Ott, J.B. and Cardon, D.L.J., *J. Chem. Thermodyn.* **8**, 505, 1976.
115. Morrison, J.A. and Richards, E.L., *J. Chem. Thermodyn.* **8**, 1033, 1976.
116. Chang, E.T. and Westrum Jr., E.F., *J. Phys. Chem.* **69**, 2176, 1965.
117. Boots, H.M.J. and Bokx, P.K., *J. Phys. Chem.* **93**, 8240, 1989.
118. Mondieig, D., Espeau, P., Robles, L., Haget, Y., Oonk, H.A.J. and Cuevas-Diarte, M.A., *J. Chem. Soc. Faraday Trans.* **93**, 3343, 1997.
119. Calvet, M.T., Cuevas-Diarte, M.A., Haget, Y., van der Linde, P. and Oonk, H.A.J., *CAL PHAD: Coupling Phase Diagrams Thermochem.* **15**, 225, 1991.
120. López, D.O., Salud, J., Tamarit, J.Ll., Barrio, M. and Oonk, H.A.J., *Chem. Mater.* **12**, 1108, 2000.
121. van der Kemp, W.J.M., Blok, J.G., van Genderen, A.C.G., van Ekeren, P.J. and Oonk, H.A.J., *Thermochim. Acta* **196**, 301, 1992.
122. Walling, J.F. and Halsey, G.D., *J. Phys. Chem.* **62**, 752, 1958.
123. Calvet, T. and Oonk, H.A.J., *CALPHAD: Coupling Phase Diagrams Thermochem.* **19**, 49, 1995.
124. Sellers, C.M. and Maak, F., *Trans. Metall. Soc. AIME* **236**, 457, 1966.
125. Okamoto, H. and Massalsky, T.B., *Bull. Alloy Phase Diagrams* **6**, 229, 1985.
126. van der Kemp, W.J.M., Blok, J.G., van der Linde, P., Oonk, H.A.J., Schuijff, A. and Verdonk, M.L., *CALPHAD: Coupling Phase Diagrams Thermochem.* **18**, 255, 1994.
127. van der Kemp, W.J.M., Blok, J.G., van der Linde, P., Oonk, H.A.J. and Schuijff, A., *Thermochim. Acta* **225**, 17, 1993.
128. Tanaka, T., Gokcen, N.A. and Morita, Z., *Z. Metallkd.* **81**, 49, 1990.
129. Adriani, J.H., *Z. Phys. Chem.* **33**, 453, 1900.

10 Condensed Phases of Inorganic Materials: Metallic Systems*

M.H. KAYE, K.M. JAANSALU and W.T. THOMPSON
Department of Chemistry and Chemical Engineering
Royal Military College of Canada
Kingston, Canada

* This article has previously appeared under the title "Phase equilibrium in metallic systems", *Canadian Metallurgical Quarterly*, **42**(4), October 2003, pp. 393–410.

Measurement of the Thermodynamic Properties of Multiple Phases
R.D. Weir and Th.W. de Loos (Editors)

10 CONDENSED PHASES OF INORGANIC MATERIALS: METALLIC SYSTEMS

Phase equilibrium in binary metallic systems has been extensively studied in support of metallurgical engineering. The early work, a century or more ago, put emphasis on such experimental methods as thermal analysis and metallography, and resulted in the landmark collection of phase diagrams by Hansen in 1936 [1]. In the years following, the greater range of superior experimental methods and a developing interest in the underlying thermochemical principles of phase equilibria led to the international metallic phase diagram evaluation programmes [2–5] culminating in the volumes edited by Massalski [6].

Phase equilibrium for a binary metallic system is usually represented on an isobaric temperature–composition diagram. This very common selection of axes recognizes the major variables of interest in metallurgical processing. Although it is most often secondary to the intended use, these diagrams may be regarded as maps showing the phase or phases that provide the lowest Gibbs energy at a particular temperature, pressure and composition. In principle, the phase diagram may be developed from an independent knowledge of the relative Gibbs energies for the various possible phases. Although this has been recognized since the landmark paper of Gibbs [7], it is seldom a reliable practical approach to phase diagram construction, since relatively small uncertainties in measured Gibbs energy differences between components in the phases generate substantial uncertainties in the placement of the phase boundaries.

The matters that make the computation of phase diagrams unreliable when based on a variety of independent direct thermochemical measurements imply that thermochemical properties can be quite well inferred from a phase diagram when the underlying principles are applied. Indeed, the determination of any feature of a phase diagram by whatever method constitutes a *bona fide* method to establish thermochemical properties that are quite reliable. Therefore, compilations of assessed phase diagrams constitute a rich source of thermochemical solution properties. The development of phase diagrams from Gibbs energies may appear to have limited practical value. It may seem that the exercise does little more than demonstrate that the features of the diagram are consistent with the constraints of thermodynamic principles – reassuring but not far reaching. However, the process of critical analysis via modelling brings together, in a *self-consistent way*, various kinds of independent thermochemical property measurements with the phase diagram as the keystone. As a result, the analysis isolates improbable measurements and places bounds on accuracy. Until the widespread use of advanced computers, this approach was impractical, but in the past 25 years it has become well recognized.

The solution properties inferred from phase diagram modelling are valuable in other ways. For example, thermochemical data on the behaviour of a binary metallic solution, when combined with other data, such as the Gibbs energy of formation of metal oxides, may be useful in understanding equilibrium in a three-component metal–metal–oxygen system. Another

example of interest is in the vacuum processing of alloys, where a phase diagram showing the placement of the vapour field under reduced pressure can be calculated. Furthermore, reasonable predictions of phase diagrams can be computed for multi-element metallic systems based upon an understanding of the component binary metallic systems. The predictions, at the very least, guide experimental investigations towards regions of particular interest.

10.1 Solution Thermodynamics and Phase Diagram Development

Since the principles of phase equilibrium computations are well covered elsewhere [8–11], only the cornerstone ideas will be highlighted here. The underlying principle in extracting thermodynamic data from phase diagrams is the equality of chemical potential or partial molar Gibbs energy for each of the components in the coexisting phases. Therefore, for component A, distributed between coexisting phases α and β:

$$\bar{G}_A^{\alpha} = \bar{G}_A^{\beta}, \tag{10.1}$$

With reference to Figure 10.1, the partial molar Gibbs energy for component A in the α phase, can be interpreted graphically as the intercept of a tangent to the Gibbs energy of the α phase at the composition of interest.

The partial molar Gibbs energy must be expressed relative to a standard condition of concentration. For pure A, the difference illustrated in Figure 10.1 can be related to the activity of the component in solution α at the composition given by the point of tangency. That is,

$$\bar{G}_A^{\alpha} - G_A^{o\alpha} = RT \ln a_A^{\alpha}, \tag{10.2}$$

where a_A^{α} is the activity at temperature T.

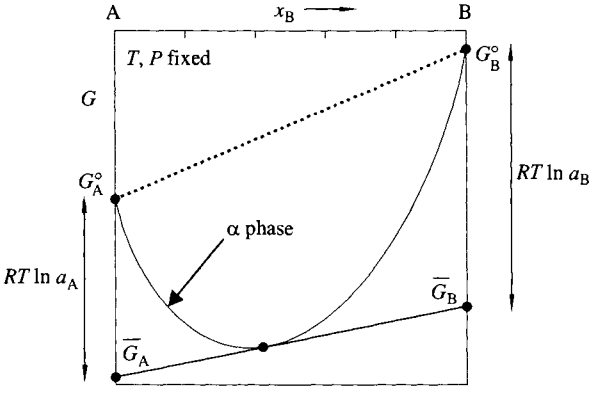

Figure 10.1 Relationship of molar Gibbs energy of a solution to the partial molar Gibbs energies and activities of the components.

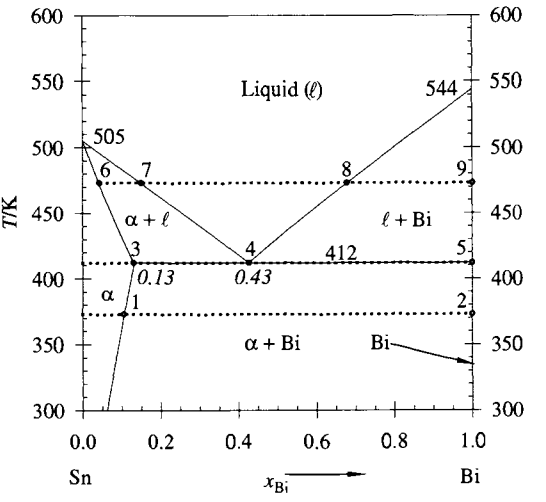

Figure 10.2 Isobaric (Sn + Bi) temperature–composition phase diagram.

Table 10.1 Gibbs energy data for (Sn + Bi) binary system [12].

1. Sn (pure component):
   $G^{o,\ell}_{Sn} = 0\,J \cdot mol^{-1}$ (reference phase)
   $\Delta^{g}_{\ell}G^{\circ}_{Sn} = -7029.1 + 13.917\,(T/K)\,J \cdot mol^{-1}$
2. Bi (pure component):
   $G^{o,\ell}_{Bi} = 0\,J \cdot mol^{-1}$ (reference phase)
   $\Delta^{hR2}_{\ell}G^{\circ}_{Bi} = -11296.8 + 20.766\,(T/K)\,J \cdot mol^{-1}$
   $\Delta^{g}_{\ell}G^{\circ}_{Bi} = -4331.8 + 20.766\,(T/K)\,J \cdot mol^{-1}$
3. Sn-rich tI4 solution (α-solid phase):
   For $(1 - x)\ Sn_{\alpha\text{-solid}} + (x)\ Bi_{\alpha\text{-solid}} = ((1 - x)Sn + (x)Bi)_{\alpha\text{-solid sln}}$
   $\Delta_{mix}G^{\alpha} = (1 - x)RT\ln(1 - x) + (x)RT\ln(x)\,J \cdot mol^{-1}$
4. Liquid phase:
   For $(1 - x)Sn_{\ell} + (x)\ Bi_{\ell} = ((1 - x)Sn + (x)Bi)_{\ell\ sln}$
   $\Delta_{mix}G^{\ell} = (1 - x)\,RT\ln(1 - x) + (x)RT\ln(x) + (1 - x)(x)(606 + 194(1 - x))\,J \cdot mol^{-1}$

The temperature–composition phase diagram for the system (Sn + Bi) is shown in Figure 10.2.

A thermodynamic model for the system (Sn + Bi) [12] is given in Table 10.1.

Gibbs energy isotherms for all phases (liquid (ℓ), Sn-rich solid solution (α) and virtually pure solid (Bi)) are shown in Figure 10.3 at three temperatures. The hydrostatic pressure is understood to be constant at 101.325 kPa (1 atm), although for practical purposes there is little influence on the Gibbs energy of condensed phases for changes of a few atmospheres.

At $T = 473$ K it is possible to construct a common tangent between the Gibbs energy isotherms for the Sn-rich solid solution phase (α) and the liquid (ℓ), ($\alpha + \ell$). In view of the significance of the tangent intercepts at the extremes of composition, this construction satisfies the basic requirement of Equation (10.1) for both components simultaneously.

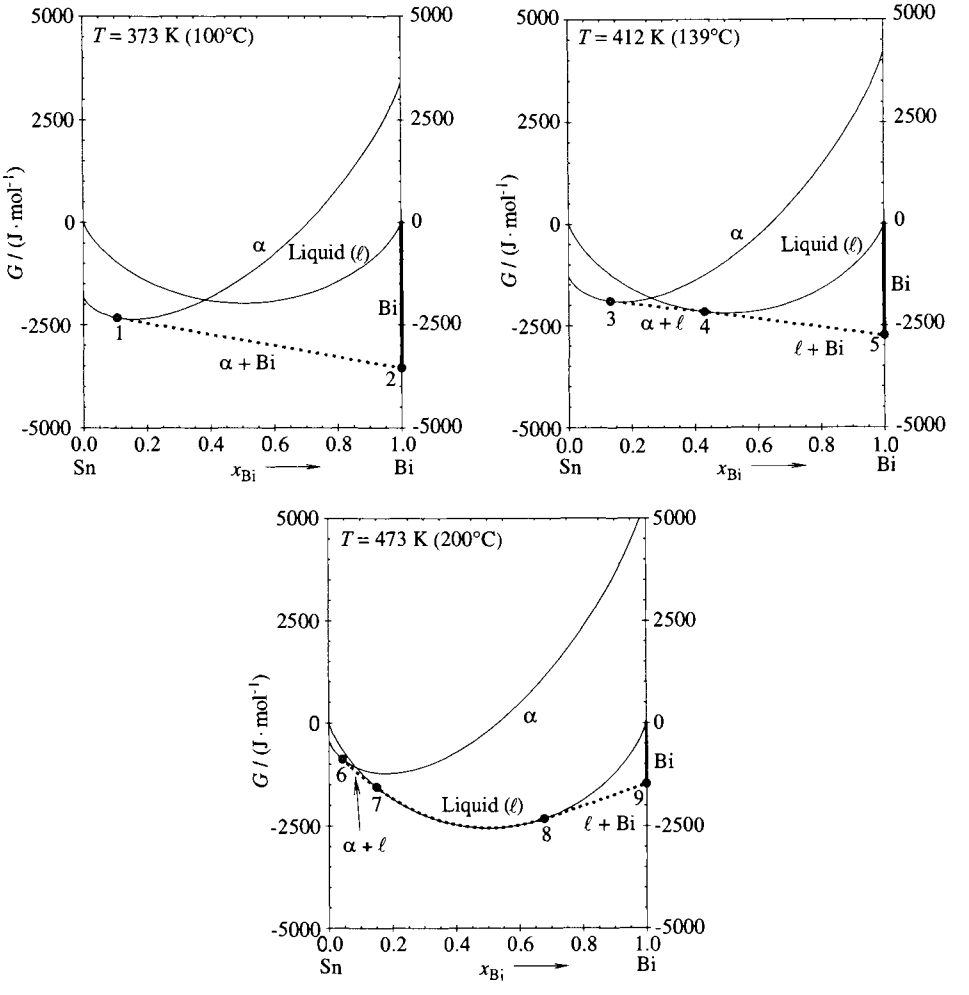

Figure 10.3 Gibbs energy isotherms for the system (Sn + Bi).

Moreover, it is clear that no other phase between the points of tangency has Gibbs energy lower than a mixture of these two phases. This collection of ideas, leading to the ends of the tie line (points 6 and 7) shown in Figure 10.2 at $T = 473$ K is termed the *lowest common tangent* construction.

At $T = 473$ K, when the overall Bi concentration is higher, there is another pair of coexisting phases, namely points 8 and 9 in Figure 10.2. The construction in Figure 10.3 can still be described as the *lowest common tangent* if the point representing the Gibbs energy of pure solid Bi is interpreted as the lower extremity of a "curve" (shown as the bold line), which ascends sharply upward near the right edge of Figure 10.3. This might be offered as a thermochemical explanation of the negligible solubility of Sn in solid Bi.

At $T = 412$ K, the temperature of the eutectic, the two common tangents are now collinear. That is to say, one tangent touches all three isotherms simultaneously (points 3, 4 and 5).

This situation typically arises only at one temperature or, in the language of the Phase Rule, when the system is invariant. At $T = 373\,\mathrm{K}$, there is only one common tangent connecting virtually pure solid Bi to the Sn-rich α-solid solution (points 1 and 2). The liquid-phase isotherm does not cut this tangent and is, therefore, not as stable as the two solid phase combination depicted on the phase diagram.

Since the elements may not exist as all crystal types, it is usually necessary to be able to assign a hypothetical structure in order to construct the Gibbs energy of mixing curve over the entire composition range. Therefore, it is useful to mention in connection with this idea and Figure 10.3 the concept of *lattice stability* attributed to Kaufman [13], and with data compiled and reviewed by Dinsdale [14]. As it might not be possible to locate the Gibbs energy isotherm for the α-solid solution in an experimental sense relative to the other phases for high concentrations of Bi, a hypothetical structure was postulated. However, the meaning of the Bi rich extreme of the isotherm is the Gibbs energy Bi *would have if it could exist* in the α-phase (tI4) [15]. This lattice stability of Bi in the tI4 structure can be expressed relative to Bi in its more stable rhombohedral structure (hR2) [16]. In Table 10.1 this is treated as a constant:

$$(-4331.8 - (-11\,296.8)) = 6965\,\mathrm{J \cdot mol^{-1}}.$$

Of course, when Gibbs energies for all phases are known as functions of temperature, the enthalpy and entropy contributions to the Gibbs energy are, in effect, known as well. This opens the possibility of calculating other phase diagrams for the same system using other coordinates. In Figure 10.4, the temperature, or thermal potential, axis in Figure 10.2 has been replaced by the relative thermal energy or enthalpy change, with respect to a mechanical mixture of the two pure solid components at $T = 298\,\mathrm{K}$.

This diagram not only connects phase equilibrium with scanning calorimetry, but is useful in a practical sense to understand thermal effects associated with solidification or melting, which is a matter of interest for this particular alloy system in view of its use in lost core moulding of hollow polymer components, which involves repetitive melting and solidification.

Since, for the case of most metallic solution phases, the component atoms interchange on lattice sites, the ideal Gibbs energy of mixing for a mole of solution represented by

$$(\mathrm{A} + \mathrm{B})_{\mathrm{Solution}} = x_{\mathrm{A}}(\mathrm{A}) + x_{\mathrm{B}}(\mathrm{B}), \tag{10.3}$$

and is given by

$$\Delta_{\mathrm{mix}} G^{\ell} = x_{\mathrm{A}} RT \ln x_{\mathrm{A}} + x_{\mathrm{B}} RT \ln x_{\mathrm{B}}, \tag{10.4}$$

which is a form used in Table 10.1 for the liquid and α-phases.

The Gibbs energy provided by Equation (10.4) is brought into agreement with thermochemical measurements or phase diagram features by the addition of an excess Gibbs term, G^{E}, that itself can be subdivided into an enthalpy of mixing and excess entropy contribution:

$$G^{\mathrm{E}} = \Delta_{\mathrm{mix}} H - TS^{\mathrm{E}}. \tag{10.5}$$

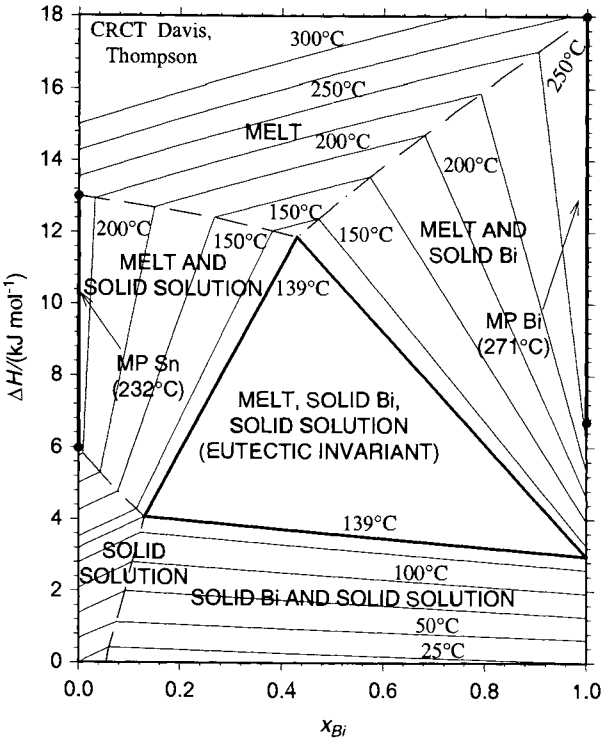

Figure 10.4 Enthalpy–composition phase diagram for (Sn + Bi).

The simplest form is given by an empirical series, which is usually arranged as follows:

$$G^{E} = x_A x_B(a + bx_B + cx_B^2 + \cdots). \tag{10.6}$$

For many systems G^{E} is not very dependent on temperature, which implies that S^{E} is near zero, and the random atomic mixing assumption inherent in the form of Equation (10.4) provides a close approximation to the actual entropy of mixing. In this case, the excess Gibbs energy is numerically equivalent to the enthalpy of mixing. When G^{E} is temperature dependent each coefficient in Equation (10.6) may be expressed by an expansion in T; usually a linear relationship is sufficient.

To complete the mathematical positioning of a Gibbs energy isotherm, for example the liquid phase in Figure 10.4, the ends of the curve at each extreme of composition must be located. This may be done by arbitrarily selecting a reference phase for each component (the phases need not be the same) and by expressing the ends of the isotherm with respect to these selections. For the (Sn + Bi) system shown in Table 10.1, the point of reference for each component is the pure liquid.

Figure 10.5 shows the phase diagram for (Mg + Si). Five phases are involved, of which two are solution phases. All of the numerical data to establish the relative placement

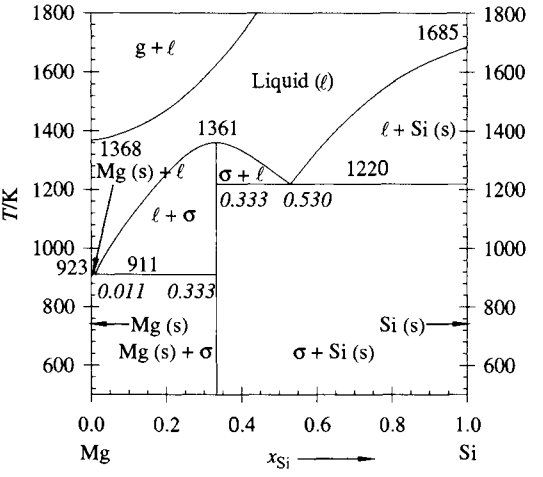

Figure 10.5 Computed binary phase diagram for the (Mg + Si) system using the data in Table 10.2 (P = 101.325 kPa (1 atm)).

Table 10.2 Gibbs energy data used in the construction of Figures 10.5 through 10.8.

1. Mg (pure component):
   $G^{o,\ell}_{Mg} = 0\,J \cdot mol^{-1}$ (reference phase)
   $\Delta^{s}_{\ell} G^{o}_{Mg} = -8479 + 9.186\,(T/K)\,J \cdot mol^{-1}$
   $\Delta^{g}_{\ell} G^{o}_{Mg} = 127\,847 - 93.476\,(T/K) + RT \ln (P/atm)\,J \cdot mol^{-1}$
2. Si (pure component):
   $G^{o,\ell}_{Si} = 0\,J \cdot mol^{-1}$ (reference phase)
   $\Delta^{s}_{\ell} G^{o}_{Si} = -50\,212 + 29.80\,(T/K)\,J \cdot mol^{-1}$
   $\Delta^{g}_{\ell} G^{o}_{Si} = 384\,540 - 109.613\,(T/K) + RT \ln (P/atm)\,J \cdot mol^{-1}$
3. Mg_2Si (intermetallic compound, σ):
   For $\frac{2}{3}Mg_{\ell} + \frac{1}{3}Si_{\ell} = \frac{1}{3}Mg_2Si_s$
   $\Delta_{mix}G^{\sigma} = -211\,373 + 1096.8\,(T/K) - 133.427\,(T/K) \ln (T/K)\,J \cdot mol^{-1}$;
4. Vapour phase:
   For $(1 - x)\,Mg_{(g,\,P\,atm)} + (x)\,Si_{(g,\,P\,atm)} = ((1 - x)\,Mg + (x)\,Si)_{(g\,sln,\,P\,atm)}$
   $\Delta_{mix}G^{g} = (1 - x)\,RT \ln (1 - x) + (x)\,RT \ln (x)\,J \cdot mol^{-1}$;
5. Liquid phase:
   For $(1 - x)Mg_{\ell} + (x)Si_{\ell} = ((1 - x)Mg + (x)Si)_{\ell\,sln}$
   $\Delta_{mix}G^{\ell} = (1 - x)\,RT \ln (1 - x) + (x)\,RT \ln (x) + (1 - x)(x)(-26\,751 - 70.809(T/K))$
   $+ (1 - x)(x)^2\,(74\,838)\,J \cdot mol^{-1}$

of the Gibbs energy curves consistent with Figure 10.5 is given in Table 10.2. This provides the basis for constructing the Gibbs energy isotherms in Figure 10.6 at T = 1300 K.

By applying the lowest common tangent construction it is seen that Figures 10.5 and 10.6a are self-consistent at this temperature. As for Table 10.1, the data in Table 10.2 may be regarded as a formal way of storing the phase diagram, or as thermodynamic data useful for other purposes. Consider the development of the temperature–composition diagram

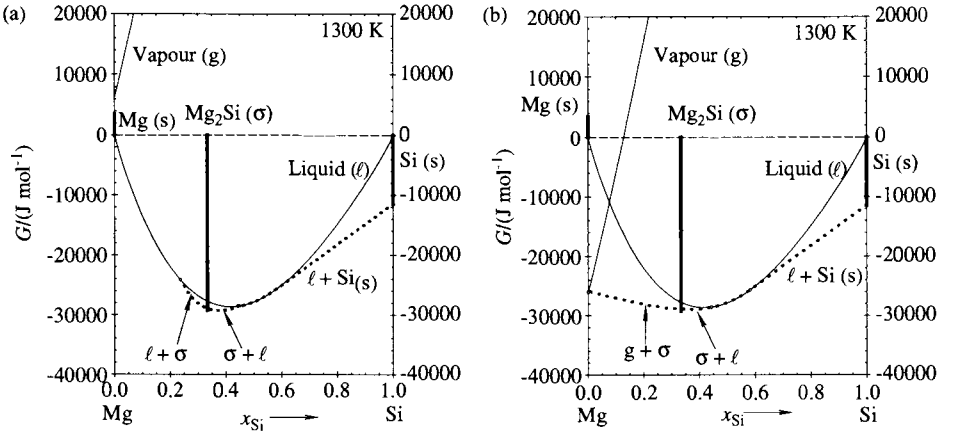

Figure 10.6 Gibbs energy isotherms for the (Mg + Si) system at $T = 1300$ K. The effect of pressure reduction on the placement of the vapour phase isotherm is shown in (b).

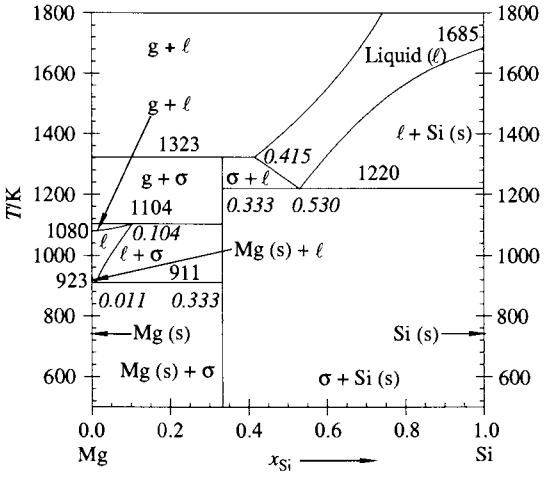

Figure 10.7 Computed binary phase diagram for the (Mg + Si) system using the data in Table 10.2 ($P = 5.066$ kPa (0.05 atm)).

at a constant pressure of 5.066 kPa (0.05 atm). The isotherm for the vapour phase in Figure 10.6b is lowered by $RT \ln P$ and the lowest common tangent construction is repeated. At $T = 1300$ K, the construction shows that the vapour phase is stable for pure Mg and is part of the two-phase mixture of (g + σ) at low concentrations of Si. This is shown in the resulting phase diagram, Figure 10.7.

The ability to rapidly compute the diagram at various pressures naturally leads to an isothermal *log P-composition* diagram, shown in Figure 10.8 at $T = 1300$ K.

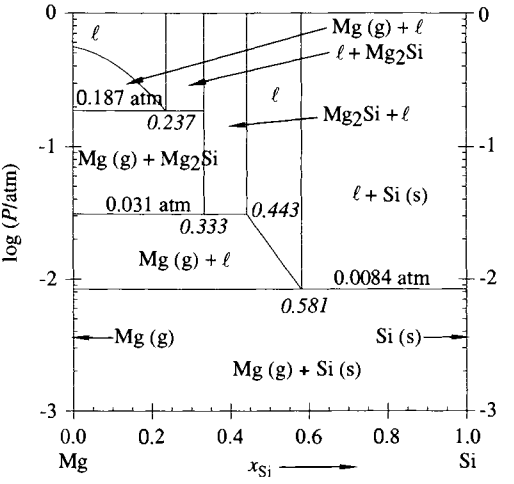

Figure 10.8 Computed isothermal pressure versus composition phase diagram for the (Mg + Si) system using the data in Table 10.2 (T = 1300 K).

The data in Table 10.2 are reasonably reliable insofar as relative Gibbs energies are concerned. The computed diagram, in which the eutectic compositions and temperatures are well represented, is evidence. However, the enthalpy and entropy changes inferred from the Gibbs energies are less reliable. For example, the constant preceding the $T \ln T$ term in the Gibbs energy for the formation of Mg_2Si implies a large difference in the heat capacities between the product and reactants associated with the formation of Mg_2Si. Further, the magnitude of the temperature dependence in the Gibbs energy of mixing of the liquid phase implies a large departure from random atom mixing. This underlines the need to couple phase diagram modelling to experimental measurement.

10.2 Experimental Methods

A very wide variety of experimental techniques bear upon the study of phase equilibrium in metal systems. It is typical of a great fraction of the experimental work reported that specialized equipment, unique to the alloy under study, has been custom assembled for a particular purpose. A catalogue of specific techniques would, therefore, imply a degree of experimental standardization and off the shelf equipment that does not exist. The approach here will be to broadly classify the main techniques used, with reference to binary systems, although all of the techniques can apply to multi-component systems. The selection of a particular technique is usually dictated by heating requirements, available materials of construction and the chemical reactivity or volatility of component elements. Materials of construction pose a major problem and, if this matter is not a part of the experimental plan from the outset, the containment materials may become inadvertent minor components of the system under study.

10.2.1 Microscopic Phase Examination

The detection of phases by microscopic means for alloys of known composition and thermal history is a cornerstone in the development of metallic phase diagrams. By working backwards with the computational ideas discussed in the previous section, thermodynamic information of the phases can be deduced.

Optical microscopic methods for metals are based on the reflection of light from polished and etched metal surfaces [16]. To determine the liquidus and solidus, an alloy is heated and annealed in a protective atmosphere at a known temperature. A rapid quench follows, which freezes in the microstructure at that temperature [17]. By examining the microstructure, the number and identity of the phases present at that temperature can be determined [18]. An example of a typical optical micrograph for a (Mo + Rh) alloy is shown in Figure 10.9 [19]. Several days or even weeks of annealing may be required to reach equilibrium depending on the temperature. Alloys with an increasing fraction of a second element are examined and the composition when a second phase appears at a particular temperature is noted. The relative mass or atomic fraction of the phases can be obtained from the observed phase fractions, which in turn can be related to a tie line on the phase diagram.

By plotting the phase assemblages determined by microscopy at each alloy composition against temperature, a general indication of the phase diagram is obtained. The example

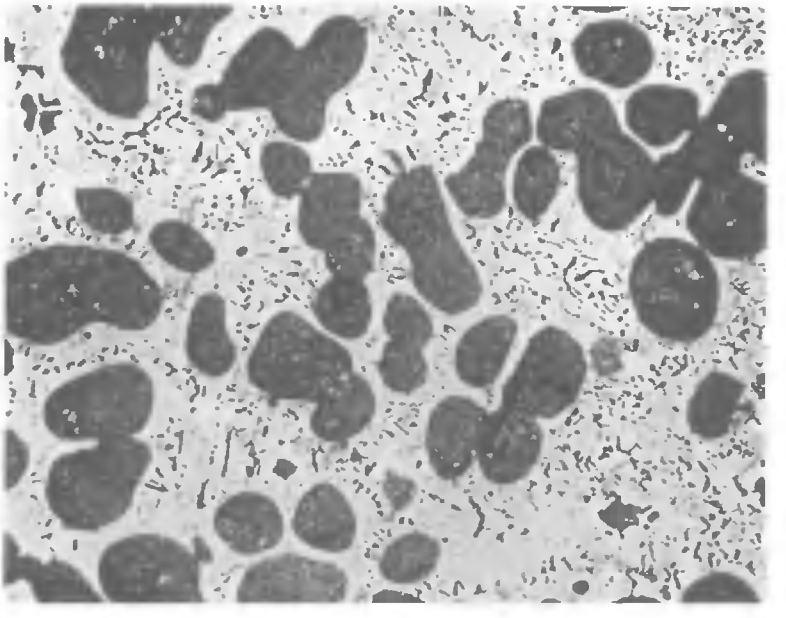

Figure 10.9 Mo-30 at.% Rh alloy quenched from the condition identified in Figure 10.10, at a temperature just above the eutectic in the two-phase field (α + liq). The dark regions are the Mo-rich phase (α-Mo), surrounded by the two-phase mixture associated with the eutectic solidification of the liquid phase. The sample was etched in solutions diluted from a stock solution of: 9 g NaOH, 2.5 g $K_3Fe(CN)_6$, and 380 g H_2O. Magnification is 200× [19], used with permission of IOM[3].

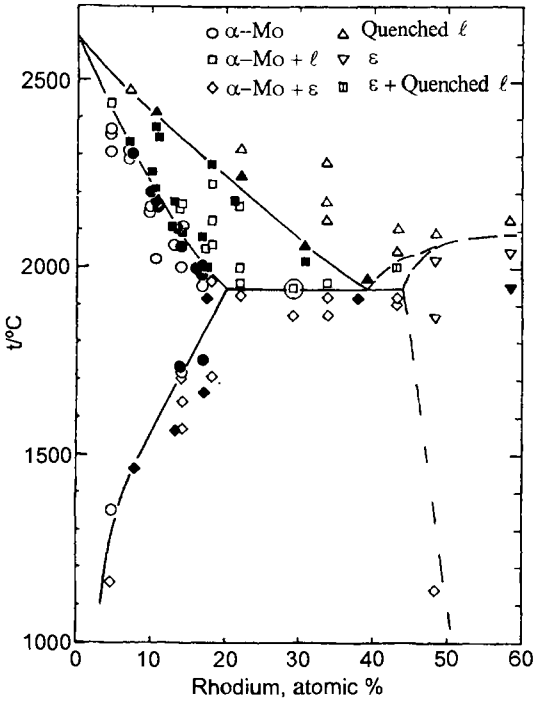

Figure 10.10 A partial phase diagram for (Mo + Rh) as determined by metallography [19]. Note the point (as circled) for the Mo-30 at.% Rh alloy depicted in Figure 10.9, used with permission of IOM[3].

for the molybdenum–rhodium system is shown in Figure 10.10 [19]. Note that the relative proportions of α-Mo and transformed liquid phase (from Figure 10.9) are consistent with the lever rule construction in Figure 10.10.

A superior method, in principle, is hot-stage microscopy where the phases can be directly observed at the temperature of interest in a vacuum or protective atmosphere. This approach does not depend on interpretational matters that arise when phase transformations occur during quenching, but is otherwise similar to the venerable annealing–quenching technique.

For the scanning electron microscope (SEM) or electron probe micro-analyser (EPMA), an electron beam interacts with the atoms in the sample, and X-rays are emitted that are characteristic of the elements present. The X-rays are detected and analysed using energy dispersive (EDS) or wavelength dispersive spectrometers (WDS). The SEMs are routinely coupled to an EDS system for concurrent chemical analysis. For microchemical analysis in metallurgical work, an EPMA has one or more WDS attached. The SEM and EPMA instruments make use of the same physical principles, but the emphasis is different. The SEM is an imaging device; EPMA a chemical analysis tool. As such with an EPMA, the instrument is designed to control the position of the electron beam, which must be held stationary for long periods of time, tightly aimed and focussed. Detailed information on these techniques and their applications can be found in references [20–23]. The relative

merits of the WDS, sometimes called a crystal dispersive spectrometer, over the EDS is that the WDS has a higher resolution of the X-ray spectrum and better detection limits of trace elements, but this comes at the cost of increased data collection times. The impact of these differences is well discussed by Lifshin [24].

In the study of phase equilibrium, the main advantage of an SEM/EDS system is the capability to provide relatively rapid compositional information that can be used to locate the ends of tie lines. Routinely, images are collected that indicate the distribution of specific elements. This requires some capability of the SEM to hold the electron beam at a specific location for a pre-set time, similar to the EPMA. As the EDS system acquires the entire spectrum, as opposed to the WDS, which scans only the wavelengths of interest, data collection for the EDS system is relatively rapid.

Advances in SEM/EDS have resulted in better and faster means of determining the composition of the phases. In particular, the advances in detector technology, digital pulse processing, and computer storage have expanded the utility of energy-dispersive spectrometry [25]. Older detection systems are restricted to detecting aluminium and heavier elements. Detector construction and the development of atmospheric thin windows have improved the detection of light elements, such as carbon and oxygen, to the point where they can be detected reliably and their proportions derived. Present day systems can detect elements as light as beryllium. Of particular note are the advances in low-voltage electron microscopy, which prevents charge build-up on the sample. Thus, conductive coatings are not required and a better EDS analysis is obtained for light elements.

The transmission electron microscope (TEM) is an extremely valuable tool in examining precipitates on the order of a few hundred nanometres. Although it is primarily used for the investigation of submicron features of microstructures, the TEM has also been used to provide information relating to the placement of phase boundaries for metallic systems [21]. In a TEM, an electron beam is passed through a thin section of material. Similar to the SEM or EPMA, the X-rays emitted can be analysed with a EDS or WDS system to give the composition of the phase examined. An electron diffraction pattern is also obtained concurrently, giving the structure of the phase.

10.2.2 X-Ray Diffraction

Since the first structure determination by Bragg in 1912 [26], X-ray diffraction has been used to characterise the arrangement of atoms [27]. Metal phases and their crystal structures have been so extensively studied that the method is now used to identify phases and is primarily used as a complement to metallographic or microscopic techniques. The X-ray powder diffraction has been reviewed in great detail recently [28] and application to metallurgy can be found in general texts [29–31] and in specific publications [27].

Construction of phase diagrams from X-ray data exploits the fact that there is a continuous change in the lattice parameter with changing proportions of atoms of different size. Typically, alloy specimens equilibrated at high temperature are quenched to room temperature to preserve the equilibrium. For a continuous solid solution, such as (Co + Ni) alloys, the lattice parameter varies nearly linearly with composition in accordance with Vegard's law. This variation is shown for the (Co + Ni) system in Figure 10.11 [32].

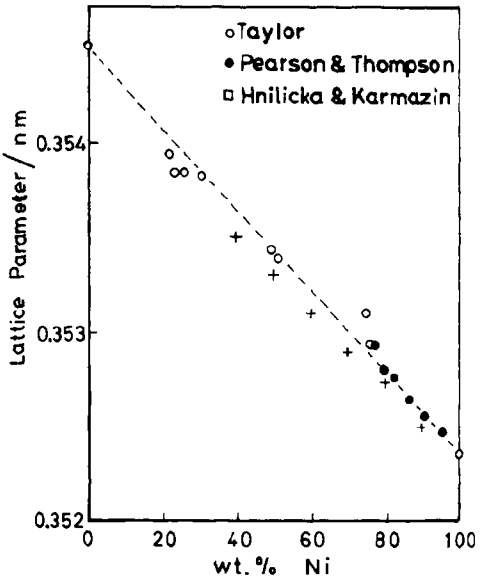

Figure 10.11 Lattice parameter of (Co + Ni) alloys at room temperature [32], used with permission of ASM International.

Where there are two phases possible at a particular temperature, there is an arrest in the lattice parameter variation with composition and diffraction peaks associated with a second phase that begin to appear. This is evident for the (Ni + Ti) system shown in Figure 10.12 [33]. The discontinuity identifies the phase boundary or solid solubility at $T = 1023$ K.

For comparison purposes, the (Ni + Ti) phase diagram [6] is shown in Figure 10.13, with the point on the phase boundary determined in Figure 10.12 circled.

Approximate relative proportions of the phases in the powder, usually accurate to a few percent, can be determined by intensity variation. To do so requires that standards of known proportions be prepared and used to create a calibration plot. Relative proportions can also be determined by Rietveld refinement, which is growing in popularity [34]. This technique originally grew out of the analysis of neutron diffraction patterns and has been applied to X-ray diffraction patterns. The interpretational software requires some knowledge of the space group, and atomic positions within the unit cell. This is generally not a problem for metallic systems. One recent application has been to quantitatively determine the mass fraction and mean size evolution of the δ' precipitates in an Al–Li alloy [35,36]. The software is freely available [37] and guidelines for the Rietveld refinement have been published recently [38].

10.2.3 Emf Cells

Generally speaking, this approach provides the relative partial molar Gibbs energy of one component in the system as a voltage measured under open-circuit conditions [39]. The experimental program must first demonstrate reproducibility in the measured potentials

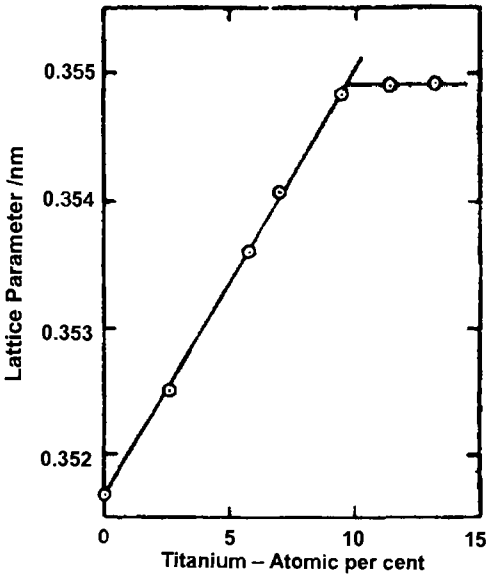

Figure 10.12 Lattice parameter of (Ni + Ti) alloys, nickel-rich region at $T = 1023\,K$ [33], used with permission of IOM[3].

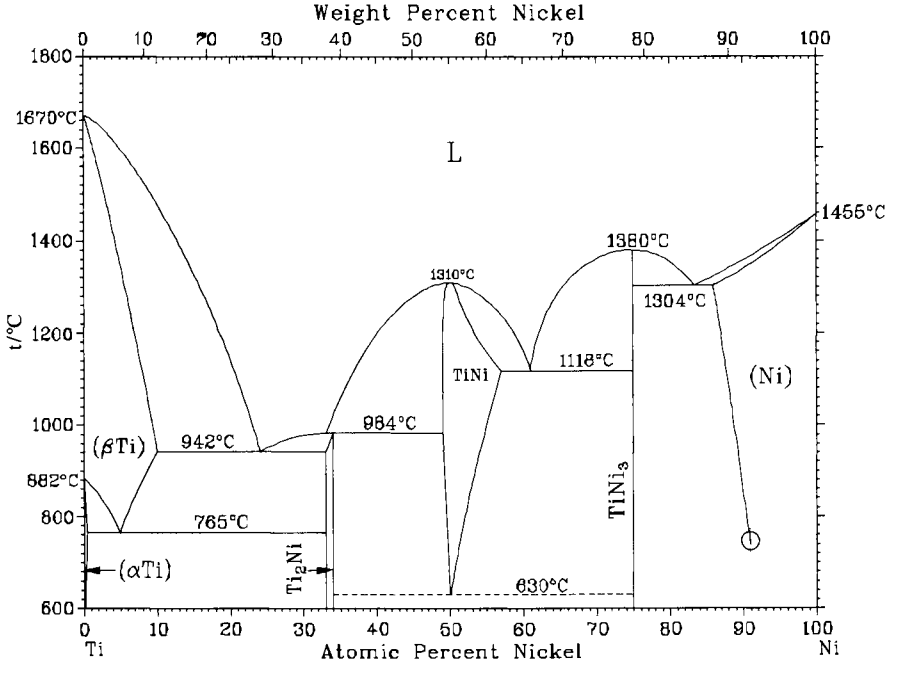

Figure 10.13 The (Ni + Ti) phase diagram [6]. The circled point on the lower right relates to the discontinuity shown in Figure 10.12, used with permission of ASM International.

following a disturbance, such as the momentary passage of a small current or excursion in temperature. By gathering sufficient information on the compositional dependence of one component over the extremes of composition change, the Gibbs–Duhem equation may be integrated to determine the relative partial molar Gibbs energy of the other component and the Gibbs energy of mixing, depicted in Figure 10.1.

Consider a binary system (M + N) in which M is the more easily oxidized element. An electrochemical concentration cell may be constructed of the type

$$- M|M^{z+}|(\mathrm{M} + \mathrm{N}) +. \tag{10.7}$$

The electrolyte containing the M^{z+} ion must be suitably conductive and non-volatile at the temperature of interest. Typically, a molten salt mixture is employed to provide a suitably low eutectic [40–42]. The diluent salts for the M^{z+} ion must be sufficiently stable so that there is no chemical exchange with the alloying elements. The reversible open circuit cell voltage E gives the relative partial Gibbs energy of M by

$$\Delta\bar{G}_{\mathrm{M}} = -zFE, \tag{10.8}$$

where F is the Faraday constant.

To permit measurements at higher temperatures, where even a molten electrolyte may be too volatile, a solid electrolyte may be employed. In this technique, a metal–metal oxide equilibrium may be used to establish an oxygen partial pressure in the half-cells. The difference in the effective oxygen partial pressure on either side of the solid O^{2-} conducting electrolyte generates an emf that can be related to the activity of the metal component under study in the alloy phase.

To take the case of palladium–rhodium alloys, the thermodynamic properties have been measured between $T = 950\,\mathrm{K}$ and $1350\,\mathrm{K}$ [43]. The galvanic cell, shown in Figure 10.14, is schematically represented by

$$- \underbrace{\mathrm{Rh},\ \mathrm{Rh_2O_3}}_{(P_{\mathrm{O_2}})_1} | \underbrace{\mathrm{Y_2O_3 \cdot ZrO_2}}_{\text{solid oxide electrolyte}} | \underbrace{\mathrm{Pd_{1-x}Rh_x},\ \mathrm{Rh_2O_3}}_{(P_{\mathrm{O_2}})_2} +, \tag{10.9}$$

where the oxygen partial pressure at each electrode is controlled by

$$2\mathrm{Rh} + 1.5\mathrm{O_2} = \mathrm{Rh_2O_3}. \tag{10.10}$$

The results take the form of plots of E in volts versus temperature for each alloy composition, as shown in Figure 10.15.

The emf, corresponding to the virtual oxygen transfer, reaction (10.11), is given by Equation (10.12):

$$\mathrm{O_{2(alloy\text{-}side\ 2)}} \xrightarrow[4F]{} \mathrm{O_{2(pure\ Rh\text{-}side\ 1)}}, \tag{10.11}$$

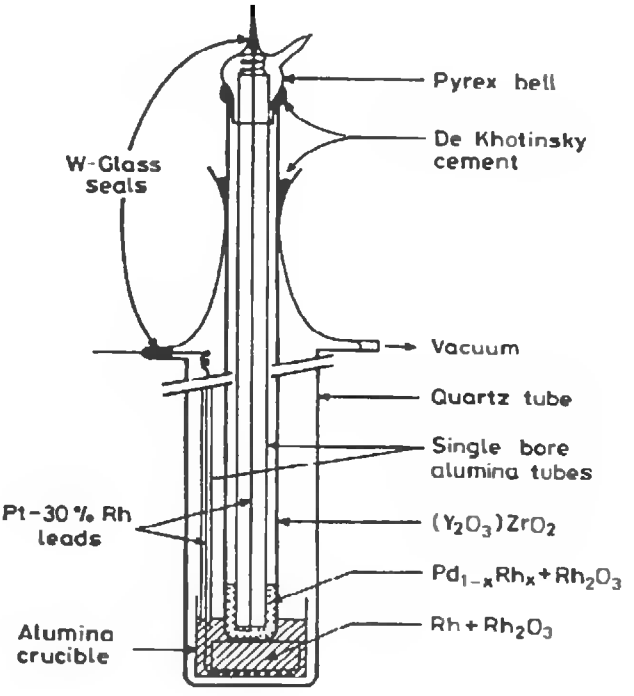

Figure 10.14 Schematic diagram of a galvanic cell [43], used with permission of ASM International.

$$E = \frac{-RT}{4F} \ln \left[\frac{(P_{O_2})_1}{(P_{O_2})_2} \right]. \tag{10.12}$$

Combining the previous concepts, the activity of the rhodium (a_{Rh}) is directly related to the emf by Equation (10.13) [43]:

$$-3FE = \Delta_{mix} \bar{G}_{Rh} = RT \ln a_{Rh}. \tag{10.13}$$

From the temperature dependence of the activity, the partial enthalpy and entropy for Rh can be computed. By using the Gibbs–Duhem equation, the corresponding properties for Pd can be derived. This leads to a thermodynamic model describing the solution behaviour of the solid in the (Pd + Rh) system, in the range of temperatures where continuous solid solutions can be expected, as shown in Figure 10.16 [44]. The form of the equation is similar to that shown in Table 10.1 for the liquid phase of the (Sn + Bi) system (small positive deviations from ideal behaviour).

Gibbs energy isotherms for the (Pd + Rh) system at $T = 1000$ and 1300 K are shown in Figure 10.17. Note that in Figure 10.17a the miscibility gap depicted in the phase diagram is defined by the common tangent to the cF4-phase.

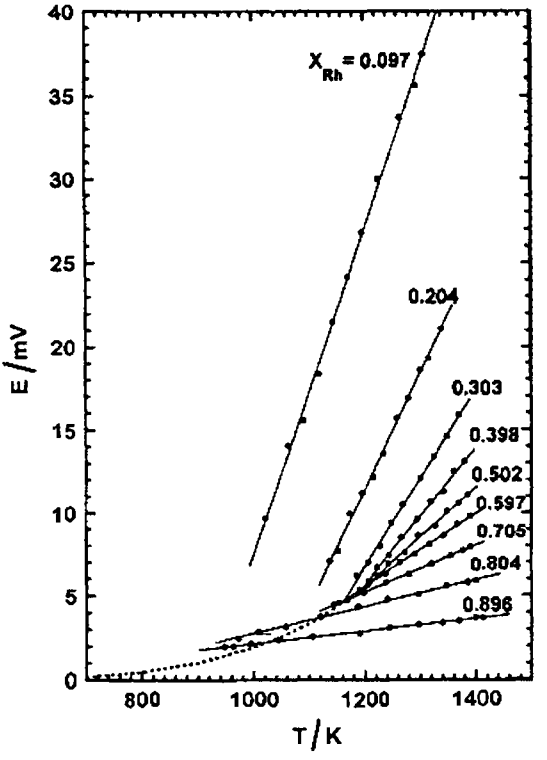

Figure 10.15 Sample set of results for emf measurements for (Pd + Rh) alloys [43], used with permission of ASM International.

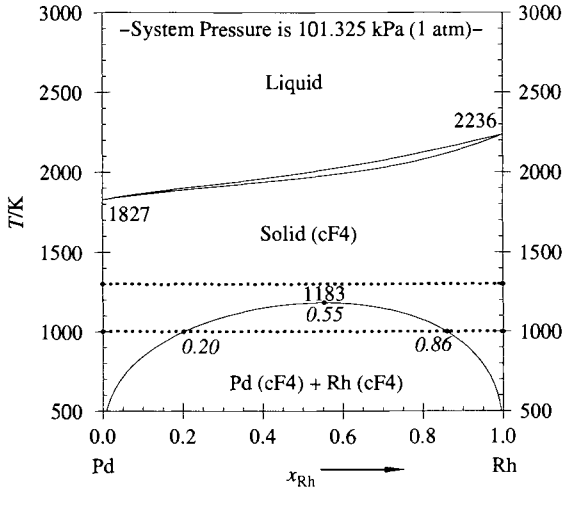

Figure 10.16 (Pd + Rh) phase diagram [44].

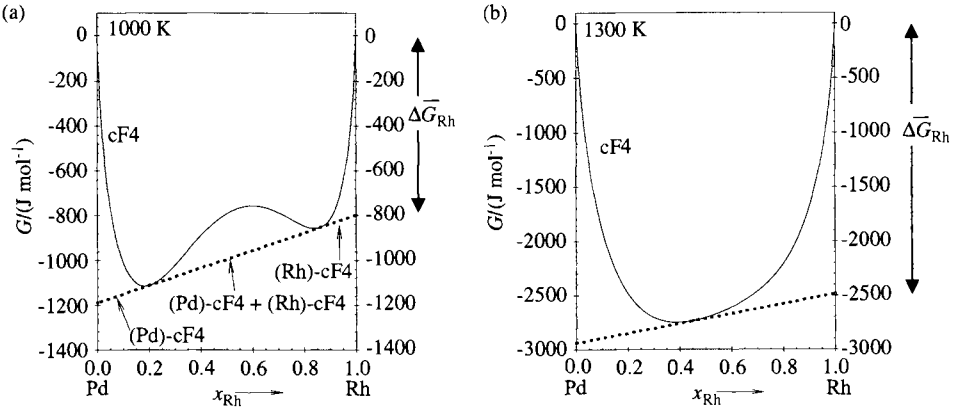

Figure 10.17 Gibbs energy isotherms for the (Pd + Rh) system at $T = 1000$ and 1300 K.

10.2.4 Vapour Pressure Techniques

Vapour pressure measurements provide another way of measuring a relative partial molar Gibbs energy. Since the temperatures involved in most metal system investigations are relatively high and the partial pressure of the most volatile component is typically low, it is quite appropriate to employ ideal gas behaviour in the following way:

$$\Delta_{\text{mix}}\,\bar{G}_i = \bar{G}_i - G_i^{\circ} = RT \ln\left[\frac{P_i}{P_i^{\circ}}\right] = RT \ln a_i. \qquad (10.14)$$

This experimental approach of gathering Gibbs energy data is limited to systems where there is only one component that is a substantial contributor to the vapour phase and also when the molar mass of the volatile species is not in question. Fortunately for most metals, the dominant vapour species is usually monatomic.

In the transpiration or transport technique, an inert gas is passed through or over a condensed sample such that the partial pressure of the vapour is taken to be in equilibrium with the condensed phase [45–47].The mass transport is monitored through the weight loss of the condensed phase or through the weight gain of a cold finger or trap that is positioned downstream. The vapour species are condensed and analysed with a suitable technique. A simple transpiration apparatus is presented in Figure 10.18 [46]. Such an apparatus would be used for the determination of the vapour pressures of solids. Care must be taken to ensure that the flow of the carrier gas is slow enough for equilibrium to be reached but also fast enough to render insignificant any diffusion of the vapour downstream to the cold trap. Material depletion is another factor: material evaporated from the condensed system must not affect the overall composition to a significant extent.

In principle, the transpiration technique could be applied to the (Mg + Si) system noted in Section 10.2. The measurements for a particular composition and temperature would give, in effect, a point on the vapour phase boundary in Figure 10.7. The collection of sufficient data of this type yields the relative partial molar Gibbs energy of Mg in the

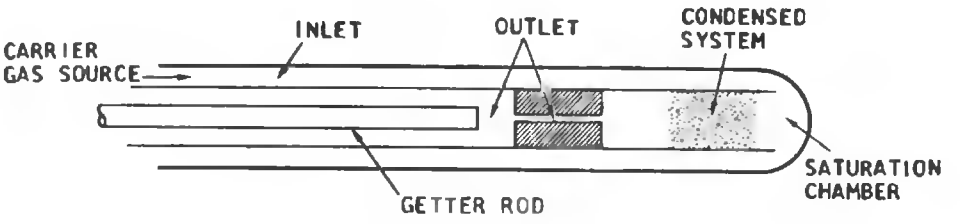

Figure 10.18 Simple high-temperature transpiration apparatus, after Norman and Winchell [46]

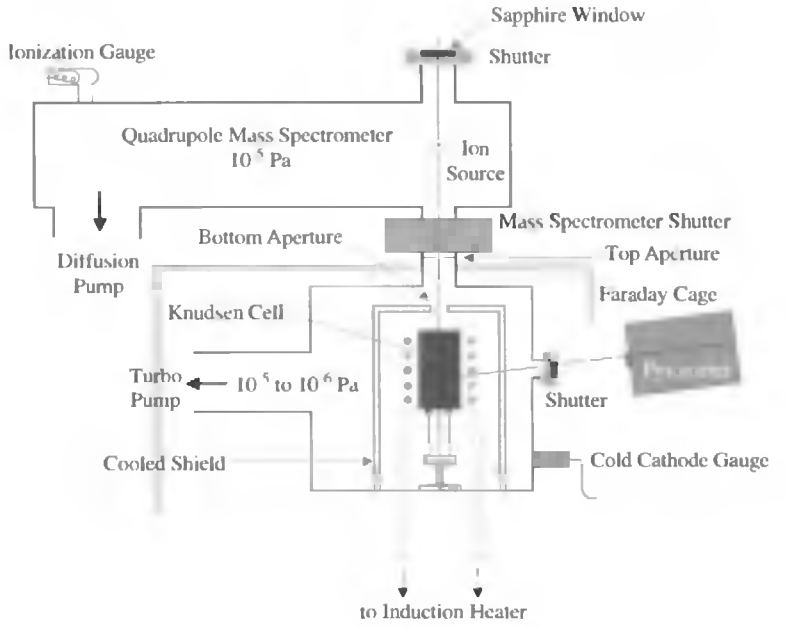

Figure 10.19 Mass spectrometer/Knudsen cell apparatus.

liquid phase as a function of temperature. By the application of the Gibbs–Duhem equation, the corresponding relative partial molar Gibbs energy for Si could be derived. The Gibbs energy of mixing could then be found, which becomes the basis for the computation of the phase diagram for (Mg + Si), by the lowest common tangent methodology.

The modern embodiment of vapour pressure methods employs superior detection systems. One such arrangement, appropriate to systems with quite low volatility, for example (Pd + Rh), is shown in Figure 10.19 [48]. A Knudsen cell made of inert material encloses the alloy under study. The effusing vapour is detected by mass spectrometric means.

The signal provides a partial pressure for each isotope of Pd, the more volatile element. The relative isotopic abundance of vapour species is used to refine the computation of the total partial pressure expressed in Equation (10.14) as P_i. Typical data for a (Pd + Rh)

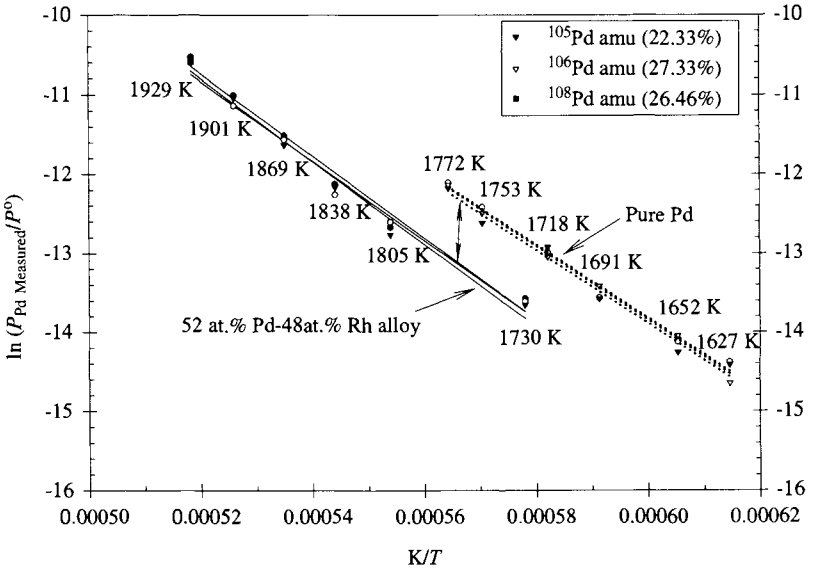

Figure 10.20 Typical partial pressure data for a 52 at.% Pd–48 at.% Rh alloy [48].

alloy are shown in Figure 10.20 for both pure Pd and an alloy [48]. The displacement of the two lines provides a measurement of the activity of Pd in the alloy. In this case, it is slightly greater than the atomic fraction of Pd in the condensed phase.

When the volatility is much higher, continuous recording of thermogravimetric (TGA) means could be employed in the detection system. Vapour effusing from the hot Knudsen cell, swept away by an inert carrier gas, condenses in a cold trap downstream. The mass loss from a chamber, in which saturation must be demonstrated, provides the partial pressure using classical effusion equations.

10.2.5 Thermal Methods

In the simplest embodiment of this technique, the temperature is continuously recorded during slow heating or cooling. Phase changes that take place alter the rate of temperature change with time due to the heat effects associated with the transformation. The most effective use of this technique is the study of liquid–solid transformation since the phase transformations are generally not sluggish in metallic systems.

A variation on this technique is differential thermal analysis (DTA) in which two thermocouples are used. One is placed in a non-transforming reference material and the other in the system under study. A spike occurs in the temperature difference when a transformation is encountered. An example of the application of DTA is shown in Figure 10.21 for a (Pd + Rh) alloy [48].

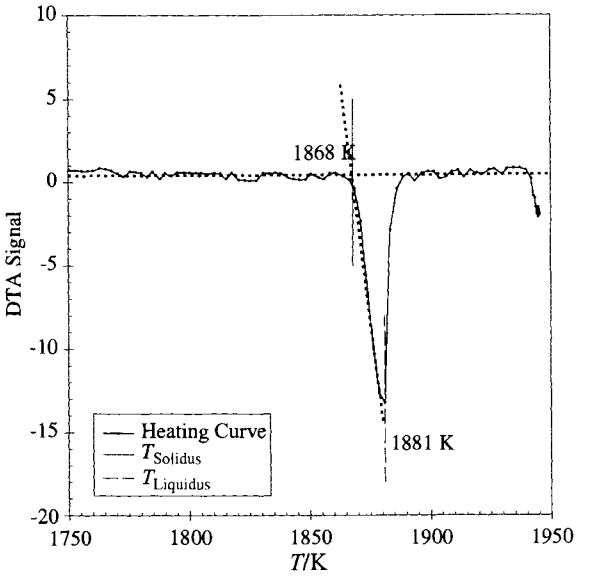

Figure 10.21 A typical DTA curve for an 80 at.% Pd–20 at.% Rh alloy. The extrapolated onset indicates that the solidus temperature is 1868 K [48].

Thermal analysis techniques put emphasis on the temperature at which a transformation commences, since the temperature at which a transformation concludes may not be reliably detected. For example, the solidus in a cooling binary metal system is usually achieved by segregation associated with the slow diffusion of the components in the crystallizing solid. Advancement on DTA is the quantification of the thermal effect associated with the peak height/area, which leads to scanning calorimetry.

10.2.6 Scanning Calorimetry

There are the two principal types of differential scanning calorimeters (DSC). Boersma [49] introduced the heat flux DSC in 1955, and Watson and O'Neill [50,51] developed the Power Compensation DSC in 1963. With these two techniques, it is possible to make quantitative measurements of the transformation energy, which had not been possible with traditional DTA [52]. In the heat flux method, the heat of transformation is detected as a temperature difference with respect to an adjacent reference material [49]. In the power compensating method, the power required to keep the sample and the reference material at the same temperature is recorded [50].

A typical result for (Sn + Bi) alloy is shown in Figure 10.22. It can be seen from this figure that the onset of transformation temperature is calculated as $T = 412$ K. This corresponds to the eutectic temperature in Figure 10.3 [53].

Table 10.3 summarizes the experimental work [53] for several additional compositions of (Sn + Bi) alloys. For the process of raising the temperature from 373 to 483 K, with all

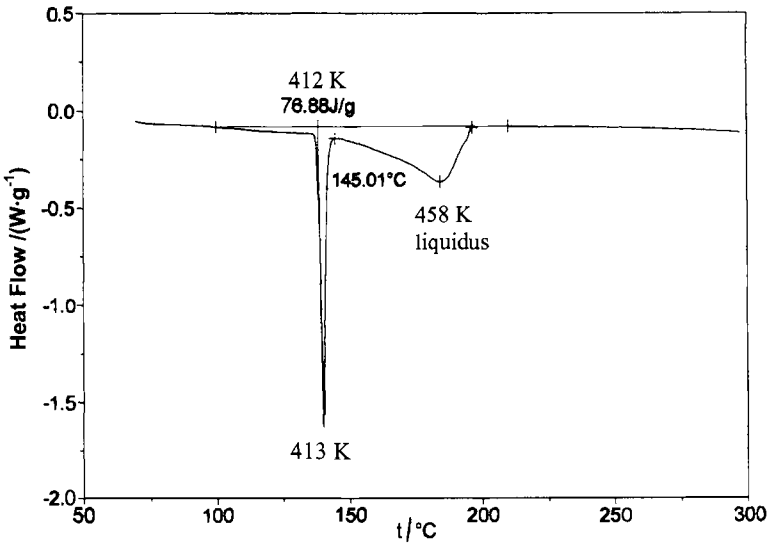

Figure 10.22 DSC heating profile for a 20 at.% Bi in Sn alloy. The eutectic temperature, determined by the extrapolated onset, is 412 K and the liquidus temperature is 458 K [53].

Table 10.3 Thermal effects for fusion of (Sn + Bi) alloys.

x_{Bi}	Measured ΔH ($J \cdot mol^{-1}$)	Calculated ΔH ($J \cdot mol^{-1}$)	Difference	
			($J \cdot mol^{-1}$)	%
0.197	10103	10496	−393.1	−3.75
0.312	10890	11074	−184.3	−1.66
0.390	11846	11455	391.7	3.42
0.475	11623	11863	−240.0	−2.02

accompanying phase changes, a measured ΔH is recorded in Table 10.3. This can be compared to the calculated ΔH, determined from Figure 10.4. The difference in the values is typical of the precision that may be expected from scanning calorimetry as it applies to alloy transformations that involve melting.

The liquidus temperatures were determined from the return to baseline, as marked in Figure 10.22. These are shown in Table 10.4 and compared with modelled temperatures from Figure 10.2.

Heating rates affect the results obtained using scanning calorimetry to a limited degree. An indication of this is shown in Table 10.5.

Figure 10.23 shows a series of representative DSC curves for various alloy compositions in a more complex binary system [54]. At compositions indicated by 1, 2 and 3 (pure B; compound D with a congruent melting temperature; and the eutectic composition, respectively), the curves have very sharp peaks, indicating a temperature invariant phase change. However, alloys 4–8 have melting ranges as indicated on the phase diagram. For alloys 4–7,

Table 10.4 Liquidus temperatures T_ℓ for the (Sn + Bi) alloys.

x_{Bi}	Observed T_ℓ/K	Modelled T_ℓ/K
0.197	458	463
0.312	430	438
0.390	425	421
0.475	423	424

Table 10.5 Effect of heating rate on observed eutectic temperature T_e and liquidus temperature T_ℓ for sample 3 (x_{Bi} = 0.39).

Heating rate ($K \cdot min^{-1}$)	Observed T_e(K)	Observed T_ℓ(K)
10	412.6	425.2
2	412.6	424.1
0.5	412.5	423.7

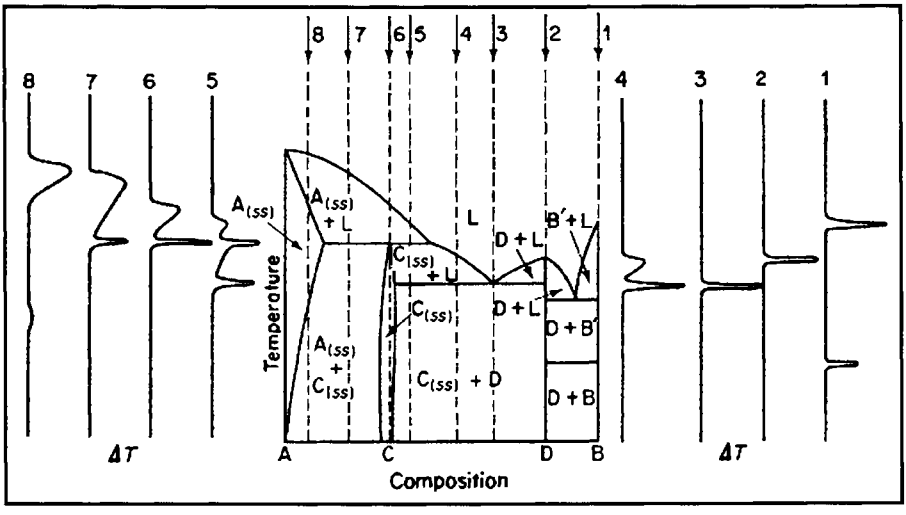

Figure 10.23 The (A + B) phase diagram, showing representative DSC curves for various alloy compositions, indicated by the dashed lines, after Gutt and Majumdar [54]. *Note*: (ss) indicates solid solution.

the eutectic and peritectic temperatures correspond to the extrapolated onset of the sharp peak, but the heating curve does not return immediately to the baseline, which is similar to the behaviour shown in Figure 10.22. In the cases where the cooling path only passes through one region of solid plus liquid (alloys 4, 6 and 7), the DSC curve moves towards a second extreme value, which corresponds to the liquidus temperature. For curve 5, the

eutectic and peritectic temperatures are indicated by sharp peaks, and the liquidus by the final peak.

Alloy 8 in Figure 10.23 has a path that does not cross a eutectic or peritectic tie line. Instead, the solidus is determined by where the extrapolated onset occurs for the larger peak, with the liquidus occurring at the peak extremity, similar to that of Figure 10.21. The temperature of the solidus is approximately indicated by the bump in the DSC curve at the lower temperature. However, the heat effect here is rather small and difficult to resolve, since it is a solid to solid reaction. X-ray diffraction (Section 10.2.2) would be better suited to determining the placement of this phase boundary.

Calorimetric Methods

Although enthalpies of formation and heat capacity do not deal directly with the subject matter of this review, these data do bear upon phase transformations since they contribute to the development of Gibbs energy equations exemplified by Mg_2Si in Table 10.2.

The calorimetric techniques applied to metallurgy are well reviewed in [45]. Practical considerations in reaction calorimetry are well reviewed in Chapter 3A of Ref. [55]. With respect to solution calorimetry, the IUPAC has recently published a book by that title, which describes the various techniques now commonplace today. In particular, Chapter 6 of Ref. [56] gives an excellent review of this technique as applied to metallurgical systems.

10.3 Multi-Component Systems

Phase equilibrium in systems of contemporary commercial interest almost invariably involve more than two components. Experimental studies, based upon methods outlined in the previous sections, are being guided to a considerable degree, by predictive methods based upon the substantial body of thermodynamic data collected over the past 25 years [6,57]. Two types of multi-component systems may be distinguished, *viz.* those involving a solvent element with several dilute solutes, and those covering the extremes of composition for all components.

When there is a dominant metal component, the simplifications associated with dilute solution thermodynamics may be applied. There are many systems of commercial interest that fall into this category. Principally a knowledge of the Henry's activity coefficient for each solute and its variation with temperature is required. In many cases, it is sufficient to treat the activity coefficients as independent of composition within the limited range of concentration for those dilute solutes and to ignore, as an initial approximation, the effect of one solute on the activity coefficient of another.

Consider the case of a lead battery electrode alloy containing small concentrations of Ca, Sn and Ag. The activity of Ca dissolved in Pb can be found by formulating the solubility product from the Gibbs energy of formation of $CaPb_3$, via reaction (10.15), and using a portion of the binary (Pb + Ca) phase diagram, shown in Figure 10.24 [58–60].

$$Ca + 3Pb = CaPb_3. \qquad (10.15)$$

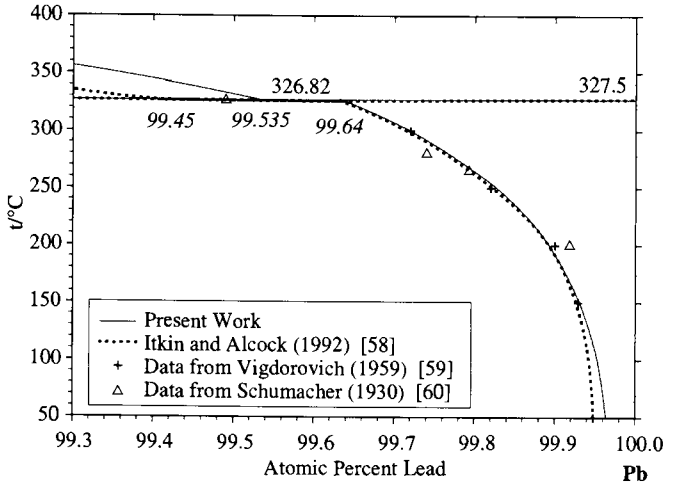

Figure 10.24 The (Ca + Pb) phase diagram, enlarged at the Pb-rich side.

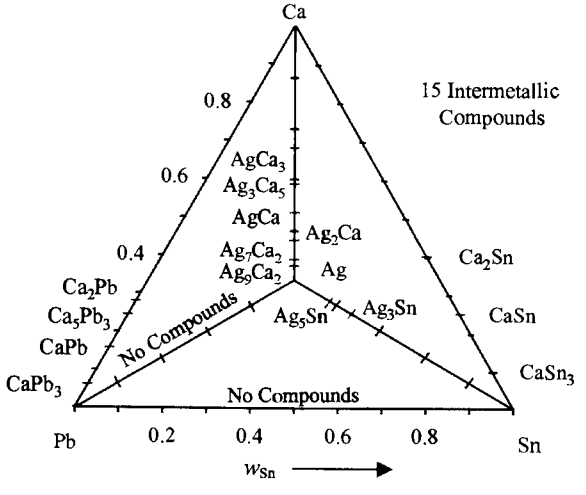

Figure 10.25 The (Pb + Sn + Ca + Ag) quaternary system.

Taking the activity of Pb in the lead-rich phase to be the atom fraction, the activity coefficient of Ca can be found for alloys saturated with $CaPb_3$, using equation.

$$\Delta_f G^{\circ}_{CaPb_3} = RT \ln x_{Ca} + RT \ln \gamma_{Ca} + RT \ln x_{Pb}. \qquad (10.16)$$

The Henrian activity may be found, broadly speaking, in a similar manner for the other solutes. The phase equilibrium involving the possible coexistence of the lead-rich solid solution with intermetallic phase(s) can now be calculated. Figure 10.25 depicts the compositions of all the possible intermetallic phases involving the four elements in question.

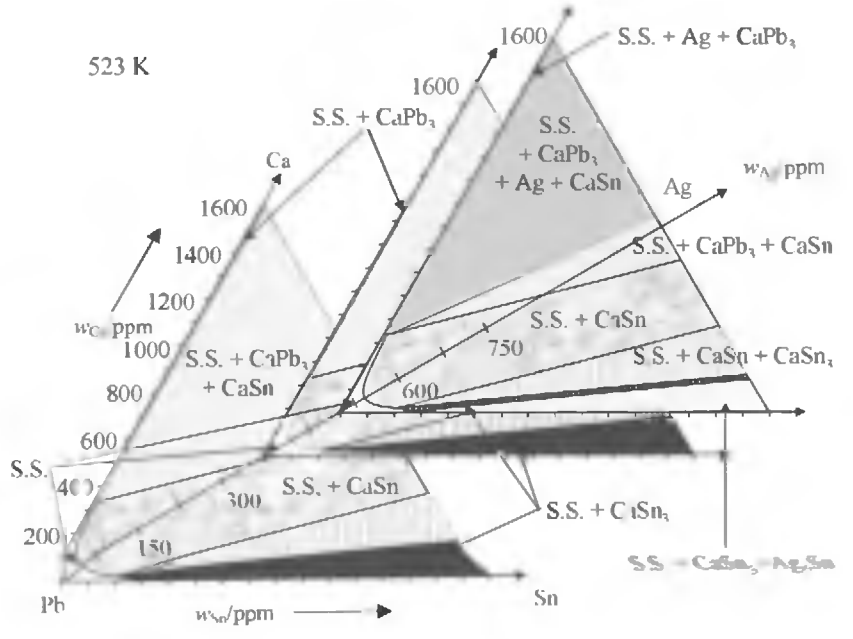

Figure 10.26 Ternary slices from (Pb + Sn + Ca + Ag) quaternary, at constant levels of Ag.

With the Gibbs energy of formation for these nearly stoichiometric phases, there is sufficient data to develop the phase diagram in the lead-rich corner by Gibbs energy minimization methods incorporated into computational software [61]. The estimated phase equilibrium is depicted in Figure 10.26 for $T = 523$ K.

It is also possible to compute, for a series of temperatures, the most stable phase assemblages, and identify those temperatures associated with the appearance of new phases. These results are organized in Table 10.6, with the asterisks indicating the temperature for the appearance of a new phase. This information, made possible by bringing together a variety of experimental measurements, modelling the binary phase diagrams to rationalize those data, and using modern computational tools, is revealing in terms of the genesis of phases. In particular, it is important to know from which phase (solid or liquid) a particular intermetallic precipitate first appears. This affects the metallurgical microstructure with a consequent impact on mechanical properties.

When the phase equilibrium is to be developed for a system where dilute solution simplifications do not apply, interpolation methods may be used to estimate Gibbs energies based upon experimental studies for the binary metal combinations. Consider the case of (Mo + Pd + Rh + Ru) alloys. This system is encountered as metallic inclusions in spent nuclear fuel. The Kohler interpolation scheme [62], which will here suffice to represent others [63], proportionally weights, from each binary system, the contribution of the thermodynamic property of interest, as given below.

$$G_{\mathrm{p}}^{\mathrm{E}} = (1 - x_{\mathrm{X}})^2 \, G_{\mathrm{a}}^{\mathrm{E}} + (1 - x_{\mathrm{Y}})^2 \, G_{\mathrm{b}}^{\mathrm{E}} + (1 - x_{\mathrm{Z}})^2 \, G_{\mathrm{c}}^{\mathrm{E}}. \tag{10.17}$$

Table 10.6 The mass percentages of the various phases for the slow cooling of a Pb alloy with 600 ppm Ca, 6000 ppm Sn and 500 ppm Ag.

T/K	Liquid solution	$CaSn_3$	Solid solution	Ag_5Sn
773.0	100			
727.0	100	*		
599.5	99.475	0.525	*	
589.7	0	0.564	99.436	
534.0	0	0.592	99.408	*
473.0	0	0.593	99.365	0.042

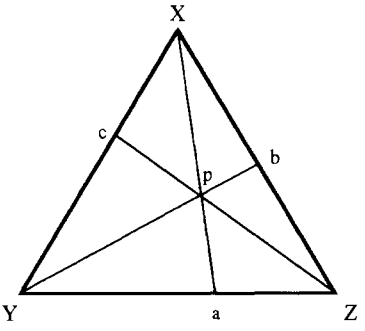

Figure 10.27 Representation of Kohler Interpolation; the property (G^E) at p may be estimated from a knowledge of properties at compositions a, b and c [62].

This is illustrated in Figure 10.27, where the excess Gibbs energy of mixing at point p, is estimated from the known excess Gibbs energy of mixing at points a, b and c, which are found by extending line segments from each of the corners on the ternary diagram, to the opposite binary system.

The form of the interpolation scheme for the excess Gibbs energy is consistent with regular solution behaviour of each component dissolved in a solvent involving a fixed proportion of the other two components. This methodology has been found suitable in many cases as a predictive approach to provide ternary and multi-component excess solution property estimates when no experimental data exist. As experimental data are gathered for the multi-component system, departure terms may be added to the basic interpolation. These terms, usually only 1 or 2 are necessary or justified, take the form of products of all mole fractions raised to different powers times a temperature-dependent coefficient. The correction terms vanish in the binary subsystems. Figure 10.28 shows the phase equilibrium for the ternary faces of the quaternary alloy at $T = 2000$ K computed using this interpolation method [64]. The phase boundaries for the (Pd + Rh) binary alloy may be compared with the binary diagram in Figure 10.16.

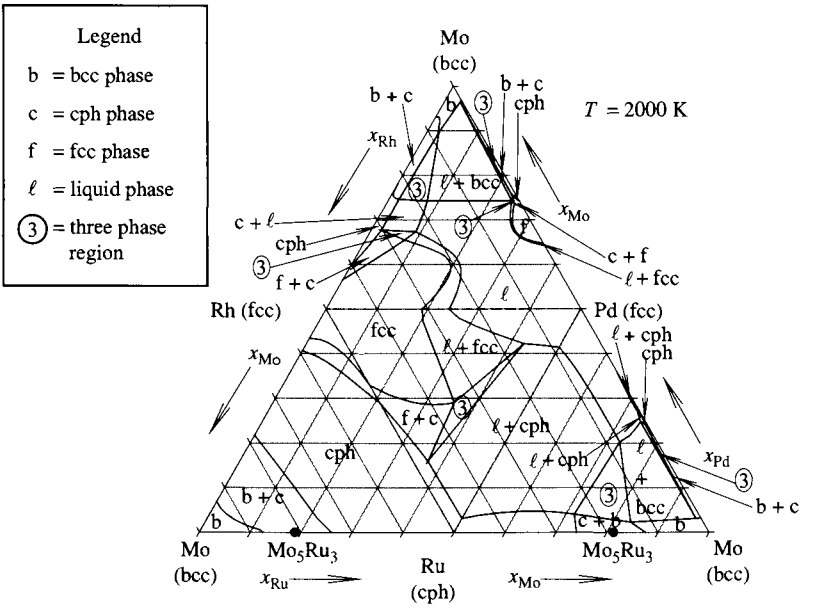

Figure 10.28 Four ternary diagrams for the (Mo + Pd + Rh + Ru) system at $T = 2000$ K [64].

10.4 Conclusions

Phase equilibrium expressed using binary temperature–composition phase diagrams has long been recognized as central to metallurgical processing. For the greater part of the last century, the development of these diagrams was almost exclusively undertaken as an experimental activity involving the substantial use of microscopy, X-ray diffraction and thermal analysis. The widespread use of computers in the past 25 years awakened a more fundamental understanding of the thermodynamic principles of phase diagram construction that was dormant for a century. This has enabled experimental measurements of thermodynamic solution properties to contribute in greater measure to phase diagram development, and assist in major international assessment programs leading to comprehensive compilations. This modelling/assessment process not only gives assurance that the phase diagram is self-consistent and respects underlying principles, but also provides a degree of confidence in extrapolating to conditions of temperature, pressure or composition that may be difficult to study experimentally. Furthermore, phase equilibrium information, stored as self-consistent equations for the thermochemical properties of the phases, permits diagrams with unconventional axes to be rapidly developed for special applications. With the addition of interpolation equations to forecast multi-component solution behaviour from the binary subsystems, likely phase diagrams for systems with many components can now be calculated to help focus future time-consuming experimental effort.

References

1. Hansen, M., *Der Aufbau der Zweistofflegierungen*, Springer, Berlin, 1936.
2. Hansen, M., *Constitution of Binary Alloys*, McGraw-Hill, New York, NY, 1958.
3. Elliott, R.P., *Constitution of Binary Alloys-First Supplement*, McGraw-Hill, New York, NY, 1965.
4. Skunk, F.A., *Constitution of Binary Alloys-Second Supplement*, McGraw-Hill, New York, NY, 1969.
5. Moffatt, W.G., *The Handbook of Binary Phase Diagrams*, G.E. Company, Schenectady, NY, 1977.
6. Massalski, T.B., *Binary Alloy Phase Diagrams, 1 & 2*, ASM, Metals Park, OH, 1986.
7. Gibbs, J.W., in *The Collected Works of J. Willard Gibbs, Vol I – Thermodynamics*, Yale University Press, New Haven, CT, pp. 55–371, 1957.
8. Darken, L.S., *Thermodynamics in Physical Metallurgy*, ASM, Cleveland, OH, 1952.
9. Oonk, H.A.J., *Phase Theory: The Thermodynamics of Heterogeneous Equilibria, Studies in Modern Thermodynamics, Vol 3*, Elsevier Scientific, Amsterdam, 1981.
10. Gaskell, D.R., *Introduction to Metallurgical Thermodynamics*, McGraw-Hill, New York, NY, 1981.
11. Lupis, C.H.P., *Chemical Thermodynamics of Materials*, Elsevier Science Publishers, Amsterdam, 1983.
12. Thompson, W.T. and Davis, B.R., *29th International Metallographic Society*, Pittsburgh, PA, 1996.
13. Kaufman, L., in *Phase Stability in Metals and Alloys*, P.S. Rudman, J. Stringer and R.I. Jaffee, eds., McGraw-Hill, New York, NY, 1967.
14. Dinsdale, A.T., *CALPHAD*, **15**, 317–425, 1991.
15. Okamoto, H., *J. Phase Equilibr.* **12**, 623–643, 1991.
16. Boyer, H.E. and Gall, T.L., eds., *Metals Handbook Desk Edition*, ASM, Metals Park, OH, 1985.
17. Chu-Kun, K., Zu-Xiang, L. and Dong-Sheng, Y., *High Temperature Phase Equilibria and Phase Diagrams*, Pergamon Press, Beijing, 1990.
18. Kehl, G.L., *The Principles of Metallographic Laboratory Practice*, McGraw-Hill, New York, NY, 1949.
19. Haworth, C.W. and Hume-Rothery, W., *Inst. Met. J.* **87**, 265–272, 1958–1959.
20. Goldstein, J.I. and Newbury, D.E., eds., *Scanning Electron Microscopy and X-Ray Microanalysis: A Text for Biologists, Materials Scientists, and Geologists*, 2nd ed., Plenum Press, New York, NY, 1992.
21. *Metallography and Microstructures*, ASM Handbook, *Vol 9*, ASM International, Materials Park, OH, 1985.
22. *Materials Characterization*, ASM Handbook, *Vol 10*, ASM International, Materials Park, OH, pp. 473–476, 1986.
23. ASTM Standard E 1508-98, *Standard Guide for Quantitative Analysis by Energy-Dispersive Spectroscopy*, ASTM, 1999.
24. Lifshin, E., in *Characterization of Materials*, R.W. Cahn, P. Haasen and E.J. Kramer, eds., *Materials Science and Technology, Vol 2B*, VCH, New York, NY, p. 351–421, 1994.
25. Freil, J.J. and Greenhut, V.A., *Adv. Mater. Proc.* **156**, 28–32, 1999.
26. Bragg, W.L., in *The Crystalline State: Volume 1 – General Survey*, W.H. Bragg and W.L. Bragg, eds., G. Bell and Sons, London, pp. 268–286, 1933.
27. Taylor, A., *X-ray Metallography*, Wiley, New York, NY, 1961.
28. Jenkins, R. and Snyder, R.L., *Introduction to X-ray Powder Diffractometry, Chemical Analysis, Vol 138*, Wiley, New York, NY, 1996.
29. Cullity, B.D., *Elements of X-Ray Diffraction*, 2nd ed., Addison-Wesley, Reading, MA, 1978.
30. Reed-Hill, R.E., *Physical Metallurgy Principles*, Van Nostrand, Princeton, NJ, 1964.
31. Kostorz, G., in *Physical Metallurgy*, 3rd ed., Ch. 12., R.W. Cahn and P. Haasen, eds., North-Holland, New York, NY, 1983.

32. Nash, P., ed., *Phase Diagrams of Binary Nickel Alloys*, ASM International, Materials Park, OH, 1991.
33. Taylor, A. and Floyd, R.W., *Inst. Met. J.* **80**, 577–587, 1951–1952.
34. Young, R.A., ed., *The Rietveld Method, IUCr Monographs on Crystallography 5*, Oxford University Press, Oxford, 1993.
35. Pérez-Landazábal, J.I., Nó, M.L., Madariaga, G. and San Juan, J., *J. Appl. Crystallogr.* **30**, 107–113, 1997.
36. Pérez-Landazábal, J.I., Nó, M.L., Madariaga, G., Recarte, V. and San Juan, J., *Acta Mater.* **48**, 1283–1296, 2000.
37. Collaborative Computational Project Number 14 – Single Crystal and Powder Diffraction, Homepage: http://www.ccp14.ac.uk/main.htm.
38. McCusker, L.B., Von Dreele, R.B., Cox, D.E., Louër, D. and Scardi, P., *J. Appl. Crystallogr.* **32**, 3650, 1999.
39. Mikula, A., in *High Temperature Materials Chemistry IX*, K.E. Spear, ed., The Electrochemical Society Inc., pp. 187–193, 1997.
40. Thompson, W.T., Leung, A. and Hurkot, D.G., *Can. Metal. Q.* **12**, 421–433, 1973.
41. Kleppa, O.J., *J. Am. Chem. Soc.* **71**, 3275–3280, 1949.
42. Kleppa, O.J., *J. Am. Chem. Soc.* **72**, 3346–3352, 1950.
43. Jacob, K.T., Priya, S. and Waseda, Y., *J. Phase Equilibr.* **19**, 340–350, 1998.
44. Gürler, R., Cornish, L.A. and Pratt, J.N., *J. Alloys Compd.* **191**, 165–168, 1993.
45. Kubaschewski, O., Alcock, C.B. and Spencer, P.J., *Materials Thermochemistry*, 6th ed., Pergamon Press, Oxford, pp. 64–112, 1993.
46. Norman, J.H. and Winchell, P., in *Physicochemical Methods in Metal Research, Part I*, R.A. Rapp, ed., *Techniques of Metals Research, Vol IV*, Wiley, New York, 1970.
47. Margrave, J.J., in *Physicochemical Measurements at High Temperatures*, J.O'M. Bockris, J.L. White and J.D. Mackenzie, eds., Butterworths, London, pp. 225–246, 1959.
48. Kaye, M.H., *A Thermodynamic Model for Noble Metal Alloy Inclusions in Nuclear Fuel Rods and Application to the Study of Loss-of-Coolant Accidents*, Doctoral Thesis, Queen's University, Kingston, ON, 2001.
49. Boersma, S.L., *J. Am. Cer. Soc.* **38**, 281–284, 1955.
50. Watson, E.S., O'Neill, M.J., Justin, J. and Brenner, N., *Anal. Chem.* **36**, 1233–1238, 1964.
51. O'Neill, M.J., *Anal. Chem.* **36**, 1238–1245, 1964.
52. Sykes, C., *Proc. Roy. Soc.* **148**, 422–446, 1935.
53. From unpublished experimental work performed by M.H. Kaye.
54. Gutt, W. and Majumdar, A.J., in *Differential Thermal Analysis, Vol 2*, Ch. 29, R.C. Mackenzie, ed., Academic Press, London, pp. 79–117, 1972.
55. Leach, J.S.L., in *Physicochemical Methods in Metal Research, Part I*, R.A. Rapp, ed., *Techniques of Metals Research, Vol IV*, Wiley, New York, 1970.
56. Marsh, K.N. and O'Hare, P.A.G., eds., *Experimental Thermodynamics, Vol IV*, IUPAC Chemical Data Series #39, Blackwell Scientific Publications, London, 1994.
57. *J. Phase Equilibr.* (previously *Bull. Alloy Phase Diagrams*), ASM, Metals Park, OH.
58. Itkin, V. and Alcock, C.B., *J. Phase Equilibr.* **13**, 162–169, 1992.
59. Vigdorovich, V.N. and Ya. Nashel'skii, A., *Russ. J. Inorg. Chem.* **4**, 922–925, 1959.
60. Schumacher, E.E. and Bouton, G.M., *Met. Alloys* **1**, 405–409, 1930.
61. Bale, C.W., Pelton, A.D. and Thompson, W.T., *Facility for the Analysis of Chemical Thermodynamics – User Manual 2.1*, Ecole Polytechnique de Montreal-McGill University, 1996.
62. Kohler, F., *Monats. Chem.* **91**, 738–740, 1960.
63. Chartrand, P. and Pelton, A.D., *J. Phase Equilibr.* **21**, 141–147, 2000.
64. Kaye, M.H., Thompson, W.T. and Lewis, B.J., *Trans. Am. Nucl. Soc.* **79**, 123–125, 1998.

11 Condensed Phases of Inorganic Materials: Ceramic Systems

N.S. JACOBSON
NASA John H. Glenn Research Center at Lewis Field
Cleveland, USA

R.L. PUTNAM
Los Alamos National Laboratory
Los Alamos, USA

A. NAVROTSKY
Thermochemistry Facility
Department of Chemical Engineering and Materials Science
University of California
Davis, USA

Measurement of the Thermodynamic Properties of Multiple Phases
R.D. Weir and Th.W. de Loos (Editors)

11 CONDENSED PHASES OF INORGANIC MATERIALS: CERAMIC SYSTEMS

Ceramic materials include oxides, nitrides, carbides, and borides. Many applications for these materials involve high temperatures where their chemical stability is critical. Thermodynamics provide a useful tool for predicting chemical stability, particularly at high temperatures. Thus there is a continuing need for accurate thermodynamic data for existing and future ceramic materials.

Methods of obtaining thermodynamic data for ceramic materials are generally similar to those employed for metallic materials. However, there are a number of critical issues for ceramic materials, which are emphasized here. In general, ceramic materials are used at higher temperatures and therefore, high-temperature thermodynamic data are needed. Obtaining thermodynamic data at high temperature sometimes requires the use of extreme conditions that are incompatible with typical thermodynamic methods and instruments. One particular challenge is the need for an inert reaction container at high temperatures. Ceramic materials also present a wide range of thermodynamic stabilities. Certain refractory oxides are exceptionally stable, *e.g.* ThO_2, whereas certain carbides, nitrides, and borides are barely more stable than the constituent elements, *e.g.* Mo_2C [1].

To characterize a system thermodynamically, the following data are needed at a minimum [2]:

(1) The standard molar enthalpy of formation from the elements in their standard states, *e.g.* $\Delta_f H^0_m$ (298.15 K) for $M(s) + \frac{1}{2}O_2(g) = MO(s)$.
(2) Standard entropy, usually at 298.15 K, S^0 (298.15 K).
(3) Heat capacity to high temperatures, $C_p^0(T)$.
(4) Enthalpies of phase transformation, $\Delta_{tr}H(T)$.

These data are usually obtained by calorimetry. The formation enthalpies are typically measured using some form of combustion or solution calorimetry. Heat capacities are commonly measured using adiabatic, drop, or differential scanning calorimetry. From the heat capacity and the formation enthalpy, high-temperature values for H, G, and S can easily be obtained using Equations (11.1)–(11.3) [2].

$$\Delta_f H^0(T) = \Delta_f H^0(298) + \int_{298}^{T} C_p^0(T)\,dT, \tag{11.1}$$

$$S^0(T) = S^0(298) + \int_{298}^{T} \frac{C_p^0(T)}{T}\,dT, \tag{11.2}$$

$$\Delta_f G^0(T) = \Delta_f H^0(T) - T\Delta S^0(T). \tag{11.3}$$

In some materials with disorder, a configurational entropy term must be included in Equation (11.2) [3].

Many ceramic materials form solid solutions with wide ranges of non-stoichiometry. Examples include $ZrO_{2-\delta}$ and $MoC_{1-\delta}$. For these compounds, it is important to know the partial thermodynamic quantities, such as the thermodynamic activities. The most common experimental methods are gas equilibration, vapour pressure, and electromotive force (emf) measurements. The measured activities are related to the partial molar Gibbs energy by [4]

$$\Delta\bar{G}_i = RT \ln a_i, \tag{11.4}$$

which allows the derivation of the partial molar enthalpy and entropy by

$$\Delta\bar{S}_i = -\left(\frac{\partial\Delta\bar{G}_i}{\partial T}\right)_p, \tag{11.5}$$

$$\Delta\bar{H}_i = \Delta\bar{G}_i + T\Delta\bar{S}_i = \Delta\bar{G}_i - T\left(\frac{\partial\Delta\bar{G}_i}{\partial T}\right)_p. \tag{11.6}$$

As noted by Kubachewski *et al.* [2], caution should be taken in ascribing too much significance to data derived from slopes and intercepts. Generally, entropies determined from calorimetric measurements or their estimates are preferred. Estimates may be made either from spectroscopic data or by comparison with similar compounds.

If the activities are determined for each component, then the Gibbs energy of formation can be calculated. Consider the oxide formation example:

$$M(s) + \tfrac{1}{2}O_2(g) = MO(s) \quad \Delta_f G^0 = RT \ln a_M a_{O_2}^{1/2}. \tag{11.7}$$

Ideally, this can be compared with the value determined calorimetrically.

In this section, we begin with a discussion of calorimetry as applied to ceramic materials. We then cover gas equilibration, vapour pressure, and emf techniques. This will cover the major approaches in use today for obtaining thermodynamic quantities of ceramic materials. The references will provide the reader with more details on these and other techniques.

11.1 Techniques Yielding Formation Enthalpies

Highly pure, single-phase materials are the most desirable for enthalpy measurements. If the highest purity material is unavailable, then impurities should be identified and compensated for in the thermodynamic calculations yielding the standard molar enthalpy of formation from the elements, $\Delta_f H_m^0$ (298.15 K). This requires that any impurity phases be known and have known thermodynamic functions.

11.1.1 Combustion Calorimetry

Combustion calorimetry is a powerful calorimetric tool used to determine the enthalpy of formation of many materials. The most common forms of combustion calorimetry on

ceramic materials involve the reaction of a precursor with fluorine or oxygen gas to measure the energies of reactions of the type:

$$\mathrm{M1M2\,(s)} + \tfrac{n}{2}\mathrm{X_2\,(g)} = \mathrm{M1X}_n\,\mathrm{(s\ or\ g)} + \mathrm{M2X}_n\,\mathrm{(s\ or\ g)}, \tag{11.8}$$

where X = O or F. Several requirements must be met for combustion calorimetry to be useful on ceramic materials. A candidate for combustion calorimetry must react completely with the oxidant to be used, *e.g.* (Si_3N_4 + O_2) [5]. The reaction products must be known, reproducible in composition and crystal structure, and have known or measurable enthalpies of formation.

Recently, O'Hare [6,7] and Tomaszkiewicz *et al.* [8,9] have determined the enthalpies of formation of several MSi_{2+x} alloys where M = W or Mo. Their studies used fluorine F_2 bomb calorimetry, since each component in their system (Si, W, and Mo) reacts completely with F_2 to form exactly one known product {SiF_4 (g), WF_6 (g), and MoF_6 (g)}. Calculation of an enthalpy of formation is straightforward once the enthalpy of combustion is known. Using $WSi_{2.060}$ as an example [6], the molar enthalpy of combustion, $\Delta_c H^0_m$, after corrections unique to each calorimeter, represents the reaction:

$$\mathrm{WSi_{2.060}\,(cr)} + 7.12\ \mathrm{F_2\,(g)} = \mathrm{WF_6\,(g)} + 2.06\ \mathrm{SiF_4\,(g)}\ \ \Delta_c H^0_m. \tag{11.9}$$

With the standard enthalpies of formation for the products $\Delta_f H^0_m(WF_6, g, 298.15\,K)$ [10] and $\Delta_f H^0_m(SiF_4, g, 298.15\,K)$ [11], the enthalpy of formation for $WSi_{2.060}$ can thus be calculated by,

$$\Delta_f H^0_m(\mathrm{WSi_{2.06}}, \mathrm{cr}, 298.15\,\mathrm{K}) = 2.06\ \Delta_f H^0_m(\mathrm{SiF_4}, \mathrm{g}, 298.15\,\mathrm{K}) + \Delta_f H^0_m(\mathrm{WF_6}, \mathrm{g}, 298.15\,\mathrm{K}) - \Delta_c H^0_m. \tag{11.10}$$

Leonidov and O'Hare have recently reviewed [12] F_2 bomb calorimetry. An oxygen bomb calorimeter is simpler in design to that described by O'Hare, but the basic technique remains the same. Generally, combustion bomb calorimetry is limited to non-oxide ceramics or alloys including carbides, nitrides, and some borides. A difficulty in forming oxides by combustion is their tendency to form poorly crystalline or finely grained (nanophase) materials.

11.1.2 Solution Calorimetry

Solution calorimetry is a common method for measuring formation enthalpies of ceramic materials. The material is dissolved in a solvent and the energies associated with the reaction are measured in a calorimeter. Two general types of solution calorimetry are used on ceramic materials. Aqueous solution calorimetry [13–17] employs aqueous acidic solutions at T = (298–335) K as a solvent and is thus used for less refractory, easily soluble materials. These materials tend to be the higher valence oxides and water containing materials while many of the newer, more technologically interesting materials tend to be more refractory and less susceptible to aqueous solution calorimetry. High-temperature

oxide-melt solution calorimetry [18–29] relies on a molten oxide-melt at elevated temperatures to dissolve more refractory materials that often cannot be dissolved using aqueous techniques. We emphasize the oxide-melt technique in this discussion and refer the reader to the more detailed references on aqueous solution calorimetry for examples of its use. The basic thermodynamics of the two techniques are the same.

There is one principal requirement for solution calorimetry. Samples must dissolve completely and rapidly in the solvent and must form reproducibly solvated species. It is convenient for oxide-melt solution calorimetry if solutions are dilute enough to be in the Henry's law regime, so that the enthalpy of solution depends neither on the amount of solute added nor on the presence of comparable amounts of other solutes. In aqueous acid solution calorimetry, this is not possible because of the presence of the acid, care must therefore be taken that the final concentration of dissolved species in the reference experiment is equivalent to the final concentration dissolved species from the unknown sample. This is because in aqueous solution calorimetry the measured enthalpy is concentration dependent.

There are several techniques for sample introduction into the solvent. Table 11.1 lists some sample introduction techniques and a brief description of each. In most cases, a blank or control experiment is necessary to correct for heat effects caused by sample introduction. For example, the heat effect of ampoule breakage or dissolution must be compensated for if an ampoule is used to introduce the sample.

The typical instrument used for oxide-melt solution calorimetry is a twin cell calorimeter described in detail by Navrotsky [18,19] and designed to operate isothermally at a given temperature, T_2 in the example below, for an extended period of time, and with

Table 11.1 Sample introduction techniques for solution calorimetry.

Sample introduction technique	Description
Inert sealed ampoule: aqueous experiments	Sealed: a small ampoule, usually glass, is broken and its contents mixed into the solvent allowing dissolution of the sample
Inert capsule: oxide-melt experiments	Capsule: an uncovered and inert, usually Pt pan or capsule is dropped into the solvent where the contents are dissolved
Soluble ampoule: oxide-melt experiments	A small ampoule, usually made of hardened solvent material, is dropped into the solvent where it, along with the sample, dissolves
Inert platform: both aqueous and oxide-melt experiments	A platform on the end of a manipulation rod is equilibrated above the solvent and then lowered into the solvent and then agitated to allow for sample dissolution. Correction for mechanical stirring
Pellet: oxide-melt experiments	A pressed pellet of the sample material is dropped into the solvent where it dissolves. No correction is required

Table 11.2 Examples of materials studied using high-temperature oxide-melt solution calorimetry.

Material studied/reference	Points of interest in study	Solvent and temperature used
$CaZrTi_2O_7$ [21], $CaHfTi_2O_7$ [22]	Nuclear waste materials and highly refractory oxides	$2PbO–B_2O_3$ 973, 1043, and 1073 K
$Ca_3Al_2[(OH)_4]_3$ [23]	Hydrous phases	$2PbO–B_2O_3$, 969 K
$MgAl_2O_4$ [24]	Nanophase materials	$2PbO–B_2O_3$, 975 K
Li_3BN_2, Li_3AlN_2, $Ca_3B_2N_4$ [25] α-Si_3N_4, β-Si_3N_4 [26]	Nitrides	$3Na_2O–4MoO_3$, 979 K 52 wt% $LiBO_2$–48 wt% $NaBO_2$ $K_2O–3V_2O_5$
SiO_2, Al_2O_3 [27]	Element partitioning in silicate melts	$K_2O–SiO_2$, 1760 K $K_2O–3SiO_2$
Zeolites [28]	Zeolites, meso-, and microporous materials	$2PbO–B_2O_3$, 977 K
$YBa_2Cu_4O_8$, Y_2BaCuO_5, $Y_2Cu_2O_5$, and $BaCuO_{2.01}$ [29]	Superconductor materials and mixed valencies	$2PbO–B_2O_3$, 977 K

a number of different solvents. Table 11.2 lists examples of ceramic materials that have been examined recently and the calorimeter temperatures and solvents used for calorimeters of this design [18,19].

The dissolution of a sample in a solution calorimeter results in a reaction of the form

$$ABO_x\,(\text{cr}, T_1) = AO_y\,(\text{sol}, T_2) + BO_{x-y}\,(\text{sol}, T_2) \quad \Delta_r H^0_m(ABO_x, \text{cr}, T_1), \qquad (11.11)$$

where T_1 is the sample temperature before introduction and T_2 is the calorimeter and solvent temperature. T_1 and T_2 are not necessarily the same temperature and $\Delta_r H^0_m(ABO_x, \text{cr}, T_1)$ is the measured heat effect of the reaction. In fact, in most cases of high-temperature solution calorimetry, T_1 and T_2 are of necessity different to accommodate a molten oxide-melt as the solvent. One exception occurs in the experiments where an inert platform (Table 11.1), is used for sample introduction. We use the notation AO_{x-y} (sol, T_2) to indicate that little is known or needs to be known about the actual speciation of the solute to derive an enthalpy of formation. We need only to know that the material dissolves in the solvent.

An enthalpy of formation for ABO_x (cr) at $T = T_1$ can then be obtained using Equation (11.12) if the values of $\Delta_r H^0_m$ for AO_y (cr, T_1) and BO_{x-y} (cr, T_1) are known or have been similarly measured. Equivalent equations or thermodynamic cycles can be written for non-oxide materials. Typically, experiments are designed to have $T_1 = 298.15$ K, yielding $\Delta_f H^0_m$ (298.15 K) directly.

$$\Delta_f H^0_m\,(ABO_x, \text{cr}, T_1) = \Delta_r H^0_m(AO_y, \text{cr}, T_1) + \Delta_r H^0_m(BO_{x-y}, \text{cr}, T_1) - \Delta_r H^0_m\,(ABO_x, \text{cr}, T_1). \qquad (11.12)$$

11.2 Techniques Yielding Heat Capacities and Entropies

In addition to the enthalpy of formation, as shown by Equation (11.3), the entropy is needed to calculate the Gibbs energy of formation for a ceramic material. Several techniques are used in determining $C_p = f(T)$ for the determination of $S^0(T)$ [Equation (11.2)].

Adiabatic calorimetry yields most of the low temperature ($T < 100$ K), a good portion of the intermediate temperature ($100 < T < 500$ K), and even some of the high temperature ($500 < T/\mathrm{K} < 1500$) C_p data with accuracies near 0.1 per cent. Differential scanning calorimetry (DSC) is used primarily for obtaining high temperature ($T > 500$ K) data, but also has been used for some low-temperature work ($T > 100$ K). It is limited in its accuracy to about (3–5) per cent, under normal conditions, and with extreme care, can be improved to roughly (1–2) per cent. A third technique, drop calorimetry, is limited only to the high-temperature region, although in theory it could be applied at low temperature given a specialized calorimeter. The accuracy of drop calorimetry is comparable with DSC derived data. We start our discussion of entropy measurements by examining each of these techniques for obtaining C_p. Calorimeters capable of drop calorimetry and the DSC instruments are available commercially, while adiabatic calorimeters are custom-built instruments and their use is limited to a few specialized laboratories [30–35].

11.2.1 Drop Calorimetry

A common technique for obtaining high-temperature C_p on ceramic materials is drop calorimetry. Two forms of drop calorimetry are used. Transposed temperature, namely cold to hot, drop calorimetry (TTDC) is similar to the high-temperature oxide-melt solution calorimetry described above, but does not use a solvent. A sample, at some temperature T_1, is dropped into a calorimeter maintained at some higher temperature T_2. The calorimetric effect, $\Delta_{T1}^{T2}H$, is the enthalpy increment of the sample from T_1 to T_2 and is related to C_p by

$$C_p^* = \frac{(\Delta_{T1}^{T2}H)}{\Delta T}, \tag{11.13}$$

where C_p^* is defined as the average heat capacity from T_1 to T_2 and is normally attributed to the mid-point temperature, T^*, between T_1 and T_2. Regular drop (hot to cold) calorimetry (DC) maintains the sample in a temperature controlled and heated dropping mechanism at T_2 and the sample is dropped from the higher temperature (T_2) into a calorimeter maintained at a lower temperature (T_1). The heat effect measured is still $\Delta_{T1}^{T2}H$ and Equation (11.13) is still applied. The accuracy of C_p determinations using drop calorimetry is limited only by the sensitivity of the calorimeter to the measurement of $\Delta_{T1}^{T2}H$ and to the magnitude and accuracy of ΔT. Successive measurements of $\Delta_{T1}^{T2}H$ while varying the value of T_2 can allow for the determination of $C_p = f(T)$ needed for Equation (11.2) as shown by the following example:

Example. $\Delta_{T1}^{T2}H$ is measured n times for ABO_3 with T_2 being increased from 600 K to T_n in 25 K increments. Measured are: $\Delta H_1 = \Delta_{T1}^{600\,K}H$, $\Delta H_2 = \Delta_{T1}^{625\,K}H$, $\Delta H_n = \Delta_{T1}^{Tn}H$. The heat capacity $C_p = f(T)$ is obtained by fitting the curve determined by the $n - 1$ points defined by

$$_{i=1\text{to }n}(C_p^*(i),\, T^*(i)) = \left(\left\{\frac{\Delta H_{i+1} - \Delta H_i}{25}\right\},\, \{612.5 + 25(i-1)\}\right).$$

With care, determinations of $C_p = f(T)$ including phase transitions [36] can be obtained to within a few per cent. However, this method is usually reserved for situations where the accuracy of a more difficult technique, adiabatic calorimetry, is not required. It is also used for obtaining C_p at temperatures significantly above room temperature.

11.2.2 Differential Thermal Methods

DSC can be used in two ways to obtain heat capacities. These are the scanning method and the enthalpic method. We will briefly describe each method here and refer the reader to Boerio-Goates and Callanan [37] and their accompanying references for greater detail.

The scanning method for obtaining heat capacities from DSC requires that scans of an empty pan, a reference material, and the unknown sample be taken over a large range in temperature, usually at least 150 K. The heat capacity of the sample is derived by difference using the DSC traces of the reference material and the unknown material after the contribution of the empty sample pan has been subtracted from each. Errors associated with instrumental drift with time and resulting from the need for three different DSC runs, one each for the sample, the reference, and the empty pan, per experiment contribute to the accuracy of determining C_p by this technique. Some of this error can be compensated by means of bracketing the sample run by run using the reference material, which necessitates a fourth DSC run. In this way, some of the errors associated with instrumental drift can be compensated for by assuming that any difference in the two reference runs is a result of instrumental drift.

In the enthalpic (step scan) method, a series of short heat pulses are introduced into the sample. Each pulse is followed by a short equilibration time. The DSC signal, which resembles a series of high peaks caused by the heat pulses, followed by valleys of a low, nearly linear, signal during the thermal equilibration periods, can then be used to determine C_p. The heat capacity is calculated using Equation (11.13) where the area under an individual peak is related to $\Delta_{T1}^{T2}H$, and T^* is the mid-point temperature between T_1 and T_2. Calibration of $\Delta_{T1}^{T2}H$ requires that control experiments be run on an empty pan and a reference sample. Because of the use of small heat pulses and the need for short equilibration times of a few minutes, this technique is less sensitive to instrumental drift; however, errors are associated with the multiple DSC runs per experiment.

It is possible to modify these DSC techniques to allow both the sample and the reference material to be run simultaneously reducing the number of DSC runs per experiment [37]. In this case, a compensated measurement, yielding ΔC_p between the sample and the reference material is obtained. Using ΔC_p and C_p of the reference material, the heat capacity of the sample may be derived.

11.2.3 Adiabatic Calorimetry

Adiabatic calorimetery is a more accurate technique than either DSC or drop calorimetry. Accuracies to within 0.1 per cent at $T = 298.15$ K are typically attained. The range in temperature over which C_p measurements can be made begins near $T = 0$ K and extends

as high as $T = 1500$ K. This temperature region is not accessible by a single calorimeter due to the complex and exacting design requirements [38] for adiabatic calorimeters that require significant modifications for operations at temperatures above 350 K. Typically, cryogenic calorimeters are used for work from near $T = 0$ to about 400 K [30–35]. High-temperature designs are used for work from room temperature to near $T = 1500$ K [32,34].

The principle behind the use of an adiabatic calorimeter is the stepwise addition of heat into a known sample mass followed by a measurement, after thermal equilibration has been attained, of the change in temperature caused by that addition of heat. Throughout the experiment, heat exchange between the sample and the surroundings must be eliminated to attain true adiabatic conditions. Through the use of resistive heating over a given amount of time, a known energy input, ΔE, causes a change in temperature, ΔT, from T_1 to T_2 and allows the calculation of C_p using a modification of Equation (11.13):

$$C_p^* = \frac{\Delta E}{\Delta T}. \tag{11.14}$$

As in drop calorimetry, the temperature, T^*, at which this heat capacity point is determined is the mid-point of T_1 and T_2. Through careful control of the magnitude of ΔT in an adiabatic sample environment, $C_p = f(T)$ is obtained through a series of equivalent experiments over a range of temperatures.

Ideally, adiabatic conditions for the sample would mean that no heat is exchanged with the surroundings through radiation, conduction, or convection. True adiabaticity is not attainable however, and therefore minimization of heat exchange is sought. The necessary shielding and control electronics that minimize these heat exchanges lead to the complexity of adiabatic calorimeters [33–35,38].

Many materials have been studied with a combination of solution calorimetry and high-temperature heat capacity data to yield thermodynamic quantities from $T = 0$ to 1500 K. Examples of such studies are given in references [21,22,30,34].

11.3 Techniques Yielding Partial Molar Quantities

We now turn to techniques for obtaining partial molar quantities in ceramics such as thermodynamic activities. The most common techniques are gas equilibration, Knudsen cell vapour pressure techniques, and emf techniques.

11.3.1 Gas Equilibration Techniques

One of the oldest and most useful techniques for determining partial molar quantities is gas equilibration. Consider the equilibration of metal carbide, MC, with a CH_4/H_2 mixture

$$CH_4\,(g) = C\,(\text{in MC}) + H_2\,(g), \quad K = \frac{a(\text{C in MC})\,P(H_2)}{P(CH_4)}. \tag{11.15}$$

Here K is the known equilibrium constant for the above reaction, a(C in MC) is the activity of carbon in the metal carbide, $P(H_2)$ is the partial pressure of hydrogen, and $P(CH_4)$ is the partial pressure of methane. Thus, measurements of the partial pressures of hydrogen and methane are used to calculate a carbon activity in the metal carbide. An independent chemical analysis of the carbon content of the carbide is done after the experiment. Table 11.3 [39], lists some commonly used gas mixtures [40–45]. Gases are allowed to flow continuously or re-circulated over the sample. The mixtures are analysed with a variety of techniques including gas chromatography, mass spectrometry, and various spectroscopic techniques.

There are a number of critical issues in these experiments. The gases must be at the same temperature as the sample, the gases analysed must be of the same composition as those that equilibrate with the sample, and thermal diffusion effects must be minimized. The latter leads to migration of lighter gases to the hot furnace regions and heavier gases to the cold furnace regions. Thermal diffusion is minimized by pre-heating the inlet gases, using a gas mixture containing an inert gas and by increasing flow rates [41]. In general, experiments should be done at several flow rates.

The CH_4/H_2 mixture is particularly susceptible to moisture effects and gases must be thoroughly dried. To avoid any errors due to moisture, Wada *et al.* [42] have used solid iron along with their unknowns. Since the activity of carbon in iron as a function of composition is well known, this gives the activity for a given methane to hydrogen ratio, eliminating any errors from the gas analysis. Another factor with the hydrogen containing gas mixtures is reactions with silica-containing refractories to form SiO (g), which may lead to silicide formation in the samples. Therefore it is best to use highly pure alumina or zirconia refractories in the hot zone. The use of ammonia to set a nitrogen potential is useful only to about 600°C, since ammonia decomposes above this temperature [43]. Thus at higher temperatures, nitrogen gas is used directly to set nitrogen activities.

Table 11.3 also lists a metal/metal oxide mixture to set an oxygen potential [44] or metal/metal sulphide mixture to set a sulphur potential [45] over another condensed phase material. This is referred to as a 'Rhines Pack' and is generally done in a sealed ampoule with the metal/metal oxide mixture on one end and the metal to be treated on the other. Again care must be taken to avoid SiO (g), which forms if low oxygen potentials are present in a silica ampoule. In addition, the effects of a static gas in the ampoule as opposed to a flowing gas in the gas mixtures must be considered. However, deleterious effects of secondary gas mixture components are avoided [45].

Table 11.3 Gas mixtures for setting chemical potentials.

Reactant mixture/reference	Potential set
$CO–CO_2$ [40]	O_2, C
$H_2–H_2O$ [41]	O_2
$CH_4–H_2$ [42]	C
$NH_3–H_2$ [43]	N_2
MO, M [44]	O_2
MS, M [45]	S_2

11.3.2 Knudsen Cell Methods

Knudsen cell-based methods have been extensively reviewed by a number of authors [46–49] and are summarized here as they apply to ceramic materials. The Knudsen cell technique enables direct measurement of the component thermodynamic activities in a solid from the component vapour pressures over that solid, which will be the focus of this section. First, general considerations in the Knudsen cell technique are discussed and then specific methods of vapour analysis are discussed.

A Knudsen cell is a small enclosure typically ~1 cm in diameter and ~1 cm high, which allows a condensed phase to equilibrate with its vapour. A small orifice of well-defined dimensions allows the vapour to be sampled. Dimensions of the orifice are such that molecule/wall collisions dominate over molecule/molecule collisions. A good deal of information is available on the proper geometrical design of a Knudsen cell [46–49 and associated references].

The cell material must be inert to both the condensed phase and the vapour above it. Table 11.4 lists some selected studies on ceramics and the choice of cell material. In general, refractory metals (Pt, Ir, Re, Mo, W, Ta) [48] are the most inert with ceramic materials. Caution must be taken however, if tantalum is to be used, due to its high affinity for oxygen. With Mo and W cells, the volatile metal oxide equilibria can be used to determine a partial pressure of oxygen in the cell [48]. Consider the MoO_2 (g) and MoO_3 (g) equilibria:

$$MoO_2(g) + \tfrac{1}{2}O_2(g) = MoO_3(g), \quad K = \frac{P(MoO_3)}{P(MoO_2)[P(O_2)]^{1/2}}. \tag{11.16}$$

Since the partial pressures of MoO_2 and MoO_3 can be measured and the equilibrium constant is well known, a value for the partial pressure of oxygen can be calculated. This is clearly an important parameter in a thermodynamic study of oxides. Rhenium is an inert container for many oxide materials, but expensive and difficult to machine. The silicon

Table 11.4 Representative Knudsen cell studies of ceramics and choice of cell materials.

Ceramic/reference	Knudsen cell material
SiC [50,51]	Graphite
Si_3N_4 [52,53]	Si_3N_4
Al_2O_3 [54]	Mo, W
ZrO_2–Y_2O_3 [55]	W
SiO_2 [56]	Ta with ZrO_2 liners
Y_2O_3 [57]	W
Y_2O_3 [58]	Ir, thoria
U–UO_2 [59]	Urania
TiC, ZrC, HfC, ThC [60]	W, Ta with graphite liners
AlN [61]	Graphite

component in SiC and Si_3N_4 is very reactive and there is no material that is completely inert to silicon [50–53].

The Knudsen cell may be heated by resistance heating, electron bombardment, or by induction heating. Precise temperature measurement is done by means of a thermocouple attached to the cell or through the use of optical pyrometry.

Ceramic materials often exhibit kinetic barriers to vaporization and the measured vapour pressure from a Knudsen cell may be different from the equilibrium value. The Whitman–Motzfeld [62–64] equation has been used to correct for some of this effect:

$$P_m = P_{eq} - \left(\frac{1}{\alpha} + \frac{1}{W_A} - 2\right)\frac{P_m W_B B}{A}. \tag{11.17}$$

Here P_m is the measured vapour pressure, P_{eq} the equilibrium vapour pressure, W_A the Clausing factor of the cell, W_B the Clausing factor of the orifice, A the cross-sectional area of the cell, B the cross-sectional area of the orifice, and α the vaporization coefficient. The Clausing factor is simply the fraction of molecules that escape under molecular flow conditions [46]. Measurements are taken with several orifice sizes and a plot of P_m against $\left(\frac{P_m W_B B}{A}\right)$ yields P_{eq} as the intercept and $\left(\frac{1}{\alpha} + \frac{1}{W_A} - 2\right)$ as the slope. Thus, the vaporization coefficient may be extracted from the slope. The vaporization coefficient may be defined as the ratio of the number of molecules that should leave the surface to generate an equilibrium vapour pressure to the number of molecules that actually do leave the surface. There are numerous discussions of the vaporization coefficient [65] and modifications of Equation (11.17) [48]. However, the important point is that vaporization coefficients for ceramic materials are often less than unity and this type of extrapolation is necessary to obtain equilibrium vapour pressures.

The vapour effusing from the cell may be analysed via a variety of methods. These include: weight loss, torsion effusion, target collection, and mass spectrometry. Weight loss or thermo-gravimetric methods are extremely useful. Weight changes may be measured *in situ* with an automatic recording balance or by weighing the sample before and after heating. The weight loss per unit time area of the orifice is a flux, which can be related to vapour pressure according to the Hertz–Knudsen–Langmuir equation:

$$J = P\sqrt{\frac{M}{2\pi RT}}. \tag{11.18}$$

Here P is the pressure (in units of force per unit area), M the molar mass of the vapour species, R the gas constant, and T the absolute temperature. Note that the molar mass of the effusing species must be known.

As pointed out by Cater [46], effusate collection and weighing has advantages over weight change measurements of the cell. Any weight changes incurred by the cell itself are now not considered. However, the vapour must be readily condensable and a very accurate weighing or assay is necessary. Tuenge *et al.* [66] have used an electron microprobe. For a radioactive element, accurate assaying is possible.

Vapour pressure can be directly measured via a torsion effusion apparatus [67]. In this case, two Knudsen cells are mounted in a small rectangular box that is suspended from a wire in the centre. The cell orifices are located equidistant from the centre and facing

opposite directions. Thus the vapour effusing from the cells creates a torque on the wire. The total vapour pressure is given by

$$P_T = \frac{2\tau\theta}{A_1 d_1 f_1 + A_2 d_2 f_2} \approx \frac{\tau\theta}{Ad}. \tag{11.19}$$

Here P_T is the total vapour pressure, τ the torsion constant of the wire, A_1 and A_2 are the areas of the two torsion orifices, d_1 and d_2 the distances between the suspension axis and the two effusion orifices, and f_1 and f_2 the Searcy–Freeman correction factors [68]. This elegant technique is a direct measurement of vapour pressure and has been used to study a variety of ceramic systems. Kulkarni and Worrell [69] have examined chromium carbides by measuring CO (g) vapour pressures. In theory, torsion effusion can be applied to all ceramic systems. The variation of the torsion constant of a wire suspended from a cold zone to a hot zone may limit the technique to lower temperature systems. Selenides [70], sulphides [71], and sulphates [72] have been successfully studied with torsion effusion techniques.

The torsion effusion and weight loss techniques have been combined into one apparatus. Edwards [73] has developed such a system with fully automated data collection. Simultaneous measurement of flux and pressure leads to an average vapour molar mass, by substitution of Equation (11.19) into Equation (11.18). This technique has been used very successfully to describe the complex decomposition behaviour of sulphates [72] and chromates [74].

A versatile method of vapour analysis is mass spectrometry. Magnetic sector, quadrupole, and time-of-flight instruments have been used to analyse the molecular beam emerging from the Knudsen cell. Magnetic sector instruments are generally preferred due to the lack of mass discrimination and high sensitivity. The instruments are differentially pumped, with high-speed pumps on the Knudsen cell chamber and clean, oil-free pumps on the ionization and detection chambers. There are numerous excellent reviews on the technique [47–49,75].

Knudsen cell mass spectrometric studies of ceramic materials involve the same consideration discussed previously, namely the selection of an inert cell material, the fact that vaporization coefficients are often much less than one, and the need for high temperatures. A fourth consideration is that ceramic materials vaporize to complex species. For example, SiC vaporizes to Si_n (g) (n = 1–7), SiC_2 (g), Si_2C (g), SiC (g), Si_2C_2 (g), Si_3C (g), Si_4C (g), Si_3C_2 (g) and determination of the thermodynamic activity of silicon in SiC requires selection of the appropriate solid/vapour species equilibria [50,51].

The ultimate issue in mass spectrometry is to relate precisely measured ion intensity to a vapour pressure of a parent molecule. The assignment of observed ions to neutral parents has been discussed extensively [75]. Once the parent molecule has been unambiguously identified, the measured current of that particular ion must be converted to the vapour pressure of the parent molecule. In mass spectrometry, the ion current I is related to vapour pressure P by the following expression:

$$P = \frac{kIT}{\sigma}. \tag{11.20}$$

Here k is the machine constant and σ the ionization cross section.

First consider the machine constant. This is determined by means of a calibration material of known vapour pressure, such as gold and silver, although CsCl, ThO_2, and La_2O_3 have also been used [48]. A problem with this calibration technique is the variation of k from run to run. Near perfect alignment of the cell and ion source and constancy of the ionization process are required to achieve a constant k. Some mass spectrometers have been designed for this, while most have not.

In order to circumvent the problem of a varying calibration constant, there are two major approaches. One involves the use of ion–current ratios and Gibbs–Duhem integration [76]. This approach has been applied to numerous metallic alloy systems and some ceramic systems as well [48]. Consider a compound AB. The ion–current ratios $I(B^+)/I(A^+)$ are measured across the composition range and the activity of A, a_A, is given by a graphical integration.

$$\ln a_A = -\int_{x_B=0}^{x_B=x_B} x_B \, d \ln \frac{I(B^+)}{I(A^+)}. \tag{11.21}$$

Here x_B is the mole fraction of B. This technique has been extensively used and is discussed in more detail for ceramics in reference [48].

The second approach involves the use of multiple cells [77]. Assume a solution AB in one cell and a standard A in an adjacent cell at the same temperature. The cells are translated in and out of the sampling region in the mass spectrometer. Thus the activity of component A is simply:

$$a_A = \frac{P_A(\text{in AB})}{P_A^0(\text{in pure A})}. \tag{11.22}$$

The complication with this technique is mixing between the effusing vapour of A from the solution and the standard. To avoid this, Chatillon used an ionization chamber entrance aperture smaller than the Knudsen cell orifice so that the ionizer effectively 'sees' only inside the cell [77]. Alternatively another standard may be used, with appropriate corrections for difference in vapour pressures and ionization cross sections [78].

Precise determination of ionization cross sections, σ, remains a major issue in mass spectrometry. For atoms, several recent measurements [79] and compilations present reliable data [80]. However, for molecules such as those often encountered in vaporization of ceramics, this remains a problem. Generally, the additivity rule is used [81], but this gives an estimate that is too large. Experimental studies with dimers suggest a factor of 0.75 should be applied to the sum of the ionization cross sections [48]. This has been extended to larger molecules, but it is only an approximation.

11.3.3 Electrochemical Techniques

Solid-state electrochemical measurements to determine Gibbs energies were first demonstrated by Kiukkola and Wagner [82]. Since then, the technique has evolved into one of the most versatile and widely used methods in recent years. This has been possible due to the development of solid electrolytes with nearly total ionic conductivity. Several excellent reviews are available on this technique [2,83,84].

Consider a general cell for determining the Gibbs energy of formation of the oxide MO:

$$\text{Pt} \mid \text{M}', \text{M}'\text{O} \mid \text{ZrO}_2\,(+\text{Y}_2\text{O}_3) \mid \text{M}, \text{MO} \mid \text{Pt}. \tag{11.23}$$

According to standard notation, the vertical lines represent phase boundaries. The reference is the oxygen potential set by a known mixture, designated as M′, M′O. The electrolyte is ZrO_2 doped with Y_2O_3, which is an oxygen anion conductor. The two half reactions, which occur at the right- and left-hand side of the electrolyte are

$$2e^- + AO = A + O^{2-} \tag{11.24a}$$

$$B + O^{2-} = BO + 2e^- \tag{11.24b}$$

$$B + AO = BO + A. \tag{11.24c}$$

The net reaction (11.24c) is known as a 'virtual reaction' since such a cell is designed for 'open circuit' operation with no net flow of current. The measured emf, E, from the above cell is related to the activity gradient through the electrolyte as

$$E = \frac{RT}{zF}\int_{a'_{O_2}}^{a''_{O_2}} t_{O_2}\, \mathrm{d}\ln a_{O_2}. \tag{11.25}$$

Here R is the gas constant, T the temperature, z the number of electrons transferred, F the Faraday constant, t_{O_2} the transference number, and a_{O_2} the activity of oxygen with the prime and double prime indicating each electrode. In the case of the above displacement reaction (11.24c) and a pure ionic conductor, Equation (11.25) reduces to

$$\Delta G^0 = -2FE. \tag{11.26}$$

Here ΔG^0 is the Gibbs energy change associated with reaction (11.24c). The entropy and enthalpy of the above reaction can be determined from the temperature dependence of the measured emf in Equations (11.5) and (11.6). There are numerous experimental considerations in developing such a cell. Foremost, is the electrolyte selection. It must be a purely ionic conductor and impervious to gas. Dense pellets of the electrode and electrolyte are made and put into a furnace with high-purity argon. In instances where the electrodes have high vapour pressure, it may be necessary to isolate the atmosphere of each electrode. Table 11.5 lists the three most common electrolytes and some illustrative applications [82,85–88].

Table 11.5 Sample solid electrolyte studies.

Solid electrolyte	Example of study/reference
Stabilized ZrO_2	$\Delta_f G$ for FeO [82] a(NiO) in NiO-MgO [85]
ThO_2	$\Delta_f G$ TiO [86] $\Delta_f G$ for α-SiC, β-SiC [87]
CaF_2	$\Delta_f G$ for Mn Carbides [88]

The necessary stabilizing compounds for ZrO_2, typically (10–15) mole% CaO, MgO, or Y_2O_3, introduce oxygen anion lattice vacancies and lead to ionic conduction. Additions are also made to ThO_2 to increase ionic conductivity. The use of ThO_2 extends the lower oxygen potential limit. The CaF_2 exhibits ionic conductivity over the widest range of temperatures and activities. However, particular care must be taken in the handling of CaF_2 to avoid oxidation and hydration.

There are numerous variations on the basic cell described above. Although the cell above is measuring the Gibbs energy change in a simple displacement reaction, it can also be regarded as a concentration cell. Consider the following cell:

$$\text{Pt, } O_2 \mid ZrO_2\ (+Y_2O_3) \mid \text{M, O dissolved.} \tag{11.27}$$

So the virtual reaction is

$$\text{O (M)} = \tfrac{1}{2}O_2\ (g),\ \Delta G^0 = RT \ln P_{O_2}. \tag{11.28}$$

Note that the reference in this cell is air or oxygen. As Pratt [84] points out, this has the advantage of maintaining ionic conductivity in the reference side of the cell and thus allowing measurements to lower oxygen potentials. However, particular care must be taken to avoid permeation of the electrolyte by oxygen gas.

Rickert [84] describes two types of cells. For cells of the first type, the activity of a species that is the same as the mobile species in the electrolyte is measured. Examples of these are the oxygen activity cells that have been discussed. For cells of the second type, the activity of a species that is different from the mobile species in the electrolyte is measured. This second type of cell allows application of this technique to a wide range of ceramic materials. Under the second type of cells, there are two sub-categories.

In the first sub-category are cells where oxygen potential with an oxide anion conductor is measured and related to another species chemical potential. This is illustrated by a recent elegant study of α-SiC and β-SiC by Klekamp [87]. He uses the cell

$$\text{Pt} \mid \text{Re} \mid \beta\text{-SiC, C, } SiO_2 \mid Th(Y)O_2 \mid SiO_2\text{, C, } \alpha\text{-SiC} \mid \text{Re} \mid \text{Pt}. \tag{11.29}$$

The Re phases are barriers to prevent reactions between the Pt and Si. The two half reactions are

$$\beta\text{-SiC} + 2O^{2-} = SiO_2 + C + 4e^-, \tag{11.30a}$$

$$SiO_2 + C + 4e^- = \alpha\text{-SiC} + 2O^{2-}. \tag{11.30b}$$

Thus the oxygen activity measured is due to the small difference between β-SiC/SiO_2 and α-SiC/SiO_2. The measured emf indicates the small Gibbs energy difference between the two phases of SiC. Prior to this study, this quantity had not been measured.

The second sub-category involves primarily the CaF_2 electrolyte. Although the mobile ion in CaF_2 is F^-, it can be applied to measure oxygen activities as well [89,90]. Ramanarayanan *et al.* [89] have shown that conduction is due to the fluorine ion. The oxygen

at the surface of the CaF_2 electrolyte reacts to generate this mobile F^- species. The wide range of ionic conductivity of CaF_2 makes it a particularly attractive electrolyte.

11.4 Conclusions

The major techniques for thermodynamic studies of ceramic materials have been discussed. Total molar quantities are determined from calorimetry and are the heats of reaction, heat capacities, and heats of transformation. Partial molar quantities are determined from gas equilibration techniques, Knudsen cell-based vapour pressure measurements, and emf techniques. In each case, the problems unique to ceramics have been emphasized.

References

1. Searcy, A.W., in *Chemical and Mechanical Behavior of Inorganic Materials*, A.W. Searcy, D.V. Ragone and U. Colombo, eds., Wiley-Interscience, New York, pp. 33–56, 1970.
2. Kubachewski, O., Alcock, C.B. and Spencer, P.J., eds., *Materials Thermochemistry*, 6th ed., Pergamon Press, New York, 1993.
3. Stevens, R., Hom, B.K., Boerio-Goates, J., Woodfield, B.F., Putnam, R.L., Gutierriez, J. and Navrotsky, A., *J. Chem. Thermodyn.* **33**, 1441, 2001.
4. Gokcen, N.A. and Reddy, R.G., eds., *Thermodynamics*, 2nd ed., Plenum Press, New York, 1996.
5. O'Hare, P.A.G., Tomaszkiewicz, I., Beck, C.M. II and Seifert, J., *J. Chem. Thermodyn.* **31**, 303, 1999.
6. O'Hare, P.A.G., *J. Chem. Thermodyn.* **24**, 1323, 1992.
7. O'Hare, P.A.G., *J. Chem. Thermodyn.* **25**, 1333, 1993.
8. Tomaszkiewicz, I., Hope, G.A., Beck, C.M. II and O'Hare, P.A.G., *J. Chem. Thermodyn.* **27**, 585, 1995.
9. Tomaszkiewicz, I., Hope, G.A., Beck, C.M. II and O'Hare, P.A.G., *J. Chem. Thermodyn.* **28**, 29, 1996.
10. O'Hare, P.A.G. and Hubbard, W.N., *J. Phys. Chem.* **70**, 3353, 1966.
11. Johnson, G.K., *J. Chem. Thermodyn.* **18**, 801, 1986.
12. Leonidov, V.Y. and O'Hare, P.A.G., *Fluorine Calorimetry: History, Applications, Results*, Begell House, New York, NY, 2000.
13. Hemingway, B.S. and Robie, R.A., *J. Res. U.S. Geol. Survey* **5/4**, 413, 1977.
14. Morss, L.R., Williams, C.W., Choi, I-K. and Fuger, J., *J. Chem. Thermodyn.* **15**, 1093, 1983.
15. Fuger, J., Morss, L.R. and Williams, C.W., *J. Chem. Thermodyn.* **17**, 561, 1985.
16. Patarin, J., Kessler, H., Soulard, M. and Guth, J.L., in *Zeolite Synthesis; ACS Symposium Series 298*, M.L. Occelli and H.E. Robson, eds., American Chemical Society, Washington, DC, pp. 221–232, 1989.
17. Hovis, G., *Am. Mineral.*, **82**, 149, 1997.
18. Navrotsky, A., *Phys. Chem. Miner.* **89**, 2, 1977.
19. Navrotsky, A., *Phys. Chem. Miner.* **24**, 222, 1997.
20. Topor, L. and Kleppa, O.J., *J. Chem. Thermodyn.* **16**, 993, 1984.
21. Putnam, R.L., Navrotsky, A., Woodfield, B.F., Boerio-Goates, J. and Shapiro, J.L., *J. Chem. Thermodyn.* **31**, 229, 1999.
22. Putnam, R.L., Navrotsky, A., Woodfield, B.F., Shapiro, J.L., Stevens, R. and Boerio-Goates, J., *Scientific Basis for Nuclear Waste Management*, Materials Research Society, 1998.

23. Schoenitz, M. and Navrotsky, A., *Am. Mineral.* **84**, 389, 1999.
24. McHale, J.M., Navrotsky, A. and Kirkpatrick, R.J., *Chem. Mater.* **10**, 1083, 1998.
25. McHale, J.M., Navrotsky, A. and DiSalvo, F.J., *Chem. Mater.* **11**, 1148, 1999.
26. Liang, J.J., Topor, L., Navrtosky, A. and Mitomo, M., *J. Mater. Res.* **14**, 1959, 1999.
27. Wilding, C.M. and Navrotsky, A., *N. Jb. Miner. Abh.* **172**, 177, 1998.
28. Navrotsky, A., Petrovic, I., Hu, Y., Chen, C. and Davis, M.E., *Microporous Mater.* **4**, 95, 1995.
29. Zhou, Z. and Navrotsky, A., *J. Mater. Res.* **7**, 2920, 1992.
30. Woodfield, B.F., Boerio-Goates, J., Shapiro, J.L., Putnam, R.L. and Navrotsky, A., *J. Chem. Thermodyn.* **31**, 245, 1999.
31. Callanan, J.E., Weir, R.D. and Westrum, E.F., *J. Chem. Thermodyn.* **30**, 1483, 1998.
32. Stolen, S., Johnson, H.B., Abe, R., Atake, T. and Grande, T., *J. Chem. Thermodyn.* **31**, 465, 1999.
33. Ogata, Y., Kobayashi, K., Matsuo, T. and Suga, H., *J. Phys. E: Sci. Instrum.* **17**, 1054, 1984.
34. Huntelaar, M.E., Booij, A.S., Cordfunke, E.H.P., van der Laan, R.R., van Genderen, A.C.G. and van Miltenburg, J.C., *J. Chem. Thermodyn.* **32**, 465, 2000.
35. Van Oort, M.J.M. and White, M.A., *Rev. Sci. Instrum.* **58**, 1239, 1987.
36. Guyot, F., Richet, P., Courtial, P. and Gillet, P., *Phys. Chem. Miner.* **20**, 141, 1993.
37. Boerio-Goates, J. and Callanan, J.E., in *Physical Methods of Chemistry, 2nd ed., Vol 6, Determination of Thermodynamic Properties*, B.W. Rossiter and R.D. Baetzold, eds., Wiley, New York, pp. 621–717,1992.
38. Westrum, E.F. Jr., Furukawa, G.T. and McCullough, J.P., in *Experimental Thermodynamics, Vol 1*, J.P. McCullough and D.W. Scott, eds., Butterworths, London, pp. 133–214, 1968.
39. Richardson, F.D. and Alcock, C.B., in *Physicochemical Measurements at High Temperatures*, J.O'M. Bockris, J.L. White and J.D. Mackenzie eds., Butterworths, Scientific Publishers, London, 1959.
40. Smith, R.P., *JACS* **68**, 1163, 1948.
41. Dastur, M. and Chipman, J., *Trans. Am. Inst. Metall. Eng.* **185**, 441, 1949.
42. Wada, T., Wada, H., Elliot, J.F. and Chipman, J., *Metall. Trans.* **2**, 2199, 1971.
43. Corney, N.S. and Turkdogan, E.T., *J. Iron Steel Inst.* **180**, 344, 1955.
44. Rhines, F.N., *Trans. Am. Inst. Min. Metall. Eng.* **137**, 246, 1940.
45. Smith, P.J. and Smeltzer, W.W., *Oxid. Met.* **28**, 291, 1987.
46. Cater, D.E., in *Proc. 10th Mater. Res. Symp. High Temp. Vapors Gases*, J. Hastie, ed., NBS Special Publication 561/1, Washington, pp. 3–38, 1979.
47. Hilpert, K., *Rapid Commun. Mass Spec.* **5**, 175, 1991.
48. Stolyarova, V.L. and Semenov, G.A., *Mass Spectrometric Study of the Vaporization of Oxide Systems*, Wiley, Chichester, 1994.
49. Stolyarova, V.L., *Rapid Commun. Mass Spec.* **7**, 1022, 1993.
50. Rocabois, P., Chatillon, C. and Bernard, C., *High Temp. – High Press.* **27/28**, 3, 1995/1996.
51. Rocabois, P., Chatillon, C., Bernard, C., and Genet, F., *High Temp. – High Press.* **27/28**, 25, 1995/1996.
52. Rocabois, P., Chatillon, C. and Bernard, C., *J. Am. Ceram. Soc.* **79**, 1351, 1996.
53. Rocabois, P., Chatillon, C. and Bernard, C., *J. Am. Ceram. Soc.* **79**, 1361, 1996.
54. Drowart, J., DeMaria, G., Burns, R.P. and Inghram, M.G., *J. Chem. Phys.* **32**, 1366, 1960.
55. Belov, A.N. and Semenov, G.A., *Russ. J. Phys. Chem.* **59**, 342, 1985.
56. Zmbov, K.F., Ames, I.I. and Margrave, J.L., *High Temp. Sci.* **5**, 235, 1973.
57. Liu, M.B. and Wahlbeck, P.G., *High Temp. Sci.* **6**, 179, 1974.
58. Panish, M.B., *J. Chem. Phys.* **34**, 1079, 1961.
59. Ackermann, R.J., Rauh, E.G. and Chandrasekharaiah, M.S., *J. Phys. Chem.* **73**, 762, 1969.
60. Kohl, F.J. and Stearns, C.A., *High Temp. Sci.* **6**, 284, 1974.
61. Hildenbrand, D.L. and Hall, W.F., *J. Phys. Chem.* **67**, 888, 1963.

62. Whitman, C.I., *J. Chem. Phys.* **20**, 161, 1952.
63. Motzfeld, K., *J. Phys. Chem.* **59**, 139, 1955.
64. Jacobson, N.S., Lee, K.N. and Fox, D.S., *J. Am. Ceram. Soc.* **75**, 1603, 1992.
65. Searcy, A.W., Ragone, D.V., Colombo, U., eds., *Chemical and Mechanical Behavior of Inorganic Materials*, Wiley-Interscience, New York, pp. 109–131, 1970.
66. Tuenge, R.T., Laabs, F. and Franzen, H.F., *J. Chem. Phys.* **65**, 2400, 1976.
67. Freeman, R.D., in *The Characterization of High Temperature Vapors*, J.L. Margrave, ed., Wiley, New York, pp. 152–192, 1967.
68. Freeman, R.D. and Searcy, A.W., *J. Chem. Phys.* **22**, 762, 1954.
69. Kulkarni, A.D. and Worrell, W.L., *Metall. Trans.* **3**, 2363, 1972.
70. Brunetti, B., Guido, M. and Piacente, V., *High Temp. Mater. Sci.* **37**, 159, 1997.
71. Steinbrunner, B.S. and Edwards, J.G., *High Temp. Sci.* **32**, 167, 1991.
72. Lau, K.H., Brittian, R.D., Lamoreaux, R.H. and Hildenbrand, D.L., in *Proc. High Temp. Mater Chem-III*, Z.A. Munir and D. Cubiciotti, eds., The Electrochemical Society, Pennington, NJ, pp. 36–46, 1986.
73. Edwards, J.G., in *Proc. 10th Mater. Res. Symp. High Temp. Vapors Gases*, J.W. Hastie, ed., NBS Special Publication 561/1, Washington, DC, pp. 67–82, 1979.
74. Brittian, R.D., Lau, K.H. and Hildenbrand, D.L., *J. Electrochem. Soc.* **134**, 2900, 1987.
75. Drowart, J. and Goldfinger, P., *Angew. Chem. Intern. Ed.* **6**, 581, 1967.
76. Belton, G.R. and Fruehan, R.J., *Metall. Trans.* **244**, 781, 1970.
77. Chatillon, C., Senillou, C., Allibert, M. and Pattoret, A., *Rev. Sci. Instrum.* **47**, 334, 1976.
78. Jacobson, N.S. and Brady, M.P., in *Proc. 9th Int. Conf. High Temp. Mater. Chem.*, K. Spear, ed., The Electrochemical Society, Pennington, NJ, pp. 695–703, 1997.
79. Fruend, R.S., Wetzel, R.C., Shul, R.J and Hayes, T.R., *Phys. Rev. A* **41**, 3575, 1990.
80. Drowart, J., Chatillon, C., Hastie, J. and Bonnell, D., *Pure Appl. Chem.* **77**, 683, 2005.
81. Otvos, J.W. and Stevenson, D.P., *JACS* **78**, 546, 1956.
82. Kiukkola, K. and Wagner. C., *J. Electrochem. Soc.* **104**, 308, 1957.
83. Rickert, H., in *Treatise on Solid State Electrochemistry, Vol 4*, N.B. Hannay, ed., Plenum, New York, pp. 281–331, 1976.
84. Pratt, J.N., *Metall. Trans.* **21A**, 1223, 1990.
85. Jakobsson, A., Sichen, Du. and Seetharaman, S., *Metall. Trans.* **24B,** 1023, 1993.
86. Tetot, R., Picard, C. and Gerdanian, P., *J. Phys. Chim. Solids* **44**, 1059, 1983.
87. Kleykamp, H., *Ber. Bunsenges. Phys. Chem.* **102**, 1231, 1998.
88. Sichen, Du., Seetharaman, S. and Staffansson, L., *Metall. Trans.* **19B**, 951, 1988.
89. Ramanarayanan, T.A., Narula, M.L. and Worrell, W.L., *J. Electrochem. Soc.* **126**, 1360, 1979.
90. Chou, S.F. and Rapp, R.A., in *High Temperature Metal Halide Chemistry*, D.L. Hildenbrand and D.D. Cubicciotti, eds., The Electrochemical Society, Princeton, NJ, pp. 392–400, 1978.

12 Condensed Phases of Inorganic Materials: Molten Salts

B. DAVIS
Department of Mining Engineering
Queen's University
Kingston, Canada

Measurement of the Thermodynamic Properties of Multiple Phases
R.D. Weir and Th.W. de Loos (Editors)

12 CONDENSED PHASES OF INORGANIC MATERIALS: MOLTEN SALTS

Experimental work in molten salts has changed significantly since its high point in the 1960s and early 1970s. At that time, relatively simple systems were studied generally for one of two reasons. First, there were limited thermodynamic data available for most salt systems and many of these binary systems were being studied only for the first or second time. Much of this work was focussed on the light metals industry of aluminium (cryolite) and magnesium (molten chlorides), on carbonate-based fuel cells, and on thermal energy storage (alkali metal nitrates and sulphates). Second, since molten salts were relatively new in the field of chemistry, workers sought to understand better the ionic interactions in the melt. An improved understanding of these interactions allowed the development of models, based on the composition and temperature of the melt, to represent the thermodynamic properties of the melt. These models were relatively simple at first, but with better access to computers, more complex treatments of the salt systems were developed. The goal of this modelling work was to provide a framework to represent experimental thermodynamic data. Also, given the large number of binary systems and virtually inexhaustible number of ternary and higher order systems, general models were required to allow estimates of the properties of systems that had yet to be investigated.

Present work on the thermodynamics of molten salts is limited. Most binary systems in the more common categories, such as alkali/alkaline earth metal halides, nitrates, carbonates, etc., have been studied at least once. There are sufficient data in many cases to model multi-component systems in terms of their thermodynamic properties. Today, experimental work in molten salts is aimed at multi-component systems (3+ components) to validate models that use interpolation techniques to combine binary system data into comprehensive models. There is also some experimental work done on less common systems for specific reasons, such as rare earth chloride systems for the electrolytic production of rare earth metals.

The large amount of data available to those wishing to model salt systems is a great benefit. However, due to the variety of sources and methods used to obtain thermodynamic data on salt systems, there will often be conflicting data. For this reason, the modelling effort requires understanding of the experimental techniques used and their respective reliabilities. Then, with the modeller's judgement, weighting for each source of data can be assigned prior to finding the parameters for a given model.

12.1 Structure of Molten Salts

Molten salts can be classified based on the ionic make up of the salt system. The simplest type to consider is the case of univalent single atoms, as in the case of NaCl and KCl. Here, the cations all have the same environment, namely the common anion, and energy changes due to mixing must result from short-range interactions between different cations. Unless there is a strong interaction between cations, they will be more or less randomly distributed on

the cation sites. The complexity of the system increases with differently charged ions, as in $MgCl_2$ + NaCl. The charge of 2+ on magnesium attracts the chloride ions more tightly than does the sodium ion. The result is that complex ion formation occurs with the formation of $MgCl_4^{2-}$. The occurrence of complex ions is usually denoted by a sharp change in the enthalpy of mixing and by a large value of the excess entropy. Naturally, systems with a complex anion, such as nitrates or carbonates, will also disrupt the short-range order of the melt, requiring modifications to models used to represent the thermodynamic mixing properties. Reciprocal systems, those with two anions and two cations, such as NaI, KCl, NaCl, KI, also have special types of models that are used to fit the thermodynamic properties [1]. These models are generally composed of a modification of the ideal mixing term as explained below.

The presence of short-range order in molten salts associated with coulombic interaction among anions and cations [2] provides the basis for structural models. The concept of ideal molten salt behaviour is credited to Temkin [3]. This work is the cornerstone for most of the subsequent efforts in molten salt chemistry on mixing of cations and anions on separate interpenetrating 'sublattices'. In the ideal case, for the enthalpy of mixing of pure liquid component chlorides,

$$\Delta_{mix}H^{id} = 0. \tag{12.1}$$

For the binary system, AY–BZ, assuming that entropy is solely a function of the configuration of the ions, the ideal integral entropy of mixing is given by

$$\Delta_{mix}S^{id} = -R[(\Sigma x^+)(n_{A^+} \ln n_{A^+} + n_{B^+} \ln n_{B^+}) + (\Sigma x^-)(n_{Y^-} \ln n_{Y^-} + n_{Z^-} \ln n_{Z^-})], \tag{12.2}$$

where Σx^+ and Σx^- are the number of moles of cations and anions, respectively, in one mole of solution and n are the ionic fractions of each of the eight ionic species. Since the ideal enthalpy of mixing is zero, it follows that the ideal Gibbs energy of mixing, $\Delta_{mix}G^{id}$, is

$$\Delta_{mix}G^{id} = -T\Delta_{mix}S^{id}. \tag{12.3}$$

Binary systems that are approximately ideal (*i.e.* $CdCl_2$ + AgCl) typically have a small enthalpy of mixing associated with them. Molten salt systems with a significant enthalpy of mixing (*i.e.* $CdCl_2$ + KCl), which are often exothermic, form complex ions, such as $CdCl_3^-$ and $CdCl_6^{4-}$. These complex ions usually correspond to solid compounds that appear in the binary phase diagram. Therefore, initial estimates of the mixing behaviour of salt systems can generally be predicted based on whether the phase diagram shows any compounds. Those that do are likely to mix non-ideally and will have a large enthalpy of mixing close to the mole fraction associated with a complex [4].

12.2 Experimental Determination of Thermodynamic Properties

Techniques for measuring thermodynamic properties of solutions can be divided into two categories: those that produce measurements associated with the formation of the solution by the

mixing of components (integral property) and those that investigate the contribution that individual components make to the solution property (partial property). Frequently, the partial properties of only one component can be found in a multi-component solution; however, when the properties of only one component can be found *for all compositions*, the partial properties of the other components can be calculated from the Gibbs–Duhem equation. This differential equation interrelates the isothermal partial properties of all components in the solution.

12.2.1 Calorimetric Measurements

Calorimetric techniques provide researchers with a means of accurately determining integral enthalpies of formation, solution and reaction as well as heat capacities. In the field of chloride salts, Kleppa [5] and Orekhova [6] have produced a large body of accurate work from mixing calorimetry. The standard type of calorimeter is the isoperibol calorimeter in which the temperature of the surroundings is kept constant and the temperature of the reaction chamber is measured before, during and after the mixing process. Common to all types of calorimeters is that each has a known mass and specific heat; the increase or decrease in temperature of the instrument provides the heat of reaction or solution. Kleppa used a twin differential reaction calorimeter, one acting as a reference, with a thermopile for each calorimeter to register a thermo-electromotive force (emf) should there be a change in the temperature of the calorimeter vs. the surroundings. The two thermopiles, one for each calorimeter, are connected in series such that one thermopile opposes the other. This negates the effect of any small drift in temperature of the jacket, since it will affect both of the calorimeters, but a change in the temperature of one calorimeter due to an enthalpy of mixing will be detected. The experimental error is said to be as low as 0.5 per cent. A detailed discussion on these techniques can be found in general works on thermochemistry [7,8].

This type of work provides the integral heat of mixing. When the integral enthalpy of mixing is known as a function of composition at a particular temperature, the partial molar enthalpy of the species can be obtained through differentiation:

$$\Delta_{\text{mix}}\bar{H}_i = (1 - x_i)\frac{\partial \Delta_{\text{mix}}H}{\partial x_i} + \Delta_{\text{mix}}H. \tag{12.4}$$

12.2.2 Incorporation of Calorimetric Data into a Thermodynamic Model for Molten Salts

Since calorimetry measurements deal only with enthalpies, the activities of the components in the melt are not readily attainable. Activities can be obtained, but only through the involvement of other data. Consider the $MgCl_2$–NaCl phase diagram in Figure 12.1.

At all compositions along the $MgCl_2$ liquidus the following equation relating the partial Gibbs energy for $MgCl_2$ in the melt (l) and the coexisting solid phase(s) applies:

$$\bar{G}^{\text{s}}_{\text{MgCl}_2} = \bar{G}^{\text{l}}_{\text{MgCl}_2}. \tag{12.5}$$

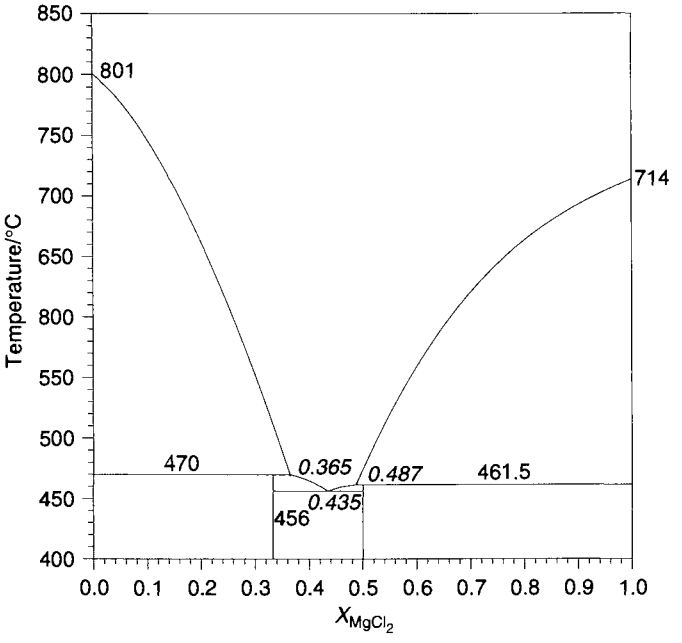

Figure 12.1 Binary phase diagram for ($MgCl_2$ + NaCl).

Expressing these partial Gibbs energies in terms of activities and standard Gibbs energies yields:

$$G^{0,s}_{MgCl_2} + RT \ln a^{s}_{MgCl_2} = G^{0,l}_{MgCl_2} + RT \ln a^{l}_{MgCl_2}. \tag{12.6}$$

Since NaCl does not dissolve appreciably in solid $MgCl_2$, the activity of solid $MgCl_2$ along the $MgCl_2$ liquidus is virtually unity. Thus, Equation (12.6) becomes

$$(G^{0,l} - G^{0,s})_{MgCl_2} = \Delta_{fus}G = -RT \ln a^{l}_{MgCl_2} \tag{12.7}$$

and with knowledge of the change in the Gibbs energy of melting with temperature, the activity of $MgCl_2$ with respect to the pure liquid can be found at any temperature along the $MgCl_2$ liquidus. When the relative partial Gibbs energy and relative partial enthalpy are known at a particular composition on the $MgCl_2$ liquidus, the relative partial entropy of mixing of $MgCl_2$, $\Delta_{mix}\bar{S}_{MgCl_2}$, can be determined using

$$\Delta_{mix}\bar{S}_i = \frac{\Delta_{mix}\bar{H}_i - \Delta_{mix}\bar{G}_i}{T}. \tag{12.8}$$

Since $\Delta_{mix}\bar{S}_{MgCl_2}$ is not a strong function of temperature, this value can be used to find the partial Gibbs energy, and hence the activity, of $MgCl_2$ at temperatures above the liquidus.

12.2.3 Vapour Pressure Methods

For cases in which one of the vapour pressures of the components of the melt is much greater than the others, vapour pressure techniques may be applied. In these situations, the activity of species i in a solution can be determined from the vapour pressure using

$$a_i = \frac{P_i}{P_i^0}, \tag{12.9}$$

where P_i is the partial pressure of i over the solution at a given temperature and P_i^0 is the partial pressure of i over pure liquid i at the same temperature. This assumes, of course, ideal gas behaviour of the vapour that is almost always a reasonable assumption at elevated temperatures and moderate total pressures. The partial molar Gibbs energy of mixing of component i as a function of temperature can be obtained from the activity using

$$\Delta_{\text{mix}}\bar{G}_i = RT \ln a_i, \tag{12.10}$$

and the partial molar enthalpy of mixing of component i can be calculated from the temperature dependency of $\Delta_{\text{mix}}\bar{G}_i$ at any particular melt composition:

$$\Delta_{\text{mix}}\bar{H}_i = R\frac{\mathrm{d} \ln a_i}{\mathrm{d}(1/T)}. \tag{12.11}$$

The partial molar entropy of mixing can also be established from the equation

$$\Delta_{\text{mix}}\bar{S}_i = -\frac{\mathrm{d}\, \Delta_{\text{mix}}\bar{G}_i}{\mathrm{d}T}. \tag{12.12}$$

Since the partial enthalpy and entropy obtained by this method are seldom of high precision, vapour pressure data are best used with calorimetric data. For example, the partial entropy of mixing component i can be found using Equation (12.12).

Vapour pressure measurements established by mass spectrometry are very useful in cases where the vapour pressure is due to more than one component or where dimerization occurs. The Gibbs–Duhem equation, which interrelates the isothermal component partial pressures in the manner

$$x_A\, d \ln P_A + x_B\, d \ln P_B + \cdots = 0, \tag{12.13}$$

provides a check on self-consistency [9]. The use of mass spectroscopy will be discussed later.

12.2.4 Electrochemical Methods

Many accurate measurements of the Gibbs energy change of a species in molten salt solutions have been made using reversible galvanic cells. The measured emf for a process that

would occur upon shorting the cell is directly related to the Gibbs energy of the reaction by the relationship:

$$\Delta_r G = -nFE, \tag{12.14}$$

where n is the number of Faradays of charge required per mole of species, F the Faraday constant, and E is the reversible emf. The accuracy of these measurements can be quite high when reversibility can be demonstrated. The typical uncertainty in these measurements is in the order of 1–2 mV. This translates to approximately 200–400 $J \cdot (g\,eq)^{-1}$, which is considered quite accurate. Through careful cell design and operation, measurements of reversible emf will generate accurate Gibbs energy changes for the formation of the most easily decomposed component. The most easily decomposed component will also be that which will form most readily if the cell electrodes are shorted.

Emf cells can be divided into two categories: concentration cells and formation cells. Concentration cells permit the examination of the process of transferring a component over a sharp concentration gradient maintained between two phases. The electrolyte used must be one that allows only the transfer of one component from one-half cell to the other when current is passed. The cell can be represented as

$$+[M]_1/M^{Z+}/[M]_2^- \tag{12.15}$$

for which the Nernst equation may be written as

$$E = -\frac{RT}{zF} \ln \frac{a_{[M]_2}}{a_{[M]_1}}, \tag{12.16}$$

where $a_{[M]_1}$ and $a_{[M]_2}$ are the activities of M in the high and low concentration zones (half cells). In this case, the activity of any species can be obtained immediately in one-half cell, when the activity in the other is known. For example, in $MgCl_2$ + NaCl solution, an Na^+-glass electrolyte could be used as the membrane between pure NaCl(l), Cl_2(g) and a solution of $MgCl_2$–NaCl(l), with Cl_2(g). It may not always be possible to find an electrolyte permeable with respect to the desired ion and also non-reactive when in contact with the phases being studied.

Formation cells generate the voltage associated with a reaction between components. The measured voltage pertains to the formation of the most easily decomposed component. A typical reaction might be

$$Mg + Cl_2 = MgCl_2. \tag{12.17}$$

The salt acts as the electrolyte and it is not necessary that it conducts the current by only one ion. It is important that the salt that would be formed at closed circuit be less stable than the other components in the electrolyte. Otherwise, the displacement reactions involving the other components such as

$$Mg + 2NaCl = MgCl_2 + 2Na, \tag{12.18}$$

would lead to slow changes in electrolyte composition even when the cell is at open-circuit. Electrodes of magnesium metal and chlorine must be in contact with the electrolyte. The necessity for gaseous halides to be involved poses an experimental difficulty for halide-based molten salts, and therefore some systems with highly toxic components are poor candidates for emf measurements.

The Gibbs energy of formation as a function of temperature, and therefore the corresponding enthalpy and entropy changes, of the most easily decomposed salt is readily attained from the experimental data generated from the electrochemical cell. The difference between the extensive property change for the formation of $MgCl_2$ in a solution and pure $MgCl_2$ provides the relative partial molar properties of $MgCl_2$. The partial properties ($\Delta_{mix}\bar{G}_i$, $\Delta_{mix}\bar{H}_i$ and $\Delta_{mix}\bar{S}_i$) of the other components may be calculated using the Gibbs–Duhem equation but only if measurements systematically explore the extremes of variations in the composition of the electrolyte. The integral properties of mixing of the melt can be obtained by summing the relative partial properties of each component multiplied by their respective mole fractions.

The relationship between the Gibbs energy change for $MgCl_2$ formation and the open-circuit voltage (emf) is the starting point for the calculation of all thermodynamic properties. This relationship becomes apparent through the rearrangement of the Nernst equation

$$RT \ln a_{MgCl_2} = -2F(E - E^{\circ}) = \Delta_{mix}\bar{G}_{MgCl_2}. \tag{12.19}$$

The partial Gibbs energy of mixing is the change in Gibbs energy per mole of $MgCl_2$ that occurs when a negligible amount of the pure salt in a specified phase is added to a solution of predetermined composition. This is therefore calculated by taking the difference in Gibbs energy to form one mole of $MgCl_2$ in the electrolyte solution and in pure liquid $MgCl_2$ as shown in Equation (12.19).

The linearity, or near linearity, in the plot of the emf (E) against T indicates that the corresponding enthalpy and entropy are independent of temperature. Often experimental emf points are fit to $E = c_1 - c_2T$, but highly accurate emf measurements can determine the temperature effect on $\Delta_{mix}H$ and $\Delta_{mix}S$ for some systems. This is, however, more accurately determined by means of calorimetry.

The constants c_1 and c_2 provide a means to calculate $\Delta_{mix}\bar{H}_{MgCl_2}$ and $\Delta_{mix}\bar{S}_{MgCl_2}$ as in:

$$-2F[E - E^{\circ}] = \Delta_{mix}\bar{G}_{MgCl_2} = \Delta_{mix}\bar{H}_{MgCl_2} - T\Delta_{mix}\bar{S}_{MgCl_2}. \tag{12.20}$$

Thus, the partial enthalpy of mixing, $\Delta_{mix}\bar{H}_{MgCl_2}$, is directly proportional to the difference of intercepts between that of a particular composition and that of pure $MgCl_2$. Similarly, the partial entropy of mixing, $\Delta_{mix}\bar{S}_{MgCl_2}$, is proportional to the difference in slope.

The partial excess Gibbs energy of $MgCl_2$ is given by

$$\bar{G}^E_{MgCl_2} = \Delta_{mix}\bar{H}_{MgCl_2} - T\bar{S}^E_{MgCl_2} = RT \ln \gamma_{MgCl_2}, \tag{12.21}$$

where γ_{MgCl_2} is the activity coefficient of $MgCl_2$ in the electrolyte solution. The resulting data can then be fit to a number of different models [10,11].

12.2.5 Solubility Measurements

Thermodynamic properties can be obtained through solubility measurements. These experiments are relatively simple and are often used to examine the thermodynamic properties of an oxide in a halide melt with the view to electrolysis, such as in the aluminium industry. The electrolyte is saturated with the additive and samples are taken periodically and analysed until there is no change in the concentration of the additive. The activity coefficient of the additive can be calculated from knowledge of the thermodynamic properties of the pure solid additive (A). At saturation,

$$\bar{G}_A^{\mathrm{l}} = G_A^{0,\mathrm{l}} + RT \ln a_A^{\mathrm{l}} = G_A^{0,\mathrm{s}}, \tag{12.22}$$

which can be rearranged as

$$\Delta_{\mathrm{fus}} G_A^0 = RT \ln a_A^{\mathrm{l}}. \tag{12.23}$$

Therefore, with knowledge of the additive's solubility as a function of temperature, the activity coefficient can be calculated.

12.2.6 Cryoscopy

The freezing point depression of one salt in another can be used to extract Henrian (dilute) activity coefficients. The binary salt system cannot contain a solid solution. The activity of the solvent s in the saturated solution is given as

$$\ln a_{\mathrm{s}} = \frac{-\Delta_{\mathrm{fus}} H_{\mathrm{s}}^0}{R} \left(\frac{1}{T} - \frac{1}{T_{\mathrm{fus,s}}} \right) - \frac{\Delta_{\mathrm{fus}} C_{\mathrm{p,s}}}{R} \left[\left(\frac{T_{\mathrm{fus,s}}}{T} \right) - \frac{T_{\mathrm{fus,s}} - T}{T} \right]. \tag{12.24}$$

The $T_{\mathrm{fus,s}}$ and $\Delta_{\mathrm{fus}} H_{\mathrm{s}}^0$ are the melting temperature and the enthalpy of fusion of the solvent, respectively. This method is effective due to its simplicity since the apparatus is simple to construct. However, it is severely limited in that it is only able to determine practically the Henrian activity coefficient for the salt.

12.3 Thermodynamic Properties from Phase Diagrams

Often, the thermodynamic properties of molten salts can be determined from knowledge of only the properties of the gaseous or solid phases and an accurate phase diagram. In conjunction with this, some information such as enthalpies of mixing is often available and can be incorporated into the modelling effort. Modelling thermodynamic properties from phase diagrams requires judgement on the credibility of conflicting data.

The modelling is based on the fact that the integral Gibbs energies of the compound and solution are equal when both are present (*i.e.* eutectic). With data for the solid compounds,

the liquid solution can then be modelled from the phase diagram by equating the Gibbs energies of the solid and liquid phases at special points on the diagram.

Generally, cooling curve data have an accuracy of about ± 1 K. Enthalpy data tend to be more reliable than emf measurements, and so the enthalpy of mixing of the solution is usually accepted as measured and the entropy (if available) is adjusted within reason to provide critical features on the phase diagram (eutectics and peritectics) within 1 K. This method of using phase diagrams to generate thermodynamic data for molten salt solutions is quite effective in providing initial estimates of the thermodynamic properties of the solution.

12.4 Solid and Gas Phases

Although this section deals with experimental techniques with molten salts, methods for the determination of the solid and gaseous phase properties should also be mentioned for reasons just discussed. There are a number of methods used to analyse molten salt interactions with solid and gas phases and two of the most common techniques are mentioned here.

12.4.1 Differential Thermal Analysis (DTA)

DTA is commonly used to identify the liquidus in binary or ternary salt systems. It is most effective with systems that have a large enthalpy of transformation, but the high precision of modern DTA instruments and the ability to generate a relatively large number of data points result in accuracies of under 5 K. Typical sample size is 10–50 mg. Any phase transition will register a significant change in the temperature profile of the DTA signal.

Since DTA is not well suited for the accurate determination of stoichiometric phases, X-ray diffraction (XRD) is used to identify the presence of solid phases. The reader is directed to a number of papers [12,13] on salt systems that combine the use of thermodynamic results with DTA, XRD and cooling curves to generate a model of the system under investigation.

12.4.2 Mass Spectroscopy

Thermodynamic properties of molten salts can be obtained through gas phase studies as previously mentioned. However, polymerization of gaseous species is a common occurrence in molten salts and therefore, mass spectroscopy often is a necessary tool. A Knudsen cell is used to effuse a portion of the sample vapour as a molecular beam that is then ionized by electron impact. Analysis of molecular species can be assisted by the use of isothermal vaporization techniques and temperature-dependence studies. The partial pressure of a gaseous species can be calculated as the product of the ion intensity, sample temperature and a proportionality constant that contains factors such as the ionization cross section, multiplier efficiency and ionizing-electron energy [14]. However, the use of a dual Knudsen cell system can remove the uncertainty associated with estimates for the constant. With a sound knowledge of the gas phase speciation, the thermodynamic properties of the vapour phase can be used to assist in the development of a model for the molten salt.

12.5 Conclusions

There are various experimental techniques that can be used to generate thermodynamic data for molten salt systems. There are advantages and drawbacks to each method. When results from a number of studies (emf, cooling curves and calorimetry) are combined with a view to their source and respective accuracies, a suitable representation of the thermodynamic properties of the molten salt can be produced. This expression can then be used to model the entire system including solid- and gaseous phases when data from other experiments on these phases are available.

References

1. Pelton, A.D., Talley, P.K. and Sharma, R.A., *J. Phase Equilibr.* **13**(4), 384–390, 1992.
2. Levy, H.A. and Danford, M.D., *Diffraction Studies of Molten Salts*, M. Blander, ed., Interscience Publishers, New York, 1964.
3. Temkin, M., *Acta Physichim. URSS.* **20**, 411, 1945.
4. Kleppa, O.J. and McCarty, F.G., *J. Phys. Chem.* **70**, 1249, 1966.
5. Hong, K.C. and Kleppa, O.J., *J. Phys. Chem.* **82**, 1596, 1978.
6. Orkheva, A.I., *Izvest Vyssh Ucheb Zaved, Tsvetn Metall.* **2**, 59–62,1978.
7. Kubachewski, O. and Deuch, W.A., *Physicochemical Measurements at High Temperatures*, J.O.M. Bockris, ed., Butterworths, London, 1959.
8. Kubachewski, O., Evans, E.L. and Alcock, C.B., *Metallurgical Thermodynamics,* 4th ed., Pergamon, London, 1967.
9. Belton, G.R. and Fruehan, R.J., *J. Phys. Chem.* **71**, 1403, 1967.
10. Davis, B.R. and Thompson, W.T., *Can. Metal. Q.* **34**(4), 347–352, 995.
11. Tomiska, J., *CALPHAD* **5**(2), 81–92,1981.
12. Zhiyu, Q., Sangster, J. and Pelton, A.D., *CALPHAD* **11**(3), 277–286, 1987.
13. Perry, G.S. and Fletcher, H., *J. Phase Equilibr.* **14**(2), 172–178, 1993.
14. *The Characterization of High Temperature Vapours*, J.L. Margrave, ed., Wiley, New York, 1967.

13 Measurement of Limiting Activity Coefficients: Non-Analytical Tools

J. DAVID RAAL and D. RAMJUGERNATH
School of Chemical Engineering
University of Kwazulu-Natal
Durban, South Africa

Measurement of the Thermodynamic Properties of Multiple Phases
R.D. Weir and Th.W. de Loos (Editors)

13 MEASUREMENT OF LIMITING ACTIVITY COEFFICIENTS: NON-ANALYTICAL TOOLS

13.1 Experimental Methods

Experimental measurement of both high- and low-pressure vapour–liquid equilibrium has been covered elsewhere in this volume. Although accurate and thermodynamically consistent data can be obtained from both static and dynamic apparatus such as described in Chapter 5, the greatest experimental difficulty and the largest measurement errors usually occur in the very dilute regions of concentration. These, however, may be precisely the regions of greatest importance in separation processes for high-purity chemicals and in the separation of pollutants from the environment. In distillation a large proportion of both the equipment and operating costs may arise in the removal of impurities to trace levels.

Infinitely dilute activity coefficients, γ_i^∞ give the best description in the dilute regions and have also found many applications in characterizing solution behaviour. As pointed out by Thomas *et al.* [1], they can be used to generate binary parameters for solution models, to predict the existence of an azeotrope and (less successfully) to estimate mutual solubilities. If the two limiting activity coefficients γ_1^∞, γ_2^∞ are measured for a binary system and then used to model the full concentration range, this clearly represents an economy of experimental effort. This possibility is excluded for systems with maxima or minima in the activity coefficient curves. Lobien and Prausnitz [2] have produced procedures for estimating γ_2^∞ from γ_1^∞ (or vice versa) from pure component properties and, for alkanols, through use of a self-associating equilibrium constant. This has considerable potential since, for many systems, γ_2^∞ may be difficult or impossible to measure, *e.g.* where γ_1^∞ is found by GC methods.

Since extrapolation of data measured in the non-dilute areas to obtain limiting activity coefficients frequently produces results of dubious quality, much effort has been devoted to procedures for direct measurement of limiting activity coefficients. The principal methods that have been developed for measuring γ_i^∞ are:

- differential ebulliometry, also referred to as comparative ebulliometry,
- use of static differential apparatus,
- inert gas stripping,
- gas chromatographic methods.

Dew-point measurement by Suleiman and Eckert [3] and measurement of molar refraction by Dutt and Prasad [4] have also been proposed, but these methods have found only limited use. Gas chromatographic methods are reviewed elsewhere in this volume and we will survey here only the first three methods listed above. Ideally, methods for measuring infinitely dilute activity coefficients should be rapid and accurate, be independent of any model for activity coefficients or excess Gibbs energy and preferably avoid measurement of very dilute concentrations. These requirements can be met by static and dynamic methods if the equipment is carefully designed and operated, and if accurate allowance is made

for holdup of vapour or vapour and liquid in parts of the equipment when the true equilibrium liquid composition x_1 is calculated from the charge composition, x_1^s.

If a choice is to be made in choosing either a static or dynamic differential method, several important considerations arise:

(a) In differential ebulliometry the steady state can be achieved fairly rapidly and, at low pressures, no troublesome and time-consuming degassing of the components is required.

(b) The steady-state however, may not represent a true equilibrium state since this must be achieved in a single pass of liquid and vapour through the Cottrell tube, including the discharge onto the thermowell. Repeated circulation will not improve the steady-state approach to equilibrium and, as also pointed out elsewhere in this volume, the Cottrell tube is not particularly suited to attain equilibrium except perhaps on a very local scale.

(c) A further potential problem in dynamic ebulliometry is that the liquid in the boiling chamber may become superheated and at low pressures particularly, below about 13 kPa, may produce "bumping" and temperature fluctuations [5]. Also, the superheat may not be fully discharged where the liquid–vapour mixture impinges on the temperature sensor. For certain classes of pure fluids there is no "plateau region" where the boiling temperature remains invariant with changing vapour production rate, as noted by Kneisl *et al.* [6]. This phenomenon, not related to solvent purity, will produce error in the measured temperature. Poorly behaved fluids, characterised by a plateau region with slopes exceeding $300\,\mu K \cdot W^{-1}$, were classified according to their dipole moment size and a molecular association parameter. This problem is discussed further below.

(d) In a static differential method, pure solvent and a very dilute solution of solute in the same solvent are contained in separate sealed flasks maintained at the same temperature in a thermostatted bath. At equilibrium, achieved most conveniently by magnetic stirring, the pressure *difference* is measured and used to calculate the limiting activity coefficient. Since the two (or more) equilibrium flasks are sealed, there is no danger of loss of the volatile components. In dynamic ebulliometry however, there is an inert gas–vapour interface in the condenser above the equipment and considerable care is necessary in the condenser design and operation to prevent loss of volatiles. The latter can be detected by failure to reach a steady-state temperature over an extended period. Absorption of inert gas into the condensate can become a problem at higher pressures as pointed out by Ambrose [7].

(e) In the static differential method even the smallest amount of dissolved gas in the equilibrium liquid can render the $P-x$ measurements meaningless, as pointed out by Abbott [8] and confirmed experimentally by Alessi *et al.* [9]. Degassing, whether by vacuum sublimation, repeated freezing–evacuation–thawing cycles (*e.g.* [10]) or by distillation under total reflux [11], may require up to 24 h.

(f) Differential ebulliometry typically produces isobaric data whereas the static method produces isothermal data. For systems where the temperature change due to fluctuations in the controlled pressure, $(\partial T/\partial p)_x$, in the dilute range is very large, accurate measurement by the dynamic method becomes difficult and the equipment may be unsuitable for such systems or in such regions. The converse applies to static differential methods, where $(\partial p/\partial T)_x$ must be small to eliminate or reduce pressure fluctuations due to bath temperature variations. Fischer and Gmehling [12] for example, with their highly

refined static apparatus, were unable to measure γ_i^∞ for *N*-methyl pyrrolidone (1) in C_5 or C_6 hydrocarbons (2). Expressions for estimating $(\partial p/\partial T)_{x_1}$ in the dilute regions are given below.

(g) Finally, computation of the true equilibrium liquid composition x_1 from the charge composition x_1^s to allow for the effect of vapour holdup is a comparatively simple task for static apparatus. The corresponding task for a dynamic ebulliometer is a much more difficult proposition and requires characterization of the ebulliometer and accurate determination of the vaporization ratio ϕ. Measurement of the latter quantity has presented considerable problems to researchers in the past and has largely been responsible for limiting the dynamic method to systems of low relative volatility. More rigorous, new procedures for solving this problem have now been developed and are described below.

Although considerable numbers of dynamic and static apparatus for measuring γ_1^∞ have been proposed and used, they are generally representative of a few basic types. We will survey here only a few proven designs and procedures representative of present technology.

13.2 Differential Ebulliometry and Equipment

In differential ebulliometry, the difference is measured between the boiling point of a pure solvent and that of a dilute solution at the same pressure. This temperature difference ΔT is then plotted against the equilibrium liquid composition x_1 and the limiting slope $(\partial T/\partial x_1)_p^\infty$ as $x_1 \to 0$ is found. The latter is related to γ_1^∞ by well-known equations. A convenient form with correction for vapour-phase non-ideality by the truncated virial equation of state (EOS), is given by Pividal and Sandler [13]:

$$\gamma_1^\infty = \frac{\varepsilon_1^\infty P_2^{sat}}{P_1^{sat}}\left[1 - \beta \frac{d \ln P_2^{sat}}{dT}\left(\frac{\partial T}{\partial x_1}\right)_P^{x_1 \to 0}\right], \tag{13.1}$$

where

$$\varepsilon_1^\infty = \exp\left[\frac{(B_{11} - v_1^l)(P_2^{sat} - P_1^{sat}) + \delta_{12} P_2^{sat}}{RT}\right],$$

$$\beta = 1 + P_2^{sat}\left(\frac{B_{22} - v_2^l}{RT}\right),$$

$$\delta_{12} = 2B_{12} - B_{11} - B_{22}.$$

The B_{ii} and B_{ij} are second virial coefficients for like and unlike species respectively, the p_i^{sat} are pure component vapour pressures and v_i^l is the liquid molar volume. A convenient low-pressure simplification is given by: $\varepsilon_1 = 1 = \beta$.

A successful ebulliometer, developed by the Eckert group (*e.g.* [5,14]), is shown in Figure 13.1. To promote smooth boiling, 30-mesh ground glass particles were fused to the inner wall of the boiler. The system pressure was controlled with a MKS Baratron system to 0.04–0.15 Torr and temperature differences were measured with a precision of

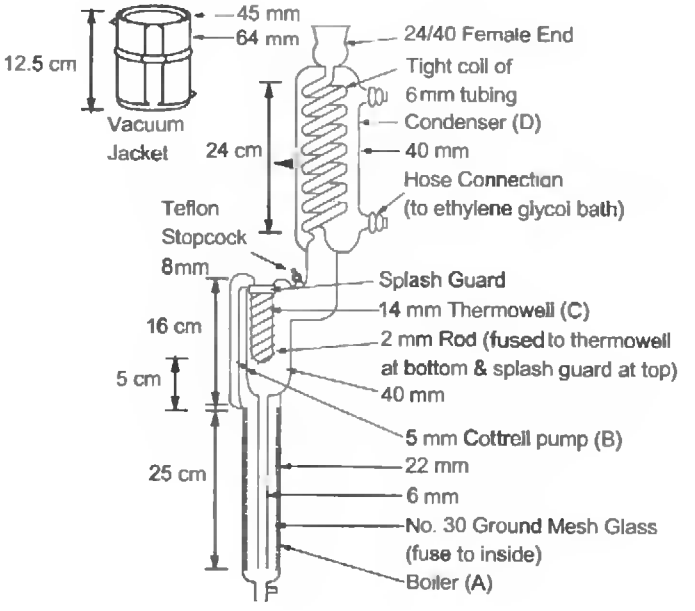

Figure 13.1 Ebulliometer of Trampe and Eckert [14]. (With permission of the American Chemical Society.)

0.0001 K. The later design incorporated magnetic stirring in the boiler. The coolant in the condenser was circulated at $T = 253\,\text{K}$ (−20°C). Several ebulliometers were connected to a common manifold with ballast to reduce pressure fluctuations, with pure solvent in one unit and dilute solutions of four different solutes in the remaining four. Data were presented for a considerable number of systems. Vapour and liquid holdups were estimated [5] or physically measured [14] to obtain the equilibrium liquid composition x_1 from the charge composition x_1^s.

The less compact ebulliometer developed by Rogalski *et al.* [15] is shown in Figure 13.2. The vapour take-off *below* the thermowell in a later version prevents cooled condensate from impinging on the thermowell, but may produce stagnant vapour in the upper reaches.

The ebulliometer used by Raal and Ramjugernath [16] is shown in Figure 13.3. To characterise the ebulliometer, a magnetically stirred sampling point is introduced in the downcomer for analysing the combined liquid-condensed vapour stream F, of composition z_i. To produce smooth boiling and for fine boiling control, the boiling chamber contains an internal heater (not shown) with micro-roughened surfaces, and is magnetically stirred. Provision is also made for measuring the "superheat" temperature T_s just below the entrance to the Cottrell pump, useful for determining the vaporization ratio ϕ, as shown below. The splashguard prevents cooled condensate arising from any surges in the boiling rate from impinging on the thermowell (in an earlier version). A superior design is proposed in Figure 13.3(b). The inner tube containing the temperature sensor is vacuum-jacketed and the arrangement is such that the superheat should be discharged in the upper regions before equilibrated liquid impinges on the sensor part. The system pressure was controlled

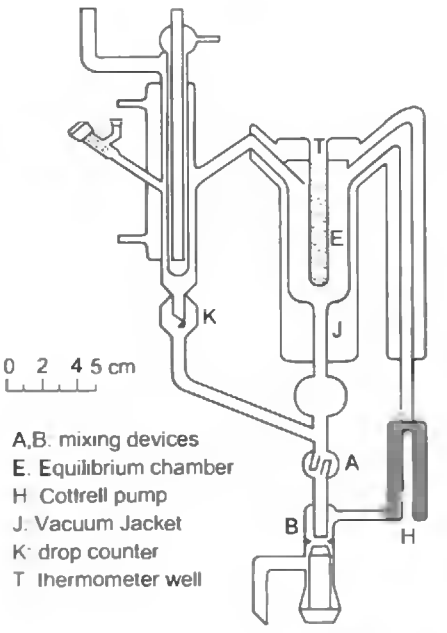

Ebulliometer for determining the liquid-vapour equilibrium.

Figure 13.2 Ebulliometer of Rogalski *et al.* [15] A, B, mixing devices; E, equilibrium chamber; C, Cottrell pump; H, heater; J, vacuum jacket; K, drop counter; T, thermowell.

with a commercial pressure controller but a more precise computer-controlled regulation such as that of Joseph *et al.* [17] is now being implemented. The new design gives very stable temperatures, a broad plateau region and vapour pressures in close agreement with literature values, which themselves often show appreciable discrepancies.

Pressures and temperatures were measured respectively with a SENSOTEC Super TJ straingauge pressure transducer and with Pt-100 resistance elements read through a HP 6 ½ digit multimeter model HP 33401A.

13.3 Characterization of an Ebulliometer

To obtain accurate γ_i^∞ data, particularly for systems of large relative volatility, the true liquid equilibrium composition x_1 must be determined from the charge composition $x_1^\S$ with the highest possible accuracy. To accomplish this, the reboiler "static" holdup (R' moles) and that of the equilibrium liquid and vapour in the upper part of the apparatus (L' and V') must be accurately determined. The V' represents vapour of composition y_1 and generally will comprise both gaseous and condensed forms, *i.e.* the *volume* of vapour in the equilibrium chamber (B) and associated areas will not be a satisfactory measure. A procedure has been found however by Raal [18] for determining all static holdups based only on material balances and equilibrium relationships, together with measurement of the composition z_1 for

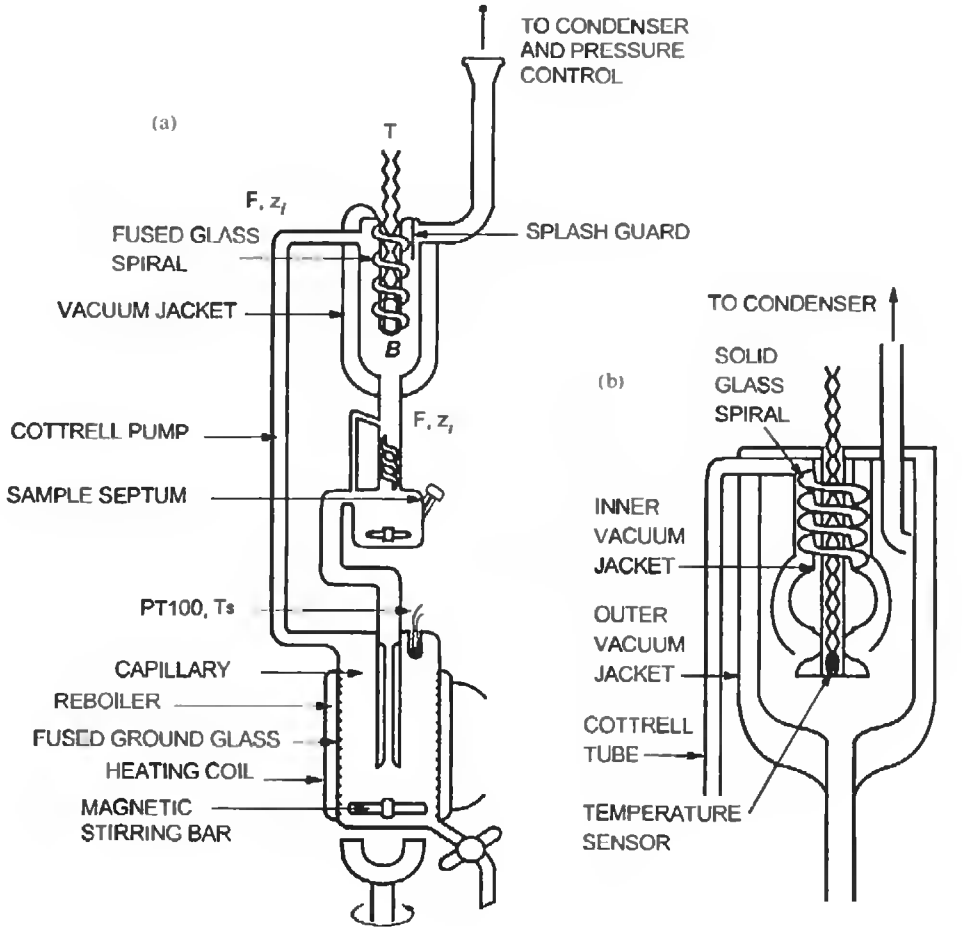

Figure 13.3 (a) Raal and Ramjugernath ebulliometer, (b) proposed modification of equilibrium chamber.

a system of known phase equilibrium behaviour. A considerable advantage of the procedure is that the regions of the various holdups need not be specifically demarcated.

13.3.1 Principal Ebulliometer Equation

The principal equation relating x_1 and x_1^s is readily derived as follows:

Consider the distribution of the charge, S' (moles) between the reboiler (R') and the liquid and vapour holdup quantities L' and V' at any instant after equilibrium has been established:

$$S' = R' + L' + V'. \tag{13.2}$$

For component 1 of a binary,

$$S' x_1^s = R' z_1 + L' x_1 + V' y_1. \tag{13.2a}$$

In Equation (13.2), it has been tacitly assumed that in the reboiler the overall composition z_1^R equals the overall composition z_1 in the Cottrell tube. This would be exact if the Cottrell tube merely acts as a mechanical pump without overall composition change. At the other extreme, if only vapour entered the Cottrell tube, its composition would differ considerably from z_1^R. Since the dynamic vaporization ratio $\phi = V/F$ usually lies somewhere between 0.02 and 0.08, the assumption $z_1^R = z_1$ should be satisfactory for all practical purposes.

The upper portion of the ebulliometer acts as an adiabatic flash chamber, for which the following equation applies:

$$x_1 = \frac{z_1(1+f)}{1+K_1 f}. \tag{13.3}$$

The K_1 is the equilibrium constant, y_1/x_1, and f is the dynamic ratio,

$$f = V/L = \phi/(1 - \phi). \tag{13.4}$$

Incorporation of Equations (13.3) and (13.4) into Equations (13.1) and (13.2) gives, after some arrangement:

$$x_1 = \frac{x_1^s}{1+(K_1 - 1)E}, \tag{13.5}$$

where the ebulliometer characterizing parameter E is given by:

$$E = V'/S' + (R'/S')\phi. \tag{13.6}$$

Evaluation of parameter E thus permits *exact* calculation of x_1 from x_1^s by an iterative procedure, since K_1 is not known *a priori*. Also, if E is known for a few values of ϕ from different boil-up rates, a plot of E *against* ϕ will produce the dimensionless holdup quantities (V'/S') and (R'/S') as the intercept and slope respectively.

13.3.2 Evaluation of E Parameter

The parameter E can be evaluated by measuring z_1 from a sampling point (see Figure 13.3) for a system of known phase equilibrium behaviour. Further relationships between ϕ and E, other than Equation (13.6), are however required. The first equation is found from the well-known relationship for a multicomponent flash, *e.g.* the Rachford and Rice equation as given by King [19]:

$$\sum_{i=1}^{m} \frac{z_i (K_i - 1)}{(K_i - 1)\phi + 1} = 0. \tag{13.7}$$

This enforces the necessary condition $\Sigma x_i = 1$.

Written for a binary and solved for ϕ, this gives:

$$-\phi = \frac{z_2}{K_1 - 1} + \frac{z_1}{K_2 - 1}. \tag{13.8}$$

A further useful equation relating E and ϕ is found by combination of Equations (13.3) and (13.5) (see *e.g.* [18]):

$$x_1^s = z_1\left\{\frac{1 + (K_1 - 1)E}{1 + (K_1 - 1)\phi}\right\}. \tag{13.9}$$

A satisfactory iterative procedure for determining E, ϕ and x_1 was found [18] as follows:

(a) Estimate x_1, *e.g.* $x_1^{(1)} = z_1$ (measured).
(b) Determine $\gamma_1^{(1)}(x_1)$ and $\gamma_2(x_1)$ from a one- or two-constant correlating equation such as the Margules or Wilson equations. In the very dilute regions, we have found the one-constant Margules equation surprisingly effective and the one-constant Wilson equation to be excellent even for highly non-ideal systems, *viz.*

$$\ln \gamma_i = A(1 - x_i)^2. \tag{13.10}$$

and for the Wilson equation,

$$G_{21} = G_{12} \exp[2\ln(v_1^l/v_2^l) - \beta(\Delta_{vap}H_2 - \Delta_{vap}H_1)(RT)^{-1}], \tag{13.11}$$

v_i^l and $\Delta_{vap}H_i$ are liquid molar volumes and enthalpy of vaporization of component i, respectively at the experimental temperature. The single fitting parameter G_{12} is related to γ_1^∞ by

$$\ln \gamma_1^\infty = -\ln G_{12} + 1 - G_{12} \exp[2\ln(v_1^l/v_2^l) - \beta(\Delta_{vap}H_2 - \Delta_{vap}H_1)(RT)^{-1}], \tag{13.12}$$

with $\beta = 2/Z$ (Z = coordination number).
(see Raal and Ramjugernath [20] for application of the Wilson equation).
(c) Determine $K_i^{(1)}$ from $K_i = \gamma_i p_i^{sat}/p$.
(d) Estimate $\phi^{(1)}$ from Equation (13.8).
(e) Calculate $E^{(1)}$ from Equation (13.9).
(f) Recalculate x_1 from Equation (13.5).
(g) Repeat steps (b)–(f) until convergence is achieved.

Note that a simpler more direct procedure for finding x_1 is also possible in principle from a plot of temperature against x_1, which can be generated from the expression for $(\partial T/\partial x)_p$ in Chapter 5 of this volume by a marching procedure.

13.3.3 Evaluation of Holdups (R′/S′) and (V′/S′)

When a converged set of ϕ, E and x_1 values have been obtained, the energy input to the reboiler can be changed to a larger or smaller value at the same pressure and with the same charge

composition x_1^s still in the apparatus. The measured temperature T and composition z_1 should change. The above sequence of calculations is then repeated to obtain a second set of E, ϕ and x_1 results. A plot of E against ϕ will then produce (V'/S') and (R'/S'), as discussed above. The procedure is admittedly demanding both experimentally and computationally.

Once (V'/S') and (R'/S') have been obtained, however, they should remain virtually constant for any new system provided that the same *volume* of charge is used as in the characterising experiment. Model calculations on two hypothetical systems of widely different molar masses and liquid density, for example, suggest that R'/S' will be unchanged and that V'/S' will change only from 0.018 to 0.022, quite satisfactory for determining E. If greater accuracy is required, the new V'/S' can be calculated but such elaboration does not seem worthwhile. The above procedures when applied to the systems {ethyl acetate (1) + toluene (2)} and {cyclohexane (1) + ethyl acetate (2)} gave the following characterization for the ebulliometer shown in Figure 13.3(b):

$$E = 0.892 + 0.0548\phi. \tag{13.6b}$$

13.3.4 Determination of the Vaporization Ratio ϕ

From the equations and procedures discussed above, it is clear that accurate determination of ϕ for each individual ebulliometric measurement is pivotal in finding accurate γ_i^∞, particularly for systems of large relative volatility (≡large K_1 in the dilute regions). Resolution of this difficult problem has been sought in a variety of ways by others, Dohnal and Novotna [21], Rogalski *et al.* [15] (three methods) and Raal and Ramjugernath [16] (two methods). Two satisfactory procedures, based on entirely different information are now available.

Iterative Procedure

For the first, it appears that the information contained in a few sets of $\Delta T - x_1^s$ data at constant pressure, together with the equations presented above, provided the holdups (R'/S') and (V'/S') are available, contain sufficient information when used with a correlating equation for $\gamma_1(x_1)$ to provide unique values of both ϕ and γ_1^∞. The iterative calculation procedure, a variation of the one presented in Section 13.3 for characterization of an ebulliometer, contains the following steps:

(a) Estimate a trial value of γ_1^∞, *e.g.* somewhat larger than the value obtained from $(\partial T/(\partial x_1^s)^\infty)$ depending on the system relative volatility.
(b) Calculate the constant in a one-parameter equation for γ_1, *e.g.* $\ln \gamma_1(x_1) = Ax_2^2$ and $A = \ln \gamma_1^\infty$.
(c) Estimate a value for x_1, *e.g.* somewhat smaller than x_1^s.
(d) Calculate the system pressure, $P_\Sigma = \Sigma x_i \gamma_i p_i^{sat}$, and compare with the measured pressure P_{exp}. If P_{exp} cannot be obtained with a realistic value of x_1, choose a larger or smaller value for γ_1^∞.
(e) Assume a value for ϕ and calculate E from Equation (13.6).

Table 13.1. Ebulliometric data for the system {*n*-hexane (1) + ethyl acetate (2)}.

x_1^s	T/(K)	T_s/(K)	x_1	z_1	ϕ
0	320.0943	321.4975		0	–
0.003603	319.854	321.2572	0.00310	0.003364	0.0280
0.005804	319.684	322.0872	0.0050	0.005424	0.0290
0.008402	319.4555	320.8587	0.0073	0.00787	0.0264

x_1, z_1, ϕ calculated by iterative procedure.
System pressure = 33.549 k.

(f) Calculate $K_1(=\gamma_1 P_1^{sat}/P)$ and then z_1 from Equation (13.9)

$$z_1 = x_{s1}\left\{\frac{1 + (K_1 - 1)\phi}{1 + (K_1 - 1)E}\right\}. \tag{13.9}$$

(g) Recalculate ϕ from Equation (13.8):

$$-\phi = \frac{z_2}{K_1 - 1} + \frac{z_1}{K_2 - 1} \tag{13.8}$$

In calculating K_2, $\gamma_2(x_1)$ can be taken as 1.00 for very dilute solutions.
Repeat steps (e)–(g) until ϕ from Equation (13.8) matches the assumed value.

(h) Check the value of x_1 with Equation (13.5). Repeat steps (c)–(f) until values of ϕ, x_1 and z_1 satisfy all the equations. Do steps (c)–(h) for all experimental points.
From the new set of $\{x_1 - (-\Delta T)\}$ for all measured points, redetermine γ_1^∞ from the improved $(\partial T/(\partial x_1)^\infty)$ from Equation (13.1) until convergence for γ_1^∞ is found.

An example of experimental results obtained with the apparatus of Figure 13.3, together with converged values of x_1, z_1 and ϕ is given in Table 13.1 for the system {*n*-hexane (1) + ethyl acetate (2)}. The limiting activity coefficient obtained, $\gamma_1^\infty = 2.838$ (at $T = 320.1$ K), is in close agreement with the 2.85 value of Thomas *et al.* [5]. The extensive iterative calculations involved in the above procedure, and the potential difficulties of non-convergence, can be avoided by a direct procedure requiring only measurement of the superheat temperature T_s and accurate latent heats and liquid heat capacities for the solvent. The procedure is based on the macroscopic energy balance applied across the Cottrell tube as follows:

Procedure Based on Macroscopic Energy Balance

Application of the macroscopic energy balance across the Cottrell tube from a point below its entrance, where T_s is measured, to the point of discharge on the thermowell where T is measured, is readily shown to give:

$$\phi = \frac{\bar{C}_p^l(T_s - T) + \phi_s \Delta_{vap}H_{T_s} - g\Delta Z_{eff}M + V(1 - \beta T)(p_s - p)}{\Delta_{vap}H_T}, \tag{13.13}$$

where g is the gravitational acceleration, M the molar mass, V the molar volume, β the liquid volume expansivity, p_s the pressure at the entrance to the Cottrell tube, and ΔZ_{eff} is the effective height of the two-phase mixture in the Cottrell pump. The third and fourth terms on the right-hand side account for the effective hydrostatic head and the effect of pressure on liquid enthalpy and have been found to be negligible for the system reported in the section on "Iterative Procedure". The $\bar{C}_p^l$ is the average solvent liquid heat capacity over the temperature interval $(T_s - T)$, and $\Delta_{vap}H_{T_s}$ and $\Delta_{vap}H_T$ are solvent enthalpy of vaporization at T_s and T, respectively. Heat loss to the surroundings from the Cottrell tube has been omitted since the loss *per unit mass of fluid*, $\dot{Q}$, is generally negligible. For systems measured at elevated temperatures, the Cottrell tube can be insulated as in the latest version of our equipment. The ϕ_s is the vaporization ratio at the entrance to the Cottrell tube, which is unknown and will be smaller than ϕ.

The unknown ϕ_s ratio can be eliminated by the very simple expedient of running experiments with the pure solvent at two (or more) slightly different pressures so that two sets of temperatures (T_1, T_{s1} and T_2, T_{s2}) differing by a few degrees from T, T_s, are obtained with a constant energy input.

Assuming ϕ and ϕ_s to remain constant for a small temperature change, permits its elimination by subtraction. Neglecting the insignificant last two terms from Equation (13.13), we obtain:

$$\phi = \frac{\bar{C}_p^l(T_s - T) - \dfrac{\Delta_{vap}H_{T_s}}{\Delta_{vap}H_{T_{s1}}}\bar{C}_{p1}^l(T_{s1} - T_1)}{\Delta_{vap}H_T - (\Delta_{vap}H_{T_1})(\Delta_{vap}H_{T_s}/\Delta_{vap}H_{T_{s1}})} \cdot \tag{13.14}$$

Since the assumption of constant vaporization ratios with changing temperature contains some approximation, the two (or more) values for ϕ obtained from Equation (13.14) are plotted against the temperature difference, $\delta T = (T - T_i)$, and extrapolated to zero. Calculations from data for the system {*n*-hexane (1) – ethyl acetate (2)} gave the following results:

$$\phi_{\delta T=4.9\,K} = 0.0734, \quad \phi_{\delta T=7.9\,K} = 0.1028, \quad \phi_{\delta T=0\,K} = 0.0253.$$

This last value is in remarkable agreement with the average for the three runs, by the iterative procedure, *viz.* 0.0271 from Table 13.1, since quite different information is used in the two procedures. Experiments still in progress on other solvents have shown, however, that the surprisingly strong dependence of vaporization rates and ratios on system pressure should be taken into account more explicitly in solving Equation (13.2) at two different pressures. With guidance from nucleate boiling heat transfer theory, "pressure independent" ϕ ratios were defined by $\phi P_r^{0.6}$ and $\phi_s P_r^{0.6}$, where P_r is the reduced pressure. Introduction of these reduced pressure ratios gave highly satisfactory results for several solvents, details of which are presented by Raal *et al.* [36]. This new procedure, although subjected so far only to limited testing, represents a powerful method for finding the difficult-to-determine vaporization ratio. We believe that together with the rigorous set of equations governing ebulliometry, this represents a significant advance in ebulliometry.

13.4 Static Differential Methods

An example of a superior static cell apparatus is that of the Gmehling group [22,23] and is shown in Figure 13.4. Degassing of the pure solvents was done by vacuum rectification (~5 h) after which the solvent was distilled into a separate flask to eliminate any less volatile impurities [23]. The degassed solvents were metered into the evacuated equilibrium flask with proportioning pumps kept in a thermostatted bath. Differential arrangements with two flasks, one containing pure solvent and the other a very dilute solution of the solute were used by Alessi *et al.* [9] and by Pividal *et al.* [24].

An arrangement with six precision bore glass tubes (with inside diameters accurate to 0.005 mm) attached to a common manifold was used by Hartwick and Howat [25]. Two of the tubes had mechanically driven pistons for fluid metering. These authors studied the effect of several possible error sources for the (acetone + water) system. A static cell can also be attached directly to a degassing condenser, as in the six-cell static cluster of Raal and Mühlbauer [26] (see Figure 13.5). The multiwalled condenser is fitted with a vapour draft tube in which a magnetically driven impeller induces a slow downward vapour flow to improve mixing and to speed up equilibration.

In all static differential methods, the solvent must be of the highest purity. Since charge composition is determined directly from the metering pumps (if used), the latter must be capable of very high accuracy. A microliquid dispenser developed in our laboratories for GC calibration purposes is shown in Figure 13.6. It has a dual mode of operation selectable by an electromagnetic clutch, so that either cm^3 or below mm^3 quantities can be

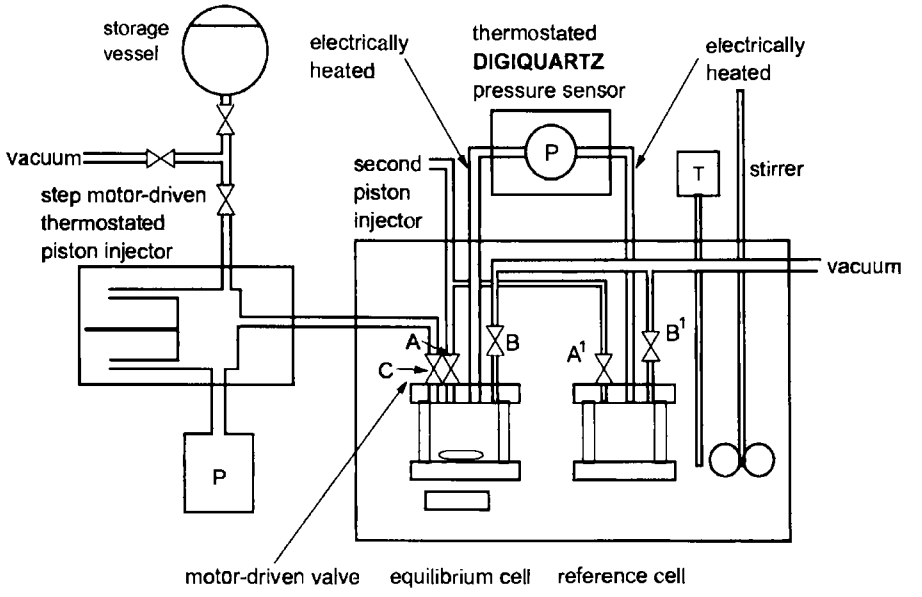

Figure 13.4 Schematic diagram of the differential static apparatus of Kolbe and Gmehling [22].

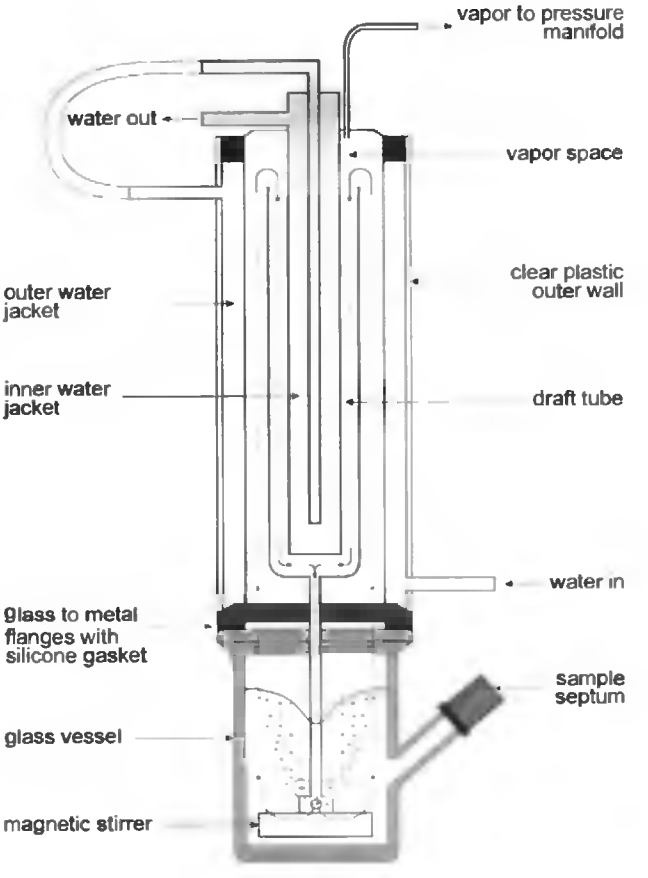

Figure 13.5 One unit of the six-cell static cluster of Raal and Mühlbauer [26].

dispensed. In the latter mode, the volume dispensed is exactly proportional to the travel of the uniform, polished stainless-steel rod propelled into the gas-free liquid in the cylinder. The unit can produce high pressures or operate against low vacuum and should be ideally suited for introducing small amounts of degassed solute into a static cell. Since the rod diameter is measured to ± 0.01 mm and can be electropolished, no calibration is required.

13.4.1 Calculation of Equilibrium Liquid Composition, x_1

The equilibrium liquid composition x_1, is related to the charge composition x_1^s by the exact relationship

$$x_1 = \frac{x_1^s}{1 + (K_1 - 1)E}, \tag{13.15}$$

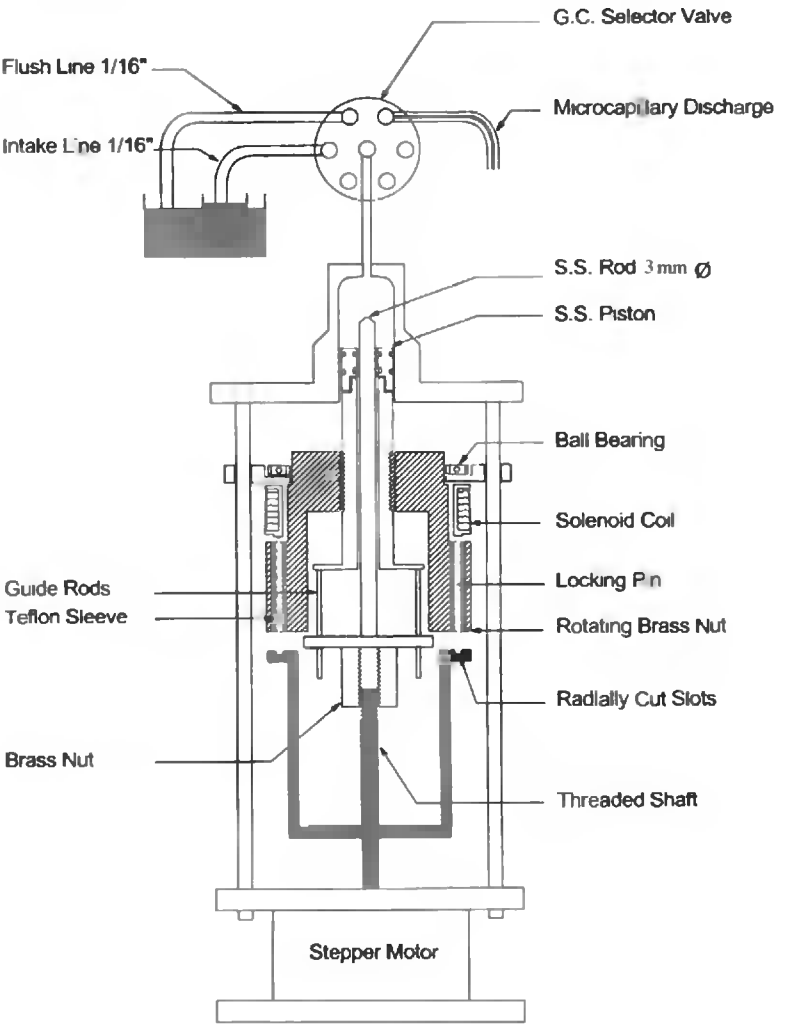

Figure 13.6 Microliquid dispenser with dual-mode operation, selectable by electromagnetic clutch.

with

$$E = (V'/S') = \frac{R_T - 1}{R_G - 1}. \tag{13.16}$$

The dimensionless groups R_T and R_G are given by

$$R_T = \frac{v^{TOT}}{S'} \frac{\rho_L}{M_L}, \qquad R_G = \frac{RTz}{P} \frac{\rho_L}{M_L}. \tag{13.16a}$$

The S' and V' are the number of moles of charge and the number of moles of vapour at equilibrium respectively and v^{TOT} is the total equipment volume. (See Raal and Ramjugernath [20] and also Chapter 5 in this volume for more detail including the iterative procedure required to calculate x_1.)

13.4.2 Calculation of Activity Coefficient at Infinite Dilution γ_i^∞

A typical data set from a static differential apparatus will consist of pressure differentials ΔP between the solvent and dilute solutions of increasing concentrations at corresponding values of x_1^s. Once x_1 has been calculated, γ_1^∞ can be obtained from the limiting pressure gradient $(\partial P/\partial x_1)^\infty$. A suitable expression, based on the virial equation of state for describing the vapour phase, is given by Pividal *et al.* [24]:

$$\gamma_i^\infty = \varepsilon_i^\infty \frac{P_j^{sat}}{P_i^{sat}}\left(1 + \beta_j \frac{1}{P_j^{sat}}\left(\frac{\partial P}{\partial x_i}\right)_T^{x_i \to 0}\right), \tag{13.17}$$

where

$$\varepsilon_i^\infty = \exp\left[\frac{(B_{ii} - v_i^l)(P_j^{sat} - P_i^{sat}) + \delta_{ij}P_j^{sat}}{RT}\right],$$

$$\beta_j = 1 + P_j^{sat}\left(\frac{B_{jj} - v_j^l}{RT}\right), \quad \delta_{ij} = 2B_{ij} - B_{ii} - B_{jj}.$$

At low pressure, approximation is $\varepsilon_i = 1 = \beta_j$.

To find $(\partial P/\partial x_1)^\infty$ from ΔP–x_1 data, various fitting procedures have been used, *e.g.* polynomials up to third order [24], and Legendre polynomials [12]. An attractive procedure however is that of Maher and Smith [27], based on earlier proposals by Ellis and Jonah [28]. It was found that plots of P_D/x_1x_2 versus x_1, or its inverse were frequently linear in the dilute regions. The limiting pressure gradient is then found from

$$(\partial P/\partial_{x_1})^\infty = (P_D/x_1x_2)_{x_1=0} + p_1^{sat} - p_2^{sat}, \tag{13.18}$$

$$\text{where } P_D = \text{"deviation pressure"} = P - \Sigma x_i p_i^{sat}. \tag{13.18a}$$

Finally, the sensitivity of measured pressure to fluctuations of bath temperature $(\partial P/\partial T)_x$ (or its inverse) can be readily computed for the dilute regions if an estimate of γ_1^∞ is available. The expression, developed in Chapter 5 of this volume is

$$\left(\frac{\partial T}{\partial p}\right)_{x_1} = \frac{B\gamma_1\{x_1 \mathrm{d}\ln\gamma_1/\mathrm{d}x_1 + 1\}}{(1 + Bx_1\gamma_1 \mathrm{d}\ln p_1^{sat}/\mathrm{d}T)(p_1^{sat}\gamma_1 - p_2^{sat}\gamma_2)\left\{1 - x_2\dfrac{\mathrm{d}\ln\gamma_2}{\mathrm{d}x_1}\right\}}, \tag{13.19}$$

where

$$B = \frac{(K_1 - 1)\, p_1^{\text{sat}}\, RT^2}{PK_1K_2x_2^2\Delta_{\text{vap}}H_2}. \tag{13.19a}$$

$\Delta_{\text{vap}}H_2$ is the enthalpy of vaporization of the solvent.

Note that Equation (13.19) can also be used to correct measured temperatures at slightly different pressures, (or vice versa) to a common value, iteratively if γ_1^∞ is not known.

13.5 Inert Gas Stripping

Since the earlier pioneering efforts of Leroi *et al.* [29], inert gas stripping has become a popular method for measuring systems with large γ_1^∞. The method is comparatively rapid and the equipment can be reasonably simple. Experimentally, the decrease in gas phase solute concentration is monitored with a GC as a function of time as the solute is stripped from its dilute solution in a solvent by the passage of finely dispersed bubbles of an inert gas. An advantage of the method is that the GC detector, although it must have a linear response, need not be calibrated. Nor is it necessary to know the initial solute concentration.

Calculation of γ_1^∞ is based on the assumption that bubbles exiting the liquid are in equilibrium with the stirred uniform liquid. The vapour phase must be of uniform concentration and partial condensation must be avoided. The subject is a large one and the reader is referred to the publications by Leroi *et al.* [29], Li *et al.* [30], Duhem and Vidal [31], Ritter and Adams [32], Richon *et al.* [33] and Hradetzky *et al.* [34] amongst others. We can sketch here only briefly some salient points.

13.5.1 Attainment of Equilibrium

The rate of transfer of solute from its mixture in the liquid to the interior of the carrier gas bubble depends on the mass transfer resistances in both the gas and liquid phases. These are dependent on a considerable number of factors such as fluid viscosity and density, bubble size and velocity and the two respective diffusion coefficients. Although gaseous diffusion, particularly in helium, is considerably faster than in the liquid phase, convective contributions in a magnetically stirred liquid phase may surpass those in the nearly stagnant interior of a bubble. In a detailed study, Richon *et al.* [33] reached the following conclusions:

(a) The viscosity of the liquid has comparatively little effect on the approach to equilibrium, even for $\mu^l = 0.040$ Pa s.
(b) The liquid phase mass transfer coefficient is sensitive to bubble velocity but not to bubble diameter.
(c) For bubble sizes $R_b < 1.25$ mm, gas phase diffusion resistance is negligible compared with the resistance of the mass transfer in the liquid phase.

Most researchers have attempted to ensure a close approach to equilibrium by having very small bubble sizes, either by using a sintered glass distributor of very fine porosity, *viz.* (4–8 μm [30]), or by a set of vertical capillaries of 0.3 mm ID [35].

13.5.2 Calculation of Activity Coefficient at Infinite Dilution γ_1^∞

The γ_1^∞ is obtained from the slope of a plot of $\ln(A/A^0)$ against Ft, where A and A^0 are the integrator peak areas at any time t and at any designated starting time t^0 respectively. The equation relating GC peak area to gas flowrate F and time t, derived by Duhem and Vidal [31], is conveniently given by Li *et al.* [30]. (The equation excludes the vapour phase correction):

$$\ln\left(\frac{A}{A^0}\right) = -\frac{\alpha F}{RT\beta}\frac{t}{[1-\bar{n}\alpha/P\beta]}, \tag{13.20}$$

$$\text{where } \alpha = \gamma_1^\infty p_1^{sat}/N; \quad \beta = 1 + \frac{Vp_1^{sat}\gamma_1^\infty}{RTN}. \tag{13.20a,b}$$

Also, N = number of moles of solvent (2) in the cell and $\bar{n}$ = log average of solute moles in cell = $(n - n_0)/\ln(n/n_0)$.

The bracketed term in Equation (13.20) accounts for loss of solvent, important if the latter is relatively volatile. For Equation (13.20) to be valid, the temperature, pressure and flow-rate must remain constant. To reduce or eliminate solvent loss, a presaturating cell can be used in series with the measuring cell. Excellent linearity for a plot of $\ln(A/A^0)$ against Ft was demonstrated by Li *et al.* [30] for {benzene(1) + water(2)} provided flowrates were kept below about 11 $cm^3 \cdot min^{-1}$. They found good agreement with published values for other systems measured by different procedures. Satisfactory results were limited to systems with gas–water partition coefficients greater than 0.3.

For solutes of low volatility, gas phase analysis by chromatography may become difficult or very time-consuming. For such systems, analysis of the remaining liquid provides a more attractive route [34].

13.6 Conclusions

Accurate measurement of limiting activity coefficients can be made for systems of diverse properties by a variety of static and dynamic methods if the equipment is constructed and operated carefully. For the most highly non-ideal systems, inert gas stripping and the static differential method are favoured. New developments in differential ebulliometry should permit extension of the technique to systems of high relative volatility, but this will remain a challenging task.

References

1. Thomas, E.R., Newman, B.A., Long, T.C., Wood, D.A. and Eckert, C.A., *J. Chem. Eng. Data* **27**, 399–405, 1982.
2. Lobien, G.M. and Prausnitz, J.M., *Ind. Eng. Chem. Fund.* **21**, 109–113, 1982.
3. Suleiman, D. and Eckert, C.A., *J. Chem. Eng. Data* **39**, 692–696, 1994.

4. Dutt, N.V.K. and Prasad, D.H.K., *Fluid Phase Equilibr.* **45**, 1–5, 1989.
5. Thomas, E.R., Newman, B.A., Nicolaides, G.L. and Eckert, C.A., *J. Chem Eng. Data* **27**, 233–240, 1982.
6. Kneisl, P., Zondlo, J.W. and Whiting, W.B., *Fluid Phase Equilibr.* **46**, 84–94, 1989.
7. Ambrose, D., in *Experimental Thermodynamics, Vol 2*, Ch. 13, B. Le Neindre and B. Vodar, eds., Butterworths, London, pp. 607–656, 1975.
8. Abbott, M.M., *Fluid Phase Equilibr.* **29**, 193–207, 1986.
9. Alessi, P., Fermeglia, M. and Kikic, I., *Fluid Phase Equilibr.* **29**, 249–256, 1986.
10. Maher, P.J. and Smith, B.D., *J. Chem. Eng. Data* **24**, 16–22, 1979.
11. Fischer, K. and Gmehling, J., *J. Chem. Eng. Data* **39**, 309–315, 1994.
12. Fischer, K. and Gmehling, J., *Fluid Phase Equilibr.* **119**, 113–130, 1996.
13. Pividal, K.A. and Sandler, S.I., *J. Chem. Eng. Data* **33**, 438–445, 1988.
14. Trampe, D.M. and Eckert, C.A., *J. Chem. Eng. Data* **35**, 156–162, 1990.
15. Rogalski, M., Rybakiewicz, K. and Malanowski, S., *Ber. Bunsenges. Phys. Chem.* **81**, 1070–1073, 1977.
16. Raal, J.D. and Ramjugernath, D., *AIChE J.* **49**, 538–545, 2003.
17. Joseph, M.A., Raal, J.D. and Ramjugernath, D., *Fluid Phase Equilibr.* **182**, 157–176, 2001.
18. Raal, J.D., *AIChE J.* **46**, 210–220, 2000.
19. King, C.J., *Separation Processes*, McGraw-Hill, New York, 1971.
20. Raal, J.D. and Ramjugernath, D., *Fluid Phase Equilibr.* **187**, 473–487, 2001.
21. Dohnal, V. and Novotna, M., *Collect. Czech. Chem. Commun.* **51**, 1393–1401, 1986.
22. Kolbe, B. and Gmehling, J., *Fluid Phase Equilibr.* **23**, 213–226, 1985.
23. Fischer, K. and Gmehling, J., *J. Chem. Eng. Data* **39**, 309–315, 1994.
24. Pividal, K.A., Birtigh, A. and Sandler, S.I., *J. Chem. Eng. Data* **37**, 484–487, 1992.
25. Hartwick, R.P. and Howat, C.S., *J. Chem. Eng. Data* **40**, 738–745,1995.
26. Raal, J.D. and Mühlbauer, A.L., *Phase Equilibria: Measurement and Computation*, Taylor & Francis, Washington, p. 60, 1998.
27. Maher, P.J. and Smith, B.D., *Ind. Eng. Chem. Fund.* **18**, 354–357, 1979.
28. Ellis, S.M.R. and Jonah, D.A., *Chem. Eng. Sci.* **17**, 971–976, 1962.
29. Leroi, J.-C., Masson, J.-C., Renon, H., Fabries, J.-F. and Sanmei, H., *Ind. Eng. Chem. Process. Des. Dev.* **16**, 139–144, 1977.
30. Li, J., Dallas, A.J., Eikens, D.I., Carr, P.W., Bergmann, D.L., Hait, M.J. and Eckert, C.A., *Anal. Chem.* **65**, 3212–3218, 1993.
31. Duhem, P. and Vidal, J., *Fluid Phase Equilibr.* **2**, 231–235, 1978.
32. Ritter, J.J. and Adams, N.K., *Anal. Chem.* **48**, 612–619, 1976.
33. Richon, D., Antoine, P. and Renon, H., *Ind. Eng. Chem. Process. Des. Dev.* **19**, 144–147, 1980.
34. Hradetzky, G., Wobst, M., Vopel, H. and Bittrich, H.J., *Fluid Phase Equilibr.* **54**, 133–145, 1990.
35. Legret, D., Desteve, J., Richon, D. and Renon, H., *AICHE J.* **29**, 137–144, 1983.
36. Raal, J.D., Gadodia, V., Ramjugernath, R. and Jalari, R., *J. Mol. Liquids* 2005, accepted for publication.

14 Measurement of Limiting Activity Coefficients Using Analytical Tools

V. DOHNAL
Department of Physical Chemistry
Institute of Chemical Technology
Prague, Czech Republic

Measurement of the Thermodynamic Properties of Multiple Phases
R.D. Weir and Th.W. de Loos (Editors)

14 MEASUREMENT OF LIMITING ACTIVITY COEFFICIENTS USING ANALYTICAL TOOLS

The limiting activity coefficient, γ_1^∞, is the fundamental thermodynamic quantity describing the behaviour of a non-electrolyte solute (1) at a state of its infinite dilution in a solvent (2) and the key parameter governing fluid-phase equilibria in highly dilute solutions (Henry's law region). Due to the essential importance of γ^∞ data for both practice and theory, their determination has been attracting interest of experimentalists for half of a century. The effort has been focussed on the development of specialized methods allowing precise and accurate measurements directly in the highly dilute range, since extrapolations from measurements on concentrated solutions yield generally unreliable results. A wide variety of such specialized vapour–liquid equilibrium (VLE) measurement techniques have been developed for this purpose. The primary property measured by these techniques is the solute's volatility or vapour–liquid partitioning at infinite dilution as expressed alternatively by one of the following quantities: the limiting relative volatility, Henry's law constant, gas–liquid partition coefficient, or liquid–gas partition coefficient. The definitions of these quantities and their relations to γ_1^∞ are summarized in Table 14.1. In these relations, as well as in the text of the entire chapter, the gas-phase non-ideality and the effect of pressure on the properties of the liquid phase are neglected for the sake of lucidity. At atmospheric and lower pressures, the error caused by this approximation is usually

Table 14.1 Common VLE partitioning characteristics and their relation to limiting activity coefficient.[a]

Quantity	Definition	Relation to γ_1^∞[b]
Limiting relative volatility	$\alpha_{12}^\infty = \lim_{x_1 \to 0} \left(\frac{y_1/x_1}{y_2/x_2} \right)$	$\gamma_1^\infty = \frac{\alpha_{12}^\infty p_2^{\mathrm{sat}}}{p_1^{\mathrm{sat}}}$
Henry's law constant (mole fraction based)	$H_{12} = \lim_{x_1 \to 0} \left(\frac{f_1^{\mathrm{l}}}{x_1} \right)$	$\gamma_1^\infty = \frac{H_{12}}{p_1^{\mathrm{sat}}}$
Henry's law constant (molar concentration based)	$H_{12}^c = \lim_{c_1^{\mathrm{l}} \to 0} \left(\frac{f_1^{\mathrm{l}}}{c_1^{\mathrm{l}}} \right)$	$\gamma_1^\infty = \frac{H_{12}^c \rho_2^{\mathrm{l}}}{p_1^{\mathrm{sat}} M_2}$
Gas–liquid partition coefficient (dimensionless Henry's law constant)	$K^{\mathrm{gl}} = \lim_{c_1^{\mathrm{l}} \to 0} \left(\frac{c_1^{\mathrm{g}}}{c_1^{\mathrm{l}}} \right)$	$\gamma_1^\infty = \frac{K^{\mathrm{gl}} RT \rho_2^{\mathrm{l}}}{p_1^{\mathrm{sat}} M_2}$
Liquid–gas partition coefficient	$K^{\mathrm{lg}} = \lim_{c_1^{\mathrm{l}} \to 0} \left(\frac{c_1^{\mathrm{l}}}{c_1^{\mathrm{g}}} \right)$	$\gamma_1^\infty = \frac{RT \rho_2^{\mathrm{l}}}{K^{\mathrm{lg}} p_1^{\mathrm{sat}} M_2}$

[a]Denotation: y_i and x_i are the mole fractions of component i in the vapour and the liquid phase, respectively, f_i its fugacity, c_i its molar concentration, p_i^{sat} and ρ_i^{l} the pure component vapour pressure and liquid density, respectively and M_i is its molar mass.

[b]The vapour-phase non-ideality and the effect of pressure on the liquid-phase fugacity are neglected.

within 1–2 per cent, which for moderately precise measurements is often negligible compared with other experimental uncertainties. For more accurate work, low-boiling solutes and/or experiments at higher than atmospheric pressure, the vapour-phase non-ideality correction should however be taken into account. The respective correcting expressions, elaborated for various experimental situations and based typically on the truncated virial equation of state, can be found in the literature [1–7].

The existing techniques to determine γ^{∞} can be categorized in a number of ways. Two basic clear-cut categories are identified by distinction whether a given technique employs an analytical tool or not. The non-analytical techniques rely on precise measurements of minute changes in the equilibrium temperature or the equilibrium pressure with varying composition of a synthetically prepared dilute mixture. As stability and sensitivity limitations do not usually allow such measurements to be performed directly in the Henry's law region but only in its close vicinity, some slight extrapolation is necessary to obtain the desired infinite dilution properties. These techniques, involving comparative ebulliometry, comparative tensimetry and dew-point temperature determinations, have been discussed in Chapter 13.

This section deals with the analytical measurement techniques that determine the infinite dilution VLE characteristics by means of suitable analytical tools and methods. Gas chromatography and UV spectrometry are the most applicable, but liquid chromatography, interferometry, Karl–Fischer titration, scintillation counting of labelled solute and other methods of analysis have been also conveniently utilized. The sensitivity and detection capabilities of analytical tools are such that one can work at solute concentrations where Henry's law is obeyed accurately. In addition, if a selective analytical method is used, the effect of impurities is efficiently suppressed. Among the analytical methods, gas–liquid chromatography (GLC) is unique: apart from being a sensitive and selective tool for analysis, its underlying gas–liquid partitioning process proper lends itself for the determination of partition characteristics by measuring the solute retention in a column loaded with the solvent.

Some surveys of the topic are available. In Chapter 2 of Experimental Thermodynamics, Volume II, Letcher [1] described in detail the determination of infinite dilution activity coefficients by classical GLC retention measurements. Conder and Young in their monograph Physicochemical Measurements by Gas Chromatography [2] gave a full account of this method. Since the mid-1970s, a number of other methods have been developed; their past overviews can be found in references [8–11]. Later review papers from 1996 [12–16], addressing environmental issues, all focussed on experimental techniques suitable for aqueous solutions of volatile organic compounds (VOC); here, the reviews of Turner *et al.* [15] and Kojima *et al.* [16] are more detailed than those of other authors.

Various analytical γ^{∞} measurement techniques described in this chapter are categorized into five groups as follows: (1) retention measurements in GLC, (2) headspace analysis method, (3) static mass balance methods, (4) rate measurements on continuous gas–liquid separation processes and (5) distillation methods. Solubility measurements are not considered here. Though the inverse mole fraction of the liquid solubility provides an accurate estimate of γ_1^{∞} for systems where the mutual solubilities of components are sufficiently small, reviewing the techniques for the measurement of liquid solubilities is beyond the scope of this section. Retention measurements in liquid–liquid chromatography are omitted because of unreliable results obscured by prevailing adsorption phenomena.

14.1 Retention Measurements in GLC

14.1.1 Conventional GLC

As recognized soon after the inception of GLC, gas–liquid partitioning characteristics can be conveniently determined by measuring the gas chromatographic retention. This route of γ^{∞} determination, which was pioneered in the years 1956–1959 and refined during the 1960s, has become extremely popular thanks to the availability of commercial instrumentation and speed with which the measurement could be done. The widespread use of the GLC technique has led to a wealth of publications and an amount of γ^{∞} data that are more extensive than those for any other method. The conventional GLC method working with essentially non-volatile solvents is well established. Since comprehensive accounts of its theory and practice presented as early as in the 1970s by Letcher [1] and Conder and Young [2] have remained essentially up to date, only few comments and updating remarks are given here.

In the last 25 years, thanks to incorporated technical innovations, commercial gas chromatographs have greatly improved thereby enabling new γ^{∞} determinations precision of 1 per cent without modifications and without auxiliary devices previously needed. Complete computer control of current research GCs allows efficient long-term stabilization and on-line monitoring of all experimental parameters. In this respect, the improved GC oven thermostatization and built-in electronic mass flow control are especially beneficial, as constancy of the column temperature and of the carrier gas flow rate is an important pre-requisite for precise and correct results to be obtained.

In sharp contrast with the high achievable precision of the method is that some portion of existing GLC data are considerably in error. The known major sources of error in the GLC method, *i.e.* inaccurate column loadings and adsorption of the solute on various surfaces in the column resulting in parasite retention, are most probably those responsible for this worrying situation. Interfering adsorption effects are especially critical for systems of strongly polar and associating solutes in non-polar solvents, such as alkanols in alkanes. Recent careful re-examinations of the problem have indicated that eliminating or just correcting for adsorption effects for such systems may be more complicated than had been assumed [17–20].

Accurate determination of the solvent mass in the column is particularly difficult for volatile solvents; a volatile stationary phase is continuously stripped from the column by the carrier gas flow, which causes a continuous change of the retention of injected solute samples. A common practice to overcome this problem is to pre-saturate the carrier gas by the solvent vapour [21–23]. This procedure however solves the problem only partially: though the elution of the volatile stationary phase decelerates, it does not completely cease due to the pressure drop across the column and the accurate knowledge of the solvent amount in the column continues to be required for the calculation of γ^{∞}. Another option to account for the solvent loss by evaporation is through weighing the column, but apart from obvious inconvenience this can be rather inaccurate. It is better to calculate the actual amount of the solvent n_2 according to

$$n_2 = n_2^0 - \frac{p_2^{\text{sat}} Ft}{RT}, \tag{14.1}$$

where n_2^0 is the initial amount of the solvent loaded in the column, F the carrier gas flow rate at the column outlet and t is the time elapsed from the start of the gas flow. If the saturated vapour pressure p_2^{sat} is not known, one can measure the net retention volume V_N as a function of t and fit the data to the following linear relation:

$$\frac{V_N}{n_2^0} = \frac{RT}{\gamma_1^\infty p_1^{sat}} - \frac{p_2^{sat} Ft}{\gamma_1^\infty p_1^{sat} n_2^0} = a + bt. \tag{14.2}$$

The values of γ_1^∞ and p_2^{sat} are then obtained from the fitted parameters a and b. This method was proposed originally by Olsson *et al.* [24]; Equation (14.2) however corresponds to a later presentation by Bayles *et al.* [25] that allows data from several columns to be processed simultaneously. The method requires the exact knowledge of initial solvent amount in each of the columns and, as a result, it is applicable only to solvents of very moderate volatility ($p_2^{sat} \approx 10^2$ Pa). Another way how to cope with the problem of a volatile stationary phase is to periodically determine γ^∞ of a particular solute chosen as a reference [26]. Such a practice is already closely similar to relative GLC retention measurements that are discussed below as a distinct method suitable for substantially volatile solvents.

The conventional GLC is a powerful and precise technique that is capable of producing accurate γ^∞ data if its inherent limitations are respected. The covered range of gas–liquid partition coefficients is approximately $0.0005 < K^{gl} < 0.05$, if retention times are to be kept reasonable. Among the plethora of application works that have appeared since the 1970s are, of particular note, the systematic studies on the solvent screening for solvent-aided separations conducted at the Oldenburg University, Germany, at the Natal University, South Africa and the St Petersburg State University, Russia, and published respectively in the Journal of Chemical and Engineering Data, the Journal of Chemical Thermodynamics and available as a cumulative compilation [27]. Accurate measurements on aqueous systems carried out by Mash and Pemberton [28] at the National Physical Laboratory, Teddington, UK, and by their successors [23,29,30] using a sophisticated medium high-pressure GLC apparatus represent another notable achievement. The most recent application of the conventional GLC, addressed by Heintz *et al.* [31–33] and Letcher *et al.* [34–36], is for the study of VOCs in ionic liquids.

14.1.2 Relative GLC

The method of relative GLC stems from a suggestion by Freeguard and Stock [37] made as early as in 1962, but to determine γ^∞ it was successfully applied for the first time in 1970s by Tassios [38]. More extensive and accurate measurements of γ^∞ by the relative GLC method were presented however only in 1990s by Sandler *et al.* [3,39].

In this method a mixture of two solutes is injected into a GLC column, one of which is the reference serving as an internal standard. For the ratio of the γ^∞ values of the two solutes, it follows from the theory of classical GLC (leaving out the vapour-phase non-ideality correction)

$$\frac{\gamma_1^\infty}{\gamma_{ref}^\infty} = \frac{p_{ref}^{sat}}{p_1^{sat}} \frac{(t_{R,ref} - t_D)}{(t_{R,1} - t_D)}, \tag{14.3}$$

where $t_{R,1}$, $t_{R,ref}$ and t_D are the retention times for the solute under study, the reference solute and a non-sorbed marker, respectively. As seen from this equation, if the limiting activity coefficient of the reference solute in the solvent loaded in the column under the conditions of experiment is known, the γ^∞ value for the other solute can be obtained only from the measurements of the retention times, the determinations of the amount of solvent on the column and of the carrier gas flow rate being no longer needed.

The relative GLC technique is applicable to a wide range of solvent volatilities; its application to appreciably volatile solvents brings however major benefits. Also, a volatile solvent can be directly injected into a general-purpose column filled with a bare inert solid support instead of preparing a special column for each solvent under study. Solutes must be of course more volatile than the solvent. The carrier gas flow rate can be adjusted from injection to injection in order to obtain reasonable values of retention times or better separation.

Retention time ratios can be easily measured to a precision of 5 per cent and better [3]. The relative character of the measurements makes this experimental procedure quite robust because various imperfections and complicating factors affecting absolute measurements cancel out or at least tend to compensate. Reasonably accurate γ^∞ values obtained by relative GLC for highly hydrophobic halogenated substances in water [39] appear to demonstrate that adsorption effects may compensate as well, in particular if the internal standard is selected so that it is chemically closely similar to the solute under study. While a distinct merit of this method is that the knowledge of the stationary phase amount is not at all needed, the γ^∞ determination fully relies on the knowledge of γ^∞ for a reference solute. The following procedure, denoted as non-steady-state gas–liquid chromatography (NSGLC), requires neither of these entries.

14.1.3 Non-Steady-State GLC

This technique for determination of limiting activity coefficients of volatile solutes in volatile solvents proposed and applied by Belfer *et al.* [40–42] is based on the measurement of the retention time of repetitively injected solute samples as a function of the time of their injection. Instead of correcting for the effect of solvent loss from the column, NSGLC utilizes this feature outlined in Figure 14.1 as the measurement principle. Under isothermal conditions and at a constant carrier gas flow rate, the amount of the solvent decreases linearly with time and so does the retention time of a solute injected repeatedly over that time. The decrease in retention time with the change in time of injection is directly related to the solute limiting activity coefficient, the respective relation derived by Belfer and Locke [41] being

$$\gamma_1^\infty = -\frac{p_2^{sat}/p_1^{sat}}{dt_R/dt}. \tag{14.4}$$

As seen from this remarkably simple equation, the only parameter to be determined from a NSGLC experiment is the derivative dt_R/dt, which is the so-called retention differential parameter that is characteristic of a given solute–solvent pair at a given temperature and represents the negative reciprocal of the limiting relative volatility. This parameter can be

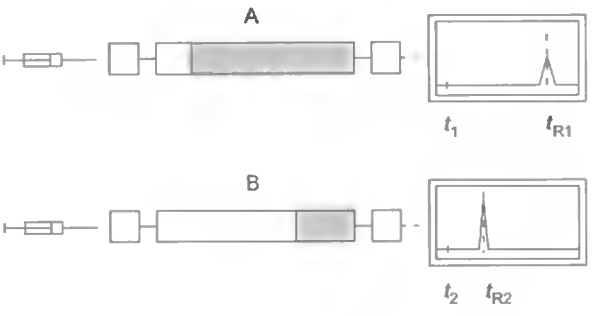

Figure 14.1 Representation of the change in retention time over time in non-steady-state GLC. The early stage (A) and the late stage (B) of the column lifetime. (Reproduced with permission from reference [42]. Copyright 1991 Am. Chem. Soc.)

conveniently evaluated as the slope of a plot of the retention time against injection time using linear regression.

Either packed columns with bare inert solid support or uncoated wide-bore fused-silica open tubular columns [43] may be used. The solvent is typically introduced *in situ* by injecting it through the respective hot injection port. In NSGLC, neither the amount of the solvent in the column nor the retention of a non-sorbed substance need to be known, and in addition some effects tend to cancel that are difficult to correct for in the classical GLC. Despite the several advantages, the NSGLC technique appears to be considered less accurate than other methods (the uncertainty of NSGLC measurements reported by Belfer *et al.* [41, 43] was 10 per cent) and has been only rarely used.

Very recently, a refined NSGLC method has been developed at the Prague Institute of Chemical Technology and shown to be suitable for accurate determination of limiting activity coefficients of VOCs in water [44]. Among several modifications suggested, the most essential one is that Equation (14.4) should be changed to

$$\gamma_1^{\infty} = -\frac{p_2^{\mathrm{sat}}/p_1^{\mathrm{sat}}}{\mathrm{d}(jt_{\mathrm{R}})/\mathrm{d}t}, \tag{14.5}$$

where j is the James–Martin compressibility correction. Although Equations (14.4) and (14.5) look very similar, the replacement of the retention time by the corrected retention time $t_{\mathrm{R}}^0 = jt_{\mathrm{R}}$, as inferred from the refined theory, has important consequences. Since $j < 1$, Equation (14.4) leads to systematically lower values of γ_1^{∞} than those calculated by Equation (14.5). Even for relatively small pressure gradients 30–40 kPa, corresponding to a short packed column, the difference attains a level of 15–20 per cent. The application of Equation (14.5) additionally requires the pressure drop to be monitored during the entire NSGLC experiment as well as the column outlet atmospheric pressure to be determined. The refined NSGLC method has proved to perform correctly and with better accuracy (3 per cent). The measurement precision has been improved to an even greater extent, thanks mainly to technical refinements of the experimental procedure.

In general, the applicability of the NSGLC method is constrained by system volatility conditions. The basic requirement is that the volatility of the solute from its dilute solution

must exceed the volatility of the solvent, otherwise the solvent elutes before the solute. The upper bound of the infinite dilution relative volatility α_{12}^{∞} follows from the fact that the measured derivative dt_R^0/dt approaches zero as α_{12}^{∞} increases and its determination is thus greatly affected by experimental errors. The concrete value of the upper bound depends on the measurement precision and the error tolerance; a practical upper bound may be around $\alpha_{12}^{\infty} = 100$. With respect to the volatility of the solvent, there are also constraints. High solvent vapour pressures lead to prohibitively short column lifetimes, while low p_2^{sat} values cause the solvent elution from the column (*i.e.* the driving mechanism of NSGLC) to be too slow. In both these cases, problems of precision arise. As a result, the applicability of NSGLC for water as the solvent is expected to be in the range from the room temperature to about 350 K. From the technical point of view, the applicability of NSGLC depends on the possibility to detect minute solute amounts in solvent saturated carrier gas streams. In this respect, the use of a flame ionization detector instead of a thermal conductivity one for aqueous solutions is considerably beneficial.

14.2 Headspace Method of Analysis

The conventional headspace analysis (HSA) method for the determination of limiting activity coefficients in gas chromatography involves the measurement of the equilibrium solute partial pressure established under static conditions above a sufficiently dilute solution of known composition [45]. Assuming that vapour-phase aliquots are dosed into the GC at constant T and p, the detector is linear, and pressures are low so that vapour-phase non-ideality can be neglected, then γ_1^{∞} can be evaluated from

$$\gamma_1^{\infty} = \frac{k_1(A_1/x_1)^{\infty}}{p_1^{sat}}, \tag{14.6}$$

where $(A_1/x_1)^{\infty}$ is the limiting ratio of the headspace solute peak area A_1 to the solute liquid mole fraction x_1 and k_1 is the proportionality response factor in $p_1 = k_1 A_1$, which must be established by calibration. If detection capabilities of the GC system allow the experiment to be done in the Henry's law region, $(A_1/x_1)^{\infty}$ can be determined from a measurement at a single composition, otherwise A_1 is measured as a function of x_1 and A_1/x_1 extrapolated to infinite dilution. Alternatively, activity coefficients at individual compositions can be evaluated and their extrapolation to infinite dilution done by a suitable thermodynamic model. The calibration is carried out using either specifically prepared gas standards or the headspace vapour above the pure liquid solute. The gas standard can be prepared by the total vaporization technique, *i.e.* by injecting a known, sufficiently small amount of liquid standard into a vessel of precisely known volume and allowing the sample to evaporate completely. However, the latter calibration technique using the saturated solute vapour is faster and especially convenient when the detector linearity extends to loadings as large as those corresponding to p_1^{sat}; then Equation (14.6) becomes

$$\gamma_1^{\infty} = \frac{(A_1/x_1)^{\infty}}{A_1^{sat}}, \tag{14.7}$$

where A_1^{sat} is the headspace peak area for the pure liquid solute. As seen from Equation (14.7), γ_1^∞ can be determined without knowing the solute vapour pressure, which is an important advantage, if p_1^{sat} value is not known accurately or even missing. However, it should be noted that this calibration route is practical only for systems exhibiting enhanced positive deviations from ideality ($\gamma_1^\infty > 10$), or else the measured HSA response (A_1) and its calibration (A_1^{sat}) become prohibitively disparate. Options (though less convenient) might be then to calibrate with the vapour above a highly dilute solution of the given solute in a different solvent in which γ_1^∞ is known [46] or to make use of a different solute as the reference with known γ_{ref}^∞ as an internal standard.

Variations of equipment and procedures for applying HSA are almost as numerous as the literature references themselves. In the simplest version, manual sampling of headspace with a syringe is employed [47,48]. Apart from obvious inconvenience, the problem with such a sampling is a rather indeterminate temperature of the sample and its possible adsorption or condensation in the syringe. Due to a difference of the headspace pressure and the ambient pressure, precision gas-tight, valve-locking syringes must be used to avoid uncontrolled sample dilution. Commercial headspace gas chromatographs, the earliest use of which is described in the work of Rohrschneider [46], may offer complete automation and a great improvement of precision, but their flexibility for accurate thermodynamic measurements is sometimes limited. *Ad hoc* headspace analysers have been therefore constructed for the measurement of limiting activity coefficients, the customized design improving especially the process of equilibration and sample transfer. The most notable HSA device was built by Hussam and Carr [4] at the University of Minnesota. This multiple cell apparatus with an assembly of valves implementing the sample transfer by vacuum yielded in the 1980s and in the first-half of 1990s a considerable amount of accurate data [17,49,50]. A new modification with a single cell and a solvent dosing pump to vary the composition of a solution in the cell continues to be equally productive [51]. Multi-cell instruments similar in design to that used in Minnesota have been described recently by Whitehead and Sandler [52] and Asprion *et al.* [53], the latter authors using, however, a vial pressurization system for the sample transfer.

The recent implementation of HSA method at the Prague Institute of Chemical Technology [54] employs a single equilibrium cell to which solute is added gravimetrically and the vapour phase is continuously circulated through the liquid phase and the gas-sampling valve of GC by an inert pump. A similar arrangement was used as early as 1967 by Pollak and Cave [55]. It has distinct advantages over designs with "pressure-vent" or "vent-to-vacuum" sampling techniques, in particular absence of any perturbation of the equilibrium during sampling, rapid equilibration and suppression of sorption effects due to continuous sample renewal.

The direct HSA method yields under good conditions a target precision of 1–5 per cent. It is a reliable technique applicable to wide ranges of solvent and solute volatilities. The lower limit of the solute volatility is imposed only by the GC sensitivity and its upper limit is related to the fact that the composition of the liquid phase to be used in Equations (14.6) or (14.7) is established from the synthetic, gravimetric or volumetric, preparation of the solution. While for a low solute volatility from solution ($K^{gl} < 0.001$), the correction for the material in the headspace is negligible, for a very high solute volatility ($K^{gl} > 0.1$) it may become critical, thereby limiting the applicability of this method. Sampling and

analysing both the gas and the liquid phase may resolve the problem, but the procedure is then rather cumbersome. Indirect HSA methods, conveniently utilizing the principle of mass balance constrained partitioning, offer an attractive alternative.

14.3 Static Mass Balance Methods

In a closed equilibrium gas–liquid system, the concentration of a given volatile solute in either phase depends on the gas-to-liquid volume ratio $\beta = V^g/V^l$. The interrelation is governed by the mass conservation and the condition of equilibrium, the latter being represented in the region of infinite dilution by the solute partition coefficient K^{gl}. By measuring the solute equilibrium concentration in one of the phases as a function of β, the partition coefficient, as a parameter in this relation, can then be determined. The principle of the mass balance constrained VLE partitioning forms also a basis of some extraction techniques where the solute is depleted from one phase by means of the other phase in a defined manner. The reported procedures deal mostly with gas phase and use headspace GC as a sensitive and selective analytical tool. By their nature the static mass balance methods are best suited for solutes exhibiting greatly enhanced volatilities from their highly dilute solutions and, as a result, they have been almost invariably applied to aqueous organics.

14.3.1 Equilibrium Partitioning in Closed Systems

The equilibrium partitioning in closed systems (EPICS) method developed by Lincoff and Gossett [56] involves a comparison of the equilibrium headspace concentrations c_1^g and $(c_1^g)'$ of a solute in two identical closed vessels whose solvent loadings V^l and V'^l are widely different. The masses of the solute m_1 and m_1' in the two vessels are equal or their ratio is known [57]. The headspace solute concentrations are determined by GC and, assuming proportional GC responses, K^{gl} is obtained from this measurement as follows:

$$K^{gl} = \frac{1 - r}{r\beta' - \beta}, \tag{14.8}$$

where

$$r = \frac{A_1' V'^l / m_1'}{A_1 V^l / m_1}. \tag{14.9}$$

Since the method involves determination of relative rather than absolute concentrations, no calibration is required. Further advantages are that no special apparatus is needed and the measurement can be easily automated using a commercial headspace analyser.

The EPICS method has become popular in the community of environmental researchers who have applied it to a variety of aqueous solutes [58–61]. Experience and theoretical error analysis [57,59] show that the technique is inherently well suited for solutes exhibiting greatly enhanced values of the gas–liquid partition coefficient, the

appropriate range being $0.1 < K^{gl} < 1$. In the indicated range the precision of this technique is moderate (about 5 per cent), but for lower K^{gl} values it deteriorates markedly. By combining the EPICS method with the solid-phase micro-extraction (SPME) sampling technique, Dewulf *et al.* [62] have recently achieved a partial improvement in precision of the determination of lower solute volatilities, basically because the SPME allowed the use of higher loading ratios V'^{l}/V^{l}.

A technique similar to EPICS and called vapour-phase calibration (VPC) was proposed by Kolb *et al.* [63]. In this technique equal small amounts of a solute under study are injected into two headspace vials of an identical volume V, one vial being originally empty and the other containing the solvent of a volume V^{l}. The one-phase system prepared by the total vaporization of the solute in the former vial serves as an external standard for the headspace of the latter vial where the solute undergoes vapour–liquid partitioning. Provided the detector is linear, the respective partition coefficient K^{gl} is obtained by the VPC technique without determining the exact composition of liquid phase from

$$K^{gl} = \frac{A_1 V^{l}}{A_1^{c} V - A_1 (V - V^{l})}, \tag{14.10}$$

where A_1^{c} denotes the headspace peak area for the gas standard.

14.3.2 Phase Ratio Variation (PRV) Method

Ettre *et al.* [64] and Robbins *et al.* [65] developed independently a static mass balance technique that might be considered as an elegant improvement of the EPICS method. In their method, denoted as PRV, aliquots of a highly dilute solution having different volumes but the same concentration are introduced into a series of identical closed vessels and the equilibrated headspace samples are analysed by GC. Provided the GC response is proportional to the solute concentration, the reciprocal peak areas $1/A_1$ plotted against gas-to-liquid volume ratios β follow a straight line whose slope divided by its intercept yields the value of K^{gl}. For reliable results, the straight-line parameters should be evaluated by linear regression with appropriate statistical weighting factors, since the dispersions of the transformed experimental variables considerably vary within the dataset [66]. This procedure, which implies measuring more than just two necessary data points, not only increases the target precision, but provides a straightforward check of the internal consistency of measured data, including the GC response linearity.

As shown by Ramachandran *et al.* [67], an analogous procedure can be implemented also for the EPICS method, where the respective linear transformation is obtained by plotting $m_1/(A_1 V^{l})$ vs. β. The EPICS method and the PRV method are very similar. The essential advantage of the PRV method is that it avoids the direct dosing of very small solute amounts replacing it by the dosing of much larger amounts of a highly dilute working solution. The PRV method, in comparison to the EPICS method, gives a possibility to use significantly smaller liquid-phase loadings. Chai and Zhu [68] demonstrated, both experimentally and by means of error analysis calculations, that by using small liquid loadings the PRV method

can be extended to determine low gas–liquid partition coefficients ($K^{gl} \approx 0.001$). The target precision obtained with aqueous lower alkanols appears to be better than 10 per cent [69].

Vitenberg and coworkers [70] developed similar techniques based on mass conservation and variation of phase ratio for variable volume devices.

14.3.3 Headspace Stepwise Extraction Methods

McAuliffe [71] was the first who described a method to measure gas–liquid partition coefficients based on successive headspace extractions. In his implementation, a thermostatted gas-tight syringe was used to hold and manipulate the sample. The syringe was flushed with a highly dilute solution under study and a sample of it retained. The rest of the total syringe volume was then filled with an inert gas and the syringe closed. After equilibration, the gas phase was sampled and analysed. The entire gas phase was then discharged and replaced by the neat inert gas. The system was re-equilibrated and the gas phase was analysed again. If the GC response is proportional to solute headspace concentration, $\ln A_1^{(i)}$ values obtained in such a repetitive extraction decrease linearly with each step i according to the relation

$$\ln A_1^{(i)} = -i \ln(1 + K^{gl}\beta) + \ln A_1^{(0)}, \tag{14.11}$$

allowing K^{gl} to be determined from the slope.

A number of other researchers dealt with the multiple headspace extraction employing different experimental arrangements [72,73]. In their specialized set-up, Brown and Wasik [74] replaced the manual syringe by a valve with a sampling loop that provided direct injection of the gas phase onto GC. Allen *et al.* [75] presented recently a single-step extraction method using *in situ* optical absorbance measurements of the liquid phase. Incorporation of a spectrometer with fibre-optic dip probes permitted data to be collected without taking headspace samples and disturbing the equilibrium. Thanks to a large gas-to-liquid volume ratio ($\beta = 200$) of their apparatus, measurements of K^{gl} values as low as 10^{-4} were possible, though with a rather compromised precision of 10–15 per cent.

14.4 Rate Measurements on Continuous Gas–Liquid Separation Processes

14.4.1 Inert Gas Stripping

The method of inert gas stripping (IGS) to measure gas–liquid partitioning was first described and applied by Burnett in 1963 [76] but it was only in 1977, when Leroi *et al.* [77] substantially improved the experimental design and clearly demonstrated good performance and convenience of this technique promoting its later widespread use. Since then, the IGS technique has been applied to a great variety of systems and the experimental set-up and procedure has been further developed and modified to extend its applicability, few representative references of many relevant being [5,78–85].

The method consists in measuring the rate of elution of a solute as an entraining inert gas is passed through a highly dilute solution ($x_1 < 10^{-3}$) kept well mixed and under isothermal conditions in an equilibrium-stripping cell. The inert gas is introduced into the cell and dispersed in small bubbles, at a constant flow rate. The outlet gas, assumed to be in equilibrium with the liquid solution in the cell, is periodically analysed for the solute content by gas chromatography to determine the rate of the solute removal. The temperature T, the total pressure p, the flow rate of the pure inert gas entering the cell F, the total amount of solvent in the cell n_2 and the detector response (peak area) to the solute A_1 as a function of time t are measured. As shown by Leroi *et al.* [77], when the partial pressure of the solute is small compared with the total pressure, vapour-phase non-ideality corrections and the effect of the vapour space of the cell are neglected, the rate of the solute elution from a non-volatile solvent follows a simple exponential first-order kinetics pattern. Provided the detector is linear, the limiting activity coefficient can be determined from the measurements outlined above as follows:

$$\gamma_1^{\infty} = \frac{n_2 RT}{p_1^{\mathrm{sat}} F} \left(- \frac{\mathrm{d} \ln A_1}{\mathrm{d}t} \right), \tag{14.12}$$

with a plot of $\ln A_1$ against t giving a straight line.

For solvents of appreciable volatility, the amount of the solvent in the cell decreases during the experiment, which requires the use of another, more complicated relation to calculate γ_1^{∞} [77] and imposes some experimental restrictions. Thus, a simpler and preferred practice applicable to volatile solvents is to keep n_2 constant by pre-saturating the stripping gas with the solvent vapour. Upon the pre-saturation, the flow rate of the stripping gas changes by a factor $1/(1 - p_2^{\mathrm{sat}}/p)$ and then

$$\gamma_1^{\infty} = \frac{n_2 RT}{p_1^{\mathrm{sat}} F} \left(- \frac{\mathrm{d} \ln A_1}{\mathrm{d}t} \right) (1 - p_2^{\mathrm{sat}}/p). \tag{14.13}$$

The approximation provided by Equations (14.12) or (14.13) is often sufficiently accurate. However, when a better accuracy is needed or the simplifying assumptions underlying Equations (14.12) and (14.13) are violated appreciably, *e.g.* for solutes of high volatility ($H_{12} > 1$ MPa), these simplifications should be eliminated. This leads to rather involved relations [76,78]. Alternatively, using a perturbation approach, the above given equations can be amended by respective correcting factors [5]; *e.g.* Equation (14.13) may be then extended, leaving out the vapour-phase non-ideality correction, as $\gamma_1^{\infty} = \gamma_1^{\infty}$ (Eq 13) $\xi_1 \xi_2$ where

$$\xi_1 = 1 - \frac{(\bar{n}_1/n_2)\gamma_1^{\infty} p_1^{\mathrm{sat}}}{p - p_2^{\mathrm{sat}}} \tag{14.14}$$

corrects for the change of the stripping gas flow rate due to the saturation of the gas stream by solute vapour in the cell, and

$$\xi_2 = 1 + \frac{\gamma_1^{\infty} p_1^{\mathrm{sat}} V^{\mathrm{g}}}{n_2 RT} \tag{14.15}$$

accounts for the amount of the solute in the vapour space of the cell assuming its complete mixing. In these equations, $\bar{n}_1$ is the mean amount of the solute in the cell during the measurement obtained from

$$\bar{n}_1 = n_1^0(A_1^f/A_1^0 - 1)/\ln(A_1^f/A_1^0), \tag{14.16}$$

where n_1^0 is the initial solute amount in the cell, A_1^f and A_1^0 are the GC responses to the solute at the end and at the beginning of the IGS experiment, respectively and V^g denotes the vapour space volume. As seen from Equations (14.14) and (14.15), the effects of ξ_1 and ξ_2 compensate partially and this is what makes the uncorrected formulae given above to work quite well at moderately enhanced solute volatilities. Nevertheless, for high $H_{12} = \gamma_1^\infty p_1^{sat}$, the corrections ξ_1 and ξ_2 considerably increase and it is necessary to take them into account. To keep these corrections and the involved uncertainty small, it is recommendable to minimize the vapour space and to use solutions as dilute as possible. Another convenient possibility is to perform a relative measurement [85] using a suitable internal standard; if its Henry's law constant is equal to that of the examined solute, the corrections cancel completely.

The basic pre-requisite for correct performance of the method is that equilibrium is attained between the gas and the liquid phase in the stripping cell. This is obviously dependent on the residence time of a bubble in the liquid, the bubble size and many physicochemical properties of the solute–solvent system. Mass transfer calculations give some insight into this problem [80]. The real situation in the cell is, however, much more complex, so the design of the cell and its operation is therefore largely empirical. In general, the diameter of bubbles should be as small as possible (preferably $\leq$1 mm) and their coalescence suppressed. Fine porosity frits, narrow bore capillaries or special perforated tips can be used for the purpose. The coalescence can be avoided only at low flow rates of the stripping gas when the number of bubbles in the solution is small. Keeping F small also helps to eliminate the liquid droplet entrainment and other undesirable effects. The suitable working range of the flow rates can be identified by examining the effect of the inert gas stripping flow rate on the measured value of γ^∞. Stripping gas flow rates as low as $0.2\,cm^3 \cdot s^{-1}$ appear to be required for aqueous solutions of volatile hydrophobic solutes [5,85]. A vigorous stirring contributes substantially to appropriate equilibration. Not only does it provide the necessary composition uniformity of the liquid, but also dramatically changes hydrodynamic conditions in the cell. A vortex is formed and, by virtue of its suction, bubbles are held in the liquid for a considerably longer time. The equilibration in a vigorously mixed system is further supported by the enlargement of the vapour–liquid interface and its constant renewal resulting from the vortex formation. A well-known general condition for the appropriate equilibration in all dynamic phase-equilibrium separation processes is to maintain a sufficiently low rate in the separation. Experience acquired with a variety of systems studied over the years at the Prague Institute of Chemical Technology indicates that this condition is met for the IGS technique at relative elution rates $0.01\,min^{-1}$ or lower. To cope efficiently with this requirement, one should have the possibility of choosing for each system the equilibrium cell of a suitable volume.

Major advantages favouring the IGS technique over some other methods are its applicability to a broad range of solute volatilities, its accuracy, no need for the calibration of the

GC detector and no or rather marginal importance of knowing exactly the initial solute concentration. The IGS method is suitable for systems where $10\,\text{kPa} < H_{12} < 10^5\,\text{kPa}$ and $p_2^{\text{sat}} < 50\,\text{kPa}$, for which the best target uncertainty (1 per cent) can be attained. Measurements outside these ranges can be done, but a compromised accuracy is then inevitable. For analytical convenience, the GC analysis of the gas phase may be replaced by that of the liquid phase [84] or other analytical techniques can be employed [86]. Obvious problems with highly viscous and foaming systems can be overcome using the special cell design of Richon *et al.* [81]. The IGS method has been shown to be well suited also for measuring γ_1^∞ in mixed solvents [87–89].

14.4.2 Exponential Saturator Method

The method of the exponential saturator (EXPSAT) [90] is a novel technique that has been recently developed for accurate determination of large limiting activity coefficients at the Prague Institute of Chemical Technology. This technique is similar to that of inert gas stripping but contrary to stripping it deals with the reverse process, *i.e.* with saturation. The essence of the method consists in measuring the rate of solvent saturation by the solute when an inert gas pre-saturated with the solute vapour is passed through the solvent in the equilibrium cell. The EXPSAT method is inherently suited for solutes of high limiting activity coefficients ($\gamma_1^\infty > 1000$) and enhanced volatilities ($H_{12} > 1$ MPa), being thus an ideal tool to study aqueous solutions of hydrophobic organics.

A scheme of the EXPSAT experimental set-up is shown in Figure 14.2. The equilibrium cell, kept at constant temperature T and pressure p, is composed of two compartments,

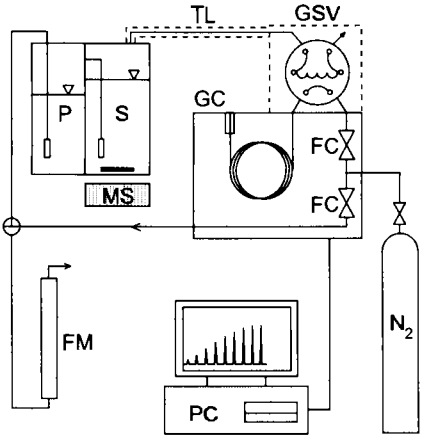

Figure 14.2 Schematic diagram of the EXPSAT experimental setup. GC, gas chromatograph; GSV, thermostated pneumatic gas sampling valve; TL, heated transfer line; P, pre-saturator of the EXPSAT cell; S, saturator of the EXPSAT cell; MS, magnetic stirrer; N_2, inert gas source; FC, digital mass flow controllers; FM, bubble flow meter; PC, personal computer. (Reproduced with permission from reference [90]. Copyright 1999 Am. Chem. Soc.)

pre-saturator and saturator, which are loaded with pure solute and a known amount n_2 of pure solvent, respectively. The saturator contents are thoroughly mixed. The inert gas is firstly introduced into the solute in the pre-saturator and dispersed in small bubbles, at a constant flow rate F. The gas, being thus saturated with the solute vapour, proceeds into the saturator where it is again dispersed into small bubbles. Some of the solute carried by the gas stream dissolves in the solvent, forming a highly dilute solution of a continuously increasing concentration. The outlet gas, equilibrated with the dilute solution formed, is periodically analysed to monitor the progress of solvent saturation. The rate of solute absorption, which is highest at the beginning of the process, continuously diminishes and, for highly non-ideal solutions assumed, the solute concentration in the cell thus approaches exponentially a steady-state value corresponding to the solubility according to the Henry's law.

Considering high dilution and detector linearity, it can be shown that the GC response (solute peak area) A_1 as a function of time obeys the following equation:

$$\frac{p_1^{\text{sat}}}{p - p_1^{\text{sat}}} \frac{A_1}{A_1^{\infty}} - \ln\left(1 - \frac{A_1}{A_1^{\infty}}\right) = \frac{\gamma_1^{\infty} p_1^{\text{sat}}}{(1 - p_1^{\text{sat}}/p)^2(1 - p_2^{\text{sat}}/p)} \frac{F}{n_2 RT} t, \qquad (14.17)$$

where A_1^{∞} denotes the GC response at the steady state. Written in the form $Y(A_1) = kt$, Equation (14.17) indicates that a plot of Y against t gives a straight line through the origin, the slope k being the time constant of the saturation process from which γ_1^{∞} can be calculated. It is also seen that no external calibration of the detector is needed provided the measurements are carried out until the steady state is effectively attained. To obtain the time constant k, the $Y(t)$ data should be fitted to a straight line by the *weighted* least-squares method. Appropriate statistical weighting is essential here, because uncertainties in the transformed variable Y vary greatly as a result of the propagation of analytical errors. For best accuracy, it is also necessary to modify Equation (14.17) by incorporating corrections for some minor technical effects complicating the basic EXPSAT principle, namely for the vapour space of the cell, for a pressure drop between the pre-saturator and the saturator, and for a rather indeterminate time origin of the experiment.

Accord of EXPSAT measurements with data obtained by various well-established methods has been demonstrated [90] over broad ranges of solution non-idealities ($500 < \gamma_1^{\infty} < 10^5$) and solute volatilities (1 MPa $< H_{12} <$ 100 MPa). Close agreement found between values measured by the EXPSAT and the IGS methods is especially important. Since the mass transfer processes in these two gas–liquid partitioning techniques approach the equilibrium from opposite directions, this agreement indicates that appropriate equilibration is attained in the both experimental techniques.

The determination of gas–liquid partitioning characteristics (H_{12}, K^{gl}) and limiting activity coefficients can be done very precisely, typically with an uncertainty of 1–2 per cent. With the EXPSAT method, there is no need for external calibration of the involved analytical method or for the preparation of any solution of a known concentration. Another major advantage is that the typical lengthy dissolution of a hydrophobic liquid to prepare the dilute solution to be studied, as required *e.g.* in the IGS method, is avoided, since the solution in the EXPSAT method is formed by absorbing the solute from the vapour phase in the course of the measurement process itself.

14.5 Distillation Methods

In these types of methods, one-stage distillation devices are employed to determine the solute limiting relative volatility and to this end two characteristic *liquid* samples are taken and analysed, the ratio of their concentrations rather than the absolute values of their concentrations being decisive. As a rule, analytical methods yielding a proportional response to the solute concentration are used because then no calibration is needed. The treatment involves the approximation $\alpha_{12}^{\infty} = \lim_{x_i \to 0}(y_1 x_2 / y_2 x_1) \cong y_1/x_1$ and hence, to keep it accurate, sufficiently dilute solutions must be used. The greater the departure of α_{12}^{∞} from unity, the higher the dilution required. The two samples taken are either those of the initial solution to be distilled and the distillation remainder (Rayleigh distillation) or those of the equilibrium liquid and the vapour phase condensate (differential distillation, circulation still).

14.5.1 Rayleigh Distillation Method (RDIST)

In the present variant of the Rayleigh distillation method (RDIST), developed at the Prague Institute of Chemical Technology [6], a known mass of a highly dilute solution ($x_1 < 10^{-3}$) is subjected to the one-stage distillation, which is accomplished by bubbling an inert gas through the thermostatted and vigorously stirred solution under study. Having distilled off a suitable amount of the original solution, the remainder is weighed and, using a suitable analytical method, the ratio of the solute concentrations in the original solution and in that remained is determined. Assuming proportionality of the analytical response to the solute concentration and leaving out the vapour-phase non-ideality correction, one can readily calculate the limiting activity coefficient as follows:

$$\gamma_1^{\infty} = \frac{p_2^{\text{sat}}}{p_1^{\text{sat}}} \left[1 + \frac{\ln(A_1/A_1^0)}{\ln(m/m^0)} \right], \tag{14.18}$$

where m^0, m are the masses of the solution before and after the stripping, respectively, and A_1^0, A_1 are the corresponding analytical responses.

In an early variant of this method, employed in 1950s by Russian investigators Zelvenskii and Shalygin [91], the distillation was performed in a classical manner by boiling the solution at a given pressure. However, this mode of distillation, necessarily involving superheating and being realized at a high distillation rate, could not be a truly equilibrium one. On the other hand, the rate of the isothermal distillation promoted by inert gas stripping can be well controlled and kept sufficiently low. In the present design, the inert gas (N_2) dispersed into small diameter bubbles by means of a frit is introduced into about 35 cm^3 of a highly dilute solution continuously mixed in the glass equilibrium cell. The flow rates below 0.6 $cm^3 \cdot s^{-1}$ (0.2 $cm^3 \cdot s^{-1}$) for non-aqueous (aqueous) solutions typically ensure complete saturation of the inert gas by the solution vapour. The attainment of the equilibrium conditions can be verified by repeated measurements at varied flow rates.

The present RDIST method is both very simple and very accurate. Its good performance has been demonstrated for various systems, non-aqueous [6,92] and aqueous ones

[54]. The technique can be regarded as a hybrid of the classical distillation and the inert gas stripping. The main difference from the IGS method is that neither the inert gas flow rate nor the time needs to be measured. The method has been shown to be well suited for systems with appreciably volatile solvents and solute relative volatilities in the range $1 < \alpha_{12}^{\infty} < 70$, for which it can safely reach precision of 1 per cent if the extent of the distillation is properly set according to the error analysis to minimize analytical errors [6]. For less volatile solvents and α_{12}^{∞} close to unity rather long distillation times are required; since no operator attendance is required during the distillation experiments this may not be however a serious drawback.

14.5.2 Differential Distillation

In this technique [93], a relatively small amount is distilled off by one-stage equilibrium flask-to-flask distillation from a batch of a highly dilute solution under study so that its composition remains effectively unchanged. Samples of the collected distillate and the batch solution are then analysed by a suitable analytical method. Provided the analytical response is proportional to the solute concentration and vapour-phase non-ideality is neglected, the ratio of the responses for the distillate and the batch solution, $A_1^{\mathrm{g}}/A_1^{\mathrm{l}}$, gives directly α_{12}^{∞} and hence

$$\gamma_1^{\infty} = \frac{p_2^{\mathrm{sat}}}{p_1^{\mathrm{sat}}}\left(\frac{A_1^{\mathrm{g}}}{A_1^{\mathrm{l}}}\right). \tag{14.19}$$

The stripping by an inert gas at isothermal conditions is used instead of heating to conduct the distillation as an equilibrium process. The procedure resembles the transpiration technique for the determination of vapour pressures of pure substances and it is sometimes referred to by this name. Some variants of the differential distillation method exist in which only a captured vapour-phase sample is analysed [94]; here however must be the analytical method calibrated, the composition of liquid phase known and the passed amount of inert gas measured.

Differential distillation (DDIST) is a simple old technique that proved its good performance in early thermodynamic studies of dilute solutions [95,96]. Current examinations of the DDIST method at the Prague Institute of Chemical Technology show that under some ordinary experimental precautions, this technique yields accurate results. Although by its nature DDIST is not suitable for systems with $\alpha_{12}^{\infty} \gg 1$, it is a unique technique giving prospects to study solutions with $\alpha_{12}^{\infty} \ll 1$ that can be hardly studied by other methods. Since relatively large batches of solution are required for differential distillation experiments, this technique is to be mainly used with water or some other inexpensive solvents.

14.5.3 Measurements by Circulation Stills

A VLE circulation still may be alternatively used to provide samples with corresponding vapour and liquid equilibrium compositions in the region of high dilution [97–100]. The still is operated at a constant, usually atmospheric or sub-atmospheric, pressure maintained by a manostat. As the solution is highly dilute, its boiling temperature is practically

indistinguishable from that of the pure solvent at a given pressure and hence no measurement of temperature is needed. Measurements by circulation stills are practical in a range of about 30 K below the normal boiling temperature of the solvent. If the samples of the equilibrium phases are analysed by a method responding proportionally to the solute concentration, the value of γ_1^∞ is obtained as in the case of DDIST method from Equation (14.19). This method performs well for systems with moderate departures of α_{12}^∞ from unity, normally $0.1 < \alpha_{12}^\infty < 30$. With increasingly greater departures of α_{12}^∞ from unity, exceedingly longer times are needed to obtain representative equilibrium samples and much depends on the quality and operation of the still since any possible imperfection becomes then critical. Under good conditions, the target uncertainty appears to be within 3–5 per cent [98,100].

14.6 Concluding Remarks

Most of the techniques for the determination of limiting activity coefficients described here are capable of a reasonable precision of 5 per cent or better. However, as often encountered, differences in results obtained by different methods and/or different laboratories can be considerably larger than the combined stated uncertainties. This typical situation is illustrated in Figure 14.3a for 1-butanol in water. The literature data shown, despite being in abundance and over a temperature interval of 80 K, hardly allow any temperature dependence to be determined because of a huge scatter.

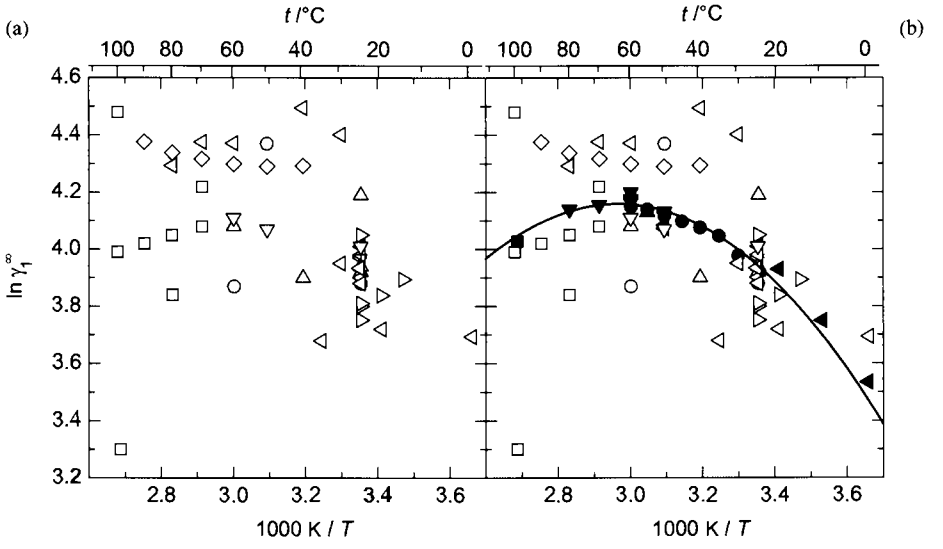

Figure 14.3 Limiting activity coefficient of 1-butanol in water as a function of temperature. In (a) values from the literature measured by □, ebulliometry; ○, tensimetry; △, GLC; ▽, relative GLC; ◇, PRV; ◁, HSA; ▷, IGS; and in (b) these amended with values from the author's laboratory measured by ■, circulation still; ●, tensimetry; ▲, NSGLC; ◀, HSA; ▼, RDIST; together with the simultaneous fit of all γ_1^∞ data with calorimetric data on limiting partial molar excess enthalpies and heat capacities.

There are many problems that may complicate the measurement of limiting activity coefficients and adversely affect the accuracy of results. The principal sources of systematic error in the determination of limiting activity coefficients are: interfacial adsorption; incomplete equilibration; incomplete separation of phases; failure to account properly for vapour space or hold-up; impurity effects; volatilization losses; lack of linearity of the analytical response; and inaccurate vapour pressure data for pure components. Nature of each individual measurement method dictates its sensitivity to these various types of systematic error and the possibility of its application to a certain type of system and conditions. None of the methods is sufficiently universal; the applicability is constrained especially by the volatilities of components, their solubility or the non-ideality of their mixture, temperature and other analytical and chemical factors. In order to obtain accurate results, the recommended policy is therefore to select for each particular case a suitable experimental method, respecting its inherent features and considering the characteristics of the system to be studied. Application of two or more suitable techniques is desirable; if the results mutually agree, their credibility will greatly increase. In case the objective is to establish $\gamma_1^\infty(T)$ in a broader temperature range, the use of several experimental methods is unavoidable due to the applicability limitations. The route of choice for determining $\gamma_1^\infty(T)$ consists then in combining the γ_1^∞ data with calorimetric data on limiting partial molar excess enthalpies and heat capacities and processing the information simultaneously by a thermodynamically consistent treatment [54]. The result of the outlined procedure for 1-butanol in water shown in Figure 14.3b is seen to resolve efficiently the issue indicated by Figure 14.3a.

In summary, since measurement versatility can be achieved only through a diversity of methods of complementary character, further developments in experimental determination of γ_1^∞ are still required. Methods applicable to low solute volatilities ($\alpha_{12}^\infty \ll 1$) have been still lacking and hence these are of a particular need.

References

1. Letcher, T.M., in *Experimental Thermodynamics, Vol II*, Ch. 2., B. Le Neindre and B. Vodar, eds., Butterworths, London, 1975.
2. Conder, J.R. and Young, C.L., *Physicochemical Measurements by Gas Chromatography*, Wiley, New York, 1979.
3. Orbey, H. and Sandler, S.I., *Ind. Eng. Chem. Res.* **30**, 2006, 1991.
4. Hussam, A. and Carr, P.W., *Anal. Chem.* **57**, 793, 1985.
5. Hovorka, Š. and Dohnal,V., *J. Chem. Eng. Data* **42**, 924, 1997.
6. Dohnal, V. and Horáková, I., *Fluid Phase Equilibr.* **68**, 173, 1991.
7. Dohnal, V. and Novotná, M., *Fluid Phase Equilibr.* **23**, 303, 1985.
8. Tiegs, D., Gmehling, J., Medina, A., Soares, M., Bastos, J., Alessi, P. and Kikic, I., *Activity Coefficients at Infinite Dilution. Part 1, 2*, DECHEMA, Frankfurt/Main, 1986.
9. Gmehling, J., Menke, J. and Schiller, M., *Activity Coefficients at Infinite Dilution. Part 3, 4*, DECHEMA, Frankfurt/Main, 1994.
10. Alessi, P., Fermeglia, M. and Kikic, I., *Fluid Phase Equilibr.* **29**, 249, 1986.
11. Bergmann, D.L. and Eckert, C.A., *ACS Symp. Ser.* **509**, 218, 1992.
12. Eckert, C.A. and Sherman, S.R., *Fluid Phase Equilibr.* **116**, 333, 1996.

13. Sherman, S.R., Trampe, D.B., Bush, D.M., Schiller, M., Eckert, C.A., Dallas, A.J., Li, J. and Carr, P.W., *Ind. Eng. Chem. Res.* **35**, 1044, 1996.
14. Sandler, S.I., *Fluid Phase Equilibr.* **116**, 343, 1996.
15. Turner, L.H., Chiew, Y.C., Ahlert, R.C. and Kosson, D.S., *AIChE J.* **42**, 1772, 1996.
16. Kojima, K., Zhang, S. and Hiaki, T., *Fluid Phase Equilibr.* **131**, 145, 1997.
17. Dallas, A.J. and Carr, P.W., *J. Phys. Chem.* **98**, 4927, 1994.
18. Zhang, Y., Dallas, A.J. and Carr, P.W., *J. Chromatogr.* **638**, 43, 1993.
19. Castells, R.C., Romero, L.M. and Nardillo, A.M., *J. Chromatogr. A* **848**, 203, 1999.
20. Romero, L.M., Filgueira, M.R., Gagliardi, L.G., Nardillo, A.M. and Castells, R.C., *Phys. Chem. Chem. Phys.* **1**, 3351, 1999.
21. Barker, P.E. and Hilmi, A.K., *J. Gas Chromatogr.* **5**, 119, 1967.
22. Pemberton, R.C. and Mash, C.J., *NPL Rep. Chem. (UK, Natl. Phys. Lab., Div. Chem. Stand.)* **33**, 1, 1974.
23. Barr, R.S. and Newsham, D.M.T., *Fluid Phase Equilibr.* **35**, 189, 1987.
24. Olsson, A.-M., Mathiasson, L., Jonsson, J.A. and Haraldson, L., *J. Chromatogr.* **128**, 35, 1976.
25. Bayles, J.W., Letcher, T.M. and Moollan, W.C., *J. Chem. Thermodyn.* **25**, 781, 1993.
26. Thomas, E.R., Newman, B.A., Long, T.C., Wood, D.A. and Eckert, C.A., *J. Chem. Eng. Data* **27**, 399, 1982.
27. Gaile, A.A., Proskuryakov, V.A., Semenov, L.V., Pul'tsin, M.N., Parizheva, N.V., Zakharov, A.P., Apter, Yu.M. and Solodova, N.I., *Limiting Activity Coefficients of Hydrocarbons in Specific Solvents: A Handbook*, St Petersburg State University, St Petersburg, 2002.
28. Mash, C.J. and Pemberton, R.C., *NPL Rep. Chem. (UK, Natl. Phys. Lab., Div. Chem. Stand.)* **111**, 1, 1980.
29. Cooling, M.R., Khalfaoui, B. and Newsham, D.M.T., *Fluid Phase Equilibr.* **81**, 217, 1992.
30. Khalfaoui, B. and Newsham, D.M.T., *Fluid Phase Equilibr.* **98**, 213, 1994.
31. Heintz, A., Kulikov, D.V. and Verevkin, S.P., *J. Chem. Eng. Data* **46**, 1526, 2001.
32. Heintz, A., Kulikov, D.V. and Verevkin, S.P., *J. Chem. Eng. Data* **47**, 894, 2002.
33. Heintz, A., Kulikov, D.V. and Verevkin, S.P., *J. Chem. Thermodyn.* **34**, 1341, 2002.
34. Letcher, T.M. and Deenadayalu, N., *J. Chem. Thermodyn.* **33**, 1697, 2001.
35. Letcher, T.M., Soko, B., Ramjugernath, D., Deenadayalu, N., Nevines, A. and Naicker, P.K., *J. Chem. Eng. Data* **48**, 708, 2003.
36. Letcher, T.M., Soko, B., Reddy, P. and Deenadayalu, N., *J. Chem. Eng. Data* **48**, 1587, 2003.
37. Freeguard, G.F. and Stock, R., in *Gas Chromatography*, Ch. 7, M. Van Swaay, ed., Butterworths, London, 1962.
38. Tassios, D.P., *Ind. Eng. Chem. Process Des. Dev.* **11**, 43, 1972.
39. Tse, G., Orbey, H. and Sandler, S.I., *Environ. Sci. Technol.* **26**, 2017, 1992.
40. Belfer, A.J., *Neftekhimiya* **12**, 435, 1972.
41. Belfer, A.J. and Locke, D.C., *Anal. Chem.* **56**, 2485, 1984.
42. Landau, I., Belfer, A.J. and Locke, D.C., *Ind. Eng. Chem. Res.* **30**, 1900, 1991.
43. Belfer, A.J., Locke, D.C. and Landau, I., *Anal. Chem.* **62**, 347, 1990.
44. Dohnal, V. and Ondo, D., *J. Chromatogr. A*, submitted.
45. Kolb, B. and Ettre, L.S., *Static Headspace-Gas Chromatography. Theory and Practice*, Wiley, New York, 1997.
46. Rohrschneider, L., *Anal. Chem.* **45**, 1241, 1973.
47. Przyjazny, A., Chrzanowski, W.W. and Staszewski, R., *J. Chromatogr.* **280**, 249, 1983.
48. Hansen, K.C., Zhou, Z., Yaws, C.L. and Aminabhavi, T.M., *J. Chem. Eng. Data* **38**, 546, 1993.
49. Park, J.H., Hussam, A., Couasnon, P., Fritz, D. and Carr, P.W., *Anal. Chem.* **59**, 1970, 1987.
50. Cheong, W.J. and Carr, P.W., *J. Chromatogr.* **500**, 215, 1990.
51. Castells, C.B., Eikens, D.I. and Carr, P.W., *J. Chem. Eng. Data* **45**, 369, 2000.

52. Whitehead, P.G. and Sandler, S.I., *Fluid Phase Equilibr.* **157**, 111, 1999.
53. Asprion, N., Hasse, H. and Maurer, G., *J. Chem. Eng. Data* **43**, 74, 1998.
54. Hovorka, Š., Dohnal, V., Roux, A.H. and Roux-Desgranges, G., *Fluid Phase Equilibr.* **201**, 135, 2002.
55. Pollak, P. and Cave, G.C.B., *Can. J. Chem.* **45**, 3089, 1967.
56. Lincoff, A.H. and Gossett, J.M., in *Gas Transfer at Water Surfaces*, W. Brutsaert and G.H. Jirka, eds., Reidel, Dordrecht, 1984.
57. Gossett, J.M., *Environ. Sci. Technol.* **21**, 202, 1987.
58. Ashworth, R.A., Howe, G.B., Mullins, M.E. and Rogers, T.N., *J. Hazard. Mater.* **18**, 25, 1988.
59. Dewulf, J., Drijvers, H. and Van Langenhove, H., *Atmos. Environ.* **29**, 323, 1995.
60. Ryu, S.A. and Park, S.J., *Fluid Phase Equilibr.* **161**, 295, 1999.
61. Gorgenyi, M., Dewulf, J. and Van Langenhove, H., *Chemosphere* **48**, 757, 2002.
62. Dewulf, J., Van Langenhove, H. and Everaert, P., *J. Chromatogr. A* **830**, 353, 1999.
63. Kolb, B., Welter, C. and Bichler, C., *Chromatographia* **34**, 235, 1992.
64. Ettre, L.S., Welter, C. and Kolb, B., *Chromatographia* **35**, 73, 1993.
65. Robbins, G.A., Wang, S. and Stuart, J.D., *Anal. Chem.* **65**, 3113, 1993.
66. Ramachandran, B.R., Allen, J.M. and Halpern, A.M., *Anal. Chem.* **68**, 281, 1996.
67. Ramachandran, B.R., Allen, J.M. and Halpern, A.M., *J. Chem. Educ.* **73**, 1058, 1996.
68. Chai, X.S. and Zhu, J.Y., *J. Chromatogr. A* **799**, 207, 1998.
69. Gupta, A.K., Teja, A.S., Chai, X.S. and Zhu, J.Y., *Fluid Phase Equilibr.* **170**, 183, 2000.
70. Vitenberg, A.G., Ioffe, B.V., Dimitrova, Z. and Butaeva, I.L., *J. Chromatogr.* **112**, 319, 1975.
71. McAuliffe, C., *CHEMTECH* **1**, 46, 1971.
72. Ioffe, B.V. and Vitenberg, A.G., *Head-space Analysis and Related Methods in Gas Chromatography*, Wiley, New York, 1984.
73. Miller, M.E. and Stuart, J.D., *Anal. Chem.* **72**, 622, 2000.
74. Brown, R.L. and Wasik, S.P., *J. Res. Natl. Bur. Stand.* **78A**, 453, 1974.
75. Allen, J.M., Balcavage, W.X., Ramachandran, B.R. and Shrout, A.L., *Environ. Toxicol. Chem.* **17**, 1216, 1998.
76. Burnett, M.G., *Anal. Chem.* **35**, 1567, 1963.
77. Leroi, J.C., Masson, J.-C., Renon, H., Fabries, J.-F. and Sannier, H., *Ind. Eng. Chem. Process Des. Dev.* **16**, 139,1977.
78. Duhem, P. and Vidal, J., *Fluid Phase Equilibr.* **2**, 231, 1978.
79. Mackay, D., Shiu, W.Y. and Sutherland, R.P., *Environ. Sci. Technol.* **13**, 333, 1979.
80. Richon, D., Antoine, P. and Renon, H., *Ind. Eng. Chem. Process Des. Dev.* **19**, 144, 1980.
81. Richon, D., Sorrentino, F.P. and Voilley, A., *Ind. Eng. Chem. Process Des. Dev.* **24**, 1160, 1985.
82. Endler, I., Hradetzky, G. and Bittrich, H.-J., *J. Prakt. Chem. (Leipzig)* **327**, 693, 1985.
83. Wobst, M. and Hradetzky, G., *Z. Phys. Chem. (Leipzig)* **269**, 555, 1988.
84. Hradetzky, G., Wobst, M., Vopel, H. and Bittrich, H.-J., *Fluid Phase Equilibr.* **54**, 135, 1990.
85. Li, J., Dallas, A.J., Eikens, D.I., Carr, P.W., Bergmann, D.L., Hait, M.J. and Eckert, C.A., *Anal. Chem.* **65**, 3212, 1993.
86. Nielsen, F., Olsen, E., Fredenslund, A., *Environ. Sci. Technol.* **28**, 2133, 1994.
87. Bao, J.-B. and Han, S.-J., *Ind. Eng. Chem. Res.* **35**, 2773, 1996.
88. Hovorka, Š., Dohnal, V., Carrillo-Nava, E. and Costas, M., *J. Chem. Thermodyn.* **32**, 1683, 2000.
89. Krummen, M., Gruber, D. and Gmehling, J., *Ind. Eng. Chem. Res.* **39**, 2114, 2000.
90. Dohnal, V. and Hovorka, Š., *Ind. Eng. Chem. Res.* **38**, 2036, 1999.
91. Zelvenskii, Ya.D. and Shalygin, V.A., *Zh. Fiz. Khim.* **31**, 1501, 1957.
92. Vrbka, P., Dohnal, V., Trejo, L.M. and Costas, M., *Fluid Phase Equilibr.* **137**, 133, 1997.
93. Andon, R.J.L., Cox, J.D. and Herington, E.F.G., *J. Chem. Soc.* **50**, 3188, 1954.
94. Christie, A.O. and Crisp, D.J., *J. Appl. Chem.* **17**, 11, 1967.

95. Butler, J.A.V., Ramchandani, C.N. and Thomson, D.W., *J. Chem. Soc.* 280–285, 1935.
96. Butler, J.A.V. and Ramchandani, C.N., *J. Chem. Soc.* 952–955, 1935.
97. Andon, R.J.L., Cox, J.D. and Herington, E.F.G., *Discuss. Faraday Soc.* **15**, 168, 1953.
98. Dohnal, V. and Fenclová, D., *J. Chem. Eng. Data* **40**, 478, 1995.
99. Olson, J.D., *Fluid Phase Equilibr.* **150–151**, 713, 1998.
100. Christensen, S.P., *Fluid Phase Equilibr.* **150–151**, 763,1998.

15 Measurement of Surface and Interfacial Tension

M.J.B. EVANS
Department of Chemistry & Chemical Engineering
Royal Military College of Canada
Kingston, Canada

Measurement of the Thermodynamic Properties of Multiple Phases
R.D. Weir and Th.W. de Loos (Editors)

15 MEASUREMENT OF SURFACE AND INTERFACIAL TENSION

The phenomena associated with the surface tension (ST) of liquids have attracted the attention of scientists, mathematicians, artists, and others for centuries. Many known more for contributions in other areas of science also showed an interest in the properties of liquid surfaces. The names of Gauss, Gibbs, Laplace, Lord Kelvin, and Thomas Young are associated with equations describing surface behaviour. Other prominent 19th and 20th century scientists including Bohr, Einstein, Schrödinger, and van der Waals published papers on some aspects of surfaces. The ephemeral beauty of soap bubbles has fascinated mankind for eons, and has been captured by such artists as Millais and Manet, and by countless photographers. The surface physics of these bodies has been discussed non-mathematically by Boys in his classic book on soap bubbles [1]. More recently, Isenberg [2] has written an equally fascinating account of the behaviour of soap films and their uses. No account of ST and interfacial tension (IFT) would be complete without the mention of D'Arcy Wentworth Thompson's book "On Growth and Form" [3] in which the influence of surface forces on the shapes of natural objects in the realms of zoology and botany is discussed with many striking illustrations.

The basic principles behind many of the methods developed over the past 150 years for the measurement of ST and IFT have not changed, but several of these methods have taken advantage of modern instrumentation to improve accuracy, reduce tedium, and to allow measurements to take place under what might be termed extreme conditions. The development of new industrial processes, including the production of ultra-pure semiconductors, high-performance polymers, and the manufacture of composites containing a variety of materials, involves techniques that depend critically on the ST of fluids. New processes for ceramic and metallurgical processing are being developed, in some instances following studies of ST effects under microgravity in orbiting laboratories.

The IFT at liquid–liquid phase boundaries is also of great significance in the field of emulsion technology. Emerging technologies in the biomedical field, the food industry, and in petroleum extraction provide further examples where the measurement and control of IFTs are of considerable importance. Here also, methods for the determination of the IFT have taken advantage of advances in image analysis and data processing. The once laborious task of deducing the IFT from the shape of an interface can now be done in seconds with the help appropriate optical equipment and a small computer. For several techniques, correction factors required in the calculation of ST from experimentally determined quantities can be calculated quickly and accurately, rather than having to interpolate tabulated values.

With few exceptions, static methods for the determination of ST and IFT are based on an equation that has generated considerable discussion over the question of the identity of its originator. The history of this debate would fill many pages, but for the purpose of this account, it will simply be referred to here as the Young–Laplace equation. One representation of the equation in its most general form relates the pressure difference across a fluid–fluid interface at a point to the mean curvature, J, of the interface at that point,

$$p^{\alpha} - p^{\beta} = \gamma J, \tag{15.1}$$

where p^{α} and p^{β} are the hydrostatic pressures in the bulk fluid phases α and β separated by the interface in question. The constant of proportionality, γ, is known as the ST or IFT. The equation was first stated in this form by Laplace in 1806 [4]. The mean curvature, J, can be expressed in terms of the principal radii of curvature of a surface at a point, R_1 and R_2,

$$J = \frac{1}{R_1} + \frac{1}{R_2}. \tag{15.2}$$

If an arc of infinitesimal length is drawn through any point on a curved interface, the arc lying in the surface, and then the arc is rotated about the normal to the surface passing through that point until its radius is at a maximum, this radius and that of the orthogonal arc drawn through the same point and also lying in the surface are the principal radii of curvature of the surface at that point. For a spherical bubble, the two radii are equal and have the same value at all points on the interface. A cylinder is also a constant curvature surface, one principal radius of curvature being infinite, the other being the radius of the cylinder. However there are other surfaces of constant curvature for which R_1 and R_2 vary with position on the surface. Of these, the catenoid is perhaps the best known, it being the surface formed by rotation about the x-axis of the catenary

$$y = c_1 \cosh\left(\frac{x - c_2}{c_1}\right), \tag{15.3}$$

where c_1 and c_2 are constants. The catenoid has, in fact, zero mean curvature, since at all points on its surface the radii of curvature are equal but opposite in sign.

Constant curvature surfaces are formed in zero gravity or under pseudo zero gravity situations such as exist for systems of two immiscible fluids having the same density. The interface in such systems is spherical if it is not in contact with a solid, or that of a figure of revolution of a catenoid, nodoid or an unduloid. These shapes are illustrated in Figure 15.1. Plateau [5] was the first to show that the limiting length of the unduloid [Figure 15.1(f)] was π times its diameter. The stability of some of these shapes in a gravitational field is of critical concern in the electronics industry, where the growth of ultra-pure single crystals by the floating zone technique is the key to the manufacture of microelectronic devices containing silicon, germanium, or other semiconductors.

In addition to a number of methods for the determination of ST and IFT under static conditions, there are several techniques that used to be described as detachment methods. These involve forming an interface and slowly extending it until instability arises. These are not strictly static methods, so they should be used with caution for the determination of ST and IFT in systems where slow migration of species to or from an interface may occur. However, two of these so-called detachment methods described below can, in fact, be modified to measure ST and IFT under conditions that are essentially static.

The third class of methods for ST and IFT measurement involves processes such as the motion of capillary waves and oscillating of jets or drops, which are the traditional methods used for studying surface ageing effects. More recently, measurement of changes in ST and IFT has become possible over both short and long time scales by the use of high-speed

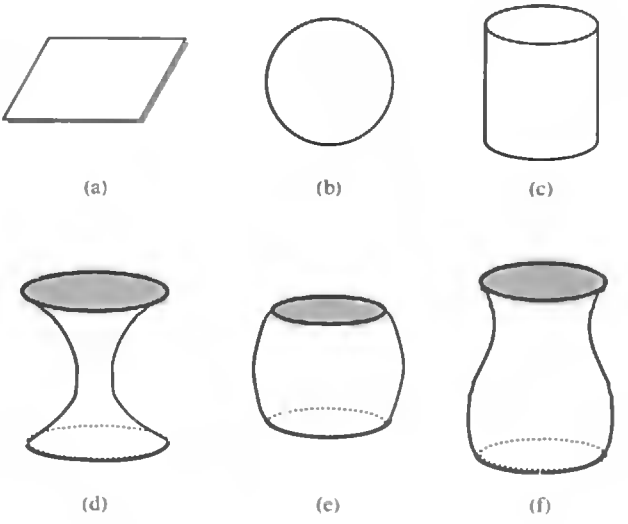

Figure 15.1 The six possible types of surfaces having constant curvature: (a) plane; (b) sphere; (c) cylinder; (d) catenoid; (e) nodoid; (f) unduloid. The last four are shown in contact with solid disks.

data acquisition systems and computer control with several of the techniques described in Sections 15.3 and 15.4.

15.1 Terminology

Recommended terminology and symbols in colloid and surface chemistry were published by the Commission on Colloid and Surface Chemistry including Catalysis in 1972 [6]. As indicated in that document, the term surface tension is normally used when one is considering the interface between a liquid and a gas or vapour. The more general term interfacial tension (IFT) is used when the interface in question is between two condensed phases, although it can be used for any type of interface. The fact that interfaces have finite thickness is not relevant to any discussion of the experimental determination of ST and IFT, since these quantities are defined as the tension that would exist per unit length in the interface if it were a layer of zero thickness separating two phases. Also, the issue of whether there exists a line tension along the line of contact of three phases in equilibrium is not considered here.

Although IUPAC recognizes both γ(gamma) and σ(sigma) as symbols for ST or IFT, the former seems to appear more commonly in the literature, and will be used here. Where a distinction between static and dynamic values needs to be made, γ^{st} will be used for the former, and γ^{dyn} for the latter. On some occasions, it is necessary to distinguish between the IFT between various phases, in which case $\gamma^{\alpha\beta}$ would represent the IFT between phases α and β. To avoid ambiguity, the ST of a liquid α in a system containing more than one condensed phase would be represented by γ^{α}.

Since from their definitions, the dimensions of ST and IFT are force per unit length, these quantities are usually expressed $mN \cdot m^{-1}$. The value in $mN \cdot m^{-1}$ is conveniently the same as in $dyne \cdot cm^{-1}$, the units used in most older publications.

15.2 Static Methods

15.2.1 Capillary Rise and Related Methods

To a first approximation the capillary rise h of a liquid in a capillary tube of radius r is given by the Young–Laplace equation [Equation (15.1)] in the form

$$h\Delta\rho g = \frac{2\gamma}{r\cos\theta}, \tag{15.4}$$

where $\Delta\rho$ is the difference in density between the liquid and the gas or vapour in equilibrium with it, g the acceleration due to gravity, and θ the contact angle between the liquid and the wall of the tube, measured through the liquid. Figure 15.2 illustrates the simple set-up required. For higher precision, the temperature should be controlled, and corrections made for the gravitational distortion of the meniscus. If the liquid completely wets the capillary, which is normally made of glass, *i.e.* $\theta = 0$, the correction is easily made using tables such as those of Sugden [7] and the ST calculated.

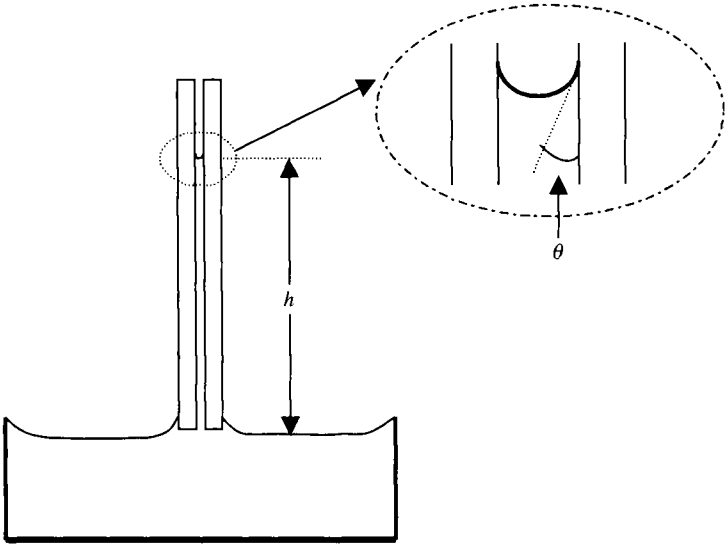

Figure 15.2 Capillary rise experiment. Inset shows contact angle, θ, at the three phase line of contact for a liquid that does not wet the tube material, *i.e.* $\theta > 0$.

If the radius of curvature at the lowest point of the meniscus is b, and the contact angle zero, then the exact form of Equation (15.4) is

$$h\Delta\rho g = \frac{2\gamma}{b}. \tag{15.5}$$

The smaller the tube radius, the closer will the value of b be to the tube radius, or in other words, the closer the meniscus will be to a hemisphere. Defining the capillary constant, a, as

$$a = \left(\frac{2\gamma}{\Delta\rho g}\right)^{\frac{1}{2}}, \tag{15.6}$$

then

$$a^2 = bh. \tag{15.7}$$

Using the tube radius as the first approximation for b, measurement of h enables an initial estimate of a to be calculated, and hence a value for r/a. Sugden's table giving r/b for various values of r/a is then used iteratively until the value of a does not change between iterations. Tables have also been compiled by Padday and Pitt [8], among others. In order to avoid error due to capillary rise in the annular ring between the tube and the liquid reservoir, the diameter of the latter should be at least 15 times that of the capillary tube. Thus, the method is not suitable when only a small volume of liquid is available. For a thorough description of the method and other options for making corrections to obtain the value of ST, see, for example, Adamson and Gast [9].

The capillary rise method can be adapted for the measurement of the IFT between two liquids. Other variations of the method have been introduced to allow measurement of ST when only small quantities of the liquid are available. Of these, the capillary u-tube technique first used by Sugden [7] is the best known. The apparatus consists simply of two capillaries of different internal diameters joined in the form of a U as illustrated in Figure 15.3(a). If the liquid completely wets the tube material, the difference in height, h, between the menisci in the two branches of the U is measured and the two tube radii. If the radii of the two tubes are r_1 and r_2, then

$$h\Delta\rho g = \gamma\left(\frac{1}{r_2} - \frac{1}{r_1}\right). \tag{15.8}$$

Correction for the gravitational distortion of the menisci using tables referred to above greatly increases the accuracy of the result. The correction procedure is slightly more cumbersome than with the simple method since two tube radii are involved, but if one radius is considerably smaller than the other, little error is introduced and the process much simplified by assuming that the meniscus in the smaller tube is hemispherical. An ingenious

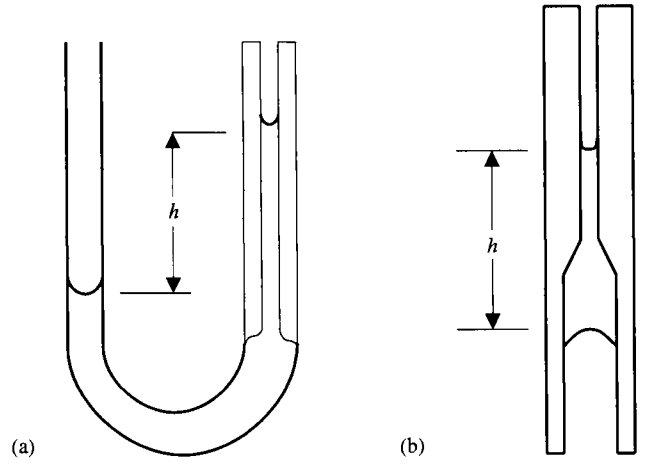

Figure 15.3 Differential capillary rise: (a) U-tube method; (b) Natelson and Pearl's method [9].

variation on this method that has received scant attention was described by Natelson and Pearl [10], who used the technique to determine the ST of biological fluids. Applicable in situations where the amount of liquid available is of the order of 0.1 mL, two capillary tubes of different radius are joined and held vertically, with the smaller tube uppermost, as shown in Figure 15.3(b). A drop of liquid is introduced into the tube and allowed to adjust to its equilibrium configuration. The length of the column of liquid, h, represents the difference between the pressure drop across each of the liquid–vapour interfaces. Assuming the tube radii and the density of the liquid are known, the ST can be calculated using Equation (15.8) and Sugden's correction factors. The method can also be used to determine the IFT between two immiscible liquids of known density.

For systems in which the liquid does not completely wet the solid, the capillary rise methods are less convenient than most other techniques, many of which do not require measurement or knowledge of the contact angle.

15.2.2 Drop and Bubble Shape Methods

The equation of Young and Laplace in its general form [Equation (15.1)] can be used to describe the profile of any static axisymmetric drop or bubble in a gravitational field. If the vertical axis of symmetry is chosen as the z-axis, and a horizontal tangent to the base or apex of the drop or bubble is chosen as the x-axis, the profile of the fluid body lies in the x–z plane. For a pair of immiscible fluids of different density, four configurations are possible. If one of the phases is a gas or vapour and the other a liquid, the four possibilities are referred to as pendent and sessile drops, and captive and emergent bubbles. Profiles of these fluid bodies are illustrated in Figure 15.4.

Taking the pendent drop as an example, if the pressure difference across the interface at the base of the drop is $h\Delta\rho g$, then at some point (x, z) on the profile above the base of the

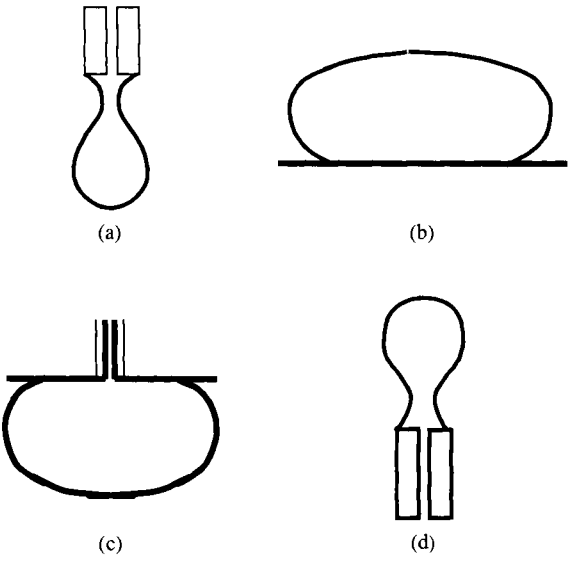

Figure 15.4 Four axisymmetric fluid bodies in a gravitational field, each constrained by contact with a solid surface: (a) pendent drop; (b) sessile drop; (c) captive bubble; (d) emergent bubble.

drop, the pressure difference is $(h - z)\Delta\rho g$. Thus for any point on the profile, the Young–Laplace equation can be written as

$$(h - z)\Delta\rho g = \gamma\left(\frac{1}{R_1} + \frac{1}{R_2}\right), \tag{15.9}$$

R_1 and R_2 being the principal radii of curvature of the interface at that point. One can express R_1 and R_2 in terms of x and the angle Φ between the tangent to the profile at point (x, z) and the horizontal. The relationships are $R_1 = \mathrm{d}x/\mathrm{d}(\sin\Phi)$, $R_2 = x/\sin\Phi$. To avoid problems in solving these equations by numerical integration, it is convenient to use as the independent variable the distance s along the profile from the origin rather than x. Equation (15.9) then becomes

$$(h - z)\Delta\rho g = \gamma\left(\frac{\mathrm{d}\Phi}{\mathrm{d}s} + \frac{\sin\Phi}{x}\right), \tag{15.10}$$

since

$$\mathrm{d}(\sin\Phi) = \cos\Phi, \quad \text{and} \quad \cos\Phi = \frac{\mathrm{d}x}{\mathrm{d}s}. \tag{15.11}$$

Before using these equations to calculate pendent drop profiles, it is usual to use dimensionless quantities for the coordinates and for h, the hydrostatic pressure across the interface

at the origin. Two approaches have been used, one dating back more than a century to the publication in 1883 of tables of pendent and sessile drop shapes by Bashforth and Adams [11]. Their tables were based on calculations mostly made by C. Powalky, as was fleetingly acknowledged by Bashforth and Adams. The tables, which required a vast number of calculations involving Taylor series expansions to be performed by hand, are remarkable for their extent and even more so for their accuracy. Extensions to the pendent drop tables have been published by Fordham [12] and for sessile drops by White [13] among others. A collation of several sets of tables for pendent and sessile drop profiles was published by Padday [14], and computer-generated tables of profiles of several types of axisymmetric fluid bodies have been produced by Hartland and Hartley [15]. However, the availability of high-speed desk-top computers has largely rendered these tables obsolete since profiles can be computed rapidly as required [16].

Bashforth and Adams introduced a shape factor β defined by the equation

$$\beta = \frac{-\Delta\rho g b^2}{\gamma}, \tag{15.12}$$

where b is the radius of curvature at the origin. Dimensionless parameters were then obtained by dividing x and z by b. The alternative approach is to use the capillary constant a, defined by Equation (15.6) to obtain dimensionless quantities $X\,(=x/a)$, $Z\,(=z/a)$ and the shape factor $H\,(=h/a)$. Either way, the system of differential equations can be solved to generate drop profiles for various shape factors, which can then be compared with experimentally determined profiles. The ST of the liquid can be deduced if the densities of the liquid and the surrounding phase are known. Inversion of these calculated profiles gives those of emergent bubbles, while those of sessile drops and captive bubbles, can be generated by changing $(h - z)$ in Equation (15.10) to $(h + z)$. A strong argument for the use of H as the shape factor rather than β, and reducing drop dimensions by dividing by a rather than b to obtain reduced quantities is that for any given liquid, the relative sizes of drops are the same in terms of their real and their reduced dimensions if a is used as the reducing parameter. This is not true when using b, since it is a function of β. One can also compare drop volumes directly when H is used, but not when β is the shape factor.

The task of comparing the profiles of drops and bubbles with those calculated by the numerical integration of Equations (15.10) and (15.11) has been greatly simplified by the use of imaging systems supported by computer software developed for the purpose. A number of axisymmetric drop shape analysis (ASDA) systems for the determination of ST and IFT and, for sessile drops, contact angle are now available commercially. In a recent discussion of the various strategies used for drop shape analysis, del Río and Neumann [17] examined several variations in the analytical procedure which usually involves the use of the fourth- or higher-order Runge–Kutta method to solve what is known as an initial value problem [18]. They concluded that measurement of the volume and equatorial diameter of a sessile drop can be used to estimate the ST to within 2 per cent. The same comment applies to pendent drops with a neck. Better accuracy (<0.5 per cent) is obtained when the fitting procedure is based on the measurement of the coordinates of a number of points on the profile of a drop. This option seems to have been adopted by several of the designers of the

commercially available ASDA systems. In a comprehensive review of drop shape analysis techniques, Lahooti *et al.* [19] discuss the optimal number of data points and the effects of various systematic errors as well as the experimental set-up. They also describe extension of the method for the determination of ultra-low IFTs (*ca.* 5×10^{-3} mN · m^{-1}) and use the method as an alternative to a film balance to study the change in surface pressure with area of an interface.

15.2.3 Spinning Drop Method

Despite the name, this technique is indeed a static method, and the one method well suited for the determination of extremely low IFTs, such as are found in studies of micro-emulsions. A small bubble, or quantity of a liquid of lower density is introduced into a liquid in a horizontally mounted precision-bore glass tube. After sealing the ends of the tube, it is rotated about its horizontal axis, the centrifugal field causing the drop or bubble to elongate (see Figure 15.5). At a sufficiently high speed of rotation, which can be in excess of 15 000 rpm, the drop or bubble is more or less cylindrical in shape. Under such conditions, the potential energy at a distance r from the axis of revolution is $\omega^2 r^2 \Delta\rho/2$, where ω is the speed of revolution, $\Delta\rho$ the density difference. Integrating this quantity from 0, the axis of revolution, to r_0, the radius of the drop, the potential energy of the drop due to the centrifugal forces is $\pi\omega^2\Delta\rho r_0^4 l/4$, l being the length of the cylindrical drop. The interfacial free energy of the drop is $2\pi r_0 l\gamma$, and its volume $\pi r_0^2 l$, so that its total energy, E, is given by

$$E = (\pi\omega^2\Delta\rho r_0^4 l/4) + 2\pi r_0 l\gamma. \tag{15.13}$$

In the steady state for the rotating drop, the differential of E with respect to r_0 will be zero, hence, since the drop volume is $\pi r_0^2 l$,

$$\gamma = \frac{\omega\Delta\rho r}{4}. \tag{15.14}$$

The justification of this equation, first presented by Vonnegut [20] has been discussed by Princen *et al.* [21], who also analysed the situation for rotating drops and bubbles for which the assumption of cylindrical shape was invalid, as is the case when the ST or IFT is large.

The method has been used particularly in academic and industrial research on emulsions and micro-emulsions, including studies of enhanced oil recovery, where low IFTs are

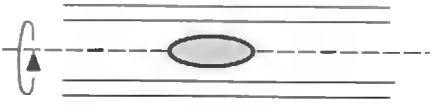

Figure 15.5 Spinning drop method for the determination of surface tension. Droplet or bubble elongated by rotation of horizontal capillary tube about its axis.

exploited in order to facilitate displacement of an organic liquid phase by surfactant solutions. Use of the technique has recently been extended to studies of the IFT and coalescence of polymer melts [22]. Commercial instruments are available which manufacturers claim can be used to determine IFTs from 1 $mN \cdot m^{-1}$ to as low as 10^{-6} $mN \cdot m^{-1}$.

Normally, a drop of the less dense organic phase is placed in the capillary tube, the remainder of the tube being filled with the denser aqueous phase, which wets the glass. In systems where the organic phase is the denser of the two fluids, the tube has to be rendered hydrophobic to prevent the drop of the aqueous phase forming a pendular ring in the tube. This extension of the spinning drop technique has been successfully demonstrated by Cai and Mohanty [23], who determined the IFT between dense non-aqueous phase liquids and aqueous surfactant solutions.

15.2.4 Oscillating Drop Method

This technique offers the benefit of there being no contact between the liquid and any potentially contaminating surface. First discussed by Raleigh [24], it has recently been used for the determination of the ST of liquids including molten metals under both normal gravity and microgravity. A droplet of liquid is acoustically or electromagnetically levitated, and the frequency of small-amplitude oscillations in the assumed spherical droplet is determined.

As shown by Raleigh, the frequency of oscillation is a function of the drop density, ρ, and its ST. For the Lth resonant mode,

$$f_L^2 = \frac{L(L+2)(L-1)\gamma}{\rho R^3} \tag{15.15}$$

where R is the radius of the spherical drop. An account of the investigation that involves acoustic levitation of droplets of several pure liquids and solutions by Trinh *et al.* [25] includes discussion of the effects of viscosity and other sources of experimental uncertainty. Uncertainties of less than 6 per cent in the value of the ST were claimed. However, in an analysis of the frequency spectrum arising from the oscillation of non-spherical acoustically or electromagnetically levitated drops, Suryanarayana and Bayazitoglu [26] have shown that by the appropriate assignment of spectral groups, the uncertainty in the ST can be reduced to close to 1 per cent. In a later paper, Bayazitoglu and co-workers extended their analysis to electromagnetically levitated molten metal drops [27] and showed that it is possible to assign unambiguously the frequencies of oscillation, thus enabling the technique to be used to determine with greater accuracy the ST of liquid metals and alloys under normal gravity and in microgravity experiments.

15.3 Quasi-Static ("Detachment") Methods

The four methods described in this section are all commonly used to determine the static ST of liquids. Interfacial tensions can also be determined by suitable modification of the

techniques, albeit with larger uncertainties. Although often referred to as detachment methods, two of the four methods can, in fact, be used in a manner that does not involve any sudden detachment of a fluid from a solid surface. For the other two methods in which detachment always occurs, namely the drop volume–weight and the maximum bubble pressure methods, some dynamic effects may be observed if the rate of drop or bubble production is varied. Thus these methods should be used with caution where dynamic effects are to be expected.

15.3.1 Drop Volume–Weight

The determination of ST and IFT from the mass or volume of a drop that detaches from the lower tip of a vertically mounted tube is based on experimental data obtained by Harkins and Brown [28] for a number of liquids. Although the advent of computers has provided the tool that would allow the analysis of the dynamics of drop detachment to be undertaken, those employing the method for the determination of ST and IFT still use the table of empirical correction factors determined by Harkins and Brown, portions of which are found in many textbooks on surfaces and on physical chemistry. In discussing this method, reference is sometimes made to Tate's law, which may be expressed mathematically as

$$mg = 2\pi r\gamma, \tag{15.16}$$

m being the mass of liquid that detaches from the base of a tube of radius r. Tate in fact only claimed that "the weight of a drop of liquid is proportional to the diameter of the tube in which it is formed" [29]. The actual mass of liquid hanging from a tube is given by the equation

$$mg = 2\pi r\gamma \sin \Phi - \pi r^2 \gamma \left(\frac{1}{R_1} + \frac{1}{R_2} \right), \tag{15.17}$$

the first term on the right-hand side representing the vertical component of the ST forces acting around the line of contact of the drop with the tube tip. The second term is due to the pressure difference across the interface at the three-phase line of contact, R_1 and R_2 being the radii of curvature of the interface at this point. If the drop is allowed to grow, a portion of it will eventually detach (see Figure 15.6). The mass or volume of the detached drop is then determined. Harkins and Brown [28] determined the mass of a large number of drops mostly of water or benzene that fell from glass tubes of various diameters. They also used brass tubes for some experiments on water. They analysed their results using two "corrected" versions of Equation (15.16), namely

$$mg = 2\pi r\gamma f\left(\frac{r}{a}\right), \tag{15.18}$$

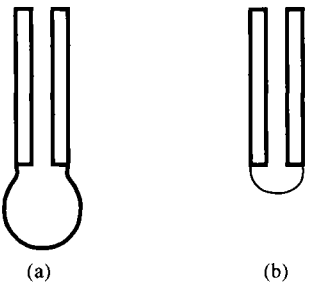

Figure 15.6 Drop weight/volume method showing (a) drop prior to detachment, and (b) residual drop following detachment.

and

$$mg = 2\pi r\gamma f\left(\frac{r}{V^{1/3}}\right), \tag{15.19}$$

where m is the mass of the detached drop and V the volume of the drop that falls. The correction factors $f(r/a)$ and $f(r/V^{1/3})$ are often assumed (erroneously) to represent the fraction of the drop that actually falls. From the drop masses, tube diameters, STs, and densities of the liquids used, Harkins and Brown plotted $f(r/a)$ against (r/a), and $f(r/V^{1/3})$ against $(r/V^{1/3})$. They found all their data fell on smooth curves. The original curves, or tabulated data taken from them, are used as the basis of the drop volume–weight method despite the fact that only a very limited range of liquids was used to produce them. The data of Harkins and Brown have also been fitted to a polynomial expression by Lando and Oakley [30], who then used the equation to generate a table of $f(r/V^{1/3})$ for a wide range of $(r/V^{1/3})$ values. An extension of the tables of Harkins and Brown to lower values of $r/V^{1/3}$ to allow use of the method for the determination of STs of molten metals has been produced by Wilkinson and Aronson [31] using measurements on pure mercury. More recently a study of the ST of molten refractory metals in ultra-high vacuum [32] included the following empirical relationships between the correction factor and $r/V^{1/3}$,

$$f\left(\frac{r}{V^{1/3}}\right) = 0.998 - \frac{1.073r}{V^{1/3}}, \quad 0.06 < \frac{r}{V^{1/3}} < 0.17 \tag{15.20}$$

$$f\left(\frac{r}{V^{1/3}}\right) = 0.992 - \frac{1.2355r}{V^{1/3}} + 1.161\left(\frac{r}{V^{1/3}}\right)^2, \quad 0.17 < \frac{r}{V^{1/3}} < 0.30. \tag{15.21}$$

The authors made no reference to the work of Wilkinson and Aronson, whose values of $r/V^{1/3}$ differ from those predicted by Equations (15.20) and (15.21) by less than 2 per cent.

Several manufacturers presently produce drop volume systems, often referred to as tensiometers, for the determination of ST and IFT. The drop is generally dispensed from syringe fitted with a glass or stainless-steel capillary tube, the end of which is carefully

ground so as to be perpendicular to the bore. The tip should be roughened slightly to ensure that it is completely wetted by the liquid, so that the three-phase line of contact is at the outer edge of the tip. Either the volume or the mass of the detached drop is determined. One advantage of the method over those in which the liquid is held in a reservoir is that ST measurements can be made when as little as $250 \times 10^{-6}\,cm^3$ of liquid is available. The speed at which the drop forms can usually be varied to determine whether or not ageing of the interface occurs due to diffusion to or from the surface, but at too high a drop rate hydrodynamic effects can lead to erroneous values of ST. Studies on the use of the drop weight method to determine dynamic STs have established an empirical relationship between drop rate and drop mass for liquids having viscosities in the range (0.39–15.4) cP [33]. Using this relationship, the equilibrium ST can be determined from the masses of drops detaching at several drop rates. The simplicity of the method is attractive, but, as discussed in later sections, there are several methods for the measurement of dynamic ST and IFT that do not depend on any correction factors or empirical relationships, and are therefore more reliable for the determination of the dynamic properties of interfaces.

15.3.2 du Noüy Ring

One of the most commonly used method for routine ST measurement, and also one of the quickest and simplest techniques, the du Noüy ring method [34], like the drop weight method, requires the use of a correction factor. Unlike the empirical correction factor of drop weight method, this can be calculated precisely using the Young–Laplace equation, as was first done by Freud and Freud [35]. Tables of an empirical correction factor published by Harkins and Jordan [36] are also still used, as they are easier to use than the graphs of Freud and Freud. In a paper in which the theory of ring tensiometry is analysed rigorously, Huh and Mason [37] found that Harkins and Jordan's values of the correction factor agreed with those obtained by Freud and Freud to within 0.5 per cent for ST, and 1 per cent for IFT measurement.

The method uses a horizontally positioned wire ring made of an inert material such as platinum or platinum–iridium alloy, suspended from a balance or force transducer. To determine the ST of a liquid, the ring is immersed below the surface of the liquid that is contained in a cylindrical vessel of diameter considerably larger than that of the ring. The vessel is then slowly lowered until the ring first reaches the surface of the liquid and then raises a meniscus attached to the ring (Figure 15.7). The force acting on the ring is monitored until it reaches a maximum, after which it falls sharply before the ring finally breaks away from the liquid surface. In automated versions of the apparatus now available commercially, the maximum force can be measured without the ring detaching from the surface of the liquid. The reservoir may then be raised and the experiment repeated several times to determine whether there are any time dependent changes in the ST due to adsorption or the migration of species to or from the interface. When operated in this mode detachment is avoided, and the method is not subject to the criticism that the system is not at equilibrium at the critical moment in the measurement as is the case for the drop weight method.

Assuming that the ring is completely wetted by the liquid, then the downward forces acting on the ring arise from the ST of the liquid, and the mass of liquid is raised above the

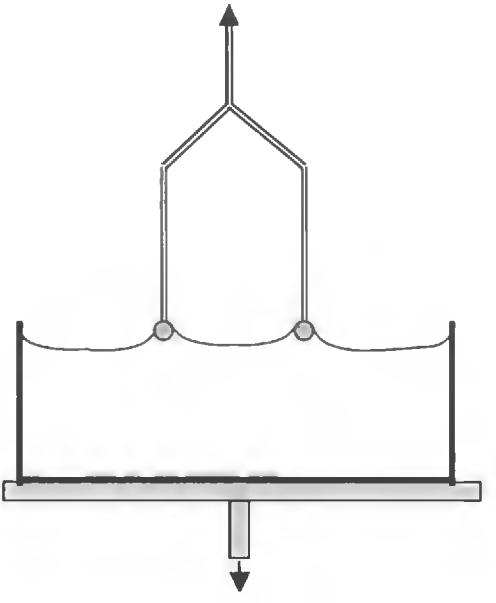

Figure 15.7 du Noüy ring method in which a platinum-iridium ring suspended from a force transducer is pulled from the surface of a liquid as the reservoir is slowly lowered. The maximum force prior to detachment is measured.

general level of liquid in its reservoir. Neglecting the latter, and assuming that the ST forces act vertically on the ring, then to a first approximation

$$f = 4\pi R\gamma, \tag{15.22}$$

where R is the ring radius. The radius of the wire, r, is assumed to be negligible compared to R. Clearly this relationship is erroneous, for the reasons already mentioned. However, as with the drop weight method, the introduction of a correction factor into this equation allows one to determine the ST of the liquid from the measurement of either the maximum force or the applied force at the moment of detachment. A clear distinction should be made between these two quantities, as the former can be significantly larger than the latter. The tables of Harkins and Jordan [36] contain values of the correction factor as a function of two dimensionless variables, R^3/V and R/r. The meniscus volume, V, is determined from the measured force and the density of the liquid.

Several factors contribute to the accuracy of the method. These include the flatness of the ring, its horizontal positioning, and the wettability of the ring, which strongly depends on its cleanliness. The method can easily be adapted to measure the IFT between two liquids. The reservoir can either be moved upwards or downwards through the interface, and the maximum force measured just prior detachment. The direction of motion should be such that the ring starts in the liquid that completely wets it. Padday [38] cautions that problems can arise due to the inconsistent contact angle between the ring and the two liquids at the

three-phase line of contact. However, provided that one of the liquids completely wets the ring, this potential source of error is no greater than that encountered in measuring the ST of a liquid that does not completely wet the ring.

A number of manufacturers offer du Noüy ring tensiometers ranging from simple manually operated torsion balances to fully automated instruments employing electronic microbalances and data acquisition systems. The more advanced versions can be operated over several ranges, with resolution claimed to be within $\pm 0.1\ \text{mN} \cdot \text{m}^{-1}$.

15.3.3 Wilhelmy Plate

This method first described by Wilhelmy [39] also involves measurement of the force acting on a solid as it is pulled from the surface of a liquid. Traditionally, the solid is a rectangular glass microscope slide suspended from a balance or force transducer and partially immersed in the test liquid with its longer edge horizontal. Modern versions of the apparatus utilize a microscopically roughened platinum plate that often reduces the contact angle to zero, and also allows easier cleaning and hence more reproducible behaviour. The technique is often preferred to that of du Noüy since it does not suffer from some of the experimental difficulties inherent in the ring method, particularly problems arising from distortion of the ring and the difficulty of positioning it horizontally. However it is not as well suited to the determination of IFT as the du Noüy ring method.

The downward force on the plate due to ST acting at an angle θ to the vertical (Figure 15.8) is given by

$$f = 2\gamma(l + t)\cos\theta, \tag{15.23}$$

where l and t are the length and thickness of the plate, respectively. If the liquid does not completely wet the plate, the contact angle θ must be known. The buoyancy of the portion of the plate that is immersed must also be taken into account. The buoyancy correction can be eliminated by either raising the plate, or lowering the reservoir, until the lower edge of the plate is at the general level of the liquid. The force exerted on the plate at this point is then measured. Justification of the above equation has been examined by Lillebuen [40], Jordan and Lane [41], and Princen [42], who also addresses the problem of the uncertainty in the length of the plate perimeter introduced by roughening the plate. Pre-equilibration of the plate with vapour is recommended.

By careful manual operation of the apparatus, or by the use of automatic control, the motion of the reservoir can be reversed shortly after the force maximum has been reached, and the experiment repeated several times without the slide becoming detached from the liquid surface, thus allowing one to determine whether the ST is changing due to the existence of some dynamic process. Like the ring method, and unlike the drop weight method, the Wilhelmy plate method can therefore be operated in a static mode.

There are a number of computer controlled Wilhelmy plate tensiometers available commercially. The control and measurement system is usually configured such that both the ST and contact angle can be measured and also the density of the liquid. Typically, ST values

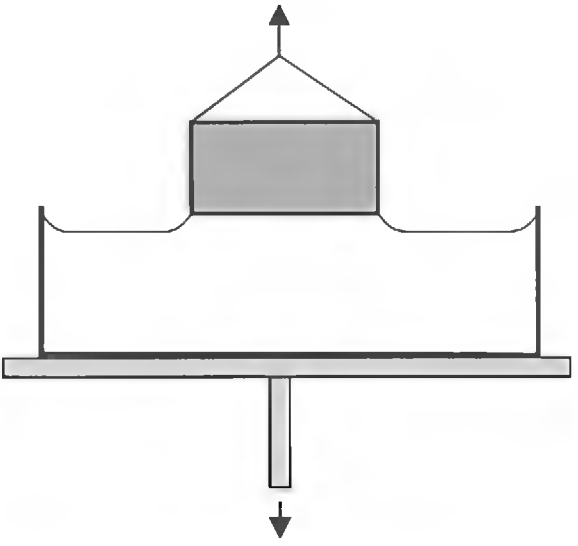

Figure 15.8 Wilhelmy slide (plate) method in which a roughened platinum plate is pulled from the surface of the liquid by lowering the reservoir. The maximum force prior to detachment is measured.

can be measured with a resolution of $\pm 0.1\,\mathrm{mN \cdot m^{-1}}$ to an accuracy of $\pm 0.2\,\mathrm{mN \cdot m^{-1}}$. Interfacial tension can also be determined, but the need to apply buoyancy corrections can reduce the accuracy of such measurements.

15.3.4 Maximum Bubble Pressure

The maximum bubble pressure (MBP) method first used by Sugden [43,44], like the drop weight method, is one that does not require elaborate equipment, but can also be fully automated so as to allow repeated measurement. An inert gas of low solubility in the liquid is used to form bubbles at the lower end of a vertically mounted capillary tube partially immersed in the liquid. As a bubble grows, the pressure within it increases until it reaches a maximum value. The pressure then decreases as the bubble volume increases further, until the bubble detaches and makes its way to the surface of the liquid. In the absence of gravitational distortion, the maximum pressure within the bubble would occur when the bubble was hemispherical, since the radius of curvature is at a minimum at this point. Sugden used the tables of Bashforth and Adams [11] to draw up a table of correction factors for gravitational distortion. If the tip at which the bubbles are formed is a distance h beneath the surface of the liquid, the pressure difference between the gas in the bubble and that in the surrounding atmosphere in the absence of gravitational distortion of the meniscus is given by

$$\Delta p = h\Delta\rho g + 2\frac{\gamma}{r}, \tag{15.24}$$

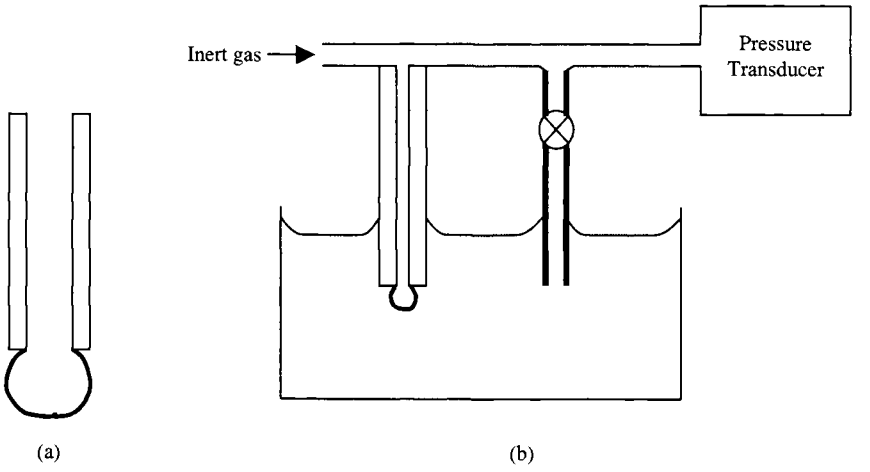

Figure 15.9 Maximum bubble pressure method showing (a) gas bubble development at the end of a tube, and (b) differential version of the technique in which bubbles form at the base of the narrower tube when the stopcock is closed, and at the base of the wider tube when it is open.

where r is the bubble radius. In reality, the bubble is flattened by gravity, as it is formed trapped below the capillary tube under the liquid surface. Its profile is that of a captive bubble, *i.e.* an inverted sessile drop. If the liquid completely wets the tube material, as shown in Figure 15.9, the three-phase line of contact has a radius equal to that of the internal radius of the tube. For bubbles formed at a tip beneath a non-wetting liquid, as would occur with a glass tube in liquid mercury, the line of contact would be around the outer edge of the tip.

As with the capillary rise method, to a first approximation the radius of curvature at the base of the bubble can be equated with the internal or external radius of the tube, depending on whether it is wetted or not. An iterative procedure similar to that used in the capillary rise method is then employed with Sugden's or similar tables to determine ST.

Some interesting variations on the technique have been devised. When operated as a differential method using two tubes of different diameters immersed to the same depth in the liquid, the need to know the depth of immersion is eliminated. This, and the fact that measurement of the pressure in the bubble can take place at some distance from the liquid, makes the method suitable for the determination of the ST of molten materials at high temperatures. If the density of the liquid is unknown, it can be determined by measuring the differential pressure and then lowering both tubes a known distance further into the liquid and measuring the differential pressure again.

Commercial MBP instruments are available from several manufacturers. The precision to which ST values can be determined is claimed to be of the order of $\pm 0.1\ \text{mN} \cdot \text{m}^{-1}$.

15.4 Dynamic Surface and Interfacial Tension

Many of the methods described above can also be used to determine changes in ST or IFT of newly created or perturbed interfaces as they progress towards equilibrium. The choice of the

most suitable method depends on several factors of which the time scale over which the variation in ST of IFT has to be measured is probably the most important. Another major consideration is the extent to which internal motion within one or both of the fluids resulting from the manner in which the interface is created influences transport phenomena in the system. The fact that in some methods the surface area of the interface necessarily changes during the measurement renders these methods less suitable for the study of changes in ST or IFT and other surface properties. In systems in which very short time scales following the creation of the interface are of interest, the oscillating or vibrating jet method, described below, is the most suitable. If changes in ST or IFT are to be monitored over time scales of minutes to hours, several of the standard static methods may be used, provided that the fluid motion or change in interfacial area inherent in some methods does not interfere with the processes leading to the establishment of equilibrium in the composition or structure of the interface. For recent detailed discussion of the pros and cons of the applicability of various static methods to dynamic tension studies, the review by Chang and Franses is recommended [45]. Horozov and Arnaudov [46] in a paper outlining a novel drop method, which is described briefly below, also make some useful comments on the suitability of various methods for the measurement of dynamic ST and IFT.

The speed and data storage capacity of currently available microcomputers allow drop shape techniques involving automatic image analysis to monitor changes in ST or IFT with sufficient rapidity to make the pendent drop and related methods suitable for the study of the dynamics of most interfacial phenomena. Acquisition rates of up to 25 images per second were reported several years ago [46] and are likely to continue to increase significantly. However, the time taken to form the drop may not allow measurement to begin as early in the life of the interface as might be required in some cases. Of the other static methods used for dynamic studies, the MBP method is still commonly used on account of its simplicity. Several variations in the method have been introduced and are described below. However, as with the drop weight method which is also occasionally used for dynamic studies, the MBP method is not able to furnish values of ST or IFT as an interface progresses towards equilibrium but rather an instantaneous value at a somewhat arbitrary point in the bubble's evolution when the interface undergoes a catastrophic change. Conditions can be varied so as to determine the ST or IFT at different times in the history of a number of similar bubbles, but the fact that the bubble area is not held constant introduces an additional variable that complicates attempts to use the method to study the dynamics of adsorption at an interface, for instance. Further comments on the suitability of the methods for dynamic studies can be found below.

15.4.1 Oscillating Jet Method

First described by Lord Rayleigh in 1879, the method involves measurement of the distance, λ, between nodes of an oscillating jet of liquid issuing from an elliptical orifice [47] (Figure 15.10). If ST of the liquid changes with time due to adsorption, then the distance between the nodes will vary as the interface approaches its equilibrium state by the migration of species to or from the surface. Instead of Raleigh's original equation, a more

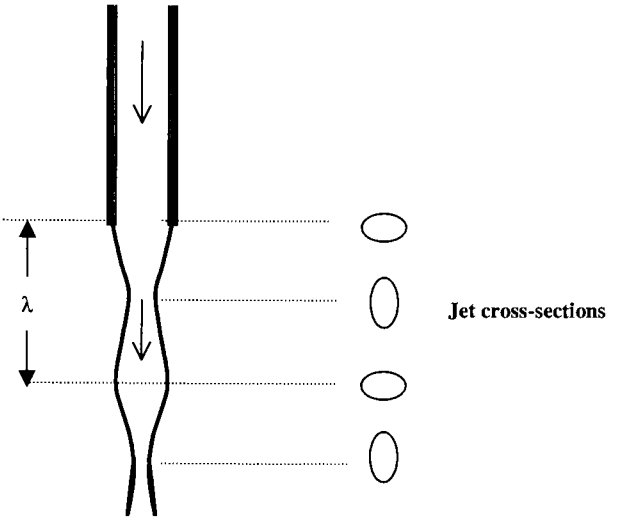

Figure 15.10 Oscillating jet issuing from a tube having an elliptical cross section. The wavelength, λ, of the oscillation is measured.

rigorous analysis of the oscillating jet by Bohr [48] led to Equation (15.25) that is normally used

$$\gamma = \frac{2\rho\upsilon^2(1 + 37\, b^2/24r^2)}{3r\lambda^2(1 + 5\pi r^2/3\lambda^2)}, \tag{15.25}$$

where υ is the volume flow rate of the jet, and ρ the liquid density. The terms r and b are half the sum of the minimum and maximum diameters at a node, and half their difference, respectively. Using an ingenious apparatus in which a laser light source and a cylindrical lens produce an image of the oscillating jet, Sato *et al.* [49] have not only determined the dynamic STs of aqueous salt and surfactant solutions, but also shown that the ST of these solutions is lowered by the application of an electric field.

The method is the only one that allows measurement of changes in ST in the 1–100 msec range. At least one commercial version of this instrument is available, and allows measurements to be made up to 320°C. The jet is viewed by means of a video camera.

15.4.2 Capillary Wave Methods

ST is the principal restoring force associated with thermally induced surface or capillary waves. Laser scattering has been used to characterize capillary waves in studies of the dynamic ST of air/polymer solutions [50] and liquid crystal interfaces [51], the ST being obtained using an equation first formulated by Kelvin. For low bulk viscosities, in its simplest form the equation can be written

$$\gamma = \rho\omega^2/q^3, \tag{15.26}$$

where ω represents the frequency and q the wave number of the capillary wave. The analysis of light scattering from surface waves can also be used to determine surface viscosity, surface dilation properties, adsorption, and structural transitions. One severe limitation of the technique is the need to minimize vibrations from external sources. As a means of determining either static or dynamic STs, methods based on the characteristics of surface waves do not have any distinct advantages over much simpler ones unless other surface properties are also being investigated. A review of capillary wave techniques including surface laser light scattering by Langevin [52] is recommended for those interested in further details of these methods.

15.4.3 Oscillating Drop and Bubble Methods

Two categories of oscillating drop techniques exist. The first involves drops, or bubbles, levitated by acoustical or electromagnetic means, as mentioned in Section 15.2.4. These methods offer the advantage of the fluid–fluid interface not being in contact with any solid surface, allowing unhindered diffusional transport processes to occur uniformly over the entire interface. Using acoustic levitation, Hsu and Apfel [53] monitored changes in IFTs of (water + butane) and (water + propane) systems over a period of up to 2 h under conditions in which the organic phase was in the form of a superheated droplet.

In the other category not mentioned earlier are some novel techniques designed specifically for the investigation of adsorption and other surface processes, as well as ST and IFT measurement. In these methods, a small drop or bubble is created at and remains attached to a capillary tip and is made to oscillate by sinusoidal changes in volume produced by means of a syringe pump or similar device. In a study of several aqueous polymer solutions, Myrvold and Hansen [54] determined the variation of ST with time over periods of up to 10^4 s by capturing 25 images per second of the profile of a 50×10^{-6} cm^3 bubble, the volume of which was held constant. The volume of the bubble was then oscillated by approximately 5 per cent at 0.2–2 Hz while the bubble profile was monitored. From the phase angle between the ST and area variations, the frequency dependence of the dynamic surface elasticity and viscosity of the surface layer were determined.

A similar technique had been employed by Chang and Franses [55] for the investigation of the dynamic ST of aqueous octanol solutions and by Johnson and Stebe [56] in a study of the adsorption of 1-decanol at the air/water interface. Chang and Franses [55] used a commercial instrument based on a design by Enhorning [57]. The bubble was assumed to be spherical and fluctuations in pressure were monitored as the bubble pulsated. In Johnson and Stebe's study, equipment requirements were simplified by the use of a photoelectric sensor to monitor radial fluctuations, obviating the need for a high-speed image analysis system. These versions of the technique might better be classified as capillary pressure methods, but the similarity to other oscillatory methods and the fact that other surface properties may be investigated warrants their inclusion here rather than in Section 15.4.3.

15.4.4 Maximum Bubble Pressure Method

Measurement of dynamic ST by the MBP method has been reported by a number of authors. However, despite its simplicity, the use of this method for dynamic measurements seems to be declining in favour of other methods, possibly as a result of the uncertainty in the age of the interface and the fact that its area does not remain constant during measurement. Attempts to address the question of surface age have been made by Austin [58], Kloubek [59] and Bendure [60], among others. Their findings have been reassessed by Garrett and Ward [61] in studies of the ST of aqueous sodium dodecyl sulphate solutions. Garrett and Ward concluded that the MBP method is suitable for surface ages in the (20–200) ms range and well as in the (1–100) s range considered by Bendure, provided that correction is made for the so-called "dead time" during which the bubble grows rapidly and detaches from the capillary tip. The question of dead time correction and other uncertainties associated with the MBP methods were the subject of a series of papers by Mysels [62], including one in which he reported that even for a pure liquid such as water, the ST appears to change significantly as the bubble formation time is reduced until it approaches the dead time. It should be pointed out that in Garrett and Ward's apparatus the capillary is oriented so that the tip points upwards allowing the bubble to break away more easily than in the normal situation in which the tip at the lower end of the capillary, and that the bore of the tube is considerably smaller than that used in the conventional version of the MBP method. What can be considered as further variations on the MBP method are discussed in the following section. In these methods, uncertainty in the age of the interface is largely eliminated.

15.4.5 Capillary Pressure and Related Methods

The development of highly sensitive pressure transducers has resulted in a number of studies of dynamic ST and IFT being made using techniques that involve monitoring the pressure difference across an interface between immiscible fluid phases as a small drop or bubble is formed. The technique can be viewed as a combination of the pendent drop and MBP methods in which changes in pressure differential and profile shape are monitored as a function of time. The advantage over the conventional pendent drop method is that the interface is formed much more rapidly, enabling changes in ST or IFT to be followed almost immediately after the formation of a relatively fresh surface. The uncertainty in the surface age is smaller than that experienced in the MBP method. In developing the method for use in a microgravity laboratory, Liggieri *et al.* [63] devised an apparatus in which a hemispherical drop formed at the tip of a small capillary is expanded rapidly, increasing its area by a factor of approximately 40. The pressure difference across the newly formed interface is then monitored along with the drop profile. Under normal gravity in the system studied, the density difference between the two fluids was such that the gravitational distortion of the meniscus was significant. Measurement of both drop height and width enabled correction for this effect to be made by assuming that the profile was elliptical.

Other versions of the technique use essentially the same apparatus but monitor capillary pressure and drop radius as a function of time, as the drop volume is expanded at various rates. The experimental procedures and details of the data analysis for studies of the

dodecane/aqueous surfactant interface have been published by Nagarajan and Wasan [64]. MacLeod and Radke [65] have used the technique extensively, measuring dynamic ST and IFTs for several systems. They conclude that the method can be used to study non-equilibrium interfaces over time periods ranging from 10 ms to hours.

A novel fast-formed drop technique devised by Horozov and Arnaudov [46], also a capillary pressure method, uses a different approach to form a fresh surface. By suddenly stopping flow of a liquid emerging as a jet from the tip of a capillary, a new surface is formed as a nearly hemispherical drop extending across the base of the capillary. If the external diameter of the capillary is sufficiently small, the drop can be regarded as a spherical cap, and the radius of curvature calculated from the tip diameter and the drop height. By measuring the capillary pressure as a function of time, the ST of pure liquids and solutions, and the IFTs between immiscible liquids can be determined over long time periods starting shortly (*ca.* 40 ms) after the formation of the interface. The authors point out that in order to create a relatively fresh interface using the expanded drop methods discussed above, the drop size after expansion must be far larger than in the fast-formed drop method. Consequently, not only is the interface formation process much more rapid, but also the gravitational distortion of the interface is much smaller than in the fast-formed drop method. The use of this technique therefore, appears to be well worth considering for systems in which the kinetics of adsorption or other surface processes are such that it is important to follow changes in ST or IFT over long periods of time, starting as early as 40 ms after the formation of the new interface if required. Another advantage of the method is that little instrumentation is required beyond a travelling microscope and a fast response pressure transducer with some means of recording its output.

References

1. Boys, C.V., *Soap-Bubbles: Their Colours and the Forces Which Mould Them*, SPCK, London, 1890; unabridged reprint edition, Dover, New York, 1959.
2. Isenberg, C., *The Science of Soap Films and Soap Bubbles*, Tieto, Clevedon, UK, 1978; reprint edition, Dover, New York, 1992.
3. Thompson, D.W., *On Growth and Form*, 2nd ed., Cambridge University Press, Cambridge, 1963; reprint of 1942 edition.
4. de Laplace, P.S., *Mécanique Céleste: Supplément au livre X*, Courcier, Paris, 1806.
5. Plateau, J., *Statique expérimentale et théoretique des liquides soumis aux seules forces moléculaires*, Gauthier-Villars, Paris, 1873.
6. Everett, D.H., *IUPAC Manual of Symbols and Terminology for Physicochemical Quantities and Units. Appendix II: Definitions, Terminology and Symbols in Colloid and Surface Chemistry, Part I*, Butterworths, London, 1972.
7. Sugden, S., *J. Chem. Soc.* **121**, 1483–1492, 1921.
8. Padday, J.F. and Pitt, A., *J. Colloid Interf. Sci.* **38**, 323–334, 1972.
9. Adamson, A.W. and Gast, A.P., *Physical Chemistry of Surfaces*, Ch. 2, 6th ed., Wiley-Interscience, New York, 1997.
10. Natelson, S. and Pearl, A.H., *J. Am. Chem. Soc.* **57**, 1520–1523, 1935.
11. Bashforth, F. and Adams, J.C., *An Attempt to Test the Theories of Capillary Action by Comparing the Theoretical and Measured Forms of Drops of Fluid*, Cambridge University Press, Cambridge, 1883.

12. Fordham, S., *Proc. Roy. Soc. (London) A* **194**, 1–16, 1948.
13. White, D.W.G., *A Supplement to the Tables of Bashforth and Adams*, Queen's Printers, Ottawa, 1967.
14. Padday, J.F., *Phil. Trans. Roy. Soc. (London)* **269**, 265–293, 1971.
15. Hartland, S. and Hartley, R.W., *Axisymmetric Fluid–Liquid Interfaces*, Elsevier, Amsterdam, 1976.
16. Boucher, E.A., Evans, M.J.B. and Jones, T.G.J., *Adv. Coll. Interface Sci.* **27**, 43–80, 1988.
17. del Río, O.I. and Neumann, A.W., *J. Colloid Interf. Sci.* **196**, 136–147, 1997.
18. Lambert, J.D., *Numerical Methods for Ordinary Differential Systems: The Initial Value Problem*, Wiley, New York, 1976.
19. Lahooti, S., del Río, O.I., Neumann, A.W. and Cheng, P., in *Applied Surface Thermodynamics*, A.W. Neumann and J.K. Spelt, eds., Dekker, New York, pp. 497–500, 1996.
20. Vonnegut, B., *Rev. Sci. Instrum.* **13**, 6–9, 1942.
21. Princen, H.M., Zia, I.Y.Z. and Mason, S.G., *J. Colloid Interf. Sci.* **23**, 99–107, 1967.
22. Schoolenberg, G.E. and During, F., *Polymer* **39**, 757–763, 1998.
23. Cai, Z.T. and Mohanty, K.K., *J. Colloid Interf. Sci.* **195**, 408–410, 1997.
24. Strutt, J.W. (Lord Rayleigh), *The Theory of Sound*, Dover, New York, p. 371, 1986.
25. Trinh, E.H., Marston, P.L. and Robey, J.L., *J. Colloid Interf. Sci.* **124**, 95–103, 1988.
26. Suryanarayana, P.V.R. and Bayazitoglu, Y., *Phys. Fluids A* **3**, 967–977, 1991.
27. Bayazitoglu, Y., Sathuvalli, U.B.R., Suryanarayana, P.V.R. and Mitchell, G.F., *Phys. Fluids* **8**, 370–383, 1996.
28. Harkins, W.D. and Brown, F.E., *J. Am. Chem. Soc.* **41**, 499–524, 1919.
29. Tate, T., *Philos. Mag.* **27**, 176, 1864.
30. Lando, J.L. and Oakley, H.T., *J. Colloid Interf. Sci.* **25**, 526–530, 1967.
31. Wilkinson, M.C. and Aronson, M.P., *J. Chem. Soc. Faraday Trans. I* **69**, 474–480, 1973.
32. Vinet, B., Garandet, J.P. and Cortella, L., *J. Appl. Phys.* **73**, 3830–3834, 1993.
33. Jho, C. and Burke, R., *J. Colloid Interf. Sci.* **95**, 61–71, 1983.
34. du Noüy, Lecomte P., *J. Gen. Physiol.* **1**, 521–524, 1919.
35. Freud, B.B. and Freud, H.Z., *J. Am. Chem. Soc.* **52**, 1772–1782, 1930.
36. Harkins, W.D. and Jordan, H.F., *J. Am. Chem. Soc.* **52**, 1751–1772, 1930.
37. Huh, C. and Mason, S.G., *Coll. Polymer Sci.* **253**, 566–580, 1975.
38. Padday, J.F., in *Surface and Colloid Science, Vol 1*, E. Matijevic, ed., Wiley Interscience, New York, pp. 29–131, 1969.
39. Wilhelmy, L., *Ann. Phys.* **119**, 177, 1863.
40. Lillebuen, B., *Acta Chem. Scand.* **24**, 3287–3292, 1970.
41. Jordan, D.O. and Lane, J.E., *Austral. J. Chem.* **17**, 7, 1964.
42. Princen, H.M., *Austral. J. Chem.* **23**, 1798–1799, 1970.
43. Sugden, S., *J. Chem. Soc.* **121**, 858–866, 1922.
44. Sugden, S., *J. Chem. Soc.* **125**, 27–31, 1924.
45. Chang, C.-H. and Franses, E.I., *Colloids Surf.* **100**, 1–45, 1995.
46. Horozov, T. and Arnaudov, L., *J. Colloid Interf. Sci.* **219**, 99–109, 1999.
47. Raleigh, Lord., *Proc. Roy. Soc. London* **29**, 71–97, 1879.
48. Bohr, N., *Philos. Mag.* **209**, 281–317, 1909.
49. Sato, M., Kudo, N. and Saito, M., *IEEE Trans. Ind. Appl.* **34**, 294–300, 1998.
50. Huang, Q.R. and Wang, C.H., *Langmuir* **15**, 634–637, 1999.
51. Sohl, C.H., Miyana, K. and Ketterson, J.B., *Rev. Sci. Instrum.* **49**, 1464–1469, 1978.
52. Langevin, D., ed., *Light Scattering by Liquid Surfaces and Complementary Techniques.* Surfactant Science Series 41, Dekker, New York, 1992.
53. Hsu, C.-J. and Apfel, R.E., *J. Colloid Interf. Sci.* **107**, 467–476, 1985.

54. Myrvold, R. and Hansen, F.K., *J. Colloid Interf. Sci.* **207**, 97–105, 1998.
55. Chang, C.-H. and Franses, E.I., *Chem. Eng. Sci.* **49**, 313–325, 1994.
56. Johnson, D.O. and Stebe, K.J., *J. Colloid Interf. Sci.* **182**, 526–538, 1996.
57. Enhorning, G., *J. Appl. Physiol: Respir. Environ. Exercise Physiol.* **43**, 198–203, 1977.
58. Austin, M., Bright, B.B. and Simpson, E.A., *J. Colloid Interf. Sci.* **23**, 108–112, 1967.
59. Kloubek, J., *J. Colloid Interf. Sci.* **41**, 1–22, 1972.
60. Bendure, R.L., *J. Colloid Interf. Sci.* **35**, 238–248, 1971.
61. Garrett, P.R. and Ward, D.R., *J. Colloid Interf. Sci.* **132**, 475–490, 1989.
62. Mysels, K.J., *Langmuir* **5**, 442–447, 1989.
63. Liggieri, L., Ravera, F. and Passerone, A., *J. Colloid Interf. Sci.* **169**, 226–237, 1995.
64. Nagarajan, R. and Wasan, D.T., *J. Colloid Interf. Sci.* **159**, 164–173, 1993.
65. MacLeod, C.A. and Radke, C.J., *J. Colloid Interf. Sci.* **160**, 435–448, 1993.

16 Critical Parameters

A.S. TEJA and J. MENDEZ-SANTIAGO
School of Chemical Engineering
Georgia Institute of Technology
Atlanta, GA, USA

Measurement of the Thermodynamic Properties of Multiple Phases
R.D. Weir and Th.W. de Loos (Editors)

16 CRITICAL PARAMETERS

The vapour–liquid critical point of a substance, discovered experimentally by Cagniard de la Tour [1], is the point on the P, v, T surface of the substance where the vapour and liquid properties become identical and, therefore, where the visible meniscus between the vapour and liquid phases disappears. The critical point is defined mathematically by the equations:

$$P > 0; \quad \left(\frac{\partial P}{\partial v}\right)_T = 0; \quad \left(\frac{\partial^2 P}{\partial v^2}\right)_T = 0; \quad \left(\frac{\partial^3 P}{\partial v^3}\right)_T < 0. \tag{16.1}$$

It is the maximum point on the coexistence curve of a pure substance, although not necessarily the maximum temperature or pressure at which vapour and liquid can coexist in a mixture. Implicit in Equation (16.1) is the assumption that the Helmholtz energy is a continuous, differentiable function of T and v, which leads to a coexistence curve that is quadratic in volume. The latter cannot be reconciled with modern theories, which show that the Hemholtz energy is non-analytic in the critical region, and the coexistence curve is approximately cubic in volume. However, the classical view of the critical point, as the state where the orthobaric densities of the coexisting phases become equal, provides an adequate working definition for the purposes of the present review.

Since the work of van der Waals [2], considerable effort has been devoted to the measurement of critical properties of pure substances for application in thermodynamic models based on the principle of corresponding states. Several reviews of experimental methods and data have also been published, the most notable of which are the reviews by Kobe and Lynn [3], Kudchadker *et al.* [4], Mathews [5] and Ambrose and Young [6]. The present work discusses the more widely used experimental techniques for the measurement of critical properties of pure substances, with special emphasis on methods that have been used to obtain the critical properties of substances that are thermally unstable. In principle, the critical point of a substance that decomposes at a temperature below its critical temperature cannot be measured experimentally. However, rapid heating techniques have been developed that can lead to a hypothetical critical state of the non-decomposed substance by extrapolation. It should be noted that rapid changes in temperature and pressure are required in order to minimise the time that a thermally unstable substance is exposed to elevated temperatures during an experiment. On the other hand, the measurement of the critical properties of a thermally stable substance requires fine temperature control to obtain data of high precision. Methods to achieve both these conditions are discussed below.

16.1 Experimental Techniques

16.1.1 Sealed Ampoule Method

Perhaps the most popular method for the measurement of the critical temperature of a substance is the sealed ampoule method. In this method, a small amount m of an air-free substance

is placed in a glass ampoule of volume V. The ampoule is first sealed and then heated until the meniscus separating the vapour and liquid phases disappears. Subsequent cooling of the ampoule results in the reappearance of the meniscus, and this process of meniscus disappearance and reappearance by successive heating or cooling may be repeated several times. The critical temperature is generally obtained by averaging the temperatures of meniscus disappearances and reappearances. However, the mass m loaded into the ampoule must be such that the quantity m/V is approximately equal (within 1–2 per cent) to the critical density of the substance. In this case, the meniscus will disappear or reappear exactly at the position of the half-volume $V/2$ of the ampoule. If the loading density is higher than the critical density, then the meniscus will rise until a single liquid phase is obtained. Similarly, if the loading density is lower than the critical density, the meniscus will fall until a single vapour phase is obtained. This is illustrated in Figure 16.1.

The temperature of meniscus disappearance or reappearance will not vary with time (or rate of heating) if the substance under study is thermally stable at its critical temperature. This is illustrated in Figure 16.2, which shows meniscus disappearances and reappearances as the n-hexane is alternatively heated and cooled through its critical region in a sealed ampoule. Note that the average temperature of meniscus disappearance and reappearance yields a precise estimate of the critical temperature when heating and cooling are controlled precisely. In the case of a thermally unstable substance, the temperature of meniscus disappearance or reappearance varies with time because each measurement represents the critical temperature of a mixture of the original substance and the reaction products formed during the heating of the sample. This behaviour is illustrated in Figure 16.3, where an experiment with n-nonanal is shown. It is apparent from the figure that the data must be extrapolated back to obtain the 'true' critical temperature of the unreacted substance.

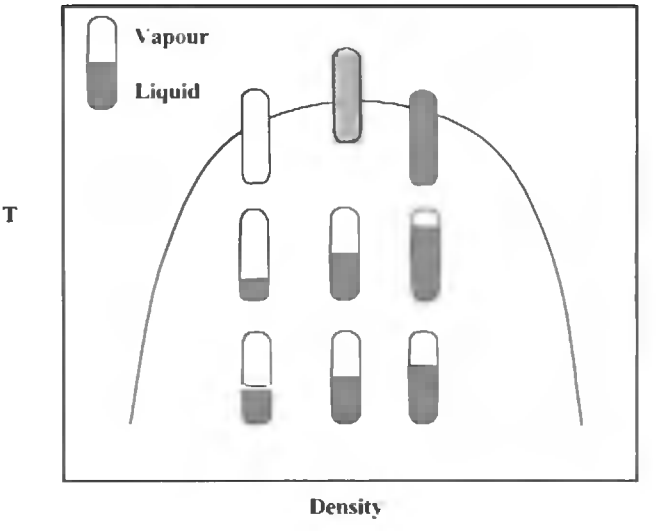

Figure 16.1 The effect of loading density on the disappearance of the vapour–liquid meniscus

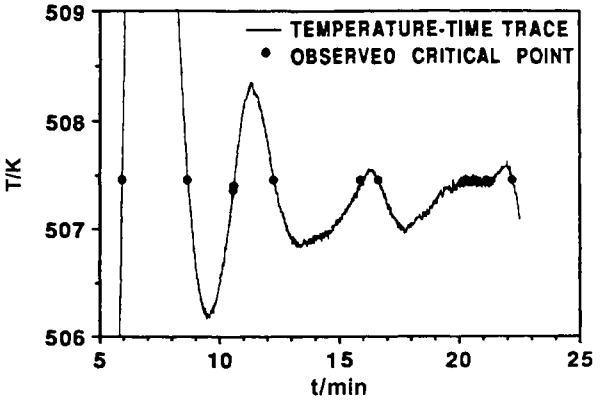

Figure 16.2 Plot of temperature against time for the heating and cooling of n-hexane in the critical region.

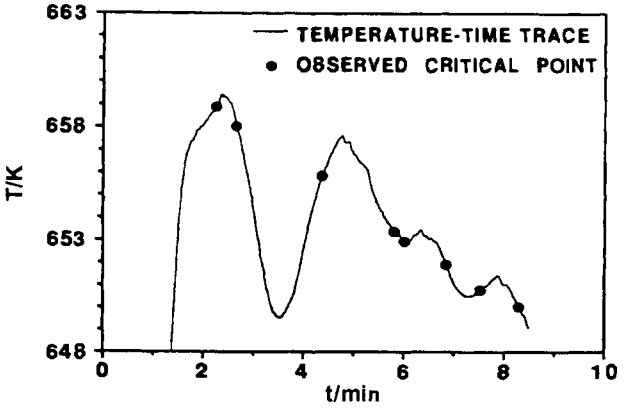

Figure 16.3 Plot of temperature against time for the heating and cooling of n-nonanal in the critical region.

The sealed ampoule technique has been used for over 70 years to determine the critical temperature of substances [7–10]. The various apparatuses differ in the heating technique employed, in the way that temperature is measured, in the type of ampoule used, and whether the contents are stirred or not. Early designs of this method include the use of an electric tube furnace to heat the substance [7,8]. Eaton and Porter [10] modified the equipment by using a gas burner for heating, which allowed for rapid heating of the sample up to $T = 640$ K in 45 s. Mixing of the ampoule was also incorporated, which allowed for thermal equilibrium to be achieved and resulted in measurements that were more accurate than those obtained without mixing.

Ambrose and co-workers [11–14] employed an electrically heated metal block for heating. A sealed ampoule containing the sample was inserted into the furnace, and the temperature of meniscus disappearance was obtained by means of a thermocouple inserted

into the furnace. A rapid heater, consisting of a copper tube with two observation holes, was also designed for thermally unstable substances [13]. Temperatures of 670–770 K were obtained within a few minutes in this apparatus. However, there were significant temperature gradients within the heater, so that an accuracy of only ±1 K could be obtained in the temperature measurements.

Mogollon *et al.* [15] designed a rapid heater consisting of a platinum film deposited on the outside surface of a quartz tube to serve as an electrical resistor. A sealed ampoule was inserted into the coated tube, which could be heated by supplying power to the platinum coating. The ampoule was constructed of borosilicate glass, and had a small thermo-well at one end where a thermocouple could be inserted as shown in Figure 16.4. The furnace was pre-heated to the estimated critical temperature before inserting the ampoule. This allowed for very rapid heating, which was necessary for thermally unstable substances. Teja and co-workers [16–21] used a modified version of this design, illustrated in Figure 16.5, to measure the critical properties of many organic substances. They were able to obtain very rapid heating of the substance, but cooling was relatively slow. Nevertheless, the fine control of heating and cooling led to very precise estimates of the temperatures of meniscus disappearance and reappearance. A magnified image of the ampoule superimposed with the time–temperature trace during the experiment was recorded by a video camera. The critical point could then be determined by examination of the videotape.

Gude and Teja [21] designed a gas heater for substances that decomposed rapidly at temperatures below their critical temperatures. Their ampoule was contained in a stainless-steel box, which protected the experimenter against any explosions. Two windows located 180° apart were placed in the box for visual observation. A hot nitrogen gas stream was used to heat the ampoule, whereas cooling was achieved by mixing the hot nitrogen stream with a cold nitrogen stream. This allowed for very rapid cooling and heating of the sample,

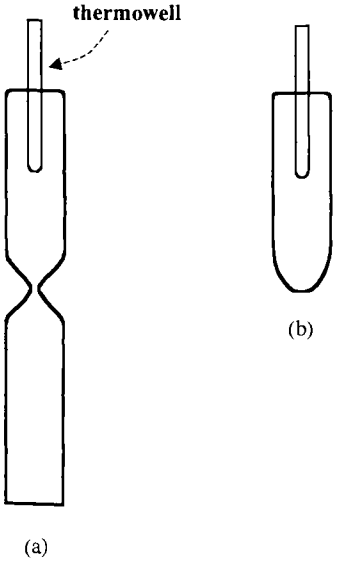

Figure 16.4 Ampoule used by Mogollon *et al.* [15]: (a) before sealing, (b) after sealing.

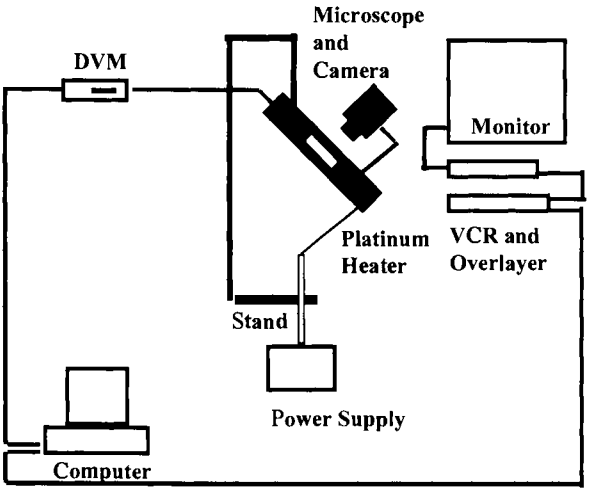

Figure 16.5 Sealed ampoule method of Gude and Teja [21].

making the technique suitable for thermally unstable substances. A magnified image of the ampoule superimposed with the time–temperature trace was also recorded for careful determination of the critical temperature.

The ampoules used in critical point experiments have generally been made from thick-walled glass of 0.5–3 mm internal diameter and ~5–10 cm in length. The critical point is more sharply defined in ampoules with a smaller diameter [22,23]. However, it is more difficult to load these small diameter ampoules with the correct amount of substance. Metal cells with sapphire windows have also been used [24], although these are not as common for critical point measurements. The earliest measurements were made without stirring the contents of the ampoule. Recent measurements, however, have employed a rocking motion to stir the samples [21]. Finally, to obtain good thermal contact between the temperature-measuring device, usually a thermocouple, and the fluid, an ampoule with a thermo-well was designed by Kay and co-workers [15].

The critical density may be determined from the mass m loaded into the ampoule and the ampoule volume V if the meniscus disappears exactly at the half-volume $V/2$. If this is not the case, then the critical density may be calculated by linear interpolation of the results of several experiments with meniscus disappearance–reappearance above or below the half-volume location, which indicates that the loading densities were higher or lower than the critical density. Details of this procedure are described by Anselme *et al.* [19].

16.1.2 Flow Method

The flow method was first proposed by Roess [25] for the measurement of the critical temperature and pressure of petroleum fractions. Roess noted that the typical static method, such as the sealed ampoule method described above, could not be used for petroleum fractions,

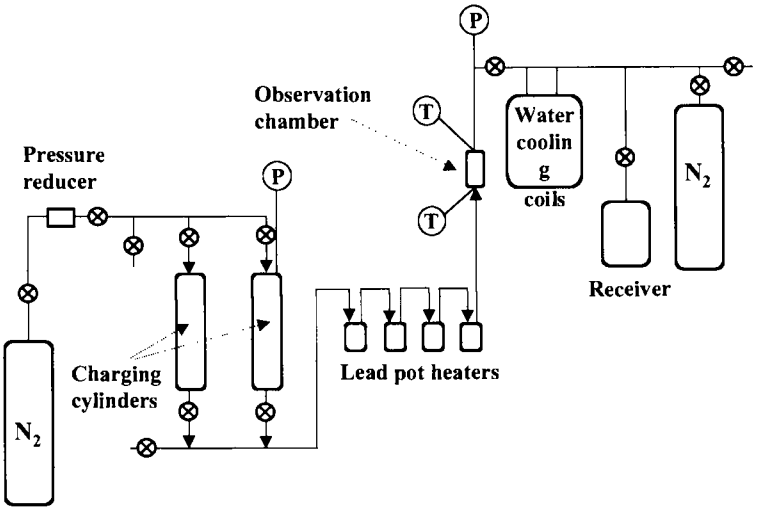

Figure 16.6 Flow apparatus used by Roess [25].

because petroleum fractions decompose before their critical temperature is reached. As a result, the 'critical temperature' observed in static experiments would be less than the 'true' value because of the presence of decomposition products. Roess proposed a flow method, illustrated in Figure 16.6, which minimises the time that the substance is exposed to high temperatures. In this method, the test substance was pressurised from a nitrogen cylinder and heated to a temperature where there would be no decomposition ($T = 675$ K in the experiments reported by Roess) as it flowed through several coils immersed in lead baths. The critical state was attained in a special quartz view cell immersed in the last lead bath. The temperature was measured by two thermocouples at the entrance and exit of the view cell. Variations of 3–6 K were noted between the two readings, and an average of the two temperatures was assumed to yield the critical temperature of the substance. The apparatus used in these experiments was large, with typical flow rates of the order of 35–50 $dm^3 \cdot h^{-1}$ and typical run times of the order of 15–30 min. Moreover, three observers were needed to run the experiments, one to read the flow rate, one to operate the potentiometer (thermocouples) and one to observe the critical phenomena and to control the temperature and pressure. It should be added that the apparatus could be used to measure critical temperatures up to 810 K. Finally, the critical pressure could be obtained by placing a pressure gauge at the exit of the view cell.

Teja and co-workers [18,26] modified the flow method by decreasing both the size of the equipment and the residence time of the fluid in the view cell (Figure 16.7). The view cell used in their work had an internal volume of 1.5 cm^3. The degassed sample was pumped through the cell by a non-pulsing syringe pump at flow rates of the order of 10 $cm^3 \cdot min^{-1}$ (0.6 $dm^3 \cdot h^{-1}$). The cell was placed inside a furnace, where it could be maintained at any desired temperature. The fluid was heated as it passed through the furnace such that the critical state was attained inside the view cell. The critical point was detected by observation of critical opalescence and the disappearance of the meniscus. Increasing the flow rate, or

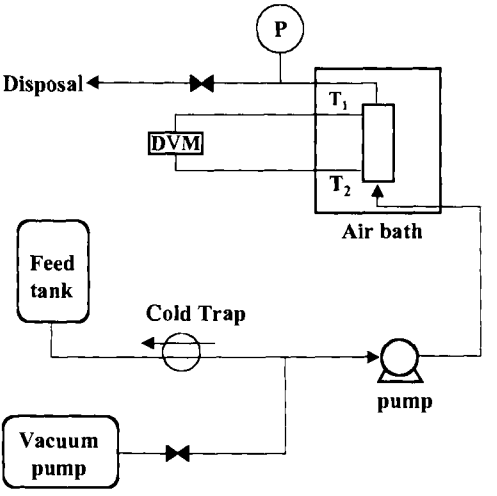

Figure 16.7 Flow apparatus used by Rosenthal and Teja [26].

reducing the flow pressure, resulted in the reappearance of the meniscus. The position of the thin band of opalescence in the view cell could be manipulated by changing the conditions of pressure, temperature and flow rate until the band moved to the tip of a thermocouple placed inside the view cell. The critical temperature was measured directly by this thermocouple and the pressure was measured by an in-line pressure gauge located at the exit of the cell. The residence time of the substance in the view cell was estimated to be 10 s at the highest flow rate. This method allowed the measurement of the critical properties with an accuracy of ± 0.6 K and ± 0.01 MPa for stable substances. In the case of unstable substances, the apparent critical temperature of the substance and its reaction products could be measured as a function of the residence time in the view cell. The data were then extrapolated to zero residence time to obtain the 'true' critical temperature of the substance [26]. Since the residence time in this method was generally below about 10 s, thermal reactions could be kept to a minimum and the extrapolation was generally within the error bounds reported by Rosenthal and Teja [26].

Wilson *et al.* [27] designed a similar flow apparatus to measure the critical properties of reactive or thermally unstable substances. Their design consisted of a visual cell of volume 16 cm^3 connected to two motorised syringe pumps and a hand-operated syringe pump. The critical temperature was measured with a platinum resistance thermometer inserted into a thermo-well in the visual cell. The average residence time of the material in the oven was ~0.4–8 min. The claimed accuracies of their measurements were ± 0.05 K and ± 5 kPa.

16.1.3 Spontaneous Boiling Methods

An explosive boiling technique to determine the spinodal curve of a substance has been proposed by Spirin and Cherezov [28,29]. Since the critical point is located at the upper end point of the spinodal curve, the method can also be used to determine the critical point.

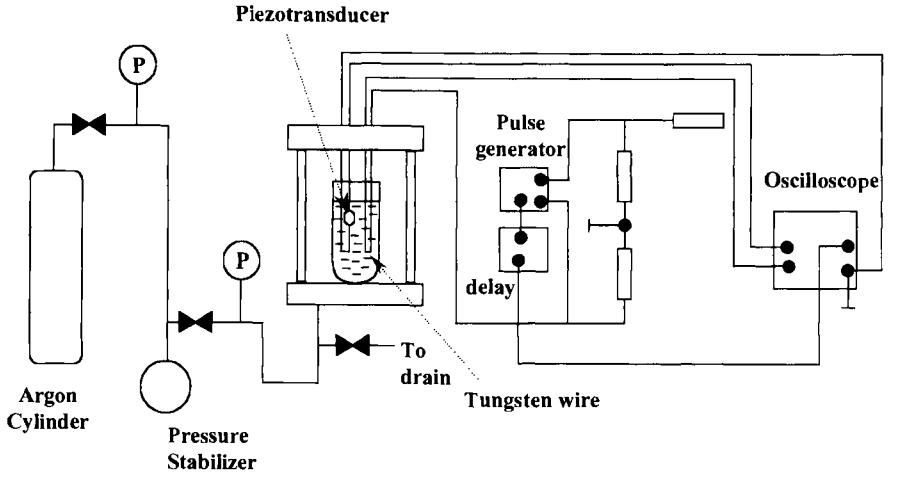

Figure 16.8 Apparatus used by Spirin and Cherezov [28,29] for the determination of the spinodal curve.

The apparatus proposed by Spirin and Cherezov is shown in Figure 16.8. A fine tungsten wire was submersed in a fluid, inside a cylindrical glass vessel. A very short voltage pulse was then applied to the wire resulting in the heating of a small portion of the fluid. When the spinodal curve is reached (after ~300 μs), homogeneous nucleation and explosive boiling occur and the rapid increase in pressure generates a sound wave. This sound wave was recorded with a piezo-pressure transducer located about 1 mm from the wire. The acoustic wave disappears at the critical point, and the temperature at which this occurs was taken to be the critical temperature.

Nikitin *et al.* [30] proposed a similar method for the measurement of critical temperature and pressure, which involves measuring the variation of the temperature of attainable superheat (spontaneous boiling) with pressure. This temperature tends to the critical temperature of a fluid as the pressure increases. The liquid under study was used to fill a chamber connected to a pressure gauge, and then heated by applying electrical pulses for 0.01–1 ms duration to a platinum wire 0.02 mm in diameter and 1–3 cm long. When spontaneous boiling occurred, temperature perturbations could be detected because of the change in heat transfer from the probe to the liquid. The temperature of spontaneous boiling was determined from the resistance of the platinum wire when the perturbations are first detected, and the pressure was measured by a pressure gauge. As the pressure in the chamber increases, the temperature perturbations decrease to zero. The pressure at which the perturbations decrease to zero was taken to be the apparent critical pressure and the corresponding temperature was taken to be the apparent critical temperature. Corrections were applied as described by Nikitin [31] to yield the 'true' critical temperature and pressure. In the case of thermally unstable substances, an extrapolation procedure based on the kinetics of decomposition of the substance was used to obtain the 'true' critical constants. Although the method is not as accurate as the methods described previously, *e.g.* the method yields T_c = 731.1 ± 7 K for n-heptadecane, the pulsed heating technique is capable of measuring the critical properties of highly unstable substances since residence times at high temperatures are generally <1 ms.

16.1.4 Open Tube Methods

Open tube methods were employed more than 100 years ago by Andrews [32] and Cailletet [33], and more recently by Kay and co-workers [34–40], and others. An air-free sample of the substance is confined over mercury in a thick-walled capillary tube, and the mercury is used to transmit the pressure to a measuring device. Ramsay and Young [41] enclosed the tube in a vapour jacket for the control of temperature. The tube is generally calibrated so that the volume of the sample can be obtained as a function of the height of mercury in the tube. Kay introduced a magnetic ball bearing into the sample, which could be manipulated by an external magnet to provide mixing. The critical point of the substance was determined by observation of the disappearance of the meniscus in the tube as the pressure and temperature were varied (Figure 16.9).

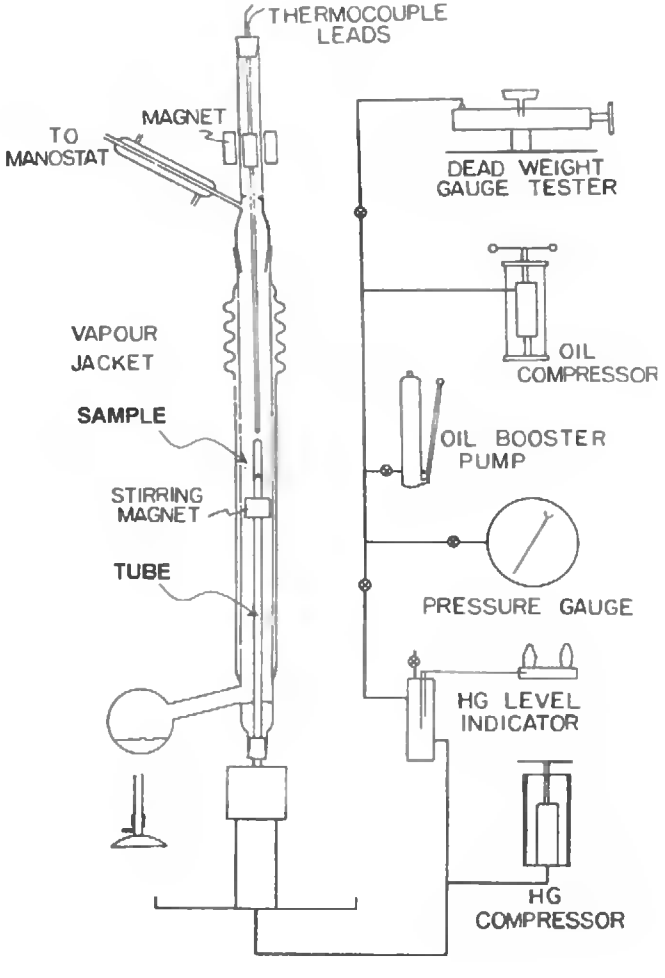

Figure 16.9 Open tube apparatus developed by Kay and co-workers.

Altschul [42] described an open tube method in which the top end of the tube was kept at a temperature above the critical temperature of the substance, whereas the lower end was kept below the critical temperature. Meniscus disappearance was then recorded at some intermediate temperature and pressure in the tube. A more refined version of this apparatus is by Ambrose and Townsend [43], who kept the mercury in the lower part of the tube at room temperature and only subjected the sample to higher temperatures. This arrangement is particularly suitable for substances whose critical temperatures exceed about 573 K when mercury has a significant vapour pressure.

More recent versions of the open tube apparatus have replaced the vapour jacket by electrical furnaces with suitable provision for visual observation of the sample. Ambrose *et al.* [14,44] added two electrical probes, which assisted in the location of the mercury level. Their furnace also allowed a standard platinum resistance thermometer to be inserted for temperature measurement. Temperature gradients of 0.04 K were observed in the furnace. Dickinson and McLure [45] therefore modified the design so that the temperature could be measured at concentric positions around the sample tube by a 10-junction chromel–aluminium thermocouple.

Open tube methods are capable of providing data of great accuracy. Under favourable conditions, the disappearance and reappearance of the meniscus can be manipulated by very small changes in pressure at constant temperature.

16.1.5 Methods Based on the *PvT* Behaviour of a Substance

The critical point of a pure substance can also be determined by examining the horizontal inflection point on the critical isotherm. This criterion is used by several investigators [46–48] for critical point measurements. An example of an apparatus used for this purpose is described by Keyes [46]. A known amount of the substance was confined in a bomb of about 200 cm^3. Mercury was used to control the volume by using a mercury compressor with a 210 cm^3 displacement, which was connected to the bomb by steel capillaries. The bomb was placed in an oil bath whose temperature was regulated by the use of three heaters at temperatures from 300 to 600 K. Measurements were made along the isochores as well as along isotherms. The equipment was limited to pressures below 50 MPa because of hysteresis in the dilation of the apparatus, which affected the accuracy of volume measurements. Also, above $T = 600$ K, uncertainties were introduced by the presence of appreciable amounts of mercury vapour. The apparatus is similar in principle to the open tube apparatus described above. The *PvT* data and vapour–liquid coexistence curves can be obtained using this approach. The data are then fitted with a modified Benedict-Webb-Rubin-type equation, and the critical parameters obtained by applying the criticality conditions (Equation (16.1)) to the equation of state [47].

If the densities of the coexisting vapour and liquid phases are obtained using the above method, then the critical density may be obtained from the rectilinear diameter. Cailletet and Mathias [49] were the first to observe that the arithmetic mean of the coexisting vapour and liquid densities is, to a good approximation, a linear function (rectilinear diameter) of temperature. If this line is extrapolated to the critical temperature, then the mean density is the critical density of the substance. More accurate measurements have shown that the plot

of rectilinear diameter has a slight curvature. More realistic equations have therefore been developed for obtaining the critical density and are described below.

The pressure–temperature behaviour of the substance at constant volume can also be used to obtain the critical point, as shown by Cailletet and Colardeau [50]. Different amounts of a substance, *i.e.* different loading densities, are placed into a constant volume cell and the pressure–temperature behaviour of the substance is measured. In the sub-critical region, the vapour pressure does not depend on the density, whereas in the supercritical region the pressure changes with the loading density. Data from several experiments are then used to determine the critical point by extrapolation. The critical point is the point at which the pressure–temperature curves diverge, as shown in Figure 16.10. All three critical properties may be obtained in this way. However, the accuracy is limited because of the extrapolation involved. Ambrose *et al.* [44] modified the technique by demonstrating that a plot of the residual log P against T provides better estimates of the critical properties. In their work, the residual log P was defined as the logarithm of the observed vapour pressure minus the logarithm of the vapour pressure calculated by extrapolation of the American Petroleum Institute (A.P.I.) equation for the vapour pressure of the substance.

16.1.6 Other Methods

Measurements of the speed of sound have shown a pronounced minimum in this property in the vicinity of the critical point, as illustrated in Figure 16.11 [51]. This criterion can therefore be used to identify the critical point of a substance. The sound velocity c is given by

$$c = \left[-\frac{v^2 C_P}{C_v} \left(\frac{\partial P}{\partial v} \right)_T \right]^{\frac{1}{2}}. \tag{16.2}$$

At the critical point, $(\partial P/\partial v)_T$ tends to zero and C_P and C_v diverge so that a minimum is observed in the speed of sound.

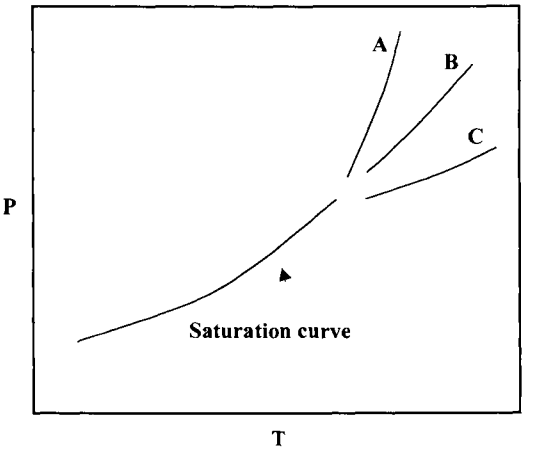

Figure 16.10 Plot of temperature against pressure at different loading densities (A–C) – method of Cailletet and Colardelau [50] for critical point determination.

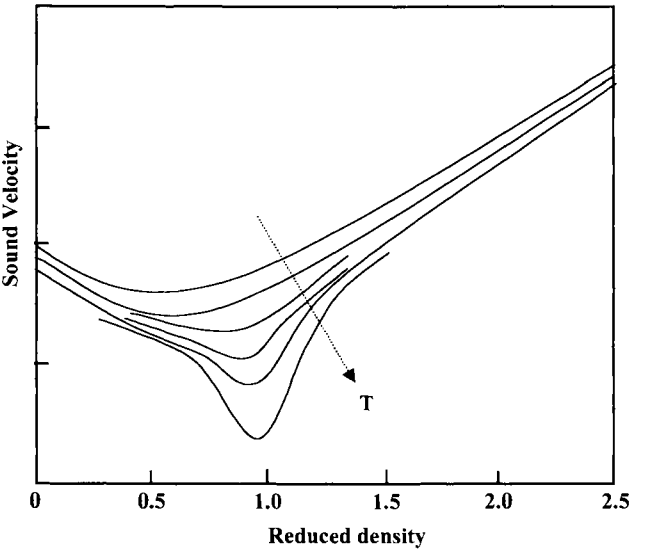

Figure 16.11 Plot of the speed of sound against reduced density [51].

Methods that utilise this behaviour have been described by Chase *et al.* [52], Schneider [53], Chynoweth and Schneider [54] and Kozhevnikov *et al.* [55]. However, direct measurements near the critical point were not possible in these approaches because of the large attenuation in the speed of sound. Colgate and co-workers [56,57] have described an acoustic resonance method that can be employed very close to the critical point. In their method, the substance under study was confined to a spherical cavity and stimulated by a piezoelectric transducer situated at the end of a circular channel opening into the cavity. Resonant modes of vibration were detected by an identical receiving transducer located at 90° to the transmitter. The cavity was charged to a set density. Then the resonant frequency, pressure and temperature of the constant volume system were measured. The resonant frequency against temperature curve shows an abrupt change at a phase boundary, and this change is sharpest at the critical temperature. Critical points of pure substances as well as mixtures were measured using this technique.

Laser interferometry can also be used to determine the coexistence curve as shown by Morofuji *et al.* [58]. A series of Fraunhofer diffraction patterns, arising from the density fluctuations near the critical point, were photographed by the use of a laser holographic technique. The data were then fitted to a simple power law in Equation (16.3) from which the critical temperature was obtained

$$\frac{\rho_L - \rho_v}{\rho_c} = B\left|\frac{T - T_c}{T_c}\right|^{\beta}. \tag{16.3}$$

This expression may also be used if densities of coexisting phases are obtained from NMR measurements [59] or refractive index data [60–62]. Near the critical temperature, the

NMR frequency difference between the vapour and the liquid phase is proportional to the density difference defined as the density of the liquid phase minus the density of the vapour phase. Similarly, the difference between the refractive index of the liquid and that of the vapour phase is asymptotically equivalent to the difference between the vapour and liquid densities. These data may therefore be used to estimate the critical temperature and density using the simple power law given by Equation (16.3).

16.2 Note on Experimental Errors

The isothermal compressibility and the isobaric expansion coefficient of a substance are known to diverge strongly near the critical point. As a result, very large fluctuations of the density can be obtained with small changes of temperature and pressure. This can lead to large experimental errors if the temperature and pressure are not controlled adequately. Temperature gradients in the sample therefore need to be minimised.

Another phenomenon that has been shown to have a significant effect on the shape of the coexistence curve in the critical region is gravity. The weight of the sample itself will cause density gradients because of the large compressibility [63]. Density measurements must therefore be obtained using small samples. More details of gravity effects are reported by Moldover *et al.* [64] and Chang *et al.* [65].

The rate of heating the substance can also influence the accurate determination of the critical point. If the sample is heated very rapidly, then thermocouple lag can lead to lower values of the critical temperature. However, for thermally unstable substances, rapid heating is essential to minimise the decomposition of the sample.

Finally, sample purity can influence the values of the critical properties obtained in these experiments. This is demonstrated by the work of Anselme and Teja [66] and of Gude and Teja [67] on dilute mixtures. A considerable increase in the critical parameters was observed by the introduction of very small amounts, mole fraction <0.01, of a compound with higher critical parameters.

16.3 Extrapolation Techniques

For stable substances, the critical point does not vary with time and therefore the critical temperature and pressure can be obtained by simply averaging several measurements obtained over a period of time. However, if the substance is thermally unstable, the critical temperature will decrease with the time that the substance is exposed to a high temperature, whereas the critical pressure will increase. The opposite behaviour is obtained for reactive substances, *e.g.* when oligomers form upon heating as discussed in reference [68]. Several extrapolation techniques have been developed to determine the 'true' critical properties of the substance.

The simplest technique extrapolates the data to the beginning of the experiment at $t = 0$. This technique was used by Ambrose [13] to determine the critical temperature of several organic compounds, and also by Mogollon *et al.* [15] to determine the critical temperature of n-alkanes. A polynomial fit was used in the extrapolation [60–62]. A linear extrapolation was employed by Rosenthal and Teja [26] because their data were obtained using

a low residence time flow apparatus, where the substance is only exposed to high temperatures for a short period of time.

Extrapolation of the critical property versus time trace to zero time can lead to high values of the critical temperature or low values of the critical pressure when the decomposition temperature is much higher than the temperature at the beginning of the experiment. Lyons [69] therefore proposed an extrapolation to the decomposition temperature of the substance. The latter was determined by exposing the substance to different temperatures and analysing the reaction products obtained.

Smith *et al.* [17] proposed a technique that incorporates reaction kinetics in the extrapolation. An irreversible first-order reaction was assumed to produce a straight line from the data, and the latter were extrapolated to the point where no reaction had occurred. The amount reacted was determined by analysing the sample by gas chromatography. The results compared with those obtained by Lyons [69] and showed a significant decrease of the critical temperature when compared with the technique used by Mogollon *et al.* [15]. A similar procedure was also employed by Nikitin [31].

The method proposed by Smith *et al.* [17] is not suitable for very rapidly decomposing substances, since the reaction rate increases rapidly with time. Teja and Smith [70] proposed another technique in which a low-boiling substance is added to the rapidly decomposing substance to reduce the decomposition rate. The critical parameters of the binary mixture can then be measured, and extrapolation along the critical locus of the binary mixture to the pure component leads to the critical parameters of the highly decomposing substance. The authors found that this extrapolation was accurate when the ratio of the critical temperatures of the two components was close to one.

If the kinetics of the reaction are not known, Anselme and Teja [20] proposed another extrapolation technique, which assumes that the critical locus of a multi-component mixture is linear with the amount of the impurity. This leads to a linear behaviour of the critical temperature–time curve. The critical temperature was assumed to lie between the first observed meniscus disappearance and the temperature resulting from the extrapolation to the time of zero decomposition. An average of the values was taken as the true critical temperature. A stability test was also developed to determine the time at which the substance was stable.

As mentioned previously, the experimental determination of the 'true' critical point of a thermally unstable substance is probably not possible. However, an estimate of the hypothetical critical state of the non-decomposed substance is provided by many of the methods described above. The values obtained are obviously not as certain as those for stable substances. Nevertheless, they provide input for many corresponding states calculations in practical applications.

References

1. Cagniard de la Tour, *Ann. Chim. Phys.* **2**, 127–132, 1822.
2. van der Waals, J.D., *On the Continuity of Gaseous and Liquid State*, Ph.D. Thesis, Leiden, Holland, 1873.
3. Kobe, K.A. and Lynn, R.E., *Chem. Rev.* **52**, 117–236, 1953.

4. Kudchadker, A.P., Alani, G.H. and Zwolinski, B.J., *Chem. Rev.* **68**, 659–735, 1968.
5. Mathews, J.F., *Chem. Rev.* **72**, 71–100, 1972.
6. Ambrose, D. and Young, C.L., *J. Chem. Eng. Data* **40**, 345–357, 1995.
7. Zeitfuchs, E.H., *Ind. Eng. Chem.* **18**, 79–82, 1926.
8. McKee, R.H. and Parker, H.H., *Ind. Eng. Chem.* **20**, 1169–1172, 1928.
9. McKee, R.H. and Szayna, A., *Ind. Eng. Chem.* **22**, 952–956, 1930.
10. Eaton, G.L. and Porter, C.A., *Ind. Eng. Chem.* **24**, 819–822, 1932.
11. Ambrose, D. and Grant, D.G., *Farad. Soc. Trans.* **53**, 771–778, 1957.
12. Ambrose, D., Cox, J.D. and Townsend, R., *Farad. Soc. Trans.* **56**, 1452–1459, 1960.
13. Ambrose, D., *Farad. Soc. Trans.* **59**, 1988–1993, 1963.
14. Ambrose, D., Broderick, B.E. and Townsend, R., *J. Appl. Chem. Biotechnol.* **24**, 359–372, 1974.
15. Mogollon, E., Kay, W.B. and Teja, A.S., *Ind. Eng. Chem. Fundam.* **21**, 173–175, 1982.
16. Smith, R.L., Anselme, M. and Teja, A.S., *Fluid Phase Equilibr.* **31**, 161–170, 1986.
17. Smith, R.L., Teja, A.S. and Kay, W.B., *AIChE J.* **33**, 232–238, 1987.
18. Teja, A.S., Gude, M. and Rosenthal, D.J., *Fluid Phase Equilibr.* **52**, 193–200, 1989.
19. Anselme, M.J., Gude, M. and Teja, A.S., *Fluid Phase Equilibr.* **57**, 317–326, 1990.
20. Anselme, M.J. and Teja, A.S., *Fluid Phase Equilibr.* **40**, 127–134, 1988.
21. Gude, M.T. and Teja, A.S., *AIChE Symp. Ser.* No. 298, **90**, 14–22, 1994.
22. Kennedy, H.T., *J. Am. Chem. Soc.* **51**, 1360–1366, 1929.
23. Ambrose, D., *Trans. Faraday Soc.* **52**, 772–781, 1956.
24. Tanikawa, S., Kabata, Y., Sato, H. and Watanabe, K., *J. Chem. Eng. Data* **35**, 381–385, 1990.
25. Roess, L.C., *J. Inst. Petrol. Tech.* **22**, 665–705, 1936.
26. Rosenthal, D.J. and Teja, A.S., *AIChE J.* **35**, 1829–1834, 1989.
27. Wilson, L.C., Wilding, W.V., Wilson, H.L. and Wilson, G.M., *J. Chem. Eng. Data* **40**, 765–768, 1995.
28. Spirin, G.G. and Cherezov, A.N., Translated from *Teplofizika Vysokikh Temperatur* **21**, 255–259, 1983.
29. Spirin, G.G. and Cherezov, A.N., Translated from *Teplofizika Vysokikh Temperatur* **19**, 368–372, 1981.
30. Nikitin, E.D., Pavlov, P.A. and Skripov, P.V., *J. Chem. Therm.* **25**, 869–880, 1993.
31. Nikitin, E.D., *High Temp.* **36**, 322–337, 1998.
32. Andrews, T., *Philos. Trans. R. Soc. London* **A159**, 575–590, 1869.
33. Cailletet, L.C., *R. Hebd. Seances Acad. Sci.* **68**, 395–398, 1869.
34. Bahlke, W.H. and Kay, W.B., *Ind. Eng. Chem.* **24**, 291–301, 1932.
35. Kay, W.B., *Ind. Eng. Chem.* **28**, 1014–1019, 1936.
36. Kay, W.B., *Ind. Eng. Chem.* **30**, 459–465, 1938.
37. Kay, W.B., *J. Am. Chem. Soc.* **69**, 1273–1277, 1947.
38. Barber, J.R., Kay, W.B. and Teja, A.S., *AIChE J.* **28**, 134–138, 1982.
39. Mandlekar, A.V. and Kay, W.B., *Fluid Phase Equilibr.* **23**, 79–88, 1985.
40. Hissong, D.W., Kay, W.B. and Rainwater, J.C., *J. Chem. Eng. Data* **38**, 486–493, 1993.
41. Ramsay, W. and Young, S., *J. Chem. Soc.* **47**, 640–657, 1885.
42. Altschul, M., *Z. Phys. Chem., Stoechem. Verwandtschaftsl* **11**, 577–597, 1893.
43. Ambrose, D. and Townsend, R., *J. Chem. Soc.* 3614–3625, 1963.
44. Ambrose, D., Broderick, B.E. and Townsend, R., *J. Chem. Soc. A, London* **4**, 633–641, 1967.
45. Dickinson, E. and McLure, I.A., *J. Chem. Soc. Farad. Trans. I* **70**, 2313–2320, 1974.
46. Keyes, F.G., *Proc. Am. Acad. Arts Sci.* **68**, 505–564, 1933.
47. Momoda, K., Uematsu, M. and Watanabe, K., *Ber. Bunsenges. Phys. Chem.* **88**, 1007–1010, 1984.

48. Thomas, W. and Zander, M., *Int. J. Thermophys.* **1**, 4, 1980.
49. Cailletet, L. and Mathias, E., *C.R. Acad. Sci.* **104**, 1563–1571, 1886.
50. Cailletet, L. and Colardeau, E., *Compt. Rend. Seances Acad. Sci.* **106**, 1489–1494, 1888.
51. Levelt Sengers, J.M.H., in *High Pressure Technology, Vol 2*, Ch. 5, I.L. Spain and J. Paauwe, eds., New York, p. 161, 1977.
52. Chase, C.E., Williamson, R.C. and Tisza, Ll., *Phys. Rev. Lett.* **13**, 467–469, 1964.
53. Schneider, W.G., *Can. J. Chem.* **29**, 243–252, 1951.
54. Chynoweth, A.G. and Schneider, W.G., *J. Chem. Phys.* **20**, 1777–1783, 1952.
55. Kozhevnikov, V., Arnold, D., Grodzinskii, E. and Naurzakov, A., *Fluid Phase Equilibr.* **125**, 149–157, 1996.
56. Colgate, S.O., Sivaraman, A., Dejsupa, C. and McGill, K.C., *Rev. Sci. Instrum.* **62**, 198–202, 1991.
57. Colgate, S.O., Sivaraman, A. and Dejsupa, C., *Fluid Phase Equilibr.* **76**, 175–185, 1992.
58. Morofuji, K., Fujii, K., Uematsu, M. and Watanabe, K., *Int. J. Thermophys.* **7**, 17–28, 1986.
59. Hayes, C.E. and Carr, H.Y., *Phys. Rev. Lett.* **39**, 1558–1561, 1977.
60. Chae, H.B., Schmidt, J.W. and Moldover, M.R., *J. Phys. Chem.* **94**, 8840–8845, 1990.
61. Defibaugh, D.R., Gillis, K.A., Moldover, M.R., Morrison, G. and Schmidt, J.W., *Fluid Phase Equilibr.* **81**, 285–305, 1992.
62. Schmidt, J.W. and Moldover, M.R., *J. Chem. Eng. Data* **39**, 39–44, 1994.
63. Weinberger, M.A. and Schneider, W.G., *Can. J. Chem.* **30**, 422–437, 1952.
64. Moldover, M.R., Sengers, J.V., Gammon, R.W. and Hocken, R.J., *Rev. Mod. Phys.* **51**, 79–99, 1979.
65. Chang, R.F., Levelt Sengers, J.M.H., Doiron, T. and Jones, J., *J. Chem. Phys.* **79**, 3058–3066, 1983.
66. Anselme, M.J. and Teja, A.S., *AIChE J.* **36**, 897–906, 1990.
67. Gude, M.T. and Teja, A.S., *Fluid Phase Equilibr.* **83**, 139–148, 1983.
68. Rosenthal, D.J., Gude, M.T., Teja, A.S. and Mendez-Santiago, J., *Fluid Phase Equilibr.* **135**, 89–95, 1997.
69. Lyons, R.L., *The Determination of Critical Properties and Vapor Pressures of Thermally Stable and Unstable Compounds*, Master's thesis, University of Pennsylvania, 1985.
70. Teja, A.S. and Smith, R.L., *AIChE J.* **33**, 1560–1562, 1987.

Subject Index

Chemical Substance Index